Apport de la géochimie isotopique du Nickel à l'étude des dépôts métallifères océaniques

Bleuenn Guéguen

THÈSE / UNIVERSITÉ DE BRETAGNE OCCIDENTALE
sous le sceau de l'Université européenne de Bretagne
pour obtenir le titre de
DOCTEUR DE L'UNIVERSITÉ DE BRETAGNE OCCIDENTALE
Mention : Géosciences Marines
École Doctorale des Sciences de la Mer

présentée par

Bleuenn Gueguen

Préparée au laboratoire Domaines Océaniques (UBO) et au laboratoire de Géochimie et métallogénie (Ifremer)

Apport de la géochimie isotopique du nickel à l'étude des dépôts métallifères océaniques

Thèse soutenue le 22 novembre 2013
devant le jury composé de :

Frédéric MOYNIER
Mr, IPGP / *Professeur*

Mark REHKAMPER
Mr, Imperial College of London / *Professeur*

Andrea KOSCHINSKY
Mme, Jacobs University Bremen / *Professeur*

Jean-Alix BARRAT
Mr, UBO / *Professeur*

Olivier ROUXEL
Mr, IFREMER / *Chercheur*

Yves FOUQUET
Mr, IFREMER / *Chercheur*

Apport de la géochimie isotopique du nickel à l'étude des dépôts métallifères océaniques

Contribution of nickel isotope geochemistry to the study of oceanic metalliferous deposits

« O mer, nul ne connaît tes richesses intimes »
Charles Baudelaire (« L'homme et la mer », Les fleurs du mal)

Remerciements :

Mes trois premières années en tant que jeune chercheuse s'achèvent. Mais l'aboutissement de ces trois années de recherche n'aurait pu se faire sans toutes les personnes qui ont, à quelque niveau que ce soit, participé à cette aventure et que je tiens à remercier ici.

Tout d'abord je tiens à remercier vivement mes deux directeurs de thèse Yves Fouquet et Olivier Rouxel pour m'avoir donnés l'opportunité de travailler sur ce sujet passionnant et prometteur et de m'avoir accordés leur confiance pour mener ce projet de thèse. Leur enthousiasme, leur souci de faire en sorte que la science soit toujours une discipline vivante et en mouvement, et leur curiosité furent et sont encore une grande source d'inspiration. Je les remercie également de m'avoir donnés l'occasion de participer à la campagne océanographique BIONOD 2012 dans l'océan Pacifique mais aussi à des congrès internationaux au cours de ces trois ans de thèse.

Je tiens à remercier Olivier Rouxel pour ses nombreux conseils et ses critiques constructives qui m'ont aidés à toujours donner le meilleur de mon travail, mais aussi et surtout pout son expertise et ses connaissances scientifiques qui ont grandement amélioré la qualité de mon travail et mes connaissances scientifiques. Je le remercie d'avoir eu la patience de me former au travail de préparation des échantillons en salle blanche et aux techniques analytiques de spectrométrie de masse. Merci de m'avoir permis d'avoir de multiples collaborations avec notamment Andrey Bekker, Brandy Toner et Jeffry Sorensen qui ont été des collaborations très enrichissantes.

Je remercie Dan Asael pour ses précieux conseils et sa convivialité lorsque nous avons partagé un bureau.

Je remercie tous les membres, chercheurs, techniciens, gestionnaires, ingénieurs, post-doc, et thésards du Laboratoire Domaines Océaniques pour leur soutien et leurs encouragements au cours de ces trois ans de thèse. Un grand merci notamment à tous les géochimistes. Claire, Céline, Philippe, Marie-Laure et Kévin, merci pour leur aide précieuse, leurs conseils et leur gentillesse. Merci à Arnaud, Stefan, Pierre et Gilles pour tous leurs conseils, encouragements mais aussi pour leur énorme joie de vivre qui ont bien animé les bureaux !

Je tiens à remercier à Priscilla, qui fut ma co-bureau pendant un an, pour son extrême gentillesse, sa joie de vivre, pour tous ses encouragements et surtout pour avoir apporté beaucoup de pétillant dans notre bureau. Je te souhaite courage et réussite pour la suite !

Bien que ma présence se soit faite plus discrète au Laboratoire de Géochimie et de métallogénie, je remercie les membres de ce laboratoire pour leur convivialité et leur aide pour les manips que j'ai eu à effectuer.

Un grand merci à Yoan et Manu pour leur bonne humeur, leur gentillesse, et surtout pour leur disponibilité lors des nombreux moments que j'ai passés en salle blanche et devant le spectro. Je remercie Philippe Saget pour son aide et son expertise sur les nodules et aussi pour sa convivialité !

Je remercie Nima et Nolwenn pour leur gentillesse, leur accessibilité et pour toutes les discussions que nous avons pu avoir en salle blanche et qui ont animé nos manips. Merci Nolwenn pour tes précieux encouragements.

Je remercie les membres de l'équipe scientifique française et allemande ainsi que l'équipage qui ont participé à la campagne océanographique BIONOD 2012 sur l'Atalante pour échantillonner les nodules sur le permis minier français dans la zone Clarion/Clipperton, et durant laquelle nous avons fait 42 jours de mer de Manzanillo au Mexique à Suva aux Fidji.

Merci à Lénaïck Menot, chef de mission, d'avoir accepté que je participe à cette campagne qui fut la première pour moi, pour le bon déroulement de la campagne et de son organisation, mais aussi pour tous les agréables moments passés à bord et qui rendirent cette première expérience inoubliable. Je remercie Alexis Khripounoff, Patrick Briand, Joëlle Galéron, Richard Cosson pour leur gentillesse et tous les bons moments passés ensemble à bord de l'Atalante.

Je remercie très chaleureusement ma colocataire de cabine Laure Perret-Gentil pour sa gentillesse et pour m'avoir permis de passer une très agréable campagne en mer. Merci aussi pour le chocolat suisse ! Je n'oublierai pas notre baptême de ligne lorsque nous avons traversé l'Equateur ! Je remercie l'équipage de la campagne pour leur aide, leur disponibilité et pour avoir fait en sorte que la campagne se déroule bien. Merci également pour leur très bonne organisation de la journée du baptême de ligne !

Je remercie Vesselin Dekov, pour d'une part tout l'aide qu'il m'a fournie lors de la campagne en mer, mais aussi pour sa gentillesse, son amitié et tout le soutien qu'il m'a apporté au cours de ces trois années de thèse.

Merci à Jean-Claude Caprais d'avoir répondu à mes questions concernant les techniques d'extraction des eaux interstitielles qui m'ont été nécessaires pour ma campagne en mer, et à Dominique Birot pour m'avoir prêté la borne d'eau mQ que j'ai pu embarquer sur l'Atalante.

Je remercie Franck Poitrasson, Christophe Cloquet et Jean-Alix Barrat d'avoir accepté de faire partie de mon comité de thèse. Les discussions que nous avons eues lors de la réunion de ce comité m'ont beaucoup aidées dans la réflexion que j'ai pu ensuite mener sur l'ensemble de mes résultats.

Je remercie Frédéric Moynier, Mark Rehkamper, Andrea Koschinsky et Jean-Alix Barrat pour avoir accepté de faire partie de mon jury de thèse.

Enfin, je remercie vivement ma famille : Klervie, Thomas (et le petit Loulou), Enora, mes grands-parents et mes parents. Je ne les remercierai jamais assez pour leurs nombreux encouragements et leur soutien incommensurable. Merci de m'avoir redonné confiance dans tous les moments où j'ai douté, d'avoir toujours cru en moi et de m'avoir donné la sérénité qui me fait parfois défaut. Vous êtes une source d'inspiration quotidienne dont je ne saurais me passer.

Je remercie toutes les personnes qui ont été présentes durant ces années et toutes celles que j'aurais malencontreusement pu oublier de mentionner ici.

Résumé:

Les explorations scientifiques menées depuis une quarantaine d'années ont permis d'identifier la diversité et la complexité des processus géologiques et géochimiques conduisant à la concentration des métaux dans les grands fonds océaniques. Les dépôts métallifères riches en hydroxydes de Fer et de Manganèse, tels que les encroûtements hydrogénétiques et hydrothermaux et les nodules polymétalliques, présentent des enrichissements variés en éléments d'intérêts économiques tels que le Ni, Cu, Co, Te, Pt et les Terres Rares. Bien que la minéralogie et la géochimie de ces dépôts aient été largement étudiées dans la littérature, les sources de métaux restent encore mal déterminées. Par conséquent, comprendre la géochimie de ces dépôts implique d'une part, de connaître les processus participant à leur genèse, et d'autre part d'avoir de meilleures connaissances sur les sources impliquées (par ex. flux continental et hydrothermal) et leur importance dans les grands cycles biogéochimiques des métaux dans les océans.

Afin d'apporter de nouveaux éléments de réponse, notre approche a consisté à utiliser les compositions isotopiques des métaux comme traceurs biogéochimiques. Ce projet est structuré autour de deux hypothèses, (1) le développement et l'utilisation d'un nouveau outil géochimique que sont les isotopes du Ni pour tracer les sources et les processus d'enrichissements en métaux dans les dépôts métallifères océaniques ; (2) la combinaison de plusieurs systèmes isotopiques tels que Fe, Pb, Cu et Zn (et Ni) dans les encroûtements de fer-manganèse comme proxy de la composition isotopique de l'eau de mer profonde.

Après avoir développé une méthode d'analyse des isotopes du Ni par MC-ICP-MS et estimé la variabilité isotopique du Ni dans les systèmes naturels par la caractérisation des grands réservoirs terrestres, nous avons évalué expérimentalement le fractionnement isotopique du Ni lors de son adsorption sur les oxyhydroxydes de Fe et Mn comme analogue à ce qui pourrait se produire dans les dépôts de Fe-Mn naturels. Les résultats indiquent que lors de l'adsorption du Ni, la phase solide est enrichie en isotopes légers par rapport à la solution avec des facteurs de fractionnement ($\Delta^{60/58}Ni_{min/sol}$) variant de -1 ‰ pour la birnessite, -0.9 ‰ pour la goethite et -0.4 ‰ pour la ferrihydrite.

A partir de ces résultats et d'autres études récentes, nous avons pu appuyer l'hypothèse selon laquelle d'un point de vue global la variabilité isotopique du Ni dans les dépôts métallifères océaniques riches en Fe et Mn s'explique par des processus d'enrichissement et de formation lors de l'incorporation des métaux dans les phases minérales de Fe et Mn plutôt que par des variations des compositions isotopiques des sources. Ainsi les encroûtements hydrogénétiques formés lentement à partir de l'eau de mer ne montrent pas de fractionnement isotopique du Ni, tandis que les dépôts hydrothermaux formés par des processus rapides liés aux apports hydrothermaux montrent des fractionnements du Ni plus importants.

Puis, afin d'évaluer la possibilité d'utiliser les signatures isotopiques du Ni comme nouveaux traceurs paléocéanographiques, nous avons mené une étude comparative sur des encroûtements collectés dans le Pacifique Nord (proche de Hawaii) et le Pacifique Sud (proche de Tahiti). Dans ce contexte, les encroûtements de fer-manganèse formés par précipitation très lente de l'ordre de quelques mm/Ma entre 1500 et 3000 m de profondeur, fournissent un enregistrement de plusieurs millions d'années des métaux dissous dans l'eau de mer. Après avoir réalisé une étude minéralogique et géochimique (éléments majeurs et traces) et calibré les taux de croissance des encroûtements, nous avons mesuré pour la première fois les compositions isotopiques du Ni, Fe, Zn, Cu et Pb sur la même série temporelle.

Dans les encroûtements du Nord Pacifique (Apuupuu), les résultats des isotopes du Fe et du Pb montrent une corrélation entre ces deux systèmes isotopiques indiquant probablement des mélanges de masses d'eau. Les compositions isotopiques en Fe négatives (< -0.7 ‰) pourraient être dues à un apport hydrothermal local issu par exemple de l'activité magmatique du point chaud de Hawaii et ayant affecté les masses d'eau. En revanche, les isotopes du Ni dans ces mêmes séries temporelles indiquent que la composition isotopique du Ni de l'eau de mer est restée constante au cours des 15 derniers millions d'années, mais que des fractionnements isotopiques important (~1.5 ‰) peuvent se produire lors de processus d'altération après dépôt. Ces résultats apportent donc de nouveaux éléments d'interprétation des isotopes du Fe et Ni dans ce type de dépôt.

Enfin, nous avons démontré pour la première fois une corrélation unique entre les isotopes du Cu et Zn dans les encroûtements mondiaux qui semble avoir pour origine des signatures isotopiques des masses d'eau différentes qui ont évoluée au cours des derniers 6 Ma. Grâce à une approche intégrée et multi-isotopique, cette étude ouvre donc de nouvelles perspectives en termes de processus de genèse des dépôts métallifères océaniques et de paléocéanographie.

Abstract:

Scientific explorations implemented for around forty years allow to identifying the diversity and the complexity of geological and geochemical processes conducting to metals concentration on the deep seafloor. Fe- and Mn-rich metalliferous deposits such as hydrogenetic and hydrothermal ferromanganese (Fe-Mn) crusts and polymetallic nodules, present various enrichment in elements of economic interests like Ni, Cu, Co, Te, Pt and Rare Earth Elements. Although the mineralogy and geochemistry of these deposits have been largely studied in the literature, metal sources remain poorly determined. Accordingly, understanding the geochemistry of these deposits implies to know which processes are involved in their formation but also to have a better knowledge of the sources (e.g. the continental and hydrothermal fluxes) and their importance in the global oceanic metal biogeochemical cycles.

In order to fill this gap, our approach consisted in using metal stable isotope compositions as biogeochemical tracers. This project is organized around two hypotheses, (1) development and utilization of a new geochemical tool, namely Ni isotopes, for tracing metal enrichment sources and processes in oceanic metalliferous deposits; (2) combination of several isotope systematics such as Fe, Pb, Cu, Zn (and Ni) in Fe-Mn crusts as proxies of the deep seawater isotope composition.

Upon developing an analytical method for measuring Ni isotopes by MC-ICP-MS and estimating the Ni isotopes variability in natural systems through the characterization of terrestrial reservoirs, we experimentally evaluated Ni isotope fractionation during adsorption on Fe- and Mn-oxyhydroxides since similar processes may potentially occur in natural Fe-Mn deposits. Results indicate that after Ni adsorption, the solid phase is enriched in light Ni isotopes relatively to the solution with fractionation factors ($\Delta^{60/58}Ni_{min/sol}$) varying from -1 ‰ for birnessite, -0.9 ‰ for goethite and -0.4 ‰ for ferrihydrite.

These results, and other recent studies, strengthen our hypothesis according to which Ni isotopes variability in Fe- and Mn-rich metalliferous deposits can be explained by enrichment and formation processes during metal incorporation in Fe and Mn mineral phases rather than variations in the isotopic composition of the sources. Thus, hydrogenetic Fe-Mn crusts formed slowly from seawater dissolved metals do not show significant Ni isotope fractionation, whereas hydrothermal deposits formed by relatively rapid processes as a result of hydrothermal inputs exhibit important Ni isotope fractionation.

Then, in order to evaluate the possibility of using Ni isotope signatures as new paleoceanographic tracers, we have led a comparative study on Fe-Mn crusts collected in the North Pacific (Hawaii area) and in the South Pacific (Tahiti area). In this framework, Fe-Mn crusts formed by slow precipitation in the order of mm/Ma between 1500 and 3000 meters water depth provide a record of more several million years of seawater dissolved metals. Upon implementing a mineralogical and geochemical study (major and trace elements) and calibrating Fe-Mn crusts growth rates, we have measured for the first time Ni, Fe, Cu, Zn and Pb isotope compositions on the same time-series.

In North Pacific Fe-Mn crusts (Apuupuu), Fe and Pb isotopes results show a correlation between these two isotope systematics and probably indicate mixing between water masses. Negative Fe isotope compositions (<-0.7 ‰) could be due to local hydrothermal inputs from the Hawaii hotspot activity in seawater. On the other hand, Ni isotopes in these same time-series indicate that Ni isotope composition of deep seawater remains stable over the last 15 million years, but that important isotope fractionation (~1.5 ‰) may occur during post-depositional alteration processes. These results provide new

evidence to the interpretation of Ni and Fe isotopes variability in metalliferous deposits. Finally, we have demonstrated for the first time a unique correlation between Cu and Zn isotope compositions in Fe-Mn crusts that seems to demonstrate that isotopic signatures of different water masses have evolved over the last 6 Ma.

This integrated multi-isotopes approach paves the way to new perspectives for the characterization of oceanic metalliferous deposits genesis and paleoceanographic processes in oceans.

Table des matières

Liste des figures

Liste des tableaux

Introduction générale : Contexte de l'étude et concepts généraux sur la systématique des isotopes stables du nickel dans les environnements océaniques

1. Les dépôts métallifères océaniques : découverte et historique

Les premiers dépôts métallifères océaniques furent découverts lors de la campagne océanographique du navire britannique *H.M.S (His/Her Majesty's Ship) Challenger* qui parcouru les mers du globe durant plus de trois ans de Décembre 1872 à Mai 1876 pour y échantillonner à la fois sur les fonds marins, mais également sur les nombreuses îles visitées par le navire, la faune, la flore, les eaux de mer des différents océans à différentes profondeurs, des échantillons géologiques (Figure I.1). Les scientifiques réalisèrent également des mesures de température et d'autres paramètres physico-chimiques tels que la température et la salinité (Murray and Renard 1891). Bien que Blaise Pascal ait dit dans son ouvrage *Pensées* que « curiosité n'est que vanité le plus souvent », d'un autre côté Victor Hugo relevait justement que « ne voir dans la mer qu'une masse d'eau, c'est ne pas voir la mer ». Et en effet, il faut admettre que la richesse des échantillons récoltés, des découvertes réalisées et des descriptions naturalistes reportées à la suite de la campagne océanographique du *H.M.S Challenger* ont marqué le début de la conquête scientifique des océans et ouvert le champ à des découvertes majeures qui se poursuivent encore maintenant. Il faut rappeler qu'à cette époque les océans sont encore des zones bien mystérieuses alors qu'ils recouvrent près de 70 % de la surface de notre Terre. Durant cette expédition les premiers sédiments très riches en manganèse et en fer furent collectés lors de dragages sur les fonds océaniques de tous les océans. Ils furent dénommés nodules de manganèse, bien que des encroûtements de fer-manganèse étaient aussi présents dans leur échantillonnage. Ils furent méticuleusement décrits et les scientifiques mentionnèrent l'abondance de ces dépôts sur le plancher océanique.

***Figure I.1** : Dessins d'observation de nodules polymétalliques et d'encroûtements de fer-manganèse collectés lors de l'expédition océanographique du navire H.M.S Challenger de Décembre 1872 à Mai 1876 extraits du rapport scientifique de l'expédition (Murray and Renard, 1891).*

Ces dépôts métallifères formées d'hydroxydes de manganèse et de fer renferment des enrichissements variables mais parfois importants en autres métaux de transition comme le Ni, le Cu et les Terres Rares (surtout en Terres Rares lourdes) pour les nodules métalliques, le Co et les éléments du groupe des platinoïdes pour les encroûtements, par rapport aux réserves exploitées actuellement sur les continents (Hein et al. 2013). De plus, en raison de l'accroissement continu de la demande en métaux stratégiques, certains de ces dépôts sédimentaires très enrichis en métaux ont un intérêt économique non négligeable en tant que ressources minières potentiellement exploitables.

A partir des années 1950 l'émergence de nouveaux pays industrialisés, l'industrialisation toujours croissante des pays et le développement des nouvelles technologies ont provoqué un besoin croissant pour l'apport en métaux de transition. Dans un contexte géopolitique en pleine tension durant la guerre froide, et dans un souci d'indépendance, les états ne cessent de vouloir protéger leurs ressources ou d'en acquérir de nouvelles. De ce fait les océans qui recouvrent 70% de la surface terrestre contenant de potentielles ressources minières apparaissent comme des lieux privilégiés d'exploration. Mais bien qu'en 1959 John Mero préconise déjà d'exploiter les nodules polymétalliques pour leur richesse en métaux, ce n'est que plus tard dans les années 1970 que ces dépôts ont réellement connu un regain d'intérêt important car de nombreuses compagnies minières ont commencé à s'intéresser à ces dépôts métallifères. Afin de mieux gérer l'accès des pays à cette ressource potentielle qui se situe dans les eaux internationales, les Nations Unies ont mis en place un cadre juridique pilotée par l'ISA (International Seabed Authority ou Autorité Internationale des Fonds Marins pour la traduction française). Elle fut notamment chargée d'attribuer des zones de permis miniers dans la zone Clarion/Clipperton de l'océan Pacifique équatorial aux pays demandeurs, ce qui leur permit de procéder à l'exploration de leur zone en vue d'établir la faisabilité d'une exploitation future. Il a donc fallu estimer la ressource disponible et prendre en compte les phénomènes d'impact environnemental lors des phases d'exploration. En France, l'Ifremer (anciennement CNEXO) fut chargé de mener ces travaux. Ainsi, de nombreuses campagnes océanographiques furent réalisées dans les champs de nodules du Pacifique équatorial (par exemple les nombreuses campagnes NIXO).

Parallèlement, à la fin des années 1970 l'Ifremer fut partie des pionniers dans l'exploration des océans avec notamment la mise en place du programme *FAMOUS* en 1974 (French-American Mid-Ocean Undersea Study), une collaboration entre équipes française et américaine qui a permis la découverte de fumeurs noirs sur la dorsale médio-atlantique grâce au sous-marin américain *Alvin* (Corliss et al. 1979; Francheteau et al. 1979; Spiess et al. 1980; Edmond 1981). Plus tard en 1984, la mise à l'eau du sous-marin français *Nautile* permis aux équipes françaises de poursuivre l'exploration des fonds marins par la découverte et l'échantillonnage de plusieurs champs hydrothermaux formés le long des 60000 km de montagnes océaniques qui jalonnent les fonds marins. Ces campagnes furent réalisées dans tous les océans du globe procédant ainsi à la constitution d'une collection très remarquable et conséquente d'échantillons hydrothermaux et d'autres minéralisations affleurant sur le plancher océanique. Les sulfures hydrothermaux présentent des enrichissements conséquents en métaux de base, et se présentent à la fois sous forme de cheminées hydrothermales actives et de monts hydrothermaux. Les dépôts de sulfures massifs, analogue actuels des VMS (Volcanogenic Massive Sulfides) exploités à terre, correspondant à des dépôts inactifs pouvant constituer d'importantes réserves en métaux (Hannington et al. 2011).

Depuis les années 1980 de nombreuses campagnes océanographiques de l'IFREMER ont été menées dans le but de caractériser les fonds marins et la ZEE (Zone Economique Exclusive) française. En particulier, des échantillons d'encroûtements riches cobalt et platine ont été décrit sur de nombreux monts sous-marins situés dans le Sud du Pacifique (notamment dans l'archipel des îles de la Société, Polynésie Française). L'étude de la composition chimique et de l'étendue spatiale de ces dépôts n'est encore que préliminaire, ne permettant pas encore une estimation des ressources en métaux. Outre les fortes teneurs en Fe et en Mn, des enrichissements significatifs en certains métaux (Co, Te, Bi, Pb,…) par rapport aux gisements exploités à terre sont observés (Hein et al. 2013).

Bien que la littérature s'attachant à comprendre les mécanismes de formation de ces dépôts riches en Fe et en Mn abonde, l'origine des métaux ainsi que les mécanismes d'enrichissement liés aux processus géochimiques et biologiques de ces dépôts ne sont pas encore complètement résolus. En réalité, bien que ces dépôts puissent être classés en différentes catégories (par ex. hydrothermal, hydrogénetique et diagénétique), il existe bien souvent une continuité entre ces catégories à la fois spatiale et temporelle. C'est dans la perspective de combler ces lacunes que s'inscrivent les objectifs de cette étude. Il s'agit de trouver de nouveaux outils géochimiques ou de nouvelles approches, adaptés à la fois à la compréhension des processus de métallogenèse de ces dépôts et des sources des métaux, mais également à la compréhension des processus océanographiques et de l'évolution des cycles biogéochimiques des métaux dans les océans pouvant intervenir dans la genèse de ces dépôts. Par conséquent, nos interrogations vont bien au-delà de la notion de ressources minérales et concernent d'une manière générale les processus contrôlant le cycle biogéochimique des métaux – en particulier le Ni - dans les environnements marins actuels et anciens.

2. Définition et terminologie des dépôts métallifères océaniques

Les métaux de transition sont généralement présents à l'état de traces dans les roches affleurant à la surface de la Terre, or ils sont particulièrement enrichis dans les dépôts métallifères océaniques (Bonatti and Joensuu 1966; Burnett and Piper 1977; Li and Schoonmaker 2003; Schulz and Zabel 2006; Hein et al. 2013). Quatre principaux types de dépôts métallifères océaniques peuvent être distingués : les nodules polymétalliques (ou nodules de manganèse), les encroûtements cobaltifères, les sulfures hydrothermaux et les boues métallifères.

- *Les nodules polymétalliques (ou nodules de manganèse) :*

Il s'agit de concrétions d'hydroxydes de fer et de manganèse ayant précipités en couches concentriques autour d'un nucleus généralement constitué d'un débris animal (coquille, dent de requin, etc) ou d'un débris rocheux de diamètre de 3 à 10 centimètres (cf. Figure I.2). Ils sont notamment enrichis en Cu, Ni, Tl, Te, Mo et Terres Rares par rapport à la croûte continentale moyenne (Nicholson et al. 1997; Cronan 2000; Maynard 2003; Verlaan et al. 2004; Schulz and Zabel 2006). Les sources d'enrichissement en métaux dans les nodules de manganèse sont variés, (1) métaux dissous dans l'eau de mer, (2) altération des sédiments argileux et des roches volcaniques du plancher océanique, et (3) métaux contenus dans les eaux interstitielles et le sédiment sous-jacent. Par ailleurs, les processus produisant ces enrichissements sont également multiples, (i) précipitation des colloïdes d'oxydes de Fe et

de Mn formé dans la colonne d'eau de mer, (ii) réactions chimiques de précipitation des oxydes de Fe et de Mn dans le sédiment, et (iii) bio-minéralisations produites par l'activité biologique (Wang and Muller 2009; Wang et al. 2009). Le sédiment et les eaux interstitielles ont probablement un rôle prédominant dans la genèse des nodules car ils agissent comme un réservoir où les métaux libérés lors de la dégradation des organismes biologiques (Froelich et al. 1979; Klinkhammer 1980; Klinkhammer et al. 1982) sont accumulés puis recyclés pour ensuite nourrir la croissance des nodules.

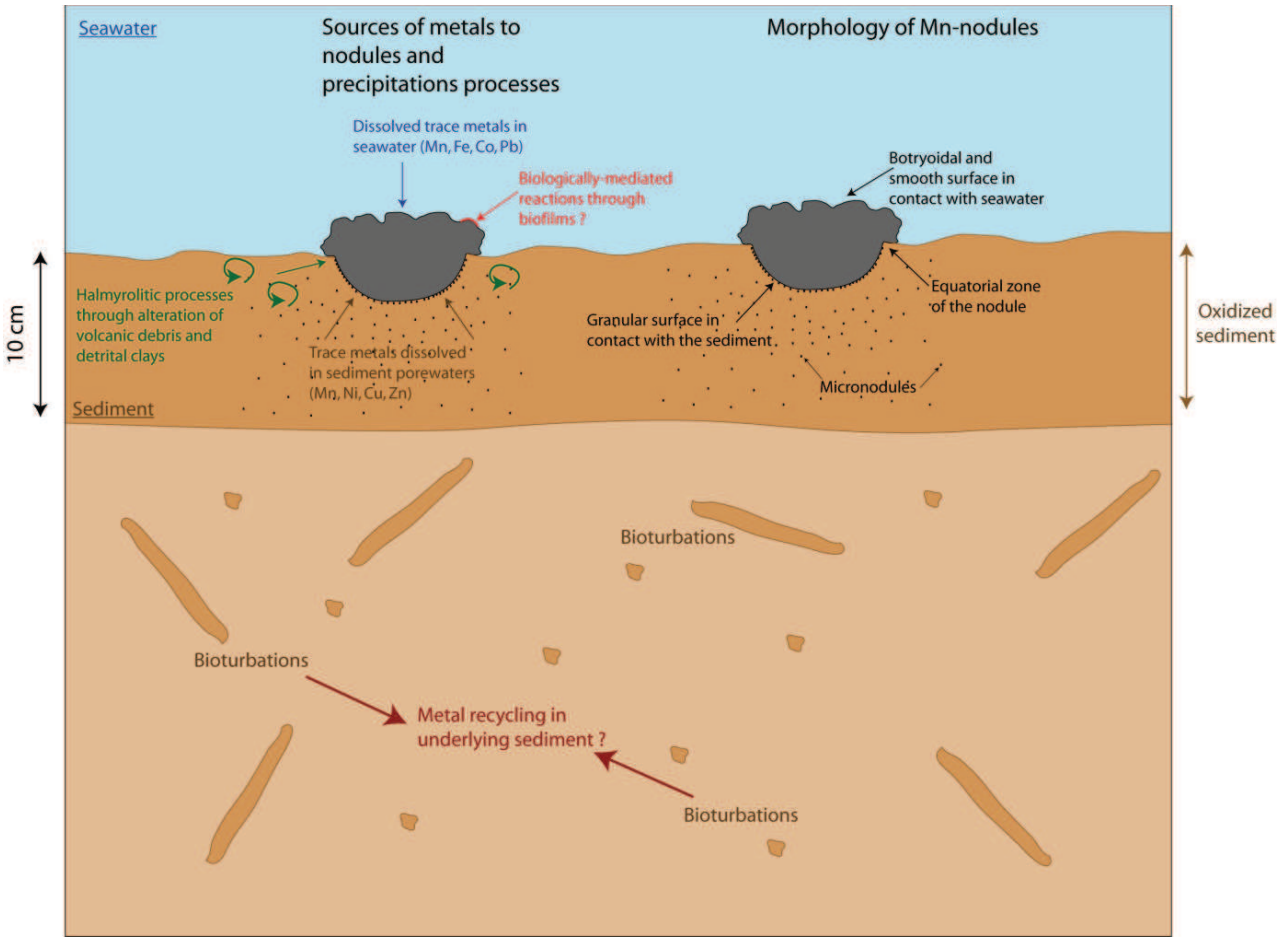

***Figure I.2** : Coupe schématique à travers les premiers centimètres de sédiments sur lesquels sont déposés les nodules polymétalliques montrant les différents facteurs biogéochimiques impliqués dans la croissance des nodules.*

Toutefois, bien qu'une documentation importante soit disponible sur la caractérisation minéralogique et géochimique de ces objets, il reste encore de nombreuses inconnues quant à la formation de ces dépôts et les paramètres contrôlant les facteurs d'enrichissements en certains métaux, et en particulier le rôle quantitatif et la contribution de chacune des sources de métaux évoquées ci-dessous.

- *Les encroûtements cobaltifères ou hydrogénétiques :*

Ces dépôts, composés d'un assemblage de phases minérales d'hydroxydes de fer et de manganèse, se sont formés par précipitation sur un substrat rocheux ou sédimentaire. On les trouve généralement sur le flanc des monts sous-marins où la sédimentation pélagique est très faible en raison de la mise en place de courants océaniques circulant de la base vers

le sommet du volcan cf. Figure III.1 et Figure III.2 du chapitre III). Ils sont présents dans tous les océans du globe. Leur taux de précipitation sont très lents, de l'ordre de 1 à 6 mm/Ma, et certains encroûtements ont des âges allant jusqu'à plus de 60 Ma (Bonatti and Joensuu 1966; Pratt and McFarlin 1966; Bonatti et al. 1972c; Burnett and Piper 1977; Halbach et al. 1983; Manheim 1986; Manheim and Lanebostwick 1988). Ces dépôts constituent donc en quelque sorte une archive géologique de l'évolution du cycle des métaux traces dans l'eau de mer au cours du Cénozoïque.

Contrairement aux nodules de manganèse dont l'origine des métaux est multiple et complexe, les encroûtements sont directement formés par précipitation des colloïdes d'oxydes de fer et de manganèse formés dans la colonne d'eau de mer à partir des métaux traces dissous. L'absence de sédimentation importante de particules détritiques et carbonatés associée à un très faible taux de déposition permet d'obtenir des enrichissements très importants en métaux traces tels que Ni et Cu même si les enrichissements sont moins importants que dans les nodules polymétalliques, Co, Te, Bi, Mo, Pb, Cd, les éléments du groupe du platine (Rh, Ru, Os, Pd) mais surtout le platine lui-même qui peut atteindre des concentrations de 3 ppm, et les Terres Rares (Halbach et al. 1983; Halbach et al. 1984; Hein et al. 1988; Halbach et al. 1989; ISA 2002; Hein et al. 2003; Hein et al. 2010; Hein et al. 2013). Ainsi les encroûtements figurent parmi les ressources minérales les plus riches en Co sur Terre, d'où le fait qu'on les désigne aussi souvent sous le terme « d'encroûtements cobaltifères » (Pichocki and Hoffert 1987; Hein et al. 1988; Lesuave et al. 1989; Nicholson et al. 1997; Koschinsky and Hein 2003; Hein et al. 2013). Une synthèse plus étoffée de l'état actuel des connaissances sur les modes de formation des encroûtements de fer-manganèse est fournie dans l'introduction du chapitre III de ce manuscrit.

- *Les sulfures hydrothermaux et les dépôts hydrothermaux riches en Fe et en Mn*

Les sulfures hydrothermaux se déposent dans des contextes géodynamiques où l'activité volcanique et magmatique est importante tels que les rides médio-océaniques, les bassins d'arrière-arcs, les volcans intraplaques (Mills and Elderfield 1995; Seyfried and Ding 1995; Von Damm 1995; Fouquet 1997), et ces minéralisations sont le résultat de la circulation hydrothermale. L'activité tectonique associée aux dorsales océaniques lors de l'écartement des plaques lithosphériques et de la formation d'une nouvelle croûte océanique implique la présence d'un réseau de failles important. Lorsque l'eau de mer s'infiltre dans ces fractures et pénètre en profondeur, elle se réchauffe au contact de la source de chaleur générée par la remontée de magma asthénosphérique. A la suite de diverses réactions chimiques se produisant lors des interactions eaux-roches la partie supérieure de la croûte océanique, - généralement des basaltes mais aussi les zones où affleurent des roches ultrabasiques (e.g. les dorsales lentes) - et impliquant des changements de conditions de pression et température, cette eau de mer va peu à peu devenir un fluide hydrothermal riche en métaux. Ce fluide chaud va ensuite remonter vers l'interface eau de mer/plancher océanique pour finalement retourner dans l'eau de mer et former ces impressionnantes cheminées hydrothermales. Ces structures sont en partie composées de sulfures qui ont précipités lors du contact entre le fluide hydrothermal chaud et riche en métaux et en soufre avec l'eau de mer relativement froide, oxydante et surtout pauvre en métaux (Corliss et al. 1979; Edmond et al. 1979; Francheteau et al. 1979; Hekinian et al. 1980; Edmond 1981; Hekinian et al. 1983; Humphris et al. 1995; German and Von Damm 2003; Tivey 2007).

Néanmoins outre ces sulfures hydrothermaux formés à proximité de l'axe d'accrétion des dorsales océaniques, la circulation hydrothermale génère également d'importantes quantités

de dépôts d'oxydes de fer et de manganèse (De Carlo et al. 1983; Rona 1984; Fouquet et al. 1991; Hein et al. 1994; Mills and Elderfield 1995; Mills et al. 2001). Ces dépôts se localisent généralement en périphérie des sites hydrothermaux de haute température, et se forment à partir de fluides hydrothermaux de plus basse température issus d'un mélange en sub-surface entre le fluide chaud et l'eau de mer (Wheat and Mottl 2000; Wheat et al. 2002). De facto, la géochimie des dépôts hydrothermaux riches en Fe et en Mn sera très différente des dépôts métallifères profonds tels que les nodules polymétalliques ou les encroûtements hydrogénétiques.

- *Les sédiments pélagiques profonds riches en métaux et les boues métallifères de la Mer Rouge*

Certaines argiles des fonds océaniques sont riches en métaux, notamment les argiles rouges déposées dans les plaines abyssales du Pacifique Sud. Les taux de sédimentation dans ces environnements sont très faibles car dépourvus d'une sédimentation carbonatée (sous la CCD, Calcite-Compensation-Depth) et l' apport en sédiments terrigènes est faible, le tout empêchant la dilution des métaux traces enrichis dans les phases authigéniques (généralement un assemblage d'oxyhydroxydes de fer et de manganèse) par une forte sédimentation carbonatée et détritique (Boström and Peterson 1966; Boström et al. 1969; Li and Schoonmaker 2003; Schulz and Zabel 2006). Par conséquent, ces sédiments profonds sont enrichis en métaux par rapport aux autres sédiments marins tels que ceux déposés près des rides médio-océaniques (sédimentation carbonatée importante) ou près des marges continentales (sédimentation détritique importante). La bonne corrélation entre l'enrichissement en REE et l'extension de l'anomalie positive en $^{3}He/^{4}He$ mesurée dans la colonne d'eau démontrant la dispersion des flux hydrothermaux émis par la dorsale Est Pacifique, indique que ces apports hydrothermaux fournissent les particules d'oxydes de fer et de manganèse sur lesquelles peuvent s'adsorber les Terres Rares qui sont ensuite déposées dans les sédiments profonds (Boström and Peterson 1966; Bonatti et al. 1972c; Kato et al. 2011). De la même manière, les sédiments pélagiques de l'Océan Pacifique montrent des enrichissements en Cu par rapport à la moyenne de la croûte continentale et qui pourraient être dû aux apports de métaux par les fluides hydrothermaux de la dorsale Est-Pacifique (Figure I.3 (Hannington 2013).

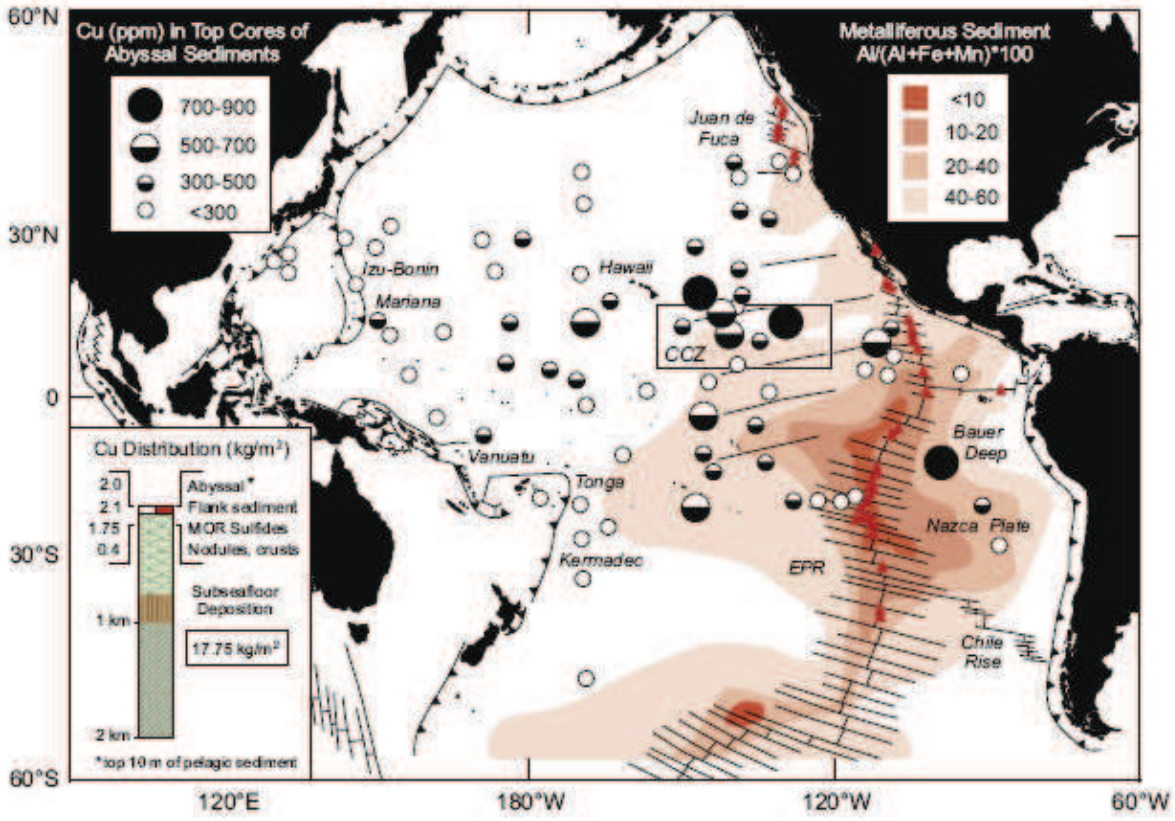

Figure I.3 : *Concentrations en Cu (ppm) des sediments pélagiques de l'Océan Pacifique (partie supérieure des carottes sédimentaires. La zone influencée par les apports hydrothermaux de la dorsale Est-Pacifique sont représentés par le rapport Al/(Al+Fe+Mn) x 100. La figure est extraite de Hannington (2013).*

Un autre type de sédiments riches en métaux de transition comprend les sédiments métallifères déposés en Mer Rouge. La fosse Atlantis II de la Mer Rouge est un bassin anoxique (pauvre en oxygène) présentant de fortes concentrations en Fe mais qui ne contient pas d'hydrogène sulfuré qui aurait, dans le cas contraire, titré le Fe dissous pour précipiter dans des sulfures. Les eaux de ce bassin sont riches en métaux dissous et résultent de l'accumulation de fluides hydrothermaux formant des saumures à la suite du contact de l'eau de mer avec les sédiments évaporitiques présent de la pile sédimentaire recouvrant le plancher océanique (Anschutz and Blanc 1995; Anschutz et al. 1995). Bien que des niveaux à argiles néoformées (nontronite) et hydroxydes de Fe et Mn (goethite, hématite, manganite, todorokite) soient observés, une grande partie des dépôts est composée de sulfures (sphalérite, pyrite, chalcopyrite).

Enfin, malgré un niveau d'enrichissement en métaux moindre en comparaison aux dépôts présentés ci-dessus et le fait qu'ils ne fassent pas partie des dépôts métallifères proprement dit, les sédiments riches en matière organique peuvent avoir des concentrations en métaux de transition importantes, notamment ceux déposés près des marges continentales résultant de la présence de courants d' « upwelling », (Brumsack 1980; Brumsack 2006).

3. Les enjeux scientifiques: genèse des dépôts métallifères océaniques riches en Fe et Mn et cycle biogéochimique des métaux dans les océans modernes

L'étude des sources et des processus d'enrichissement en métaux dans les dépôts métallifères marins riches en Fe et Mn offre deux niveaux de compréhension. Il faut d'une part comprendre les processus biogéochimiques se produisant dans l'eau de mer influant sur le cycle global des métaux dans les océans et qui, d'une manière ou d'une autre, affectent la géochimie des dépôts métallifères marins. Et d'autre part il faut pouvoir déchiffrer qualitativement mais également quantitativement les processus et sources qui entrent en jeu lors de la formation des dépôts (processus *in-situ*), tels que les mécanismes de précipitation, par l'environnement géologique de formation, les vitesses de formation, les sources hydrothermales ou diagénétiques etc. En s'appuyant sur les connaissances reportées dans la littérature concernant la géochimie des dépôts d'une manière générale, mais également la minéralogie et le contexte géologique, notre objectif est d'apporter de nouveaux outils géochimiques qui permettront d'affiner cette classification et d'aller encore plus loin dans notre compréhension de la genèse des dépôts métallifères océaniques.

3.1. Cycles biogéochimiques des métaux de transition dans les océans modernes

Le premier niveau de compréhension porte sur la connaissance du comportement des métaux dans la colonne d'eau de mer et l'évaluation de la contribution des différentes sources aux métaux dissous dans l'eau de mer ainsi que des puits. Ces deux paramètres sont très importants car ils conditionnent l'estimation du temps de résidence des éléments chimiques dans l'eau de mer. Ces diverses sources comprennent les apports continentaux via les fleuves transportant les produits issus de l'érosion continentale, les particules atmosphériques, et probablement la décharge d'eaux souterraines au niveau des marges continentales passives ; les sources hydrothermales des rides médio-océaniques déchargeant des fluides riches en métaux (Elderfield and Schultz 1996; Hannington 2013) ; et les apports extraterrestres via les flux de poussières cosmiques. La contribution de chacune de ces sources au bilan global des éléments dissous dans l'eau de mer sera différente suivant les métaux de transition. Par exemple, de nombreux travaux se sont attachés à comprendre les variations dans le passé des changements globaux tels que les variations climatiques influant directement sur les flux de matière provenant de l'érosion des continents, grâce à l'utilisation des variations des compositions isotopiques des éléments radiogéniques tels que Pb, Sr, Nd et Os dans les encroûtements de fer-manganèse (Abouchami et al. 1997; Ling et al. 1997; Frank et al. 1999; van de Flierdt et al. 2003). Ces traceurs radiogéniques ont également permis de reconstituer la circulation océanique au cours du Cénozoïque affecter par des changements paléocéanographiques majeurs tels que la mise en place de l'isthme de Panama entre 8 et 6 Ma (Frank 2002), l'intensité du transport des masses d'eau de l'Atlantique Nord vers l'océan de l'Atlantique Sud (Frank et al. 2002). Quant aux puits océaniques des métaux ils concernent les différents dépôts sédimentaires marins que ce soient des dépôts métallifères ou non.

Par ailleurs, le cycle biogéochimique des métaux dans les océans est fortement influencé par l'activité biologique et il n'est plus à démontrer que la biosphère interagit avec l'environnement géologique. Que ce soit près des sources hydrothermales qui regorgent d'écosystèmes biologiques diversifiés et abondants ; dans les basaltes profonds enfouis où la présence de vie a été démontrée (Lever et al. 2013) ; ou tout simplement dans les océans avec l'activité phytoplanctonique des eaux de surface où par exemple le Fe et le Zn sont des

micronutriments et sont donc des éléments bio-limitant pour la production primaire phytoplanctonique de surface (Morel et al. 2003; Morel and Price 2003). Les variations de la disponibilité des métaux dans les eaux de surface au cours du temps a pu avoir des effets sur l'activité biologique. De plus, il est probable que la productivité biologique de surface influe sur l'enrichissement en Cu et Ni des nodules polymétalliques (Cronan 1975; Aplin and Cronan 1985; Verlaan et al. 2004). Néanmoins, ces considérations restent souvent soit hypothèses soit des interprétations qualitatives et qui méritent donc d'être évaluées quantitativement.

Il est également nécessaire de considérer le rôle de la zone d'oxygène minimum (OMZ) (primordiale pour la genèse des encroûtements hydrogénétiques) et de la zone de compensation de la calcite (CCD) sur le cycle biogéochimique des métaux. La zone d'oxygène minimum (présente entre 500 et 1500 m de et variant suivant les océans) est un précurseur de la formation des encroûtements de fer-manganèse. Elle permet d'accumuler et de transporter du Mn dissout qui, une fois recyclé hors de cette couche, sera oxydé et pourra précipiter sous forme d'oxydes de Mn capable de piéger les métaux dissous dans l'eau de mer (Koschinsky and Halbach 1995; Koschinsky and Hein 2003). Notez également que l'épaisseur et la profondeur de cette couche varie avec l'intensité de l'activité biologique des eaux de surface.

3.2. Formation des dépôts métallifères océaniques riches en Fe et Mn

Le deuxième niveau de compréhension est inhérent aux types de dépôts et aux processus *in-situ* en jeu lors de leur dépôt, car les environnements géologiques, les réactions de précipitation chimiques et surtout les taux de précipitation et d'accumulation varient suivant les dépôts. Comme nous l'avons mentionné dans les paragraphes précédents, la littérature décrivant les environnements de dépôt, la minéralogie et la composition géochimique de ces dépôts métallifères est assez conséquente. Néanmoins, il subsiste encore des lacunes dans notre compréhension des modes de formation de certains de ces dépôts. Alors que les encroûtements hydrogénétiques se forment très probablement uniquement à partir des métaux dissous dans l'eau de mer, la formation des nodules de manganèse sur les sédiments pélagiques profonds résulte de l'intégration complexe de plusieurs processus d'enrichissement des métaux: la précipitation à partir des métaux de l'eau de mer, l'altération des roches encaissantes (sédiments, substrats basaltique) par halmyrolyse, la diagenèse précoce incluant le recyclage des métaux dans les eaux interstitielles suite à la désintégration des organismes biologiques dans le sédiment relâchant les métaux contenus dans leurs tissus (Klinkhammer 1980; Klinkhammer et al. 1982; Heggie et al. 1986), la contribution de tapis microbiens à la genèse des phases minérales (Wang and Muller 2009; Wang et al. 2009). Pourtant la contribution des différentes sources et la variété des mécanismes de formation aux enrichissements en métaux ne sont pas complètement résolues. Par ailleurs, nous avons mentionné également que les particules hydrothermales pouvaient être transportées dans l'eau de mer loin de leurs sources pour se déposer dans les sédiments pélagiques (Boström et al. 1969). Ces derniers s'accumulant lentement, ils peuvent ainsi être enrichis en métaux et notamment en REE (Kato et al. 2011). Cet apport hydrothermal distant pourrait donc être une source supplémentaire de métaux aux sédiments et indirectement aux nodules polymétalliques. Enfin, la genèse des dépôts hydrothermaux, elle est bien évidemment dépendante de la géochimie des fluides hydrothermaux et donc de l'environnement géologique, c'est-à-dire de

la nature des roches encaissantes (basique, ultrabasique) et du contexte géodynamique (bassin d'arrière-arc, dorsale lente ou dorsale rapide, volcanisme intraplaque, etc). Ceci suggère donc la relative complexité des différents paramètres qui entrent en jeu dans la formation des dépôts hydrothermaux.

Jusqu'à présent les dépôts métallifères océaniques sont communément classés dans un diagramme ternaire défini par trois pôles élémentaires: Fe, Mn et Ni+Cu+Co (Bonatti et al. 1972c; Hein et al. 1994). Ce diagramme permet de dsitinguer les différents types de dépôts suivant trois domaines indiquant l'origine prédominante des métaux de transition, c'est-à-dire les dépôts hydrogénés, les dépôts hydrothermaux et les dépôts diagénétiques (Figure X). Ces domaines définissent eux-mêmes les trois principaux types de mécanismes ayant conduit aux enrichissements en métaux de transition de ces formations métallifères. Néanmoins cette classification ne permet pas d'entrer réellement dans le niveau de complexité relatif aux modes de genèse des dépôts métallifères océaniques. Elle reste relativement grossière et comme nous l'avons vu pour les nodules polymétalliques les sources de métaux peuvent avoir des origines multiples et variées. De facto, elle ne permet pas de distinguer de manière précise les différentes sources d'enrichissement et les processus de formation.

3.3. Quels outils utiliser pour l'étude des dépôts métallifères océaniques ?

Compte tenu de la multitude des processus de formation et des sources impliquées dans la genèse des dépôts métallifères océaniques, il convient dans un premier temps de privilégier l'étude des encroûtements de fer-manganèse. Etant seulement précipités à partir de l'eau de mer, ils sont moins complexes à considérer d'un point de vue processus de formation. L'étude d'une série d'échantillons d'encroûtements en provenance de bassins océaniques variés permettra d'avoir une approche spatiale sur les facteurs globaux (environnement géodynamique, masses d'eau océaniques, etc) pouvant influencer sur les compositions géochimiques des dépôts métallifères marins. D'un autre côté, la réalisation de séries temporelles à travers plusieurs encroûtements de fer-manganèse provenant de différentes localités géographiques sera un moyen d'obtenir des réponses sur les facteurs locaux qui influent sur l'évolution dans le temps des cycles biogéochimiques des métaux dans les océans modernes (sur les derniers 60 Ma). L'avantage de cette méthodologie est qu'elle intègre à la fois le facteur spatial et le facteur temporel.

Le défi majeur qui est au cœur de notre étude est de trouver de nouveaux traceurs biogéochimiques fiables et ingénieux qui puissent répondre simultanément à ces deux niveaux de compréhension. A l'instar de la classification de Bonatti (1972) qui prend notamment en compte la composition en Fe, Mn, et Ni, Cu, Zn et Co, nous proposons d'établir une nouvelle classification à partir de la composition isotopique de ces éléments, à savoir les isotopes du Fe, Ni, Cu et Zn (sachant que Co et Mn sont par ailleurs mono-isotopiques). L'objectif est d'utiliser les variations des compositions isotopiques en Ni dans les dépôts métallifères océaniques comme nouveaux traceurs biogéochimiques dans les océans modernes, en y intégrant également d'autres traceurs isotopiques des métaux.

4. Les isotopes stables des métaux comme traceurs biogéochimiques dans les environnements marins : exemple du Ni, Fe, Cu et Zn

4.1. Théorie générale sur les fractionnements isotopiques

Plus de 75% des éléments présents dans la nature possèdent au moins deux isotopes, ces éléments ont un numéro atomique identique (même nombre de protons) mais leur nombre de neutrons est différent ce qui leur confèrent des masses différentes. Par conséquent, les isotopes d'un même élément auront les mêmes propriétés chimiques, mais les différences de masse peuvent engendrer des comportements physiques différents. C'est sur cette différence de masse entre les isotopes que s'appuie le fondement de la théorie des fractionnements isotopiques.

Au milieu du XXe siècle l'émergence de travaux majeurs sur les fractionnements isotopiques ont permis de mieux comprendre les processus qui gouvernent ces fractionnements (Bigeleisen and Mayer 1947; Urey 1947; Bigeleisen 1965). Les lois de thermodynamique ont mis en évidence que la différence de masse entre les isotopes produit des différences dans les fréquences de vibrations des isotopes qui sont à l'origine de variations dans leur état fondamental d'énergie quantique. Ainsi, les isotopes lourds ont des fréquences de vibration plus petites que les isotopes légers. Cette différence dans la fréquence de vibration se traduit dans le point-zéro d'énergie (ZPE) es liaisons chimiques. Le point-zéro d'énergie définit la différence d'énergie entre les atomes dissociés et les atomes engagés dans une liaison chimique. Plus cette valeur est faible, plus la différence d'énergie entre l'atome dissocié et l'atome lié sera grande. Par conséquent l'énergie à apporter pour briser une liaison chimique ayant un point-zéro bas sera plus élevée que pour une liaison chimique ayant un point-zéro plus élevé. En résumé, la liaison chimique impliquant un isotope lourd sera plus forte et plus stable donc plus difficile à dissocier qu'une liaison chimique impliquant un isotope léger.

On distingue deux types de fractionnement isotopique : le fractionnement cinétique et le fractionnement à l'équilibre. Le premier se produit suite à une différence entre les vitesses de réaction plus lentes pour les composés comprenant les isotopes lourds que ceux ayant des isotopes légers et qui réagissent plus vite en raison de leur plus faible masse. Le deuxième type de fractionnement concerne les fractionnements à l'équilibre qui résultent de la différence entre les ZPE des liaisons chimiques impliquant les isotopes. Supposons une réaction entre un composé AB dans lequel A est un élément possédant deux isotopes, A^L le plus léger et A^H le plus lourd, et un composé C. D'une manière simple, on peut visualiser le fractionnement à l'équilibre par une différence entre les constantes d'équilibre de la réaction,

$$A^HB + C \rightarrow A^HC + B \qquad (1)$$

où A^HB a une stabilité plus importante (ZPE plus bas) ce qui rend ce composé plus difficile à dissocier que le composé A^LB impliqué dans la réaction,

$$A^LB + C \rightarrow A^LC + B \qquad (2)$$

Ainsi, le produit global de la réaction AB + C → AC +B sera enrichit en A^LC. Outre la différence de masse entre les isotopes, le fractionnement isotopique dépend également de la température, de sorte que pour les réactions chimiques se produisant à basse température, la différence entre les fréquences de vibrations des différents isotopes sera plus importante que pour les réactions ayant lieu à haute température. Par conséquent, l'amplitude des fractionnements isotopiques est plus importante à basse température qu'à haute température (Urey 1947). Cet effet a permis notamment d'utiliser les isotopes stables légers tels que O, C, et H comme traceurs paléocéanographiques et comme géothermomètres.

Les fractionnements isotopiques peuvent être produits soient par des processus abiotiques tels que la précipitation chimique, l'incorporation de l'élément chimique dans une phase minérale lors de la cristallisation, l'adsorption sur des phases minérales, les réactions

d'oxydoréductions ou bien encore les processus d'altération ; soient par des réactions biologiques telles que l'assimilation des métaux comme micronutriment.

- *Isotopes stables « traditionnels » et « non-traditionnels »*

Les compositions isotopiques sont quantifiées par la mesure des rapports isotopiques, conventionnellement l'isotope lourd correspond au numérateur et l'isotope léger se trouve au dénominateur.

Traditionnellement, les variations des compositions isotopiques des systèmes d'isotopes stables ont communément d'abord été étudiées pour les éléments légers (par exemple S, C, H, N et O), de ce fait ils ont nommés les « systèmes d'isotopes stables traditionnels ». L'un des avantages des éléments légers par rapport aux éléments lourds est que les plus larges fractionnements isotopiques observables rendent plus facilement mesurables les variations des rapports isotopiques, qui sont eux-mêmes dus à des différences de masse entre les isotopes moindres que pour les éléments légers. De plus, les éléments légers tels que C, O et H par exemple sont des éléments très communs sur Terre et ce sont des éléments structurant des écosystèmes biologiques, ils sont donc très souvent utilisés pour étudier les processus se produisant dans les environnements de surface ou sub-surface, ou pour des études impliquant les organismes biologiques en général.

En progressant dans le tableau périodique vers les éléments plus lourds nous atteignons le groupe des métaux de transition. Certains de ces éléments chimiques comportent plusieurs isotopes, Fe, Cu, Zn, Ni, Tl, Mo, Cd, Hg – pour ne citer que les plus étudiés - et si les processus dont lesquelles sont impliqués ces éléments chimiques sont susceptibles de produire des fractionnements isotopiques, il sera ainsi possible de quantifier ces fractionnements par des mesures de rapports isotopiques. Ce sont les isotopes stables dits « non-traditionnels ». Cependant, à l'inverse des éléments légers, la différence de masse entre les isotopes d'éléments lourds est plus petite, par conséquent la détection de variations significatives des compositions isotopiques pour les éléments lourds nécessite des techniques analytiques de haute précision. Les techniques d'analyse usuellement utilisées pour les isotopes légers ne conviennent pas pour les éléments lourds dont les métaux de transition (Albarede and Beard 2004; Johnson et al. 2004; Anbar and Rouxel 2007).

Au cours des dernières décennies, le développement des techniques analytiques utilisant les spectromètres de masse pourvus de multi-collecteurs (MC-ICPMS, Multi Collector Inductively-Coupled Plasma Mass Spectrometry) a grandement favorisé l'émergence de l'étude de nouveaux systèmes isotopiques, en particulier les éléments lourds dont les métaux de transition, grâce à la détection de variations significatives des compositions isotopiques dans les matériaux terrestres par exemple (Zhu et al. 2002; Albarede and Beard 2004; Albarède et al. 2004; Williams et al. 2006; Anbar and Rouxel 2007). Au vu de cette perspective, l'étude des métaux de transition a attiré de plus en plus l'attention des géochimistes et de nouveaux terrains d'investigation ont alors peu à peu émergés, en particulier les études s'attachant à explorer et comprendre les relations entre biosphère et géosphère (Anbar and Rouxel 2007).

La représentation conventionnelle des compositions isotopiques des systèmes d'isotopes stables est la notation delta exprimée en pour mille (3). Cette notation permet d'une part une meilleure lisibilité des résultats car les variations des compositions isotopiques sont généralement sont de petite amplitude, et d'autre part elle exprime une déviation de la composition isotopique de l'échantillon par rapport à la composition isotopique d'un standard que l'on déterminera comme une valeur de référence. Elle permet

ainsi de visualiser rapidement si notre échantillon est enrichi ou appauvri en tel isotope par rapport à notre référence isotopique.

$$\delta^{x/y}E\ (‰) = 1000 \times (R_{ech}/R_{STD} - 1) \qquad (3)$$

Où $^{x/y}E$ spécifie le rapport isotopique de l'élément E avec x et y représentant les masses isotopiques utilisées dans le rapport et x>y; R_{ech} est le rapport mesuré de l'échantillon et R_{STD} est le rapport connu et fixe du standard.

4.2. Le nickel dans les environnements marins modernes

- *Sources, puits et temps de résidence du Ni dans les océans modernes*

Une simple revue de la littérature montre que le temps de résidence du Ni dans les océans modernes est mal estimé. Alors que certains auteurs proposent un temps de résidence du Ni de l'ordre 10000 ans (Sclater et al. 1976; Tribovillard et al. 2006), valeur qui concorde également avec celle nouvellement estimée par Gall et al. (2013) de 6900 à 14500 ans, d'autres auteurs proposent une valeur près de 30 fois supérieure à la précédente (Algeo and Maynard 2008). Cette incertitude du temps de résidence provient d'une mauvaise estimation des flux et des puits de Ni dans les océans modernes. On peut toutefois noter, que quel que soit le scénario envisagé, le temps de résidence du Ni est nettement supérieur au temps de mélange des océans d'environ 1500 ans.

Les estimations des sources de Ni aux océans établies par Gall et al. (2013) sont, (1) l'érosion continentale via l'apport des fleuves et les décharges d'eaux souterraines au niveau des marges continentales passives, (2) les poussières et particules atmosphériques d'origine continentale dont les émissions volcaniques, (3) les fluides hydrothermaux, et (4) les particules cosmiques (Gall et al. 2013). Gall et al. (2013) préconisent que les sources majeures de Ni aux océans sont les apports continentaux (atmosphérique et fluviatile) et hydrothermaux. D'un autre côté, ces auteurs distinguent deux principaux puits, les sédiments pélagiques et les encroûtements de fer-manganèse (Figure I.4).

En partant de ces nouvelles estimations de flux, on remarque que des incertitudes importantes demeurent. Alors que la concentration en Ni des fluides hydrothermaux formés au niveau des dorsales rapides de type dorsale Est-Pacifique dans un encaissant de composition basaltique sont pauvres en Ni, les fluides émanant de sources hydrothermales formées dans des encaissants ultrabasiques (par exemple au niveau de la dorsale médio-atlantique) montrent des enrichissements en Ni (Charlou et al. 1998; Charlou et al. 2002; Fouquet et al. 2010). Il y a donc probablement une variabilité importante dans les flux de Ni délivrés par la circulation hydrothermale compliquant l'estimation de ce flux. Par ailleurs, Gall et al. (2013) ont sous-estimé (voire non pas mentionné) l'influence des activités anthropiques sur le flux de Ni des fleuves mais également des particules atmosphériques. Ainsi, l'apport anthropique de Ni dans les rivières et les fleuves pourrait induire une surestimation de la concentration en Ni naturelle en provenance des sources continentales naturelles. Ces apports anthropiques sont par exemple les résidus d'exploitation des mines, les fonderies, les rejets issus de la combustion du charbon, mais également l'impact des activités agricoles en général. Le Ni des apports anthropiques est généralement plus facilement mobilisable que le Ni provenant des sources naturelles (Gaillardet et al. 2003). En outre, on peut également imaginer que les rivières qui traverseront un substrat basaltique auront des

teneurs en Ni différentes de celles ayant traversés des mines en exploitation créant ainsi une variabilité locale liée aux apports des sources anthropiques.

La deuxième inconnue concernant les sources de Ni est la source halmyrolitique (altération de la croûte océanique) qui pourrait être un flux important si l'on considère également l'altération des affleurements de roches ultrabasiques (riches en Ni) au niveau des dorsales lentes.

Enfin, il faudrait mentionner une estimation du puits de Ni dans les sédiments organiques. En effet, le Ni est enrichi dans les sédiments organiques (cf. paragraphes suivants), et ce puits pourrait notamment être important au niveau des marges continentales passives où sont présentes les zones d' « upwelling ».

- *Comportement du Ni dans l'eau de mer*

La concentration du Ni dans les océans figure parmi les plus élevée des métaux traces dans l'océan et varie entre 2 nmol/kg en surface et 12 nmol/kg en profondeur (Sohrin and Bruland 2011), ce qui explique que son temps de résidence soit parmi des plus élevés des métaux traces dans les océans. Cette différence de concentration entre les eaux de surface et les eaux profondes est due à l'activité biologique en surface consommant du Ni, et au recyclage en profondeur de cette matière organique libérant le Ni. C'est un élément qui a donc un profil d'élément nutritif dans les océans comme c'est également le cas du Fe, Zn et Cd par exemple (Morel and Price 2003). Ces éléments sont des micronutriments, et le Ni (et Zn) se comporte comme la silice (Calvert and Pedersen 1993).

Dans les environnements naturels le Ni est majoritairement présent sous sa forme divalente Ni^{2+}. Jusqu'à présent, on pensait que les espèces de Ni aqueux étaient sous la forme ($NiOH^{+}$) (Bruland and Lohan 2003; Gaillardet et al. 2003). D'autres études, dont certaines plus récentes, montrent que plus de 50% du Ni est présente sous la forme $NiCl^{+}$ et $NiCO_3^{+}$ (Glasby and Schulz 1999; Fujii et al. 2011). Bien que la complexation du Ni des ligands organiques n'a pas encore été établie dans l'eau de mer actuelle, il est très probable qu'elle est un rôle non négligeable voire peut-être prédominant comme c'est le cas pour le Zn par exemple (Robbins et al. 2013; Scott et al. 2013). La spéciation organique pourrait avoir un impact sur la stabilisation du Ni dans l'eau de mer et par exemple cela pourrait améliorer le transport du Ni émis par les sources hydrothermales dans l'océan, comme cela a déjà été démontré pour d'autres métaux tels que le Fe et le Cu (Toner et al. 2009; Sander and Koschinsky 2011). C'est donc une problématique qu'il faudra pouvoir résoudre dans le futur.

- *Rôle du Ni lors de l'activité biologique*

Comme une grande partie des métaux de transition (e.g. Fe, Cu, Zn, Co, Cd), le Ni est un élément important pour l'activité biologique (on peut le qualifier d'élément « bio-essentiel »), bien qu'il ne soit pas bio-limitant comme le Fe, et son rôle dans le cycle biologique est démontré par son profil d'élément nutritif dans la colonne d'eau.

Dans les systèmes biologiques, le Ni est principalement impliqué dans deux réactions biologiques: la méthanogenèse, et la consommation du nickel par le phytoplancton marin car le Ni est un co-facteur enzymatique nécessaire à l'assimilation de l'azote et du dioxyde de carbone durant l'hydrolyse de l'urée (Watt and Ludden 1999; Dupont et al. 2010). Ce dernier paramètre est fondamental il explique pourquoi le Ni suit un profil d'élément nutritif dans les océans.

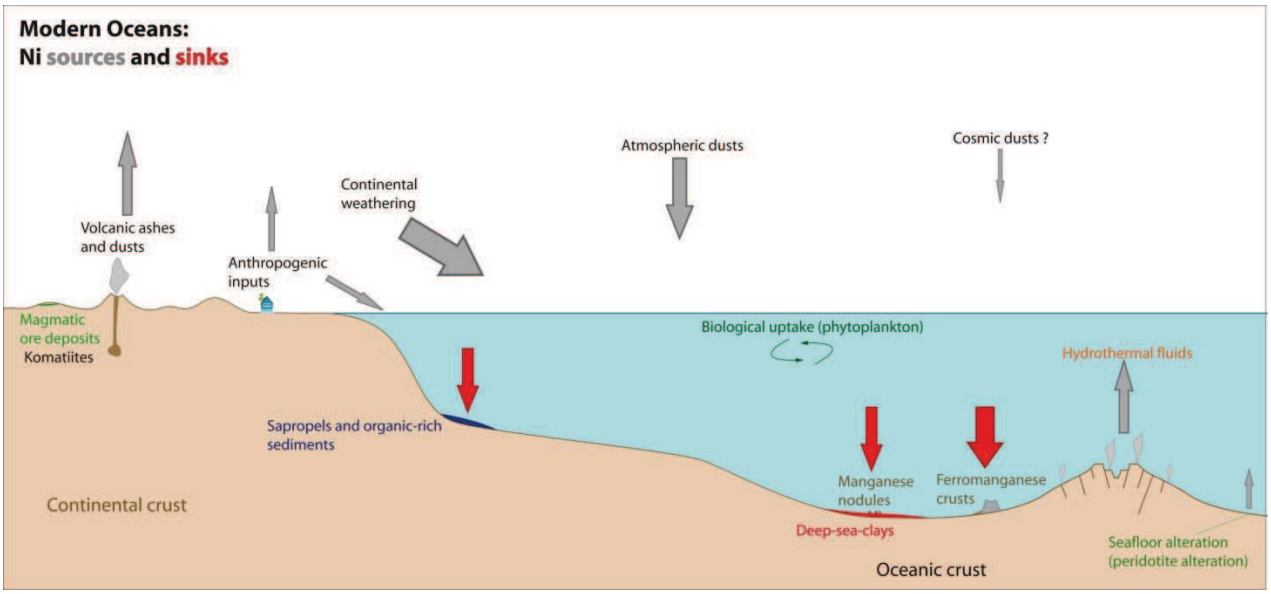

Figure I.4 *: Vue schématique des sources et des puits de Ni dans les océans modernes.*

4.3. Variations isotopiques du Ni dans les roches terrestres et dans les environnements marins : les isotopes du Ni comme nouveau traceur biogéochimique

Lors de l'initiation de ce projet, les études ayant reportées les variations isotopiques du Ni dans les systèmes naturels terrestres étaient encore très parcellaires. Ainsi, une synthèse succincte des résultats disponibles à ce jour dans la littérature sur la systématique isotopique du Ni est rappelé ici. Le paragraphe précédent a montré les caractéristiques géochimiques du Ni dans les environnements marins modernes pertinentes pour ce projet. De plus, avant de s'intéresser au Ni en tant que nouveau traceur biogéochimique, il est nécessaire de faire un état des lieux des connaissances sur la variabilité isotopique naturelle du Ni dans les roches terrestres.

Le nickel comporte cinq isotopes stables présents dans la nature, ^{58}Ni, ^{60}Ni, ^{61}Ni, ^{62}Ni, ^{64}Ni, dont les abondances sont les suivantes 68%, 26%, 1.1%, 3.6%, et 0.9% respectivement. La composition isotopique en Ni des échantillons sera reportée en utilisant le rapport ^{60}Ni/^{58}Ni par rapport au standard isotopique international NIST SRM 986 :

$$\delta^{60/58}\text{Ni (‰)} = 1000 \times [(^{60}\text{Ni}/^{58}\text{Ni}_{\text{ech}})/(^{60}\text{Ni}/^{58}\text{Ni}_{\text{NIST986}}) - 1] \qquad (4)$$

Après accrétion de la Terre lors de la formation du système solaire, la Terre s'est différenciée en différentes couches de compositions chimiques différentes. Durant cet épisode de différenciation, la formation du noyau composé d'un alliage Fe-Ni a concentré une majeure partie du Ni présent initialement après le stade d'accrétion. Le manteau inférieur et le manteau supérieur composé de roches ultrabasiques sont plus riches en Ni que les roches formant la croûte océanique et la croûte continentale. Enfin, cette dernière, formée de matériaux différenciés, est encore relativement moins riche en Ni que la croûte océanique formée de roches basiques.

- *Roches magmatiques*

Le Ni est un élément compatible au cours des processus magmatiques (affinité de l'élément pour la phase minérale aux dépens du liquide magmatique, par exemple lors des processus de cristallisation fractionnée) et il est particulièrement enrichi dans les roches ultramafiques telles que les péridotites ou les laves archéennes de type komatiites. L'enrichissement en Ni est notamment important dans les sulfures magmatiques formés à partir de la ségrégation de magmas sulfurés dans les laves komatiitiques. La composition isotopique du Ni mesurée dans les roches magmatiques basiques et ultrabasiques varient peu. Elle est proche de 0 ‰ dans les basaltes de la croûte océanique, tandis que dans les péridotites le fractionnement isotopique par rapport à cette valeur n'excède pas ~0.2 ‰ au total (Cameron et al. 2009; Gall et al. 2012; Gall et al. 2013). A noter que certains de ces résultats ont été publiés au cours de la thèse. L'ensemble de ces compositions isotopiques en Ni ont permis d'estimer une composition isotopique moyenne du réservoir de Ni dans la croûte terrestre à +0.05 ±0.05 ‰ (cf. chapitre 1).

- *Roches sédimentaires des environnements marins anciens*

Il n'existe pas encore dans la littérature de données sur les compositions isotopiques du Ni dans les sédiments anciens. La thèse de Sarah Porter (Université de Durham, UK, 2012) est à ce jour la seule reportant la composition isotopique du Ni dans des sédiments d'environnements marins anciens riches en matière organique (Porter 2012). Les sédiments riches en matière organique tels que les sapropels (dépôts modernes) et les schistes noirs ou « Black Shales » (dépôts anciens) sont généralement enrichis en métaux de transition tels que Co, Cu, Ni, Cr, V, Cd, Mo and Re (Warning and Brumsack 2000; Brumsack 2006; Piper and Calvert 2009). Ces enrichissements ont été favorisés par l'enfouissement rapide de quantités importantes de matière organique dans le sédiment empêchant l'oxydation et donc la destruction de cette matière organique à l'interface sédiment/eau de mer, mais également par les conditions d'oxydo-réductions permettant un transfert efficace des métaux traces de l'eau de mer vers le sédiment ainsi que la préservation des métaux contenus dans la matière organique. Par exemple, la présence fréquente de pyrite (ou ses précurseurs de type mackinawite) dans les dépôts de sapropels montre que les conditions redox étaient favorables à la présence d'H_2S permettant la précipitation de sulfures et le piégeage des métaux de transition.

Le Ni est particulièrement enrichi dans les sédiments organiques car il est préservé dans les tétrapyrroles (au même titre que le vanadium), molécules organiques qui dérivent principalement de la chlorophylle et l'hème (Lewan and Maynard 1982; Lewan 1984; Tribovillard et al. 2006). Au cours des réactions de métallation ayant lieu lors des processus de diagenèse précoce des molécules organiques provenant de la matière organique accumulée, le magnésium contenu dans la chlorophylle est remplacé par le Ni pour former des porphyrines qui vont ainsi conserver efficacement cet élément dans le sédiment. Au cours de cette étude, nous avons donc pu prendre connaissance des résultats des travaux de thèse de Porter (2012) sur des enregistrements sédimentaires riches en matière organique qui montrent une large gamme de variations des compositions isotopiques en Ni allant de +0.28 à +2.50 ‰, soit un enrichissement systématique en isotopes lourds. Ces résultats montrent qu'au-delà du seuil de concentration 1% du carbone organique total (TOC), l'augmentation des compositions isotopiques en Ni est corrélée avec l'augmentation de la concentration en TOC suggérant que le fractionnement des isotopes du Ni est contrôlé par l'enrichissement en matière organique. En-dessous du seuil de 1% carbone organique total toute corrélation disparaît avec les isotopes du Ni. On peut également souligner que les tétrapyrroles (dans lesquels est contenu l'essentiel du Ni) sont très stables face aux

élévations de température qui pourraient se produire lors de la diagenèse par exemple. Ainsi, les liaisons chimiques du Ni dans les tétrayrroles ne seront pas détruits excluant que les fractionnements isotopiques du Ni soient associés aux destructions ou au remaniement des tétrapyrroles après sédimentation.

- *Roches sédimentaires déposées dans les environnements marins actuels*

Dans les dépôts métallifères des océans modernes (nous utiliserons le terme « modernes » ou « actuels » car replacés sur l'échelle des temps géologiques ces dépôts sont relativement jeunes et ne peuvent pas être plus vieux que l'âge maximal de la croûte océanique d'environ 180 Ma), le Ni est particulièrement enrichi dans les encroûtements de fer-manganèse, les nodules de manganèse et d'une manière générale dans toutes les précipitations authigènes d'oxydes de Fe et de Mn des sédiments océaniques profonds tels que les argiles rouges (Nicholson et al. 1997; Cronan 2000). Le Ni est également enrichi dans les sédiments organiques, et dans les océans modernes les conditions les plus favorables à la formation de sédiments riches en matière organique sont les marges continentales où des courants d' « upwellings » sont présents telles que la marge du Pérou ou la marge Ouest-Africaine, et les bassins océaniques confinés tels que la Mer Noire, les fjords norvégiens ou encore le Golfe du Mexique (Brumsack 2006).

Très récemment, Gall et al. (2013) ont publiés les premières données sur l'isotopie du Ni dans les encroûtements de fer-manganèse montrant de larges variations de +0.9 à +2.5‰. Les données ont été reportées à la fois sur des encroûtements roche totale provenant de tous les océans du globe, mais ils ont également réalisé des analyses sur une série temporelle d'un échantillon d'encroûtement. Chacune des différents couches de la croûte dont le rapport isotopique a été déterminé a été préalablement datée permettant d'obtenir une stratigraphie des variations isotopiques du Ni au cours du Cénozoïque dans l'Océan Pacifique. Selon les auteurs, les variations observées dans cet échantillon, montrent que la diminution des compositions isotopiques en Ni est liée à un apport hydrothermal. De plus, ils remarquent que les encroûtements (roche totale) formés à proximité des sources hydrothermales ont des valeurs proches de ~+1.5‰. Ainsi, ils proposent que les fluides hydrothermaux aient probablement des compositions isotopiques proches de cette valeur.

Les variations isotopiques du Ni dans les encroûtements roche totale ne montrent aucune corrélation avec la localisation géographique, indiquant que ces variations n'ont pas de lien directe avec des différences potentielles entre les masses d'eau des océans du globe. En revanche, il semblerait que les échantillons collectés proches des marges continentales soient enrichis en isotopes lourds du Ni. Les explications qu'ils fournissent à ces observations est que l'altération de roches silicatées produit des enrichissements en isotopes légers des matériaux altérés et ceci est cohérent avec la composition isotopique mesurée sur un échantillon de saprolite. Ceci implique que le Ni lessivé lors de l'altération des continents et entrant dans le réservoir océanique sera enrichi en isotopes lourds.

En revanche, un point crucial qu'il faut évaluer est le fractionnement isotopique qui pourrait se produire entre le Ni présent dans l'eau de mer et le Ni incorporé dans les phases d'oxy-hydroxydes de Mn et de Fe des encroûtements de fer-manganèse lors de l'adsorption. Ce type d'expérimentation sur oxy-hydroxydes de Fe et de Mn sont largement documentés dans la littérature pour d'autres systèmes isotopiques tels que Fe, Cu, Zn et Mo (Barling and Anbar 2004; Pokrovsky et al. 2005; Pokrovsky et al. 2008; Goldberg et al. 2009; Wu et al. 2011). Sans ce paramètre il sera difficile d'émettre des hypothèses raisonnables quant aux variations isotopiques du Ni dans les dépôts métallifères océaniques.

- *Fractionnement isotopique du Ni par les organismes biologiques*

L'utilisation du Ni par les méthanogènes (micro-organismes biologiques pratiquant la méthanogenèse) montre des fractionnements isotopiques de plus de 1 ‰ avec une incorporation préférentielle des isotopes légers par les méthanogènes (Cameron et al. 2009).

- *Fractionnement isotopique du Ni entre les différentes espèces présentes dans l'eau de mer*

Il a été démontré qu'un fractionnement isotopique du Ni de l'ordre de 2.5‰ pouvaient se produire entre les espèces organiques et les espèces inorganiques présentes dans l'eau de mer (Fujii et al. 2011), or l'amplitude de ces fractionnements est dans la gamme de variation observée dans les dépôts marins (cf. paragraphes précédents).

4.4. Apport de l'utilisation couplée des compositions isotopiques en Fe, Cu et Zn (et Ni) dans les dépôts métallifères océaniques

En parallèle du développement du Ni comme nouveau traceur biogéochimique des océans modernes, nous avons également exploré la possibilité et le potentiel dont pourrait bénéficier une approche multi proxy par l'analyse intégrée de plusieurs systèmes isotopiques des métaux tel que le Fe, Cu et Zn (et Ni). Bien que l'ensemble des facteurs contrôlant les cycles biogéochimiques de ces métaux traces dans l'eau de mer ne soient pas encore compris dans leur intégralité (hydrothermalisme, circulation océanique, productivité biologique, éruptions volcaniques, etc), les comportements élémentaires et isotopiques du Fe, Cu et Zn dans les environnements naturels sont néanmoins différents (cf. la synthèse de (Anbar and Rouxel 2007) par exemple). Ainsi, une étude intégrant ces systèmes isotopiques permettrait peut-être de mieux appréhender les causes des variations isotopiques chaque système apportant des informations différentes mais complémentaires.

5. Les hypothèses de travail et les étapes du déroulement de l'étude

5.1. Hypothèses et objectifs sur l'utilisation des fractionnements isotopiques du Ni dans les dépôts métallifères océaniques

- Au commencement de cette étude, notre connaissance sur la systématique des isotopes du Ni était limitée par le peu d'études disponibles (les résultats de l'équipe de L. Gall ont été publiés bien postérieurement au début de cette étude). En particulier, peu d'échantillons terrestres n'avaient été caractérisés pour leur composition isotopique en Ni, laissant ainsi les variations isotopiques naturelles du Ni étaient mal connus.

Est-il possible de mesurer les compositions isotopiques en Ni dans les différents systèmes terrestres ? Les variations isotopiques sont-elles significatives et qu'elle est la gamme de variabilité des compositions isotopiques en Ni ? Le premier chapitre du manuscrit a pour objectif de répondre à ces questions. Une meilleure compréhension de la manière dont se comporte le Ni dans les différents environnements terrestres, ainsi qu'une meilleure appréhension de la variabilité naturelle affectant la systématique isotopique du Ni est un prérequis pour cette étude. Par ailleurs, la mise en place des techniques expérimentales et analytiques requises pour mesurer les compositions isotopiques en Ni n'en étaient qu'à leurs prémices et des ajustements étaient nécessaires pour valider un protocole final.

Ainsi, excepté les échantillons choisis pour mettre en place cette méthode expérimentale et analytique, l'amplitude des fractionnements isotopiques du Ni se produisant dans les environnements naturels sera évalué en analysant différentes roches représentatives des réservoirs terrestres importants pour cet élément. En outre, ce travail initial s'accompagnera de l'estimation d'un paramètre essentiel qui s'agit de la valeur isotopique en Ni de la Terre Globale (« Bulk Silicate Earth », BSE). Cette « Terre Globale » est considérée comme étant la composition isotopique de référence du réservoir global terrestre.

- Une grande partie des travaux présentés dans cette thèse porte sur les encroûtements de fer-manganèse. Mais comme cela a déjà été développé précédemment il faut évaluer si la composition isotopique en Ni mesurée dans les encroûtements reflète celle de sa source, l'eau de mer. *Quelle est la magnitude du fractionnement isotopique lors de l'incorporation du Ni dans les phases minérales riches en Fe et Mn ?* Les expériences d'adsorption du Ni sur des phases d'oxy-hydroxydes de Fe et de Mn permettront de répondre à cette question. Ces travaux ont été réalisés avec des chercheurs de l'Université du Minnesota aux Etats-Unis.

- Dans un troisième temps, l'analyse des compositions isotopiques de dépôts de Fe-Mn hydrothermaux et de celles de dépôts Fe-Mn hydrogénés permettra d'évaluer si les isotopes du Ni sont sensibles aux différentes sources desquelles ils proviennent. *Est-ce que le Ni incorporé dans des dépôts hydrothermaux a une composition isotopique distincte du Ni dans des dépôts provenant exclusivement de l'eau de mer ?*

Le temps de résidence du Ni dans les océans étant bien supérieur au temps de mélange des océans, on peut supposer d'une part, que les compositions isotopiques en Ni sont homogènes dans tous les océans, et d'autre part qu'elles ne sont pas influencées par l'effet de sources locales. Néanmoins, en supposant que le Ni incorporé dans les encroûtements hydrogénétiques est un proxy de la composition isotopique de l'eau de mer profonde, Gall et al. (2013) suggèrent que les sources hydrothermales auraient en fait un impact sur la variabilité isotopique du Ni produisant des compositions isotopiques enrichies en isotopes légers.

Dans ce contexte, la combinaison des résultats obtenus sur roche totale de dépôts riches en Fe et Mn d'origine hydrothermale et l'analyse de séries temporelles effectuées sur plusieurs encroûtements hydrogénétiques en provenance de localités géographiques différentes, permettra de déterminer si effectivement les variations des compositions isotopiques en Ni sont le résultat, de variabilité dans les sources (avec des compositions différentes), de masses d'eau océanique n'ayant pas la même composition isotopique, ou encore d'un effet minéralogique.

- Ultimement, les objectifs portent sur une meilleure compréhension de la genèse des encroûtements hydrogénétiques et des nodules polymétalliques et des processus ayant produit les enrichissements importants en certains métaux de transition. Cela suppose de mieux comprendre l'importance des sources hydrothermales dans le cycle biogéochimique des métaux dans les océans, l'influence de la productivité biologique, et l'impact des flux issus de l'érosion continentale sur la disponibilité des métaux dans les océans, en évaluant aussi les variations temporelles potentielles qui ont pu se produire et leur intensité. *Quels sont les processus affectant le cycle biogéochimique des métaux dans les océans ? et comment ceux-ci ont-ils variés au cours du temps ?* Des approches couplées incluant la minéralogie fine, l'analyse des compositions en éléments majeurs, traces et Terres Rares, et

des compositions isotopiques en métaux (Ni, Fe, Cu et Zn par exemple) permettront de disposer d'une boîte à outils substantielle pour répondre à nos lacunes de compréhension.

- Enfin, si nous avons une bonne compréhension du cycle biogéochimique des métaux dans les océans modernes et de la manière dont les compositions isotopiques en métaux ont été enregistrées dans les archives géologiques, cela nous aidera à mieux comprendre ce qu'il s'est passé dans les océans anciens à travers les dépôts anciens comme par exemple les formations ferrifères rubanées (« BIFs »).

5.2. Plan de l'étude

Ce manuscrit est divisé en six chapitres. Chaque chapitre est présenté sous la forme d'une publication scientifique. Ce choix rédactionnel implique que le lecteur rencontrera parfois des répétitions dans le texte. Le manuscrit de thèse s'organise de la manière suivante :

- Le chapitre 1 expose les méthodes expérimentale et analytique utilisées au cours de la thèse et la première partie de ce chapitre constitue un article publié en 2013 dans *Geostandards and Geoanalytical Research* sur les méthodes d'analyses des isotopes du Ni. Dans la seconde partie est présentée une méthode d'analyse des isotopes du Ni dans l'eau de mer.
- Le chapitre 2 s'intéresse aux résultats obtenus sur les fractionnements isotopiques lors de l'adsorption du Ni sur les des oxy-hydroxydes de fer et de manganèse en conditions expérimentales.
- Le chapitre 3 traite dans une première partie des variations des compositions isotopiques du Ni dans plusieurs types de dépôts métallifères océaniques riches en Fe et en Mn hydrothermaux et hydrogénétiques. La seconde partie présente les résultats des compositions isotopiques en Ni obtenues sur une séquence stratigraphique d'argiles pélagiques profondes. Et enfin la troisième partie est une synthèse du bilan de masse du Ni dans les océans modernes et son temps de résidence. Ce chapitre est précédé d'une introduction résumant l'état des connaissances sur les encroûtements de fer-manganèse.
- Le chapitre 4 discute des résultats des variations temporelles des compositions isotopiques en Ni obtenues lors des études haute résolution réalisées sur les encroûtements de fer-manganèse provenant de Tahiti et Hawaii.
- Le chapitre 5 s'intéresse à l'intérêt d'une approche couplée par l'utilisation des compositions isotopiques de plusieurs métaux tels que Fe, Cu et Zn, sur les séries temporelles d'encroûtements de fer-manganèse présentés dans le chapitre 4.
- Enfin, la synthèse des résultats permettra de mettre en avant les perspectives d'étude notamment les applications possibles aux dépôts métallifères formés dans les océans anciens tels que les formations de fer rubanées archéennes et protérozoïques.

En annexe figure deux manuscrits d'articles scientifiques : un article publié dans la revue *Mineralium Deposita* sur la formation de sulfures riches en Ni de massifs komatiitiques auquel j'ai contribué en y incluant une discussion autour des compositions isotopiques en Ni de ces sulfures (Hofmann et al. 2013), et un article soumis à *Geochimica et Cosmochimica Acta* sur la spéciation et la minéralogie fine du Fe à travers d'une section de nodule polymétallique. La troisième annexe présente le projet d'étude des échantillons de la campagne BIONOD 2012 (nodules, sédiments et eaux interstitielles collectés dans l'océan

Pacifique Central), et les annexes 4 et 5 correspondent à deux posters de communications scientifiques réalisées lors de congrès internationaux.

6. Références bibliographiques

Abouchami, W., Goldstein, S. L., Galer, S. J. G., Eisenhauer, A. and Mangini, A. (1997). "Secular changes of lead and neodymium in central Pacific seawater recorded by a Fe-Mn crust." Geochimica Et Cosmochimica Acta 61(18): 3957-3974.

Albarede, F. and Beard, B. (2004). "Analytical Methods for Non-Traditional Isotopes." Reviews in Mineralogy and Geochemistry 55(1): 113-152.

Albarède, F., Telouk, P., Blichert-Toft, J., Boyet, M., Agranier, A. and Nelson, B. (2004). "Precise and accurate isotopic measurements using multiple-collector ICPMS." Geochimica Et Cosmochimica Acta 68(12): 2725-2744.

Algeo, T. J. and Maynard, J. B. (2008). "Trace-metal covariation as a guide to water-mass conditions in ancient anoxic marine environments." Geosphere 4(5): 872-887.

Anbar, A. D. and Rouxel, O. (2007). "Metal stable isotopes in paleoceanography." Annual Review of Earth and Planetary Sciences 35: 717-746.

Anschutz, P. and Blanc, G. (1995). "Chemical mass balances in metalliferous deposits from the Atlantis II Deep, Red Sea." Geochimica Et Cosmochimica Acta 59(20): 4205-4218.

Anschutz, P., Blanc, G. and Stille, P. (1995). "Origin of fluids and the evolution of the Atlantis II deep hydrothermal system, Red Sea: Strontium isotope study." Geochimica Et Cosmochimica Acta 59(23): 4799-4808.

Aplin, A. C. and Cronan, D. S. (1985). "Ferromanganese oxide deposits from the Central Pacific Ocean, II. Nodules and associated sediments." Geochimica Et Cosmochimica Acta 49(2): 437-451.

Barling, J. and Anbar, A. D. (2004). "Molybdenum isotope fractionation during adsorption by manganese oxides." Earth and Planetary Science Letters 217(3-4): 315-329.

Bigeleisen, J. (1965). "Chemistry of isotopes." Science 147(3657): 463.

Bigeleisen, J. and Mayer, M. G. (1947). "Calculation of equilibrium constants for isotopic exchange reactions." Journal of Chemical Physics 15(5): 261-267.

Bonatti, E. and Joensuu, O. (1966). "Deep-sea iron deposit from South Pacific." Science 154(3749): 643-&.

Bonatti, E., Kraemer, T. and Rydell, H. (1972c). Classification and genesis of submarine iron-manganese deposits, Washington DC, Nat. Sci. Found.

Boström, K. and Peterson, M. N. A. (1966). "Precipitates from hydrothermal exhalations on the East Pacific rise." Economic Geology 61(7): 1258-1265.

Boström, K., Peterson, M. N. A., Joensuu, O. and Fisher, D. E. (1969). "Aluminum-poor ferromanganoan sediments on active oceanic ridges." Journal of Geophysical Research 74(12): 3261-3270.

Bruland, K. W. and Lohan, M. C. (2003). Controls of Trace Metals in Seawater. Treatise on Geochemistry. D. H. Heinrich and K. T. Karl. Oxford, Pergamon**:** 23-47.

Brumsack, H.-J. (2006). "The trace metal content of recent organic carbon-rich sediments: Implications for Cretaceous black shale formation." Palaeogeography, Palaeoclimatology, Palaeoecology 232(2-4): 344-361.

Brumsack, H. J. (1980). "Geochemistry of cretaceous Black Shales from the Atlantic Oceans (DSDP Legs 11, 14, 36 and 41)." Chemical Geology 31(1-2): 1-25.

Burnett, W. C. and Piper, D. Z. (1977). "Rapidly-formed ferromanganese deposit from Eastern Pacific Hess Deep." Nature 265(5595): 596-600.

Calvert, S. E. and Pedersen, T. F. (1993). "Geochemistry of Recent oxic and anoxic marine sediments: Implications for the geological record." Marine Geology 113(1–2): 67-88.

Cameron, V., Vance, D., Archer, C. and House, C. H. (2009). "A biomarker based on the stable isotopes of nickel." Proceedings of the National Academy of Sciences of the United States of America 106(27): 10944-10948.

Charlou, J. L., Donval, J. P., Fouquet, Y., Jean-Baptiste, P. and Holm, N. (2002). "Geochemistry of high H_2 and CH_4 vent fluids issuing from ultramafic rocks at the

Rainbow hydrothermal field (36 degrees 14 ' N, MAR)." Chemical Geology 191(4): 345-359.

Charlou, J. L., Fouquet, Y., Bougault, H., Donval, J. P., Etoubleau, J., Jean-Baptiste, P., Dapoigny, A., Appriou, P. and Rona, P. A. (1998). "Intense CH_4 plumes generated by serpentinization of ultramafic rocks at the intersection of the 15 degrees 20 ' N fracture zone and the Mid-Atlantic Ridge." Geochimica Et Cosmochimica Acta 62(13): 2323-2333.

Corliss, J. B., Dymond, J., Gordon, L. I., Edmond, J. M., Herzen, R. P. V., Ballard, R. D., Green, K., Williams, D., Bainbridge, A., Crane, K. and Vanandel, T. H. (1979). "Submarine thermal springs on the Galapagos rift." Science 203(4385): 1073-1083.

Cronan, D. S. (1975). "Manganese nodules and other ferromangese oxide deposits from Atlantic Ocean." Journal of Geophysical Research-Oceans and Atmospheres 80(27): 3831-3837.

Cronan, D. S., Ed. (2000). Handbook of marine mineral deposits, CRC Press London.

De Carlo, E. H., McMurtry, G. M. and Yeh, H.-W. (1983). "Geochemistry of hydrothermal deposits from Loihi submarine volcano, Hawaii." Earth and Planetary Science Letters 66(0): 438-449.

Dupont, C. L., Buck, K. N., Palenik, B. and Barbeau, K. (2010). "Nickel utilization in phytoplankton assemblages from contrasting oceanic regimes." Deep Sea Research Part I: Oceanographic Research Papers 57(4): 553-566.

Edmond, J. M. (1981). "Hydrothermal activity at mid-ocean ridge axes." Nature 290(5802): 87-88.

Edmond, J. M., Measures, C., Mangum, B., Grant, B., Sclater, F. R., Collier, R., Hudson, A., Gordon, L. I. and Corliss, J. B. (1979). "On the formation of metal-rich deposits at ridge crests." Earth and Planetary Science Letters 46(1): 19-30.

Elderfield, H. and Schultz, A. (1996). "Mid-ocean ridge hydrothermal fluxes and the chemical composition of the ocean." Annual Review of Earth and Planetary Sciences 24: 191-224.

Fouquet, Y. (1997). "Where are the large hydrothermal sulphide deposits in the oceans?" Philosophical Transactions of the Royal Society a-Mathematical Physical and Engineering Sciences 355(1723): 427-440.

Fouquet, Y., Cambon, P., Etoubleau, J., Charlou, J. L., Ondréas, H., Barriga, F. J. A. S., Cherkashov, G., Semkova, T., Poroshina, I., Bohn, M., Donval, J. P., Henry, K., Murphy, P. and Rouxel, O. (2010). Geodiversity of Hydrothermal Processes Along the Mid-Atlantic Ridge and Ultramafic-Hosted Mineralization: A New Type of Oceanic Cu-Zn-Co-Au Volcanogenic Massive Sulfide Deposit.

Fouquet, Y., von Stackelberg, U., Charlou, J. L., Donval, J. P., Foucher, J. P., Erzinger, J., Herzig, P., Mühe, R., Wiedicke, M., Soakai, S. and Whitechurch, H. (1991). "Hydrothermal activity in the Lau back-arc basin:Sulfides and water chemistry." Geology 19(4): 303-306.

Francheteau, J., Needham, H. D., Choukroune, P., Juteau, T., Seguret, M., Ballard, R. D., Fox, P. J., Normark, W., Carranza, A., Cordoba, D., Guerrero, J., Rangin, C., Bougault, H., Cambon, P. and Hekinian, R. (1979). "Massive deep-sea sulfide ore-deposits discovered in the East Pacific Rise." Nature 277(5697): 523-528.

Frank, M. (2002). "Radiogenic isotopes: Tracers of past ocean circulation and erosional input." Reviews of Geophysics 40(1).

Frank, M., O'Nions, R. K., Hein, J. R. and Banakar, V. K. (1999). "60 Myr records of major elements and Pb–Nd isotopes from hydrogenous ferromanganese crusts: reconstruction of seawater paleochemistry." Geochimica Et Cosmochimica Acta 63(11–12): 1689-1708.

Frank, M., Whiteley, N., Kasten, S., Hein, J. R. and O'Nions, K. (2002). "North Atlantic deep water export to the Southern Ocean over the past 14 Myr: Evidence from Nd and Pb isotopes in ferromanganese crusts." Paleoceanography 17(2).

Froelich, P. N., Klinkhammer, G. P., Bender, M. L., Luedtke, N. A., Heath, G. R., Cullen, D., Dauphin, P., Hammond, D., Hartman, B. and Maynard, V. (1979). "Early oxidation of

organic matter in pelagic sediments of the eastern equatorial Atlantic: suboxic diagenesis." Geochimica Et Cosmochimica Acta 43(7): 1075-1090.

Fujii, T., Moynier, F., Dauphas, N. and Abe, M. (2011). "Theoretical and experimental investigation of nickel isotopic fractionation in species relevant to modern and ancient oceans." Geochimica et Cosmochimica Acta 75(2): 469-482.

Gaillardet, J., Viers, J. and Dupré, B. (2003). Trace Elements in River Waters. Treatise on Geochemistry. D. H. Editors-in-Chief: Heinrich and K. T. Karl. Oxford, Pergamon**:** 225-272.

Gall, L., Williams, H., Siebert, C. and Halliday, A. (2012). "Determination of mass-dependent variations in nickel isotope compositions using double spiking and MC-ICPMS." Journal of Analytical Atomic Spectrometry 27(1): 137-145.

Gall, L., Williams, H. M., Siebert, C., Halliday, A. N., Herrington, R. J. and Hein, J. R. (2013). "Nickel isotopic compositions of ferromanganese crusts and the constancy of deep ocean inputs and continental weathering effects over the Cenozoic." Earth and Planetary Science Letters 375(0): 148-155.

German, C. R. and Von Damm, K. L. (2003). Hydrothermal Processes. Treatise on Geochemistry. D. H. Editors-in-Chief: Heinrich and K. T. Karl. Oxford, Pergamon**:** 181-222.

Glasby, G. P. and Schulz, H. D. (1999). "E_H, pH diagrams for Mn, Fe, Co, Ni, Cu and As under seawater conditions: Application of two new types of E_H, pH diagrams to the study of specific problems in marine geochemistry." Aquatic Geochemistry 5(3): 227-248.

Goldberg, T., Archer, C., Vance, D. and Poulton, S. W. (2009). "Mo isotope fractionation during adsorption to Fe (oxyhydr)oxides." Geochimica et Cosmochimica Acta 73(21): 6502-6516.

Halbach, P., Kriete, C., Prause, B. and Puteanus, D. (1989). "Mechanisms to explain the platinum concentration in ferromanganese seamount crusts." Chemical Geology 76(1-2): 95-106.

Halbach, P., Puteanus, D. and Manheim, F. T. (1984). "Platinum concentrations in ferromanganese seamount crusts from the Central Pacific." Naturwissenschaften 71(11): 577-579.

Halbach, P., Segl, M., Puteanus, D. and Mangini, A. (1983). "Co-fluxes and growth rates in ferromanganese deposits from Central Pacific seamount areas." Nature 304(5928): 716-719.

Hannington, M., Jamieson, J., Monecke, T., Petersen, S. and Beaulieu, S. (2011). "The abundance of seafloor massive sulfide deposits." Geology 39(12): 1155-1158.

Hannington, M. D. (2013). "The role of black smokers in the Cu mass balance of the oceanic crust." Earth and Planetary Science Letters(0).

Heggie, D., Kahn, D. and Fischer, K. (1986). "Trace metals in metalliferous sediments, MANOP Site M: interfacial pore water profiles." Earth and Planetary Science Letters 80(1–2): 106-116.

Hein, J. R., Conrad, T. A. and Staudigel, H. (2010). "Seamount mineral deposits: a source of rare metals for high-technology industries." Oceanography 23(1): 184-189.

Hein, J. R., Koschinsky, A. and Halliday, A. N. (2003). "Global occurrence of tellurium-rich ferromanganese crusts and a model for the enrichment of tellurium." Geochimica et Cosmochimica Acta 67(6): 1117-1127.

Hein, J. R., Mizell, K., Koschinsky, A. and Conrad, T. A. (2013). "Deep-ocean mineral deposits as a source of critical metals for high- and green-technology applications: Comparison with land-based resources." Ore Geology Reviews 51(0): 1-14.

Hein, J. R., Schwab, W. C. and Davis, A. S. (1988). "Cobalt-rich and platinum-rich ferromanagenese crusts and associated substrate rocks from the Marshall islands." Marine Geology 78(3-4): 255-283.

Hein, J. R., Yeh, H. W., Gunn, S. H., Gibbs, A. E. and Wang, C. H. (1994). "Composition and origin of hydrothermal ironstones from Central Pacific seamounts." Geochimica Et Cosmochimica Acta 58(1): 179-189.

Hekinian, R., Fevrier, M., Avedik, F., Cambon, P., Charlou, J. L., Needham, H. D., Raillard, J., Boulegue, J., Merlivat, L., Moinet, A., Manganini, S. and Lange, J. (1983). "East Pacific Rise near 13 degrees N: Geology of new hydrothermal fields." Science 219(4590): 1321-1324.

Hekinian, R., Fevrier, M., Bischoff, J. L., Picot, P. and Shanks, W. C. (1980). "Sulfide deposits from the East Pacific Rise near 21 degrees N." Science 207(4438): 1433-1444.

Hofmann, A., Bekker, A., Dirks, P., Gueguen, B., Rumble, D. and Rouxel, O. (2013). "Comparing orthomagmatic and hydrothermal mineralization models for komatiite-hosted nickel deposits in Zimbabwe using multiple-sulfur, iron, and nickel isotope data." Mineralium Deposita: 1-26.

Humphris, S. E., Herzig, P. M., Miller, D. J., Alt, J. C., Becker, K., Brown, D., Brugmann, G., Chiba, H., Fouquet, Y., Gemmell, J. B., Guerin, G., Hannington, M. D., Holm, N. G., Honnorez, J. J., Iturrino, G. J., Knott, R., Ludwig, R., Nakamura, K., Petersen, S., Reysenbach, A. L., Rona, P. A., Smith, S., Sturz, A. A., Tivey, M. K. and Zhao, X. (1995). "The internal structure of an active sea-floor massive sulfide deposit." Nature 377(6551): 713-716.

ISA, Ed. (2002). Polymetallic Massive Sulphides and Cobalt-Rich Ferromanganese Crusts: Status and Prospects. Kingston, Jamaica, International Seabed Authority (ISA).

Johnson, C. M., Beard, B. L. and Albarède, F. (2004). "Overview and General Concepts." Reviews in Mineralogy and Geochemistry 55(1): 1-24.

Kato, Y., Fujinaga, K., Nakamura, K., Takaya, Y., Kitamura, K., Ohta, J., Toda, R., Nakashima, T. and Iwamori, H. (2011). "Deep-sea mud in the Pacific Ocean as a potential resource for rare-earth elements." Nature Geoscience 4(8): 535-539.

Klinkhammer, G., Heggie, D. T. and Graham, D. W. (1982). "Metal diagenesis in oxic marine-sediments." Earth and Planetary Science Letters 61(2): 211-219.

Klinkhammer, G. P. (1980). "Early diagenesis in sediments from the eastern equatorial Pacific, II. Pore water metal results." Earth and Planetary Science Letters 49(1): 81-101.

Koschinsky, A. and Halbach, P. (1995). "Sequential leaching of marine ferromanganese precipitates: Genetic implications." Geochimica et Cosmochimica Acta 59(24): 5113-5132.

Koschinsky, A. and Hein, J. R. (2003). "Uptake of elements from seawater by ferromanganese crusts: solid-phase associations and seawater speciation." Marine Geology 198(3-4): 331-351.

Lesuave, R., Pichocki, C., Pautot, G., Hoffert, M., Morel, Y., Voisset, M., Monti, S., Amosse, J. and Kosakevitch, A. (1989). "Geological and mineralogical study of Co-rich ferromanganese crusts from a submerged atoll in the Tuamotu archipelago (French Polynesia)." Marine Geology 87(2-4): 227-247.

Lever, M. A., Rouxel, O., Alt, J. C., Shimizu, N., Ono, S. H., Coggon, R. M., Shanks, W. C., Lapham, L., Elvert, M., Prieto-Mollar, X., Hinrichs, K. U., Inagaki, F. and Teske, A. (2013). "Evidence for Microbial Carbon and Sulfur Cycling in Deeply Buried Ridge Flank Basalt." Science 339(6125): 1305-1308.

Lewan, M. D. (1984). "Factors controlling the proportionality of Vanadium to Nickel in crude oils." Geochimica Et Cosmochimica Acta 48(11): 2231-2238.

Lewan, M. D. and Maynard, J. B. (1982). "Factors controlling enrichment of Vanadium and Nickel in the bitumen of organic sedimentary rocks." Geochimica Et Cosmochimica Acta 46(12): 2547-2560.

Li, Y. H. and Schoonmaker, J. E. (2003). Chemical Composition and Mineralogy of Marine Sediments. Treatise on Geochemistry. D. H. Editors-in-Chief: Heinrich and K. T. Karl. Oxford, Pergamon**:** 1-35.

Ling, H. F., Burton, K. W., O'Nions, R. K., Kamber, B. S., von Blanckenburg, F., Gibb, A. J. and Hein, J. R. (1997). "Evolution of Nd and Pb isotopes in Central Pacific seawater from ferromanganese crusts." Earth and Planetary Science Letters 146(1–2): 1-12.

Manheim, F. T. (1986). "Marine cobalt resources." Science 232(4750): 600-606.

Manheim, F. T. and Lanebostwick, C. M. (1988). "Cobalt in ferromanganese crusts as a monitor of hydrothermal discharge on the Pacific seafloor." Nature 335(6185): 59-62.

Maynard, J. B. (2003). Manganiferous Sediments, Rocks, and Ores. Treatise on Geochemistry. D. H. Editors-in-Chief: Heinrich and K. T. Karl. Oxford, Pergamon**:** 289-308.

Mills, R. A. and Elderfield, H. (1995). Hydrothermal Activity and the Geochemistry of Metalliferous Sediment. Seafloor Hydrothermal Systems: Physical, Chemical, Biological, and Geological Interactions, American Geophysical Union, Geophysical Monograph Series. 91**:** 392-407.

Mills, R. A., Wells, D. M. and Roberts, S. (2001). "Genesis of ferromanganese crusts from the TAG hydrothermal field." Chemical Geology 176(1–4): 283-293.

Morel, F. M. M., Milligan, A. J. and Saito, M. A. (2003). Marine Bioinorganic Chemistry: The Role of Trace Metals in the Oceanic Cycles of Major Nutrients. Treatise on Geochemistry. D. H. Heinrich and K. T. Karl. Oxford, Pergamon**:** 113-143.

Morel, F. M. M. and Price, N. M. (2003). "The Biogeochemical Cycles of Trace Metals in the Oceans." Science 300(5621): 944.

Murray, J. W. and Renard, A. F. (1891). "Deep-Sea Deposits. Reports on the Scientific Results of the HMS Challenger 1873–76."

Nicholson, K., Hein, J. R., Buehn, B. and Dasgupta, S., Eds. (1997). Manganese mineralization; geochemistry and mineralogy of terrestrial and marine deposits, Geological Society of London : London, United Kingdom.

Pichocki, C. and Hoffert, M. (1987). "Characteristics of Co-rich ferromanganese nodules and crusts sampled in French Polynesia." Marine Geology 77(1-2): 109-119.

Piper, D. Z. and Calvert, S. E. (2009). "A marine biogeochemical perspective on black shale deposition." Earth-Science Reviews 95(1-2): 63-96.

Pokrovsky, O. S., Viers, J., Emnova, E. E., Kompantseva, E. I. and Freydier, R. (2008). "Copper isotope fractionation during its interaction with soil and aquatic microorganisms and metal oxy(hydr)oxides: Possible structural control." Geochimica et Cosmochimica Acta 72(7): 1742-1757.

Pokrovsky, O. S., Viers, J. and Freydier, R. (2005). "Zinc stable isotope fractionation during its adsorption on oxides and hydroxides." Journal of Colloid and Interface Science 291(1): 192-200.

Porter, S. J. (2012). Nickel and osmium isotope and trace element geochemistry of organic-rich sedimentary rocks: the first investigation of Ni isotope systematics in marine sediments. Doctor of Philosophy, Durham University.

Pratt, R. M. and McFarlin, P. F. (1966). "Manganese pavements on Blake Plateau." Science 151(3714): 1080-&.

Robbins, L. J., Lalonde, S. V., Saito, M. A., Planavsky, N. J., Mloszewska, A. M., Pecoits, E., Scott, C., Dupont, C. L., Kappler, A. and Konhauser, K. O. (2013). "Authigenic iron oxide proxies for marine zinc over geological time and implications for eukaryotic metallome evolution." Geobiology: n/a-n/a.

Rona, P. A. (1984). "Hydrothermal mineralization at seafloor spreading centers." Earth-Science Reviews 20(1): 1-104.

Sander, S. G. and Koschinsky, A. (2011). "Metal flux from hydrothermal vents increased by organic complexation." Nature Geoscience 4(3): 145-150.

Schulz, H. D. and Zabel, M. (2006). Marine geochemistry. Federal Republic of Germany, Springer : Berlin, Federal Republic of Germany.

Sclater, F. R., Boyle, E. and Edmond, J. M. (1976). "On the marine geochemistry of nickel." Earth and Planetary Science Letters 31(1): 119-128.

Scott, C., Planavsky, N. J., Dupont, C. L., Kendall, B., Gill, B. C., Robbins, L. J., Husband, K. F., Arnold, G. L., Wing, B. A., Poulton, S. W., Bekker, A., Anbar, A. D., Konhauser, K. O. and Lyons, T. W. (2013). "Bioavailability of zinc in marine systems through time." Nature Geosci 6(2): 125-128.

Seyfried, W. E. and Ding, K. (1995). Phase Equilibria in Subseafloor Hydrothermal Systems: a Review of the Role of Redox, Temperature, Ph and Dissolved Cl on the Chemistry

of Hot Spring Fluids at Mid-Ocean Ridges. Seafloor Hydrothermal Systems: Physical, Chemical, Biological, and Geological Interactions, American Geophysical Union, Geophysical Monograph Series. 91**:** 248-272.

Sohrin, Y. and Bruland, K. W. (2011). "Global status of trace elements in the ocean." Trends in Analytical Chemistry 30(8): 1291-1307.

Spiess, F. N., Macdonald, K. C., Atwater, T., Ballard, R., Carranza, A., Cordoba, D., Cox, C., Diazgarcia, V. M., Francheteau, J., Guerrero, J., Hawkins, J., Haymon, R., Hessler, R., Juteau, T., Kastner, M., Larson, R., Luyendyk, B., Macdougall, J. D., Miller, S., Normark, W., Orcutt, J. and Rangin, C. (1980). "East Pacific rise: Hot springs and geophysical experiments." Science 207(4438): 1421-1433.

Tivey, M. K. (2007). "Generation of Seafloor Hydrothermal Vent Fluids and Associated Mineral Deposits." Oceanography 20(1): 50-65.

Toner, B. M., Fakra, S. C., Manganini, S. J., Santelli, C. M., Marcus, M. A., Moffett, J., Rouxel, O., German, C. R. and Edwards, K. J. (2009). "Preservation of iron(II) by carbon-rich matrices in a hydrothermal plume." Nature Geoscience 2(3): 197-201.

Tribovillard, N., Algeo, T. J., Lyons, T. and Riboulleau, A. (2006). "Trace metals as paleoredox and paleoproductivity proxies: An update." Chemical Geology 232(1-2): 12-32.

Urey, H. C. (1947). "The thermodynamic properties of isotopic substances." Journal of the Chemical Society: 562-581.

van de Flierdt, T., Frank, M., Halliday, A. N., Hein, J. R., Hattendorf, B., Günther, D. and Kubik, P. W. (2003). "Lead isotopes in North Pacific deep water - implications for past changes in input sources and circulation patterns." Earth and Planetary Science Letters 209(1-2): 149-164.

Verlaan, P. A., Cronan, D. S. and Morgan, C. L. (2004). "A comparative analysis of compositional variations in and between marine ferromanganese nodules and crusts in the South Pacific and their environmental controls." Progress in Oceanography 63(3): 125-158.

Von Damm, K. L. (1995). Controls on the Chemistry and Temporal Variability of Seafloor Hydrothermal Fluids. Seafloor Hydrothermal Systems: Physical, Chemical, Biological, and Geological Interactions, American Geophysical Union, Geophysical Monograph Series. 91**:** 222-247.

Wang, X. H. and Muller, W. E. G. (2009). "Marine biominerals: perspectives and challenges for polymetallic nodules and crusts." Trends in Biotechnology 27(6): 375-383.

Wang, X. H., Schlossmacher, U., Wiens, M., Schroder, H. C. and Muller, W. E. G. (2009). "Biogenic Origin of Polymetallic Nodules from the Clarion-Clipperton Zone in the Eastern Pacific Ocean: Electron Microscopic and EDX Evidence." Marine Biotechnology 11(1): 99-108.

Warning, B. and Brumsack, H.-J. (2000). "Trace metal signatures of eastern Mediterranean sapropels." Palaeogeography, Palaeoclimatology, Palaeoecology 158(3–4): 293-309.

Watt, R. K. and Ludden, P. W. (1999). "Nickel-binding proteins." Cellular and Molecular Life Sciences 56(7): 604-625.

Wheat, C. G. and Mottl, M. J. (2000). "Composition of pore and spring waters from Baby Bare: Global implications of geochemical fluxes from a ridge flank hydrothermal system." Geochimica Et Cosmochimica Acta 64(4): 629-642.

Wheat, C. G., Mottl, M. J. and Rudnicki, M. (2002). "Trace element and REE composition of a low-temperature ridge-flank hydrothermal spring." Geochimica Et Cosmochimica Acta 66(21): 3693-3705.

Williams, H. M., Markowski, A., Quitté, G., Halliday, A. N., Teutsch, N. and Levasseur, S. (2006). "Fe isotope fractionation in iron meteorites: New insights into metal-sulphide segregation and planetary accretion." Earth and Planetary Science Letters 250(3–4): 486-500.

Wu, L. L., Beard, B. L., Roden, E. E. and Johnson, C. M. (2011). "Stable Iron Isotope Fractionation Between Aqueous Fe(II) and Hydrous Ferric Oxide." Environmental Science & Technology 45(5): 1847-1852.

Zhu, X. K., Guo, Y., Williams, R. J. P., O'Nions, R. K., Matthews, A., Belshaw, N. S., Canters, G. W., de Waal, E. C., Weser, U., Burgess, B. K. and Salvato, B. (2002). "Mass fractionation processes of transition metal isotopes." Earth and Planetary Science Letters 200(1-2): 47-62.

Chapitre I - Méthodes expérimentale et analytique pour l'analyse des compositions isotopiques en Ni dans divers matériaux géologiques terrestres

Chapter I – Experimental and analytical methods for analysis of Ni isotope compositions in various terrestrial geological materials

Avant-propos :

Ce premier chapitre est dédié aux méthodes expérimentale et analytique des isotopes des métaux qui ont été employées au cours de cette thèse. La première partie comprend l'article publié en 2013 dans la revue *Geostandards and Geoanalytical Research* sur la description du protocole d'analyse des isotopes du Ni. Le développement et la mise en place de la méthode a constitué une part importante de ce travail de thèse. En s'appuyant sur des protocoles déjà existants et décrits dans la littérature, ceux-ci ont été adaptés de manière à obtenir une méthode générale applicable à une large gamme de matrices géologiques. Outre la description sensu-stricto de la méthode, nous avons reporté dans cette publication les compositions isotopiques en Ni de matériaux géologiques de référence variés (nodules, sédiment dévonien, charbon, sol contaminé en métaux, nodules, granite, basalte, péridotite, dunite) ainsi qu'une sélection de basaltes, météorites de fer et quelques argiles profonds. Notre but était d'une part de fournir des valeurs de référence pour les études futures et d'autre part d'obtenir un premier aperçu global des fractionnements isotopiques du Ni dans différents réservoirs terrestres. C'est ainsi que d'une manière très intéressante les premiers résultats nous ont montré des fractionnements isotopiques significatifs entre les différents réservoirs terrestres montrant que les isotopes du Ni sont sensibles aux processus géologiques.

La seconde partie s'attache à détailler la procédure de pré-concentration du Ni à partir d'une matrice d'eau de mer. Les objets géologiques sur lesquels porte cette étude concernent en grande partie les encroûtements de fer-manganèse. Or nous avons précisé dans l'introduction de ce chapitre que ces dépôts étaient formés par précipitation à partir de l'eau de mer et que par conséquent les métaux de transition enrichis dans ces dépôts avaient également une origine océanique préjugeant du fait que la composition isotopique en Ni enregistrée dans ces dépôts reflètent celle de l'eau de mer. Ainsi, la valeur isotopique de l'eau de mer est indispensable pour savoir où se situent réellement nos échantillons par rapport à l'eau de mer la source à partir de laquelle nos échantillons se sont formés.

Après plusieurs tentatives utilisant différentes méthodes de pré-concentration des métaux traces de l'eau de mer, la méthode décrite ci-après en utilisant une résine epoxy liée au complexe 8HQ, est celle qui s'est révélée être la bonne pour mesurer les compositions isotopiques en Ni.

Partie 1 – Article publié dans *Geostandards and Geoanalytical Research* (2013) “Nickel Isotope Variations in Terrestrial Silicate Rocks and Geological Reference Materials Measured by MC-ICP-MS”

Part 1 – Article published in Geostandards and Geoanalytical Research (2013) “Nickel Isotope Variations in Terrestrial Silicate Rocks and Geological Reference Materials Measured by MC-ICP-MS”

GEOSTANDARDS and GEOANALYTICAL RESEARCH

Nickel Isotope Variations in Terrestrial Silicate Rocks and Geological Reference Materials Measured by MC-ICP-MS

Bleuenn **Gueguen** (1, 2)*, Olivier **Rouxel** (1, 2), Emmanuel **Ponzevera** (2), Andrey **Bekker** (3) and Yves **Fouquet** (2)

(1) Institut Universitaire Européen de la Mer, UMR 6538, Université de Bretagne Occidentale, BP 80, F-29280, Plouzané, France
(2) IFREMER, Centre de Brest, Unité Géosciences Marines, 29280, Plouzané, France
(3) Department of Geological Sciences, University of Manitoba, Winnipeg, R3T 2N2, Canada
* Corresponding author. e-mail: bleuenn.gueguen@gmail.com

Although initial studies have demonstrated the applicability of Ni isotopes for cosmochemistry and as a potential biosignature, the Ni isotope composition of terrestrial igneous and sedimentary rocks, and ore deposits remains poorly known. Our contribution is fourfold: (a) to detail an analytical procedure for Ni isotope determination, (b) to determine the Ni isotope composition of various geological reference materials, (c) to assess the isotope composition of the Bulk Silicate Earth relative to the Ni isotope reference material NIST SRM 986 and (d) to report the range of mass-dependent Ni isotope fractionations in magmatic rocks and ore deposits. After purification through a two-stage chromatography procedure, Ni isotope ratios were measured by MC-ICP-MS and were corrected for instrumental mass bias using a double-spike correction method. Measurement precision (two standard error of the mean) was between 0.02 and 0.04‰, and intermediate measurement precision for NIST SRM 986 was 0.05‰ (2*s*). Igneous- and mantle-derived rocks displayed a restricted range of $\delta^{60/58}$Ni values between -0.13 and +0.16‰, suggesting an average BSE composition of +0.05‰. Manganese nodules (Nod A1; P1), shale (SDO-1), coal (CLB-1) and a metal-contaminated soil (NIST SRM 2711) showed positive values ranging between +0.14 and +1.06‰, whereas komatiite-hosted Ni-rich sulfides varied from -0.10 to -1.03‰.

Keywords: nickel, stable isotopes, MC-ICP-MS, geological reference materials, Bulk Silicate Earth, abiotic fractionation.

Bien que les premières études démontrent la pertinence des isotopes du nickel en cosmochimie et en tant que signature biologique, la composition isotopique du nickel des roches ignées et sédimentaires terrestres ainsi que celle des dépôts de minerais est encore très peu connue. Notre contribution s'organise en quatre axes, (a) détailler la procédure analytique pour la détermination des compositions isotopiques en nickel, (b) déterminer la composition isotopique de matériaux géologiques de référence variés, (c) estimer la composition isotopique de la Terre Silicatée Globale (BSE) par rapport au standard isotopique de référence de nickel NIST SRM 986, et (d) reporter la gamme des fractionnements isotopiques du nickel dépendants de la masse dans les roches magmatiques et les dépôts de minerais. Après purification suivant une procédure de chromatographie en deux étapes, les rapports isotopiques du nickel ont été mesurés par MC-ICP-MS puis corrigés du biais de masse instrumental par la méthode du double-spike. La fidélité de nos mesures (erreur standard de la moyenne) est comprise entre 0.02 et 0.04‰, et la précision de mesure intermédiaire pour le NIST SRM 986 est de 0.05‰ (2s). Les roches ignées et mantelliques montrent une gamme restreinte de valeurs isotopiques $\delta^{60/58}$Ni entre -0.13 et +0.16‰, ce qui suggère une composition moyenne de la BSE à +0.05‰. Les nodules de manganèse (Nod A1; P1), le shale (SDO-1), le charbon (CLB-1) et le sol contaminé en métaux (NIST SRM 271) donnent des valeurs $\delta^{60/58}$Ni positives comprises entre +0.14 et +1.06‰, tandis que les sulfures riches en nickel présents dans les komatiites ont des valeurs négatives allant de -0.10 à -1.03‰.

Mots-clés : nickel, isotopes stables, MC-ICP-MS, matériaux géologiques de référence, Terre Silicatée Globale, fractionnement abiotique.

Received 03 Aug 12 – Accepted 17 Dec 12

doi: 10.1111/j.1751-908X.2013.00209.x

Nickel has five naturally occurring isotopes, that is, ^{58}Ni, ^{60}Ni, ^{61}Ni, ^{62}Ni and ^{64}Ni, with abundances of 68%, 26%, 1.1%, 3.6% and 0.9%, respectively. To date, Ni isotope studies have been applied mainly to cosmochemical processes (e.g., Morand and Allegre 1983, Shimamura and Lugmair 1983, Tanimizu and Hirata 2006, Moynier *et al.* 2007, Cook *et al.* 2008), specifically to detect any ^{60}Ni anomaly in iron meteorites resulting from the rapid decay of ^{60}Fe, which has a half-life of 2.62 Myr (Rugel *et al.* 2009). As Ni occurs solely in one natural valence state (Ni^{2+}) in the Earth's crust, redox-controlled processes will not induce mass-dependent isotopic fractionations as is the case for other transition metals such as Fe, Mo, Cr and Cu (e.g., Albarede and Beard 2004, Anbar and Rouxel 2007). It implies that any observed fractionation in natural environments should be the result of either biotic processes, such as assimilation of Ni by micro-organisms, or abiotic processes such as chemical precipitation or adsorption in aqueous systems, or during mineral crystallisation. However, despite its potential, the understanding of Ni isotope systematics of terrestrial reservoirs lags behind other non-traditional isotope systems. An initial study by Tanimizu and Hirata (2006) demonstrates significant Ni isotope fractionation in magmatic sulfides, and only two studies subsequently report Ni isotope composition of crustal rocks (Cameron *et al.* 2009, Gall *et al.* 2012). Interestingly, a recent study demonstrated that methanogens – micro-organisms producing methane in anaerobic environments – fractionate ^{60}Ni/^{58}Ni ratios by up to 1.5‰ by preferential incorporation of the low atomic number isotope (Cameron *et al.* 2009). Identification of such biosignatures in complex natural systems, however, remains uncertain. More recently, Fujii *et al.* (2011) report theoretical and experimental constraints on abiotic Ni isotope fractionations among aqueous species (i.e., chlorides, sulfides, sulphates, carbonates and hydroxides). The experimental results indicate that fractionation among Ni ligands, such as Ni^{2+}, $NiSO_4$, $NiCO_3$, $NiHCO_3^+$, $NiCl^+$ and $NiOH^+$, is up to 2.5‰ in $\delta^{60/58}$Ni values and encompasses the magnitude of fractionation during biological processes associated with methanogens (Cameron *et al.* 2009).

Since a growing number of studies apply Ni isotope systematics to natural samples, we aimed this study at (a) developing an experimental and analytical protocol to perform high-precision Ni isotopic determination in geological samples, including igneous rocks and sediments by multicollector-inductively coupled plasma-mass spectrometry (MC-ICP-MS) and using a double-spike method to correct for instrumental mass bias; (b) providing a substantial and relevant data set of Ni isotope composition for RMs to allow a comparison of Ni isotope data among different laboratories and with the purpose of demonstrating that significant Ni isotope variations are detectable in a large range of rock types occurring on Earth; and (c) assessing Ni isotopic composition of the Bulk Silicate Earth (BSE) necessary for interpreting Ni isotope fractionation in terrestrial rocks, based on analyses of mantle-derived rocks and komatiites.

Materials and methods

Sample description

Geological reference materials: Samples analysed in this study include several USGS geological reference materials, namely BHVO-2, a basalt from Hawaii (USA); BIR-1, a basalt from Iceland; DNC-1, a dolerite sampled in North Carolina (USA); DTS-1, a dunite sample from the Twin Sisters area in the Washington state (USA); PCC-1, a peridotite sample from the Twin Sisters area in the Washington State (USA); Nod-A-1 and Nod-P-1 representing composites of manganese nodules from the Atlantic (Blake Plateau at 788 m depth) and Pacific (at 4300 m depth) oceans, respectively; CLB-1, a coal from the Lower Bakerstown coal bed (Bettinger Mine in the Castleman Coalfield, MD, USA); SDO-1, a Devonian shale from Morehead, Kentucky (USA); and the granite G-2 collected in the Sullivan quarry (Rhode Island, USA). We also analysed NIST SRM 2711, a modern soil RM affected by metal contamination (Montana, USA). Further description of these RMs and their chemical composition can be found in the study Govindaraju (1994). For Mn-nodule RMs, Axelsson *et al.* (2002) provide an intercomparison study of trace and major element concentrations. In addition, the *ca.* 3.8 Ga IF-G Banded Iron Formation geological reference material provided by the CRPG (Nancy, France) was also analysed.

Selected samples of basalts, mantle-derived rocks and marine sediments: Fresh volcanic glass and olivine from seafloor basalts from recent olivine-phyric pillow lava flows were selected from the site *FeMO Deep* at the base of Loihi Seamount (Edwards *et al.* 2011). These samples were recovered during the FeMO cruise by the R/V Thompson (University of Washington). Samples of serpentinized ultramafic rocks that were recovered from the Logatchev hydrothermal field (Rouxel *et al.* 2004, Fouquet *et al.* 2010) during the MICROSMOKE cruise by the R/V Atalante (Ifremer-Genavir) were also analysed. Olivine and fresh glass of the FeMO Deep basalts were separated by hand-picking to evaluate potential Ni isotope fractionation between olivine and glass, whilst serpentinite powders were prepared from bulk rocks. In addition, samples of altered and fresh basalts, and deep-sea clays (from the top of the stratigraphic sequence, in the first few metres below the seafloor) recovered at IODP site 1149 (hole C, Pacific

Ocean, Eastern Japan) during cruise 185 by the R/V Joides Resolution (Plank *et al.* 2000, Rouxel *et al.* 2003) were also studied. Together with volcanic rocks available as RMs, this selected set of igneous and mantle-derived rocks allowed the estimation of the BSE Ni isotope composition and potential Ni isotope fractionation during olivine crystallisation.

Komatiite-hosted Ni-rich sulfides: Bulk rock samples comprising both komatiites and associated Ni-rich sulfide ores were analysed from two areas: the Agnew-Wiluna greenstone belt in Western Australia and the Abitibi greenstone belt in Canada (Bekker *et al.* 2009). The *ca.* 2.7 Ga Agnew-Wiluna greenstone belt is composed of a deep-marine volcanic and volcaniclastic sequence with felsic and mafic to ultramafic compositions, which locally contains large lenses of volcanogenic massive sulfides, sulfidic cherts, carbonaceous shales, and laterally variable komatiites with cumulates, thin spinifex-textured units and komatiitic basalts. Mineralisation occurs as disseminated sulfides, massive sulfide ores or sulfide aggregates comprising mostly pentlandite and pyrrhotite grains. The Mount Keith and Perseverance sites of the Agnew-Wiluna greenstone belt are among the largest komatiite-hosted Ni-Cu-PGE ore deposits. Samples from the Abitibi greenstone belt in Canada are from the Alexo mine, where Fe-Ni-Cu-PGE sulfide mineralisation occurs in a komatiitic unit with olivine cumulates (Naldrett and Mason 1968, Muir and Comba 1979, Houlé *et al.* 2012). Nickel-rich sulfide ores selected for this study include massive and blebby sulfides; in addition, brown olivine associated with disseminated Ni-sulfides was also analysed.

Iron meteorites: Two iron meteorites, namely Gibeon and Nantan, were selected for testing the experimental and analytical procedure because of their very high Ni content and previously determined Ni isotope compositions (Moynier *et al.* 2007, Cook *et al.* 2008).

Experimental procedure

Reagents and materials: Ultra-pure 18.2 MΩ cm water made with a Millipore system (Milli-Q grade) was used. Both concentrated nitric and hydrochloric acids used for dissolution and column work were double-distilled from reagent-grade acids using a Cleanacids® distillation apparatus (Analab, Bischheim, France). Acids of lower molarity were prepared from these double-distilled acids. All plastic wares were cleaned with cold 1.2 mol l^{-1} HCl (reagent grade), whereas Savillex® Teflon beakers were washed with hot 8 mol l^{-1} HNO_3 (reagent grade).

The double-spike used was prepared with spikes ^{61}Ni (batch 127890) and ^{62}Ni (batch 233026) provided by the Oak Ridge National Laboratory. Original spikes in metal form were dissolved separately in concentrated distilled HNO_3 and evaporated at 70 °C. Aliquots of the spikes were mixed together in known proportion to obtain a final double-spike solution at a concentration of 500 μg g^{-1} and with a $^{61}Ni/^{62}Ni$ ratio of ~ 1. The double-spike concentration was then determined by MC-ICP-MS using the nickel NIST SRM 986 standard solution. Considering the limited amount of spike used, we did not attempt to determine the double-spike isotope composition through a gravimetric approach.

Sample digestion: Depending on their Ni concentrations, between 50 and 250 mg of sample powder was weighed in Teflon beakers. Non-siliceous materials such as Mn nodules, sulfides and iron meteorites were digested with 5 ml of concentrated HNO_3 and 5 ml of 6 mol l^{-1} HCl, whilst silicate rocks were digested with a mixture of 2 ml of concentrated HF (28 mol l^{-1} Trace Metal Grade or Suprapure grade) and 6 ml of concentrated HNO_3. Closed beakers were put on a hot Teflon plate at 70–80 °C overnight, and then caps were removed to allow evaporation to dryness. The solid residue was then dissolved in a mixture of concentrated HNO_3 and 6 mol l^{-1} HCl and further evaporated to dryness at a temperature of 70–80 °C. This latter step was repeated to achieve complete digestion of non-siliceous rocks and ensure removal of potential fluorides formed in the course of the first dissolution step of siliceous materials. Final solutions were prepared by dissolving the residue in 10 ml of 6 mol l^{-1} HCl, and one drop of optima-grade H_2O_2 was added to each sample to ensure complete oxidation of Fe.

As explained below, all sample batches, generally including twenty-four samples, were processed with duplicates of BHVO-2, DTS-1, PCC-1, Nod-P-1 or Nod-A-1 reference materials, one procedural blank and one pure mono-elemental solution of Ni (Ni Plasma Cal standard solution made by SCP Science). Note that the shale SDO-1 and the coal CLB-1 were ashed prior to digestion at 600 °C to oxidise organic matter before chemical dissolution.

Nickel chemical purification by ion-exchange chromatography columns: The chemical purification protocol used was adapted from previous work by Cameron *et al.* (2009) and Cook *et al.* (2007) and followed a two-stage procedure. The first set of ion-exchange chromatography columns (i.e., disposable polypropylene columns equipped with a large-volume (15 ml) reservoir) was filled with 3 ml (wet volume) of anionic resin AG1-X8 in the chloride form

(Bio-Rad 100-200 mesh). The washing procedure of the columns was begun by loading 15 ml of ultra-pure water, then 15 ml of 3 mol l^{-1} HNO_3, 15 ml of ultra-pure water and 5 ml of 0.24 mol l^{-1} HCl. Conditioning was carried out with 5 ml of 6 mol l^{-1} HCl followed by the loading of a fraction of the final solutions in 6 mol l^{-1} HCl on the columns. The final solutions obtained after digestion were kept as archive solutions, and only a split was taken for ion-exchange chromatography column work. Nickel elution was achieved by passing through 15 ml of 6 mol l^{-1} HCl during which Fe, Zn and most of the Co and Cu were retained on the resin. The eluted Ni fraction was then taken to dryness at 100–120 °C on a hot plate and then dissolved in 1 ml of 0.24 mol l^{-1} HCl. This solution was then purified on a second series of chromatography columns filled with a specific nickel resin commercially available from Eichrom (Ni-Spec). As discussed below, the use of the Ni-spec resin was required to ensure complete removal of all matrix elements remaining after the anion-exchange purification step, including major rock-forming elements such as alkali and alkaline earth metals.

The specific Ni-resin, made of polymethacrylate, contains a dimethylglyoxime (DMG) molecule that scavenges Ni at pH 8–9 to form an insoluble Ni-DMG complex retained on the resin. To prevent the co-precipitation of metals in the form of insoluble hydroxides, which may inhibit the formation of the Ni-DMG complex on the resin, ammonium citrate was added to buffer solutions at pH 8–9. About 0.5 ml (wet volume) of Ni-Spec resin was loaded into disposable columns and initially washed with ultrapure water. Conditioning was made using a mixture of 2.1 ml of 0.2 mol l^{-1} ammonium citrate and 11.7 mol l^{-1} optima-grade ammonia adjusted to pH 8–9. Before loading the sample onto the column, 1 ml of the initial solution in 0.24 mol l^{-1} HCl was mixed with 0.3 ml of 1 mol l^{-1} ammonium citrate and 0.1 ml of 11.7 mol l^{-1} optima-grade ammonia to maintain a pH of 8–9. The matrix was then eluted with 4.2 ml of mixed ammonium citrate and ammonia solution and 4 ml of ultra-pure water. Nickel was quantitatively eluted from the resin with 8 ml of 3 mol l^{-1} HNO_3, which ensured oxidation and destruction of the Ni-DMG complex with nitric acid. This technique therefore prevented any regeneration and reuse of the resin. The eluted Ni solution was evaporated to dryness on a hot plate at 90 °C, and the residue dissolved in 0.28 mol l^{-1} HNO_3 when it was ready for isotope determination.

Before chemical purification through the Ni-spec column, a known amount of double-spike solution was added to each sample. As explained below, the double-spike amount was chosen to be equal to the Ni content in the sample. Chemistry yields were determined using the measured spike/natural ratio (i.e., $^{62}Ni/^{58}Ni$). Chemistry blanks were also spiked, which enabled us to determine procedural blank values. Chemistry yields through Ni-spec resin were generally better than 85%, whilst yields through AG1-X8 resin were always quantitative. In contrast to another recently published experimental procedure for nickel purification (Gall *et al.* 2012), our yields were not dependent on the geological matrix and amount of nickel loaded on the column. Nickel procedural blanks were generally *ca.* 3–4 ng, and as between 0.5 and > 1 μg of nickel was generally processed through chemistry (see footnotes in Tables 3–7), this blank level was considered negligible and did not require any correction. However, when smaller sample sizes are analysed, care should be taken to reduce these blanks.

Mass spectrometry procedure and data reduction scheme

Delta notation: Nickel isotope composition is expressed following the conventional stable isotope delta notation, that is, sample isotopic ratios are expressed relative to a standard ratio as per mil deviation (‰) following:

$$\delta^{x/58}Ni = (R_{spl}/R_{NIST} - 1) \times 1000 \quad (1)$$

where R_{spl} and R_{NIST} are the isotopic ratios $^{x}Ni/^{58}Ni$ of the unknown sample and the nickel NIST SRM 986 reference material, respectively; ^{x}Ni stands for one of the following three isotopes: ^{60}Ni, ^{61}Ni or ^{62}Ni, and the light isotope, ^{58}Ni, is placed in the denominator (it is also the most abundant). However, note that following Coplen's (2011) recommendation, omission of the multiplication factor of 1000 in the delta notation could be permitted because technically it belongs to the ‰ symbol rather than to the δ notation. The ratio that will be used to describe the data in this study is $^{60}Ni/^{58}Ni$, and it will be reported as $\delta^{60/58}Ni$.

MC-ICP-MS settings: All samples were analysed on a Neptune (Thermo-Electron) MC-ICP-MS operated at the Pôle Spectrométrie Océan (PSO) located at IFREMER, Centre de Brest, France. This instrument was equipped with nine Faraday cups that allowed simultaneous measurement of ^{58}Ni, ^{60}Ni, ^{61}Ni and ^{62}Ni, ^{63}Cu and ^{65}Cu isotopes, as well as isobarically interfering Fe monitored at mass ^{57}Fe. The instrument was run in either a medium- or high-mass-resolution mode, but the medium-resolution mode was sufficient to resolve argide and oxide interferences on Ni isotopes as discussed below. Nickel ion beam intensity in a

medium-resolution mode with the ApexQ was typically ~ 50 –75 V per μg ml^{-1} on ^{58}Ni. Although both sample and skimmer cones (X cone) were made of Ni, their contribution to the Ni isotopic ratios of samples was negligible, because the measured instrumental blank signal intensity on mass ^{58}Ni did not exceed 0.5 mV and 0.2 mV on the spiked isotope ^{62}Ni. This also indicated that the use of other cone types (e.g., Al or Pt cones) was unnecessary, as already demonstrated by Moynier *et al.* (2007). The inlet system was either a spray chamber (i.e., Stable Introduction System (SiS) coupled with a 50 μl min^{-1} PFA micro-concentric nebuliser) or an ApexQ (ESI, USA) desolvation introduction system.

Fifty measurement cycles, each having an integration time of 4 s, were performed on samples, whereas washout consisted of ten measurement cycles, each with an integration time of 4 s. The total time required per analysis was therefore approximately 4 min (analysis plus washout).

The main interferences on Ni isotopes included Fe (e.g., ^{58}Fe on ^{58}Ni), Ar or other element (e.g., Ca) oxides generated in the argon plasma with identical masses (e.g., $^{40}Ar^{18}O^+$ on $^{58}Ni^+$), and doubly charged ions (e.g., $^{124}Xe^{2+}$ on ^{62}Ni). The latter was negligible considering that (a) Xe has a high first-ionisation potential, and (b) no $^{124}Xe^{2+}$ was measured on mass 62 in the blank solution; and (c) the use of ultrapure argon resulted in negligible Xe intensity, as previously reported by Fehr *et al.* (2004) for Te isotope measurements with potential important isobaric interferences from Xe isotopes. The other major potential spectral interference on ^{64}Ni is from ^{64}Zn. As the Faraday cup configuration of the mass spectrometer did not allow simultaneous measurement of the interference-free ^{66}Zn isotope, we did not attempt to measure the ^{64}Ni isotope in this study. Argide and oxide interferences included $^{36}Ar^{24}Mg^+$ and $^{44}Ca^{16}O^+$ on $^{60}Ni^+$; $^{36}Ar^{25}Mg^+$, and $^{38}Ar^{23}Na^+$ on $^{61}Ni^+$; $^{36}Ar^{26}Mg^+$, $^{38}Ar^{24}Mg^+$ and $^{46}Ca^{16}O^+$ on $^{62}Ni^+$; $^{23}Na^{35}Cl^+$, $^{40}Ar^{18}O^+$ and $^{42}Ca^{16}O^+$ on $^{58}Ni^+$. Medium-resolution (and also high-resolution) modes allowed us to resolve polyatomic interferences on $^{58}Ni^+$, which still remained significant even when using the ApexQ (ESI, USA) system due to the production of argon oxide.

Fe isotope interference correction: Consideration of isobaric interference from Fe was critical given that it affects the major isotope ^{58}Ni. Therefore, even if Fe was quantitatively separated from Ni during chemical purification prior to analysis, ^{57}Fe was systematically measured and the interference of ^{58}Fe on ^{58}Ni was corrected using Equation (2):

$$\left(^{58}Fe/^{57}Fe\right)_{measured} = \left(^{58}Fe/^{57}Fe\right)_{natural} \cdot \left(M_{58}/M_{57}\right)^{f_{Fe}} \quad (2)$$

where $\left(^{58}Fe/^{57}Fe\right)_{measured}$ is the raw ratio measured by MC-ICP-MS; $\left(^{58}Fe/^{57}Fe\right)_{natural}$ is the corrected natural iron ratio; M_{58} is the atomic weight of ^{58}Fe; M_{57} is the atomic mass of ^{57}Fe; and f_{Fe} is the mass-discrimination factor considered equivalent to the mass-discrimination factor of nickel (f_{Ni}), which is generally around 1.8. The discrimination factor was estimated based on measurements of iron and nickel mixed solution at the beginning of each analytical session. It is important to note that this correction is only an approximation because the natural Fe isotope ratio may vary by as much as 3‰ per mass unit (e.g., Dauphas and Rouxel 2006). However, this correction was negligible for Ni isotopes (< 0.1‰) given that iron interference was very small after chemical separation, when iron was quantitatively removed from the analyte. Additionally, we estimated the effect of iron on the isotopic composition of nickel by measuring several NIST SRM 986 solutions doped with various amounts of iron. The results (see Table 1) show that minor amounts of iron (Fe/Ni ratios from 0.001 to 0.010) did

Table 1.
Nickel isotopic composition (in ‰) of NIST SRM 986 solutions doped in Ca, S or Fe

Doped element	Element/Ni ratio[a]	$\delta^{60/58}$Ni (‰)[b]	2*s*[c]
Ca	0.5	-0.19	0.14
Ca	1	-0.18	0.14
Ca	2	-0.05	0.14
S	0.5	-0.01	0.14
S	1	-0.02	0.14
S	2	-0.06	0.14
Fe	0.001	-0.11	0.09
Fe	0.01	-0.06	0.09
Fe	0.001	-0.05	0.09
Fe	0.01	-0.09	0.09

[a] The elemental ratio corresponds to a ratio of element concentrations in the solution analysed by MC-ICP-MS.
[b] Isotopic compositions of NIST SRM 986 Fe doped solutions calculated without application of the Fe correction.
[c] 2*s* is the two standard deviation value calculated for all pure NIST SRM 986 solutions analysed during the session in calibrator-sample-bracketing mode.

not produce any bias in Ni isotope ratios. The Ni isotope composition of NIST SRM 986 Fe-doped solutions was corrected for instrumental mass bias using the calibrator-bracketing method (a non-doped NIST SRM 986 solution was measured before and after each Fe-doped NIST SRM 986 solution), which explains why the analytical precision was lower than for the samples corrected with the double-spike.

Interelemental correction of Ni instrumental mass bias using Cu isotopes: This method is based on adding a known amount of Cu standard solution (i.e., NIST SRM 976), which is used to correct for instrumental mass bias. As demonstrated in previous studies (e.g., Marechal *et al.* 1999), instrumental mass bias on MC-ICP-MS follows an exponential mass-fractionation law with the fractionation factor 'f' being specific for each element. The linear relationship (plot not shown) between logarithms of Ni isotope ratios of NIST SRM 986 and Cu isotope ratios of NIST SRM 976 confirmed that (a) Cu isotopes follow the same exponential mass-fractionation law as Ni isotopes; (b) f_{Cu}/f_{Ni} was constant during individual analytical sessions, which allowed us to use f_{Cu} determined on NIST SRM 976 (Equation 3) to calculate f_{Ni} (Equation 4).

$$(R_{meas}/R_{true})_{Cu} = (M^{65}Cu/M^{63}Cu)^{fCu} \quad (3)$$

$$(R_{meas}/R_{true})_{Ni} = (M^{60}Ni/M^{58}Ni)^{fNi} \quad (4)$$

Considering that nickel recovery yield on the Ni-spec resin purification step ranged from 85% to 99%, it is possible that Cu-corrected Ni isotope compositions of purified samples were affected by significant analytical artefacts. Hence, this correction method is only suitable for Ni-rich ores and iron meteorites purified through anion-exchange resin as used in previous studies (Quitté *et al.* 2006, Moynier *et al.* 2007, Cook *et al.* 2008). In addition, this approach was used to compare Ni isotope data obtained using Cu-doping and double-spike methods.

Determination of the double-spike composition: In theory, double-spike composition can be determined either gravimetrically or after normalisation to a known isotopic reference material, such as NIST SRM 986 (Gramlich *et al.* 1989). In practice, however, the gravimetric technique does not yield a sufficiently precise composition for small quantities of spike. In addition, isotope ratios might be influenced by the type of instrument and instrumental settings, and it is therefore critical to cross-calibrate both isotope reference materials and spike on the same instrument. Indeed, as discussed previously by Siebert *et al.* (2001), uncertainties on the natural spike and RM isotope composition do not introduce bias providing that both double spike and RM are calibrated on the same instrument and that isotope data are expressed as $\delta^{60/58}$Ni values.

The isotopic composition of NIST SRM 986 was first determined by internal normalisation using a $^{60}Ni/^{58}Ni$ ratio of 0.385199 ± 0.000728 (2*s*) (Gramlich *et al.* 1989). This ratio was then used to calculate the instrumental mass-discrimination factor f_{Ni}, which allowed the calculation of other isotopic ratios, that is, $^{62}Ni/^{58}Ni$ and $^{61}Ni/^{58}Ni$. The isotopic composition of the nickel double spike was then determined using the Cu-doping correction method to determine the true $^{60}Ni/^{58}Ni$, $^{61}Ni/^{58}Ni$ and $^{62}Ni/^{58}Ni$ ratios of the spike versus NIST SRM 986. A Cu-doped pure standard solution was used to calculate the f_{Cu}/f_{Ni} ratio, which was then applied to Cu-doped pure double-spike solution. To avoid cross-contamination between the standard solution and the double-spike solution, an extended rinse

Table 2.
Abundance (in %) of Ni isotopes for NIST SRM 986 and double-spike

Standard solution	Isotope	Abundance (%)	2*s*[a]
NIST SRM 986[b]	^{58}Ni	68.07689	0.00592
NIST SRM 986[b]	^{60}Ni	26.22315	0.00514
NIST SRM 986[b]	^{61}Ni	1.13989	0.00043
NIST SRM 986[b]	^{62}Ni	3.63453	0.00114
NIST SRM 986[b]	^{64}Ni	0.92555	0.00060
Double-spike	^{58}Ni	1.05106	0.00071
Double-spike	^{60}Ni	0.76974	0.00071
Double-spike	^{61}Ni	51.28893	0.04432
Double-spike	^{62}Ni	46.61106	0.04753
Double-spike	^{64}Ni	0.27920	0.00055

[a] 2*s* of double-spike isotopic composition is the two standard deviation value calculated from ratios of repeated measurements corrected for blank and Fe interference but not corrected for instrumental mass bias.
[b] NIST SRM 986 values are from Gramlich *et al.* (1989).

time and 'on-peak zero' method were used. Results are presented in Table 2.

Double-spike correction scheme: The double-spike calculation procedure was based upon the method described by Siebert *et al.* (2001) for Mo isotope determination. The double-spike method can be visualised as a three-dimensional diagram where axes represent the three measured isotopic ratios as specified above. Line and plane intercepts, defined by isotopic compositions of the double-spike, standard solution and sample measured by MC-ICP-MS, are used to determine fractionation factors between the measured and corrected isotopic ratios (Albarede and Beard 2004). A template was established to calculate those plane intercepts by making iterative calculations to account for both natural and instrumental fractionation factors, which were applied subsequently to the measured raw isotope ratios. At least two nested iterations were run to properly obtain the fractionation factors. The template could be performed either on an Excel™ (Microsoft) spreadsheet or using Matlab™ (MathWorks Inc., Massachusetts, USA).

To obtain satisfactory precision, fifty analytical cycles (~ 4 min of total integration time) were acquired during sample analysis. Each sample analysis was bracketed by the measurements of NIST SRM 986 nickel solutions at the same nickel concentration and spike/standard ratio as that of the samples. The double-spike method offers several advantages relative to the Cu-doping or sample-calibrator-bracketing methods by allowing (a) the correction of potential isotopic fractionation during chemical separation through Ni-spec resin; (b) the determination of precise and accurate nickel concentrations of samples using the isotopic dilution method; (c) better overall analytical precision (because corrected ratios were less affected by the stability of the instrumental mass bias and the assumption that f_{Cu}/f_{Ni} remained constant throughout the analytical session); and (iv) accurate measurement of very small amounts of nickel, down to 50 ng, by MC-ICP-MS.

Results of analytical method development

Measurement precision and limit of detection

For each analysis, the measurement precision is reported as a two standard error of the mean calculated on fifty cycles of measurement during MC-ICP-MS acquisition. With the double-spike correction, the precision of $\delta^{60/58}$Ni values was usually around ± 0.02–0.04‰ (2SE) for samples with nickel concentrations ranging from 100 ng g^{-1} to 1 µg g^{-1}. Precision at lower concentrations was assessed by analysing NIST SRM 986 solution at different concentrations. In Figure 1, the two standard error of the mean calculated for each analysis is reported against the nickel concentrations and shows that below 30 ng g^{-1} the precision slightly deteriorated to about ± 0.07‰, but became worse at 10 ng g^{-1} and lower concentrations, for example, 2SE = 0.59‰ at 2 ng g^{-1} of nickel.

For optimum measurement precision during isotope measurements, we usually ran samples with nickel concen-

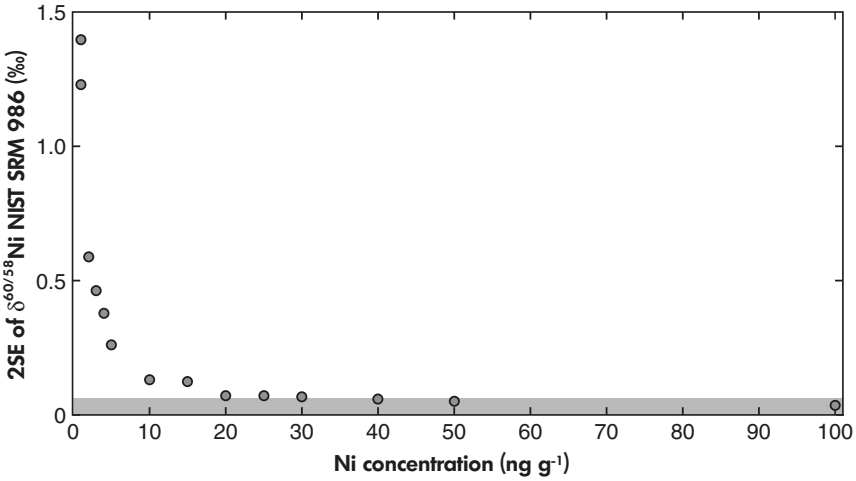

Figure 1. Plot of two standard errors (2SE) of delta values versus Ni concentration (in ng g^{-1}) of NIST SRM 986. These measurements were taken to assess the effect of Ni concentration on the precision of the determination of Ni isotopes. Nickel concentration in solution above 40 ng g^{-1} during MC-ICP-MS analysis was necessary to obtain satisfactory precision, that is, 2SE < 0.06‰, shown on the figure by the grey band (see text for further details).

Table 3.
Nickel isotope composition (in ‰) of mafic rock reference materials

Sample name	Rock type	Ni (μg g^{-1})**	$\delta^{60/58}$Ni (‰)	2SE	Number of duplicates	2*s***
USGS BHVO-2†	Basalt, Hawaii	112	0.014	0.026		
USGS BHVO-2†*	Basalt, Hawaii	110	0.023	0.031		
USGS BHVO-2††	Basalt, Hawaii	113	0.049	0.026		
USGS BHVO-2†††	Basalt, Hawaii	111	0.020	0.029		
USGS BHVO-2†††*	Basalt, Hawaii	108	-0.011	0.029		
USGS BHVO-2††††	Basalt, Hawaii	110	0.003	0.029		
USGS BHVO-2†††††	Basalt, Hawaii	115	-0.003	0.019		
USGS BHVO-2†††††*	Basalt, Hawaii	115	0.006	0.027		
USGS BHVO-2†††††*	Basalt, Hawaii	112	-0.006	0.036		
USGS BHVO-2†††††*	Basalt, Hawaii	114	-0.003	0.036		
USGS BHVO-2†††††*	Basalt, Hawaii	112	-0.030	0.032		
Average BHVO-2			**0.006**	–	***n* = 11**	**0.041**
USGS BHVO-2†††††$	*Basalt, Hawaii*	*105*	*-0.067*	*0.017*		
USGS BIR-1†	Basalt, Iceland	159	0.105	0.020		
USGS BIR-1†*	Basalt, Iceland	159	0.115	0.026		
USGS BIR-1††	Basalt, Iceland	165	0.140	0.020		
Average BIR-1			**0.120**	–	***n* = 3**	**0.035**
USGS DNC-1†	Dolerite	242	0.165	0.027		
USGS DNC-1†*	Dolerite	244	0.115	0.023		
USGS DNC-1††	Dolerite	239	0.118	0.021		
Average DNC-1			**0.132**	–	***n* = 3**	**0.056**
USGS DTS-1†	Dunite	2327	-0.061	0.028		
USGS DTS-1†*	Dunite	2451	-0.100	0.026		
USGS DTS-1††	Dunite	2171	-0.083	0.022		
USGS DTS-1†††	Dunite	2199	-0.039	0.034		
Average DTS-1			**-0.071**	–	***n* = 4**	**0.053**
USGS PCC-1†	Peridotite	2245	0.111	0.035		
USGS PCC-1†*	Peridotite	2369	0.100	0.026		
USGS PCC-1†*	Peridotite	2188	0.149	0.022		
USGS PCC-1††	Peridotite	2204	0.097	0.023		
USGS PCC-1†	Peridotite	2241	0.136	0.043		
Average PCC-1			**0.119**	–	***n* = 5**	**0.045**

*This symbol denotes the archive solution of a digested sample that was processed several times through the identical procedure of chemical purification to obtain duplicates of the same sample that were processed through the same chemistry.
†This symbol stands for different powder digestions, e.g., five digestions were made for BHVO-2 and two digestions for PCC-1.
$Samples were usually spiked prior to the second chromatography column step (Ni-spec resin), the BHVO-2 sample (in italic) was spiked only after the entire procedure of purification.
**Ni concentrations (in μg g^{-1}) were determined by isotope dilution after measurement on MC-ICP-MS. Amount of Ni processed through chemistry was between 0.5 and 25 μg.
***Two standard deviation (2*s*) calculated on values of the whole batch of identical samples (see text); number of samples (*n*) is specified.

trations of 100–200 ng g^{-1}, when using either the ApexQ or SiS introduction systems on the MC-ICP-MS instrument.

Intermediate measurement precision of NIST SRM 986 and RMs

A spiked NIST SRM 986 solution was measured before and after each sample in a manner similar to the calibrator-sample bracketing (CSB) analysis. We found that the Ni isotope ratios of NIST SRM 986 calculated using the double-spike method may deviate by up to 0.2‰ per mass unit between analytical sessions but remained constant within 0.02–0.05‰ (2*s*) during each analytical session. As a result, we normalised delta values of the samples relative to the average NIST SRM 986 Ni isotope ratios determined during the same analytical session. The large data set acquired for NIST SRM 986 allowed us to evaluate the measurement precision under intermediate precision conditions of the Ni isotope composition determined by the double-spike method. For instance, 2*s* determined using all NIST SRM 986 delta values calculated so far gave a value of 0.045‰ for 320 measurements.

The precision under intermediate precision conditions was also estimated for certified reference materials (BHVO-2, PCC-1, DTS-1, DNC-1, BIR-1, Nod-A-1 and Nod-P-1) using duplicate analyses of these samples (see footnotes of Table 3 for details). A value of 0.041‰ (2*s*) calculated for BHVO-2 duplicates (*n* = 11) was similar to the precision under repeatability conditions. This suggests that the chem-

ical purification method did not introduce additional variability in isotope measurements. One of the BHVO-2 basalt duplicates was spiked after a complete purification procedure to evaluate potential Ni isotope fractionation during chemical purification. Although only one sample was spiked subsequent to the purification procedure, the results gave similar values, that is, 0.006 ± 0.041‰ (2*s*) and -0.067 ± 0.017‰ (2SE), for the samples spiked before and after sample purification, respectively. This indicates that the incomplete recovery of Ni through the Ni-resin did not introduce Ni isotope fractionation (Table 3). Other RMs, that is, PCC-1, Nod-A-1, Nod-P-1, BIR-1, DNC-1 and DTS-1, were also analysed in duplicate, and their $\delta^{60/58}$Ni values generally did not deviate by more than 0.069‰ (2*s*; Tables 3 and 7), which is similar to the intermediate measurement precision of NIST SRM 986. It is also important to note that for BHVO-2 the isotopic composition and recovery remained invariant even for different amounts of sample material processed through the chemistry, that is, between 0.2 and 5 μg of nickel. In addition, the mono-elemental solution of Ni-PCal (Ni Plasmacal®, SCP science) processed through the entire chromatography procedure (Figure 2) yielded an average value of 0.020 ± 0.065‰ (2*s*, n = 24), which is similar to that for direct analysis of Ni-PCal standard solution.

Alternatively, another method for estimating the precision under intermediate precision conditions would be to pool all the data and to calculate the standard deviation using Equation (5) (Steele *et al.* 2011):

$$s^2 = k^{-1} \sum_i d_i^2 \quad (5)$$

where s is the standard deviation, k is the degree of freedom and d is the deviation from the mean. This method is appropriate when conditions of sample processing and measurement are similar. From data in Table 3 with five samples and 21 degrees of freedom (not including the BHVO-2 spiked after the purification procedure), 2*s* was 0.045‰; from data in Table 7 with six samples and 23 degrees of freedom (not including single measurements on USGS G-2, IF-G and NIST SRM 2711), 2*s* was 0.053‰. Taking samples from both Tables 3 and 7 (i.e., eleven samples and 44 degrees of freedom), 2*s* was 0.050‰. Hence, the 2*s* value of 0.045‰ calculated as the measurement reproducibility of NIST SRM 986 (see above) is comparable to the standard deviation calculated following the methodology of Steele *et al.* (2011), indicating that in our study both methods were adequate for assessing the measurement reproducibility ('external precision').

Optimum spike/sample ratio for Ni isotope determination

Several tests were undertaken with different spike/sample ratios (between 0.03 and 8) to evaluate the robustness of the double-spike correction. For each sample used for the tests, the concentration of NIST SRM 986 was kept fixed and different amounts of double-spike were

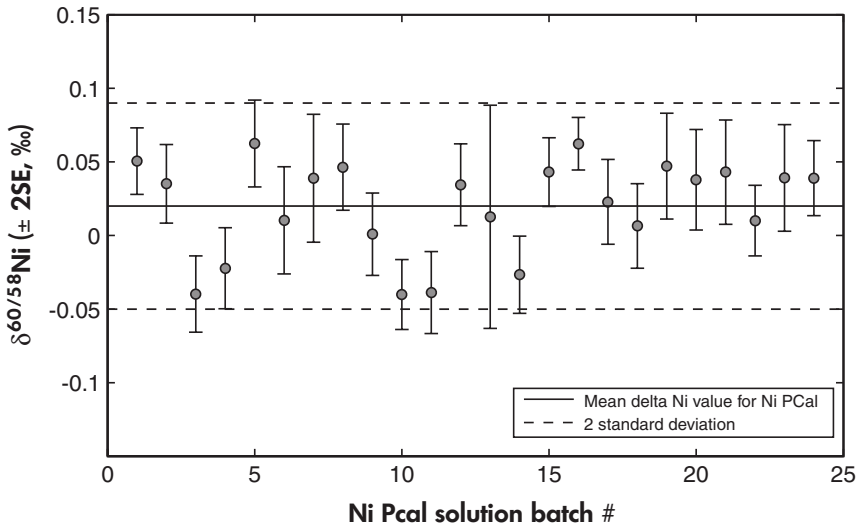

Figure 2. Isotopic composition of the mono-elemental standard solution Ni PlasmaCal® after it was processed through chemistry. This standard solution was run along with each sample batch. This figure shows the consistency of the measured value even when different amounts of nickel were processed. The dashed lines indicate the range of 2*s* (2*s* = 0.07‰ for 24 data points) calculated for the mean of Ni delta values of Ni PlasmaCal®.

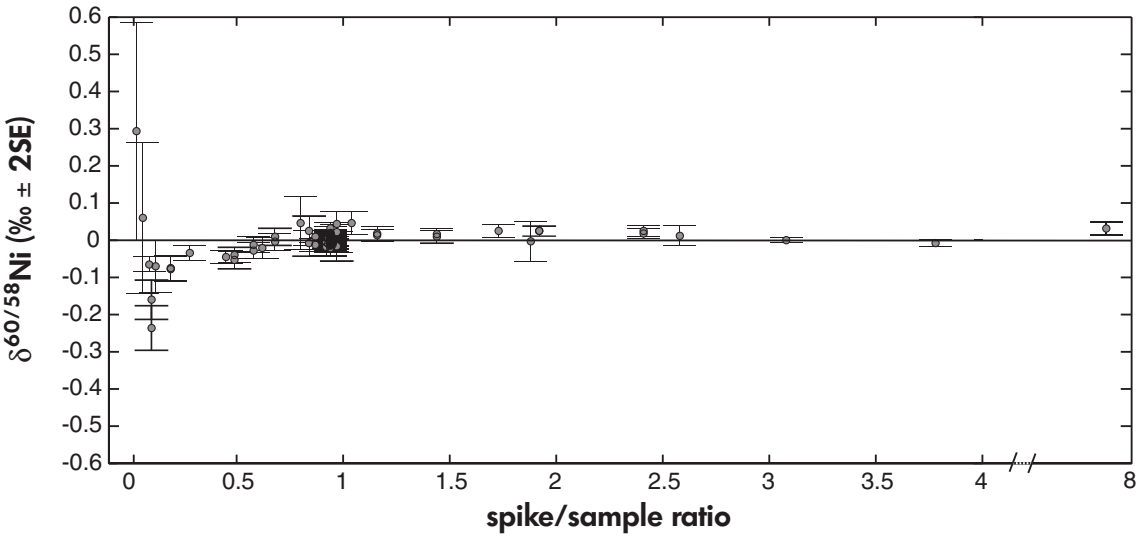

Figure 3. Plot of NIST SRM 986 delta values versus different spike/sample ratios. Under-spiked samples (ratios below 0.6) were found not to be correctly calculated by the double-spike method (wide error bars and non-zero delta values), whereas over-spiked samples up to a ratio of 7 were still correctly determined (see text for details). The black line stands for the isotopic composition of NIST SRM 986, $\delta^{60/58}$Ni = 0.00‰.

added to make final solutions with different spike/sample ratios, which is tantamount to ^{61}Ni/^{58}Ni ratios. To simply visualise the meaning of the spike/sample ratio, one should consider that nickel from the NIST SRM 986 solution is equivalent to the nickel present in a natural sample (denominator of the ratio), whereas nickel from the double-spike solution is the spike (numerator of the ratio). Instead of simply reporting a concentration ratio (concentration of spike/concentration of NIST SRM 986), the spike/sample ratio was calculated using measured intensities (corrected for instrumental mass bias), isotopic masses and true ^{61}Ni/^{58}Ni ratios of NIST SRM 986 and the double-spike mixture.

As shown in Figure 3, only under-spiked samples may not be properly corrected. Indeed, spike/sample ratios lower or equal to 0.6 yielded $\delta^{60/58}$Ni values ranging between -0.05 ± 0.02‰ (2SE) and -0.24 ± 0.06‰ for NIST SRM 986, whereas ratios higher than 0.6 yielded $\delta^{60/58}$Ni values clustering around 0.01 ± 0.02‰. Even spike/sample ratios of up to 7 gave consistent $\delta^{60/58}$Ni values of 0.04 ± 0.02‰. Although an optimum precision was obtained for spike/sample ratios between 0.7 and 8, we used a spike/sample ratio ~ 1 throughout this study.

The Matlab™ template constructed by Rudge *et al.* (2009) allowed us to further evaluate the optimum spike/sample ratio. Calculations indicated that the best results were obtained with spike/sample ratios between ~ 0.6 and ~ 4, which is consistent with our results.

Evaluation of potential matrix effect and chemical purification efficiency

Chemical purification efficiency was checked for a number of RMs (e.g., manganese nodules, basalts and shale) by measuring concentrations of matrix elements with an ICP-Quadrupole (ICP-Q-MS, X-series II) at PSO, Brest. Potassium, Na, Ca, Cr, Mn, Fe, Mo and Co concentrations in purified samples were all below the detection limit of the instrument. The estimated separation efficiency factor, defined as the mass (g) of an element loaded on resin divided by the mass of the element remaining after purification, was > 10^6 for Na and Mg, ~ 10^6 for Cu and > 10^7 for Mn. Titanium was found more difficult to separate with a separation factor as low as 10^3. On the other hand, Zn was well separated (separation efficiency factor better than 10^6), although care should be taken to avoid Zn contamination during sample preparation. As ^{64}Ni was not considered in our double-spike calculations and final results, potential isobaric interference from ^{64}Zn was not critical for our study. Iron was not detected in all analysed solutions (separation efficiency >> 10^6), which suggests that iron was quantitatively separated during the chemical procedure even if samples had high amounts of iron.

Potential matrix effects were further assessed using several NIST SRM 986 solutions doped separately with Ca and S. As several Ni-rich sulfides were analysed without Ni-spec resin column purification, we tested the influence of

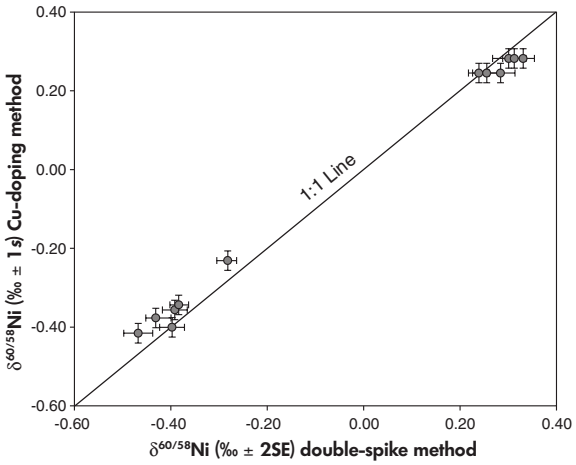

Figure 4. Comparison of values obtained with the Cu-doping and double-spike correction methods. The 1:1 linear trend was plotted on the figure to show that data points follow this line. It indicates the consistency of the two methods, but more importantly it validates use of the double-spike method for correction of instrumental mass bias when Ni isotope ratios are measured (see text for details on each method).

sulphur on the instrumental mass bias with S/Ni ratios between 2 and 0.5 in analysed solutions. The same was also done with Ca, which is a good proxy for matrix-forming elements in silicate rocks. Calcium is also a source of potential isobaric interferences from calcium oxides (e.g., $^{40}Ca^{18}O$ on ^{58}Ni). Matrix-doped nickel solutions were analysed using a CSB method and without a nickel double-spike to monitor all natural Ni isotope ratios. As shown in Table 1, the results suggest that isobaric interferences and changes in instrumental mass bias were insignificant for element/Ni ratios between 1 and 0.5, yielding $\delta^{60/58}$Ni values of -0.18 ± 0.14‰ (2*s*) and 0.02 ± 0.14‰ (2*s*) for Ca/Ni = 1 and S/Ni = 1, respectively. These results also imply that the medium-resolution mode resolved major isobaric interferences from CaO. Note that similar to the Fe-doping tests (see section on MC-ICP-MS settings), measured Ni isotope values for NIST SRM 986 doped with Ca and S were corrected for instrumental mass bias using the sample-calibrator-bracketing method. The reported precision is the two standard deviation value based on replicate measurements of non-doped NIST SRM 986.

Comparison between Cu-doping and double-spike correction methods for instrumental mass bias

Several Ni-rich sulfides as well as iron meteorites (i.e., Ni-rich meteorites) were analysed and corrected for instrumental mass bias using two different methods. One method involved sample purification through anion-exchange resin and instrumental mass bias correction based on Cu-doping. The second method involved purification through the entire procedure and double-spike correction. As shown in Figure 4, values calculated with the two methods fall within uncertainties for the total range of $\delta^{60/58}$Ni values from -0.60‰ to 0.40‰. These results further validate the reliability of the double-spike data reduction scheme.

Sample analysis results and discussion

Assessment of the BSE Ni isotope composition

It is important to have an estimate of the BSE value to interpret and compare Ni isotope fractionation in natural samples. Hence, our approach was to measure Ni isotope values in various igneous rocks, including oceanic basalts and Archaean komatiites. The former yield an estimate of the modern mantle isotope composition, whereas the latter may represent the early Earth's mantle isotope composition.

Igneous and ultramafic rock samples: As presented in Table 3 and Figure 5, mafic and ultramafic RMs (i.e., basalt, dunite and peridotite) closely clustered within a range of $\delta^{60/58}$Ni values between -0.10‰ and +0.15‰; BHVO-2 gave a near zero $\delta^{60/58}$Ni value (0.01 ± 0.04‰, 2*s*, *n* = 11). Table 4 and Figure 5 display isotopic and chemical composition of the basalt samples from Hawaii (Loihi Seamount) and serpentinite from the Mid-Atlantic Ridge (Logatchev field). Fresh pillow basalts from Loihi Seamount were selected because they were probably derived from the deep enriched Earth's mantle as indicated by their high $^{3}He/^{4}He$ ratios (Kurz *et al.* 1983). Therefore, they might represent the most primitive mantle composition, which is important for determining the BSE Ni isotope composition. Fresh glass material from Loihi yielded a value of +0.07‰, whilst hand-picked olivine crystals displayed a slightly more positive value of +0.10‰. Serpentinite from the Logatchev hydrothermal field had a $\delta^{60/58}$Ni value of -0.13‰, whereas peridotite PCC-1 had the value of +0.12‰ and dunite DTS-1 had a composition of -0.07‰. In addition, fresh and altered basalts recovered at IODP core site 1149 (Plank *et al.* 2000, Rouxel *et al.* 2003) were also analysed (Table 5 and Figure 5). They gave $\delta^{60/58}$Ni values between -0.03 and +0.10‰, without any significant difference between fresh and altered basalts, and are in agreement with Ni isotope values for other mafic igneous rocks reported in this study. In summary, all mantle-derived rocks analysed in this study, that is, RMs (BHVO-2, BIR-1, DNC-1, DTS-1 and PCC-1) and fresh and altered basalts from Loihi seamount and IODP core 1149, displayed a

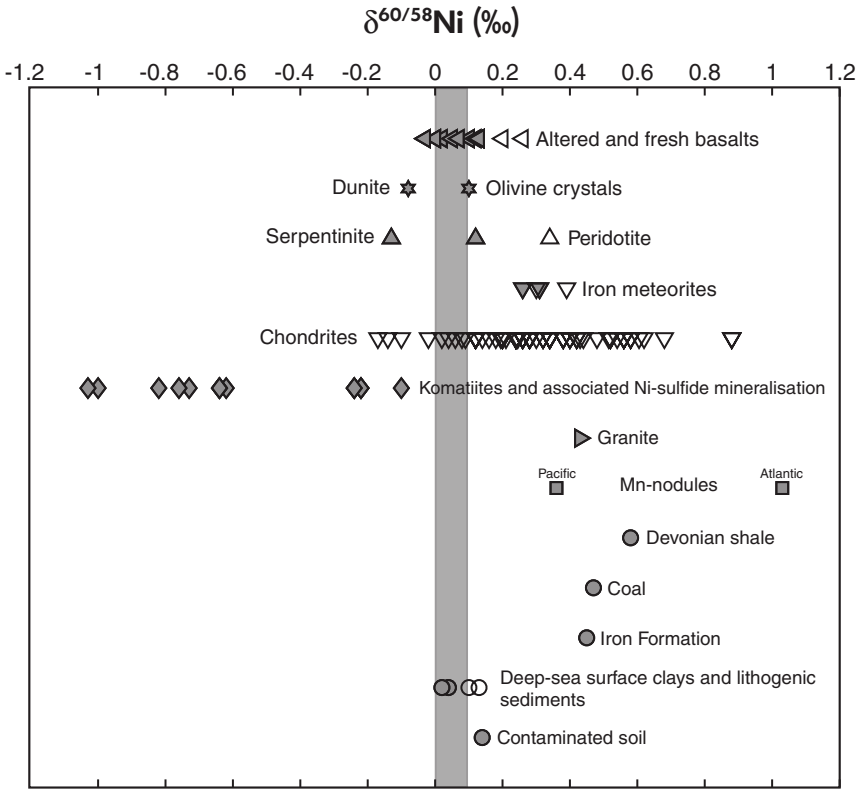

Figure 5. Plot showing Ni isotope composition in ‰ of terrestrial samples from this study and the literature. RMs, komatiites and associated Ni-sulfide mineralisation, mantle-derived rocks and deep-sea clays are shown by closed symbols, and literature data for both extraterrestrial and terrestrial materials are represented by open symbols (Cook *et al.* 2007, Moynier *et al.* 2007, Cameron *et al.* 2009, Steele *et al.* 2011). The grey bar stands for the BSE $\delta^{60/58}$Ni value of 0.05 ± 0.05‰, determined using various igneous and volcanic rocks and minerals such as altered and fresh basalts, dunite, peridotite, deep-sea clays and olivine crystals. See text for further details.

Table 4.
Concentration of some major elements (in μg g^{-1}) and Ni isotope composition (in ‰) of basaltic glass and olivine from Loihi and serpentinite from the Logatchev hydrothermal field

Sample name	Rock type	Al (μg g^{-1})[a]	Ca (μg g^{-1})[a]	Mg (μg g^{-1})[a]	Na (μg g^{-1})[a]	Mn (μg g^{-1})[a]	Fe (μg g^{-1})[a]	Co (μg g^{-1})[a]	Zn (μg g^{-1})[a]	Ni (μg g^{-1})[b]	$\delta^{60/58}$Ni (‰)	2SE
Basaltic glass (Loihi)	Basalt, Hawaii	51291	70609	98084	15661	1329	91013	80	110	603	0.074	0.029
Olivine minerals fractions (Loihi)	Olivine minerals	322	2348	280653	51	1500	104045	163	88	2250	0.104	0.030
Serpentinite (Logatchev hydrothermal field)	Serpentinite, Atlantic	2329	622	159862	2901	399	151144	473	1378	1505	-0.126	0.035

[a] Elemental concentrations (in μg g^{-1}) were determined by ICP-AES at PSO, Brest, France. Precision expressed as RSD was between 0.5% and 3%.
[b] Ni concentrations (in μg g^{-1}) were redetermined by isotope dilution after measurement using MC-ICP-MS. Amount of Ni processed through chemistry was between 0.5 and 25 μg.

small range of $\delta^{60/58}$Ni values, < 0.1‰, which is too close to the analytical uncertainty to be considered significant.

For comparison, previously published $\delta^{60/58}$Ni values (figure 5 in Cameron *et al.* 2009) are systematically heavier with values up to +0.34 ± 0.08‰ (2*s*) for PCC-1 and

Table 5.
Nickel isotope composition (in ‰) and major element concentrations (in % m/m) of deep-sea clays and altered and fresh basalts from IODP site 1149, hole C

Sample name	Depth (m) in the core	Sample type	LOI	K_2O	Fe_2O_3	SiO_2	CaO	MgO	MnO	Na_2O	P_2O_5	Al_2O_3	TiO_2	$\delta^{60/58}$Ni (‰)	2SE	Ni ($\mu g\ g^{-1}$)[a]
1149A-01H1,140	1.4	Ash and silica bearing clay	9.12	1.88	5.48	58.50	3.01	2.35	0.12	3.14	0.07	14.88	0.57	0.044	0.037	33
1149A-04H2,140	26.1	Clay	11.05	2.53	7.08	57.72	1.46	2.71	0.12	2.74	0.10	14.28	0.64	0.020	0.034	55
1149B-32R1,136	436.96	Altered basalt	5.08	0.57	10.27	47.56	8.41	6.88	0.11	2.84	0.20	16.16	1.79	0.018	0.027	73
1149B-29R3,60/D	410.31	Basalt slightly altered	2.13	0.18	7.90	50.34	11.12	7.90	0.14	2.70	0.22	15.42	1.77	0.004	0.041	71
1149D-19R1,85	435.57	Deepest fresh basalt	1.22	0.44	13.17	48.56	9.89	6.12	0.22	3.03	0.24	14.96	2.31	0.052	0.022	43
1149D-06R2,82	312.17	Altererd basalt	2.00	0.52	9.72	49.77	10.69	7.09	0.14	2.84	0.19	15.16	1.74	-0.026	0.032	61
1149D-16R3,0	408.88	Altered basalt	2.52	0.59	9.71	48.21	12.15	6.28	0.23	2.67	0.22	15.62	1.71	0.102	0.033	111

[a] Ni concentrations (in $\mu g\ g^{-1}$) were redetermined by isotopic dilution after measurement using MC-ICP-MS. Amount of Ni processed through chemistry was 1 µg.

+0.13 ± 0.03‰ (2*s*) for BHVO-2. In contrast, Gall *et al.* (2012) obtained results similar to ours for both PCC-1 and BHVO-2 (~ +0.1‰). The small discrepancy in the data, although minor, might be related to reference material heterogeneity or to an as yet unclear difference in analytical methods.

Ni isotope composition of deep-sea clays: Deep-sea clays were collected at IODP site 1149 along with altered and fresh basalts described above (Plank *et al.* 2000). Clay minerals are the most common component of sediments on the oceanic seafloor; hence, they represent an important sedimentary reservoir on Earth. Deep-sea sediments are the repository of materials of both detrital and chemical origin derived from the continents. Therefore, their Ni isotope composition can be taken as representative of the average composition of the continental crust. As expected, $\delta^{60/58}$Ni values of +0.04 and +0.02‰ for deep-sea clays (Table 5, Figure 5) clearly fall in the range of values obtained for igneous and ultramafic rocks in our study.

Ni isotope composition of komatiite-hosted Ni-sulfide ores: Our komatiite samples were representative of Ni-sulfide-mineralised ultramafic magmas. Whilst some samples were dominated by pentlandite mineralisation (AX-1, AX-2, MC-1, TD21, MKTD76), others were composed of almost pure komatiitic materials (B and A) and two samples were olivine mineral separates (BE-1 and BE-2). An unexpectedly large range of Ni isotope values was found for these samples, ranging from -0.10 to -1.03‰ (Table 6, Figure 5), but the most negative $\delta^{60/58}$Ni values, from -0.62 to -1.03‰, were determined on samples with elevated content of pentlandite, whereas olivine minerals and pure komatiite samples were close to modern basalt values, from -0.26 to -0.10‰.

The choice of these samples was essentially motivated by our attempt to assess a value for the BSE composition, and we did not expect to obtain such a large range of variation in the Ni isotope composition of komatiites. Regardless of the, as yet unclear, mechanism of Ni isotope fractionation in komatiites, our results clearly demonstrate that significant abiotic fractionation of Ni isotopes took place during the magmatic processes that formed these rocks. This interpretation is further confirmed by recent Ni isotope data for Archaean Ni-rich magmatic sulfides from Zimbabwe that show a systematic enrichment in low atomic number isotopes to values as low as -0.82 ± 0.02‰, with most values clustering around -0.40‰ (Hofmann *et al.* in press). Therefore, it seems very likely that negative Ni isotope values measured for these komatiites reflect the contribution of Ni-rich sulfides.

GEOSTANDARDS and GEOANALYTICAL RESEARCH

Table 6.
Ni, Fe and S isotope composition (in ‰) and major element concentrations (in % m/m) of selected komatiites and associated Ni-sulfide mineralisation from Canada and Western Australia

Sample name	Sample location	Drill core #	Type of mineralisation	Type of komatiite	S (% m/m)[a]	Fe (% m/m)[a]	Cu (% m/m)[a]	Ni (μg g^{-1})[b]	$\delta^{60/58}$Ni (‰)	2SE	$\delta^{56/54}$Fe (‰)[a]	$\Delta^{33/32}$S (‰)[a]
BE-1	Betheno, Yakabindie, Agnew-Wiluna Belt, Yilgarn Craton, Western Australia	MKTD 528	Olivine	Barren	0.36	5.0	< DL	7253	-0.256	0.024	-0.05	–
BE-2	Betheno, Yakabindie, Agnew-Wiluna Belt, Yilgarn Craton, Western Australia	MKTD 528	Olivine	Barren	0.36	5.0	< DL	8692	-0.243	0.028	-0.02	–
A	Jordan, Albion Downs, Agnew-Wiluna Belt, Yilgarn Craton, Western Australia	ADJD 348	Disseminated sulfides	Barren	0.87	–	0.62	3893	-0.103	0.024	–	-0.1
AX-1	Alexo Mine, Abitibi Greenstone Belt, Canada	–	Massive sulfide ores	Ni sulfide-bearing	–	53.15	1.04	58693	-1.003	0.029	-0.29	-0.9
AX-2	Alexo Mine, Abitibi Greenstone Belt, Canada	–	Massive sulfide ores	Ni sulfide-bearing	–	52.4	1.61	71462	-1.035	0.034	-0.30	-0.8
MC-1	Mount Newman, Mount Clifford, Agnew-Wiluna Belt, Yilgarn Craton, Western Australia	LMCD005	Blebby sulfides	Ni sulfide-bearing	1.07	21.7	1.70	82159	-0.621	0.029	0.03	-0.5
TD21	Spinifex Park, Mount Keith, Agnew-Wiluna Belt, Yilgarn Craton, Western Australia	MKTD21	Massive sulfide ores	Ni sulfide-bearing	41.50	44.5	0.07	77063	-0.718	0.023	-0.10	-0.6
TD21[c]	Spinifex Park, Mount Keith, Agnew-Wiluna Belt, Yilgarn Craton, Western Australia	MKTD21	Massive sulfide ores	Ni sulfide-bearing	41.50	44.5	0.07	77063	-0.817	0.033	-0.10	-0.6
MKTD96	Spinifex Park, Mount Keith, Agnew-Wiluna Belt, Yilgarn Craton, Western Australia	MKTD96	Massive sulfide ores	Ni sulfide-bearing	35.00	47.2	0.56	22418	-0.639	0.024	0.36	-0.6
MKTD96[c]	Spinifex Park, Mount Keith, Agnew-Wiluna Belt, Yilgarn Craton, Western Australia	MKTD96	Massive sulfide ores	Ni sulfide-bearing	35.00	47.2	0.56	22381	-0.643	0.030	0.36	-0.6

< DL: below detection limit.

[a] Data are from Bekker *et al.* (2009) and $\Delta^{33/32}S \approx \delta^{33/32}S\text{-}0.515c\ \delta^{34/32}S$

[b] Ni concentrations (in μg g^{-1}) were determined by isotope dilution after measurement with MC-ICP-MS. Amount of Ni processed through chemistry was between 10 and 20 μg.

[c] The same digested powder was used, but separate chemistry procedures were applied.

Table 7.
Nickel isotope composition (in ‰) of iron meteorites, granite G-2 and selected geological reference materials of sedimentary origin

Sample name	Rock type	Ni (μg g^{-1})**	$\delta^{60/58}$Ni (‰)	2SE	Number of duplicates	2*s****
USGS G-2	Granite	2	0.431	0.034		
Nantan Iron	iron meteorite (IICD)	58328	0.331	0.022		
Nantan Iron*	iron meteorite (IICD)	59370	0.301	0.029		
Nantan Iron*	iron meteorite (IICD)	61239	0.313	0.030		
Average Nantan Iron		**59645**	**0.315**	–	***n*** **= 3**	**0.030**
Gibeon Iron	iron meteorite (IVA)	69314	0.284	0.026		
Gibeon Iron*	iron meteorite (IVA)	82959	0.239	0.026		
Gibeon Iron*	iron meteorite (IVA)	74133	0.255	0.032		
Average Gibeon Iron		**75469**	**0.260**	–	***n*** **= 3**	**0.045**
USGS Nod-A-1†	Mn-nodule Atlantic	5616	1.034	0.028		
USGS Nod-A-1†*	Mn-nodule Atlantic	5413	1.062	0.031		
USGS Nod-A-1††	Mn-nodule Atlantic	5633	1.043	0.026		
USGS Nod-A-1††*	Mn-nodule Atlantic	5778	1.043	0.028		
USGS Nod-A-1†*	Mn-nodule Atlantic	5513	1.043	0.031		
USGS Nod-A-1††*	Mn-nodule Atlantic	5334	0.976	0.031		
Average Mn-nodule Atlantic		**5548**	**1.034**	–	***n*** **= 6**	**0.059**
USGS Nod-P-1†	Mn-nodule Pacific	12330	0.347	0.028		
USGS Nod-P-1†*	Mn-nodule Pacific	11961	0.412	0.028		
USGS Nod-P-1††	Mn-nodule Pacific	12208	0.401	0.034		
USGS Nod-P-1††*	Mn-nodule Pacific	12454	0.345	0.029		
USGS Nod-P-1†*	Mn-nodule Pacific	12165	0.363	0.025		
USGS Nod-P-1††*	Mn-nodule Pacific	12482	0.343	0.039		
USGS Nod-P-1†*	Mn-nodule Pacific	12605	0.304	0.032		
USGS Nod-P-1††*	Mn-nodule Pacific	11553	0.349	0.038		
Average Mn-nodule Pacific		**12220**	**0.358**	–	***n*** **= 8**	**0.069**
USGS SDO-1	Devonian shale	92	0.600	0.021		
USGS SDO-1*	Devonian shale	95	0.593	0.040		
USGS SDO-1*	Devonian shale	85	0.576	0.030		
USGS SDO-1*	Devonian shale	91	0.583	0.036		
USGS SDO-1*	Devonian shale	91	0.571	0.031		
Average SDO-1		**91**	**0.585**	–	***n*** **= 5**	**0.025**
USGS CLB-1	Coal	20	0.475	0.018		
USGS CLB-1*	Coal	21	0.502	0.046		
USGS CLB-1*	Coal	21	0.470	0.027		
USGS CLB-1*	Coal	21	0.443	0.042		
Average CLB-1		**21**	**0.473**	–	***n*** **= 4**	**0.048**
IF-G	Banded Iron Formations	20	0.455	0.032		
NIST SRM 2711	Contaminated Montana soil	18	0.140	0.019		

*, **, *** and † same as in Table 3.

All Archaean komatiite samples and associated Ni-sulfide mineralisation from this study previously yielded negative Δ^{33}S values (Table 6; Bekker *et al.* 2009). Bekker *et al.* (2009) suggest that these negative values reflect assimilation of sulphur processed through an oxygen-poor atmosphere, where it underwent mass-independent fractionation during photochemical reactions. Although S isotopes indicate crustal contribution for sulphur during komatiite emplacement, which promoted sulfide saturation to form sulfide mineralisation, Ni is unlikely to be sourced from a crustal reservoir and is most probably linked with partial mantle melting (Fiorentini *et al.* 2007; Rosengren *et al.* 2008). Therefore, the observed Ni isotope fractionations are solely the result of magmatic processes occurring at high temperatures (i.e., abiotic fractionation). Iron isotope composition of the same samples was less variable, with a range from +0.36 to -0.30‰ interpreted as being the result of either crustal contamination or high-temperature fractionation (Bekker *et al.* 2009). High-temperature Fe isotope fractionation has been documented by Teng *et al.* (2008), who show that magmatic differentiation in the Kilauea Iki lava lake (Hawaii) produced Fe isotope fractionations of

Table 8.
Compilation of published isotope composition of Tl, Mo, Cd, Fe, Cu and Zn in two Mn-nodule RMs and Ni isotope data (this study)

	Nod-P-1	2*s*	Nod-A-1	2*s*	Reference
$\delta^{60/58}Ni_{NIST986}$ (‰)	0.36	0.07	1.03	0.06	This study
$\delta^{205}Tl_{NIST997}$ (‰)[a]	nd	–	1.07	0.05	Nielsen *et al.* (2004)
$\delta^{205}Tl_{NIST997}$ (‰)[a]	0.05	0.045	0.89	0.045	Rehkämper *et al.* (2002)
$\delta^{97/95}Mo_{JMC\text{-}spec}$ (‰)	-0.42	0.1	-0.63	0.1	Barling *et al.* (2001)
$\delta^{114/110}Cd_{JMC\text{-}Cd\text{-}Mainz}$ (‰)[a,d,c]	0.020	0.016[b]	-0.018	0.016[b]	Schmitt *et al.* (2009)
$\delta^{114/110}Cd_{JMC\text{-}Cd\text{-}alfa}$ (‰)[d]	0.22	0.06[b]	0.25	0.06[b]	Horner *et al.* (2010)
$\delta^{114/110}Cd_{Cd\text{-}SPEX}$ (‰)[d]	0.13	0.12[b]	-0.07	0.12[b]	Cloquet *et al.* (2005)
$\delta^{56/54}Fe_{IRMM\text{-}14}$ (‰)	-0.50	0.10	-0.35	0.09	Rouxel, unpubl.
$\delta^{56/54}Fe_{IRMM\text{-}14}$ (‰)	nd	–	-0.42	0.07	Dideriksen *et al.* (2006)
$\delta^{65/63}Cu_{NIST976}$ (‰)	0.46	0.08	nd	–	Chapman *et al.* (2006)
$\delta^{65/63}Cu_{NIST976}$ (‰)	0.35	0.08	nd	–	Bigalke *et al.* (2010)
$\delta^{66/64}Zn_{JMC\text{-}Zn}$ (‰)	0.78	0.09	nd	–	Chapman *et al.* (2006)
$\delta^{66/64}Zn_{JMC\text{-}Zn}$ (‰)	0.87	0.08	nd	–	Bigalke *et al.* (2010)

nd, not determined.
[a] Isotope ratios were initially reported in per thousand in epsilon notation. For clarity, values are given here in per mil to express values in delta notation.
[b] Measurement precision is expressed as two standard error of the mean.
[c] Data from Schmitt *et al.* (2009) were originally reported as $^{112/110}Cd$ ratio. For more comparison with other Cd data, the data were converted to delta values expressing them as the $^{114/110}Cd$ ratio.
[d] Note that Cd isotope compositions for the three references are reported relative to different reference materials (JMC-Mainz, JMC Alfa Zürich, Spex).

~ 0.2‰. As the range of Ni isotope variations reported in our study was ~ 0.90‰, it indicates that Ni isotopes are at least as sensitive as Fe isotopes to high-temperature processes and crystallisation effects in magmatic systems. Although a detailed discussion of parameters that govern Ni isotope fractionation at high temperature is beyond the scope of this paper, these promising results coupled to their ubiquitous occurrence in mantle rocks mean that Ni isotopes could be potentially used to investigate crystallisation processes at the magmatic system scale.

Ni isotope composition of the BSE: Mantle heterogeneity and high-temperature mass-dependent fractionation processes have been inferred from studies of stable isotope systems ranging from traditional low atomic number isotopes, O and S (e.g., Eiler 2001), to non-traditional isotopes, including Mg and Fe (e.g., Young and Galy 2004, Dauphas and Rouxel 2006, Teng *et al.* 2008). Our results for Ni isotopes are, to some extent, consistent with inferences from studies of other stable isotope systems, precluding a straightforward estimate of the BSE value. However, as we observed a narrow range in $\delta^{60/58}Ni$ values from mantle-derived rocks, between ~ -0.1 and +0.1‰, we feel confident to ascribe the BSE composition to the average value of common basalts and mantle-derived rocks, which is +0.05 ± 0.05‰ (measurement reproducibility). Our BSE estimate is slightly lower than that of +0.179 ± 0.036‰ determined by Steele *et al.* (2011) on Japanese basalt JP-1 and dunite DTS-2. The large range of mantle-derived rocks analysed in our study and the inclusion of common sedimentary minerals such as deep-sea clays improve our understanding of the Ni isotope composition of BSE.

Ni isotopes in selected RMs

Organic matter–rich samples: Samples containing high contents of organic matter, namely SDO-1 Devonian Ohio shale (Morehead, KY, USA) and CLB-1 coal (Maryland, USA), gave $\delta^{60/58}Ni$ values of +0.58‰ and +0.47‰, respectively (Table 7 and Figure 5). These positive values relative to BSE provide strong evidence for Ni isotope fractionation in low-temperature environments with interesting prospects for future studies. Although shales are generally considered as a proxy for bulk crustal composition (e.g., Turekian and Wedepohl 1961), organic-rich shales are characterised by authigenic enrichments of redox-sensitive trace metals such as Mo, Ni, U, Cu, V and Zn, leading to metal/Al ratios well above crustal values (e.g., Algeo and Maynard 2004, Brumsack 2006, Tribovillard *et al.* 2006, Scott *et al.* 2008, 2011). In marine sediments nickel has a strong affinity to organic matter, forming organometallic complexes, and with iron sulfides (e.g., pyrite), which may form either in the water column or during diagenesis in sediments. Hence, positive Ni isotope values in marine organic matter–rich sediments probably reflect the contribution of isotopically heavy nickel sources, derived either directly from seawater or in association with organic matter.

Mn-nodule RMs: Geological reference materials of manganese nodules (Nod-A-1 and Nod-P-1) that represent composite samples from the Atlantic and Pacific oceans gave $\delta^{60/58}$Ni values of +1.03‰ and +0.36‰, respectively. Mn nodules are typically enriched in transition metals such as Ni, Cu, Zn and Co and form in deep-sea sediments generally at water depths between 4 and 6 km. They consist of concentrically laminated Fe-Mn oxyhydroxides precipitated at the sediment–water interface. The two Mn-nodule RMs were prepared from a large number of individual Mn nodules collected from the Atlantic and Pacific oceans (Table 7 and Figure 5). These nodules had been analysed previously for other isotopic systems (Table 8) such as Fe (Dideriksen *et al.* 2006), Zn and Cu (Chapman *et al.* 2006, Bigalke *et al.* 2010), Cd (Cloquet *et al.* 2005, Schmitt *et al.* 2009, Horner *et al.* 2010), Mo (Barling *et al.* 2001) and Tl (Rehkämper *et al.* 2002, Nielsen *et al.* 2004), highlighting differences in their isotopic composition with the exception of Mo (Anbar 2004) and Cd isotopes. The difference in Ni isotope composition between these two nodules is larger (per mass unit) than for any other studied isotope system and indicates that Ni isotopes are particularly sensitive to mechanisms involved in the formation of nodules, compared with other metal isotope systems. Several processes could be inferred to explain such variations: (a) diagenetic processes through which metals contained in subsurface sediments (e.g., associated with organic matter) were released into pore waters and then scavenged onto Mn oxides during nodule growth; (b) adsorption of metals directly from seawater onto oxyhydroxides; (c) biological productivity in surface waters, which could result in a high supply of organic matter to the sediments providing metals to pore waters during organic matter re-mineralisation; and (d) *in situ* biological activity, specifically that of microbial mats, which have been observed to cover entire nodule surfaces. It is clear that more detailed investigations regarding the contribution of each of these mechanisms to the composition of polymetallic nodules, as well as a larger data set, are needed to clearly establish which of these processes are responsible for variations in the Ni isotope composition of Fe-Mn nodules.

Rehkämper *et al.* (2002) argue that variations in Tl isotope ratios of Mn nodules reflect equilibrium fractionation during preferential adsorption of heavy Tl isotopes onto Mn oxides in a closed system developed in pore waters, which are an important source of metals for Mn-nodule growth. Similarly, Ni isotopes might be affected by this mechanism as revealed by experimental results on nickel adsorption on Fe-Mn oxides (Gueguen *et al.* 2011). Alternatively, Horner *et al.* (2010) argue that Cd isotopes incorporated with Mn oxides into Fe-Mn crusts were not fractionated compared with seawater Cd probably because of the high ionic strength of seawater. The same might hold true for Mn-nodule Cd isotope compositions that probably reflect biotic fractionations by micro-organisms rather than fractionation during adsorption on Fe-Mn oxides (Schmitt *et al.* 2009). The chemical behaviour of nickel in seawater is akin to that of cadmium (and zinc), for example, in their depletion in surface waters upon their uptake by phytoplankton. We therefore suggest that Ni isotopes in precipitated marine Fe-Mn oxides might have been also affected by biological activity, although this remains to be demonstrated.

Other RMs corresponding to major terrestrial reservoirs: The metal-contaminated soil sample NIST SRM 2711 (Table 7 and Figure 5) was found to have a $\delta^{60/58}$Ni value of +0.14‰, which is very close, within uncertainty, to lithogenic sediments such as loess and Nile river sediment with $\delta^{60/58}$Ni values of +0.10 and +0.13‰, respectively (Cameron *et al.* 2009), and to Pacific deep-sea clays (see above). In contrast, granite G-2 with very low nickel content was significantly enriched in heavy Ni isotopes with a value of +0.43‰ (Table 7 and Figure 5), suggesting variability in Ni isotope ratios within common continental rocks. Finally, the Iron Formation IF-G sample displayed an enrichment in heavy Ni isotopes of +0.45‰ (Table 7).

Ni isotope composition of iron meteorites

Our main goals in measuring iron meteorite samples were to implement our experimental and analytical procedure on Ni-rich rocks and to compare our data with results from previous studies. As the first Ni isotope measurements were made on meteoritic materials to study nucleosynthetic processes (Birck and Lugmair 1988, Cook *et al.* 2006, 2007, Moynier *et al.* 2007, Regelous *et al.* 2008, Chen *et al.* 2009), the available data set of Ni isotope determinations mainly concerns extraterrestrial reservoirs with the main focus on mass-independent Ni isotope variations.

The Gibeon and Nantan Iron meteorites both displayed fairly similar positive $\delta^{60/58}$Ni values (see Table 5; 2*s* calculated on duplicate analyses) of +0.26‰ and +0.31‰, respectively, consistent with data in Cook *et al.* (2008), who obtained a $\delta^{62/58}$Ni value of +0.37 ± 0.09‰ on Gibeon Iron. Our values are also in full agreement with the range of $\delta^{60/58}$Ni values measured in iron meteorites by Cameron *et al.* (2009) and Steele *et al.* (2011), that is, 0.24 –0.36‰. Other meteorites analysed by Moynier *et al.* (2007) and Cameron *et al.* (2009), including chondrites, are also enriched in high atomic number isotopes and have a range of values between +0.02‰ and +0.80‰ (only few meteorites in these data sets have negative Ni isotope

values). It is however important to note that Moynier *et al.* (2007) report their isotopic ratios with respect to the Aesar ICP-MS Ni standard solution batch No 066110910 and expressed their results as per mass unit.

As discussed by Regelous *et al.* (2008), the observed isotopic variations among iron meteorites and chondrites, which are mass-independent, are likely to be the result of mixing within the protosolar nebula of mineralogical phases with different nucleosynthetic origin. Steele *et al.* (2011) and Regelous *et al.* (2008) suggest that each iron meteorite class had their protolith formed in a restricted region of the protosolar nebula as was previously demonstrated for the precursor materials to the different classes of chondrites. The overlap between mass-independently fractionated Ni isotope values of iron meteorites and chondrites suggests that the source regions of parent bodies for the different classes of chondrites and iron meteorites might have also overlapped. In addition, the range of Ni isotope values among iron meteorites is also suggestive of lateral heterogeneity in the early Solar System. Alternatively, based on mass-dependent Ni isotope compositions, Moynier *et al.* (2007) and Cook *et al.* (2007) argue that all meteorites follow the same mass-dependent fractionation line as terrestrial samples and indicate fractionation from a common isotopic pool, which was homogenised in the solar nebula. In this interpretation, nickel isotope variations in meteorites reflect physicochemical reactions between distinct phases (e.g., solid-vapour, metal-silicate). Recently, Huh *et al.* (2009) experimentally demonstrated an isotopic fractionation of at least -0.3‰ between metallic and silicate phases at magmatic temperature (800 °C), with the metal being enriched in low atomic number isotopes. Altogether, these results suggest that significant Ni isotope fractionations may have occurred during Earth's core segregation and that Ni isotope composition of the Earth after its accretion may have differed from the BSE composition developed after the early differentiation of the metallic core.

Conclusions

In this paper, investigation of deep-sea clays and mantle-derived rocks of RMs and mafic and ultramafic igneous rocks and minerals such as fresh and altered basalts, komatiites and olivine crystals allowed us to establish the isotopic composition of the BSE at $\delta^{60/58}Ni = +0.05 \pm 0.05$‰. We report here the Ni isotope composition of selected geological reference materials, which show a range of $\delta^{60/58}Ni$ values more than 1‰. Interestingly, both Fe-Mn nodules and organic matter–rich shales have positive $\delta^{60/58}Ni$ values, suggesting either biotic or inorganic Ni isotope fractionations in aqueous environments. We also found that bulk rock samples of komatiites and associated Ni-sulfide mineralisation display a range of $\delta^{60/58}Ni$ values from -0.10 to -1.03‰, indicating that fractionation in high-temperature magmatic systems can explain some variations in the Ni isotope composition of natural samples. We infer that Ni-rich sulfides with negative $\delta^{60/58}Ni$ values affected the Ni isotope composition of komatiites, which otherwise, as shown by the least mineralised komatiite samples, have Ni isotope compositions close to that of BSE with a near zero value. This is an important finding because it emphasises that Ni isotope fractionations are not an unique biosignature, as was recently inferred (Cameron *et al.* 2009), but they can be also produced by abiotic processes such as high-temperature magmatic processes and, potentially, by low-temperature processes during co-precipitation of Ni with Fe-Mn oxides (Gueguen *et al.* 2011). Therefore, the Ni isotope composition of specific terrestrial reservoirs (e.g., magmatic and sedimentary rocks) relevant to the biogeochemical Ni cycle might significantly deviate from the BSE value, and, more importantly, our results demonstrate that Ni isotope fractionations are systematic, that is, positive fractionations characterise low-temperature processes, while negative fractionations mark high-temperature processes. Finally, we have demonstrated that for Ni isotopes, the double-spike correction method is appropriate for measuring a broad range of sample matrices from silicate rocks to metalliferous deposits, including sulfides, and a large range of Ni concentrations. The method allowed us to measure small but meaningful fractionations of more than ten times the analytical precision even when small amounts of Ni were processed through chemistry and determined by MC-ICP-MS. The new results for RMs and analytical methods presented here should help to make Ni isotope measurements more straightforward, and more frequently utilised in future studies of terrestrial and planetary materials.

Acknowledgements

We thank Céline Liorzou and Yoan German for laboratory assistance, Jean-Alix Barrat for iron meteorite samples, and Marco Fiorentini for samples of komatiites and associated Ni-sulfide mineralisation from Canada and Western Australia. We thank Harry Elderfield and Jeffrey Sorensen for their thoughtful comments on the first draft of this manuscript. Two anonymous reviewers and the editor Thomas Meisel are gratefully thanked for their constructive comments and corrections to this manuscript. The study was supported by funding from Ifremer, the European Marie-Curie ISOMAR project (European Reintegration grant #FP7 #247837) and Europôle Mer. Participation by AB was supported by NSERC Discovery Grant and IFREMER visiting scientist grant.

References

Albarede F. and Beard B. (2004)
Analytical methods for non-traditional isotopes. Reviews in Mineralogy and Geochemistry, 55, 113–152.

Algeo T.J. and Maynard J.B. (2004)
Trace-element behavior and redox facies in core shales of Upper Pennsylvanian Kansas-type cyclothems. Chemical Geology, 206, 289–318.

Anbar A.D. (2004)
Molybdenum stable isotopes: Observations, interpretations and directions. Reviews in Mineralogy and Geochemistry, 55, 429–454.

Anbar A.D. and Rouxel O. (2007)
Metal stable isotopes in paleoceanography. Annual Review of Earth and Planetary Sciences, 35, 717–746.

Axelsson M.D., Rodushkin I., Ingri J. and Ohlander B. (2002)
Multielemental analysis of Mn-Fe nodules by ICP-MS: Optimisation of analytical method. Analyst, 127, 76–82.

Barling J., Arnold G.L. and Anbar A.D. (2001)
Natural mass-dependent variations in the isotopic composition of molybdenum. Earth and Planetary Science Letters, 193, 447–457.

Bekker A., Barley M.E., Fiorentini M.L., Rouxel O.J., Rumble D. and Beresford S.W. (2009)
Atmospheric sulfur in Archaean komatiite-hosted nickel deposits. Science, 326, 1086–1089.

Bigalke M., Weyer S., Kobza J. and Wilcke W. (2010)
Stable Cu and Zn isotope ratios as tracers of sources and transport of Cu and Zn in contaminated soil. Geochimica et Cosmochimica Acta, 74, 6801–6813.

Birck J.L. and Lugmair G.W. (1988)
Nickel and chromium isotopes in Allende inclusions. Earth and Planetary Science Letters, 90, 131–143.

Brumsack H.J. (2006)
The trace metal content of recent organic carbon-rich sediments: Implications for Cretaceous black shale formation. Palaeogeography, Palaeoclimatology, Palaeoecology, 232, 344–361.

Cameron V., Vance D., Archer C. and House C.H. (2009)
A biomarker based on the stable isotopes of nickel. Proceedings of the National Academy of Sciences of the United States of America, 106, 10944–10948.

Chapman J.B., Mason T.F.D., Weiss D.J., Coles B.J. and Wilkinson J.J. (2006)
Chemical separation and isotopic variations of Cu and Zn from five geological reference materials. Geostandards and Geoanalytical Research, 30, 5–16.

Chen J.H., Papanastassiou D.A. and Wasserburg G.J. (2009)
A search for nickel isotopic anomalies in iron meteorites and chondrites. Geochimica et Cosmochimica Acta, 73, 1461–1471.

Cloquet C., Rouxel O., Carignan J. and Libourel G. (2005)
Natural cadmium isotopic variations in eight geological reference materials (NIST SRM 2711, BCR 176, GSS-1, GXR-1, GXR-2, GSD-12, Nod-P-1, Nod-A-1) and anthropogenic samples, measured by MC-ICP-MS. Geostandards and Geoanalytical Research, 29, 95–106.

Cook D.L., Wadhwa M., Janney P.E., Dauphas N., Clayton R.N. and Davis A.M. (2006)
High precision measurements of non-mass-dependent effects in nickel isotopes in meteoritic metal via multicollector ICP-MS. Analytical Chemistry, 78, 8477–8484.

Cook D.L., Wadhwa M., Clayton R.N., Dauphas N., Janney P.E. and Davis A.M. (2007)
Mass-dependent fractionation of nickel isotopes in meteoritic metal. Meteoritics and Planetary Science, 42, 2067–2077.

Cook D.L., Clayton R.N., Wadhwa M., Janney P.E. and Davis A.M. (2008)
Nickel isotopic anomalies in troilite from iron meteorites. Geophysical Research Letters, 35, L01203.

Coplen T.B. (2011)
Guidelines and recommended terms for expression of stable-isotope-ratio and gas-ratio measurement results. Rapid Communications in Mass Spectrometry, 25, 2538–2560.

Dauphas N. and Rouxel O. (2006)
Mass spectrometry and natural variations of iron isotopes. Mass Spectrometry Reviews, 25, 831–832.

Dideriksen K., Baker J.A. and Stipp S.L.S. (2006)
Iron isotopes in natural carbonate minerals determined by MC-ICP-MS with a ^{58}Fe–^{54}Fe double spike. Geochimica et Cosmochimica Acta, 70, 118–132.

Edwards K.J., Glazer B.T., Rouxel O.J., Bach W., Emerson D., Davis R.E., Toner B.M., Chan C.S., Tebo B.M., Staudigel H. and Moyer C.L. (2011)
Ultra-diffuse hydrothermal venting supports Fe-oxidizing bacteria and massive umber deposition at 5000 m off Hawaii. The ISME Journal, 5, 1748–1758.

Eiler J.M. (2001)
Oxygen isotope variations of basaltic lavas and upper mantle rocks. Reviews in Mineralogy and Geochemistry, 43, 319–364.

Fehr M.A., Rehkämper M. and Halliday A.N. (2004)
Application of MC-ICP-MS to the precise determination of tellurium isotope compositions in chondrites, iron meteorites and sulfides. International Journal of Mass Spectrometry, 232, 83–94.

references

Fiorentini M., Rosengren N., Beresford S., Grguric B. and Barley M. (2007)
Controls on the emplacement and genesis of the MKD5 and Sarah's Find Ni–Cu–PGE deposits, Mount Keith, Agnew–Wiluna Greenstone Belt, Western Australia. Mineralium Deposita, 42, 847–877.

Fouquet Y., Cambon P., Etoubleau J., Charlou J.L., Ondréas H., Barriga F.J.A.S., Cherkashov G., Semkova T., Poroshina I., Bohn M., Donval J.P., Henry K., Murphy P. and Rouxel O. (2010)
Geodiversity of hydrothermal processes along the mid-atlantic ridge and ultramafic-hosted mineralization: A new type of oceanic Cu-Zn-Co-Au volcanogenic massive sulfide deposit. Geophysical Monograph Series, 188, 444pp.

Fujii T., Moynier F., Dauphas N. and Abe M. (2011)
Theoretical and experimental investigation of nickel isotopic fractionation in species relevant to modern and ancient oceans. Geochimica et Cosmochimica Acta, 75, 469–482.

Gall L., Williams H., Siebert C. and Halliday A. (2012)
Determination of mass-dependent variations in nickel isotope compositions using double spiking and MC-ICP-MS. Journal of Analytical Atomic Spectrometry, 27, 137–145.

Govindaraju K. (1994)
1994 compilation of working values and sample description for 383 geostandards. Geostandards Newsletter, 18 (Special Issue), 158pp.

Gramlich J.W., Machlan L.A., Barnes I.L. and Paulsen P.J. (1989)
Absolute isotopic abundance ratios and atomic weight of a reference sample of nickel. Journal of Research of the National Institute of Standards and Technology, 94, 347–356.

Gueguen B., Rouxel O., Ponzevera E., Sorensen J.V., Toner B.M., Bekker A. and Fouquet Y. (2011)
Ni biogeochemical cycle through geological time: Insights from Ni isotope variations in modern and ancient marine metallifereous deposits. AGU Fall Meeting 2011, San Francisco, USA.

Hofmann A., Bekker A., Dirks P., Gueguen B., Rouxel O.J. and Rumble D. (in press)
Comparing orthomagmatic and hydrothermal mineralization models of komatiite-hosted nickel deposits in Zimbabwe using multiple-sulfur, iron and nickel isotope data.

Horner T.J., Schönbächler M., Rehkämper M., Nielsen S.G., Williams H., Halliday A.N., Xue Z. and Hein J.R. (2010)
Ferromanganese crusts as archives of deep water Cd isotope compositions. Geochemistry Geophysics Geosystems, 11, 1525–2027.

Houlé M., Lesher C.M. and Davis P. (2012)
Thermomechanical erosion at the Alexo Mine, Abitibi greenstone belt, Ontario: Implications for the genesis of komatiite-associated Ni–Cu–(PGE) mineralization. Mineralium Deposita, 47, 105–128.

Huh M.C., Lazar C., Young E.D. and Manning C.E. (2009)
High temperature fractionation of Ni stable isotopes between metal and silicates: Constraints from experimental study at 800 °C and 10 kbar. EOS Transactions AGU, 90.

Kurz M.D., Jenkins W.J., Hart S.R. and Clague D. (1983)
Helium isotopic variations in volcanic rocks from Loihi seamount and the island of Hawaii. Earth and Planetary Science Letters, 66, 388–406.

Marechal C.N., Télouk P. and Albarède F. (1999)
Precise analysis of copper and zinc isotopic compositions by plasma-source mass spectrometry. Chemical Geology, 156, 251–273.

Morand P. and Allegre C.J. (1983)
Nickel isotopic studies in meteorites. Earth and Planetary Science Letters, 63, 167–176.

Moynier F., Blichert-Toft J., Télouk P., Luck J.M. and Albarède F. (2007)
Comparative stable isotope geochemistry of Ni, Cu, Zn, and Fe in chondrites and iron meteorites. Geochimica et Cosmochimica Acta, 71, 4365–4379.

Muir J.E. and Comba C.D.A. (1979)
The Dundonald deposit: An example of volcanic-type nickel-sulfide mineralization. Canadian Mineralogist, 17, 351–359.

Naldrett A.J. and Mason G.D. (1968)
Contrasting Archaean ultramafic igneous bodies in Dundonald and Clergue Townships, Ontario. Canadian Journal of Earth Sciences, 5, 111–143.

Nielsen S.G., Rehkämper M., Baker J. and Halliday A.N. (2004)
The precise and accurate determination of thallium isotope compositions and concentrations for water samples by MC-ICP-MS. Chemical Geology, 204, 109–124.

Plank T., Ludden J.N., Escutia C., Abrams L., Alt J.C., Armstrong R.N., Barr S., Bartolini A., Cairns G., Fisk M.R., Guerin G., Haveman S.A., Hirono T., Honnorez J., Kelley K.A., Larson R.L., Lozar F.M., Murray R.W., Pletsch T.K., Pockalny R.A., Rouxel O., Schmidt A., Smith D.C., Spivack A.J., Staudigel H., Steiner M.B. and Valentine R.B. (2000)
Site 1149. Proceedings of the Ocean Drilling Program, Part A: Initial Reports, 185.

Quitté G., Meier M., Latkoczy C., Halliday A.N. and Günther D. (2006)
Nickel isotopes in iron meteorites-nucleosynthetic anomalies in sulphides with no effects in metals and no trace of ^{60}Fe. Earth and Planetary Science Letters, 242, 16–25.

Regelous M., Elliott T. and Coath C.D. (2008)
Nickel isotope heterogeneity in the early Solar System. Earth and Planetary Science Letters, 272, 330–338.

Rehkämper M., Frank M., Hein J.R., Porcelli D., Halliday A., Ingri J. and Liebetrau V. (2002)
Thallium isotope variations in seawater and hydrogenetic, diagenetic, and hydrothermal ferromanganese deposits. Earth and Planetary Science Letters, 197, 65–81.

references

Rosengren N., Cas R.A.F., Beresford S.W. and Palich B.M. (2008)
Reconstruction of an extensive Archaean dacitic submarine volcanic complex associated with the komatiite-hosted Mt Keith nickel deposit, Agnew-Wiluna Greenstone Belt, Yilgarn Craton, Western Australia. Precambrian Research, 161, 34–52.

Rouxel O., Dobbek N., Ludden J. and Fouquet Y. (2003)
Iron isotope fractionation during oceanic crust alteration. Chemical Geology, 202, 155–182.

Rouxel O., Fouquet Y. and Ludden J.N. (2004)
Copper isotope systematics of the Lucky Strike, Rainbow, and Logatchev sea-floor hydrothermal fields on the Mid-Atlantic Ridge. Economic Geology and the Bulletin of the Society of Economic Geologists, 99, 585–600.

Rudge J.F., Reynolds B.C. and Bourdon B. (2009)
The double spike toolbox. Chemical Geology, 265, 420–431.

Rugel G., Faestermann T., Knie K., Korschinek G., Poutivtsev M., Schumann D., Kivel N., Günther-Leopold I., Weinreich R. and Wohlmuther M. (2009)
New measurement of the ^{60}Fe half-life. Physical Review Letters, 103, 072502.

Schmitt A.D., Galer S.J.G. and Abouchami W. (2009)
Mass-dependent cadmium isotopic variations in nature with emphasis on the marine environment. Earth and Planetary Science Letters, 277, 262–272.

Scott C., Lyons T.W., Bekker A., Shen Y., Poulton S.W., Chu X. and Anbar A.D. (2008)
Tracing the stepwise oxygenation of the Proterozoic ocean. Nature, 452, 456–U5.

Scott C.T., Bekker A., Reinhard C.T., Schnetger B., Krapez B., Rumble D. and Lyons T.W. (2011)
Late Archean euxinic conditions before the rise of atmospheric oxygen. Geology, 39, 119–122.

Shimamura T. and Lugmair G.W. (1983)
Ni isotopic compositions in Allende and other meteorites. Earth and Planetary Science Letters, 63, 177–188.

Siebert C., Nägler T.F. and Kramers J.D. (2001)
Determination of molybdenum isotope fractionation by double-spike multicollector inductively coupled plasma-mass spectrometry. Geochemistry Geophysics Geosystems, 2, 1032.

Steele R.C.J., Elliott T., Coath C.D. and Regelous M. (2011)
Confirmation of mass-independent Ni isotopic variability in iron meteorites. Geochimica et Cosmochimica Acta, 75, 7906–7925.

Tanimizu M. and Hirata T. (2006)
Determination of natural isotopic variation in nickel using inductively coupled plasma-mass spectrometry. Journal of Analytical Atomic Spectrometry, 21, 1423–1426.

Teng F.Z., Dauphas N. and Helz R.T. (2008)
Iron isotope fractionation during magmatic differentiation in Kilauea Iki Lava Lake. Science, 320, 1620–1622.

Tribovillard N., Algeo T.J., Lyons T. and Riboulleau A. (2006)
Trace metals as paleoredox and paleoproductivity proxies: An update. Chemical Geology, 232, 12–32.

Turekian K.K. and Wedepohl K.H. (1961)
Distribution of the elements in some major units of the Earth's crust. Geological Society of America Bulletin, 72, 175–192.

Young E.D. and Galy A. (2004)
The isotope geochemistry and cosmochemistry of magnesium. Reviews in Mineralogy and Geochemistry, 55, 197–230.

Partie I.2 - Mesure de la composition isotopique de l'eau de mer

1. Méthode expérimentale de la séparation et purification des isotopes du Ni appliquées à des matrices d'eau de mer

La séparation des métaux traces dissous dans l'eau de mer est une étape délicate en raison de la quantité importante d'éléments alcalins et alcalino-terreux présents dans la matrice d'eau de mer. Deux autres méthodes ont été utilisées préalablement à celle-ci mais elles ont été abandonnées soit en raison de l'inefficacité lors la séparation en elle-même (très mauvais rendements), soit en raison de blancs de chimie trop élevés. Les deux méthodes testées sont la pré-concentration du Ni par co-précipitation dans des oxydes de Fe, et la pré-concentration du Ni en utilisant la résine Chelex sur des colonnes chromatographiques suivant la méthode décrite pour les isotopes du Cu et du Zn (Bermin et al. 2006). Dans un ultime essai de séparation du Ni la méthode décrite ci-dessous s'est révélée être la plus adéquate. Par ailleurs, cette méthode permet non seulement de pré-concentrer le Ni de l'eau de mer mais également les autres métaux de transition présents à l'état de trace ainsi que les Terres Rares.

2. Synthèse de la résine utilisée pour les colonnes chromatographiques lors de la pré-concentration des métaux dans l'eau de mer

La purification des métaux de transition de l'eau de mer a été réalisée en utilisant une résine polymérique macroporeuse (polymère de méthacrylate). Le complexe 5-amino,8-hydroxyquinoline.2HCl (8HQ) est un chélateur ayant de très fortes affinités avec les métaux de transition par rapport aux métaux alcalins et alcalino-terreux (Landing et al. 1986). Le principe repose sur la liaison covalente de ce complexe 8HQ avec la résine AF-epoxy-650M (Tosoh Bioscience) déjà activée dont la dimension des perles est 40-90 µm (l'ensemble sera par la suite dénommé TSK-8HQ). Ainsi la liaison des métaux de transition par chélation sur le complexe 8HQ permet une séparation efficace des métaux de transition et des Terres Rares de la matrice d'eau de mer riche en sels. Pour ce faire il est nécessaire dans un premier temps de synthétiser la réaction de liaison du complexe 8HQ sur la résine epoxy. De manière pratique, 5 grammes de de 8HQ (Sigma-Aldrich) ont été dissous dans 25 mL d'eau milliQ (Millipore®) et ajuster à un pH de 11-12 avec NaOH à 10 mol/L. Ensuite, 2.5 grammes de résine AF-epoxy-650M ont été ajoutées et le mélange entier a été mis à chauffer à 80°C durant 6 heures. La procédure de synthèse de cette résine ainsi que la procédure expérimentale de séparation sont adaptées de (Sohrin et al. 1998; Dierssen et al. 2001; Firdaus et al. 2007; Nakagawa et al. 2008).

3. Procédure de séparation sur colonnes chromatographiques

Une fois la synthèse TSK-8HQ réalisée, 0.8 mL a été prélevé puis chargé sur des colonnes chromatographiques en polypropylène. La résine a été lavée avec 20 mL d'eau milliQ et 20 mL d'un mélange de HCl à 2 mol/L et d'HNO_3 0.5mol/L, et le conditionnement a été réalisé avec 50 mL d'ammonium acétate à 0.05 mol/L tamponné à un pH de 5.3. La quantité d'échantillon d'eau de mer chargé sur la colonne est de 200 mL. De plus, afin d'évaluer précisément les rendements de Ni obtenus lors de l'entière procédure, une quantité connue de double-spike en Ni est ajoutée à chaque échantillon. Enfin les 200 mL d'échantillon sont préalablement tamponné à un pH de 5.3.

L'élution se fait ensuite en deux étapes, dans un premier temps la matrice d'eau de mer est éluée avec 15 ml d'acétate d'ammonium à 0.05 mol/L tamponné à un pH de 5.3,

puis l'élution des métaux de transition se poursuit par l'ajout de 25 mL d' HNO_3 à 0.5 mol/L. Pour terminer, la résine est rincée avec 20 mL d'un mélange de HCl à 2 mol/L et d'HNO_3 0.5mol/L, puis 10 mL d'acétate d'ammonium à 0.05 mol/L tamponné à un pH de 5.3, et enfin 10 mL d'eau milliQ.

Après évaporation totale des solutions éluées, les échantillons sont chargés sur la résine Ni-spec en suivant la procédure identique à celle utilisée pour la purification des échantillons de roche (cf. partie 1 de ce chapitre).

4. Composition isotopique du Ni de l'eau de mer

L'analyse isotopique a été réalisée sur un échantillon d'eau de mer profonde du Pacifique Nord. Pour une concentration de 18.7 nmol/L $\delta^{60/58}$Ni = +1.25 ±0.02‰.

Conclusion du chapitre I :

Outre les développements analytiques nécessaires pour l'obtention de données isotopiques en Ni précises notamment grâce à l'utilisation d'un double-spike en Ni pour corriger du biais de masse instrumental lors de l'analyse par MC-ICP-MS, ce premier chapitre a permis de rendre compte l'étendue de la variabilité des compositions isotopiques en Ni dans différents réservoirs terrestres (roches ignées, roches sédimentaires,…). En effet, lorsque nous avons commencé à nous intéresser aux isotopes du Ni nous ne disposions que de très peu de données isotopiques en Ni sur les matériaux terrestres. Ainsi, nous avons ensuite choisi de publier les données acquises sur une variété de matériaux géologiques de référence pour, d'une part montrer la grande variabilité isotopique, et d'autre part fournir un jeu de données de référence pour les études qui suivront. Enfin, cette première approche a permis de montrer que les processus de haute température (par ex. processus magmatiques) produisent des fractionnements isotopiques négatifs du Ni, alors que les processus de basse température (par ex. processus sédimentaires) produisent des fractionnements isotopiques positifs (Figure C.1).

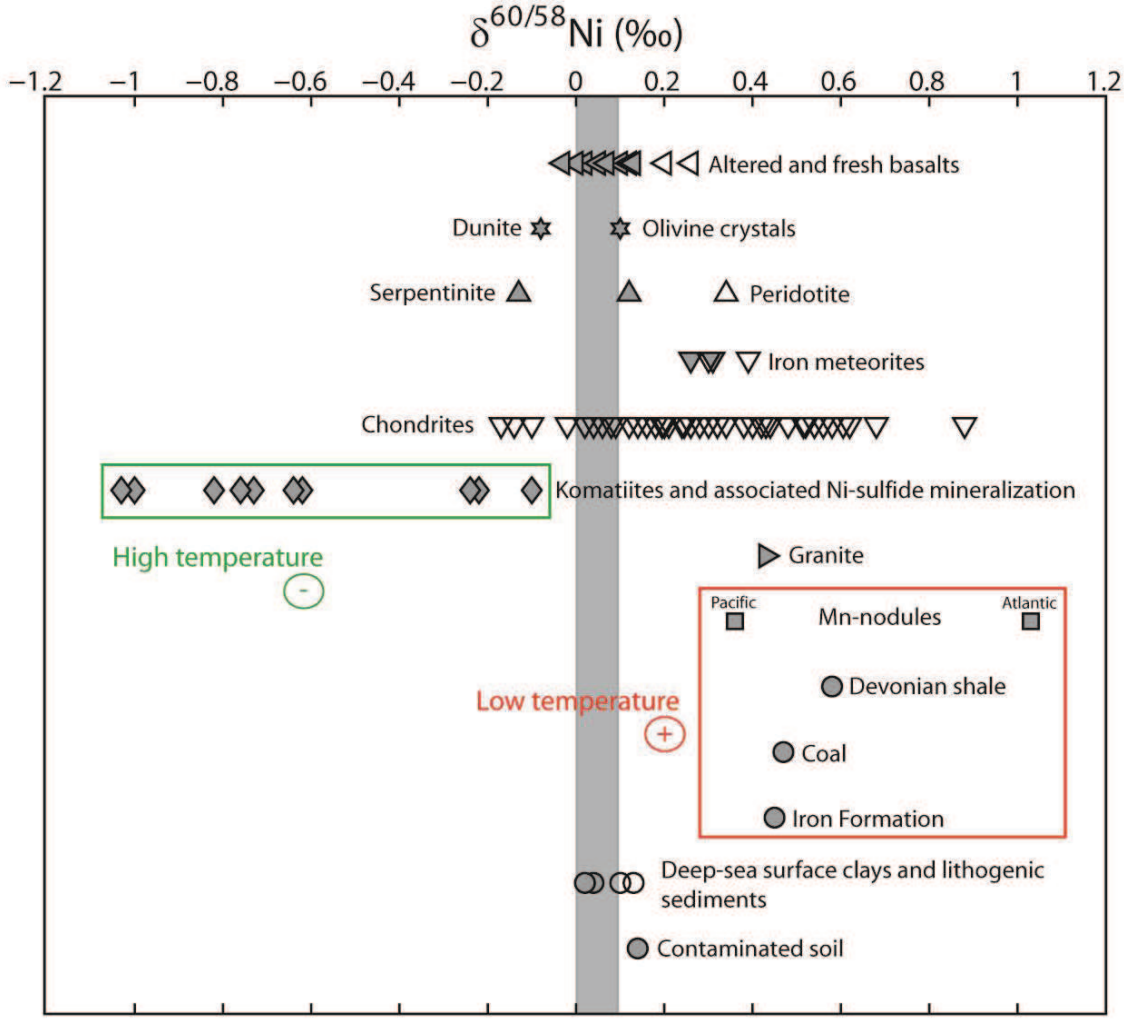

Figure C.1 : *Synthèse des données isotopiques déterminées dans différents réservoirs terrestres. Les symboles gris représentent les données de cette étude, les symboles blancs correspondent aux données de la littérature (figure modifiée de Gueguen et al. 2013).*

Chapitre II - Fractionnement isotopique du nickel lors de l'adsorption sur des oxy-hydroxydes de fer et de manganèse en conditions expérimentales

Chapter II – Experimental determination of nickel isotope fractionation during adsorption onto iron and manganese oxyhydroxides

Avant-propos :

Avant le début de ce projet de recherche, Olivier Rouxel avait initié une collaboration avec des chercheurs de l'Université du Minnesota (USA), Brandy Toner et Jeffry Sorensen, pour étudier le fractionnement isotopique du Ni qui pourrait se produire lors de son adsorption sur des phases minérales de d'oxydes de fer et de manganèse. Leur travail consistait à réaliser les expériences en laboratoire d'adsorption du Ni sur des phases minérales synthétisées, tandis que nous nous occupions des analyses isotopiques en Ni. La collaboration avec ces chercheurs est très précieuse car outre les travaux de laboratoire qu'ils ont réalisés, ce sont également des experts des techniques d'analyses de spectrométrie d'absorption des rayons X par utilisation du rayonnement synchrotron (EXAFS). En effet, l'objectif était également de déterminer la coordination du Ni dans les phases minérales et dans les solutions à partir desquelles les expériences ont été menées afin de savoir si les variations des fractionnements isotopiques du Ni en fonction des phases minérales, conditions expérimentales, etc, s'expliquaient par des changements de coordination dans le minéral ou de spéciation du Ni dans la solution. Ces expérimentations sont un atout non négligeable pour les travaux qui ont été effectués tout au long de ce projet de thèse. Les dépôts métallifères océaniques sont en majeure partie formés de phases minérales précipitées dans l'eau de mer et l'incorporation des métaux traces dans ces phases minérales se fait en grande partie via des processus d'adsorption. Or ces processus peuvent générer des fractionnements isotopiques non négligeables qu'il est important de contraindre pour interpréter de manière fiable les compositions isotopiques déterminées dans des échantillons naturels.

Les expérimentations ont été réalisées sur des oxyhydroyxdes de fer et de manganèse, qui sont les phases minérales prédominantes présentes dans les dépôts métallifères océaniques, et qui incorporent les métaux de transition dans leur réseau cristallin.

La première partie concerne les données obtenues sur les oxydes de fer rédigée sous forme d'un article. La rédaction de cette partie a déjà bénéficié de l'apport des collaborateurs, Jeffry Sorensen, Brandy Toner et Stefan Lalonde entre autres. En revanche, bien que l'acquisition des données pour les oxydes de manganèse ne soit pas encore terminée (le jeu de données isotopiques du Ni sur toutes les phases n'est pas encore complet), les résultats étant forts et importants, ils seront tout de même présenter succinctement dans une seconde partie de ce chapitre.

Partie II.1 - Fractionnement isotopique du nickel lors de l'adsorption sur des oxy-hydroxydes de fer en conditions expérimentales

Part II.1 - Experimental determination of Ni isotope fractionation during adsorption on Fe-oxyhydroxides

Article in preparation with Jeffry Sorensen, Olivier Rouxel, Brandy Toner and Stefan Lalonde

Abstract :

This study aims to provide experimental constraints on nickel (Ni) isotope fractionation during adsorption on goethite and 2-line ferrihydrite. We conducted two types of experiments: one with variable pH but constant initial Ni concentrations in solution and the other at a constant pH of 7.7 but with different initial Ni concentrations. Isotopic measurements were made both on the solid phase and the supernatant solution remaining after adsorption. Our results show a preferential uptake of lighter Ni isotopes during adsorption of Ni onto Fe-oxyhydroxides. Goethite yields the most fractionated $\Delta^{60/58}Ni_{min/sol}$ values (determined as $\Delta^{60/58}Ni_{min/sol} = \delta^{60/58}Ni_{min} - \delta^{60/58}Ni_{sol}$) down to -1.00 ±0.03 ‰, whereas 2-line ferrihydrite yields values down to -0.40 ±0.04 ‰. Isotopic data were interpreted within a framework of Ni coordination and speciation chemistry using surface complexation modeling and Extended X-Ray Absorption Fine Structure (EXAFS). Our data indicate that (1) Ni adsorption on Fe-oxides is characterized by light isotope enrichment due to equilibrium fractionation, and (2) the extent of Ni isotope fractionation is different according to the type of mineral. These results have important implications regarding the previous assumption that Fe- and Mn-rich deposits like ferromanganese crusts are a direct proxy for deep seawater Ni isotope compositions.

1. Introduction

Nickel (Ni) isotopes are an emerging tool for investigating the origin and history of oceanic metalliferous deposits like ferromanganese (Fe-Mn) crusts and manganese nodules (Gueguen et al. 2011; Gall et al. 2013; Gueguen et al. 2013). Specific attention has been given to Fe-Mn crusts, composed of Mn-oxides phases with Fe-oxides phases in a lesser abundance and covering the flank of seamounts upon which they may form massive encrustations (Koschinsky and Halbach 1995; Hein et al. 2003; Koschinsky and Hein 2003). During formation of precursor Fe-Mn colloids (amorphous vernadite δ-MnO_2 and amorphous goethite) in the water column, dissolved transition metals are scavenged from seawater by adsorption processes at the mineral surface, such that transition metals in these deposits may directly reflect the seawater pool of dissolved metals. In addition, their slow accumulation rates (1-6 mm/Ma) imply that some deposits may be as old as 60 Ma (Frank et al. 1999; Frank et al. 2002). Therefore, Fe-Mn crusts may represent a geological archive of the transition metal concentrations and isotope compositions of deep seawater, one that is already being exploited in order to understand deep ocean metal cycling throughout the Cenozoic (Frank 2002; Gall et al. 2013).

Recently, a depth profile of Ni isotope compositions through a Central Pacific Fe-Mn crust (Gall et al. 2013) led the authors to suggest that light Ni isotope excursions resulted from increased hydrothermal inputs in the Pacific. However, this hypothesis is based on the assumption that no isotope fractionation occurred between the source of Ni to the crust (seawater) and oxide mineral phases during adsorption, especially because the seawater isotope composition falls in the range of values determined for Fe-Mn crusts. But as shown in previous studies for other transition metals like Mo (Barling and Anbar 2004; Wasylenki et al. 2011), Zn (Juillot et al. 2008), Cu (Balistrieri et al. 2008), Tl (Rehkämper et al. 2002) and Fe (Skulan et al. 2002; Johnson et al. 2005; Beard et al. 2010; Wu et al. 2011; Wu et al. 2012), adsorption of metals on mineral phases is generally accompanied by isotope fractionation that may vary according to sorbant mineralogy. So far, there is no experimental data characterizing Ni isotope fractionation during adsorption and precipitation processes. Hence,

it remains unclear whether the extent of Ni isotope variability in Fe-Mn crusts depends on mechanisms of Ni uptake, the type of mineral carrier, or secular variations in seawater.

Although Ni is substantially sequestered in Mn-oxides of marine deposits from modern oceans (e.g. Fe-Mn crusts), Fe-oxides may also constitute important mineral hosts for Ni in modern marine deposits and further play a role during transport of Ni in continental run-off through Fe- and Mn-oxides coatings on riverine suspended matter. In addition, Ni present in Banded Iron Formations (BIF), Fe-rich metasediments deposited throughout much of the Precambrian, is essentially hosted in Fe-oxide minerals (Konhauser et al. 2009). Similar to the case of Fe-Mn crusts, these deposits hold strong potential for recording the Ni isotope composition of seawater in deep time. However, evaluation of potential fractionation during mineral adsorption is critical for any interpretation of the Ni isotopic record of evolving seawater that they may possess.

To address these issues we conducted Ni adsorption experiments on two types of experimentally synthesized Fe-oxyhydroxides, 2-line ferrihydrite and goethite, and at variable pH and at variable Ni concentrations, with the goal of determining Ni isotope fractionation factors associated with adsorption. Measurements of Ni isotope composition of both the solid and liquid phases were coupled to EXAFS analyses to determine the role of Ni speciation and coordination in Ni isotope fractionation.

2. Materials and methods

2.1 Synthesis of Fe-oxyhydroxides and Ni adsorption procedure

All reagents employed were analytical grade and 18.2 $M\Omega \cdot cm^{-1}$ deionized (DI) water was supplied by a Millipore system. Reaction vessels were Savillex® PFA vials that had been previously soaked in heated 50% HNO_3, rinsed with DI water, and air dried. All preparation steps and experiments were performed in the class 1000 clean lab facilities at IFREMER Brest, at ambient atmospheric pressure, and at 25°C. Atmospheric CO_2 was not excluded from the experimental solutions however the formation of Ni-carbonate complexes is negligible below pH 8 (see text below).

Goethite and 2-line ferrihydrite was synthesized according to (Schwertman and Cornell 1991). Synthesized minerals were dried and degassed at 150°C before specific surface area was measured by nitrogen adsorption and calculated according to BET theory. Mineral surface charge was determined using a ZetaPALS analyzer (Brookhaven Instruments Corp.) for 0.98 - 1.44 g/L of mineral suspended in DI water. Measurement parameters were: a conductance of 82 µS, a current of 0.34 mA, applied voltage of 7.54V, and an electric field of 9.29 V/cm, with 3 cycles of 5 measurements per mineral (Table II.1).

Ni adsorption experiments were performed as follows: a Ni standard solution of 1000 ppm used in all the experiments was made with a $Ni(NO_3)_2$-H_2O salt dissolved in 0.05M $NaNO_3$. Experimental aqueous solutions were prepared with 0.15 g of goethite and 2-line ferrihydrite mineral suspended in 150 ml of 0.05M $NaNO_3$. The first set of experiments was performed at different solution pH (pH 5, 6, 7, 7.7 and 8) with a same initial Ni concentration of 10 ppm. Each of these experiments was agitated continuously using a stir bar. After 24 hours, solids were filtered using 0.2 µm Nuclepore track-etched filters and dissolved in 6M HCl for subsequent Ni chemical purification (see below). Filtrates were also kept for isotopic analyses. A blank consisting of mineral in 0.05M $NaNO_3$ solution without Ni stock addition was included with each set of experiments and did not exceed 1% of the total amount of Ni determined in Ni-bearing experiments. Experiments were duplicated at least once.

Table II.1: Zeta potential measurements parameters.

Mineral type	Amount of mineral in solution	Conductance	Current	Applied Voltage	Zeta potential	Mobility	Relative Residual
2-line Ferrihydrite	1.44 g/L	344 µS	2.56 mA	7.54 V	-3.44 mV	-0.027	0.0093
Goethite	0.984 g/L	81 µS	0.712 mA	7.54 V	3.46 mV	0.27	0.0151

2.2 EXAFS measurements

Synchrotron-based Ni K-edge EXAFS (Extended X-ray Absorption Fine Structure) measurements were conducted at the Advanced Photon Source (Argonne National Laboratory) beamline 20-BM in transmission mode over the energy range 8130 to 9300 eV. Iron minerals on filters bearing adsorbed Ni were prepared for EXAFS analysis by being brought to room temperature and then transferred from filters to thin mylar film. The mylar film bearing the sample was then covered by another mylar film and the edges closed to form a sealed envelope around the sample. Measurements were conducted at room temperature and individual scans were examined for systematic changes in peak position or line-shape to detect photon-induced sample alteration; none was observed. All EXAFS data processing was done using the IFEFFIT software suite with the Athena program used for glitch removal, pre-edge subtraction, and post-edge normalization. The Artemis program was used to generate shell-by-shell fits for interpretation of the EXAFS spectra (Ravel and Newville 2005).

2.3 Concentration determinations and column chromatographic purification of Ni

Mineral phases were dissolved in 6M HCl at ambient temperature over a few days until all solid was completely dissolved. Solid phase mineral concentrations of Ni, Mn, and Fe were determined by quadrupole ICP-MS (X-series2, Thermo-Finnigan) at the Pôle Spectrométrie Océan (PSO, IUEM, Brest, France) prior to chromatographic separation of Ni for isotope measurements. Concentrations in the filtrate solutions were calculated by mass balance from the initial solution concentrations at the beginning of each experiment.

For column chromatographic purification of Ni, a fixed aliquot of each filtrate solution was evaporated to dryness prior to redissolution in 1 ml of 6M HCl. An identical and precisely known amount of Ni was processed for each sample. Final concentrations were recalculated after analysis by MC-ICP-MS by isotopic dilution.

A full description of the column chromatographic purification of Ni can be found in (Gueguen et al. 2013). Briefly, we used a two-step separation procedure that involved a first anion exchange chromatographic step using AG1-X8 resin to remove Fe (a primary mineral component) as well as Mn, followed by a second column step using a Ni-specific resin (manufactured by Eichrom) to separate Ni from any remaining matrix elements. This resin contains DMG (Dimethylglyoxime) complexes Ni in ammonium citrate media at pH 8-9, permitting other remaining elements to be eluted while Ni is retained on the column.

2.4. Mass spectrometry procedure and double-spike correction scheme

Nickel isotope compositions were measured by MC-ICP-MS Neptune (Thermo-Electron) at Ifremer (Brest, France) using a double-spike (composed of ^{61}Ni and ^{62}Ni) added to samples prior to loading on Ni-spec resin (second step of purification procedure) in order to correct for instrumental mass bias. An ApexQ (ESA, USA) desolvation introduction system was employed for all measurements. The nine faraday cups of the instrument allow simultaneous measurement of ^{58}Ni, ^{60}Ni, ^{61}Ni and ^{62}Ni, ^{64}Ni and ^{66}Zn isotopes as well as the potential isobaric interference ^{57}Fe. The main potential interferences include Fe (e.g. ^{58}Fe on ^{58}Ni), oxides of Ar or other elements (e.g. Ca) generated in the plasma with identical masses (e.g. $^{40}Ar^{18}O^{+}$ on $^{58}Ni^{+}$), and double-charged ions (e.g. $^{124}Xe^{2+}$ on $^{62}Ni^{+}$), the latter being negligible considering the high first-ionization potential of Xe. Argide and oxide interferences include $^{36}Ar^{24}Mg^{+}$ and $^{44}Ca^{16}O^{+}$ on $^{60}Ni^{+}$; $^{36}Ar^{25}Mg^{+}$, and $^{38}Ar^{23}Na^{+}$ on $^{61}Ni^{+}$; $^{36}Ar^{26}Mg^{+}$, $^{38}Ar^{24}Mg^{+}$, and $^{46}Ca^{16}O^{+}$ on $^{62}Ni^{+}$; $^{23}Na^{35}Cl^{+}$, $^{40}Ar^{18}O^{+}$, and $^{42}Ca^{16}O^{+}$ on $^{58}Ni^{+}$. While chromatographic purification of Ni quantitatively removes matrix elements, the instrument was operated in a medium-resolution mode such that any potential argide and oxide interferences are fully resolved.

Analysis of the samples by MC-ICP-MS is always prone to instrumental mass bias and isotope ratios must be corrected for this deviation. Rather than mass bias correction by element doping or standard-sample-bracketing (Albarede and Beard 2004; Albarede et al. 2004), we implemented a double-spike correction for Ni isotopes using the calculation method of (Siebert et al. 2001). A mixture of ^{61}Ni and ^{62}Ni isotopes was added to each sample in a known amount and for a spike/natural concentration ratio of 1 prior to the second step of the Ni purification procedure. Detailed analytical results of the Ni double-spiked correction method are reported in (Gueguen et al. 2013). For each sample, 50 cycles of measurement were performed, resulting in internal two standard error (2se) values typically between 0.02 and 0.04 ‰.

3. Results

3.1. EXAFS

Ni K-edge EXAFS spectra for 2-line ferrihydrite are presented as Fourier Transforms in Figure II.1. All 2-line ferrihydrite samples are characterized by a major peak at R+ ΔR ≈ 1.6 Å, corresponding to Ni-O scattering and a smaller, yet broad, peak at R+ ΔR ≈ 2.71 Å, corresponding to Ni-Fe scattering. Small differences are present between spectra but no systematic changes were detected across gradients.

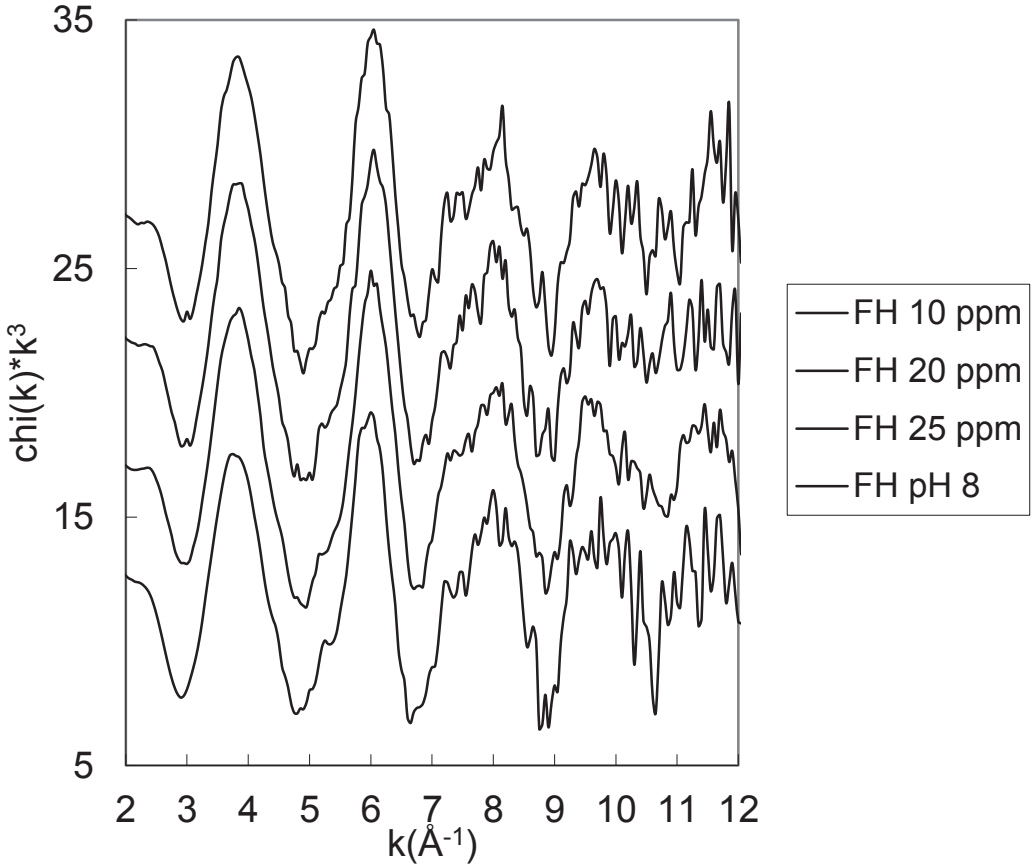

Figure II.1 *: Fourier Transform of Ni EXAFS spectra from the 2-line ferrihydrite at 25 ppm of Ni.*

Figure II.2 also shows the Fourier Transform of Ni EXAFS spectra from the 2-line ferrihydrite at 25 ppm of Ni with a rough fit for Ni-O and Ni-Fe generated using the crystallographic parameters from 2-line ferrihydrite. The Ni-Fe shell is poorly fit; the Ni-Fe scattering component was found to contain three separate scattering lengths of R+ ΔR ≈ 3.32 Å, 3.40 Å, and 3.47 Å, which our data quality did not allow us to properly constrain while maintaining acceptable structural parameters. Due to these challenges, we were able to verify that the Ni is bound to the 2-line ferrihydrite and not in another form but we were unable to determine what proportion of the Ni was incorporated into the mineral structure and how much was surface adsorbed. Ni K-edge EXAFS data collection was attempted for the goethite but due to the small amount of Ni adsorbed to the mineral surface the data quality was insufficient to provide structural data.

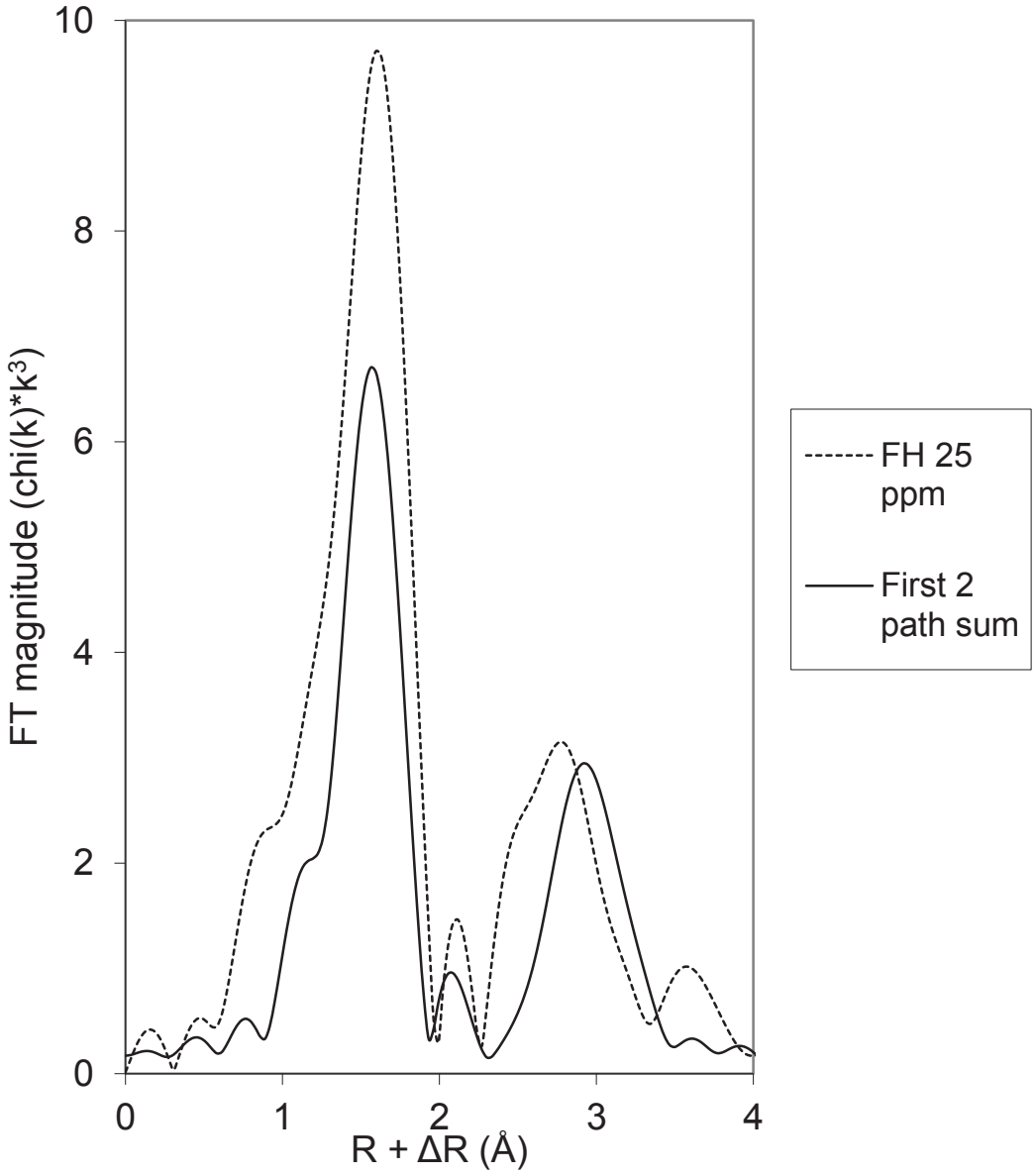

Figure II.2 : Ni K-edge EXAFS spectra for 2-line ferrihydrite presented as Fourier Transforms.

3.2. Zeta potential

Table II.1 shows the results of zeta potential measurements made on 2-line ferrihydrite and goethite at pH 7. Two-line ferrihydrite exhibits a negative surface charge with a value of -3.44 mV whereas goethite exhibits a positive surface charge with a value of 3.46 mV.

3.3. Chemistry coordination of Ni in solution

Between pH 1 and 8, Ni species in solution are mainly in the form of Ni^{2+} hydrous ions in octahedral coordination with six water molecules, and calculations using the MINEQL thermodynamic database indicates that the proportion of other species in solution, namely $Ni(OH)_{2(aq)}$ $Ni(OH)^-_3$, $NiOH^+$, $NiCO^+_3$, $NiCO_{3(aq)}$, and $NiNO^+_3$, are negligible in this pH range

and under our experimental conditions (Figure II.3). Therefore, the complex that is likely to be adsorbed on the mineral surface is Ni-xH_2O. MINEQL calculations indicate no solid precipitation in our experiments (Figure II.3), and no precipitate was observed.

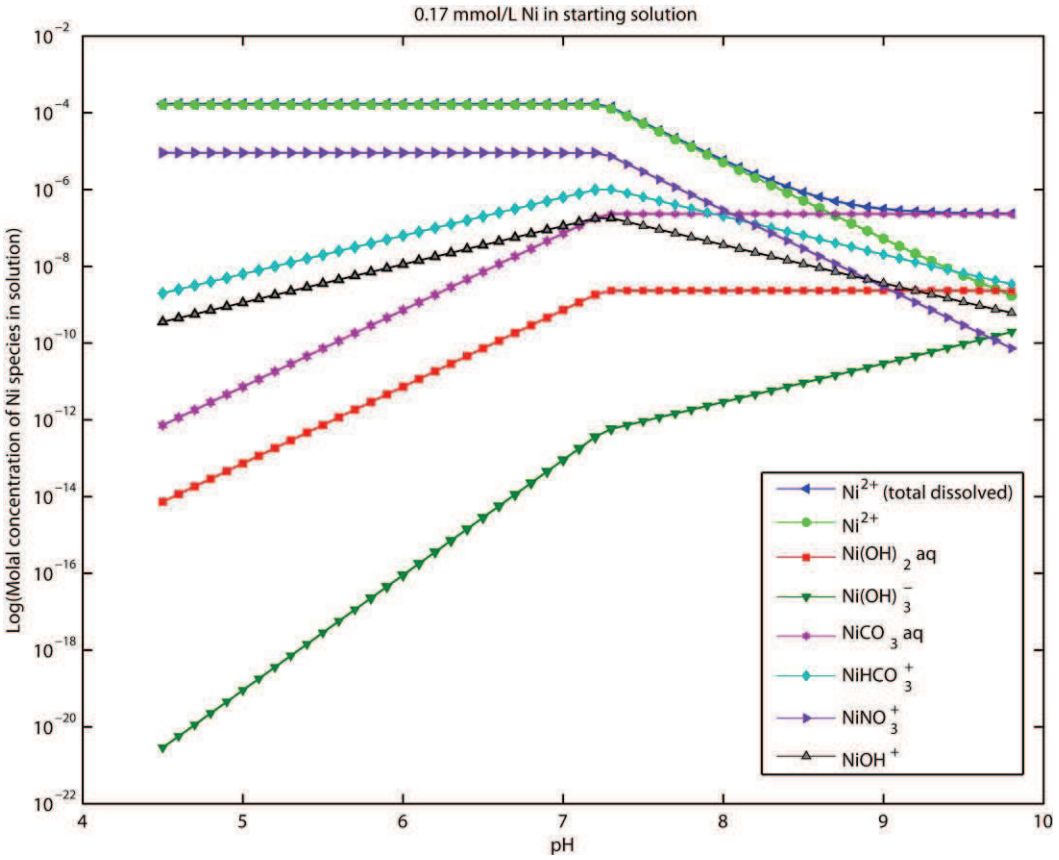

Figure II.3 *: Ni speciation modeling in solution versus pH using Visual Minteq software under experimental conditions implemented in this study. Plot show logarithm of molal concentrations of different Ni species versus pH of solution with Ni concentration in starting solution of 0.17 mmol/L.*

Previous work has also indicated that Ni is adsorbed onto Fe-oxyhydroxides primarily as the hydrous Ni^{2+} ion (Peacock and Sherman 2007a; Peacock and Sherman 2007b). According to these authors, with a 60 ppm Ni solution in 0.1M $NaNO_3$ media, $Ni(OH)_2$ begins to precipitate out at pH=7.2. Nevertheless, our calculations with MINEQL show that at 25 ppm of Ni in solution, no precipitation would occur even at pH 8. We therefore chose a pH range of between 5 and 8 for our experiments. In the second set of experiments, the varying parameter is initial Ni concentration, with values of 1, 5, 10, 20, and 25 ppm and a constant pH of 7.7. The choice of a pH of 7.7 for the second set of experiment was largely to avoid precipitation of $Ni(OH)_2$ that might occur above pH=8 (Figure II.4). For each initial concentration in these experiments, MINEQL calculations indicate that Ni was always undersaturated with respect to $Ni(OH)_2$.

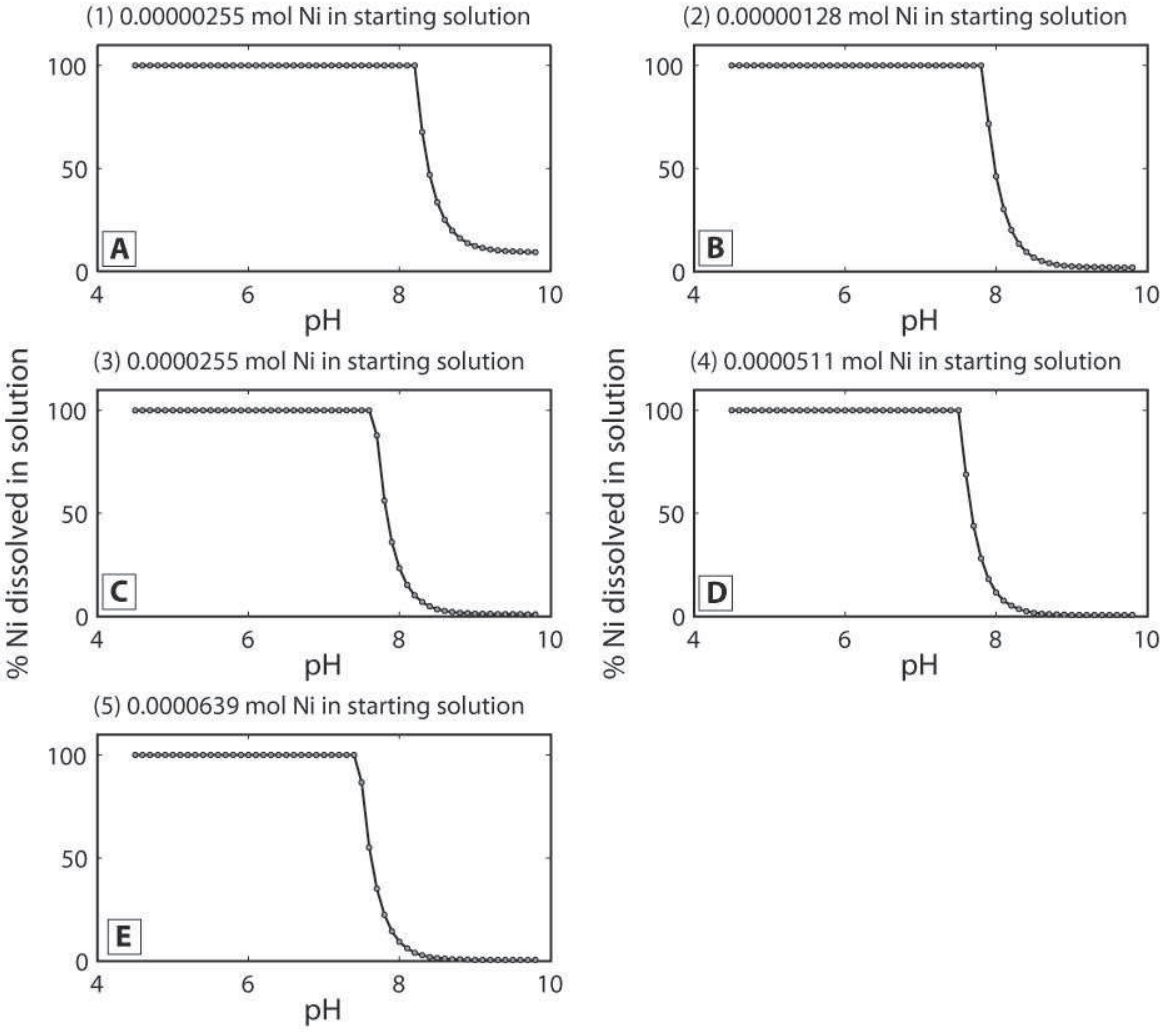

***Figure II.4**: Plots showing modeling results of adsorption percentages of Ni versus pH of solution according to different starting Ni concentration in solution. Initial Ni amount (mol) is specified on each plot.*

3.4. Surface complexation modeling

Surface complexation modeing for Ni adsorption to 2-line ferrihydrite using a constant capacitance model (CCM) was performed using adsorption parameters provided by (Dzombak and Morel 1990) (Figure II.5A). Specific surface area for the 2-line ferrihydrite used in this study was determined by BET analysis to be 119.30 m²/g. Adsorption parameters for goethite were taken from (Pokrovsky et al. 2005) and also applied in a CCM surface complexation modeling approach (Figure II.5B).

Results of our experiments on 2-line ferrihydrite are in complete agreement with the surface complexation model calculated with modeling parameters from Dzombak and Morel (1990) (Figure II.5A). However, experimental results on goethite deviate from the surface complexation model probably because little Ni was adsorbed on the mineral surface, producing small adsorption ranges. It is important to note that the CCM is a simple surface complexation model that integrates a smaller number of parameters in comparison to the diffuse-layer model and the triple-layer model (Hayes et al. 1991) and thus may not as closely approximate natural conditions.

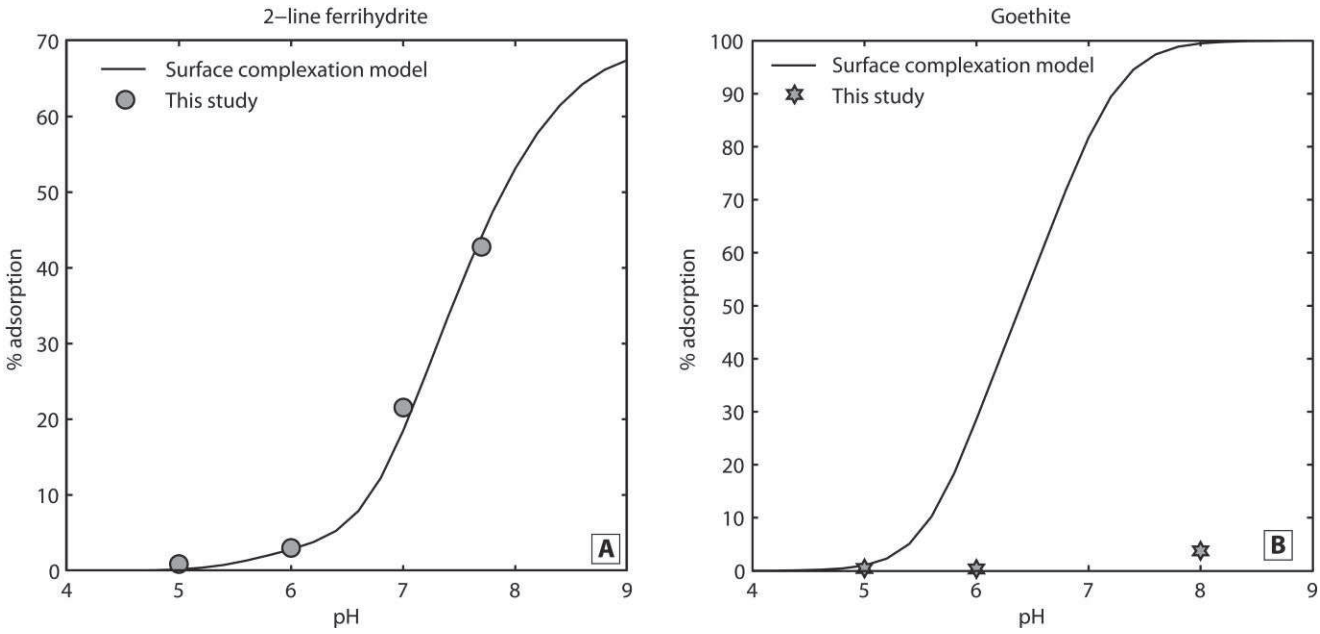

Figure II.5*: Surface complexation modeling using a Constant Capacitance Model and experimental data from this study showing Ni adsorption percentages versus pH of solution for 2-line ferrihydrite (panel A) and goethite (panel B).*

3.5. Notation for reporting Ni isotope values

Isotope ratios of sorbed and aqueous Ni are reported according to the conventional delta notation using the Ni international isotopic standard NIST SRM 986 as the standard ratio (see Gueguen et al. (2013) for more details) (1):

$$\delta^{60/58}Ni\ (‰) = (R_{sample}/R_{NIST986} - 1) \times 1000 \quad (1)$$

Different Ni loadings during batch Ni adsorption experiments were obtained by varying pH and Ni concentrations in the starting solution according to the two different experimental procedures described above. The Ni isotope composition of the initial solution used in all experiments was $\delta^{60/58}Ni = -0.33 \pm 0.05‰$ (2sd, n=4). The apparent difference in Ni isotopic composition between the mineral-adsorbed Ni and filtrate Ni remaining in solution – the fractionation factor - is expressed as $\Delta^{60/58}Ni_{min/sol}$ (Table 1) (2):

$$\Delta^{60/58}Ni_{min/sol} = \delta^{60/58}Ni_{mineral} - \delta^{60/58}Ni_{solution} \quad (2)$$

3.6. Ni adsorption experiments

pH-dependent adsorption experiments on 2-line ferrihydrite yielded adsorption percentages from 0.9% to 45.6% with $\Delta^{60/58}Ni_{min/sol}$ values ranging from -0.37 to -0.03 ‰ (Figure II.6 and Table II.2).

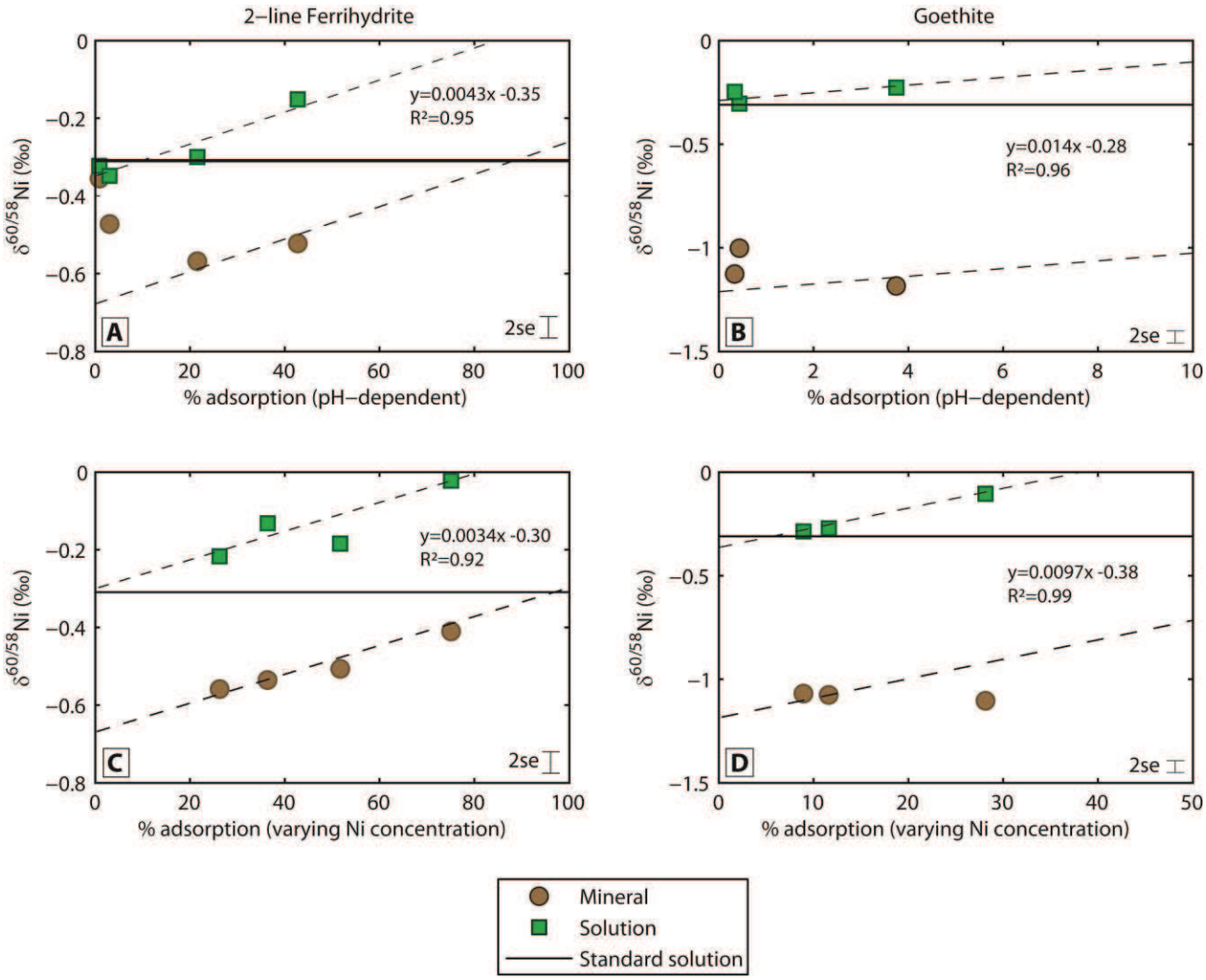

Figure II.6 *: Ni isotope composition (‰) of minerals (green squares) and supernatant solutions (brown circles) for pH-dependent experiments for 2-line ferrihydrite (panel A) and goethite (panel B), and for varying starting Ni concentration in solution experiments for 2-line ferrihydrite (panel C) and goethite (panel D). Linear fitting lines for the data and their equations are shown for panels A, C and D. The straight black line in the four plots stands for the Ni isotope composition of the starting Ni solution (*$\delta^{60/58}$*Ni = -0.33 ‰).*

At very low adsorption percentages, i.e. 0.9 and 3.0% obtained for low pH experiments (pH 5-6), Ni isotopes were not fractionated ($\Delta^{60/58}Ni_{min/sol}$ = -0.03‰) or weakly fractionated ($\Delta^{60/58}Ni_{min/sol}$ = -0.12‰) respectively (Figure II.7). The second type of experiment with varying Ni concentrations in solution at pH=7.7 produced between 26.2% and 75.1% Ni adsorption on 2-line ferrihydrite with $\Delta^{60/58}Ni_{min/sol}$ values ranging between -0.40 and -0.32 ‰ (Figure II.8).

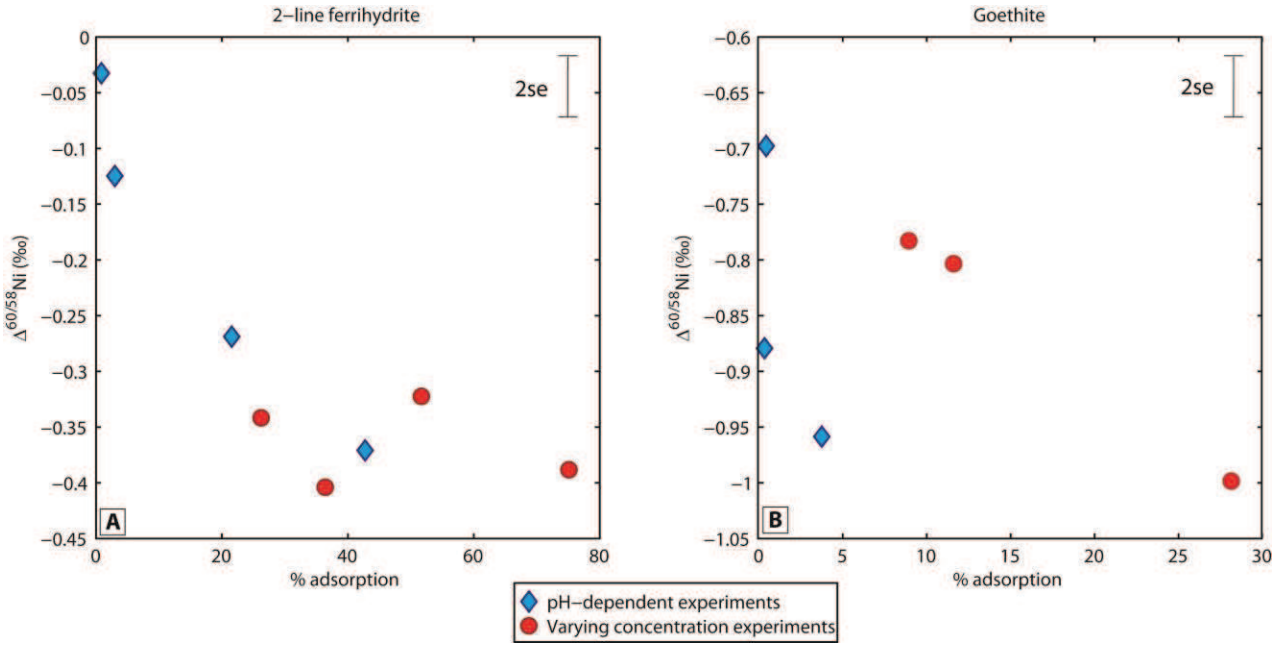

Figure II.7 *: Ni isotope fractionation factors ($\Delta^{60/58}$Ni) vs adsorption percentages for pH-dependent experiments (blue diamonds) and varying concentration experiments (red circles) plotted for 2-line ferrihydrite (panel A) and goethite (panel B).*

Ni sorption on goethite in the pH-dependent experiment was small, ranging from 0.4% to 3.7%, but Ni isotope fractionation factors yielded consistent $\Delta^{60/58}Ni_{min/sol}$ values between -0.96 and -0.70 ‰ (Figure II.6 and Table II.2). Adsorption percentages for goethite were higher in the variable Ni concentration experiments, ranging from 8.9% to 28.1%, with $\Delta^{60/58}Ni_{min/sol}$ values between -1.00 and -0.78 ‰ (Figure II.7). Similar to 2-line ferrihydrite, goethite with the lowest adsorption percentage (generally for the lowest pH) displayed less fractionated Ni isotopic compositions, with $\Delta^{60/58}Ni_{min/sol}$ = -0.70 ‰ and -0.88 ‰ for pH 5 and 6, respectively (Figure II.8). The most negative $\Delta^{60/58}Ni_{min/sol}$ value of -1.00 ‰ was observed in experiments with the highest adsorbed Ni amount (28.1%).

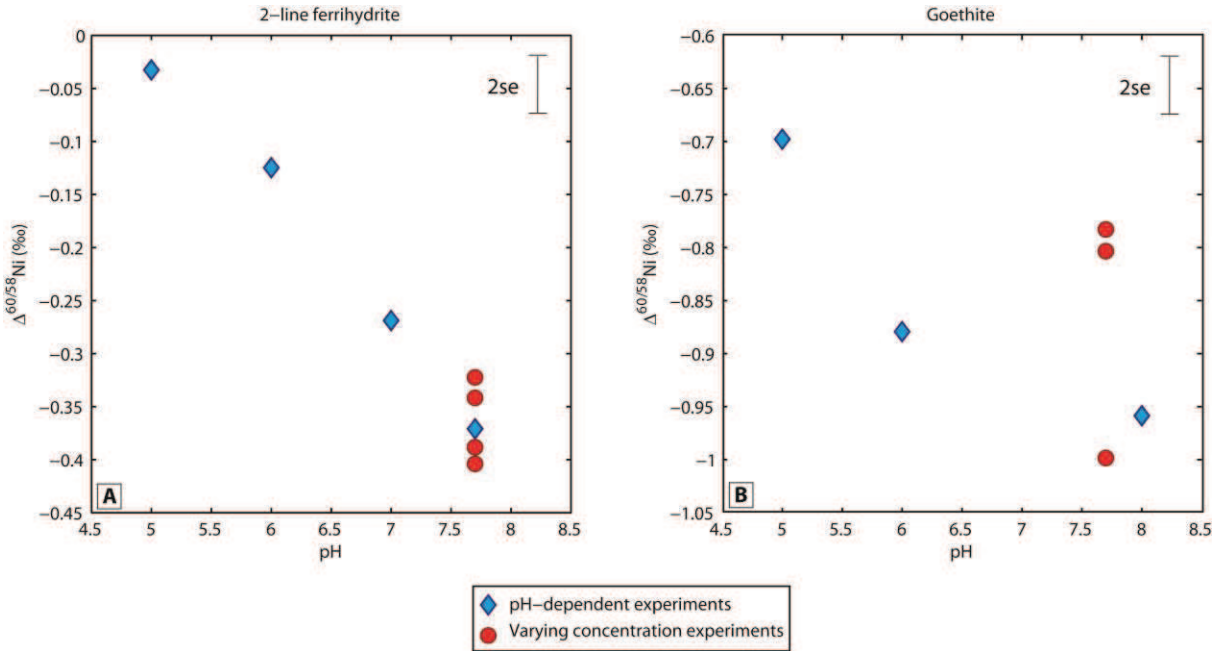

Figure II.8 *: Ni isotope fractionation factors ($\Delta^{60/58}$Ni) vs pH for pH-dependent experiments (blue diamonds) and varying concentration experiments (red circles) plotted for 2-line ferrihydrite (panel A) and goethite (panel B).*

Table II.2 : Samples information and Ni isotope composition (‰) of mineral phases and supernatant solutions for pH-dependent experiments and varying Ni concentration in solution experiments.

Mineral type	pH of solution	Type of experiment[a]	Ni (ppm) in starting solution	Ni (μg) in mineral after adsorption[b]	Ni (μg) in remaining solution after adsorption[c]	% of Ni adsorption[d]	$\delta^{60/58}Ni_{mineral}$[e]	2se	$\delta^{60/58}Ni_{solution}$[f]	2se	$\Delta^{60/58}Ni_{min/sol}$[g]
2-line Ferrihydrite	5	pH-dependent	10	16,86	1905,13	0,9	-0,36	0,02	-0,32	0,03	-0,03
2-line Ferrihydrite	6	pH-dependent	10	45,37	1466,22	3,0	-0,47	0,02	-0,35	0,03	-0,12
2-line Ferrihydrite	7	pH-dependent	10	354,16	1288,64	21,6	-0,57	0,02	-0,30	0,03	-0,27
2-line Ferrihydrite	7,7	pH-dependent	10	657,32	880,37	42,7	-0,52	0,02	-0,15	0,03	-0,37
2-line Ferrihydrite	7,7	Variable concentration	1	190,62	63,24	75,1	-0,41	0,02	-0,02	0,04	-0,39
2-line Ferrihydrite	7,7	Variable concentration	5	349,46	326,60	51,7	-0,51	0,02	-0,18	0,04	-0,32
2-line Ferrihydrite	7,7	Variable concentration	10	369,17	1039,43	26,2	-0,56	0,02	-0,22	0,04	-0,34
2-line Ferrihydrite	7,7	Variable concentration	20	949,23	1659,17	36,4	-0,54	0,03	-0,13	0,04	-0,40
Goethite	5	pH-dependent	10	9,33	2134,37	*0,4*	-1,00	0,03	-0,30	0,03	-0,70
Goethite	6	pH-dependent	10	4,95	1464,71	0,3	-1,13	0,03	-0,25	0,04	-0,88
Goethite	8	pH-dependent	10	63,99	1642,91	3,7	-1,19	0,03	-0,23	0,03	-0,96
Goethite	7,7	Variable concentration	1	162,85	415,76	28,1	-1,10	0,02	-0,11	0,03	-1,00
Goethite	7,7	Variable concentration	10	246,97	1880,32	11,6	-1,08	0,02	-0,27	0,04	-0,80
Goethite	7,7	Variable concentration	25	316,61	3225,29	8,9	-1,07	0,02	-0,29	0,03	-0,78
Ni standard solution	-			-		-	-	-	-0,32	0,03	-
Ni standard solution	-			-		-	-	-	-0,34	0,03	-
Ni standard solution							-	-	-0,30	0,03	
Ni standard solution							-	-	-0,35	0,06	
Average Ni standard solution (2SD)	**-**			**-**		**-**	**-**	**-**	**-0,33**	**0,05**	**-**

[a] Type of experiment is either pH-dependent meaning that pH of solution is variable but Ni concentration in starting solution remains constant, or consists of a varying Ni concentration in starting solution with a constant pH of 7.7 set for each experiments.

[b] Amount of Ni (µg) were first determined after analysis of minerals by ICP-AES and then by isotopic dilution after measurements on the MC-ICP-MS. The reported value is the one calculated by isotopic dilution. Amount of Ni processed through chemistry is between 2 and 10 µg.

[c] Amount of Ni (µg) of supernatant solutions were determined by isotopic dilution after analysis on the MC-ICP-MS. Amount of Ni processed through chemistry is 2 µg.
[d] Adsorption percentages were calculated using the amount of Ni determined in oxides minerals and the amount of Ni remaining in supernatant solutions. Concentrations of the latter were obtained by isotopic dilution after measurements by the Neptune MC-ICP-MS

[e] Isotopic values were measured on minerals after adsorption experiments. The error corresponds to a 2 sigma error (2se) determined for each sample.
fIsotopic values were determined on Ni remaining in supernatant solutions for each experiments. The error is as for the minerals.

[g] The difference in isotopic composition between the mineral and the supernatant solution is expressed as $\Delta^{60/58}Ni_{min/sol} = \delta^{60/58}Ni_{mineral} - \delta^{60/58}Ni_{solution}$. This value corresponds to the fractionation factor during Ni adsorption on the mineral surface.

4. Discussion

Two different mechanisms of equilibrium isotope fractionation are possible during metal adsorption onto Fe- and/or Mn-oxyhydroxides (Barling and Anbar 2004). One involves isotopic exchange among aqueous species in solution followed by preferential adsorption of one of these species onto the mineral phase. This would result in contrasting isotope composition between the fluid and mineral, as previously observed for the Mo isotope system (Siebert et al. 2003). The other process takes place directly during metal adsorption and involves preferential adsorption of one isotope from the aqueous phase onto the solid phase. However, these two mechanisms are not mutually exclusive and combination of the two mechanisms is likely to occur in natural systems. Below we discuss the effect of adsorption on Ni isotope composition in the context of these two mechanisms.

4.1. Equilibrium Ni isotope fractionation factors during Ni adsorption onto Fe-oxyhydroxides

For some experiments the fractionation factor is not constant (deviation from theoretical lines). This can be explained several ways: (1) error in the determination of percentage of adsorption (i.e. an analytical artifact), which may be especially important at very low or very high percentages of adsorption, (2) non equilibrium fractionation (i.e. kinetic processes), (3) a change in coordination chemistry with pH.

Figure II.6 presents $\delta^{60/58}$Ni values of the mineral and the filtrate solution versus corresponding percentage of adsorption. If equilibrium fractionation occurs during Ni adsorption on oxy-hydroxides, Ni isotope composition of the mineral-bound Ni and the solution will follow parallel lines, the distance between the lines being the fractionation factor. On the other hand, if Ni isotopes are affected by Rayleigh distillation, samples will follow curves as Ni adsorbed onto the mineral is isolated from the solution, leading to progressive depletion of the solution in light isotopes. When the reaction occurs in a closed system, if all Ni is adsorbed onto the mineral it will have the isotopic composition of the initial solution.

Figure II.6 shows that samples follow straight parallel lines, consistent with equilibrium fractionation in the absence of Rayleigh distillation. Deviations of the samples from these lines could be due to bias in the determination of adsorption percentages, especially for low adsorption percentages where the error is larger. Insofar as chemical equilibrium is assumed to be attained in our experiments, then we should expect to obtain similar fractionation factors for all samples of a given mineral. Indeed, in case of equilibrium isotope fractionation in a closed system, Ni isotope composition of solution and mineral-bound Ni are linearly related to the degree of Ni adsorption. On the other hand, if equilibrium is not attained and kinetic effects are the predominant processes affecting Ni isotopes during the reaction, light isotopes would be enriched in products of the reaction (i.e. in the solid phase) because they react faster, hence producing a fractionation factor α smaller than 1. Consequently, faster reactions will be more enriched in light isotopes. This effect could be particularly relevant for pH-dependent experiments, because pH can influence reaction kinetics. Finally, Rayleigh-type effects which occur in cases when equilibrium between solution and mineral is not reached could produce mineral-sorbed Ni with low isotopic values. For instance, this process could be significant for samples with a low adsorption percentage when little Ni is adsorbed onto the mineral. Hypothesis (3) can be ruled out since neither change in coordination nor in pH was observed (EXAFS measurements).

pH-dependent adsorption and varying concentration adsorption experiments are expected to provide a first assessment of the equilibrium Ni isotope fractionation factor $\Delta_{min/sol}$

between the solid Fe-oxyhydroxide phase and the supernatant solution. In the case of equilibrium fractionation, α values generally follow a simple relationship with temperature, which ultimately depends on the difference in bond strength between two species involved in the reaction, the heavier isotope being enriched in the species where it is most strongly bonded as the result of short bonds (Schauble 2004; Pokrovsky et al. 2005).

4.2. pH-dependent and varying Ni concentration experiments

For goethite, we found that during the pH-dependent experiment very little Ni was adsorbed onto the mineral (e.g. 0.3- 3.7%) and generated $\Delta^{60/58}Ni_{min/sol}$ values fall in the range -0.96 to -0.70 ‰, with an average of -0.85 ±0.27 ‰. Isotopic results of this experiment should be thus interpreted with caution because we cannot exclude that during filtering procedure significant amount of Ni from the solution was retained on the mineral surface, which would have then decreased the apparent isotope fractionation factor. Varying-concentration experiments for goethite show contrasted $\Delta^{60/58}Ni_{min/sol}$ values ranging from -1.00 to –0.78 ‰, with an average of -0.86 ±0.24 ‰ (2sd), with a general trend towards highly fractionated Ni isotopes with increasing adsorption.

The pH-dependent experiments show that for both 2-line ferrihydrite and goethite Ni adsorption increases with increasing pH with a maximum reached at pH=7.7 for 2-line ferrihydrite and at pH=8 for goethite. Experiments with 2-line ferrihydrite produced an average $\Delta^{60/58}Ni_{min/sol}$ value of -0.36 ±0.08 ‰ (2sd) for varying Ni concentrations with a range of values between -0.32 and -0.40 ‰. Excluding extreme values of -0.03 ‰ and -0.12 ‰ at low % adsorption, the pH-dependent experiments generated a similar range from $\Delta^{60/58}Ni_{min/sol}$ = -0.37 to -0.27 ‰, average $\Delta^{60/58}Ni_{min/sol}$ = -0.32 ±0.14 ‰ (2sd), for 2-line ferrihydrite.

Likewise, results on 2-line ferrihydrite have shown that very low adsorption percentages of 0.9% and 3.0% during pH-dependent experiments at pH 5 and 6 with $\Delta^{60/58}Ni_{min/sol}$ values of -0.12‰ and 0.00‰, respectively, clearly falling out of the $\Delta^{60/58}Ni_{min/sol}$ range reported above for 2-line ferrihydrite, hence suggesting that such values are probably inaccurate.

Noteworthy, for both goethite and 2-line ferrihydrite and for both types of experiments, even when excluding samples with very low values of Ni adsorbed (two extreme points for each minerals, generally at low pH), a trend is outlined with increasing negative $\Delta^{60/58}Ni_{min/sol}$ fractionation factors values (i.e. increasing light isotope enrichment of the solid phase) with increasing adsorption or pH (Figure II.7 and Figure II.8).

However, results of Ni EXAFS measurements on goethite and 2-line ferrihydrite from this study do not show any significant variation of mineral structure with pH which rules out any control of the mineral structure on the magnitude of Ni isotope fractionation. In these experiments we assumed that all Ni contained in goethite or 2-line ferrihydrite is adsorbed on their surface. Although Ni coordination in the mineral is 4 or 6, EXAFS data indicate that there is no change in Ni coordination according to pH and concentration on both Fe-oxides. Therefore Ni coordination should not be impinged by variations of environmental conditions such as varying pH.

Decreasing $\Delta^{60/58}Ni_{min/sol}$ values with pH in both goethite and 2-line ferrihydrite are, therefore, likely not controlled by the mineral itself.

4.3. Differences of Ni isotope fractionation between goethite and 2-line ferrihydrite

Nickel species in solution that are likely to be adsorbed onto minerals are mainly under the Ni^{2+} hydrous form (Peacock and Sherman 2007a). Within the pH range investigated (i.e. pH<10), therefore adsorption of $Ni(OH)_{2aq}$, which is the prevailing Ni species in solution (Figure II.3) is unfavorable on this surface. The low affinity of the positive aqueous Ni cation available in solution with goethite surface explains the small % of adsorption in the experiment albeit the SCM indicates that Ni should adsorb under these physico-chemical conditions (Figure II.5). Zeta potential measurements corroborate this observation. At pH lower than ~10, goethite has a net positive charge on the mineral surface making adsorption of hydrous Ni^{2+} energetically unfavorable, while 2-line ferrihydrite has a surface charge controlled by pH. Accordingly, the weak Ni affinity for goethite surface in comparison with 2-line ferrihydrite might also account for the difference observed in the magnitude of isotope fractionation (i.e. different fractionation factors $\Delta^{60/58}Ni_{min/sol}$) between the two minerals. However, we observe from Figure II.8 that $\Delta^{60/58}Ni_{min/sol}$ values decrease with increasing pH in 2-line ferrihydrite but also in goethite, suggesting that changes in its surface charge may affect the magnitude its fractionation factor. Obviously this effect is also related to the efficiency of adsorption since at low pH there is few Ni adsorbing on the mineral surface.

It is unclear whether different adsorbed species could explain such variations since computational modeling of occurring species in solution according to pH with MINTEQ indicates that changes in the proportion of Ni species in solution mostly occur at pH > 7 (Figure II.3).

Theory predicts that weaker bonds are formed with light isotopes rather than with heavy isotopes and the strength of the bond could be controlled by coordination of the element within the crystalline structure (Schauble 2004). Therefore, our data are consistent with the theory: goethite is enriched in light isotopes with a more negative isotope fractionation factor in comparison with 2-line ferrihydrite, since due to the weak affinity of Ni for goethite surface, weaker bonds are formed, resulting in preferential adsorption of light isotopes.

4.4. Comparison with other metal stable isotope systematics

Pokrovsky et al. (2005) reported similar light isotope enrichment in goethite during adsorption of Zn. However, their results contrast with results of adsorption experiments of Zn and Cu on oxyhydroxides reported in other studies, which reveal enrichment of the solid phase in heavy isotopes (Juillot et al. 2008). $\Delta^{66/64}Zn_{min/sol}$ values are +0.53‰ and +0.29‰ for ferrihydrite and goethite respectively (Juillot et al. 2008) consistent with $\Delta^{66/64}Zn_{min/sol}$ = +0.52‰ (Balistrieri et al. 2008). These results are best explained by a decrease of the coordination number from 6 in the aqueous species to 4 in the solid phase, induced by shortening of Zn-O bonds on Fe oxyhydroxides surfaces. Lower coordination number is associated with shorter and stronger bonds, thus producing heavy isotopes enrichment of the solid phase (Balistrieri et al. 2008). Similarly, enrichment of heavy Cu isotopes in the solid phase, i.e. $\Delta^{65/63}Cu_{min/sol}$ = +0.78‰ for goethite (Pokrovsky et al. 2008) and $\Delta^{65/63}Cu_{min/sol}$ = +0.73‰ for ferrihydrite (Balistrieri et al. 2008), is a result of changes in Cu coordination during adsorption on Fe oxy-hydroxides due to the formation of shorter Cu-O bonds than those present in aqueous species. These data agree with the value of +0.78‰ for $\Delta^{65/63}Cu_{min/sol}$ obtained on goethite by (Pokrovsky et al. 2008). Pokrovsky et al. (2005) showed that variation of the adsorption percentage does not produce any significant variation in $\Delta^{66/64}Zn_{min/sol}$. In addition, the magnitude of Zn isotope fractionation according to the solid

phase at stake during the adsorption reaction is not accounted for by coordination and first-neighbor interatomic distances changes (Pokrovsky et al. 2005).

Juillot et al. (2008) showed that the degree of Zn fractionation is different between goethite and 2-line ferrihydrite. EXAFS data on these minerals provide explanation for the difference: there is no change in Zn coordination between aqueous species and mineral phase during Zn adsorption onto goethite, whereas Zn adsorbed on 2-line ferrihydrite surface forms stronger bonds in response to a coordination shift. The authors also found that length of Zn-O bonds is different between goethite and 2-line ferrihydrite and that a larger change in the bond strength between aqueous and adsorbed Zn results in a larger isotopic fractionation.

Similarly to Ni and probably Zn, Mo adsorption on Fe-oxyhydroxides produces enrichment of the solid phase in the lighter isotopes (Goldberg et al. 2009). Although, the authors argue that fractionation factors vary according to the mineralogy of the solid phase which increases from magnetite ($\Delta^{98/95}Mo_{min/sol}$ = 0.83 ±0.60‰) to ferrihydrite ($\Delta^{98/95}Mo_{min/sol}$ = -1.11 ±0.15‰) to goethite ($\Delta^{98/95}Mo_{min/sol}$ = -1.40 ±0.48‰) and to hematite with the most fractionated value ($\Delta^{98}Mo_{min/sol}$ = -2.19 ±0.84‰), $\Delta^{98}Mo_{min/sol}$ values for hematite and goethite are rather similar when considering the large error bars. Mineralogical control on Mo isotope fractionation might in fact not be as obvious as stated by these authors. The sense of Mo isotope fractionation is the same as for Ni isotopes showing that the magnitude of Ni fractionation factor is larger for goethite than for 2-line ferrihydrite. Adsorption mechanisms of Mo favor adsorption of the molybdate complex. However, the authors explain Mo isotope results by differences in the types of reactive sites on the mineral phase that would adsorb different species present in solution. Therefore, we may assume that the decreasing trend of $\Delta^{60/58}Ni_{min/sol}$ values with increasing pH could be the result of adsorption of different Ni species present in solution.

Mo isotopes study by Barling and Anbar (2004) highlighted the fact that even with their experimental data they could not distinguish whether the fractionation they measured for Mo was the result of equilibrium fractionation among species present in seawater or among aqueous complexes and complexes forming at the oxide surface during adsorption, Goldberg et al. (2009) found that isotopic fractionations towards lighter composition increase with pH of solution due to preferential adsorption of molybdate MoO_3 on the mineral surface at higher pH. Contrarily to Ni which adsorbs under a cationic form, adsorption of Mo occurring as strong soluble oxyanions requires protonation of either the oxy-hydroxide surface or the oxyanion complex itself and this mechanism is favored at low pH. Consequently, at higher pH MoO_3 is more easily adsorbed than other protonated species and as MoO_3 is lighter than other species then it will decrease the Mo isotopic composition of the mineral (Tossell 2005; Goldberg et al. 2009). Alternatively, theoretical calculations by Tossel (2005) show that Mo isotope fractionation occurs between the different aqueous species in seawater, in particular between the most common species MoO_4^{2-} and MoO_3, the latter being enriched in light isotopes by 1.6‰ compared to MoO_4^{2-}. Thus, Tossell (2005) ascribed Mo isotope fractionation in Mn-oxides formed in seawater to preferential adsorption of MoO_3 on the mineral phase, producing enrichment in light isotopes compared to ambient seawater. However, based on spectroscopic data, (Wasylenki et al. 2008) argued that MoO_3 is unlikely to be a common species in seawater, implying that observed fractionations could not be explained by fractionation between aqueous species. Finally another hypothesis suggested by (Siebert et al. 2003) is that albeit MoO_4^{2-} is the dominant species occurring in seawater, the less abundant molybdate acid $Mo(OH)_6$ is likely the species that will be adsorbed on oxides. However, the reaction of production of $Mo(OH)_6$ from MoO_4^{2-} produces an equilibrium

isotope fractionation that enriches the product of reaction in isotopically light isotopes. Thus, scavenging of the more reactive species $Mo(OH)_6$ by oxides results in light isotope enrichment of these solid phases. What could be learned from these results is that knowing precisely metal speciation in solution is crucial for understanding the cause of metal isotope fractionation during adsorption on hydrous oxides phases, but also the role of metal speciation is still unclear and is prone to debate.

This literature review shows that many factors may be responsible for the isotopic fractionation occurring during metal adsorption in natural environments: coordination, pH, speciation, fractionation between dissolved species, etc. However, it is noteworthy that with the exception of copper, isotopically light metals are generally adsorbed on mineral surfaces. Further, the magnitude of Ni isotope fractionation during adsorption on Fe-oxides, -0.4 ‰ for 2-line ferrihydrite and -0.9 ‰ for goethite, is among the highest fractionation factors determined for metal adsorption on Fe-oxides phases.

4.5. Implications for Ni isotope composition of oceanic metalliferous deposits

The average Ni oceanic residence time of ~10000 years (Sclater et al. 1976; Gall et al. 2013) is among the most elevated for transition metals making Ni a conservative element; therefore deep waters of oceanic basins should have homogenized Ni isotope values through time. Nonetheless, Ni behaves as a nutrient in seawater because it is depleted in surface waters through consumption of Ni by biological activity and it is enriched in deep waters by recycling of the organic matter in the water column (Bruland 1980; Morel et al. 2003; Morel and Price 2003). Therefore, subtle variations in Ni concentrations in surface waters may occur among the different oceanic basins and could potentially locally impinge Ni biogeochemical cycle.

Precipitation of Ni in modern oceans deposits mostly occurs via incorporation into Mn-Fe oxyhydroxides phases in sedimentary rocks such as ferromanganese crusts, manganese nodules, pelagic sediments with auhtigenic Fe- and Mn-oxides precipitation and Mn-Fe oxides associated with mid-ocean ridges hydrothermal activity as suggested by elevated enrichment in Ni in these mineralizations (Boström and Peterson 1966; Boström et al. 1969; Bonatti et al. 1972c; Nicholson et al. 1997; Cronan 2000). Mn-nodules and Fe-Mn crusts, and pelagic sediments are the two major sinks for Ni in oceans. For the former a yearly flux of 5.1×10^8 mol was determined while a flux of 2.9×10^9 mol was estimated for the latter (Gall et al. 2013). Fe-Mn crusts and Mn-nodules are composed of a mineral assemblage of poorly crystallized Mn- and Fe oxyhydroxides. While Fe-Mn crusts are precipitated from Fe- and Mn-colloids present in seawater - implying that metals have a purely hydrogenetic origin, additional sources such as the underlying sediments reservoir of trace metals are required for the formation of Mn-nodules. However, whatever the source of metals, incorporation of metals including Ni in these mineral phases mostly occurs via adsorption processes. Consequently, in contrast to Fe isotopes that readily and quantitatively precipitates when delivered to the oceans suggesting (e.g. by hydrothermal vents) that Fe isotopes in marine deposits are mostly dependent on the composition of the sources (hydrothermal, detrital,…) (Anbar and Rouxel 2007), Ni isotope composition of Mn- and Fe-rich marine deposits should be mainly controlled by adsorption/precipitation processes at stake during their formation in seawater rather than composition of their sources. Therefore, the extent of Ni isotope fractionation during adsorption is a key parameter that must be taken into account for interpreting Ni isotope variations in metalliferous deposits. Besides a systematic isotopically light Ni enrichment in the solid phase, our results show that depending on the mineral

structure the magnitude of isotope fractionation may vary. In the natural environment, oceanic Fe-Mn-rich deposits are generally composed of mixed Fe- and Mn-oxides. According to the proportion of each mineral phase forming these deposits, it may be possible to observe apparent Ni isotope variations. Hence, isotopic variability would not be the outcome of metal sources with different Ni isotope composition but rather the outcome of intrinsic mineralogical control. However, impact of these parameters should be limited because as demonstrated by EXAFS measurements, Ni coordination in goethite and 2-line ferrihydrite does not change with pH or Ni concentration in solution.

Obviously, a simple and direct application of our results to natural systems is not straightforward. Parameters like those listed below might influence Ni adsorption processes in natural marine environments are of multiple nature.

(1) Competition of Ni with other dissolved trace metals as well as with other elements such as silicon (Konhauser et al. 2009) during adsorption on the mineral surface. For instance, at hydrothermal vents Si content could be 20 times higher than in seawater, thus it could have an important role in adsorption of Ni during precipitation of hydrothermal Fe-Mn oxides.

(2) Ni speciation in marine environment is probably the most critical parameter to be adequately reproduced in the laboratory. In aquatic systems Ni can occur as a free cation due to its relatively low Z^2/r (charge to radius) (Gaillardet et al. 2003). However, calculations yield estimates of dissolved nickel distribution in modern seawater according of 20% Ni^{2+}, 57% $NiCl^+$, 19% $NiCO_3$, 2% $NiHCO_3^+$ and 2% $NiSO_4$ (Fujii et al. 2011), minimizing the predominance of Ni^{2+} in marine environments. The presence of organic compounds should also be addressed in models because it could significantly modify the proportions of Ni species distribution. For instance, measurements of Ni concentration in Beaulieu estuary (UK) showed that Ni adsorption on particles in suspension is limited when organic matter is present and this effect is not dependent on the organic matter concentration in the system (Turner et al. 1998). Despite difficulties for measuring and determining the influence of organic ligands on dissolved Ni both in freshwater and seawaters, data indicate that eventually they probably play a non-negligible role (Turner and Martino 2006).

(3) Fujii et al. (2011) showed that fractionations up to 2.5‰ for $\delta^{60/58}Ni$ could occur during exchange reaction between inorganic and organic ligands, the latter being enriched in light isotopes. Accordingly, if one of these species which has undergone previous fractionation in aqueous conditions (e.g. in seawater) is preferentially adsorbed on the oxyhydroxide surface, the isotopic composition of the precipitate would be dependent on which aqueous species is adsorbed on the solid surface producing an isotopic fractionation independent of the adsorption process itself (Fujii et al. 2011). Moreover, the distribution of organic ligands in aqueous environments and the determination of their role during adsorption on mineral surfaces need to be evaluated in details, especially the role of organic ligands in Ni speciation in seawater.

(4) Oceanic metalliferous deposits are one of the most important sink for Ni in modern oceans where it is highly enriched in comparison to the terrestrial crust. Ni is predominantly hosted by the Mn-phase, especially in hydrogenetic deposits like ferromanganese crusts and manganese nodules (Halbach et al. 1981; Koschinsky and Halbach 1995; Peacock and Sherman 2007a; Peacock and Sherman 2007b; Peacock 2009). However, in Fe- and Mn-rich hydrothermal deposits there is a large range of Mn/Fe ratios and some deposits are essentially composed of Fe-oxides implying that Ni is hosted in that Fe phase (De Carlo et al. 1983; Rona 1984; Hein et al. 1994). In addition, the results reported here are valuable information for the study of Ni isotope variations in Precambrian metalliferous sediments.

During the Precambrian the deposition in marine environment of Banded Iron Formations (BIFs) made of successive Fe-rich and Si-rich layers indicates that Fe-oxyhydroxides were the predominant phases hosting transition metals (Bekker et al. 2010). Therefore, as many attempts are given to use key transition metal isotope composition of BIFs like Fe and Ni for instance as a paleoproxy of the Precambrian oceans chemical composition (Beard et al. 2003; Johnson et al. 2003; Johnson et al. 2008; Johnson et al. 2008; Cameron et al. 2011; Gueguen et al. 2011), possible isotope fractionation during adsorption processes need to be critically evaluated. Besides the complexity in estimating redox conditions and overall geochemistry of Precambrian seawater, our results indicate that incorporation of Ni in Fe-oxides might be prone to important isotope fractionation.

5. Conclusion

During this study we implemented experimental procedures in order to investigate Ni isotope fractionation during adsorption on Fe-oxides minerals using two different varying parameters: Ni concentration in solution and pH. We have shown that Ni isotopes significantly fractionate during adsorption on 2-line ferrihydrite and goethite. These fractionations are characterized by (1) systematic preferential incorporation of light isotopes on the solid surface for the two Fe-oxides minerals investigated yet, (2) Ni adsorbed on 2-line ferrihydrite is less fractionated than goethite, respectively $\Delta^{60/58}Ni_{min/sol}$ values range from -0.12 to -0.40 ‰ and, from -0.70 to -1.00 ‰, which is probably due to the net positive surface charge of goethite hampering quantitative Ni adsorption. Ni isotope fractionation factors are among the highest in comparison to those determined for other metals (e.g. Cu, Zn, Mo, Fe, Tl). Eventually, these results argue against previous assumptions that no isotope fractionation occurs during adsorption of Ni from the dissolved seawater pool onto Fe- (and most likely Mn-) oxides (Gall et al. 2013). It also puts some important constraints for inferring Ni isotope composition of seawater from deposits precipitated in Precambrian oceans, such as Banded Iron Formations (BIFs) which are especially enriched in Fe, as paleoceanographic tracers.

6. References

Albarede, F. and Beard, B. (2004). "Analytical Methods for Non-Traditional Isotopes." Reviews in Mineralogy and Geochemistry 55(1): 113-152.

Albarede, F., Telouk, P., Blichert-Toft, J., Boyet, M., Agranier, A. and Nelson, B. (2004). "Precise and accurate isotopic measurements using multiple-collector ICPMS." Geochimica Et Cosmochimica Acta 68(12): 2725-2744.

Anbar, A. D. and Rouxel, O. (2007). "Metal stable isotopes in paleoceanography." Annual Review of Earth and Planetary Sciences 35: 717-746.

Balistrieri, L. S., Borrok, D. M., Wanty, R. B. and Ridley, W. I. (2008). "Fractionation of Cu and Zn isotopes during adsorption onto amorphous Fe(III) oxyhydroxide: Experimental mixing of acid rock drainage and ambient river water." Geochimica Et Cosmochimica Acta 72(2): 311-328.

Barling, J. and Anbar, A. D. (2004). "Molybdenum isotope fractionation during adsorption by manganese oxides." Earth and Planetary Science Letters 217(3-4): 315-329.

Beard, B. L., Handler, R. M., Scherer, M. M., Wu, L. L., Czaja, A. D., Heimann, A. and Johnson, C. M. (2010). "Iron isotope fractionation between aqueous ferrous iron and goethite." Earth and Planetary Science Letters 295(1-2): 241-250.

Beard, B. L., Johnson, C. M., Skulan, J. L., Nealson, K. H., Cox, L. and Sun, H. (2003). "Application of Fe isotopes to tracing the geochemical and biological cycling of Fe." Chemical Geology 195(1-4): 87-117.

Bekker, A., Slack, J. F., Planavsky, N., Krapez, B., Hofmann, A., Konhauser, K. O. and Rouxel, O. J. (2010). "Iron Formation: The Sedimentary Product of a Complex Interplay among Mantle, Tectonic, Oceanic, and Biospheric Processes." Economic Geology 105(3): 467-508.

Bonatti, E., Kraemer, T. and Rydell, H. (1972c). Classification and genesis of submarine iron-manganese deposits, Washington DC, Nat. Sci. Found.

Boström, K. and Peterson, M. N. A. (1966). "Precipitates from hydrothermal exhalations on the East Pacific rise." Economic Geology 61(7): 1258-1265.

Boström, K., Peterson, M. N. A., Joensuu, O. and Fisher, D. E. (1969). "Aluminum-poor ferromanganoan sediments on active oceanic ridges." Journal of Geophysical Research 74(12): 3261-3270.

Bruland, K. W. (1980). "Oceanographic distributions of Cadmium, Zinc, Nickel, and Copper in the North Pacific." Earth and Planetary Science Letters 47(2): 176-198.

Cameron, V., Vance, D. and Poulton, S. W. (2011). "Nickel isotopes, BIFs and the Archean oceans." Mineralogical Magazine, Goldschmidt Abstracts 2011 75(3): 615.

Cronan, D. S., Ed. (2000). Handbook of marine mineral deposits, CRC Press London.

De Carlo, E. H., McMurtry, G. M. and Yeh, H.-W. (1983). "Geochemistry of hydrothermal deposits from Loihi submarine volcano, Hawaii." Earth and Planetary Science Letters 66(0): 438-449.

Dzombak, D. A. and Morel, F. M. M. (1990). Surface complexation modeling : hydrous ferric oxide. New York, Wiley.

Frank, M. (2002). "Radiogenic isotopes: Tracers of past ocean circulation and erosional input." Reviews of Geophysics 40(1).

Frank, M., O'Nions, R. K., Hein, J. R. and Banakar, V. K. (1999). "60 Myr records of major elements and Pb–Nd isotopes from hydrogenous ferromanganese crusts: reconstruction of seawater paleochemistry." Geochimica Et Cosmochimica Acta 63(11–12): 1689-1708.

Frank, M., Whiteley, N., Kasten, S., Hein, J. R. and O'Nions, K. (2002). "North Atlantic deep water export to the Southern Ocean over the past 14 Myr: Evidence from Nd and Pb isotopes in ferromanganese crusts." Paleoceanography 17(2).

Fujii, T., Moynier, F., Dauphas, N. and Abe, M. (2011). "Theoretical and experimental investigation of nickel isotopic fractionation in species relevant to modern and ancient oceans." Geochimica et Cosmochimica Acta 75(2): 469-482.

Gaillardet, J., Viers, J. and Dupré, B. (2003). Trace Elements in River Waters. Treatise on Geochemistry. D. H. Editors-in-Chief: Heinrich and K. T. Karl. Oxford, Pergamon**:** 225-272.

Gall, L., Williams, H. M., Siebert, C., Halliday, A. N., Herrington, R. J. and Hein, J. R. (2013). "Nickel isotopic compositions of ferromanganese crusts and the constancy of deep ocean inputs and continental weathering effects over the Cenozoic." Earth and Planetary Science Letters 375(0): 148-155.

Goldberg, T., Archer, C., Vance, D. and Poulton, S. W. (2009). "Mo isotope fractionation during adsorption to Fe (oxyhydr)oxides." Geochimica et Cosmochimica Acta 73(21): 6502-6516.

Gueguen, B., Rouxel, O., Ponzevera, E., Bekker, A. and Fouquet, Y. (2013). "Nickel Isotope Variations in Terrestrial Silicate Rocks and Geological Reference Materials Measured by MC-ICP-MS." Geostandards and Geoanalytical Research 37(3): 297-317.

Gueguen, B., Rouxel, O., Ponzevera, E., Sorensen, J. V., Toner, B. M., Bekker, A. and Fouquet, Y. (2011). Ni biogeochemical cycle through geological time: insights from Ni isotope variations in modern and ancient marine metallifereous deposits. AGU Fall Meeting 2011. San Francisco, USA.

Halbach, P., Scherhag, C., Hebisch, U. and Marchig, V. (1981). "Geochemical and mineralogical control of different genetic types of deep-sea nodules from the Pacific ocean." Mineralium Deposita 16(1): 59-84.

Hayes, K. F., Redden, G., Ela, W. and Leckie, J. O. (1991). "Surface complexation models: An evaluation of model parameter estimation using FITEQL and oxide mineral titration data." Journal of Colloid and Interface Science 142(2): 448-469.

Hein, J. R., Koschinsky, A. and Halliday, A. N. (2003). "Global occurrence of tellurium-rich ferromanganese crusts and a model for the enrichment of tellurium." Geochimica et Cosmochimica Acta 67(6): 1117-1127.

Hein, J. R., Yeh, H. W., Gunn, S. H., Gibbs, A. E. and Wang, C. H. (1994). "Composition and origin of hydrothermal ironstones from Central Pacific seamounts." Geochimica Et Cosmochimica Acta 58(1): 179-189.

Johnson, C. M., Beard, B. L., Beukes, N. J., Klein, C. and O'Leary, J. M. (2003). "Ancient geochemical cycling in the Earth as inferred from Fe isotope studies of banded iron formations from the Transvaal Craton." Contributions to Mineralogy and Petrology 144(5): 523-547.

Johnson, C. M., Beard, B. L., Klein, C., Beukes, N. J. and Roden, E. E. (2008). "Iron isotopes constrain biologic and abiologic processes in banded iron formation genesis." Geochimica Et Cosmochimica Acta 72(1): 151-169.

Johnson, C. M., Beard, B. L. and Roden, E. E. (2008). "The iron isotope fingerprints of redox and biogeochemical cycling in the modern and ancient Earth." Annual Review of Earth and Planetary Sciences 36: 457-493.

Johnson, C. M., Roden, E. E., Welch, S. A. and Beard, B. L. (2005). "Experimental constraints on Fe isotope fractionation during magnetite and Fe carbonate formation

coupled to dissimilatory hydrous ferric oxide reduction." Geochimica Et Cosmochimica Acta 69(4): 963-993.

Juillot, F., Marechal, C., Ponthieu, M., Cacaly, S., Morin, G., Benedetti, M., Hazemann, J. L., Proux, O. and Guyot, F. (2008). "Zn isotopic fractionation caused by sorption on goethite and 2-Lines ferrihydrite." Geochimica Et Cosmochimica Acta 72(19): 4886-4900.

Konhauser, K. O., Pecoits, E., Lalonde, S. V., Papineau, D., Nisbet, E. G., Barley, M. E., Arndt, N. T., Zahnle, K. and Kamber, B. S. (2009). "Oceanic nickel depletion and a methanogen famine before the Great Oxidation Event." Nature 458(7239): 750-754.

Koschinsky, A. and Halbach, P. (1995). "Sequential leaching of marine ferromanganese precipitates: Genetic implications." Geochimica et Cosmochimica Acta 59(24): 5113-5132.

Koschinsky, A. and Hein, J. R. (2003). "Uptake of elements from seawater by ferromanganese crusts: solid-phase associations and seawater speciation." Marine Geology 198(3-4): 331-351.

Morel, F. M. M., Milligan, A. J. and Saito, M. A. (2003). Marine Bioinorganic Chemistry: The Role of Trace Metals in the Oceanic Cycles of Major Nutrients. Treatise on Geochemistry. D. H. Heinrich and K. T. Karl. Oxford, Pergamon**:** 113-143.

Morel, F. M. M. and Price, N. M. (2003). "The Biogeochemical Cycles of Trace Metals in the Oceans." Science 300(5621): 944.

Nicholson, K., Hein, J. R., Buehn, B. and Dasgupta, S., Eds. (1997). Manganese mineralization; geochemistry and mineralogy of terrestrial and marine deposits, Geological Society of London : London, United Kingdom.

Peacock, C. L. (2009). "Physiochemical controls on the crystal-chemistry of Ni in birnessite: Genetic implications for ferromanganese precipitates." Geochimica et Cosmochimica Acta 73(12): 3568-3578.

Peacock, C. L. and Sherman, D. M. (2007a). "Sorption of Ni by birnessite: Equilibrium controls on Ni in seawater." Chemical Geology 238(1-2): 94-106.

Peacock, C. L. and Sherman, D. M. (2007b). "Crystal-chemistry of Ni in marine ferromanganese crusts and nodules." American Mineralogist 92(7): 1087-1092.

Pokrovsky, O. S., Viers, J., Emnova, E. E., Kompantseva, E. I. and Freydier, R. (2008). "Copper isotope fractionation during its interaction with soil and aquatic microorganisms and metal oxy(hydr)oxides: Possible structural control." Geochimica et Cosmochimica Acta 72(7): 1742-1757.

Pokrovsky, O. S., Viers, J. and Freydier, R. (2005). "Zinc stable isotope fractionation during its adsorption on oxides and hydroxides." Journal of Colloid and Interface Science 291(1): 192-200.

Ravel, B. and Newville, M. (2005). "ATHENA, ARTEMIS, HEPHAESTUS: data analysis for X-ray absorption spectroscopy using IFEFFIT." Journal of Synchrotron Radiation 12: 537-541.

Rehkämper, M., Frank, M., Hein, J. R., Porcelli, D., Halliday, A., Ingri, J. and Liebetrau, V. (2002). "Thallium isotope variations in seawater and hydrogenetic, diagenetic, and hydrothermal ferromanganese deposits." Earth and Planetary Science Letters 197(1-2): 65-81.

Rona, P. A. (1984). "Hydrothermal mineralization at seafloor spreading centers." Earth-Science Reviews 20(1): 1-104.

Schauble, E. A. (2004). "Applying Stable Isotope Fractionation Theory to New Systems." Reviews in Mineralogy and Geochemistry 55(1): 65-111.

Schwertman, U. and Cornell, R. (1991). Iron Oxides in the Laboratory Preparation and Characterization, VCH Publishers.

Sclater, F. R., Boyle, E. and Edmond, J. M. (1976). "On the marine geochemistry of nickel." Earth and Planetary Science Letters 31(1): 119-128.

Siebert, C., Nagler, T. F. and Kramers, J. D. (2001). "Determination of molybdenum isotope fractionation by double-spike multicollector inductively coupled plasma mass spectrometry." Geochemistry Geophysics Geosystems 2: 1032.

Siebert, C., Nagler, T. F., von Blanckenburg, F. and Kramers, J. D. (2003). "Molybdenum isotope records as a potential new proxy for paleoceanography." Earth and Planetary Science Letters 211(1-2): 159-171.

Skulan, J. L., Beard, B. L. and Johnson, C. M. (2002). "Kinetic and equilibrium Fe isotope fractionation between aqueous Fe(III) and hematite." Geochimica Et Cosmochimica Acta 66(17): 2995-3015.

Tossell, J. A. (2005). "Calculating the partitioning of the isotopes of Mo between oxidic and sulfidic species in aqueous solution." Geochimica Et Cosmochimica Acta 69(12): 2981-2993.

Turner, A. and Martino, M. (2006). "Modelling the equilibrium speciation of nickel in the Tweed Estuary, UK: Voltammetric determinations and simulations using WHAM." Marine Chemistry 102(3-4): 198-207.

Turner, A., Nimmo, M. and Thuresson, K. A. (1998). "Speciation and sorptive behaviour of nickel in an organic-rich estuary (Beaulieu, UK)." Marine Chemistry 63(1-2): 105-118.

Wasylenki, L. E., Rolfe, B. A., Weeks, C. L., Spiro, T. G. and Anbar, A. D. (2008). "Experimental investigation of the effects of temperature and ionic strength on Mo isotope fractionation during adsorption to manganese oxides." Geochimica Et Cosmochimica Acta 72(24): 5997-6005.

Wasylenki, L. E., Weeks, C. L., Bargar, J. R., Spiro, T. G., Hein, J. R. and Anbar, A. D. (2011). "The molecular mechanism of Mo isotope fractionation during adsorption to birnessite." Geochimica Et Cosmochimica Acta 75(17): 5019-5031.

Wu, L., Percak-Dennett, E. M., Beard, B. L., Roden, E. E. and Johnson, C. M. (2012). "Stable iron isotope fractionation between aqueous Fe(II) and model Archean ocean Fe–Si coprecipitates and implications for iron isotope variations in the ancient rock record." Geochimica Et Cosmochimica Acta 84(0): 14-28.

Wu, L. L., Beard, B. L., Roden, E. E. and Johnson, C. M. (2011). "Stable Iron Isotope Fractionation Between Aqueous Fe(II) and Hydrous Ferric Oxide." Environmental Science & Technology 45(5): 1847-1852.

Partie II.2 - Fractionnements isotopiques du Ni lors l'adsorption sur des oxy-hydroxydes de Mn (birnessite); premiers résultats expérimentaux

Les résultats sur le fractionnement isotopique se produisant lors de l'adsorption du Ni sur des oxyhydroxydes de fer (2-line ferrihydrite et goethite) ont été présentés dans la première par de ce chapitre. L'objectif de ce projet et de ces expériences avaient également pour but d'évaluer le fractionnement isotopique du Ni lors de son adsorption sur des oxydes de Mn. C'est un paramètre important car, comme il en sera longuement discuté dans les chapitres suivants de ce manuscrit, les dépôts métallifères océaniques des océans actuels sont en majeure partie formée par des oxydes de Mn qui piège les métaux traces présents dans l'eau de mer, le sédiment, etc.

Nous ne détaillerons pas ici les méthodes expérimentales ni les procédures analytiques (qui sont identiques à celles présentées dans la partie 1 de ce chapitre). La birnessite est un minéral qui adsorbe très facilement les métaux de transition. C'est pourquoi lors des premières tentatives d'adsorption du Ni sur les oxydes de Mn et ce dans les mêmes conditions expérimentales que pour les oxyhydroxydes de fer (cf. partie 1 de ce chapitre), le Ni présent initialement en solution était entièrement adsorbé sur la phase minérale empêchant toute détermination du fractionnement isotopique. Il a donc fallu refaire les expériences en adaptant les conditions expérimentales (concentrations en Ni plus élevées dans la solution de départ) afin de pouvoir mesurer un facteur de fractionnement entre la phase solide et la phase aqueuse. Ceci a donc entraîné un certain délai qui n'a pas permis l'achèvement complet des expériences et les analyses isotopiques sur les solutions de surnageant restant après expérience ne sont pas complètement terminées. Toutefois, au vu des premières données obtenues, nous avons estimé judicieux de reporter ces premiers résultats dans ce manuscrit car ils apportent tout de même des éléments importants à la discussion.

Ainsi, les fractionnements isotopiques déterminés sur la birnessite montrent un fort enrichissement de la phase minérale en isotopes légers jusqu'à -1 ‰, ce qui jusqu'à présent, correspond au facteur de fractionnement le plus important déterminé lors de nos expériences d'adsorption. Le facteur de fractionnement obtenu sur la ferrihydrite est de ~-0.4 ‰ tandis qu'il est de ~-0.9 ‰ pour la goethite.

Ces résultats montrent d'une part que les isotopes du Ni fractionnent lors des processus d'adsorption et se traduisent par un enrichissement préférentiel de la phase minérale en isotopes légers, et d'autre part le facteur de fractionnement dépend de la phase minérale considérée suivant un gradient de fractionnement comme suit, birnessite > goethite > 2-line ferrihydrite.

Conclusion du chapitre II :

L'objectif guidant ce projet est de s'intéresser à la variabilité isotopique du Ni dans les dépôts métallifères océaniques afin de mieux le cycle biogéochimique des métaux dans les océans modernes et les processus d'enrichissement en métaux de ces dépôts marins. Ainsi, dans le premier chapitre nous avons d'abord montré les techniques analytiques pour obtenir la composition isotopique en Ni dans une large gamme de matériaux géologiques ce qui nous a ensuite permis d'évaluer la variabilité naturelle des compositions isotopiques en Ni rencontrée dans les environnements naturels et dans différents réservoirs terrestres. Dans ce deuxième chapitre nous avons déterminé expérimentalement la magnitude du facteur de fractionnement isotopique pouvant se produire lors de l'adsorption du Ni en solution sur des phases minérales d'oxydes de Fe et de Mn (Figure C.2). C'est un paramètre fondamental à déterminer mais aussi à comprendre avant de s'intéresser précisément aux échantillons naturels. Notre étude montre qu'en effet l'adsorption du Ni sur des phases minérales peut produire des fractionnements isotopiques aussi importants que les variations isotopiques observées dans les échantillons naturels, en particulier dans les dépôts métallifères océaniques. Nous avons montré que la valeur de ce facteur de fractionnement varie suivant la minéralogie, l'oxyde de Mn birnessite étant le plus fractionné (-1 ‰) suivi de la goethite (-0.9 ‰) et de la ferrihydrite (-0.4 ‰).

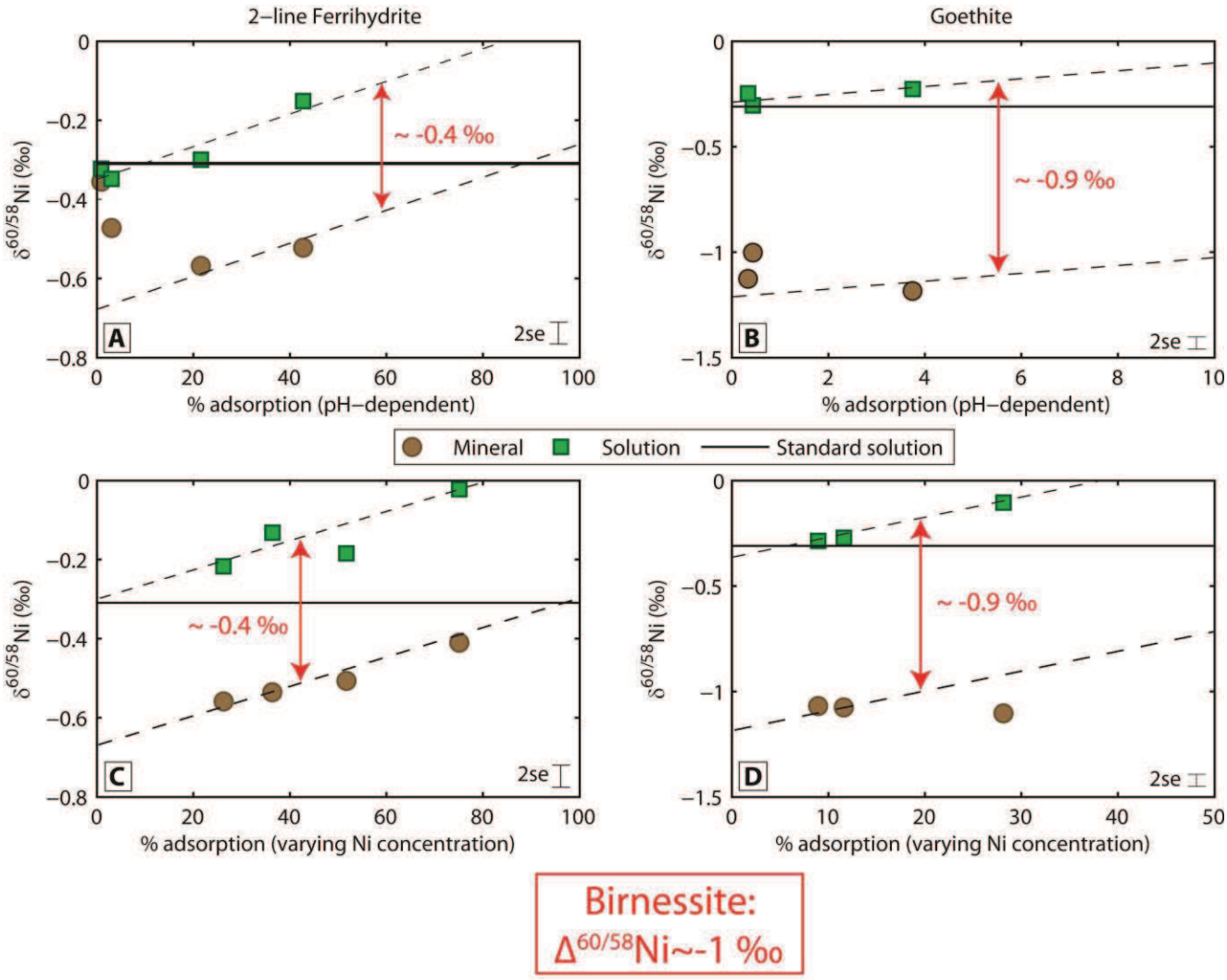

Figure C.2 : *Synthèse des résultats expérimentaux sur le fractionnement isotopique du Ni lors de l'adsorption sur des phases minérales de geothite et ferrihydrite. Les flèches rouges indiquent le facteur de fractionnement entre le minéral (symbole rond marron) et la solution (symbole carré vert). La ligne en gras noir correspond à la composition isotopique en Ni de la solution de départ avant expérience. Le facteur de fractionnement moyen calculé pour la birnessite est inséré sur la figure pour comparaison (figure modifiée et extraite de la partie 1 du chapitre II).*

Chapitre III - Variations isotopiques du nickel dans les dépôts métallifères océaniques

Chapter III – Nickel isotope variations in oceanic metalliferous deposits

Avant-propos :

Le chapitre 3 comporte trois parties. Une première partie introductive propose une revue de l'état des connaissances sur la géochimie élémentaire et isotopique des encroûtements de fer-manganèse. La deuxième partie est consacrée aux variations isotopiques du Ni dans différents dépôts métallifères riches en oxydes de fer et de manganèse dans les océans actuels. Cette première approche permet notamment d'avoir un aperçu concret de la composition isotopique du Ni les dépôts riches en Fe et Mn formés en contexte hydrothermal et de la comparer avec des dépôts purement hydrogénés. Au cours de la rédaction de ce chapitre, Gall et al. (2013) ont publié un article dans *Earth and Planetary Science Letters* reportant les compositions isotopiques en Ni d'encroûtements de fer-manganèse collectés dans les divers océans du globe terrestre. Nous avons donc intégrés ces résultats récents dans notre étude, comme éléments de comparaison, et nous proposons une nouvelle interprétation pour certains de ces résultats.
Enfin, la seconde partie expose les résultats des compositions isotopiques en Ni obtenus sur une séquence sédimentaire d'argiles profondes collectées dans l'Ouest du Pacifique. Cette étude permet notamment de déterminer le puits sédimentaire du Ni dans les sédiments pélagiques qui constituent un réservoir important de Mn et probablement de Ni dans les océans, en plus des nodules et encroûtements.

Chapitre III – Synthèse bibliographique sur la formation et la géochimie des encroûtements de fer-manganèse

Chapter III – Elemental and isotopic geochemistry of ferromanganese crusts: literature review

It is beyond the scope of this introduction to provide a comprehensive review of the literature existing on ferromanganese crusts. The goal here is rather to give a general overview of the most important points pertaining to ferromanganese crusts geochemistry and the general concepts related to their mode of formation. We also review important results on metal isotope compositions obtained in Fe-Mn crusts over the last few years.

1. Key points to the formation of ferromanganese crusts

Ferromanganese (Fe-Mn) crusts are predominantly the result of Mn-oxides precipitation as poorly crystallized vernadite δ-MnO2, whereas amorphous Fe-oxides are present as a minor phase (Hein et al. 1988; Nicholson et al. 1997). Deposition occurs on volcanic or sedimentary substrate between water depths of 1000 and 3000 m at slow precipitation rates of 1-6 mm /Ma (Figure III.1). It is generally considered that mixed Fe/Mn-oxides colloids directly precipitate from seawater from dissolved metals in the water column (Koschinsky and Halbach 1995; Hein et al. 2003; Li and Schoonmaker 2003) (Figure III.2). Therefore, Fe-Mn crusts can be envisioned as condensed Fe- and Mn-oxides-rich deposits which have recorded in their successive precipitated layers the trace metal inventory of deep seawater (Hein et al. 1992). Due to their low precipitation rate, some of these crusts may provide a record of oceanic metals for up to 60 Ma (Frank et al. 1999). Hence, they were often used for paleoceanographic studies of past continental erosion and past oceanic circulation (Abouchami et al. 1997; Frank et al. 1999; Zhu et al. 2000; Frank 2002).

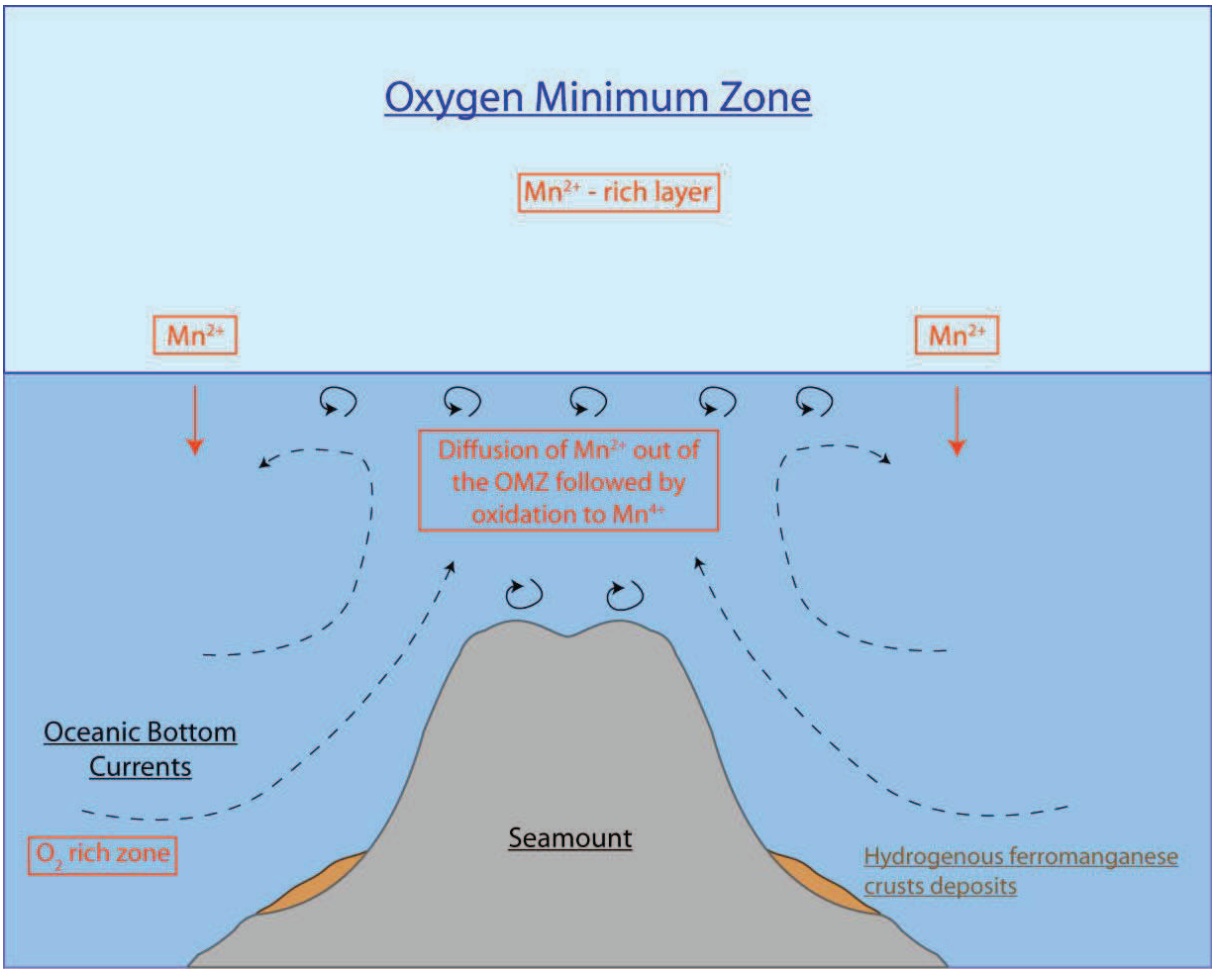

***Figure III.1**: Schematic view of mechanisms involved in ferromanganese crusts formation on seamounts (figure modified after Koschinsky and Halbach, 1995).*

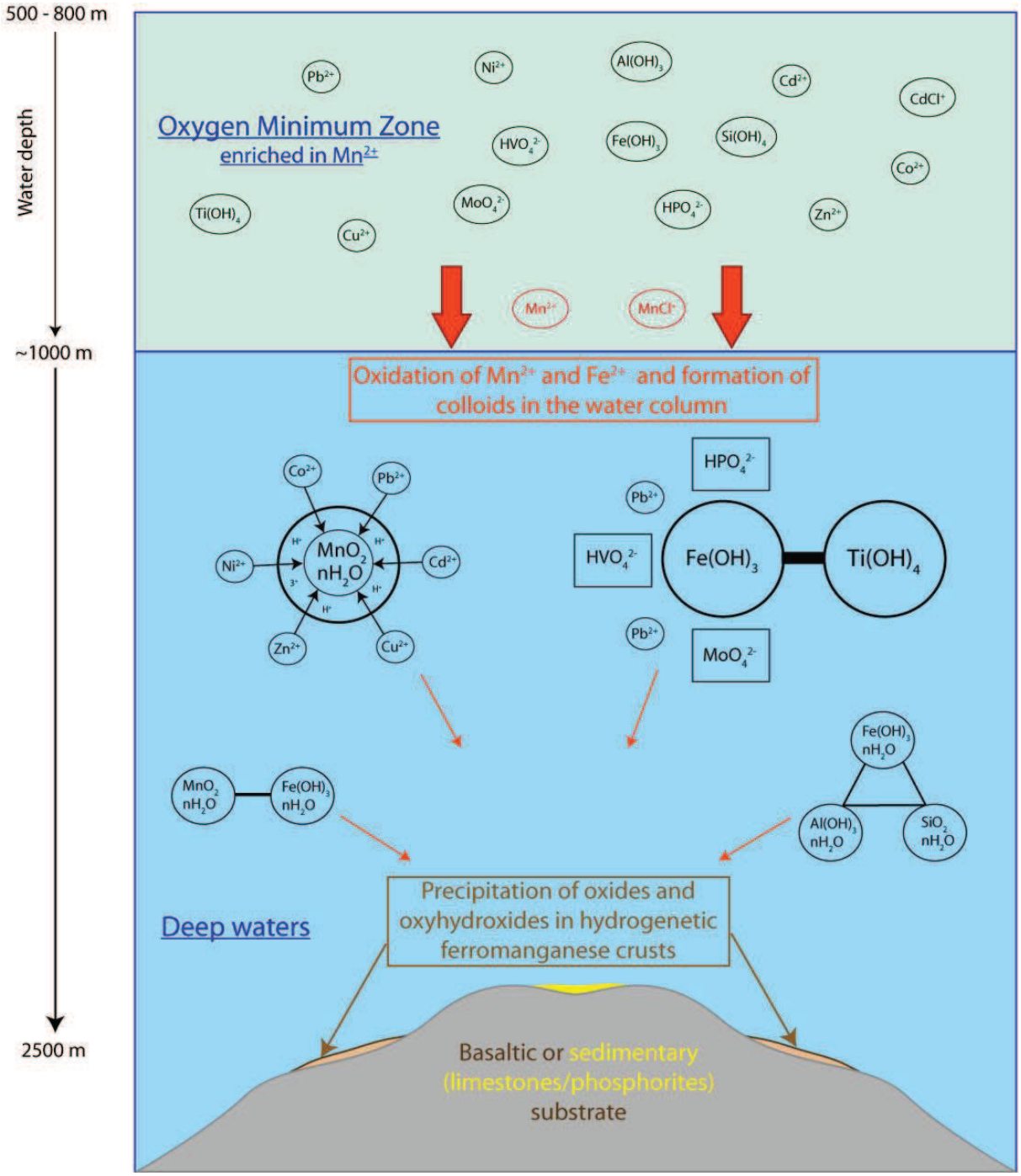

***Figure III.2**: Schematic view of metals incorporation in Fe- and Mn-colloids in the water column by adsorption processes and subsequent precipitation in ferromanganese crusts (figure modified after Koschinsky and Halbach, 1995).*

A combination of three principal environmental settings are required for the deposition of Fe-Mn crusts, (1) a limited sedimentation background preventing dilution of authigenic Fe-Mn oxides by detrital/carbonate phases, (2) inactive tectonic or magmatic environments minimizing disturbance of the surface of deposition, and (3) active oceanic currents preserving a good oxygenation of the environment by mixing with deep seawater. In addition, Fe-Mn crusts are generally associated with the presence of an oxygen-minimum-zone

(OMZ), an oxygen depleted layer present in the oceans between ~500 and 1500 m water depth, where dissolved reduced Mn accumulates (Martin and Knauer 1984; Martin and Knauer 1985). Upwelling of deep currents originating from the base of seamounts allows Mn to diffuse out of the OMZ to be subsequently oxidized and precipitated as Mn-oxides during which efficient scavenging of seawater dissolved trace metals occurs (Koschinsky and Halbach 1995; Verlaan et al. 2004).

Positively charged ions and complexes should preferentially adsorb on the negative surface charge of the manganese phase (e.g. Ni, Cu, Co, Zn, Tl, Ce), whereas negatively charged ions and oxyanions complexes would be preferentially incorporated with the amorphous FeOOH phase (e.g. P, Th, REE, As, Ti, Pb, Be, Sc, Te, Bi, V, Se, Mo) (Bau et al. 1996; Koschinsky and Hein 2003; Takahashi et al. 2007) – although Mo, Te and Pb might also be taken up by Mn-oxides depending on the growth rate. Hence, determination of such associations requires a good knowledge of both metal speciation in seawater and mineralogical phase affinity which is not straightforward. So far, the potential importance of organic ligands has not been mentioned in previous studies although this may play an important role. Current models of metal association with specific Fe and/or Mn oxide phases mainly derive from selective chemical leaching of Fe-Mn crusts (Koschinsky and Halbach 1995; Koschinsky and Hein 2003) as well as synchrotron based techniques (Hlawatsch et al. 2002; Marcus et al. 2004; Takahashi et al. 2007; Peacock 2009). In some cases, such as Mo, and Te, both approaches yield contradicting results (Koschinsky et al. 2013).

Iron occurs either in the hydrous layers of Fe-Mn crusts or in the silicate phase. A maximum concentration of dissolved Fe is generally observed in the OMZ as a result of remineralization of high Fe:C organic material formed in surface ocean and/or as a result of lateral mixing of a coastal Fe signal from the margin (Fitzsimmons et al. 2013). Colloidal forms of dissolved Fe in seawater are not particularly enriched in transition metals compared to the Mn-phase (Halbach and Puteanus 1984). Hence, Fe-Mn crusts composition should vary according to depth of precipitation and Mn/Fe ratios. Beneath the OMZ the Mn flux is intense and Fe-Mn crusts will have a higher Mn/Fe ratio and higher Ni, Cu, Co, Zn contents, whereas in deeper waters away from the OMZ and especially below the CCD (calcite-compensation-depth), the Fe flux will be more important due to biological debris remineralization. Accordingly, we have to take into account the fact that first, the CCD is variable in oceans, and second the carbonate flux is extremely dependent on the surface waters biological productivity implying a spatial and temporal variability of metal supply to deep oceanic waters.

Finally, several studies attributed high Pt concentrations to the presence of extraterrestrial materials since cosmic spherules were observed in some South Pacific Fe-Mn crusts (Halbach and Puteanus 1984; Pichocki and Hoffert 1987; Hein et al. 1988; Halbach et al. 1989; Lesuave et al. 1989; Hein et al. 2003) making these metalliferous deposits as potential mineral resources (Hein et al. 2013). Several authors attributed high Pt concentrations to the presence of extraterrestrial materials since cosmic spherules were observed in some South Pacific Fe-Mn crusts (Halbach and Puteanus 1984; Hein et al. 1988; Halbach et al. 1989). However, it should be noted that no complete agreement on the origin of Pt enrichment was really admitted.

2. Growth rates and chronology of ferromanganese crusts

One of the valuable interests of Fe-Mn crusts lies is the possibility to obtain a chronology of the successive Fe-Mn oxides layers through the last 60 Ma (Frank et al. 1999).

This allows investigating the paleoceanographic record of the evolution of metal isotope compositions of the oceans through time.

An efficient means of dating Fe-Mn crusts is the use of the cosmogenic isotope ^{10}Be (Segl et al. 1984; Bourles et al. 1989; Ling et al. 1997; Frank 2002). Radioactive ^{10}Be is produced in the atmosphere by spallation of N and is then rapidly adsorbed onto particles and mixed in the atmosphere to eventually reach the oceans through rainfalls. The method for dating Fe-Mn crusts is based on the assumption that ^{10}Be is supplied at a constant rate to the overlying oceans (von Blanckenburg et al. 1996). Therefore, ^{10}Be/^{9}Be ratio should be uniform in the surface layer of Fe-Mn crusts, but could be different between oceans. Because the half-life of ^{10}Be is 1.36 Ma, only the youngest 10 Ma can be dated with Be isotopes.

An alternative method which has been widely used to determine age of Fe-Mn crusts is the use of Co contents. This method is based on the assumption that the seawater Co flux is constant over time due to its short residence time in seawater and its efficient scavenging by Mn-colloids (Halbach et al. 1983; Halbach and Puteanus 1984; Puteanus and Halbach 1988). Therefore, Co concentration in Fe-Mn crusts layers is indicative of their growth rates, the richer in Co the slower the growth rate. Frank et al. (1999) also proposed different equations for calculating growth rates using Co concentrations, according to whether Fe-Mn crusts are rich in Co (>0.24 wt%) or poor in Co (<0.24 wt%) (Frank et al. 1999). This approach allows taking into account the precipitation depth of Fe-Mn crusts, as those precipitated further from the OMZ base receive a smaller Co flux than crusts precipitated close to the OMZ base in which Co is enriched.

Up to now, Co-dating remains the most common and useful method for dating crusts older than 10 Ma (Frank et al. 1999; Claude et al. 2005). This approach has been shown to yield good estimates of the growth rates for Pacific Fe-Mn crusts, but still remains debated for dating Atlantic Fe-Mn crusts (Frank et al. 1999). It is also important to note that this method does not account for any hiatuses during growth of the crust, which are best assessed using the Be method because it gives an absolute age.

Other dating methods include the use of U-Th isotope systematics that can be applied to younger ages of less than 400 000 yrs (Claude et al. 2005). Finally, Os and Tl isotopes may be also used for indirectly dating crusts (Klemm et al. 2005; Nielsen et al. 2011). For example, comparison of the Os isotope composition curve of Fe-Mn crusts layers with the seawater Os isotope curve of seawater allowed calibrating age of the different layers of the crust between 30 to 70 Ma (Klemm et al. 2005).

3. Effects of phosphatization events on the geochemical composition of Fe-Mn crusts

In the South Pacific Ocean two major episodes of phosphatization occurred during the Cenozoic, between 39-34 Ma and 27 and 21 Ma, in response to climatic variations that have modified oceanic circulation and phosphorus distribution in the water masses (Hein et al. 1993). Another minor phosphogenesis event occurred ca. 15 Ma. These events were attributed to major disruptions of the oceanic circulation in relation to tectonic and oceanographic changes resulting in important climatic transitions from warmer to cooler climates. Phosphogenesis generally initiates after a warm climate and a less vigorous oceanic circulation when cooling of waters intensified oceanic circulation. Since productivity in surface waters was generally high prior to phosphogenesis events promoting accumulation of dissolved phosphate – in particular in the OMZ - intensification of oceanic circulation have redistributed these large accumulated phosphorus reservoirs, thus allowing subsequent replacement of precipitated carbonate by phosphorus-rich CFA (carbonate fluorapatite).

Alternatively, more intense continental chemical weathering could have provided a high phosphorus flux to the oceans that further promoted increasing of biological productivity of surface waters (Koschinsky et al. 1997)

Intensification of bioproductivity also produced an increase of OMZ thickness. As a consequence, a phosphorus-rich OMZ would have reached the flanks and tops of seamounts onto which Fe-Mn crusts were deposited, favoring the precipitation of CFA (carbonate fluorapatite) over Fe-Mn deposits. The combination of these processes lead to the formation of phosphatized Fe-Mn crusts. Calcium in phosphatized crusts may reach values up to 15 wt% and P may be as high as 5 wt% (Koschinsky et al. 1997). The reaction of precipitation of CFA provoked partial dissolution of vernadite Mn-oxide phases and remobilization of elements bound to this phase. Although Mn can be reprecipitated as secondary todorokite, some elements that were remobilized during dissolution of vernadite may not be re-incorporated in the new todorokite phase. This mechanism can explain the depletion in Co observed in some phosphatized crusts while elements like Ni, Cu and Zn remained unchanged or even enriched due to their great affinity for the todorokite phase (Koschinsky et al. 1997). These authors also suggested that increase in Ni, Cu and Zn contents of phosphatized crusts could be due to the higher productivity of surface waters that supplied important amount of nutrient-type elements to the OMZ. Besides those elements, phosphatization has been shown to modify the overall geochemical composition, for instance REE patterns.

To date, the effect of phosphatization on Pb and Nd isotopes is considered to be minor. After investigating two Pacific ferromanganese crusts showing contrasted phosphatization extent (Ling et al. 2005) showed that the patterns of Pb and Nd of the two crusts were very identical, thus they concluded that phosphatization has a very limited impact for modifying Pb and Nd isotopic composition. Similar conclusions were drawn by (Frank et al. 1999) on Pacific Fe-Mn crusts for which they do not observed differences in Pb and Nd patterns between phosphatized and unphosphatized crusts, even though variations in the geochemical composition were observed. However, this question remains poorly documented for transition metal isotopes which may be affected not only by source changes but also by local fractionation processes during incorporation.

4. Rare Earth Elements patterns in ferromanganese crusts and other oceanic metalliferous deposits

In the natural environment, REE occur mostly in the 3+ valence state (Elderfield et al. 1981). The lanthanide contraction resulting from a decrease in REE ionic radii with increasing atomic number of the element implies that changes in their chemical properties is progressive. Therefore, REE have a very coherent geochemical behavior between each other in such a way that concentration of one REE can be deduced by interpolation from its neighboring REE and their distribution in the natural environment will be somewhat predictable (De Baar et al. 1985; German and Elderfield 1990). However, Eu and Ce are exceptions to this rule because, besides their 3+ valence state, Ce and Eu can occur in the 2+ and 4+ valence states respectively. Oxidation of Ce^{3+} to Ce^{4+} in seawater forms insoluble CeO_2 complexes that readily precipitate, generally in Fe-Mn phases, producing a typical negative Ce anomaly in the REE pattern of seawater and positive Ce anomaly in hydrogeneous Fe-Mn crusts (Bau 1999; Mills et al. 2001). Seawater REE pattern shows enrichment in heavy REE, whereas Mn-nodules and crusts are enriched in light REE. Hence, metalliferous sediments and seawater show inverse REE patterns.

De Carlo and McMurtry (1992) observed that shallower Fe-Mn crusts (<2000 m depth) were depleted in LREE relative to HREE. A similar trend was observed in Fe-Mn crusts from the Line Islands in Central Pacific (Aplin 1984) and also by Bau et al. (1996) in Fe-Mn crusts from various seamounts located in the Pacific Ocean (Bau et al. 1996). This is probably because LREE are more abundant in near surface waters due to efficient adsorption of LREE onto particles which are then released in deep waters upon dissolution of these particles (De Carlo and McMurtry 1992). Alternatively, Aplin (1984) attributed this difference to the fact that Mn-oxides exhibit enriched HREE patterns and that Mn/Fe are higher in shallower Fe-Mn crusts, thus producing HREE enriched patterns in the crust. This hypothesis was discarded by De Carlo and McMurtry (1992) on the basis that Mn-oxides have negative surface charge and preferentially adsorb positively charged species, which is in contradiction with the fact that HREE form negatively charged species. De Carlo and McMurtry (1992) also suggested that trivalent REE mostly derived from local sources and were scavenged by Fe-oxides in the water column.

Elderfield et al. (1981) showed that in ferromanganese nodules, phosphate and iron-rich minerals are the main carriers of REE. Ce is mostly incorporated in the Fe-phase, and the higher the abundance of the Fe-phase relative to the P-phase, the higher the REE content of the nodules. Eventually, the proportion of the phosphatic phase and the ferrous phase will control the REE concentration of the nodule and it is in fact the Fe-phase which is responsible for the seawater REE pattern. Authors also argue that most REE in nodules and sediments are not only precipitated from seawater but are rather supplied by organic matter particles which deposit in the sediment. Afterwards, organic matter decay within the sediment during diagenetic processes releases REE into porefluids which are then incorporated into the nodules. Nodules with low Mn/Fe ratios were formed from a higher contribution of metals from seawater, i.e. more Fe participates to Mn-nodules precipitation and more Fe-oxides are formed, thus the scavenging of Ce is more efficient and produces high positive Ce anomalies. Mn-nodules having the highest Mn/Fe ratios (indicating an important diagenetic source component) are the nodules having the smallest positive Ce anomaly (Elderfield et al. 1981).

In practice, it has been observed that top surfaces of nodules directly in contact with seawater have a more positive Ce anomaly than bottom surfaces in contact with sediment (Elderfield et al. 1981). More specifically, this general trend also applies for overall REE content which increases with decreasing Mn/Fe ratios. In addition, the slow sedimentation rate characterizing Mn-nodules environment of formation is also a prerequisite for concentrating products originating from organic matter disintegration in sediment porewaters. But in contrast to Mn-nodules, Fe-Mn crusts do not have this diagenetic component albeit REE are effectively scavenged by Fe-oxides. REE removal onto Fe-Mn crusts is dominated by surface complexation processes and the positive Ce anomaly is probably indicative of an additional process with precipitation of Ce-hydroxides on the crust surface (Bau et al. 1996). More elevated Ce anomalies may also be related with depth of occurrence of the crusts (De Carlo and McMurtry 1992). Reduction of Ce from particles entering the OMZ promotes its solubilization and accumulation in the OMZ. Thereafter, it is rapidly oxidized through formation of CeO_2 complexes at the surface of the crust. Hence, this process is more efficient in shallower crusts close to the OMZ.

Manganese nodules and Fe-Mn crusts recovered in Bauer Basin (Eastern Pacific Ocean) have a negative Ce anomaly which the authors attributed to an important input of hydrothermal iron-oxides (Elderfield and Greaves 1981). They further observed that the most

pronounced negative Ce anomaly corresponds to nodules with the lowest Mn/Fe suggesting the input of hydrothermal Fe-oxyhydroxides in the water column.

5. Radiogenic isotopes as tracers of continental erosion, climate variations and oceanic circulation during the Cenozoic

Radiogenic isotope composition of Fe-Mn crusts has long been an interesting tool for determining past oceanic circulation and tracing variations in local inputs of material from the continent to the oceans as a result of weathering and alteration processes, and/or climatic variations (Christensen et al. 1997; Frank 2002). Since Pb and Nd residence times are much smaller than oceanic mixing time of ~1500 yrs (~50 to 200 yrs for Pb and ~500 yrs to ~5000 yrs for Nd), Pb and Nd isotope compositions reflect the composition of water masses at the ocean basin-scale (Abouchami et al. 1997). Since climate is strongly related to oceanic circulation, tracing those variations through time could provide useful insights into past climate. Furthermore, variations in continental inputs may affect marine productivity in surface waters and accordingly the biogeochemical cycling of transition metals.

- Pb isotopes

Residence time of Pb in oceans is very small from ~80 to 200 yrs due to its highly particle-reactive nature. The main sources of to the oceans are the riverine component, both particulate and dissolved, produced during continental weathering; eolian dusts (including volcanic ashes), hydrothermal inputs (but it is probably minor compared to other sources), and for the last century the anthropogenic input Pb has severely affected Pb budget in modern oceans (Frank 2002). However, most of riverine Pb is removed in estuaries and does not contribute massively to seawater Pb budget. For instance, analyses of sediment in cores from North Central Pacific Ocean reveals that Asian eolian dust is the predominant source of sedimentary particles (Jones et al. 2000; Pettke et al. 2002). Thus the atmospheric input is likely to be the most important source of Pb to marine environments rather than the riverine input. However, present-day natural Pb isotope composition of seawater is not measurable directly because important anthropogenic inputs that started from the beginning of the last century (e.g. gasoil combustion) mask the natural isotopic signal; therefore it can only be determined using relevant proxies.

Frank et al. (1999) advocate the use of Pb and Nd isotopic composition of Fe-Mn crusts as reliable proxies of ambient seawater isotopic composition and natural variations of Pb isotopes in deep seawater (Figure III.3). In contrast to marine sediments that directly record Pb isotopes of the particulate fraction mainly composed of the eolian dust component, Pb isotope compositions of Fe-Mn crusts solely reflect the dissolved fraction of seawater. Fe-Mn crust will record more efficiently global oceanic circulation and changes in atmospheric circulation that modify the climate, marine sediments will archive eolian dust flux variations, i.e. the direct continental input, even if Pb residence time in oceans is very small compared to the mixing time of oceans of ~1500 yrs (Ling et al. 2005). The short residence time of Pb in oceans implies that Pb isotope composition recorded in crusts will be extremely dependent on the composition of local sources. Thus, it is very unlikely to infer any variations in pathway or intensity of large-scale oceanic currents using Pb isotopes. Such consideration is important because, for instance, oceanic circulation in the Atlantic is much more vigorous than in the Pacific, implying that efficient mixing of Pb isotope composition is very unlikely to occur in the Pacific. However, locally, weathering of old or young island arcs, old cratons, or

hot spot volcanic chains could impart different Pb isotope signatures to oceanic basins. Jones et al. (2000) showed that Pb isotope compositions of leachates of loess match the Pb isotope composition of seawater. In addition, since silicate particles are rather insoluble, it is mostly Mn-Fe oxides coatings of particles and carbonate grains that would influence seawater Pb isotope budget (Jones et al. 2000).

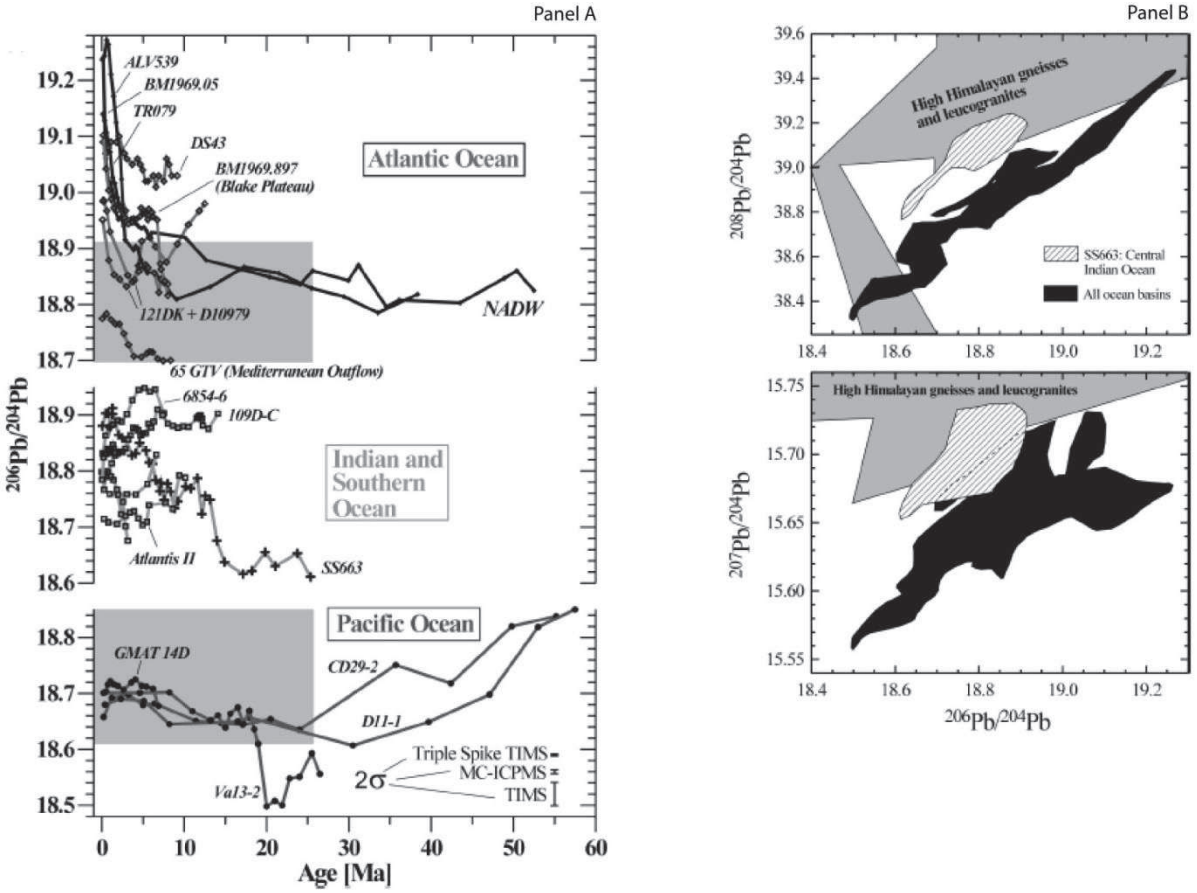

Figure III.3*: Pb isotope composition patterns through time recorded by some Fe-Mn crusts from the literature and diagram* $^{207/204}Pb$ - $^{206/204}Pb$ *isotope ratios in Fe-Mn crusts (Figures are from Frank, 2002).*

Ling et al. (2005) observed that similar patterns of Pb isotopes through age of deposition in Fe-Mn crusts and a sediment core from the North pacific likely indicate that dissolved oceanic Pb is mostly controlled by inputs from eolian dusts; therefore Fe-Mn crusts might record changes in the origin of this eolian flux. On the other hand, combined Fe and Pb isotope compositions in a Fe-Mn crust from Atlantic Ocean indicate that a positive correlation between increasing Fe isotope and increasing Pb isotope values may be attributable to mixing of continental sources (Zhu et al. 2000). This is further supported by positive Fe isotope compositions measured in loess. However, the importance of eolian inputs and their impact on Pb isotope budget of oceans, and consequently on the isotopic composition of Fe-Mn crusts, is still debated.

A study demonstrated that Pb isotope of Fe-Mn crusts from Northern Pacific do not show any variations correlated with increase in asian eolian dusts fluxes implying that this contribution is minor and is not quantitative enough to modify the oceanic Pb budget of North Pacific Ocean (van de Flierdt et al. 2003). They concluded that most of the Pb was brought

to the oceans via riverine inputs and erosion of continental basement, and that increase in $^{206}Pb/^{204}Pb$ and $^{207}Pb/^{204}Pb$ reflects an intensification of erosion of the North American margin during its uplift (Canadian Cordillera) that started in Miocene. Pb isotope variations exactly correspond to the increase in accumulation of terrigenous sediment in the Gulf of Alaska, suggesting an important Pb riverine flux from the North American margin. Conversely, similar Pb isotopes temporal patterns of Fe-Mn crusts and silicate dust from a core suggest that eolian dusts are a major contributor to dissolved Pb in North Pacific (Ling et al. 2005). Nevertheless, they noted that such assertion was only valid after 40 Ma and they ascribed this difference to hydrothermal inputs to the sediment (prior to 40 Ma) where dust was recovered, and by assuming that hydrothermal Pb does not contribute to the oceanic budget. The other hypothesis would be a contribution from unradiogenic Pb coming from erosion of volcanic arcs that surrounds the Pacific Ocean, albeit it is probably a minor source compared to eolian particles.

Interestingly, Ling et al. (2005) attempted to determine the real Pb isotope composition resulting from eolian dusts dissolution. They show that leaching experiments on China loess particles produce lower Pb isotope ratios of the leachates compared to the residue; hence this should be taken into account for the determination of eolian sources. In addition, it was demonstrated that Pb isotopes were fractionated during continental weathering with preferential remobilization of radiogenic isotopes (^{207}Pb, ^{208}Pb and ^{206}Pb), because the decay of U and Th producing these radiogenic isotopes induces distortion of the crystal lattice (Frank 2002). Radiogenic isotopes will therefore be easily removable from hosting minerals. On the other hand, diagenesis within Fe-Mn crusts layers did not affect Pb isotope composition at the interval of time recorded in Fe-Mn crusts (Henderson and Burton 1999).

Eventually, Pb isotopes were equally used as a tracer of hydrothermal inputs in Fe-Mn crusts (van de Flierdt et al. 2004). Authors attributed low Pb isotope ratios in Fe-Mn crusts to hydrothermal inputs from the extinct Galapagos rise in the Eastern Pacific.

- Nd isotopes

A significant difference between Pb and Nd in seawater is their residence time in oceans which is much longer for Nd (~500-5000 yrs) than Pb, thus they are not affected by the same secular changes of seawater. Pb isotopes will record transient changes in oceanic circulation or sources to the oceans, whereas Nd isotopes will record events occurring on a longer timescale (Figure III.4). The residence time in oceans is also one of the reasons why we do observe stratification in Nd isotope composition of seawater. Nd isotope composition varies through seawater depth, and for instance very low Nd values of bottom Central Pacific seawater are ascribed to inputs from the Northward Antarctic Bottom Water oceanic current (AABW) (Ling et al. 1997). This feature is not detectable using Pb isotope variations.

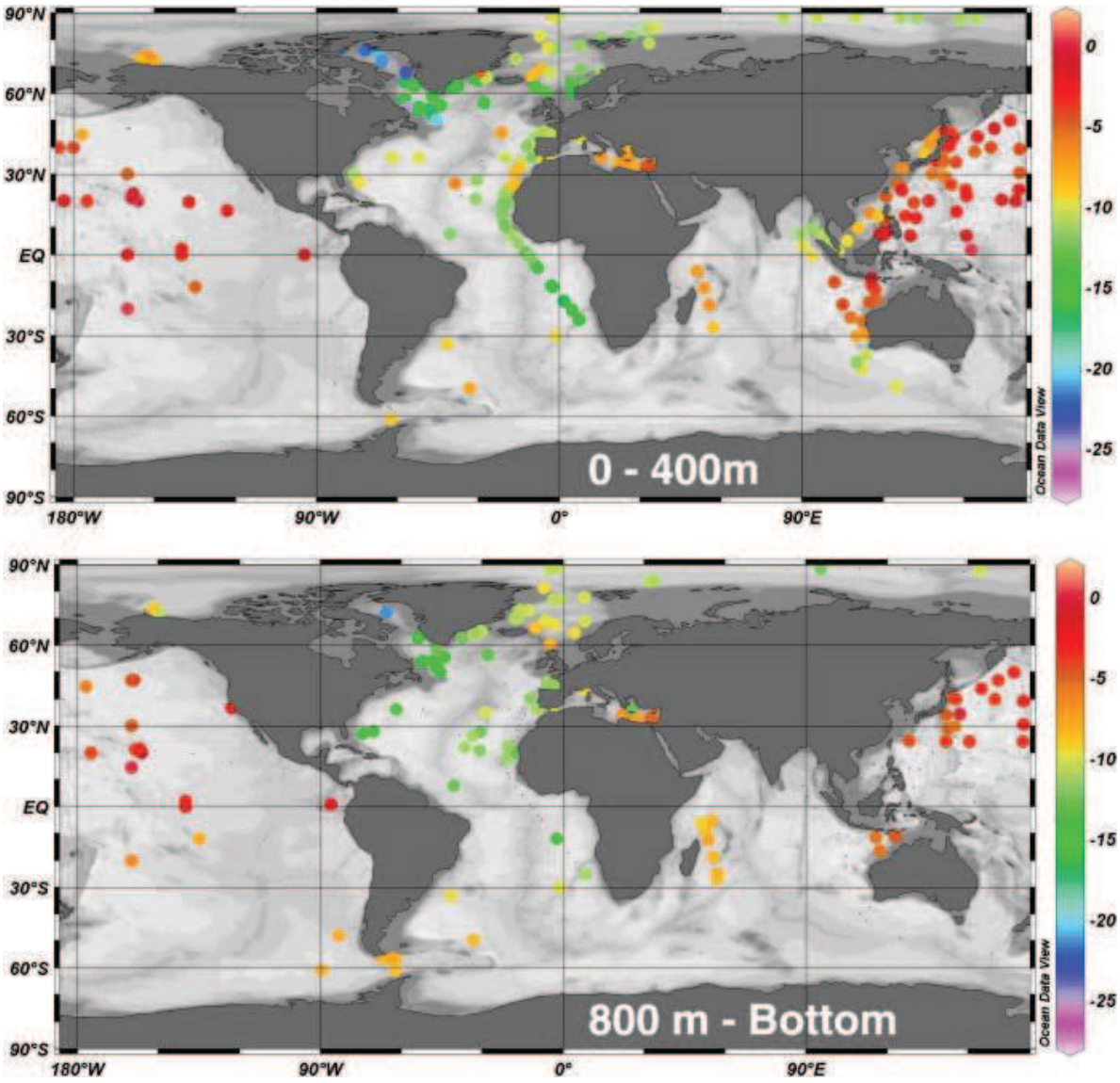

Figure III.4 *: World oceans map of ξNd composition of modern seawater (Lacan et al. 2012).*

Sources of Nd to the oceans are riverine inputs from continental weathering, eolian dusts and weathering of continental margins sediments. There is no hydrothermal Nd delivered to oceans because Nd is rapidly sequestered in precipitates near the vents (Frank 2002). While Ling et al. (2005) study of North Pacific deposits demonstrate that dissolution of the eolian dust flux is unlikely to influence REE budget of deep waters from which Fe-Mn crusts sourced their Nd content, on the contrary some authors advocates that contribution of eolian Nd is important for the ocean budget (Frank, 2002 and references therein). Nd in deep waters probably originated from volcanic arc rocks and their sediment cover. The authors also argued that Nd isotopes variations in Fe-Mn crusts are not due to modifications in the oceanic circulation, instead deep waters Nd is mostly controlled by inputs from continents and volcanic arcs through weathering processes.

Previous studies investigating radiogenic isotope composition in Fe-Mn crusts highlighted that over the last 3 Ma, North Atlantic Ocean and Arctic Ocean were prone to a more intense detrital input from the North American continent and from Greenland.

Decoupling of Pb and Nd isotopes variations through age and the geochemical composition, in particular in transition metals like Ni, Cu and Co, of nearby crusts interestingly indicates that controlling parameters of Pb and Nd isotope variations are different from those influencing transition metal contents variations (Frank et al. 1999). While radiogenic isotope proxies are efficient to providing information on paleo-circulation of oceanic currents and their potential impact on climate variations, we expect that metal isotopes will give insights into the biogeochemical evolution of seawater in terms of biological productivity – affected by availability of bioessential metals - and redox conditions.

Frank at al. (1999) discussed the possibility that variations in elemental composition of Fe-Mn crusts could be the result of diagenetic remobilization processes. However, the consistency of Pb and Nd isotope variations between phosphatized and unphosphatized Fe-Mn crusts and between crusts from distant locations led the authors to conclude that geochemical composition variations were indeed the result of modification of local parameters such as seawater chemistry, mechanisms of precipitation, and physico-chemical conditions prevailing in seawater.

Abouchami et al. (1997) observations from a high resolution study of a Fe-Mn crust from Pacific indicate that Pb and Nd isotopic composition of Central Pacific Seawater became more radiogenic probably in response to the closure of Panama isthmus.

6. Metal stable isotope systematics in oceanic metalliferous deposits: Fe, Mo, Tl, Cd, Zn and Cu

- Fe isotopes

The significance of Fe isotope composition in Fe-Mn deposits remains highly debated. A comprehensive survey of Fe isotope variations in surface layers of Fe-Mn crusts from various geographical locations within oceans ($\delta^{56/54}Fe_{IRMM-14}$ from -0.8 to -0.1 ‰) could not reveal any relationships with geographical locations and depth within oceans or the influence of variable erosional inputs to oceanic basins (Levasseur et al. 2004) (Figure III.5). This study also discounted prior hypothesis advocating that Fe isotope variability in Fe-Mn crusts is the result of changes in the relative proportion of hydrothermal vs. atmospheric fluxes to the oceans (Beard et al. 2003). It has been also proposed that light Fe isotope compositions in Fe-Mn crusts could reflect either a large-scale diagenetic (Staubwasser et al. 2006) or hydrothermal Fe sources (Chu et al. 2006). Data of $\delta^{56/54}Fe_{IRMM-14}$ of surface Fe-Mn crusts layers can be compared with the seawater Fe isotope composition range of -0.8 to +0.8 ‰ in the Atlantic Ocean (Boyle et al. 2012) and -0.39 to -0.24 ‰ in the Pacific Ocean (Conway et al. 2013).

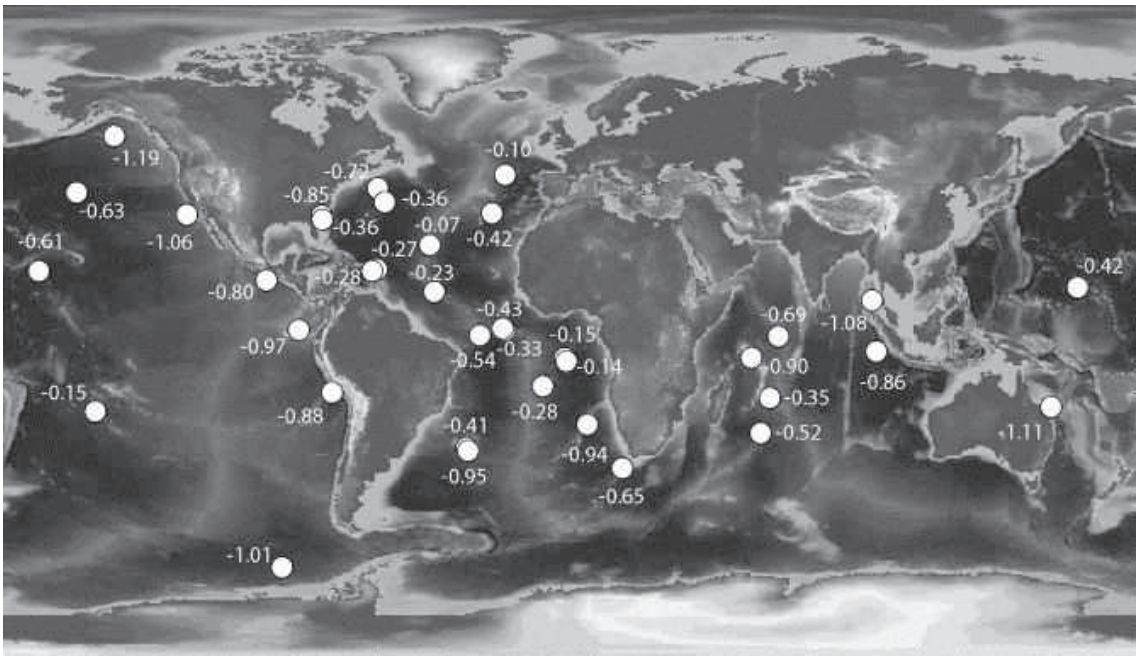

Figure III.5 *World map of $\delta^{57/54}$Fe values in surface layers of Fe-Mn crusts (Figure from Levasseur et al., 2004).*

A negative Fe isotopes excursion down to -0.95 ‰ have been reported in a Fe-Mn crust from Western Pacific (close to Izu-Bonin arc) and interpreted as resulting from a local hydrothermal pulse (Chu et al. 2006). This negative excursion is coupled to an increase in Mn, Mg, Ni, Cu, Zn, Mo and V contents of the crust layers. However, a second crust collected in the vicinity of the other crust does not record this hydrothermal pulse. The difference was accounted for by either different depths between the two sites or a localized hydrothermal pulse. The authors proposed several explanations that may account for this discrepancy, (1) crusts were not collected at locations close enough so that the diffuse and localized hydrothermal plume haven't imprinted the two crusts, (2) precision on the determination of growth rate using Co-dating method is low and could explain the apparent gap for the transition metal contents increase.

Zhu et al. (2000) reported Fe isotope and Pb isotope compositions in Atlantic Fe-Mn crusts Based on the literature, Pb isotope variations are mostly controlled by eolian and continental weathering inputs (except for purely hydrothermal deposits), while Fe isotope compositions can be strongly affected by hydrothermal inputs. Excellent co-variations between Fe isotope and Pb isotope compositions in a Atlantic Fe-Mn crust with continuous decrease from 0 to ca.2 Ma was attributed to a variation in the sources of these elements (identical for Fe and Pb) (Zhu et al. 2000). Fe isotope values measured in China loess - assumed to represent the composition of the upper continental crust, the main source of Fe to the oceans, and the predominant particles inputs to the Pacific - are comprised between -0.04 and +0.32‰. Therefore, the trend showing that, the more elevated Pb isotope ratios the more positive Fe isotope values (from -0.77 to +0.13‰), is in agreement with mixing of continental sources.

Recent analytical progresses in the measurement of Fe isotope composition of dissolved Fe in seawater are shedding new lights in this debate. So far, seawater dissolved Fe isotope ratios have been measured in the North Atlantic near Bermuda (John and Adkins 2012) and equatorial Pacific Ocean (Lacan et al. 2008; Lacan et al. 2010; Radic et al. 2011).

Surprisingly, most of the $\delta^{56/54}Fe_{IRMM-14}$ values of dissolved Fe in seawater are positive from +0.30 to +0.71‰ in the Atlantic Ocean, and from 0.01 to +0.58‰ in the Pacific Ocean. Other studies have reported negative dissolved $\delta^{56/54}Fe_{IRMM-14}$ values down to -3.45‰ for coastal O_2-deficient basins such as the San Pedro Basin (John et al. 2012) and down to -0.9‰ for coastal seawater (Rouxel and Auro 2010). Fe isotope composition of hydrothermal plumes has been been yet thoroughly investigated but are likely characterized by negative $\delta^{56/54}Fe_{IRMM-14}$ values (Rouxel et al. 2008; Bennett et al. 2009). In the light of those new results, previous work should be certainly revisited.

- Mo isotopes

Mo has a long residence time in the oceans, ca. 800 kyr, which is among the highest observed for transition metal; hence its concentration in the oceans is the highest among transition metal (ca. 105 nmol/kg) (Anbar 2004). Seawater is therefore very homogenous regarding its Mo isotope composition with $\delta^{98/95}Mo_{JMC}$ = +2.3 ‰ (Siebert et al. 2003). This value is significantly heavier than terrigenous materials and deep-sea pelagic clays ranging from -0.50 to +0.25 ‰ (Siebert et al. 2003). More recent data from seawater samples recovered within the GEOTRACES international program indicate similar Mo isotope values of +2.5‰ (relatively to Mo ICPMS standard from (Archer and Vance 2008)). A compilation of Mo isotope compositions of open-ocean seawater published in the literature (relative to the international Mo isotopic standard NIST SRM 3134) yielded an average value of $\delta^{98/95}Mo_{NIST3134}$ = 2.09 ± 0.10 ‰ (Archer and Vance 2008; Goldberg et al. 2013).

The molybdenum source to the modern oxygenated oceans is mainly derived from continental erosion and weathering. The oceanic molybdenum sink is closely associated to Mn sink, such as Fe-Mn deposits and deep-sea sediment bearing Mn-oxides. In addition, suboxic/anoxic sediments provide another important sink for oceanic Mo. In the presence of reduced sulfur H_2S in solution, Mo forms thiomolybdates which are extremely particle-reactive and quantitatively precipitate as sulfides (Anbar and Rouxel 2007).

A 60 Ma profile in three Fe-Mn crusts from the Atlantic, Pacific and Indian oceans shows that Mo isotope composition is isotopically light relative to seawater and has remained constant over 60 Ma, i.e. values are comprised in the -1.0 to -0.5 ‰ narrow range (Siebert et al. 2003).

- Tl isotopes

Although not a major mineral-forming element, Tl has generated a great deal of interest in the last 10 years. The Tl marine residence time is ~20000 yrs which is well above the oceans mixing time (Rehkämper et al. 2004). Tl isotope composition of successive layers in three Fe-Mn crusts (two from the Pacific Oceans and one from the Atlantic Ocean) reveals a systematic increase in Tl isotope values with decreasing age of the crust. Crust layers younger than 25 Ma display $\delta^{205/203}Tl_{NITS997}$ from +1.1 to +1.5 ‰, whereas base of crusts has a value comprised between +0.5 and +0.7‰ (Rehkämper et al. 2004). Large riverine inputs, enhanced benthic and eolian volcanic dusts fluxes in the early Cenozoic seawater with low Tl isotope compositions would explain the trend from low to high Tl isotope values in Fe-Mn crusts. In addition, surface layers of the crust are isotopically enriched in heavy Tl compared to seawater by about 2 ‰. The average Tl composition of Fe-Mn crusts surface layers is +1.28 ‰ whereas seawater $\delta^{205/203}Tl$ in seawater is ~ -0.6 ‰, thus Fe-Mn crusts are shifted from seawater by about 2 ‰ (Rehkämper et al. 2004). Rehkämper et al al. (2004) suggested

that this offset could be the result of, (1) fractionation during adsorption on Fe-Mn oxides, (2) fractionation between dissolved Tl^{+} and Tl^{3+}, (3) fractionation between occurring species in seawater with preferential adsorption on one species over another on the solid phase of Fe-Mn crusts. Although the authors favored an adsorption mechanism to fractionate Tl isotopes, the explanation for this offset is still unclear. One of their crusts has recorded an episode of phosphatization, but the absence of any changes in Tl isotope composition during this event demonstrates that phosphatization has no effect on Tl isotope.

Redetermination of the age of a Fe-Mn crust from the Indian Ocean using Os isotope composition allows to emphasizing resolvable Tl isotope variations that the authors ascribed to an increase in production rates of the crust rather than a possible influence from the North Atlantic Deep Water (Nielsen et al. 2011).

- Cd isotopes

As an important non-redox sensitive and nutrient-type metal in seawater, Cd isotope composition of Fe-Mn crusts may be provide paleoceanographic information that are not achievable by other metal isotope systems described above. Cd isotope compositions of Fe-Mn crusts recovered from various locations are in the range of seawater values indicating that no isotope fractionation occurs during adsorption of Cd from seawater onto Fe- (but mostly) Mn-colloids (Horner et al. 2010). $\delta^{112/110}Cd_{AlfaZurich}$ values of Fe-Mn crusts range from +0.01 to +0.23 ‰ whereas Cd isotope composition of seawater is +0.33 ‰ (Horner et al. 2010). The authors attributed the light Cd isotope composition of +0.02 ‰ in a Fe-Mn crust from the Southern Ocean at a water depth of ~3200 m to differences in the utilization of Cd in surface waters compared to other oceanic regions. It is consistent with low concentrations in nutrients probably also indicating that Cd utilization by the biological activity is lower than elsewhere. On the other hand, Schmitt et al. (2009) reported Cd isotope compositions of surface layers of Mn-nodules with a range from -0.05 to+0.20 ‰ for $\delta^{112/110}Cd_{JMC\text{-}std}$ (note the different standard of reference used in the two studies), thus in the range of Fe-Mn crusts and seawater reported by Horner et al. (2010). The authors observed a correlation between depth of Mn-nodules collection and Cd isotope composition. Shallow nodules from the surface to ~2000 m depth have isotopically heavier Cd isotopes and show decreasing $\delta^{112/110}Cd_{JMC\text{-}std}$ values from +0.1 to 0.0 ‰, whereas in nodules collected in waters > 2000 m depth $\delta^{112/110}Cd_{JMC\text{-}std}$ values are relatively constant around a near-zero value (Schmitt et al. 2009). They also concluded from their data that Cd is not significantly fractionated from seawater when incorporated into Fe-Mn oxy-hydroxides which is consistent with experimental studies of Cd adsorption on Mn-oxides (Wasylenki and Swihart 2013). Finally the heavier Cd isotope composition of surface waters was ascribed to uptake of light Cd isotopes by phytoplankton, implying that Cd isotopes may be used as a tracer of phytoplankton activity and nutrient utilization (Lacan et al. 2006; Schmitt et al. 2009). However, $\delta^{112/110}Cd_{NIST3108}$ values in GEOTRACES samples (Atlantic) are comprised between +0.22 to +0.75 ‰ with the heaviest values measured in surface seawater (Boyle et al. 2012). $\delta^{112/110}Cd_{NIST3108}$ in Pacific seawater from SAFe samples yields a restricted range of values from +0.12 to +0.14 ‰ (Conway et al. 2013).

- Zn isotopes

Zinc isotope composition reported for Fe-Mn crusts are very scarce and essentially concern three Fe-Mn crusts from the Atlantic, Indian and Pacific oceans (Little et al. 2013),

while most data reported so far pertained to manganese nodules (Maréchal et al. 2000). Values of $\delta^{66/64}Zn_{JMC\text{-}Lyon}$ measured in Fe-Mn crusts is contained in the +0.60 to +1.42 ‰ range. While the Atlantic and Pacific Fe-Mn crusts show practically no significant variability, the Indian Fe-Mn crust show a high magnitude of variation of ~0.8 ‰ (Little et al. 2013). However, interpretations of the mechanisms responsible for these variations were not the goal of the paper. Maréchal et al. (2000) reported Zn isotope composition of nodule surface layers as proxies for present-day seawater isotope composition. $\delta^{66/64}Zn_{JMC\text{-}3\text{-}0749L}$ values in surface layers of Mn-nodules collected in the Atlantic, Pacific, and Indian oceans and in the Circum-Antarctic Current vary from +0.53 to +1.16 ‰.

Zinc isotope composition measured for seawater is $\delta^{66/64}Zn_{JMC}$ = +0.05 to +0.53 ‰ (i.e. $\delta^{66/64}Zn_{NIST3168a}$ = +1.01 to +1.49 ‰) in the North Atlantic Ocean (GEOTRACES samples) (Boyle et al. 2012) which is similar to the +0.16 to +0.50 ‰ range in $\delta^{66/64}Zn_{JMC}$ (i.e. $\delta^{66/64}Zn_{NIST3168a}$ = +1.12 to +1.46 ‰) for the Pacific Ocean (SAFe Samples) (Conway et al. 2013). Experiments show little Zn isotope fractionation during adsorption on Mn-oxide birnessite $\Delta^{66/64}Zn_{solid/sol}$ = -0.17‰ indicating enrichment of the solid phase in light isotopes (Pokrovsky et al. 2005). Hence, it is surprising that $\delta^{66/64}Zn_{JMC}$ values in Mn-nodules are generally higher than seawater Zn isotope composition (~0.4 to ~0.5 ‰ higher in average).

In addition, surface seawater is enriched in light Zn isotopes compared to deep waters probably as a result of biological uptake and adsorption (Boyle et al. 2012). This explains that Zn isotope composition of seawater shows relatively important variations below 1000 m depth with a trend of heavier values with increasing depth. By contrast, deep water Zn isotopes are relatively homogenous (Conway et al. 2013).

Maréchal et al. (2000) showed that Zn isotope variations in marine sediment particles (mostly carbonates) from high latitudes locations reflect variable seasonal primary productivity in surface waters. At high latitudes, development of a thermocline during summer prevents any exchange between deep waters and surface waters (no upwelling currents), and since biological activity preferentially uptakes light Zn isotopes, the residual pool will be enriched in isotopically heavy Zn likewise carbonate forming in these waters. Conversely, during winter the absence of a strong thermocline allows upwelling currents to mix with surface waters erasing the stratification and preventing surface waters from light Zn isotopes depletion. On the other hand, low latitudes are not prone to variable strength in thermocline and carbonate particles formed in these waters will systematically have lower $\delta^{66/64}Zn$ values. The authors argued that Zn isotopes variations in Mn-nodules could not be the outcome of spatial variations in primary productivity because of the rather complex distribution of bioproductivity in surface waters that precludes the determination of any specific patterns in modern oceans and the absence of correlation with age of water masses (deep Pacific waters are older than deep Atlantic waters, thus we would expect to observe different Zn isotope compositions between nodules from different oceans) (Maréchal et al. 2000).

However, we must highlight that conversely to Fe-Mn crusts, Mn-nodules formation is a result of complex and multiple formation processes including diagenetic remobilization of metals in the underlying sediment, precipitation from dissolved seawater trace metals, scattered and far-field hydrothermal inputs and local biological activity. It is clear that the first-order assumption that Mn-nodules reflect ambient seawater metal isotope composition is probably inaccurate. As shown by Maréchal et al. (2000) study, the isotope variability recorded in surface layers of Mn-nodules cannot be used as a straightforward proxy of ambient deep seawater isotope variations.

By contrast, purely hydrogenetic Fe-Mn crusts and their long-time integrated record of seawater composition should question whether it is possible to distinguish any seasonal

signal in Zn isotopes. As for Zn isotopes from deep marine carbonates (Pichat et al. 2003), Fe-Mn crusts may record global variations of the biological productivity in surface waters that occurred over long periods as a result of, for instance, climate variations. Consequently, Zn isotope signatures in Fe-Mn crusts could be used to trace large-scale and long terms variations of biological activity in seawater.

- Cu isotopes

Despite its great potential and the wealth of studies of Cu isotope fractionation in natural environments (Anbar and Rouxel 2007), studies of Cu isotopes in marine Fe-Mn deposits are extremely scarce. The Cu isotope compositions reported for seawater vary greatly with $\delta^{65/63}Cu_{NIST976}$ = +0.4 to +1.4 ‰ (Vance et al. 2008; Boyle et al. 2012; Takano et al. 2013; Thompson et al. 2013). Cu isotope fractionation has only been documented for Fe-oxides ($\Delta^{65/63}Cu_{solid/sol}$ = +0.58 and +0.98 ‰) (Pokrovsky et al. 2008) and to the author knowledge no experimental data exist for Mn-oxides yet.

Biological activity preferentially uptakes isotopically light Cu (~up to -1.5‰) (Zhu et al. 2002; Ehrlich et al. 2004). However, Cu isotopes in modern marine sediments were measured on manganese nodules surface layers from different geographic locations (Albarede 2004), and as discussed for Zn isotopes we should be cautious about the real meaning of such isotopic signatures in comparison to seawater isotopic signatures. No specific trend has emerged from analyses of these nodules, the mean value for $\delta^{65/63}Cu_{NIST976}$ is +0.31‰ with a range of variation from +0.09 to +0.60 ‰ and no relation could be established with geographical locations or any other specific processes. The few data available for Cu isotopes in Fe-Mn crusts were reported in three Fe-Mn crusts from the Atlantic, Indian and Pacific oceans with $\delta^{65/63}Cu_{NIST976}$ values are comprised in the -0.16 to +1.19 ‰ range (Little et al. 2013). Except several outliers, the average $\delta^{65/63}Cu_{NIST976}$ values of those crust is between +0.20 and +0.54 ‰, which is within the range of deep seawater. Nevertheless, origin and significance of Cu isotope variability in Fe-Mn crusts remain cryptic.

7. Synthesis and objectives of this work

This synthesis shows that metal isotope compositions in Fe-Mn crusts vary and respond to major biogeochemical processes in the global marine environment. Although our understanding of these variations is continuously improving, we see that important processes need to be resolved. Table III.1 summarizes literature data available for metal isotope compositions (Fe, Ni, Cd, Zn, Cu, Mo and Tl), the range of variations in seawater, Fe-Mn crusts and Mn-nodules; isotope fractionation factors during adsorption on mineral surfaces; and residence time of the elements in seawater. Further attention should be paid to other metalloids such as Se and Ge in marine deposits which reveal significant isotope variability (Johnson et al. 1999; Rouxel et al. 2002; Johnson and Bullen 2004; Rouxel et al. 2006).

Table III.1: Summary of metal isotope compositions (Fe, Ni, Cd, Zn, Cu, Mo and Tl) in Fe-Mn crusts, Mn-nodules and seawater reported in the literature. Isotopic values are in permil (‰) except Cd and Tl isotopes in per thousand.

	Fe-Mn-crusts		**References**	**Mn-nodules**		**References**
	Lower range	**Higher range**		**Lower range**	**Higher range**	
$\delta^{56/54}Fe_{IRMM-14}$	-0,8	0,13	Levasseur et al., 2004; Chu et al., 2006; Zhu et al., 2000	-	-	-
$\delta^{56/54}Fe_{IRMM-14}$	-	-	-	-	-	-
$\delta^{60/58}Ni_{NIST986}$	1,14	2,47	Gall et al., 2013	-	-	-
$\delta^{60/58}Ni_{NIST986}$	-	-	-	-	-	-
$\xi^{112/110}Cd_{Alfa-Cd}$ **	-0,5	2,3	Horner et al., 2010; Schmitt et al., 2009	-	-	-
$\delta^{66/64}Zn_{JMC}$	0,6	1,23	Little et al., 2013	0,53	1,16	Marechal et al., 2000
$\delta^{66/64}Zn_{JMC}$	-	-	-	-	-	-
$\delta^{65/63}Cu_{NIST976}$	-0,16	1,19	Little et al., 2013	-	-	-
$\delta^{98/95}Mo_{JMC}$	-0,6	1,0	Siebert et al., 2003	-	-	-
$\xi^{205/203}Tl_{NIST997}$ **	5,3	15,4	Rehkamper et al., 1999; 2002; 2004; Nielsen et al., 2011	-5,3	8,9	Rehkamper et al., 2002

Table III.1 : Continued

	Seawater		Location	Reference	Residence time in seawater (years)	Reference	Fractionation factors (solid/solution) in ‰	Mineral	Reference
	Lower range	Higher range							
$\delta^{56/54}Fe_{IRMM-14}$	-0,8	0,8	Atlantic	Boyle et al., 2012	0-200	Johnson et al., 1997	0,9	Fe-oxides	Bullen et al., 2001
$\delta^{56/54}Fe_{IRMM-14}$	-0,39	-0,24	Pacific	Conway et al., 2013	-	-	-	-	-
$\delta^{60/58}Ni_{NIST986}$	~1,3	~1,6	Atlantic	Cameron and Vance, 2013	3600-14500	Gall et al., 2013	up to -0,9	Goethite	Gueguen et al., 2011
$\delta^{60/58}Ni_{NIST986}$	~1,2	~1,4	Pacific	Cameron and Vance, 2013	-	-	-	-	-
$\xi^{112/110}Cd_{Alfa-Cd}$ **	0,45*	1,35*	Atlantic	Boyle et al., 2012	50000	Schmitt et al., 2009	-0,25	Birnessite	Wasylenki and Swihart, 2013
$\delta^{66/64}Zn_{JMC}$	0,05	0,53	Atlantic	Boyle et al., 2012	11000	Little et al., 2013	-0,17	Birnessite	Pokrovsky et al., 2005
$\delta^{66/64}Zn_{JMC}$	0,16	0,50	Pacific	Conway et al., 2013	-	-	-	-	-
$\delta^{65/63}Cu_{NIST976}$	0,56	0,68	Atlantic	Boyle et al., 2012	5400	Little et al., 2013	up to +0,98	Fe-oxides	Pokrovsky et al., 2008
$\delta^{98/95}Mo_{JMC}$	2,47	2,52	Atlantic	Boyle et al., 2012	800000	Anbar, 2004	~+0,2	δ-MnO_2	Barling and Anbar, 2004
$\xi^{205/203}Tl_{NIST997}$ **	-6,6	-8,7	Atlantic	Nielsen et al., 2004	17000-21000	Rehkamper et al., 2004	up to ~-1	Birnessite	Nielsen et al., 2013

Furthermore, this framework shows that combining isotope proxies of metal isotope compositions (e.g. Fe, Cu and Zn) in deep-sea Fe-Mn crusts may yield a promising approach for unraveling both mechanisms of Fe-Mn deposits formation and metal biogeochemical cycling in seawater through time.

Among unexplored but yet promising proxy in Fe-Mn crusts, Ni which is an important base metal in Fe-Mn crusts, is currently actively developed by other several research groups as a new isotopic tool (Cameron and Vance 2013; Gall et al. 2013).

Therefore, besides developments required for the use of Ni isotopes as a new biogeochemical tracer, one of the goals of this study is to implement a multi-proxy approach using several metal isotopes proxies including Ni. In that perspective, this chapter III is dedicated to the investigation of Ni isotope variations in bulk Fe- and Mn-rich deposits and pelagic sediments in order to constrain the extent of Ni isotope variability in marine sediments. Then, in chapters IV and V our efforts will focus on Fe-Mn crusts samples to investigate the temporal patterns of several metal isotope systematics, i.e. Ni, Fe, Cu and Zn, recorded in these deposits to give an overview of the potential from using a multi-proxy approach.

8. References

Abouchami, W., Goldstein, S. L., Galer, S. J. G., Eisenhauer, A. and Mangini, A. (1997). "Secular changes of lead and neodymium in central Pacific seawater recorded by a Fe-Mn crust." Geochimica Et Cosmochimica Acta 61(18): 3957-3974.

Albarede, F. (2004). "The Stable Isotope Geochemistry of Copper and Zinc." Reviews in Mineralogy and Geochemistry 55(1): 409-427.

Anbar, A. D. (2004). "Molybdenum Stable Isotopes: Observations, Interpretations and Directions." Reviews in Mineralogy and Geochemistry 55(1): 429-454.

Anbar, A. D. and Rouxel, O. (2007). "Metal stable isotopes in paleoceanography." Annual Review of Earth and Planetary Sciences 35: 717-746.

Aplin, A. C. (1984). "Rare earth element geochemistry of Central Pacific ferromanganese encrustations." Earth and Planetary Science Letters 71(1): 13-22.

Archer, C. and Vance, D. (2008). "The isotopic signature of the global riverine molybdenum flux and anoxia in the ancient oceans." Nature Geoscience 1(9): 597-600.

Bau, M. (1999). "Scavenging of dissolved yttrium and rare earths by precipitating iron oxyhydroxide: experimental evidence for Ce oxidation, Y-Ho fractionation, and lanthanide tetrad effect." Geochimica Et Cosmochimica Acta 63(1): 67-77.

Bau, M., Koschinsky, A., Dulski, P. and Hein, J. R. (1996). "Comparison of the partitioning behaviours of yttrium, rare earth elements, and titanium between hydrogenetic marine ferromanganese crusts and seawater." Geochimica Et Cosmochimica Acta 60(10): 1709-1725.

Beard, B. L., Johnson, C. M., Von Damm, K. L. and Poulson, R. L. (2003). "Iron isotope constraints on Fe cycling and mass balance in oxygenated Earth oceans." Geology 31(7): 629-632.

Bennett, S. A., Rouxel, O., Schmidt, K., Garbe-Schonberg, D., Statham, P. J. and German, C. R. (2009). "Iron isotope fractionation in a buoyant hydrothermal plume, 5 degrees S Mid-Atlantic Ridge." Geochimica Et Cosmochimica Acta 73(19): 5619-5634.

Bourles, D., Raisbeck, G. M. and Yiou, F. (1989). "^{10}Be and ^{9}Be in marine sediments and their potential for dating." Geochimica Et Cosmochimica Acta 53(2): 443-452.

Boyle, E. A., John, S., Abouchami, W., Adkins, J. F., Echegoyen-Sanz, Y., Ellwood, M., Flegal, A. R., Fornace, K., Gallon, C., Galer, S., Gault-Ringold, M., Lacan, F., Radic, A., Rehkamper, M., Rouxel, O., Sohrin, Y., Stirling, C., Thompson, C., Vance, D., Xue, Z. C. and Zhao, Y. (2012). "GEOTRACES IC1 (BATS) contamination-prone trace element isotopes Cd, Fe, Pb, Zn, Cu, and Mo intercalibration." Limnology and Oceanography-Methods 10: 653-665.

Cameron, V. and Vance, D. (2013). Nickel Isotopic Composition of Modern Seawater and Rivers. Goldschmidt, Florence, Italy, Mineralogical Magazine.

Christensen, J. N., Halliday, A. N., Godfrey, L. V., Hein, J. R. and Rea, D. K. (1997). "Climate and ocean dynamics and the lead isotopic records in Pacific ferromanganese crusts." Science 277(5328): 913-918.

Chu, N. C., Johnson, C. M., Beard, B. L., German, C. R., Nesbitt, R. W., Frank, M., Bohn, M., Kubik, P. W., Usui, A. and Graham, I. (2006). "Evidence for hydrothermal venting in Fe isotope compositions of the deep Pacific Ocean through time." Earth and Planetary Science Letters 245(1-2): 202-217.

Claude, C., Suhr, G., Hofmann, A. W. and Koschinsky, A. (2005). "U-Th chronology and paleoceanographic record in a Fe-Mn crust from the NE Atlantic over the last 700 ka." Geochimica et Cosmochimica Acta 69(20): 4845-4854.

Conway, T. M., Rosenberg, A. D., Adkins, J. F. and John, S. G. (2013). "A new method for precise determination of iron, zinc and cadmium stable isotope ratios in seawater by double-spike mass spectrometry." Analytica Chimica Acta 793(0): 44-52.

De Baar, H. J. W., Bacon, M. P., Brewer, P. G. and Bruland, K. W. (1985). "Rare Earth elements in the Pacific and Atlantic Oceans." Geochimica Et Cosmochimica Acta 49(9): 1943-1959.

De Carlo, E. H. and McMurtry, G. M. (1992). "Rare-earth element geochemistry of ferromanganese crusts from the Hawaiian Archipelago, central Pacific." Chemical Geology 95(3–4): 235-250.

Ehrlich, S., Butler, I., Halicz, L., Rickard, D., Oldroyd, A. and Matthews, A. (2004). "Experimental study of the copper isotope fractionation between aqueous Cu(II) and covellite, CuS." Chemical Geology 209(3-4): 259-269.

Elderfield, H. and Greaves, M. J. (1981). "Negative Cerium anomalies in the rare-earth element patterns of oceanic ferromanganese nodules." Earth and Planetary Science Letters 55(1): 163-170.

Elderfield, H., Hawkesworth, C. J., Greaves, M. J. and Calvert, S. E. (1981). "Rare-earth element geochemistry of oceanic ferromanganese nodules and associated sediments." Geochimica Et Cosmochimica Acta 45(4): 513-528.

Elderfield, H., Hawkesworth, C. J., Greaves, M. J. and Calvert, S. E. (1981). "Rare-earth element zonation in Pacific ferromanganese nodules." Geochimica Et Cosmochimica Acta 45(7): 1231-1234.

Fitzsimmons, J. N., Zhang, R. and Boyle, E. A. (2013). "Dissolved iron in the tropical North Atlantic Ocean." Marine Chemistry 154(0): 87-99.

Frank, M. (2002). "Radiogenic isotopes: Tracers of past ocean circulation and erosional input." Reviews of Geophysics 40(1).

Frank, M., O'Nions, R. K., Hein, J. R. and Banakar, V. K. (1999). "60 Myr records of major elements and Pb–Nd isotopes from hydrogenous ferromanganese crusts: reconstruction of seawater paleochemistry." Geochimica Et Cosmochimica Acta 63(11–12): 1689-1708.

Gall, L., Williams, H. M., Siebert, C., Halliday, A. N., Herrington, R. J. and Hein, J. R. (2013). "Nickel isotopic compositions of ferromanganese crusts and the constancy of deep ocean inputs and continental weathering effects over the Cenozoic." Earth and Planetary Science Letters 375(0): 148-155.

German, C. R. and Elderfield, H. (1990). "Application of the Ce Anomaly as a Paleoredox Indicator: The Ground Rules." Paleoceanography 5(5): 823-833.

Goldberg, T., Gordon, G., Izon, G., Archer, C., Pearce, C. R., McManus, J., Anbar, A. D. and Rehkamper, M. (2013). "Resolution of inter-laboratory discrepancies in Mo isotope data: an intercalibration." Journal of Analytical Atomic Spectrometry 28(5): 724-735.

Halbach, P., Kriete, C., Prause, B. and Puteanus, D. (1989). "Mechanisms to explain the platinum concentration in ferromanganese seamount crusts." Chemical Geology 76(1-2): 95-106.

Halbach, P. and Puteanus, D. (1984). "The influence of the carbonate dissolution rate on the growth and composition of Co-rich ferromanganese crusts from Central Pacific seamount areas." Earth and Planetary Science Letters 68(1): 73-87.

Halbach, P., Segl, M., Puteanus, D. and Mangini, A. (1983). "Co-fluxes and growth rates in ferromanganese deposits from Central Pacific seamount areas." Nature 304(5928): 716-719.

Hein, J. R., Bohrson, W. A., Schulz, M. S., Noble, M. and Clague, D. A. (1992). "Variations in the fine-scale composition of a Central Pacific ferromanganese crust: paleoceanographic implications." Paleoceanography 7(1): 63-77.

Hein, J. R., Koschinsky, A. and Halliday, A. N. (2003). "Global occurrence of tellurium-rich ferromanganese crusts and a model for the enrichment of tellurium." Geochimica et Cosmochimica Acta 67(6): 1117-1127.

Hein, J. R., Mizell, K., Koschinsky, A. and Conrad, T. A. (2013). "Deep-ocean mineral deposits as a source of critical metals for high- and green-technology applications: Comparison with land-based resources." Ore Geology Reviews 51(0): 1-14.

Hein, J. R., Schwab, W. C. and Davis, A. S. (1988). "Cobalt-rich and platinum-rich ferromanagenese crusts and associated substrate rocks from the Marshall islands." Marine Geology 78(3-4): 255-283.

Hein, J. R., Yeh, H. W., Gunn, S. H., Sliter, W. V., Benninger, L. M. and Wang, C. H. (1993). "Two major Cenozoic episodes of phosphogenesis recorded in equatorial Pacific seamount deposits." Paleoceanography 8(2): 293-311.

Henderson, G. M. and Burton, K. W. (1999). "Using ($^{234}U/^{238}U$) to assess diffusion rates of isotope tracers in ferromanganese crusts." Earth and Planetary Science Letters 170(3): 169-179.

Hlawatsch, S., Neumann, T., van den Berg, C. M. G., Kersten, M., Harff, J. and Suess, E. (2002). "Fast-growing, shallow-water ferro-manganese nodules from the western Baltic Sea: origin and modes of trace element incorporation." Marine Geology 182(3–4): 373-387.

Horner, T. J., Schonbachler, M., Rehkämper, M., Nielsen, S. G., Williams, H., Halliday, A. N., Xue, Z. and Hein, J. R. (2010). "Ferromanganese crusts as archives of deep water Cd isotope compositions." Geochemistry Geophysics Geosystems 11: 1525-2027.

John, S. G. and Adkins, J. (2012). "The vertical distribution of iron stable isotopes in the North Atlantic near Bermuda." Global Biogeochemical Cycles 26(2): GB2034.

John, S. G., Mendez, J., Moffett, J. and Adkins, J. (2012). "The flux of iron and iron isotopes from San Pedro Basin sediments." Geochimica Et Cosmochimica Acta 93(0): 14-29.

Johnson, T. M. and Bullen, T. D. (2004). "Mass-Dependent Fractionation of Selenium and Chromium Isotopes in Low-Temperature Environments." Reviews in Mineralogy and Geochemistry 55(1): 289-317.

Johnson, T. M., Herbel, M. J., Bullen, T. D. and Zawislanski, P. T. (1999). "Selenium isotope ratios as indicators of selenium sources and oxyanion reduction." Geochimica Et Cosmochimica Acta 63(18): 2775-2783.

Jones, C. E., Halliday, A. N., Rea, D. K. and Owen, R. M. (2000). "Eolian inputs of lead to the North Pacific." Geochimica Et Cosmochimica Acta 64(8): 1405-1416.

Klemm, V., Levasseur, S., Frank, M., Hein, J. R. and Halliday, A. N. (2005). "Osmium isotope stratigraphy of a marine ferromanganese crust." Earth and Planetary Science Letters 238(1-2): 42-48.

Koschinsky, A. and Halbach, P. (1995). "Sequential leaching of marine ferromanganese precipitates: Genetic implications." Geochimica et Cosmochimica Acta 59(24): 5113-5132.

Koschinsky, A., Hein, J., Mohwinkel, D., Foster, A. and Bargar, J. (2013). Accumulation Mechanisms and Bonding of High-Tech Metals in Marine Ferromanganese Crusts. Goldschmidt, Florence, Italy, Mineralogical Magazine.

Koschinsky, A. and Hein, J. R. (2003). "Uptake of elements from seawater by ferromanganese crusts: solid-phase associations and seawater speciation." Marine Geology 198(3-4): 331-351.

Koschinsky, A., Stascheit, A., Bau, M. and Halbach, P. (1997). "Effects of phosphatization on the geochemical and mineralogical composition of marine ferromanganese crusts." Geochimica et Cosmochimica Acta 61(19): 4079-4094.

Lacan, F., Francois, R., Ji, Y. and Sherrell, R. M. (2006). "Cadmium isotopic composition in the ocean." Geochimica Et Cosmochimica Acta 70(20): 5104-5118.

Lacan, F., Radic, A., Jeandel, C., Poitrasson, F., Sarthou, G., Pradoux, C. and Freydier, R. (2008). "Measurement of the isotopic composition of dissolved iron in the open ocean." Geophysical Research Letters 35(24).

Lacan, F., Radic, A., Labatut, M., Jeandel, C., Poitrasson, F., Sarthou, G., Pradoux, C., Chmeleff, J. and Freydier, R. (2010). "High-Precision Determination of the Isotopic Composition of Dissolved Iron in Iron Depleted Seawater by Double Spike Multicollector-ICPMS." Analytical Chemistry 82(17): 7103-7111.

Lacan, F., Tachikawa, K. and Jeandel, C. (2012). "Neodymium isotopic composition of the oceans: A compilation of seawater data." Chemical Geology 300–301(0): 177-184.

Lesuave, R., Pichocki, C., Pautot, G., Hoffert, M., Morel, Y., Voisset, M., Monti, S., Amosse, J. and Kosakevitch, A. (1989). "Geological and mineralogical study of Co-rich ferromanganese crusts from a submerged atoll in the Tuamotu archipelago (French Polynesia)." Marine Geology 87(2-4): 227-247.

Levasseur, S., Frank, M., Hein, J. R. and Halliday, A. (2004). "The global variation in the iron isotope composition of marine hydrogenetic ferromanganese deposits: implications for seawater chemistry?" Earth and Planetary Science Letters 224(1-2): 91-105.

Li, Y. H. and Schoonmaker, J. E. (2003). Chemical Composition and Mineralogy of Marine Sediments. Treatise on Geochemistry. D. H. Editors-in-Chief: Heinrich and K. T. Karl. Oxford, Pergamon**:** 1-35.

Ling, H.-F., Jiang, S.-Y., Frank, M., Zhou, H.-Y., Zhou, F., Lu, Z.-L., Chen, X.-M., Jiang, Y.-H. and Ge, C.-D. (2005). "Differing controls over the Cenozoic Pb and Nd isotope evolution of deepwater in the central North Pacific Ocean." Earth and Planetary Science Letters 232(3–4): 345-361.

Ling, H. F., Burton, K. W., O'Nions, R. K., Kamber, B. S., von Blanckenburg, F., Gibb, A. J. and Hein, J. R. (1997). "Evolution of Nd and Pb isotopes in Central Pacific seawater from ferromanganese crusts." Earth and Planetary Science Letters 146(1–2): 1-12.

Little, S. H., Vance, D., Walker-Brown, C. and Landing, W. M. (2013). "The oceanic mass balance of copper and zinc isotopes, investigated by analysis of their inputs, and outputs to ferromanganese oxide sediments." Geochimica Et Cosmochimica Acta(0).

Marcus, M. A., Manceau, A. and Kersten, M. (2004). "Mn, Fe, Zn and As speciation in a fast-growing ferromanganese marine nodule." Geochimica et Cosmochimica Acta 68(14): 3125-3136.

Maréchal, C. N., Nicolas, E., Douchet, C. and Albarède, F. (2000). "Abundance of zinc isotopes as a marine biogeochemical tracer." Geochem. Geophys. Geosyst. 1(5): 1-15.

Martin, J. H. and Knauer, G. A. (1984). "VERTEX: manganese transport through oxygen minima." Earth and Planetary Science Letters 67(1): 35-47.

Martin, J. H. and Knauer, G. A. (1985). "Lateral transport of Mn in the Northeast Pacific gyre oxygen minimum zone." Nature 314(6011): 524-526.

Mills, R. A., Wells, D. M. and Roberts, S. (2001). "Genesis of ferromanganese crusts from the TAG hydrothermal field." Chemical Geology 176(1–4): 283-293.

Nicholson, K., Hein, J. R., Buehn, B. and Dasgupta, S., Eds. (1997). Manganese mineralization; geochemistry and mineralogy of terrestrial and marine deposits, Geological Society of London : London, United Kingdom.

Nielsen, S. G., Gannoun, A., Marnham, C., Burton, K. W., Halliday, A. N. and Hein, J. R. (2011). "New age for ferromanganese crust 109D-C and implications for isotopic records of lead, neodymium, hafnium, and thallium in the Pliocene Indian Ocean." Paleoceanography 26.

Peacock, C. L. (2009). "Physiochemical controls on the crystal-chemistry of Ni in birnessite: Genetic implications for ferromanganese precipitates." Geochimica et Cosmochimica Acta 73(12): 3568-3578.

Pettke, T., Halliday, A. N. and Rea, D. K. (2002). "Cenozoic evolution of Asian climate and sources of Pacific seawater Pb and Nd derived from eolian dust of sediment core LL44-GPC3." Paleoceanography 17(3).

Pichat, S., Douchet, C. and Albarede, F. (2003). "Zinc isotope variations in deep-sea carbonates from the eastern equatorial Pacific over the last 175 ka." Earth and Planetary Science Letters 210(1-2): 167-178.

Pichocki, C. and Hoffert, M. (1987). "Characteristics of Co-rich ferromanganese nodules and crusts sampled in French Polynesia." Marine Geology 77(1-2): 109-119.

Pokrovsky, O. S., Viers, J., Emnova, E. E., Kompantseva, E. I. and Freydier, R. (2008). "Copper isotope fractionation during its interaction with soil and aquatic microorganisms and metal oxy(hydr)oxides: Possible structural control." Geochimica et Cosmochimica Acta 72(7): 1742-1757.

Pokrovsky, O. S., Viers, J. and Freydier, R. (2005). "Zinc stable isotope fractionation during its adsorption on oxides and hydroxides." Journal of Colloid and Interface Science 291(1): 192-200.

Puteanus, D. and Halbach, P. (1988). "Correlation of Co concentration and growth rate — A method for age determination of ferromanganese crusts." Chemical Geology 69(1–2): 73-85.

Radic, A., Lacan, F. and Murray, J. W. (2011). "Iron isotopes in the seawater of the equatorial Pacific Ocean: New constraints for the oceanic iron cycle." Earth and Planetary Science Letters 306(1-2): 1-10.

Rehkämper, M., Frank, M., Hein, J. R. and Halliday, A. (2004). "Cenozoic marine geochemistry of thallium deduced from isotopic studies of ferromanganese crusts and pelagic sediments." Earth and Planetary Science Letters 219(1-2): 77-91.

Rouxel, O., Galy, A. and Elderfield, H. (2006). "Germanium isotopic variations in igneous rocks and marine sediments." Geochimica Et Cosmochimica Acta 70(13): 3387-3400.

Rouxel, O., Ludden, J., Carignan, J., Marin, L. and Fouquet, Y. (2002). "Natural variations of Se isotopic composition determined by hydride generation multiple collector inductively coupled plasma mass spectrometry." Geochimica Et Cosmochimica Acta 66(18): 3191-3199.

Rouxel, O., Shanks, W. C., Bach, W. and Edwards, K. J. (2008). "Integrated Fe- and S-isotope study of seafloor hydrothermal vents at East Pacific rise 9-10 degrees N." Chemical Geology 252(3-4): 214-227.

Rouxel, O. J. and Auro, M. (2010). "Iron Isotope Variations in Coastal Seawater Determined by Multicollector ICP-MS." Geostandards and Geoanalytical Research 34(2): 135-144.

Schmitt, A. D., Galer, S. J. G. and Abouchami, W. (2009). "Mass-dependent cadmium isotopic variations in nature with emphasis on the marine environment." Earth and Planetary Science Letters 277(1-2): 262-272.

Segl, M., Mangini, A., Bonani, G., Hofmann, H. J., Nessi, M., Suter, M., Wolfli, W., Friedrich, G., Pluger, W. L., Wiechowski, A. and Beer, J. (1984). "^{10}Be-dating of a manganese crust from Central North Pacific and implications for ocean palaeocirculation." Nature 309(5968): 540-543.

Siebert, C., Nagler, T. F., von Blanckenburg, F. and Kramers, J. D. (2003). "Molybdenum isotope records as a potential new proxy for paleoceanography." Earth and Planetary Science Letters 211(1-2): 159-171.

Staubwasser, M., von Blanckenburg, F. and Schoenberg, R. (2006). "Iron isotopes in the early marine diagenetic iron cycle." Geology 34(8): 629-632.

Takahashi, Y., Manceau, A., Geoffroy, N., Marcus, M. A. and Usui, A. (2007). "Chemical and structural control of the partitioning of Co, Ce, and Pb in marine ferromanganese oxides." Geochimica Et Cosmochimica Acta 71(4): 984-1008.

Takano, S., Tanimizu, M., Hirata, T. and Sohrin, Y. (2013). "Determination of isotopic composition of dissolved copper in seawater by multi-collector inductively coupled plasma mass spectrometry after pre-concentration using an ethylenediaminetriacetic acid chelating resin." Analytica Chimica Acta 784(0): 33-41.

Thompson, C. M., Ellwood, M. J. and Wille, M. (2013). "A solvent extraction technique for the isotopic measurement of dissolved copper in seawater." Analytica Chimica Acta 775(0): 106-113.

van de Flierdt, T., Frank, M., Halliday, A. N., Hein, J. R., Hattendorf, B., Günther, D. and Kubik, P. W. (2003). "Lead isotopes in North Pacific deep water - implications for past changes in input sources and circulation patterns." Earth and Planetary Science Letters 209(1-2): 149-164.

van de Flierdt, T., Frank, M., Halliday, A. N., Hein, J. R., Hattendorf, B., Günther, D. and Kubik, P. W. (2004). "Tracing the history of submarine hydrothermal inputs and the significance of hydrothermal hafnium for the seawater budget—a combined Pb–Hf–Nd isotope approach." Earth and Planetary Science Letters 222(1): 259-273.

Vance, D., Archer, C., Bermin, J., Perkins, J., Statham, P. J., Lohan, M. C., Ellwood, M. J. and Mills, R. A. (2008). "The copper isotope geochemistry of rivers and the oceans." Earth and Planetary Science Letters 274(1-2): 204-213.

Verlaan, P. A., Cronan, D. S. and Morgan, C. L. (2004). "A comparative analysis of compositional variations in and between marine ferromanganese nodules and crusts in the South Pacific and their environmental controls." Progress in Oceanography 63(3): 125-158.

von Blanckenburg, F., O'Nions, R. K., Belshaw, N. S., Gibb, A. and Hein, J. R. (1996). "Global distribution of beryllium isotopes in deep ocean water as derived from Fe-Mn crusts." Earth and Planetary Science Letters 141(1-4): 213-226.

Wasylenki, L. E. and Swihart, J. (2013). Cd Isotope Fractionation during Sorption to Mn Oxide at Low and High Ionic Strength. Goldschmidt, Florence, Italy.

Zhu, X. K., Guo, Y., Williams, R. J. P., O'Nions, R. K., Matthews, A., Belshaw, N. S., Canters, G. W., de Waal, E. C., Weser, U., Burgess, B. K. and Salvato, B. (2002). "Mass fractionation processes of transition metal isotopes." Earth and Planetary Science Letters 200(1-2): 47-62.

Zhu, X. K., O'Nions, R. K., Guo, Y. L. and Reynolds, B. C. (2000). "Secular variation of iron isotopes in North Atlantic Deep Water." Science 287(5460): 2000-2002.

Partie III.1 – Les isotopes du Ni comme traceurs des sources et des processus d'enrichissement des dépôts marins hydrothermaux et hydrogénétiques riches en Fe et en Mn

Part III.1 - Ni isotope constraints of Ni sources and enrichment processes in hydrothermal and hydrogenetic Fe- and Mn-rich deposits in the oceans

Abstract:

Much attention is now being given to Ni isotopes as new biogeochemical tracers in marine environments. The goal of this study is to evaluate the influence of sources and enrichment processes on Ni isotope composition of marine metalliferous deposits and to propose a model explaining Ni isotope variability in these deposits.
We investigated the Ni isotope compositions ($\delta^{60/58}$Ni) of Fe- and Mn-rich deposits from contrasted marine environments, including hydrothermal deposits and hydrogenous crusts. Samples include hydrogenetic Fe-Mn crusts from various locations in the Atlantic and Pacific Oceans, old hydrothermal deposits from the Lau back-arc basin and hydrothermal deposits from active vent sites of Loihi seamount (South Hawaii).
Purified samples were measured by MC-ICP-MS using a double-spike (^{61}Ni and ^{62}Ni) correction method. Compared to relatively homogenous Ni isotope composition in crustal rocks, ferromanganese (Fe-Mn) crusts collected in the Atlantic and Pacific Oceans yield $\delta^{60/58}$Ni values from +0.76 to +1.80 ‰, which are both higher and lower than the range of Ni isotope composition in modern seawater. No systematic differences between the Atlantic and the Pacific Oceans have been observed. In general, the highest $\delta^{60/58}$Ni values are observed in hydrogenous crust that also display typical positive Ce anomalies (Ce/Ce*), suggesting a direct uptake of Ni from seawater with limited isotope fractionation. Local variations in $\delta^{60/58}$Ni values reflect either different Ni sources or Ni isotope fractionation during Ni adsorption onto Fe- and Mn-oxides. Mixed hydrothermal-hydrogenous crust from the Bauer Basin yield a $\delta^{60/58}$Ni value of +0.33 ‰ and REE patterns displaying negative Ce anomalies. The results are interpreted as reflecting the larger extent of Ni isotope fractionation during seawater-derived Ni scavenging in hydrothermal plume environments rather than direct hydrothermal input. Pure hydrothermal Fe-Mn deposits from the Lau basin hydrothermal field are characterized by a strong negative Ce anomaly and Ni isotope values are comprised between +0.51 and +1.11 ‰. These deposits originally formed through diffuse hydrothermal fluid precipitation, resulting in post-depositional scavenging of seawater-derived Ni and REE. In marked contrast, actively forming hydrothermal Fe-Mn deposits at the base of Loihi Seamount yield negative $\delta^{60/58}$Ni values from -0.73 to -1.49 ‰ suggesting that Ni is derived directly from diffuse hydrothermal fluids with relatively minor seawater uptake. Overall, the results are integrated within a genetic model of Fe-Mn deposits that combines REE and Ni isotope systematics.

1. Introduction

It has long been recognized that oceanic metalliferous deposits show large diversity with respect to their sources of metals, mineralogy, rates and processes of formation and geodynamic settings (Bonatti et al. 1972c; Cronan 2000). Major types of ferromanganese (Fe-Mn) deposits include (i) Mn nodules formed on the abyssal plains (>4000 m depth) where pelagic sedimentation and tectonic activity are very limited (Cronan 1975; Halbach et al. 1982; Dymond et al. 1984; Aplin and Cronan 1985); (ii) ferromanganese (Fe-Mn) crusts covering the flank of seamounts, often referred as hydrogenetic crusts, and (iii) hydrothermal Fe-Mn(Si) oxides deposits resulting from low temperature diffuse hydrothermal venting and showing a large range of composition from Mn-rich to Mn-poor deposits, including ironstone or umber deposits (Hein et al. 1994; Hein et al. 1996; Edwards et al. 2011). Owing to their very slow rate of formation, Fe-Mn crusts and Mn-nodules typically show extreme enrichment of metals compared to the average crust e.g. Co, Te and Pt in Fe-Mn crusts (Halbach et al.

1984; Hein et al. 1988; Halbach et al. 1989; Hein et al. 2003), and Ni and Cu in Mn-nodules (Cronan 1975; Hein et al. 2013). In contrast, hydrothermal Fe-Mn deposits are generally poorly enriched in transition metals besides Fe and Mn.

Fe-Mn crusts are found covering the flank of seamounts that serves as a substrate for these encrustations. Seamounts enhance the circulation of oceanic currents, leading to Fe-Mn particles precipitation from seawater in area areas that are kept sediment-free for millions of years (Nicholson et al. 1997; Frank et al. 1999). Since Fe-Mn crusts are solely precipitated from seawater (i.e. hydrogenetic deposits), they have attracted considerable interest as proxies for deep seawater composition over million years time-scale. In contrast, Fe-Mn hydrothermal deposits form rapidly near active oceanic ridges. It was demonstrated that the formation of such hydrothermal deposits could be the result of either direct precipitation from diffuse hydrothermal venting (e.g. Lau Basin (Fouquet et al. 1993), Loihi Seamount (Edwards et al. 2011)) or other types of Fe-Mn deposits may be also related to hydrothermal plume fallout and/or lateral transport of vent-exported materials from the ridge axis (e.g. Bauer Basin (Heath and Dymond 1977; Lyle et al. 1977; McMurtry and Yeh 1981) and other areas in the Atlantic)

All of those types of Fe-Mn deposits have been largely used as paleoceanographic archives through the study of radiogenic isotopes geochemistry (Pb, Nd, Hf, Os); including primarily the Fe-Mn crusts (Ling et al. 1997; O'Nions et al. 1998; Frank et al. 1999; Reynolds et al. 1999; Frank 2002; Frank et al. 2002; Ling et al. 2005), seawater-exposed surface of manganese nodules (Abouchami and Goldstein 1995; Albarede et al. 1998) and hydrothermally affected sediments (Ravizza and McMurtry 1993). Similar approaches were implemented for transition metals like Fe, Cu and Zn as a proxy of ambient seawater isotope composition (Anbar and Rouxel 2007). Isotope composition of Fe, Cd, and Tl have been previously reported in Fe-Mn crusts either on bulk samples or on surface layers fractionation in order to evaluate potential relationships between oceanic basins and variations in metal isotope composition (Rehkämper et al. 2002; Levasseur et al. 2004; Rehkämper et al. 2004; Schmitt et al. 2009; Horner et al. 2010). On the other hand, Zn and Cu isotope compositions were only reported in manganese nodules (Maréchal et al. 2000; Albarede 2004). However, while no resolvable variations were observed for Cd and Tl isotopes according to their locations in the oceans or the geodynamic settings, large Fe isotopes variations measured in surface layers of Fe-Mn crusts from various locations have yielded ambiguous results for deciphering between local and global effects on metal sources to the oceans (Beard et al. 2003; Levasseur et al. 2004).

In order to shed light on our understanding of metal isotope variations in marine environments and their potential as biogeochemical tracers, attention is now given at developing Ni isotope systematics (Cameron et al. 2009; Gueguen et al. 2011; Gall et al. 2012; Cameron and Vance 2013; Gueguen et al. 2013; Vance et al. 2013). Ni isotopes in various terrestrial rocks indicate significant variations between, for instance, rocks formed at high temperature like Ni-rich sulfides (Gueguen et al. 2013; Hofmann et al. 2013) and low temperature rocks such as marine sediments (Gueguen et al. 2013). These previous studies suggested an average value of 0.0 to 0.05 ‰ for the Bulk Silicate Earth (Gall et al. 2012; Gueguen et al. 2013).

First Ni isotope composition of Fe-Mn crusts reported by Gall et al. (2013) ranges from +0.9 to +2.5 ‰ with no obvious distinction between oceanic basins. The authors argued that no isotope fractionation occurs between Fe-Mn crusts and seawater, and that variations are related to different Ni sources contribution in seawater. However, Gueguen et al. (2011) demonstrated that Ni adsorption on Fe- and Mn-oxides produces Ni light isotopes enrichment

in the mineral phase, with values between -0.4 and -1 ‰. Gall et al. (2013) inferred from the variations of Mn concentrations and $\delta^{60/58}$Ni values through a hydrogenetic Fe-Mn crust from the Central Pacific Ocean that a non-negligible part of Ni in seawater may be derived from hydrothermal inputs. A major issue with such interpretation is that hydrothermal input of Ni is very limited and is mostly found in ultramafic setting (Charlou et al. 2002; Douville et al. 2002). It is also not clear whether such local input may shift seawater Ni isotope composition considering the relatively long residence time of Ni in seawater. Measurements of pure hydrothermal crusts and even hydrothermal fluids are also required to test such hypothesis. Although the study of Gall et al. (2013) provides an important baseline of Ni isotope composition of Fe-Mn deposits, further studies are required to address local vs. global effects on Ni isotope variations in seawater and hydrothermal vs. lithogenic Ni input.

Therefore, the purpose of this work is (1) to perform a detailed investigation of Ni isotope variations in Fe-Mn crusts and nodules and hydrothermal Fe-Mn deposits from different geological settings (2) to evaluate the influence of sources versus processes on Ni isotope fractionation by comparing with other geochemical signatures such as REE. Results of this study will enhance our understanding of the factors governing Ni isotope variations in Fe-Mn deposits and their significance for seawater chemistry and Ni biogeochemical cycling.

2. Sample description

2.1. Atlantic and Pacific hydrogenous Fe-Mn crusts

We performed analyses of bulk Fe-Mn crusts samples from the Pacific Ocean and Atlantic Ocean. Since continuous discrete layers were not specifically investigated, this sample set should integrate the Ni isotope composition over a long period of time.

Fe-Mn crusts from the Pacific Ocean were collected on Apuupuu seamount ~50 km south of Hawaii during FeMO 2009 cruise on the R/V Kilo Moana (University of Hawaii) in October 2009. These crusts were collected by ROV (Remotely Operated underwater Vehicle) Jason II (Woods Hole Oceanographic Institution). Eight samples were selected for our study between 2000 and 3000 m depth (Table III.2).

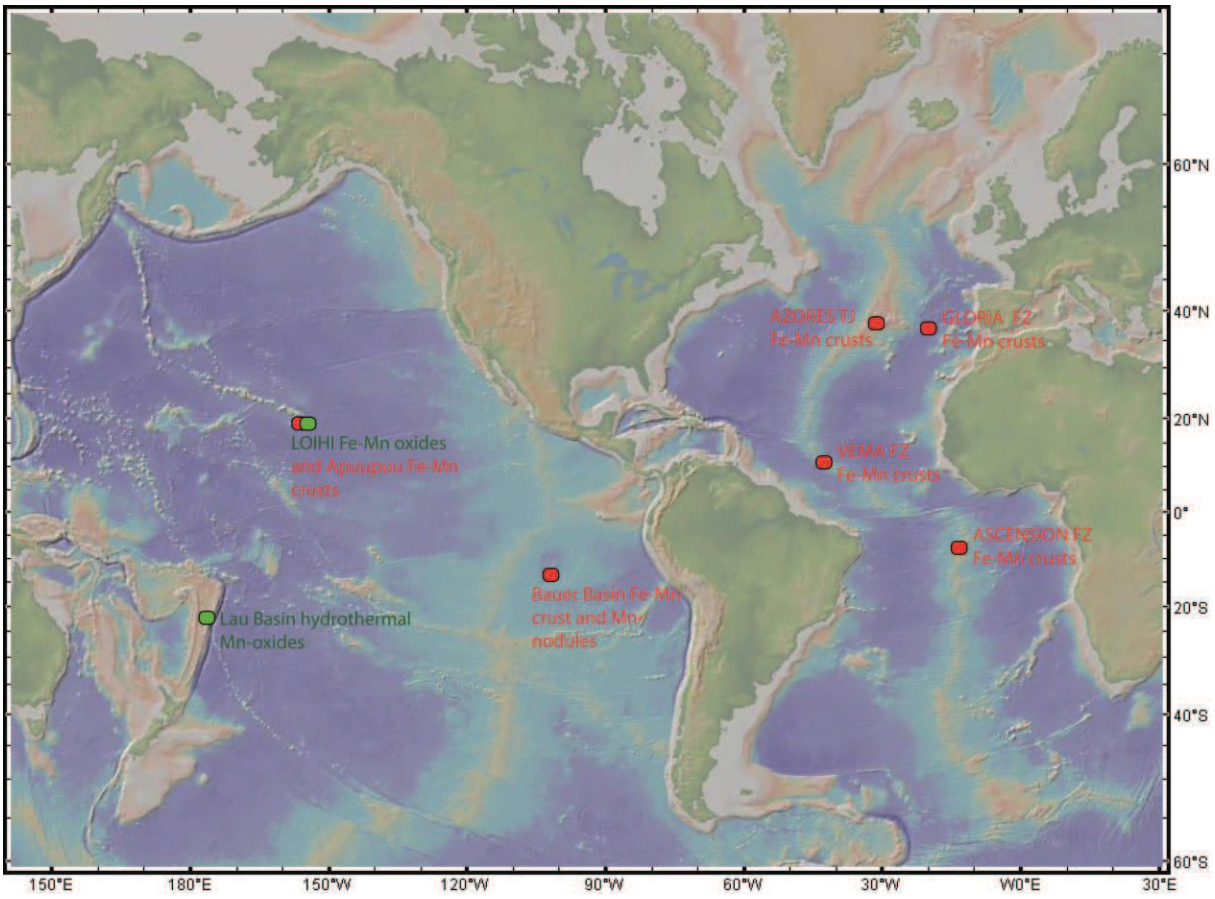

Figure III.6: *World map indicating sample locations. Bulk hydrogenetic Fe-Mn crusts are indicated in red and hydrothermal Fe-Mn deposits are shown in green.*

Table III.2: Sampling information and mineralogy of hydrogenetic Fe-Mn crusts and Lau Basin Fe-Mn deposits

Sample Name	Location	Name of cruise	Latitude	Longitude	Depth on the seafloor (m)	Mineralogy	Comments
CAP BREST 03-03	Ascension FZ	CAP BREST	7°52.05S	13°27.02W	3200	todorokite, birnessite, calcite, (quartz)	poorly crystallized
DR01-003 4-B-5	VEMA FZ	VEMA CH78	10°35.4N	42°42.9W	2800	todorokite, birnessite, goethite, (quartz)	poorly crystallized
DR-01-005 16-A-12	VEMA FZ	VEMA CH78	10°35.4N	42°42.9W	2800	todorokite, birnessite, goethite, (quartz)	poorly crystallized
DR01-005 16-A-6	VEMA FZ	VEMA CH78	10°35.4N	42°42.9W	2800	todorokite, quartz	poorly crystallized
DR01-005 16-B-11	VEMA FZ	VEMA CH78	10°35.4N	42°42.9W	2800	todorokite, birnessite, (quartz)	poorly crystallized
DR01-005 16-B-12	VEMA FZ	VEMA CH78	10°35.4N	42°42.9W	2800	todorokite, birnessite, (quartz)	poorly crystallized
DR01-005 6-C-13	VEMA FZ	VEMA CH78	10°35.4N	42°42.9W	2800	todorokite, birnessite, quartz	poorly crystallized
DR03-003 17-C-4	VEMA FZ	VEMA CH78	10°38.8N	42°41.1W	3800		
DR03-025 15#5	VEMA FZ	VEMA CH78	10°38.8N	42°41.1W	3800	todorokite, calcite, quartz	poorly crystallized
DR03-025 15-D-10	VEMA FZ	VEMA CH78	10°38.8N	42°41.1W	3800	todorokite, birnessite, (calcite), (quartz)	poorly crystallized
DR12-24 32-A-6	Gloria FZ	GIB CH30	37°02.5N	20°05.30W	3480	todoroktie, birnessite, argile, (quartz)	poorly crystallized
DR12-24 32-B-2	Gloria FZ	GIB CH30	37°02.5N	20°05.30W	3480	todorokite, birnessite, (calcite), (quartz)	poorly crystallized
DR12-24 32-B-3	Gloria FZ	GIB CH30	37°02.5N	20°05.30W	3480	todorokite, birnessite, (quartz)	poorly crystallized
DR24-09 34-A-2	AZORES TJ	GIB CH30	37°55.2N	31°06.1W	2140	todorokite	poorly crystallized
DR24-09 34-C-2	AZORES TJ	GIB CH30	37°55.2N	31°06.1W	2140	todorokite, birnessite	poorly crystallized
J2-480-R11	Apuupuu	FeMO2009	51°71N	52°49E	2078	todorokite, birnessite, fluorapatite, (quartz), (plagioclase)	poorly crystallized
J2-480-R11b	Apuupuu	FeMO2009	51°71N	52°49E	2078	todorokite, (quartz)	poorly crystallized
J2-480-R13A	Apuupuu	FeMO2009	51°71N	52°49E	2076	todorokite, birnessite, phillipsite, (quartz)	poorly crystallized
J2-480-R13A	Apuupuu	FeMO2009	51°71N	52°49E	2076	todorokite, birnessite, phillipsite, (quartz)	poorly crystallized
J2-480-R13Ab	Apuupuu	FeMO2009	51°71N	52°49E	2076	todorokite, birnessite, (quartz), (plagioclase)	nd
J2-480-R13B	Apuupuu	FeMO2009	51°71N	52°49E	2076		nd
J2-480-R14	Apuupuu	FeMO2009	51°71N	52°49E	2079	todorokite, fluorapatite, (plagioclase)	poorly crystallized
J2-480	Apuupuu	FeMO2009	51°71N	52°49E	extra sample	todorokite, fluorapatite, (plagioclase)	poorly crystallized
Y73-3-22D crust	Bauer Basin	YALOC-73	13°40S	102°8W	hand specimen	todorokite, birnessite, phillipsite, (quartz)	crystallized
NL-10-09		NAUTILAU	21°51,10'S	176°29,78'W	1908	Birnessite, (todorokite)	crystallized
NL-20-05		NAUTILAU	22°13,75'S	176°36,52'W	1650	todorokite, birnessite	crystallized

Fe-Mn crusts from the Atlantic Ocean were sampled at different locations, along the Ascension Fracture Zone (FZ), Vema FZ, Gloria FZ and the Azores Triple Junction (TJ). They were collected by dredging during several CNEXO cruises on the R/V Jean Charcot (cruises GIBRACO CH30 in August-September 1972 and BIOVEMA CH78 in October 1977) (Table III.2 and Figure III.6). Selection also includes the two USGS geostandards of manganese nodules (Nod-A-1 and Nod-P-1) collected in the Atlantic and the Pacific Oceans.

2.2. Bauer Basin Fe-Mn deposits, Southeastern Pacific

The selection comprises one Fe-Mn crust from the Bauer Basin, located Eastern of the East Pcific Rise South Eastern Pacific, collected during YALOC-73 cruise on the R/V Yaquina (Oregon State University) at latitude=13°40'S and longitude=102°8'W (Lyle et al. 1977; Elderfield and Greaves 1981). Bauer Basin (BB) is located in South Pacific Ocean between the active East Pacific Rise and the extinct Galapagos Rise. At the southern part of the basin is the Central Basin situated north of the Sala-Y-Gomez Ridge and further north of BB is the Galapagos rift zone (Heath and Dymond 1977). The Bauer deep is surrounded by oceanic ridges that are either active or inactive. Thus, Fe-Mn deposits and Fe-Mn crusts from Bauer Basin are prone to influence of hydrothermal inputs exported by seawater circulation through the ridge crests. The source of metal such as Fe and Mn have been shown to have a hydrothermal origin (Dymond and Veeh 1975; Heath and Dymond 1977; Lyle et al. 1977; Elderfield and Greaves 1981). Previous study of REE patterns revealed negative Ce anomalies in both crusts and nodules from the Bauer basin which is consistent with scavenging of seawater REE onto hydrothermal iron oxyhydroxides probably originating from the East Pacific Rise (Elderfield and Greaves 1981).

2.3. Hydrothermal deposits from the Lau basin, Southwestern Pacific

Fe-Mn oxides samples were collected in southern back-arc Lau basin at the Eastern Tonga subduction zone during NAUTILAU cruise on the R/V Nadir (Ifremer-Genavir) in April-May 1989 (Figure III.6). The Valu Fa Ridge in the Lau basin is an active back-arc spreading center where diffuse hydrothermal venting allows the deposition of Fe- and Mn-rich deposits (Fouquet et al. 1991). Some Fe-Mn-rich deposits are located on inactive sites and active hydrothermal fields were also identified: Hine Hina on the Southern Valu Fa Ridge, Vai Lili on the Central Valu Fa Ridge, and White Church on the Northern Valu Fa segment (Fouquet et al. 1993). Samples were recovered during four dives with submersible NAUTILE on inactive and active hydrothermal sites. Two samples were selected for our study: NL-20-05 is a pure 5 cm-thick manganese crust collected at 1650 m water depth at the Vai Lili site (Central Valu Fa Ridge). NL-10-09 was collected at 1908 m water depth at the White Church site (Northern Valu Fa Ridge) and consists of pieces of small inactive chimneys composed of pure porous and filamentous Mn-oxides (Fouquet et al. 1993).

2.4. Fe and Mn-rich microbial mats at Loihi seamount, Northern Pacific

Hydrothermal Fe-Mn oxides and microbial mats were collected on Loihi seamount during three oceanographic cruises: FeMO 2006 on R/V Melville (Scripps Oceanographic Institute) in October-November 2006, FeMO 2008 on R/V Thompson (University of Washington) in September-October 2008 and FeMO 2009 on the R/V Kilo Moana (University of Hawaii) in October 2009 using ROV Jason II (Woods Hole Oceanographic Institution) (Figure III.6). These cruises are part of a project called the Iron-Oxidizing Microbial Observatory (FeMO) designed to investigate iron biogeochemical reactions at Loihi hydrothermal vents. Descriptions of the samples are provided in (Glazer and Rouxel 2009; Edwards et al. 2011). Samples selected for this study were collected different location: Mkr17 located on the Fe-Mn deposits deposited between pillow lavas; and Ula Nui-Moon Mat areas located at the base of Loihi Seamount, referred to "FeMO Deep". The extensive deposits recovered at FeMO Deep are considered to originate from ultra-diffuse venting of low

temperature fluids, forming the deepest actively forming hydrothermal deposits reported so far, i.e. ~5000 m water depth (Edwards et al. 2011). Loihi samples are very fresh and are very recent deposits in comparison to Lau basin hydrothermal Fe-Mn oxides which are older deposits.

3. Methods

3.1. Mineralogy and geochemical analyses

The mineralogy of Fe-Mn deposits (Fe-Mn crusts and BB Fe-Mn crust and hydrothermal deposits from Lau Basin) was determined by X-ray diffraction at Ifremer (Brest, France) on bulk powder. Major, trace and Rare Earth elements concentrations were measured by ICP-MS-Quadrupole (Thermo-Finnigan, X-Series 2) at Pôle Spectrométrie Océan (IUEM/Ifremer, Brest, France). Samples were dissolved in HNO_3-HCl acid mixture and diluted to 200 before ICP-MS analysis. Multi-elemental solutions and geological reference materials (GRM) of Mn-nodules Nod-A-1 and Nod-P-1 were systematically run during each analytical session altogether with the samples. Concentrations were calibrated using a multi-elemental solution. Typical error obtained for all elements is generally better than 3%. Results are presented in Table III.2 (mineralogy) and Table III.3 (geochemistry).

3.2. Ni isotopes measurements

Ni isotope compositions were measured by MC-ICP-MS on a Thermo-Finnigan Neptune at Pôle Spectrométrie Océan (IUEM/Ifremer, Brest, France) (Table III.4). Detailed descriptions of the analytical and experimental methods can be found in (Gueguen et al. 2013), though a brief description of methodology is provided below.

After a two-stage purification method through ion-exchange chromatography columns using AG1-X8 (for separating Fe, Zn and most of Co and Cu) and Ni-spec Eichrom resins (for completing removal of remaining element matrix), $^{60}Ni/^{58}Ni$, $^{61}Ni/^{58}Ni$, and $^{62}Ni/^{58}Ni$ ratios were measured by MC-ICP-MS in medium or high-mass resolution with an ApexQ (ESI, USA) desolvation introduction system. Instrumental mass discrimination was corrected using double-spike method. A mix of ^{61}Ni and ^{62}Ni isotopes was added to each sample prior to second step of chemical purification, data reduction is based on calculations from (Siebert et al. 2001). A spiked solution of the international isotopic standard of nickel NIST SRM 986 was routinely analyzed during each analytical session in a similar manner as a sample-standard-bracketing method which allows to monitoring the reproducibility of each analytical session. Experimental and analytical methods are described in (Gueguen et al. 2013).
$^{60}Ni/^{58}Ni$ ratios of samples are reported as a deviation from NIST SRM 986 standard isotope composition following equation (1) in per mil:

$$\delta^{60/58}Ni = (R_{spl}/R_{NIST986} - 1) \times 1000 \quad (1)$$

Where R_{spl} is the $^{60}Ni/^{58}Ni$ ratio of the sample and R_{STD} the ratio of standard. Typical measurement precision achieved on Ni isotope composition is better than 0.04 ‰ and external precision (two-standard deviation) calculated on replicate measurements of NIST SRM 986 is ~0.05 ‰.

Table III.3 : Elemental geochemistry* (µg/g) of Fe-Mn deposits.

Sample Name	CAP BREST 03-03	DR01-003 4-B-5	DR-01-005 16-A-12	DR01-005 16-A-6	DR01-005 16-B-11	DR01-005 16-B-12	DR01-005 6-C-13
Location	Ascension FZ	VEMA FZ	VEMA FZ	VEMA FZ	VEMA FZ	VEMA FZ	VEMA FZ
Type	***Bulk Atlantic and Pacific Fe-Mn crusts***						
Si	nd***	nd	nd	nd	nd	nd	nd
Na*	15125,62	12159,62	11325,43	9648,61	11168,89	11722,46	10365,92
Mg	10941,87	12678,85	12948,22	11326,95	12447,80	13060,32	12233,93
Al	14059,44	24813,92	25855,20	24579,36	22037,97	25054,41	23814,87
Ca	29338,57	13242,72	13485,33	12471,80	13920,23	14637,38	12809,71
Ti	6414,78	4637,90	6177,88	4654,15	4799,20	5867,72	6550,25
V	818,01	844,10	877,02	701,93	911,09	867,63	749,54
Cr	8,56	45,35	39,24	31,94	31,88	23,81	22,63
Mn	121622,04	117695,71	131259,32	111603,76	136067,72	140785,04	140957,87
Fe	227965,29	200355,52	197711,46	182251,21	207151,49	194301,28	179173,56
Co	2766,96	3103,95	5004,77	2443,04	3826,34	5005,89	5442,95
Ni**	1161,95	1947,85	1946,23	1853,08	1983,38	1994,32	2127,97
Cu	743,95	943,67	801,35	794,13	695,06	662,10	732,35
Zn	442,48	457,74	477,50	442,65	495,84	509,63	526,04
Rb	2,04	9,66	9,17	7,02	4,07	5,93	4,23
Sr	853,63	683,56	623,40	521,36	701,59	738,69	648,48
Y	156,43	159,21	157,20	156,87	177,55	180,88	183,89
Nb	55,83	57,70	71,71	24,92	42,42	67,97	51,35
Mo	296,45	366,96	357,51	246,23	378,38	375,39	313,63
Cd	3,21	4,33	5,03	4,99	6,00	7,01	7,62
Te	32,59	47,71	58,65	33,24	50,01	54,84	50,89
Ba	1044,21	882,64	973,06	688,57	1072,88	1088,95	939,27
Pt	0,22	0,29	0,40	0,19	0,25	0,33	0,40
Tl	59,31	92,88	81,91	92,30	123,37	119,65	118,94
Pb	447,01	618,52	573,02	537,39	700,81	698,97	670,14
Bi	3,48	8,64	7,81	7,71	9,70	9,10	8,55
Th	17,51	56,97	73,01	43,60	57,74	60,28	52,97
U	8,45	9,61	8,58	8,19	10,10	9,55	8,96
La	232,58	232,86	233,93	171,14	249,96	237,47	187,84
Ce	896,04	1201,05	1331,19	827,93	1392,50	1524,27	1377,60
Pr	52,91	62,90	64,16	44,07	67,17	64,46	51,51
Nd	214,34	257,86	259,03	180,71	274,33	262,72	210,83
Sm	55,62	43,64	46,23	19,10	17,84	52,97	56,34
Eu	9,93	12,86	12,67	9,06	13,36	12,96	10,89
Gd	47,58	60,03	56,93	43,41	61,22	59,51	49,42
Tb	7,03	9,11	8,62	6,73	9,39	8,97	7,77
Dy	41,28	52,83	49,22	39,68	54,46	51,61	45,58
Ho	7,93	9,90	9,05	7,68	10,19	9,71	8,89
Er	23,10	28,71	26,18	22,81	29,09	28,11	26,13
Tm	3,31	4,16	3,74	3,33	4,12	4,00	3,80
Yb	21,15	25,94	23,26	20,96	25,97	24,90	23,86
Lu	3,39	4,05	3,51	3,36	3,98	3,78	3,68

Table III.3 continued

Sample Name	DR03-003 17-C-4	DR03-025 15#5	DR03-025 15-D-10	DR12-24 32-A-6	DR12-24 32-B-2	DR12-24 32-B-3	DR24-09 34-A-2
Location Type	VEMA FZ	VEMA FZ	VEMA FZ	Gloria FZ	Gloria FZ	Gloria FZ	AZORES TJ
Si	nd	nd	nd	nd	nd	nd	nd
Na*	10130,00	11232,01	11645,54	9707,37	11114,70	10968,76	16315,94
Mg	10574,06	9725,39	10679,16	13235,88	12381,33	13858,50	10614,90
Al	17807,74	16112,87	18325,81	24935,08	19919,22	25548,17	2043,37
Ca	14764,65	57239,64	15191,51	14268,46	23532,56	15370,76	25185,84
Ti	5563,20	4708,79	5043,64	17064,72	17495,58	19354,80	8460,82
V	761,45	670,53	768,57	715,77	733,75	798,01	525,88
Cr	18,08	18,90	29,45	16,73	14,05	22,91	1,58
Mn	115560,82	103275,15	109590,79	125600,31	133536,52	133039,17	236905,21
Fe	193340,77	169443,09	195224,63	188847,06	180275,77	198517,42	91919,95
Co	2910,16	2234,97	2711,03	2693,34	4034,07	3783,11	11144,82
Ni**	1631,26	1385,14	1616,82	1846,97	1803,44	1836,54	5495,08
Cu	558,38	571,33	817,19	857,07	748,44	886,95	538,78
Zn	485,67	417,58	486,36	558,36	508,78	573,78	551,84
Rb	3,82	6,57	5,81	2,01	3,57	3,47	2,01
Sr	634,38	755,97	632,98	766,00	839,08	752,24	1001,93
Y	181,89	150,64	167,29	233,35	217,94	235,26	103,06
Nb	37,06	34,25	32,64	60,20	92,87	84,06	61,89
Mo	255,51	268,28	273,58	213,97	239,55	221,38	477,94
Cd	4,03	2,97	3,71	8,08	5,89	7,44	5,38
Te	34,66	21,90	35,76	26,30	38,18	37,16	98,10
Ba	892,11	777,19	916,08	1233,06	1176,09	1163,03	1220,31
Pt	0,16	0,11	0,15	0,15	0,21	0,16	0,64
Tl	72,19	51,56	53,24	101,71	89,19	96,35	236,66
Pb	665,12	552,53	645,93	760,22	861,60	756,92	1472,60
Bi	7,82	6,50	8,75	15,32	17,28	15,46	35,38
Th	60,84	54,69	56,65	26,46	35,84	27,18	3,55
U	9,93	8,07	9,02	14,77	14,45	13,49	11,25
La	232,47	220,03	219,60	219,38	258,20	230,06	122,38
Ce	1203,44	1146,39	1138,68	1577,52	1746,30	1611,30	602,35
Pr	61,67	58,99	58,03	58,44	62,57	57,30	23,16
Nd	253,11	239,09	240,27	242,57	259,21	238,07	98,54
Sm	16,03	56,05	19,07	52,79	55,57	54,88	51,98
Eu	12,52	11,52	12,10	13,26	13,29	12,87	4,77
Gd	59,04	54,01	57,30	65,56	65,18	63,31	23,28
Tb	8,96	8,01	8,63	10,59	10,16	10,14	3,57
Dy	51,84	45,47	49,63	63,66	60,25	60,63	23,26
Ho	9,78	8,31	9,39	12,35	11,63	11,75	5,18
Er	28,21	23,43	27,10	36,25	33,82	34,39	16,47
Tm	4,04	3,29	3,82	5,25	4,91	4,98	2,43
Yb	25,51	20,54	24,10	32,89	30,93	31,04	15,30
Lu	3,95	3,13	3,71	5,05	4,69	4,68	2,48

* Elemental concentrations (µg/g) were determined by ICP-MS-Quadrupole at PSO (Pôle-spectrométrie-océan, Brest, France). Precision as RSD is comprised between 0.5% and 3%, except Loihi hydrothermal Fe-Mn oxides measured by ICP-MS Element 2.

**Ni concentration were determined by isotopic dilution after measurements through MC-ICP-MS. Amount of Ni processed through chemistry is between 2 µg and 0.5 µg.

*** nd: data not determined.

Table III.3 continued

Sample Name	DR24-09 34-C-2	J2-480-R11	J2-480-R11b	J2-480-R13A	J2-480-R13A	J2-480-R13Ab	J2-480-R13B
Location Type	AZORES TJ	Apuupuu	Apuupuu	Apuupuu	Apuupuu	Apuupuu	Apuupuu
Si	nd	nd	nd	nd	nd	nd	nd
Na*	14768,44	12325,85	12130,40	13451,17	12219,50	13594,42	11330,88
Mg	10017,56	7203,85	6741,66	6734,20	6824,89	7622,61	6445,36
Al	2488,58	11184,33	5080,41	11321,48	4294,21	9439,51	7749,91
Ca	22600,57	72293,83	14573,05	14232,18	15963,39	15887,28	15917,97
Ti	8026,60	2107,88	10421,35	8039,13	8729,13	9283,62	11877,34
V	524,07	369,69	469,27	359,76	481,20	386,99	437,88
Cr	2,08	8,43	6,97	5,14	3,21	4,44	16,13
Mn	234031,59	120004,16	173611,27	148316,97	186333,83	168124,65	110710,28
Fe	94306,03	107620,27	126941,03	119794,50	128111,42	111836,45	130431,62
Co	12549,05	1842,56	5000,38	3255,81	3861,39	3957,82	3066,11
Ni**	5114,19	2797,47	2139,21	2706,06	2874,68	1499,29	2303,89
Cu	703,72	831,51	489,57	1187,67	1581,70	1412,18	136,05
Zn	559,98	420,12	432,88	406,40	466,75	427,10	397,07
Rb	1,78	6,23	2,64	7,91	2,99	6,04	3,18
Sr	891,47	890,48	818,07	758,49	873,38	789,47	664,80
Y	106,62	185,46	130,58	120,46	113,63	121,00	133,10
Nb	57,43	0,70	16,99	15,19	13,26	22,80	33,92
Mo	388,67	191,64	289,56	248,72	359,65	249,79	170,33
Cd	4,70	2,12	3,06	2,41	2,97	3,11	2,52
Te	86,15	35,09	29,34	30,80	24,05	26,54	16,65
Ba	1053,27	1774,36	1299,68	1517,63	1543,81	1904,37	971,11
Pt	0,60	0,44	0,20	0,40	0,29	0,27	0,22
Tl	199,26	62,10	106,69	96,37	110,12	111,63	49,40
Pb	1240,66	554,88	968,59	516,96	540,36	649,42	1021,15
Bi	31,52	33,53	27,10	16,24	22,27	26,71	12,95
Th	2,71	4,79	8,65	9,74	8,27	11,96	24,64
U	9,89	7,42	10,47	7,10	8,89	8,72	9,87
La	107,90	170,85	154,76	217,77	236,75	180,84	162,03
Ce	497,19	906,04	811,61	785,97	844,11	830,23	622,60
Pr	19,78	32,43	29,93	48,40	53,47	44,88	41,11
Nd	85,45	136,59	129,76	199,71	220,07	186,94	174,97
Sm	18,61	26,72	46,73	32,81	26,00	40,77	39,24
Eu	4,07	6,69	6,44	10,10	11,03	9,91	9,24
Gd	20,51	31,31	32,39	44,31	47,80	43,73	41,92
Tb	3,09	4,60	4,92	6,61	7,27	6,72	6,46
Dy	20,24	28,30	31,50	38,40	42,36	39,82	37,93
Ho	4,51	6,06	6,66	7,18	7,81	7,60	7,41
Er	14,47	18,80	20,49	20,72	22,46	22,04	21,17
Tm	2,14	2,72	3,02	3,01	3,24	3,23	2,99
Yb	13,66	17,98	19,72	19,20	20,72	20,81	19,24
Lu	2,16	2,99	3,12	2,95	3,06	3,17	2,88

Table III.3 continued

Sample Name	J2-480-R14	J2-480	Y73-3-22D crust	NL-10-09	NL-20-05
Location	Apuupuu	Apuupuu	Bauer Basin		
Type			***Bulk Fe-Mn crust***	***Lau basin hydrothermal deposits***	
Si	nd	nd	nd	nd	nd
Na*	11262,35	12280,35	20208,03	38354,45	29920,44
Mg	5828,21	6065,40	11983,03	16024,32	15675,25
Al	5520,34	6728,88	23237,73	511,53	267,83
Ca	78606,31	76256,30	11694,77	12797,42	8231,78
Ti	751,31	935,29	2057,47	33,34	23,21
V	422,62	450,29	486,39	179,44	235,03
Cr	1,71	2,24	8,33	nd	nd
Mn	143340,10	146812,26	168004,06	450526,11	463837,57
Fe	93666,52	98608,21	165329,71	843,13	604,35
Co	2411,68	2368,42	849,35	9,58	40,23
Ni**	2333,98	1933,61	5884,71	54,26	130,04
Cu	941,23	986,20	3325,53	59,72	556,55
Zn	418,63	462,32	784,79	257,91	427,99
Rb	3,38	3,92	14,21	5,07	11,22
Sr	999,49	1036,66	457,33	362,23	348,98
Y	161,53	154,75	133,47	2,05	20,13
Nb	0,22	0,24	10,24	0,05	0,05
Mo	328,00	321,54	265,66	1014,41	507,99
Cd	2,50	2,62	7,26	7,94	6,47
Te	44,46	44,29	6,27	0,08	0,09
Ba	1954,52	2341,36	1391,44	715,02	1016,53
Pt	0,37	0,41	0,19	nd	nd
Tl	79,85	80,75	79,88	24,82	3,52
Pb	653,19	652,37	122,33	4,36	1,53
Bi	54,39	56,51	1,64	0,03	0,02
Th	2,67	2,75	1,98	nd	nd
U	8,83	9,14	3,68	3,56	5,19
La	228,67	183,16	104,91	0,37	2,44
Ce	1076,23	1140,95	105,47	0,13	0,20
Pr	41,02	35,70	20,33	0,08	0,55
Nd	170,34	146,37	89,06	0,39	3,20
Sm	42,82	28,27	57,80	0,10	0,75
Eu	8,00	7,05	4,82	0,18	0,44
Gd	37,21	31,84	23,13	0,19	2,15
Tb	5,47	4,75	3,43	0,03	0,28
Dy	33,17	28,86	22,44	0,19	1,99
Ho	6,66	5,97	4,78	0,05	0,56
Er	19,92	18,46	14,54	0,16	1,76
Tm	2,87	2,71	2,11	0,02	0,22
Yb	18,44	18,10	13,60	0,16	1,25
Lu	2,87	2,96	2,14	0,03	0,24

Table III.3 continued

Sample Name	J2-243-SS1	J2-369-SS-Red	J2-244-SS3	J2-244-SS5	J2-309-SS2A	J2-309-SS2B
Location	Mkr 17A	Mkr 17	Ula Nui	Ula Nui	Ula Nui2	Ula Nui2
Type	***Loihi hydrothermal deposits***					
Si	88386,67	-	108126,67	64820,00	97440,00	104626,67
Na*	35761,29	51586,62	45406,45	50080,65	46370,97	33164,52
Mg	16404,76	14668,26	20119,05	10461,90	18819,05	20242,86
Al	11336,00	7212,22	16796,00	1820,00	16224,00	17576,00
Ca	25714,29	20437,16	30357,14	15357,14	26214,29	28571,43
Ti	2477,92	1675,18	3751,95	362,34	3512,34	3781,17
V	242,00	239,15	107,00	8,00	99,00	119,00
Cr	90,00	47,44	110,00	nd	90,00	130,00
Mn	51157,75	55426,25	14284,51	27530,99	23254,93	15880,28
Fe	257740,00	256108,87	238280,00	295890,00	212870,00	212310,00
Co	289,00	311,27	42,00	68,00	42,00	45,00
Ni**	238,13	295,55	66,50	170,30	119,13	126,31
Cu	1990,00	3694,58	50,00	30,00	90,00	30,00
Zn	90,00	88,14	40,00	nd	50,00	30,00
Rb	nd	nd	8,00	12,00	7,00	46,00
Sr	nd	nd	681,00	555,00	555,00	574,00
Y	nd	nd	8,30	0,90	8,70	9,50
Nb	nd	nd	nd	nd	nd	nd
Mo	100,00	nd	26,00	43,00	26,00	28,00
Cd	nd	nd	nd	nd	nd	nd
Te	nd	nd	nd	nd	nd	nd
Ba	nd	nd	251,00	123,00	238,00	253,00
Pt	nd	nd	nd	nd	nd	nd
Tl	nd	nd	nd	nd	nd	nd
Pb	nd	nd	nd	nd	nd	nd
Bi	nd	nd	nd	nd	nd	nd
Th	nd	nd	nd	nd	nd	nd
U	nd	nd	nd	nd	nd	nd
La	3,20	nd	4,70	0,35	4,71	5,40
Ce	2,35	nd	9,47	0,72	10,10	10,60
Pr	0,63	nd	1,35	0,10	1,40	1,51
Nd	2,73	nd	6,43	0,49	5,96	6,58
Sm	0,59	nd	1,54	0,12	1,51	1,73
Eu	0,19	nd	0,56	0,05	0,58	0,64
Gd	0,56	nd	1,63	0,14	1,70	1,94
Tb	0,11	nd	0,27	0,02	0,27	0,28
Dy	0,77	nd	1,58	0,13	1,53	1,57
Ho	0,18	nd	0,29	0,03	0,29	0,31
Er	0,57	nd	0,80	0,07	0,81	0,90
Tm	0,08	nd	0,11	0,01	0,12	0,13
Yb	0,55	nd	0,64	0,06	0,69	0,77
Lu	0,10	nd	0,09	0,01	0,10	0,11

Table III.3 continued

Sample Name	J2-309-SS2C	J2-313-SS1-top	J2-313-SS2	J2-477-SS black-green	NOD-A-1	NOD-P-1
Location	Ula Nui2	Ula Nui 2	Ula Nui 2	Ula Nui	Atlantic	Pacific
Type					***Bulk manganese nodules (USGS geostandards)***	
Si	88386,67	65660,00	nd	nd	nd	nd
Na*	38432,26	46816,13	nd	31988,22	7475,53	15348,91
Mg	16900,00	12257,14	nd	48612,38	27334,68	18815,98
Al	14248,00	7800,00	4771,27	21010,03	20288,88	22792,53
Ca	24785,71	20642,86	19835,02	30533,96	102495,77	20869,44
Ti	3138,31	1659,74	761,43	4546,01	3505,68	3052,16
V	90,00	54,00	46,08	117,08	686,49	492,23
Cr	120,00	40,00	14,89	97,53	24,25	14,50
Mn	26585,92	63304,23	37155,78	69214,03	176519,44	286944,43
Fe	207760,00	228480,00	250000,00	196267,94	101253,11	54267,41
Co	72,00	80,00	56,10	138,53	3302,00	2364,48
Ni**	140,44	116,86	77,54	212,79	4577,88	10586,11
Cu	50,00	80,00	18,62	18,28	1117,42	11905,86
Zn	30,00	30,00	16,39	42,40	625,76	1591,26
Rb	6,00	2,00	nd	nd	9,35	22,55
Sr	522,00	516,00	nd	nd	1468,30	620,96
Y	7,80	4,10	nd	nd	106,43	80,58
Nb	nd	nd	nd	nd	304,35	267,60
Mo	nd	100,00	95,78	nd	46,89	17,45
Cd	nd	nd	nd	nd	334,70	571,69
Te	nd	nd	nd	nd	33,46	5,41
Ba	206,00	147,00	nd	nd	1412,51	2371,64
Pt	nd	nd	nd	nd	0,64	0,26
Tl	nd	nd	nd	nd	93,88	180,89
Pb	nd	nd	nd	nd	676,13	381,18
Bi	nd	nd	nd	nd	8,32	4,56
Th	nd	nd	nd	nd	18,06	13,25
U	nd	nd	nd	nd	5,51	3,38
La	4,67	2,16	nd	nd	91,23	87,84
Ce	9,63	4,61	nd	nd	669,47	287,33
Pr	1,31	0,63	nd	nd	21,84	29,34
Nd	5,69	2,75	nd	nd	90,99	123,47
Sm	1,51	0,73	nd	nd	20,05	30,00
Eu	0,54	0,26	nd	nd	4,79	7,19
Gd	1,62	0,82	nd	nd	23,70	29,34
Tb	0,24	0,13	nd	nd	3,48	4,35
Dy	1,37	0,71	nd	nd	20,73	24,80
Ho	0,26	0,13	nd	nd	4,21	4,48
Er	0,75	0,36	nd	nd	12,85	12,56
Tm	0,11	0,05	nd	nd	1,86	1,79
Yb	0,65	0,30	nd	nd	11,75	11,56
Lu	0,09	0,04	nd	nd	1,89	1,74

Table III.4: Ni isotope composition (‰), selected elemental ratios (µg/µg) and Ce/Ce* (Ce anomaly) of Fe-Mn deposits.

Sample Name		$\delta^{60/58}$Ni	2se*	Ni/Mn	Fe/Mn	Cu/Mn	Zn/Mn	Co/Mn	Co/Zn	Co/Fe	Ce/Ce*
Bulk Fe-Mn crusts											
CAP BREST 03-03	Ascension FZ	1,40	0,03	0,0096	1,87	0,0061	0,0036	0,0228	6,25	0,012	1,90
DR01-003 4-B-5	VEMA FZ	1,48	0,02	0,0165	1,70	0,0080	0,0039	0,0264	6,78	0,015	2,33
DR-01-005 16-A-12	VEMA FZ	1,37	0,02	0,0148	1,51	0,0061	0,0036	0,0381	10,48	0,025	2,55
DR01-005 16-A-6	VEMA FZ	1,51	0,04	0,0166	1,63	0,0071	0,0040	0,0219	5,52	0,013	2,24
DR01-005 16-B-11	VEMA FZ	1,45	0,02	0,0146	1,52	0,0051	0,0036	0,0281	7,72	0,018	2,52
DR01-005 16-B-12	VEMA FZ	1,33	0,02	0,0142	1,38	0,0047	0,0036	0,0356	9,82	0,026	2,89
DR01-005 6-C-13	VEMA FZ	1,33	0,02	0,0151	1,27	0,0052	0,0037	0,0386	10,35	0,030	3,29
DR03-003 17-C-4	VEMA FZ	1,27	0,02	0,0141	1,67	0,0048	0,0042	0,0252	5,99	0,015	2,36
DR03-025 15#5	VEMA FZ	1,10	0,02	0,0134	1,64	0,0055	0,0040	0,0216	5,35	0,013	2,36
DR03-025 15-D-10	VEMA FZ	1,48	0,02	0,0148	1,78	0,0075	0,0044	0,0247	5,57	0,014	2,37
DR12-24 32-A-6	Gloria FZ	1,27	0,02	0,0147	1,50	0,0068	0,0044	0,0214	4,82	0,014	3,27
DR12-24 32-B-2	Gloria FZ	0,76	0,02	0,0135	1,35	0,0056	0,0038	0,0302	7,93	0,022	3,23
DR12-24 32-B-3	Gloria FZ	0,80	0,02	0,0138	1,49	0,0067	0,0043	0,0284	6,59	0,019	3,30
DR24-09 34-A-2	AZORES TJ	1,73	0,02	0,0232	0,39	0,0023	0,0023	0,0470	20,20	0,121	2,65
DR24-09 34-C-2	AZORES TJ	1,73	0,02	0,0219	0,40	0,0030	0,0024	0,0536	22,41	0,133	2,52
J2-480-R11	Apuupuu	1,48	0,03	0,0233	0,90	0,0069	0,0035	0,0154	4,39	0,017	2,85
J2-480-R11b	Apuupuu	1,76	0,03	0,0123	0,73	0,0028	0,0025	0,0288	11,55	0,039	2,80
J2-480-R13A	Apuupuu	1,72	0,03	0,0182	0,81	0,0080	0,0027	0,0220	8,01	0,027	1,80
J2-480-R13A	Apuupuu	1,80	0,03	0,0154	0,69	0,0085	0,0025	0,0207	8,27	0,030	1,77
J2-480-R13Ab	Apuupuu	1,76	0,03	0,0089	0,67	0,0084	0,0025	0,0235	9,27	0,035	2,17
J2-480-R13B	Apuupuu	1,63	0,04	0,0208	1,18	0,0012	0,0036	0,0277	7,72	0,024	1,79
J2-480-R14	Apuupuu	1,60	0,03	0,0163	0,65	0,0066	0,0029	0,0168	5,76	0,026	2,60
J2-480	Apuupuu	1,59	0,03	0,0132	0,67	0,0067	0,0031	0,0161	5,12	0,024	3,31
Bulk Bauer Basin Fe-Mn crust											
Y73-3-22D crust	Bauer Basin	0,33	0,02	0,0350	0,98	0,0198	0,0047	0,0051	1,08	0,005	0,54

* 2se corresponds to a two-standard error of the mean calculated on the 50 measurement cycles through MC-ICP-MS and corrected using double-spike.
Ce/Ce* = CeN/(LaN+PrN)/2, where subscript N stands for normalized values to PAAS ((Taylor and McLennan 1995).
*** nd: data not determined.

Table III.4 continued

Lau basin hydrothermal deposits											
NL-10-09	Lau Basin	0,51	0,02	0,0001	0,00	0,0001	0,0006	0,0000	0,04	0,011	0,18
NL-20-05	Lau Basin	1,11	0,02	0,0003	0,00	0,0012	0,0009	0,0001	0,09	0,067	0,04
Loihi hydrothermal deposits											
J2-243-SS1	Mkr 17A	-0,74	0,02	0,0047	5,04	0,0389	0,0018	0,0056	3,21	0,001	0,39
J2-369-SS-Red	Mkr 17	-0,73	0,02	0,0053	4,62	0,0667	0,0016	0,0056	3,53	0,001	nd
J2-244-SS3	Ula Nui	nd	nd	0,0047	16,68	0,0035	0,0028	0,0029	1,05	0,000	0,88
J2-244-SS5	Ula Nui	-1,49	0,03	0,0062	10,75	0,0011	nd	0,0025	nd	0,000	0,85
J2-309-SS2A	Ula Nui 2	-0,80	0,02	0,0051	9,15	0,0039	0,0022	0,0018	0,84	0,000	0,92
J2-309-SS2B	Ula Nui 2	-0,81	0,02	0,0080	13,37	0,0019	0,0019	0,0028	1,50	0,000	0,87
J2-309-SS2C	Ula Nui2	-0,93	0,02	0,0053	7,81	0,0019	0,0011	0,0027	2,40	0,000	0,91
J2-313-SS1-top	Ula Nui 2	-1,16	0,03	0,0018	3,61	0,0013	0,0005	0,0013	2,67	0,000	0,92
J2-313-SS2	Ula Nui 2	-1,07	0,02	0,0021	6,73	0,0005	0,0004	0,0015	3,42	0,000	nd
J2-477-SS black-green	Ula Nui	-1,16	0,03	0,0031	2,84	0,0003	0,0006	0,0020	3,27	0,001	nd
Bulk manganese nodules USGS											
NOD-A-1	Atlantic	1,03	0,02	0,0259	0,57	0,0063	0,0035	0,0187	5,28	0,033	nd
NOD-A-1***	Atlantic	1,06	0,03	0,0269	0,58	0,0063	0,0037	0,0187	5,12	0,033	nd
NOD-P-1	Pacific	0,36	0,03	0,0369	0,19	0,0415	0,0055	0,0082	1,49	0,044	nd
NOD-P-1	Pacific	0,37	0,03	0,0383	0,19	0,0407	0,0055	0,0081	1,46	0,043	nd

4. Results

4.1. Ferromanganese crusts from Atlantic and Pacific oceans

The two Atlantic crusts near the Azores TJ are clearly distinct from other Atlantic crusts since they have the highest Mn, Ni, Cu, Mo concentrations but lower Fe, Al, Ti, Te and REE concentrations. Ni is more than twice more concentrated in Azores TJ crusts than in other Fe-Mn crusts, and Co is also particularly enriched. Tl, Pb and Mo are up to three-fold enriched in Azores TJ crust relatively to the other crusts (Table III.3). Generally, Fe/Mn ratios are higher for Atlantic samples, i.e. Ascension FZ, VEMA FZ and Gloria FZ, with values ranging from 1.27 to 1.87 compared to Pacific crusts (Apuupuu seamount) with Fe/Mn ratios ranging from 0.65 to 1.17, with the exception of Azores TJ Fe-Mn crusts having Fe/Mn ratios as low as 0.39. We observe that lowest Fe/Mn ratios are found for crusts recovered at shallower depths (i.e. Apuupuu and Azores TJ Fe-Mn crusts) (Table III.2). Accordingly, Azores TJ crusts also exhibit the highest Ni/Mn, Co/Mn and Cu/Mn ratios (Figure III.7).

In the same manner than Co, Ni chemical behavior in oceans is closely associated – if not dependent - from the oceanic Mn cycling, thus Ni and Co concentrations are controlled by the Mn-phase (Koschinsky and Halbach 1995; Koschinsky and Hein 2003; Koschinsky et al. 2003).

Co/Mn ratios, which have been generally used as proxy for crust growth rate because the Co flux to the oceans is assumed to be constant, vs Ni/Mn ratios allow to distinguishing between two groups: Azores TJ Fe-Mn crusts on the one hand with high Co/Mn (>0.050) and Ni/Mn (>0.020) ratios, while other hydrogenetic crusts (VEMA FZ, Ascension FZ, Gloria FZ and Apuupuu) have lower Co/Mn (<0.040) and Ni/Mn (<0.015) ratios (Figure III.7, panel A).

Plot of Cu/Mn ratios vs Ni/Mn ratios also shows some distinctions between the two groups defined above (Figure III.7, panel B). Azores TJ samples have lower Cu/Mn ratios (<0.0030) than other Fe-Mn crusts (>0.0050) with higher values observed in Apuupuu Fe-Mn crusts. Cu/Mn ratios tend to be controlled by mineralogy because Cu is more easily incorporated in todorokite than vernadite or birnessite. Todorokite crystal lattice contains some manganese in the divalent form, Mn^{2+}, which allows substitution by Cu^{2+}, Ni^{2+} and Zn^{2+}. In contrast, Mn in vernadite occurs as Mn^{4+} which facilitates incorporation of Co^{3+} by substitution (Cronan 1975; Cronan 2000).

Zn/Mn ratios, which can be an indicator of sources (e.g. hydrothermal), indicate that Azores TJ crusts have lower Zn/Mn (~0.024) than other hydrogenetic Fe-Mn crusts (>0.035) (Figure III.7, panel C).

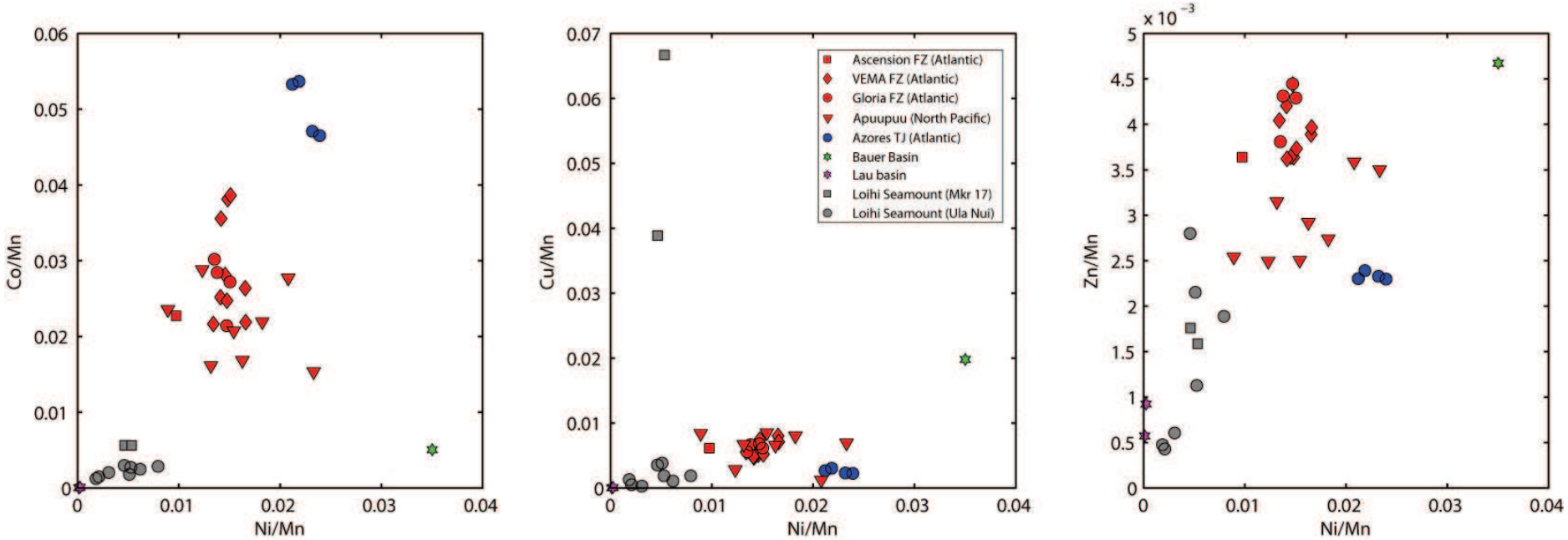

Figure III.7: *Plot of Co/Mn (panel A), Cu/Mn (panel B) and Zn/Mn (panel C) versus Ni/Mn ratios in bulk hydrogenetic Fe-Mn crusts (red and blue symbols) and Bauer Basin Fe-Mn crust (green star) and hydrothermal Fe-Mn deposits from Loihi (grey symbols) and Lau Basin (pink star).*

REE patterns normalized to PAAS (Post Archean Australian Shale (Taylor and McLennan 1995)) are typical of hydrogenous deposits exhibiting a strong positive Ce anomaly (Figure III.8). While REE are characterized by one 3+ oxidation state, Ce can undergo two oxidation states 3+ and 4+ in well-oxygenated waters. Therefore, its enrichment in marine metalliferous deposits is due to oxidation of Ce^{3+} to Ce^{4+} on Fe- and Mn-oxides surfaces which facilitates its subsequent adsorption (German and Elderfield 1990; De Carlo and McMurtry 1992; Bau 1999; Mills et al. 2001). Importantly, the kinetic of this reaction is relatively slow in seawater.

REE patterns of Fe-Mn crusts recovered between 2800 m and 3480 m (VEMA FZ, Ascension FZ and Gloria FZ) are more enriched in REE relatively to shallowest Fe-Mn crusts Apuupuu and Azores TJ. In addition, positive Ce anomalies are less pronounced in Apuupuu and Azores TJ samples (Table III.4). The Ce anomaly is defined as $Ce/Ce^* = Ce_N/(La_N + Pr_N)/2$ (Mills et al. 2001), where subscript N stands for normalized values to PAAS (Figure III.8).

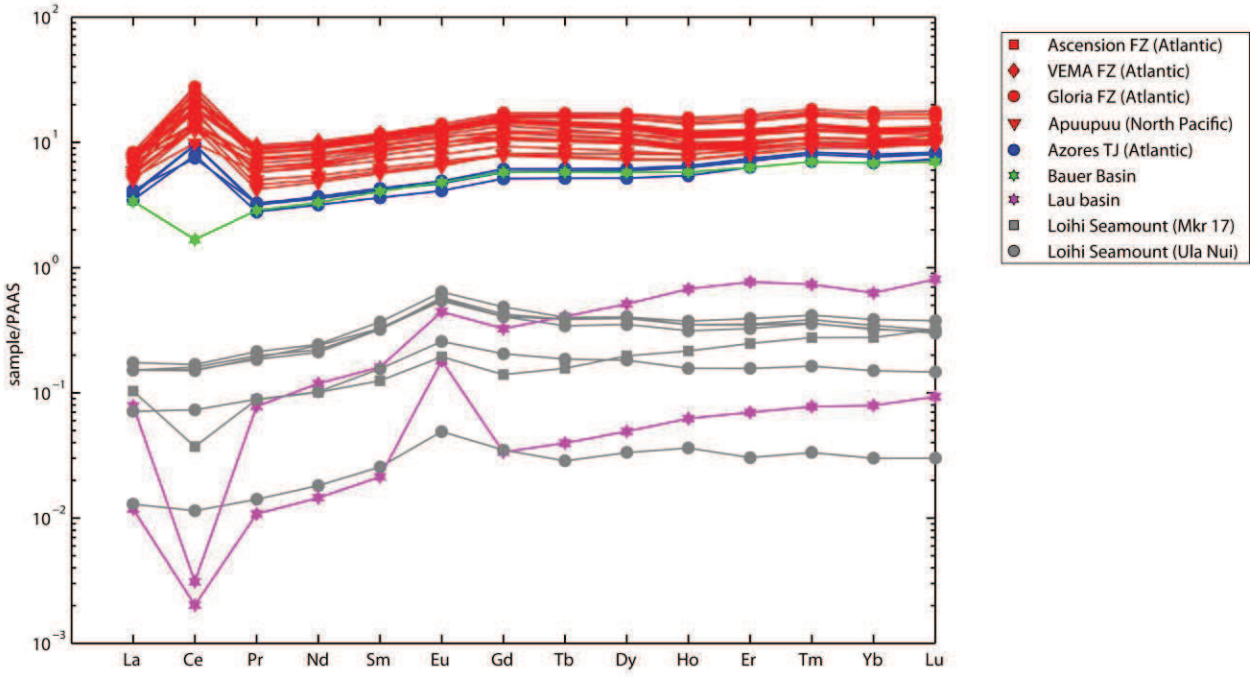

Figure III.8: *REE patterns normalized to PAAS (Post Archean average Australian Shale (Taylor and McLennan 1995)) (Taylor and McLennan 1995) in hydrogenetic Fe-Mn crusts, Bauer Basin Fe-Mn deposits, Loihi hydrothermal deposits and Lau Basin hydrothermal deposits (pink star).*

$\delta^{60/58}$Ni values range between +0.76 ‰ and +1.80 ‰ with most values clustering between +1.3 and 1.6 ‰ (Figure III.9 and Table III.4). Figure III.9 showing $\delta^{60/58}$Ni values versus Ni concentration (ppm) clearly help distinguishing Azores TJ Fe-Mn crusts from other Fe-Mn crusts. Although, Pacific Apuupuu Fe-Mn crusts display a similar range of values, Ni isotope composition of Azores TJ crusts are among the highest values from samples of this study. Ni isotope compositions are consistent with the results of Gall et al. (2013) showing an overall range of $\delta^{60/58}$Ni values between +0.9 and +2.5 ‰. In addition, there is no resolvable

Ni isotope variability among Fe-Mn crusts according to locations within the different oceans and distance to continental shelf as also reported by Gall et al (2013).

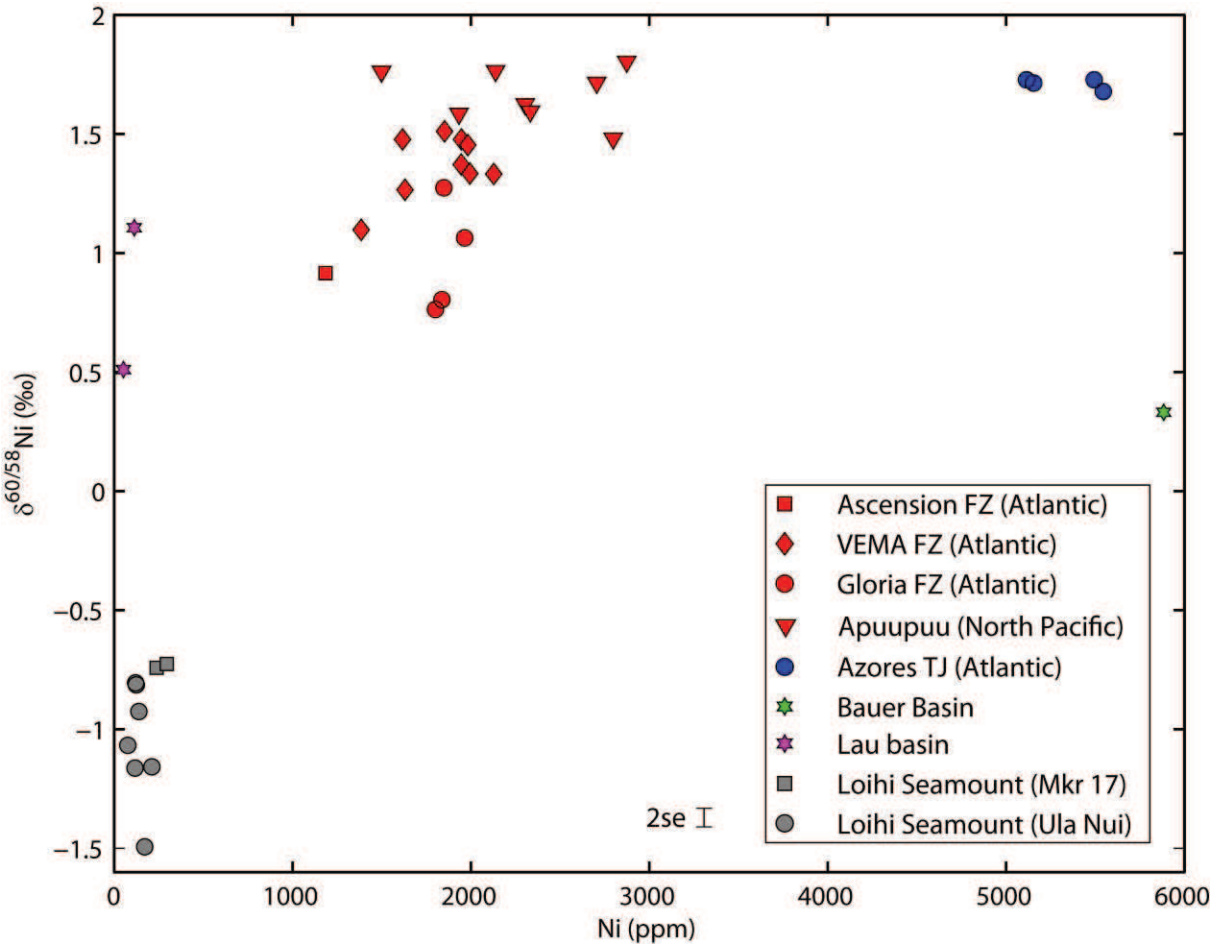

Figure III.9: *Ni isotope composition (‰) versus Ni concentration (ppm) in hydrogenetic Fe-Mn crusts (red and blue symbols), Bauer Basin Fe-Mn deposits (green star), Loihi hydrothermal deposits (grey symbols) and Lau Basin hydrothermal deposits.*

Although not statistically significant, Ni isotope composition seems to be related to the water depth since shallowest crust (~2000 m depth) have also the lowest Fe/Mn ratios and yield the most positive $\delta^{60/58}$Ni values (Figure III.10).

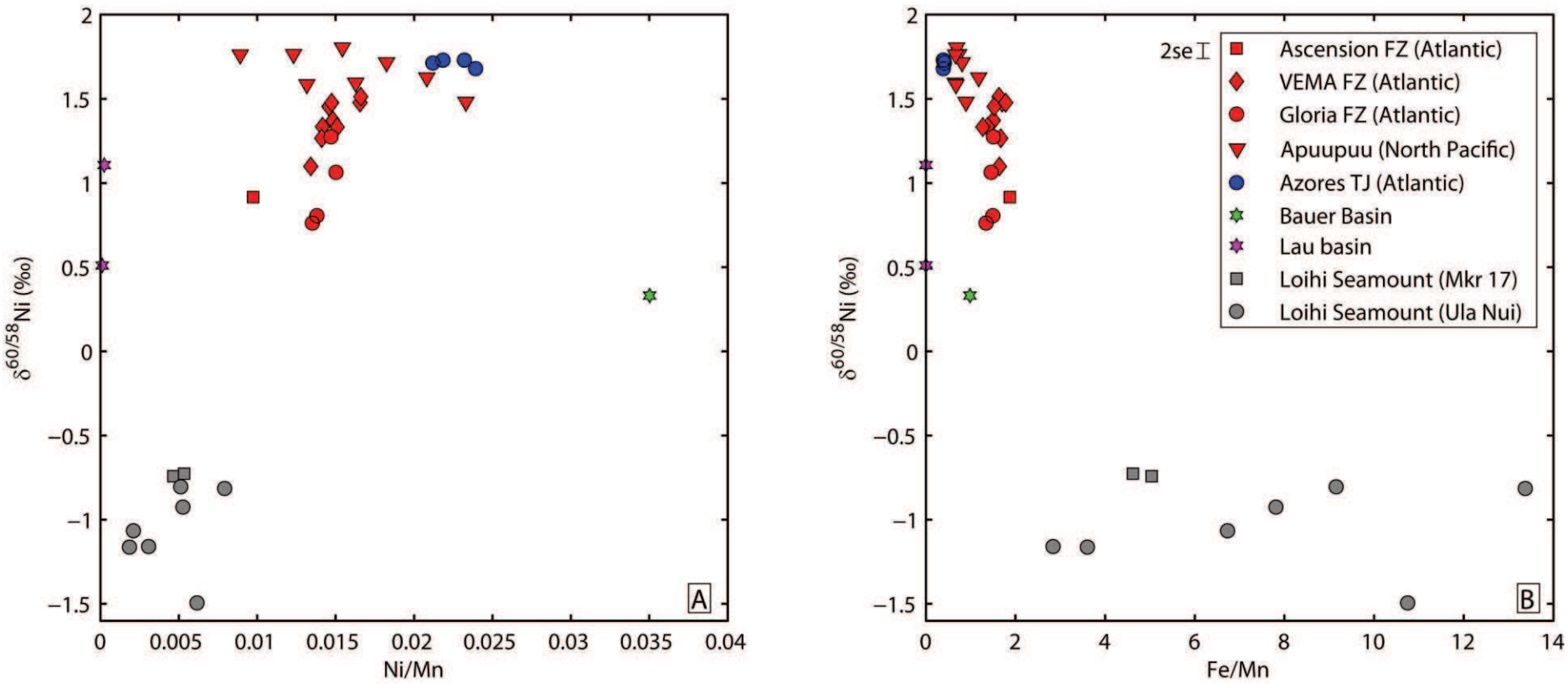

***Figure III.10**: Ni isotope composition (‰) versus Ni/Mn (panel A) and Fe/Mn (panel B) ratios in hydrogenetic Fe-Mn crusts (red and blue symbols), Bauer Basin Fe-Mn deposits (green star), Loihi hydrothermal deposits (grey symbols) and Lau Basin hydrothermal deposits.*

4.2. Ferromanganese crust from the Bauer Basin

The Fe-Mn crust sample collected in the Bauer Basin (BB) is made of a combination of crystallized todorokite and birnessite mineral phases. This sample has low Co, Pb and Te concentrations but high Ni, Cu, Zn and Cd concentrations (Table III.3) relative to typical hydrogenous Fe-Mn crusts (Hein et al. 2013). For instance, Ni is twice more enriched than average Pacific Fe-Mn crusts, Cu is more than four times enriched, and Cd more than ten times enriched in comparison to hydrogenous crusts. By contrast, typical seawater-derived elements like Co and Te are respectively more than eight times and ten times depleted compared to Fe-Mn crusts. Other elements like Mo and Tl, which are also elements derived from seawater, are in the range of hydrogenetic Fe-Mn crusts concentrations, i.e. between ~200 and 400 ppm, and ~50 and 200 ppm respectively. Finally, BB crust displays the lowest Ti and Cr contents but it has high Al concentrations

In comparison to other Pacific Fe-Mn crusts analyzed in our study, BB Fe-Mn crust has a low Fe/Mn ratio, 0.98 compared to >~1.2 for other common pure hydrogenetic crusts, Ni/Mn ratio is higher especially because of elevated Ni concentration of 5884 ppm in comparison to the range of ~2000-3000 ppm for Apuupuu and Atlantic crusts.

It has high Cu/Mn ratio (0.0198) compared to Cu/Mn <0.009 for both Atlantic and Pacific crusts, in particular because Cu concentration is almost four times higher than in other crusts. Zn content is also one of the highest (733 ppm) while Atlantic and Pacific crusts generally cluster in the 400-500 ppm range. By contrast, BB Fe-Mn crust has a very low Co/Mn (0.005) with Co concentrations of ~800 ppm whereas common other Pacific Fe-Mn crusts have Co concentrations at least three times higher (Tables III.3 and III.4). Lower Co concentrations in BB Fe-Mn crust indicate higher growth rates in comparison to common hydrogenous Fe-Mn crusts. The presence of crystallized mineral phases like todorokite is consistent with higher Cu/Mn ratio, thus it clearly shows that genetic processes were somewhat different than for hydrogenetic Atlantic and Pacific Fe-Mn crusts.

Finally, BB Fe-Mn crust has low REE contents in comparison to hydrogenetic crusts, with for instance La being twice less concentrated and shows a clear negative Ce anomaly (Figure III.8 and Table III.4) as reported previously by Elderfield and Greaves (1981).

$\delta^{60/58}$Ni value of BB Fe-Mn crust of +0.33 ‰ is very low and stands in marked contrast compared to hydrogenous crust. Low Ni isotopes are combined with high Ni concentration and high Ni/Mn ratio, while Fe/Mn ratio is lower than hydrogenous Fe-Mn crusts (Figures III.9 and III.10).

4.3. Hydrothermal fields of Loihi seamount: FeMO Deep (Ula Nui) and Mkr 17 sites

Geochemical composition of FeMO Deep and Mkr17 Fe-Mn oxides are reported in (Table III.3). Mkr 17 samples have higher Ni, Co, Cu and Zn concentrations than Ula Nui. Loihi seamount samples have the lowest Co/Mn, Cu/Mn, Zn/Mn and Ni/Mn ratios (Figure III.7) from all the samples investigated in this study and are markedly distinct from other samples in Figure III.8. Low Co concentrations are therefore directly related to a higher rate of precipitation in comparison to hydrogenous deposits formed through precipitation of dissolved seawater metals.

Ni isotope values span a range from -1.18 to -0.73 ‰ and highest $\delta^{60/58}$Ni values are correlated with highest Ni/Mn and Fe/Mn ratios (Figure III.10). There is a distinction between Mkr 17 samples and Ula Nui samples. The former have higher Ni isotope values, i.e. -0.74

and -0.73 ‰, whereas Ni isotope compositions of Ula Nui samples are generally systematically below -0.80 ‰ (Table III.4).

4.4. Hydrothermal fields of Lau basin back-arc: the Valu Fa Ridge

The major elements geochemistry of the two samples have already been published elsewhere (Fouquet et al. 1993) but in this paper we report additional geochemical data including trace elements such as REE. Mineralogy of the samples is composed of well-crystallized Mn-oxides of todorokite (especially NL-20-05) and birnessite (especially NL-10-09). These deposits are essentially composed of Mn-oxides phases as shown by their very low Fe/Mn ratios < 0.002. Samples are not particularly rich in Co and Ni. While Cu and Zn are not specifically enriched in NL-10-09, NL-20-05 displays Cu and Zn concentrations comparable to those measured in Fe-Mn crusts. The presence of todorokite in NL-20-05 in comparison to NL-10-09 is probably the reason why Cu content is higher in the former. Both samples have elevated Mo concentrations (1014 and 508 ppm) in comparison to the average value of ~400 ppm in hydrogenetic Fe-Mn crusts. Ni/Mn, Co/Mn and Cu/Mn ratios are twice higher in NL-20-05 than in NL-10-09 (Tables III.3 and III.4).

REE patterns for both samples exhibit a negative Ce anomaly and a positive Eu anomaly. The negative Ce anomaly is more pronounced for NL-20-05 than for NL-10-09. Samples are globally enriched in HREE and the overall patterns indicate that Lau basin hydrothermal deposits are depleted in REE relatively to hydrogenetic Fe-Mn crusts by 2 to 3 orders of magnitude but instead have the same level of enrichment than hydrothermal Fe-Mn deposits from Loihi (Figure III.8).

The two samples display positive Ni isotope values of +0.51 and +1.11 ‰ for NL-10-09 and NL-20-05 respectively (Table III.4).

5. Discussion

5.1. Significance of Ni isotope variations in hydrogenetic Fe-Mn crusts

Fe-Mn crusts are metalliferous sediments deposited on volcanic seamounts at depths between 1000 and 3000 m and formed by direct precipitation of Fe-Mn colloids from seawater. They grow at very slow rate of 1-6 mm/Ma in areas with very limited pelagic sedimentation background (Hein et al. 2003). Upwelling currents from the base of seamount toward the base of OMZ (Oxygen Minimum Zone) permit mixing of oxygen-rich deep waters with oxygen-deficient waters of the OMZ, leading to the reduction of colloidal Mn present in this layer. Oxidation of Mn at the base of the OMZ provides efficient scavenging of trace metals, such as Co, Ni, Zn, Tl and Cd, leading to their strong enrichment in Fe-Mn crusts (Koschinsky and Halbach 1995; Koschinsky and Hein 2003; Koschinsky et al. 2003). Therefore, these deposits are generally considered to be good proxy of deep seawater metal isotope composition.

In oceans, Ni has one of the highest residence times of ca. 10000 years among trace metals (Sclater et al. 1976; Gall et al. 2013), which is well above the mixing time of oceans of ca. 1500 years, implying that Ni isotopes should be homogenous in the deep oceans. Recently, Gall et al. (2013) made a review of the Ni oceanic biogeochemical cycling by re-estimating sources and sinks fluxes in modern oceans. They advocate that continental erosion and weathering through riverine discharges and ground water and hydrothermal fluids are the primary inputs to the oceans. Additional sources like atmospheric dusts and

volcanic particles also bring Ni to the oceans. On the other hand, Ni is retrieved from seawater during Mn-oxides precipitation in Fe-Mn crusts, Mn-nodules but mostly in overall authigenic Mn-oxides precipitation within deep-sea sediments (i.e. pelagic clays).

However, we highlight that strong uncertainties still remain regarding the residence time of Ni within oceans due to a misevaluation of these sources and sinks. For instance, while Ni concentration is very low in hydrothermal fluids formed in basalt-hosted hydrothermal vents, higher Ni concentrations were measured in fluids formed in ultramafic environments (Charlou et al. 1998; Douville et al. 2002; Fouquet et al. 2010), thus complicating the proper estimation of this flux. In addition, Gall et al. (2013) did not mention the potential influence of anthropogenic activities on the present-day Ni flux coming from rivers and they did not estimate how much Ni was deposited through the organic sink (e.g. sapropels and organic sediments deposited on continental margins), yet this sink could be important along continental margins (Brumsack 1980; Brumsack 2006). Another unknown is the halmyrolitic flux emanating from ultramafic rocks alteration on the seafloor, and since they are relatively enriched in Ni they could be a non-negligible source.

Gall et al. (2013) reported a large range of Ni isotope values in Fe-Mn crusts from +0.9 to +2.5 ‰ and they suggested that Ni isotope variations reflect mixing of different Ni sources in seawater. The authors advocate that Fe-Mn crusts formed close to continental margins have higher Ni isotope values than those precipitated away from the continents. These variations were attributed to an important contribution of riverine Ni with heavy Ni isotope composition as a source of Ni to these crusts (Gall et al. 2013). By contrast, modern seawater has an average $\delta^{60/58}$Ni value of ~+1.5 ‰, in the range of Fe-Mn crusts values, with few variations between the different oceanic basins (Cameron and Vance 2013; Vance et al. 2013). Ni isotopes time-series in a Central Pacific Fe-Mn crust measured by Gall et al. (2013) indicate negative $\delta^{60/58}$Ni values excursion and enrichment in Mn concentrations which were ascribed to local hydrothermal inputs with lighter Ni isotope compositions. On the other hand, the authors did not observe any correlation between Ni isotopes and distance of the crusts from mid-ocean ridges. An important caveat of this study is that Ni isotope fractionation during incorporation in the mineral phases is considered to be negligible.

Below, we critically evaluate alternate hypotheses that could account for the isotopic variability of Ni isotopes in hydrogenous Fe-Mn crusts besides source effects including, (1) effects of phosphogenic events, (2) mineralogical effects on Ni isotope fractionation during Ni uptake, (3) influence of Ni speciation in seawater, (4) geological settings and environmental conditions.

(1) (Halbach and Puteanus 1984) linked the phosphogenic events of Miocene age with an expansion of the OMZ due to increased surface productivity. This suboxic and phosphate-rich water layer reached down to the crust-covered slopes of the seamounts which inhibited Fe-Mn growth and and impregnated the older crusts with carbonate fluorapatite. Based on Ca/Fe ratios it is clear that at least three crusts from the Apuupuu seamount were moderately affected by phosphatization. Yet, no relationship is seen between Ca/Fe and $\delta^{60/58}$Ni values (Figure III.11) indicating that phosphatization doesn't necessarily affect Ni isotope composition.

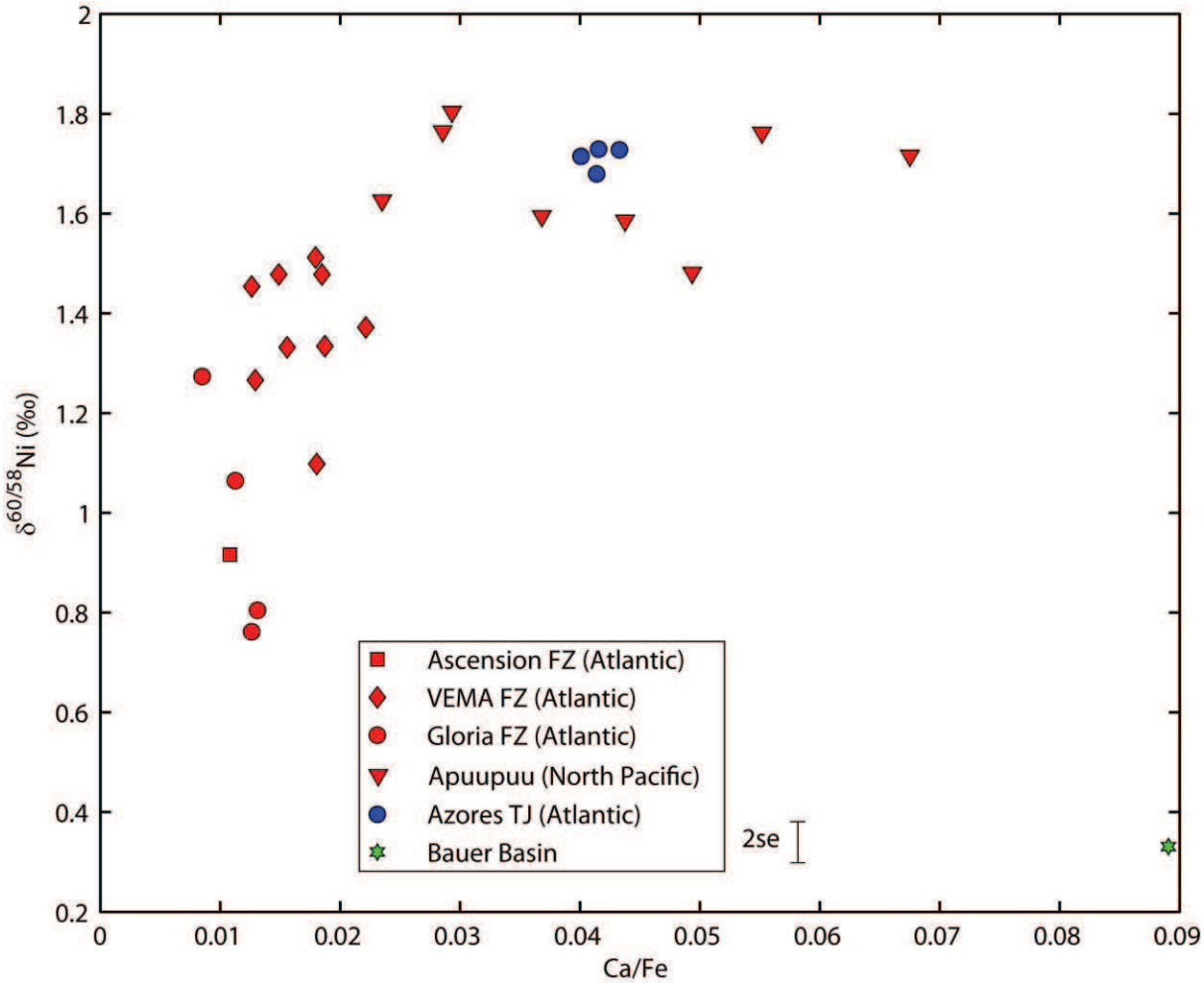

Figure III.11*: Ni isotope composition (‰) versus Ca/Fe ratios in hydrogenetic Fe-Mn crusts (red and blue symbols) and Bauer Basin Fe-Mn deposits (green star).*

(2) It has been well recognized that Ni is mostly bound to Mn-oxyhydroxides (Peacock and Sherman 2007a; Peacock and Sherman 2007b). Spectroscopic data (EXAFS) also demonstrated that Ni adsorption onto birnessite is affected by change in pH with the incorporation of Ni in the structure of the mineral being favored at higher pH. Ni adsorbed on birnessite is then structurally incorporated with time (Peacock 2009; Sorensen et al. 2011). In addition, Ni (along with Cu, Zn and Co) is primarily hosted by the Mn-phase rather than by the Fe-phase (Koschinsky and Halbach 1995; Koschinsky and Hein 2003). Initial results on experimental adsorption of Ni onto synthetic Fe- and Mn-oxides, namely goethite, 2-line ferrihydrite and birnessite, indicate that the mineral phase is enriched in light isotopes compared with the isotopic composition of the initial Ni solution (Gueguen et al. 2011). The extent of fractionation increases in the following order, 2-line ferrihdyrite, goethite and birnessite, with values of fractionation (expressed as the difference between isotopic composition of the mineral phase and the solution) of -0.4 ‰, -0.9‰, and -1.0 ‰ respectively (Gueguen et al. 2011). However, experimental results are in contrast with the observed differences in Ni isotope composition between modern seawater of ~+1.5‰ (Cameron and Vance 2013; Vance et al. 2013) and surface layer of hydrogeneous Fe-Mn crusts showing a global average of +1.6 ± 0.8‰ (Gall et al. 2013).

The discrepancy between experimental data and natural samples could be explained considering the pathways of Ni incorporation in Mn minerals. In the case of near-quantitative scavenging, identical Ni isotope composition of Fe-Mn crusts and seawater is expected. In that case, Ni incorporation in Fe-Mn crusts should proceed through continuous adsorption of Ni onto Mn-oxide surface in a closed-system reservoir. This hypothesis is however counterintuitive considering the very slow growth of Fe-Mn crusts in contact with seawater. A possible model could be that Ni (along with other dissolved trace metals in seawater) is first incorporated in Mn-oxides colloids formed in seawater with enrichment in light Ni isotopes which is consistent with equilibrium isotope fractionation factor. Then, further Ni is incorporated within the crust structure leading to near quantitative adsorption of the local Ni reservoir and producing a non-fractionated sink. It is important to note that such model is only possible if very slow enrichment processes occur during formation of the deposits.

(3) Another important factor to consider is the effect of metal speciation on isotopic fractionation which have already been highlighted for Mo for instance (Barling and Anbar 2004). However, the authors recognized that even with their experimental data they could not distinguish whether the fractionation they measured for Mo was the result of equilibrium fractionation among species present in seawater or among aqueous complexes and complexes forming at the oxide surface during adsorption. Experimental and theoretical studies on Ni isotopes showed fractionations up to 2.5 ‰ for $\delta^{60/58}$Ni during exchange reaction between inorganic and organic ligands (Fujii et al. 2011). Accordingly, if one of these species that has undergone previous fractionation in aqueous conditions is preferentially adsorbed on the oxy-hydroxide surface it would impart an apparent isotope fractionation between the isotope composition of the precipitate and the solution. Variable and chemical parameters (e.g. presence of an OMZ) may affect Ni speciation in seawater, thus potentially influencing Ni isotope fractionation in Fe-Mn crusts. Although Ni speciation in freshwaters indicates that 99.9% is bound with organic ligands (Xue et al. 2001), the role played by organic ligands on Ni speciation in seawater is presently unclear and should be evaluated in the future.

(4) There are also evidence that $\delta^{60/58}$Ni values of some crusts (e.g. shallowest Fe-Mn crusts from Azores TJ) may be even higher than seawater values, which cannot be reconcile by adsorption fractionation. In that case, other processes should be considered such as the location of Fe-Mn crusts formation and the base of the OMZ. Close to the OMZ there is an efficient recycling of Mn while in deeper waters, Mn cycling is less vigorous and less efficient scavenging of trace metals is expected. In addition, an increased Fe flux is probably generated below the CCD by the dissolution of carbonate testas from microorganisms (Halbach and Puteanus 1984), leading to higher Fe/Mn ratios in deeper crusts in comparison to shallower crusts. The observed negative trend between Fe/Mn ratios and $\delta^{60/58}$Ni values (Figure III.10) for hydrogenous Fe-Mn crusts may point toward such effect. In particular, Fe-Mn crusts collected near the Azores TJ are relatively shallow (2140 m) and yield the lowest Fe/Mn, but the highest Co/Mn and Ni/Mn ratios and one of the highest $\delta^{60/58}$Ni values. This trend could be related to enhanced precipitation of Mn-oxides vs. Fe-oxides near the base of the OMZ favoring efficient scavenging of Ni in Mn-phases with Ni isotope composition close to seawater values. In contrast, lower $\delta^{60/58}$Ni with higher Fe/Mn would point toward the importance of Fe-rich colloids in scavenging Ni leading to larger Ni isotope fractionation factor during partial Ni incorporation. Our conclusions are consistent with similar observations reported in Fe-Mn crusts from Line Islands (Pacific Ocean) (Aplin and Cronan

1985), from crusts collected in the Hawaii chain (De Carlo et al. 1987), and in Central Pacific (Halbach et al. 1984). Those authors suggested that crusts formed in shallower waters close to the OMZ would have benefited from an enhanced supply of Mn from this layer, thus allowing efficient scavenging of dissolved trace metals in Mn-oxides like Ni, Cu and Zn.

Therefore, the trend displayed by Ni isotopes with depth is consistent with hypothesis (2) because it could indicate that in shallow waters close to the OMZ, there is an important production of Mn-rich colloids producing a quantitative removal of Ni from seawater, thus no isotope fractionation is expressed between seawater and Mn-oxides.

5.2. Bauer Basin Fe-Mn deposits: assessing the impact of hydrothermal inputs on hydrogenetic Fe-Mn crusts geochemistry

It is important to make the distinction between deposits formed directly by hydrothermal processes (i.e. diffuse fluid flow venting) such as those encountered at Loihi seamount and Lau Basin hydrothermal fields, and deposits which have been influenced at various extent by far-field hydrothermal inputs (i.e. hydrothermal plume fall-out). Thus, although Fe-Mn crust from BB is recognized as being part of hydrogenetic deposits because they are not formed by hydrothermal processes *sensu-stricto*, they have been, however, affected by hydrothermal inputs from distal hydrothermal sources (Elderfield and Greaves 1981). The suggested model is that oceanic circulation would have bring seawater affected by hydrothermal inputs from the East Pacific Rise (EPR), and then would have brought this hydrothermally affected seawater in the Bauer Basin (east of the EPR) (Heath and Dymond 1977; Lyle et al. 1977; Ravizza and McMurtry 1993).

BB crust selected for this study have the highest Ni/Mn, Zn/Mn but one of the lowest Co/Mn ratios. In addition Co/Zn ratios ~1 are well below the Co/Zn > 5 found in hydrogenetic Fe-Mn crusts from the Atlantic and the Pacific. Altogether, low Co/Mn (i.e high growth rate) and low Co/Zn ratios in Fe-Mn deposits are attributed to a hydrothermal origin (Nicholson et al. 1997) because Co is exclusively derived from seawater - and it is assumed to be supplied to oceans at a constant rate - whereas hydrothermal vents could be an important source of Zn. Besides those differences, the overall geochemical composition of BB crust is closer to common hydrogenetic Fe-Mn crusts in comparison to Lau Basin Fe-Mn crusts and Loihi deposits formed by hydrothermal processes.

Hence, the formation of BB hydrogenous Fe-Mn crust involves the precipitation of Mn- and Fe-rich colloids formed in seawater combined with a flux of hydrothermal Fe- and Mn-rich particles likely derived from the East Pacific Rise. This process is consistent with the fact that REE patterns of BB sample display negative Ce anomaly typical of seawater indicating rapid scavenging. Kinetic effects on REE patterns have already been demonstrated in hydrothermal Fe-Mn deposits from TAG vent site (Mills et al. 2001). This study shows a trend between the magnitude of the Ce anomaly and the distance from hydrothermal sources. Since samples located further away from the hydrothermal source are precipitated more slowly, the magnitude of the Ce anomaly could be used as a proxy for the deposition rate of the deposits.

Considering the low concentration of Ni in hydrothermal fluids (see discussion below), the process leading to high Ni/Mn ratios in the Bauer Basin remains however unclear. BB crust sample displays a very low $\delta^{60/58}$Ni value of +0.33 ‰ indicating a marked depletion in heavy Ni isotopes in comparison to other Pacific and Atlantic hydrogenetic Fe-Mn crusts mostly ranging between +1.4 and +1.9 ‰. As shown in Figure III.12, Bauer Basin deposits have also lower Ce/Ce* (<0.5) in comparison to hydrogenetic Fe-Mn crusts. Hence, we

consider that low Ni isotope values are directly related to the rate of formation of hydrothermal Fe- and Mn-rich particles rather than the contribution of hydrothermal Ni sources. The apparent difference between $\delta^{60/58}$Ni value in BB deposits and seawater is about 1‰, which is similar to the maximum Ni isotope fractionation factor during Ni adsorption on Mn-Fe-particles (Gueguen et al. 2011). In that case, direct scavenging of Ni in the water column with hydrothermally derived Fe-Mn particles would allow the expression of such Ni isotope fractionation.

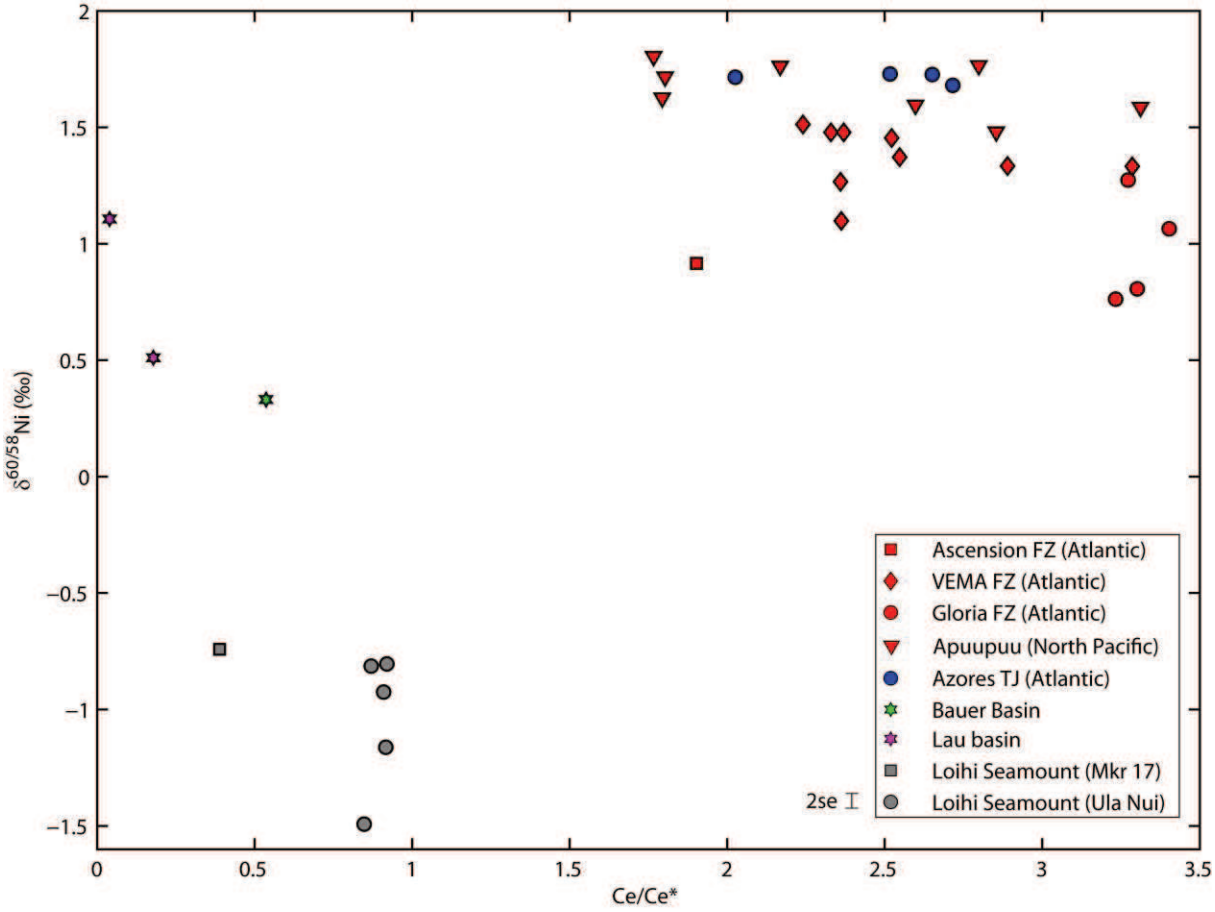

Figure III.12: *Ni isotope composition versus Ce anomaly Ce/Ce* of hydrogenetic Fe-Mn crusts and hydrothermal deposits from Lau Basin.*

5.3. Fe-rich deposits at Loihi Seamount and Ni isotope signature of hydrothermal sources

The presence of active microbial communities combined with mineralogical observations indicates that Loihi Fe-rich mats are of biogenic origin. Such bacterial activity is supported by low temperature ultra-diffuse hydrothermal venting occurring as diffusive leakage through the oceanic crust (Edwards et al. 2011). Considering that the basaltic end-member (Loihi glass) has a $\delta^{60/58}$Ni value of +0.07 ‰ (Gueguen et al. 2013), light Ni isotope values down to -1.49‰ are consistent with isotope fractionation from this near-zero basaltic end-member during Ni adsorption processes on Mn- and Fe-oxides. Mat geochemistry characterized by high Fe/Mn ratios and low metal/Mn ratios (Ni, Zn, Co) suggest that Fe-oxyhydroxides may be a significant host phase of Ni.

Experimental determination of Ni isotope fractionation of ~-1 ‰ and ~-0.9 ‰ on birnessite and goethite respectively, indicate that the mineral phase is systematically

enriched in light isotopes and that differences occur according to the mineral phase (Gueguen et al. 2011). In that sense, the variability is accounted for by a mixture between Mn-oxides and Fe-oxides for which the fractionation factor is different. The maximum difference between $\delta^{60/58}$Ni values of basalts and Fe-Mn deposits is about 1.5 ‰, which is even larger than experimentally determined Ni isotope fractionation factors. Hence, it is possible that hydrothermal Ni source at Loihi is characterized by negative values of about -0.5 ‰. Although the Ni isotope composition of hydrothermal fluids has not been determined so far, several lines of evidence suggest a hydrothermal source of Ni at Loihi. In particular, Ni concentrations up to 80 nmol/l have been measured in Loihi hydrothermal fluids (Sedwick et al. 1992) which is about 10 times seawater concentrations. These fluids are also characterized by elevated pH and low H_2S content precluding the formation of sulfides and the precipitation of Fe and other metals like Ni (Glazer and Rouxel 2009). This contrasts with the fact that Ni concentration is generally low in hydrothermal fluids formed at mid-ocean ridges with the exception of hydrothermal fields in ultramafic environments (Charlou et al. 2002; Douville et al. 2002). They have the low Ce anomaly of these deposits is further evidence that these hydrothermal deposits formed rapidly in comparison to Fe-Mn crusts (Figure 7) (Mills et al. 2001).

5.4. Hydrothermal Mn-rich deposits in Lau Basin

Fe-Mn oxides deposits of the Valu Fa Ridge in the Lau basin (LB) were formed by low temperature diffuse hydrothermal venting through the volcanic substrate. Therefore, the tectonic activity and the presence of faulting allowing seawater circulation in the oceanic crust, plays an important role on the metallogenesis of these deposits (Fouquet et al. 1993). In contrast to pure hydrogenetic Fe-Mn encrustations with Fe/Mn ratios generally comprised between 0.5 and 1, these hydrothermal deposits have extremely low Fe/Mn ratios of 0.0019 and 0.0013 for NL-10-09 and NL-20-05 respectively, with a mineralogy predominantly controlled by Mn-oxide phases such as birnessite and todorokite characteristic of hydrothermal deposits.

It has been well demonstrated that hydrothermal Fe-Mn deposits are characterized by a large range of Fe/Mn ratios because hydrothermal processes highly fractionate Fe and Mn due to their different oxidation rates and source compositions (Hein et al. 1994). As explained previously, faster precipitation rates for hydrothermal deposits have been also considered as the main parameters for explaining the limited enrichment in transition metals in hydrothermal deposits (Bonatti 1975; Heath and Dymond 1977).

The REE patterns of LB samples indicate mixing between seawater and hydrothermal fluids (Figure III.8). While the negative Ce anomaly and HREE enrichment are typical of a seawater source for REE, the positive Eu anomaly is a robust signature of REE derived from hydrothermal fluids (German et al. 1990). Further, they display very low Ce anomalies in comparison to hydrogenetic Fe-Mn crusts in the range of Loihi hydrothermal deposits and BB Fe-Mn crusts (Figure III.12). The other important distinctive characteristic of LB deposits in comparison to hydrogenetic deposits is that REE are depleted relatively to PAAS (Figure III.8). Hence, the REE pattern indicates that Fe- and Mn-oxides in LB samples formed rapidly in seawater. In addition, high concentrations of Mo in these deposits (between ~500 and 1000 ppm) provide another evidence that metals, including Ni, have a seawater origin since it is unlikely that Mo is derived from hydrothermal fluids.

In summary, the formation of LB hydrothermal deposits is relatively similar to the formation of Fe-Mn deposits at Loihi, where diffuse hydrothermal fluids provide the source of

major elements Fe and Mn as well as trace elements (e.g. REE) that co-precipitate at the seafloor. Subsequent aging of the deposits and exposure at the seafloor allows further scavenging of seawater-derived elements including REE, Mo and Ni. Following this model, positive Ni isotope values of +0.51 and +1.11 ‰ measured in LB samples are consistent with a seawater origin of Ni. As a result of Ni isotope fractionation from seawater during adsorption processes lower $\delta^{60/58}$Ni values in comparison to typical hydrogenous Fe-Mn crusts are produced as the result of reservoir effects. It is important to note that in contrast to Loihi hydrothermal Fe-rich deposits, LB deposits incorporated a significant proportion of seawater-derived metals implying that the isotopic composition of seawater-derived Ni dominates the Ni isotopic budget of LB deposits.

5.5. Towards a genetic model of hydrothermal and hydrogenous Fe-Mn deposits at the seafloor

Our study demonstrates that Ni isotope variations on Fe-Mn deposits are primarily explained by enrichment and formation processes, rather than source effects. Even for pure hydrothermal Fe-Mn deposits, a direct contribution of hydrothermal source of Ni remains rather rare, except in actively forming deposits. A genetic model of Fe-Mn deposits, linking the sources of major elements (Fe, Mn) and traces (REE, Ni) and aging of the deposits is summarized in Figure III.13. Pure hydrogenetic Fe-Mn deposits are precipitated through accumulation of Fe- and Mn-colloids formed in seawater, and as inferred from our data Ni isotopes are not fractionated relatively to seawater. A possible pathway for explaining such values is that Ni is scavenged during formation of Mn-oxides colloids in the water column but then, after precipitation of colloids in Fe-Mn crusts further Ni is additionally incorporated into the mineral structure. Due to slow precipitation kinetics of Fe- and Mn-oxides in Fe-Mn crusts (and aging of the crusts) the mineral surface is exposed to seawater during a long period of time in comparison to the time of in-situ colloids precipitation. Thus, Ni from seawater is continuously incorporated in the mineral structure producing an apparent quantitative removal of Ni. According to this process no Ni isotopic fractionation is produced.

The opposite end-member is pure hydrothermal deposits formed in presently active hydrothermal sites such as Loihi hydrothermal deposits. These deposits formed after precipitation of Fe- and Mn-rich particles during release of metals by diffuse hydrothermal fluids implying that metals including REE originate from the hydrothermal fluid. Precipitation of these particles and accumulation rates of these deposits are rapid due to a substantial and continuous hydrothermal flux. Therefore, important Ni isotope fractionation from Ni coming from the fluid and the precipitate could occur.

We have demonstrated that Ni isotope compositions of the fluids are similar to that of the basaltic substrate, around ~0.0 ‰ in Loihi for instance (Gueguen et al. 2013). In between these two end-members, there are alternative deposits composed of a mix of hydrothermal/hydrogenetic components. Some are dominated by hydrogenetic processes as in Bauer Basin Fe-Mn deposits while others are hydrothermal deposits with influence of hydrogenetic end-member as in Lau Basin deposits. These two end-members are also extremely related to the time of formation. Hydrogenetic Fe-Mn deposits formed slowly (a few mm/Ma) whereas hydrothermal deposits are sedimented rapidly.

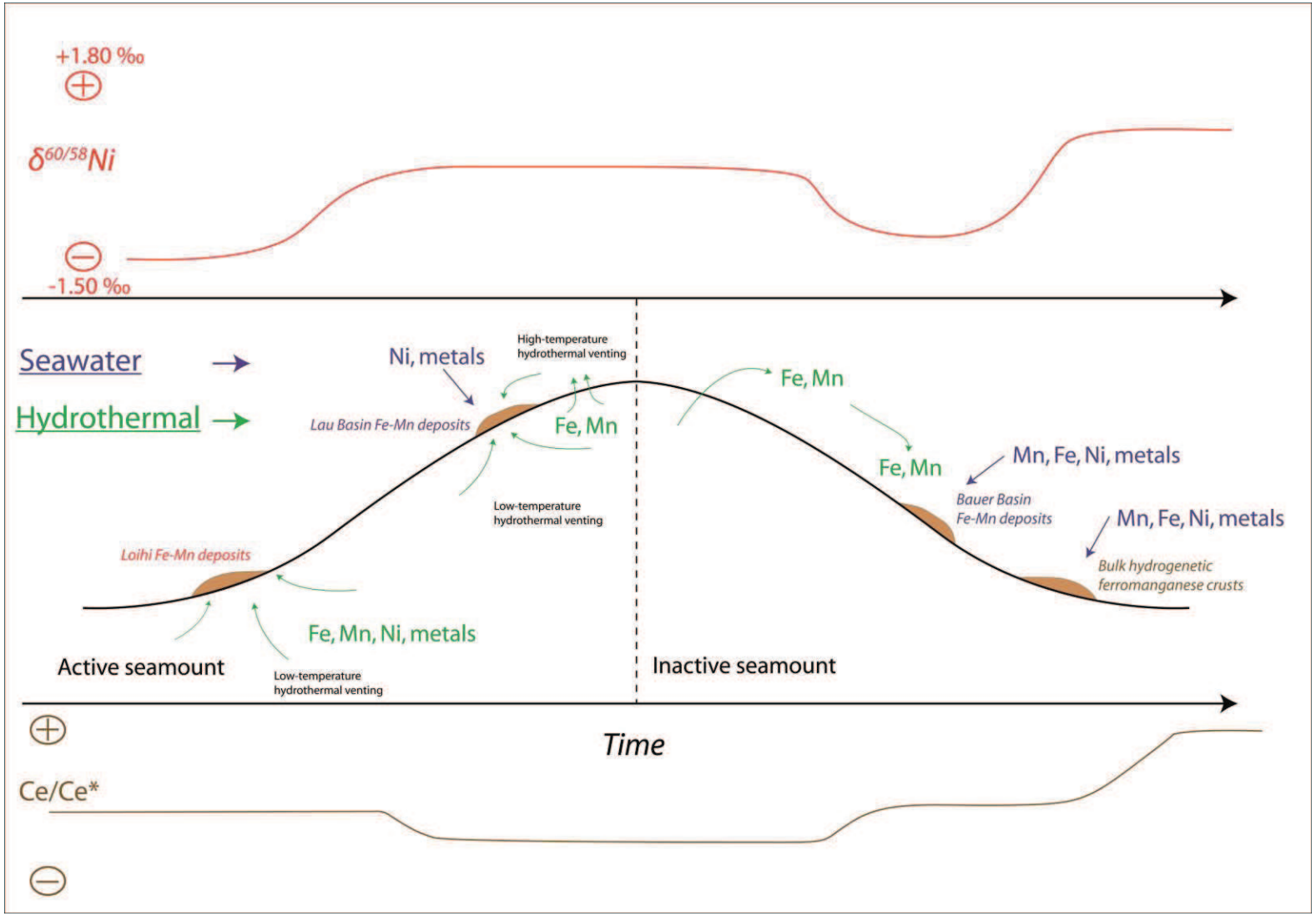

Figure III.13 *: Conceptual model showing Ni isotope variations in relation to kinetic of formation and Ce anomaly in the REE pattern.*

6. Summary and conclusions

In this study we have reported Ni isotope compositions of hydrogenetic and hydrothermal oceanic metalliferous deposits from different geological settings and geographical locations. Here we proposed a model in which deposition kinetics control Ni isotope variability in Fe- and Mn-rich deposits. Results show that slow precipitated hydrogenetic Fe-Mn crusts in both the Atlantic and the Pacific oceans have positive Ni isotope values from +0.76 to +1.80 ‰ and high positive Ce anomalies (Ce/Ce*). The fact that most values are >+1.5 ‰, i.e. in the range of seawater Ni isotope composition, implies that there is minimal or no isotope fractionation between the source and the sink. Slow precipitation of Fe- and Mn-oxides promotes quantitative removal of Ni from seawater in Fe-Mn crusts, thus no isotope fractionation is expressed with enrichment in REE and a positive Ce anomaly in the pattern. Lower Ni isotope value of +0.33 ‰ correlated with a lower Ce anomaly (Ce/Ce*) in Bauer basin Fe-Mn crust is consistent with a hydrothermal influence during genesis of the deposits which promoted higher accumulation and precipitation rates.

Hydrothermal Lau basin deposits indicate that while the processes of Fe- and Mn-oxides formation is the result of hydrothermal activity (Mn and Fe have a hydrothermal source), the source of other transition metals including Ni is hydrogenous. Variations in Ni isotope composition from +0.51 to +1.11 ‰ are due to isotope fractionation during adsorption of seawater Ni on the mineral phases. On the other hand, negative $\delta^{60/58}$Ni values from -0.04 to -1.49 ‰ in very young Fe- and Mn-oxides deposits from Loihi seamount suggest that both the source of Ni and probably other transition metals (i.e. the leached basaltic substrate) and the processes of formation are associated with hydrothermal activity. And once again Ni isotope variations are accounted for isotope fractionation during adsorption.

7. References

Abouchami, W. and Goldstein, S. L. (1995). "A lead isotopic study of circum-Antarctic manganese nodules." Geochimica Et Cosmochimica Acta 59(9): 1809-1820.

Albarede, F. (2004). "The Stable Isotope Geochemistry of Copper and Zinc." Reviews in Mineralogy and Geochemistry 55(1): 409-427.

Albarede, F., Simonetti, A., Vervoort, J. D., Blichert-Toft, J. and Abouchami, W. (1998). "A Hf-Nd isotopic correlation in ferromanganese nodules." Geophysical Research Letters 25(20): 3895-3898.

Anbar, A. D. and Rouxel, O. (2007). "Metal stable isotopes in paleoceanography." Annual Review of Earth and Planetary Sciences 35: 717-746.

Aplin, A. C. and Cronan, D. S. (1985). "Ferromanganese oxide deposits from the Central Pacific Ocean, II. Nodules and associated sediments." Geochimica Et Cosmochimica Acta 49(2): 437-451.

Aplin, A. C. and Cronan, D. S. (1985). "Ferromanganese oxide deposits from the Central Pacific ocean. 1. Encrustations from the Line islands archipelago." Geochimica Et Cosmochimica Acta 49(2): 427-436.

Barling, J. and Anbar, A. D. (2004). "Molybdenum isotope fractionation during adsorption by manganese oxides." Earth and Planetary Science Letters 217(3-4): 315-329.

Bau, M. (1999). "Scavenging of dissolved yttrium and rare earths by precipitating iron oxyhydroxide: experimental evidence for Ce oxidation, Y-Ho fractionation, and lanthanide tetrad effect." Geochimica Et Cosmochimica Acta 63(1): 67-77.

Beard, B. L., Johnson, C. M., Von Damm, K. L. and Poulson, R. L. (2003). "Iron isotope constraints on Fe cycling and mass balance in oxygenated Earth oceans." Geology 31(7): 629-632.

Bonatti, E. (1975). "Metallogenesis at oceanic spreading centers." Annual Review of Earth and Planetary Sciences 3: 401-431.

Bonatti, E., Kraemer, T. and Rydell, H. (1972c). Classification and genesis of submarine iron-manganese deposits, Washington DC, Nat. Sci. Found.

Brumsack, H.-J. (2006). "The trace metal content of recent organic carbon-rich sediments: Implications for Cretaceous black shale formation." Palaeogeography, Palaeoclimatology, Palaeoecology 232(2-4): 344-361.

Brumsack, H. J. (1980). "Geochemistry of cretaceous Black Shales from the Atlantic Oceans (DSDP Legs 11, 14, 36 and 41)." Chemical Geology 31(1-2): 1-25.

Cameron, V. and Vance, D. (2013). Nickel Isotopic Composition of Modern Seawater and Rivers. Goldschmidt, Florence, Italy, Mineralogical Magazine.

Cameron, V., Vance, D., Archer, C. and House, C. H. (2009). "A biomarker based on the stable isotopes of nickel." Proceedings of the National Academy of Sciences of the United States of America 106(27): 10944-10948.

Charlou, J. L., Donval, J. P., Fouquet, Y., Jean-Baptiste, P. and Holm, N. (2002). "Geochemistry of high H_2 and CH_4 vent fluids issuing from ultramafic rocks at the Rainbow hydrothermal field (36 degrees 14 ' N, MAR)." Chemical Geology 191(4): 345-359.

Charlou, J. L., Fouquet, Y., Bougault, H., Donval, J. P., Etoubleau, J., Jean-Baptiste, P., Dapoigny, A., Appriou, P. and Rona, P. A. (1998). "Intense CH_4 plumes generated by serpentinization of ultramafic rocks at the intersection of the 15 degrees 20 ' N fracture zone and the Mid-Atlantic Ridge." Geochimica Et Cosmochimica Acta 62(13): 2323-2333.

Cronan, D. S. (1975). "Manganese nodules and other ferromangese oxide deposits from Atlantic Ocean." Journal of Geophysical Research-Oceans and Atmospheres 80(27): 3831-3837.

Cronan, D. S., Ed. (2000). Handbook of marine mineral deposits, CRC Press London.

De Carlo, E. H. and McMurtry, G. M. (1992). "Rare-earth element geochemistry of ferromanganese crusts from the Hawaiian Archipelago, central Pacific." Chemical Geology 95(3–4): 235-250.

De Carlo, E. H., McMurtry, G. M. and Kim, K. H. (1987). "Geochemistry of ferromanganese crusts from the hawaiian archipelago. 1. Northern survey areas." Deep-Sea Research Part a-Oceanographic Research Papers 34(3): 441-467.

Douville, E., Charlou, J. L., Oelkers, E. H., Bienvenu, P., Colon, C. F. J., Donval, J. P., Fouquet, Y., Prieur, D. and Appriou, P. (2002). "The rainbow vent fluids (36 degrees 14 ' N, MAR): the influence of ultramafic rocks and phase separation on trace metal content in Mid-Atlantic Ridge hydrothermal fluids." Chemical Geology 184(1-2): 37-48.

Dymond, J., Lyle, M., Finney, B., Piper, D. Z., Murphy, K., Conard, R. and Pisias, N. (1984). "Ferromanganese nodules from MANOP Sites H, S, and R - Control of mineralogical and chemical composition by acretionary processes." Geochimica Et Cosmochimica Acta 48(5): 931-949.

Dymond, J. and Veeh, H. H. (1975). "Metal accumulation rates in the Southeast Pacific and the origin of metalliferous sediments." Earth and Planetary Science Letters 28(1): 13-22.

Edwards, K. J., Glazer, B. T., Rouxel, O. J., Bach, W., Emerson, D., Davis, R. E., Toner, B. M., Chan, C. S., Tebo, B. M., Staudigel, H. and Moyer, C. L. (2011). "Ultra-diffuse hydrothermal venting supports Fe-oxidizing bacteria and massive umber deposition at 5000m off Hawaii." The ISME journal: 1-11.

Elderfield, H. and Greaves, M. J. (1981). "Negative Cerium anomalies in the rare-earth element patterns of oceanic ferromanganese nodules." Earth and Planetary Science Letters 55(1): 163-170.

Fouquet, Y., Cambon, P., Etoubleau, J., Charlou, J. L., Ondréas, H., Barriga, F. J. A. S., Cherkashov, G., Semkova, T., Poroshina, I., Bohn, M., Donval, J. P., Henry, K., Murphy, P. and Rouxel, O. (2010). Geodiversity of Hydrothermal Processes Along the Mid-Atlantic Ridge and Ultramafic-Hosted Mineralization: A New Type of Oceanic Cu-Zn-Co-Au Volcanogenic Massive Sulfide Deposit.

Fouquet, Y., von Stackelberg, U., Charlou, J. L., Donval, J. P., Foucher, J. P., Erzinger, J., Herzig, P., Mühe, R., Wiedicke, M., Soakai, S. and Whitechurch, H. (1991). "Hydrothermal activity in the Lau back-arc basin:Sulfides and water chemistry." Geology 19(4): 303-306.

Fouquet, Y., von Stackelberg, U., Charlou, J. L., Erzinger, J., Herzig, P. M., Muehe, R. and Wiedicke, M. (1993). "Metallogenesis in back-arc environments: the Lau Basin example." Economic Geology 88(8): 2154-2181.

Frank, M. (2002). "Radiogenic isotopes: Tracers of past ocean circulation and erosional input." Reviews of Geophysics 40(1).

Frank, M., O'Nions, R. K., Hein, J. R. and Banakar, V. K. (1999). "60 Myr records of major elements and Pb–Nd isotopes from hydrogenous ferromanganese crusts: reconstruction of seawater paleochemistry." Geochimica Et Cosmochimica Acta 63(11–12): 1689-1708.

Frank, M., Whiteley, N., Kasten, S., Hein, J. R. and O'Nions, K. (2002). "North Atlantic deep water export to the Southern Ocean over the past 14 Myr: Evidence from Nd and Pb isotopes in ferromanganese crusts." Paleoceanography 17(2).

Fujii, T., Moynier, F., Dauphas, N. and Abe, M. (2011). "Theoretical and experimental investigation of nickel isotopic fractionation in species relevant to modern and ancient oceans." Geochimica et Cosmochimica Acta 75(2): 469-482.

Gall, L., Williams, H., Siebert, C. and Halliday, A. (2012). "Determination of mass-dependent variations in nickel isotope compositions using double spiking and MC-ICPMS." Journal of Analytical Atomic Spectrometry 27(1): 137-145.

Gall, L., Williams, H. M., Siebert, C., Halliday, A. N., Herrington, R. J. and Hein, J. R. (2013). "Nickel isotopic compositions of ferromanganese crusts and the constancy of deep ocean inputs and continental weathering effects over the Cenozoic." Earth and Planetary Science Letters 375(0): 148-155.

German, C. R. and Elderfield, H. (1990). "Application of the Ce Anomaly as a Paleoredox Indicator: The Ground Rules." Paleoceanography 5(5): 823-833.

German, C. R., Klinkhammer, G. P., Edmond, J. M., Mitra, A. and Elderfield, H. (1990). "Hydrothermal scavenging of rare earth elements in the ocean." Nature 345(6275): 516-518.

Glazer, B. T. and Rouxel, O. J. (2009). "Redox Speciation and Distribution within Diverse Iron-dominated Microbial Habitats at Loihi Seamount." Geomicrobiology Journal 26(8): 606 - 622.

Gueguen, B., Rouxel, O., Ponzevera, E., Bekker, A. and Fouquet, Y. (2013). "Nickel Isotope Variations in Terrestrial Silicate Rocks and Geological Reference Materials Measured by MC-ICP-MS." Geostandards and Geoanalytical Research 37(3): 297-317.

Gueguen, B., Rouxel, O., Ponzevera, E., Sorensen, J. V., Toner, B. M., Bekker, A. and Fouquet, Y. (2011). Ni biogeochemical cycle through geological time: insights from Ni isotope variations in modern and ancient marine metallifereous deposits. AGU Fall Meeting 2011. San Francisco, USA.

Halbach, P., Giovanoli, R. and Vonborstel, D. (1982). "Geochemical processes controlling the relationship between Co, Mn and Fe in early diagenetic deep-sea nodules." Earth and Planetary Science Letters 60(2): 226-236.

Halbach, P., Kriete, C., Prause, B. and Puteanus, D. (1989). "Mechanisms to explain the platinum concentration in ferromanganese seamount crusts." Chemical Geology 76(1-2): 95-106.

Halbach, P. and Puteanus, D. (1984). "The influence of the carbonate dissolution rate on the growth and composition of Co-rich ferromanganese crusts from Central Pacific seamount areas." Earth and Planetary Science Letters 68(1): 73-87.

Halbach, P., Puteanus, D. and Manheim, F. T. (1984). "Platinum concentrations in ferromanganese seamount crusts from the Central Pacific." Naturwissenschaften 71(11): 577-579.

Heath, G. R. and Dymond, J. (1977). "Genesis and transformation of metalliferous sediments from East Pacific rise, Bauer deep, and Central basin, Northwest Nazca plate." Geological Society of America Bulletin 88(5): 723-733.

Hein, J. R., Gibbs, A. E., Clague, D. A. and Torresan, M. (1996). "Hydrothermal mineralization along submarine rift zones, Hawaii." Marine Georesources & Geotechnology 14(2): 177-203.

Hein, J. R., Koschinsky, A. and Halliday, A. N. (2003). "Global occurrence of tellurium-rich ferromanganese crusts and a model for the enrichment of tellurium." Geochimica et Cosmochimica Acta 67(6): 1117-1127.

Hein, J. R., Mizell, K., Koschinsky, A. and Conrad, T. A. (2013). "Deep-ocean mineral deposits as a source of critical metals for high- and green-technology applications: Comparison with land-based resources." Ore Geology Reviews 51(0): 1-14.

Hein, J. R., Schwab, W. C. and Davis, A. S. (1988). "Cobalt-rich and platinum-rich ferromanagenese crusts and associated substrate rocks from the Marshall islands." Marine Geology 78(3-4): 255-283.

Hein, J. R., Yeh, H. W., Gunn, S. H., Gibbs, A. E. and Wang, C. H. (1994). "Composition and origin of hydrothermal ironstones from Central Pacific seamounts." Geochimica Et Cosmochimica Acta 58(1): 179-189.

Hofmann, A., Bekker, A., Dirks, P., Gueguen, B., Rumble, D. and Rouxel, O. (2013). "Comparing orthomagmatic and hydrothermal mineralization models for komatiite-hosted nickel deposits in Zimbabwe using multiple-sulfur, iron, and nickel isotope data." Mineralium Deposita: 1-26.

Horner, T. J., Schonbachler, M., Rehkämper, M., Nielsen, S. G., Williams, H., Halliday, A. N., Xue, Z. and Hein, J. R. (2010). "Ferromanganese crusts as archives of deep water Cd isotope compositions." Geochemistry Geophysics Geosystems 11: 1525-2027.

Koschinsky, A. and Halbach, P. (1995). "Sequential leaching of marine ferromanganese precipitates: Genetic implications." Geochimica et Cosmochimica Acta 59(24): 5113-5132.

Koschinsky, A. and Hein, J. R. (2003). "Uptake of elements from seawater by ferromanganese crusts: solid-phase associations and seawater speciation." Marine Geology 198(3-4): 331-351.

Koschinsky, A., Winkler, A. and Fritsche, U. (2003). "Importance of different types of marine particles for the scavenging of heavy metals in the deep-sea bottom water." Applied Geochemistry 18(5): 693-710.

Levasseur, S., Frank, M., Hein, J. R. and Halliday, A. (2004). "The global variation in the iron isotope composition of marine hydrogenetic ferromanganese deposits: implications for seawater chemistry?" Earth and Planetary Science Letters 224(1-2): 91-105.

Ling, H.-F., Jiang, S.-Y., Frank, M., Zhou, H.-Y., Zhou, F., Lu, Z.-L., Chen, X.-M., Jiang, Y.-H. and Ge, C.-D. (2005). "Differing controls over the Cenozoic Pb and Nd isotope evolution of deepwater in the central North Pacific Ocean." Earth and Planetary Science Letters 232(3–4): 345-361.

Ling, H. F., Burton, K. W., O'Nions, R. K., Kamber, B. S., von Blanckenburg, F., Gibb, A. J. and Hein, J. R. (1997). "Evolution of Nd and Pb isotopes in Central Pacific seawater from ferromanganese crusts." Earth and Planetary Science Letters 146(1–2): 1-12.

Lyle, M., Dymond, J. and Ross Heath, G. (1977). "Copper-nickel-enriched ferromanganese nodules and associated crusts from the Bauer Basin, northwest Nazca plate." Earth and Planetary Science Letters 35(1): 55-64.

Maréchal, C. N., Nicolas, E., Douchet, C. and Albarède, F. (2000). "Abundance of zinc isotopes as a marine biogeochemical tracer." Geochem. Geophys. Geosyst. 1(5): 1-15.

McMurtry, G. M. and Yeh, H.-W. (1981). "Hydrothermal clay mineral formation of East Pacific rise and Bauer Basin sediments." Chemical Geology 32(1–4): 189-205.

Mills, R. A., Wells, D. M. and Roberts, S. (2001). "Genesis of ferromanganese crusts from the TAG hydrothermal field." Chemical Geology 176(1–4): 283-293.

Nicholson, K., Hein, J. R., Buehn, B. and Dasgupta, S., Eds. (1997). Manganese mineralization; geochemistry and mineralogy of terrestrial and marine deposits, Geological Society of London : London, United Kingdom.

O'Nions, R. K., Frank, M., von Blanckenburg, F. and Ling, H. F. (1998). "Secular variation of Nd and Pb isotopes in ferromanganese crusts from the Atlantic, Indian and Pacific Oceans." Earth and Planetary Science Letters 155(1-2): 15-28.

Peacock, C. L. (2009). "Physiochemical controls on the crystal-chemistry of Ni in birnessite: Genetic implications for ferromanganese precipitates." Geochimica et Cosmochimica Acta 73(12): 3568-3578.

Peacock, C. L. and Sherman, D. M. (2007a). "Sorption of Ni by birnessite: Equilibrium controls on Ni in seawater." Chemical Geology 238(1-2): 94-106.

Peacock, C. L. and Sherman, D. M. (2007b). "Crystal-chemistry of Ni in marine ferromanganese crusts and nodules." American Mineralogist 92(7): 1087-1092.

Ravizza, G. and McMurtry, G. M. (1993). "Osmium isotopic variations in metalliferous sediments from the East Pacific Rise and the Bauer Basin." Geochimica Et Cosmochimica Acta 57(17): 4301-4310.

Rehkämper, M., Frank, M., Hein, J. R. and Halliday, A. (2004). "Cenozoic marine geochemistry of thallium deduced from isotopic studies of ferromanganese crusts and pelagic sediments." Earth and Planetary Science Letters 219(1-2): 77-91.

Rehkämper, M., Frank, M., Hein, J. R., Porcelli, D., Halliday, A., Ingri, J. and Liebetrau, V. (2002). "Thallium isotope variations in seawater and hydrogenetic, diagenetic, and hydrothermal ferromanganese deposits." Earth and Planetary Science Letters 197(1-2): 65-81.

Reynolds, B. C., Frank, M. and O'Nions, R. K. (1999). "Nd- and Pb-isotope time series from Atlantic ferromanganese crusts: implications for changes in provenance and paleocirculation over the last 8 Myr." Earth and Planetary Science Letters 173(4): 381-396.

Schmitt, A. D., Galer, S. J. G. and Abouchami, W. (2009). "Mass-dependent cadmium isotopic variations in nature with emphasis on the marine environment." Earth and Planetary Science Letters 277(1-2): 262-272.

Sclater, F. R., Boyle, E. and Edmond, J. M. (1976). "On the marine geochemistry of nickel." Earth and Planetary Science Letters 31(1): 119-128.

Sedwick, P. N., McMurtry, G. M. and Macdougall, J. D. (1992). "Chemistry of hydrothermal solutions from Pele vents, Loihi seamount, Hawaii." Geochimica Et Cosmochimica Acta 56(10): 3643-3667.

Siebert, C., Nagler, T. F. and Kramers, J. D. (2001). "Determination of molybdenum isotope fractionation by double-spike multicollector inductively coupled plasma mass spectrometry." Geochemistry Geophysics Geosystems 2: 1032.

Sorensen, J. V., Toner, B. M., Gueguen, B. and Rouxel, O. (2011). "Ni Speciation and Isotope Fractionation in Marine Ferromangenese Deposits." Goldschmidt Conference 2011 75(3): 1914.

Taylor, S. R. and McLennan, S. M. (1995). "The geochemical evolution of the continental crust." Reviews of Geophysics 33(2): 241-265.

Vance, D., Cameron, V., Little, S. and Archer, C. (2013). The Oceanic Cycles of the Transition Metals and their Isotopes. Goldschmidt 2013, Florence, Italy, Mineralogical Magazine.

Xue, H. B., Jansen, S., Prasch, A. and Sigg, L. (2001). "Nickel speciation and complexation kinetics in freshwater by ligand exchange and DPCSV." Environmental Science & Technology 35(3): 539-546.

Partie III.2 – Composition isotopique du puits de Ni dans les sédiments marins profonds : résultats du site ODP 1149 dans l'Ouest du Pacific

Part III.2 - Nickel isotope composition of the authigenic Ni sink in deep-sea sediments: Results of ODP Site 1149 in the Western Pacific

Abstract:

We investigated Ni isotope composition in a stratigraphic sequence of pelagic clays collected during IODP core leg 185 on site 1149 in Western Pacific Ocean near the Izu-Bonin subduction trench. The sequence presented here is a 170 meters-thick sequence of pelagic sediments which are deposited on one of the oldest oceanic crust of the modern seafloor. The base of the pelagic clays sequence is dated at 104 Ma. Ni isotope composition ($\delta^{60/58}Ni_{NIST986}$) varies in the range of +0.04 ±0.04 to +1.03 ±0.03 ‰. There is a correlation between increasing Mn/Fe, Mn/Al, higher transition metals concentration and depth in the stratigraphic sequence with increasing Ni isotope values. This trend is accounted for by authigenic Mn-oxides precipitation in the sediment which scavenged metals from dissolved metals in porewaters and this shows that Ni isotope composition of porewaters is similar to that of seawater at ~+1.5 ‰. The variability in Ni isotope composition could be the result of mixing between a pure deep-sea clays end-member at 0 ‰ and pure Mn-oxides end-member of ~+1.6 ‰ akin to Fe-Mn crusts and seawater Ni isotope composition. These results also allow us to estimate the Ni isotope composition (~+1.2 ‰) and the flux of Ni of the most important Ni sink in modern oceans (2.2 to 6.8x10^8 mol/yr) that effectively enters the mantle through subduction zones.

1. Introduction

It has long been demonstrated that deep-sea pelagic clays can display significant enrichment in transition metals in comparison to lithogenic and terrigenous sediments (Boström and Peterson 1966; Boström et al. 1969; Glasby 1991). Previous models, mainly relying on Mn enrichment in surface sediments as well as trace element signatures such as REE have invoked a combination of processes to explain enrichment of metals : (1) a very slow rate of deposition (<1 m/Ma) related to minor detrital inputs that would otherwise have imparted dilution effect for transition metals and (2) diagenetic processes including the decay of organic matter within oxic sediments that release transition metals within sediment pore fluids, and (3) hydrothermal input through hydrothermal plume fall-out precipitation and scavenging of seawater-derived elements from seawater.

In earlier studies, Boström et al. (1969) used a simple geochemical index based on the Al/(Al+Fe+Mn) ratio to show that pelagic sediment enrichment in transition metals in the South Pacific Ocean probably results from the far-field influence of hydrothermal inputs from the East Pacific Rise. Evidence for anomalously high $^3He/^4He$ ratios in the water column further demonstrated a major contribution of hydrothermal fluxes in seawater in the South Pacific that extend away from the ridges (Lupton 1995; Lupton 1998). Recently, Kato et al. (2011) correlated REE enrichment of pelagic clays from the South Pacific with the extent of $^3He/^4He$ anomaly in the water column suggesting that scavenging of dissolved seawater REE on hydrothermal particles which then accumulated in the sediment produced REE enrichment (Kato et al. 2011). Another major pathways of metal enrichment process in pelagic clays is related to diagenetic and even hydrogenetic processes where the decay of organic matter and biological debris remineralization in deep seawater and surface sediments provide important source of metals (Heggie et al. 1986). The diagenetic reduction of Mn-oxides to Mn^{2+}, rendering this element soluble in porewaters, could be the precursor to authigenic precipitation of Mn-oxides along with scavenging of trace metals such as Ni, Cu, Co and Zn previously released by organic matter particles (Klinkhammer 1980; Sawlan and Murray 1983). Although this mechanism of scavenging of trace metals with subsequent burial

in sediments has long been identified as an important output to the oceans (Krishnaswami 1976; Thomson et al. 1984), the estimation of the global Fe-Mn oxide sink of a range of trace metals remains difficult.

Pelagic sediments are one of the major sink for Ni in modern oceans. Yet, previous work used Fe-Mn crust and Mn-nodules to estimate Ni isotope composition of this sink(Gall et al. 2013). Therefore samples from this study will shed light on the Ni isotope composition of this sink, and here we aim to apply new advances of Ni isotope geochemistry to better constraint authigenic enrichment of Ni in sediments and evaluate whether the estimation of output flux of Ni in pelagic sediment is consistent with previous estimate based on nodules and Fe-Mn crust only. In this study we present results measured along a complete section of deep-sea pelagic clays from the ODP Site 1149 in the Western Pacific that allow determination of the Ni isotope composition of a well-characterized pelagic clay sequence.

Initial goals of drilling these sediments deposited on the oldest oceanic crust (Jurassic oceanic crust) were to evaluate the geochemical and mineralogical composition of sediments recycled in the mantle through subduction zones (Ludden et al. 2006). For instance, this stratigraphic sequence represents one of the largest records of Miocene Asian eolian and volcanic ash inputs, and siliceous plankton production of surface waters (Ludden et al. 2006).

Ni isotope composition of pelagic clays and fresh and altered basalts from this same core have been already used to determine the composition of the Bulk Silicate Earth, i.e. +0.05 ± 0.05 ‰ (Gueguen et al. 2013). Since the Ni isotope composition in Mn deposits (e.g. Fe-Mn crusts) display positive values relative to bulk continental Crust (Gall et al. 2013; Gueguen et al. 2013), there is a great potential for tracing the proportion of authigenic Ni enrichment in pelagic clays relative to detrital sources.

As pelagic clays is one the largest sediment repository on the Earth's surface and that it receives sediments from several terrestrial reservoirs, they are also good representative of the average input of sediments recycled through subduction zones. Hence, potential Ni isotope heterogeneity in global marine sediments may affect the isotopic budget of Ni buried in the mantle. Although most of the Ni recycled in the mantle occurs via recycling of the basaltic oceanic crust and the lithospheric mantle, Ni isotope composition of these deep-sea clays could be used to estimate Ni isotope composition of the authigenic Ni contained in these sediments and recycled in the mantle. For instance, it has been demonstrated that recycling of ferromanganese sediments in the Hawaiian mantle could explain Tl isotope variations of Hawaiian basalts (Nielsen et al. 2006).

2. Samples description

These pelagic sediments were recovered from an ODP core at site 1149 (hole 1149A) in the Western Pacific Ocean off Izu-Bonin Trench (Figure III.14). Sediment cores were recovered during ODP Expedition 185 onboard the R/V Joides Resolution. Full descriptions of the samples can be found in (Plank et al. 2000; Rouxel et al. 2003; Ludden et al. 2006). The core was collected ~100 km east of the Izu-Bonin trench.

The whole stratigraphic sequence consists of four different units (Figure III.14). Unit I corresponds to the first 118 meters of sediments and it is composed of biogenic silica-bearing clays and several ash layers, and the unit represents a geological period of 6.5 Ma. Sediments from this uppermost unit were deposited below the CCD at water depths of ~6000 m and they are composed of clays, silts, several volcanic ashes layers which are probably the result of volcanic eruptions in the Izu-Bonin-Mariana arc, biogenic opaline silica and siliceous microfossils like radiolarians, diatoms and silicoflagellates. Accumulation rates of

sediment are between 7 and 13 m/Ma. Unit II is a condensed sequence (from 6.5 to 104 Ma) of pelagic brown clays deposited on a thickness of 61 meters, thus sedimentation rates are very low < 2 m/Ma. Siliceous microfossils are practically absent from this unit. Finally, the lowermost part of the sedimentary sequence (Units III and IV) is composed of a 229 meters-thick unit of hard radiolarian cherts (corresponding to a period of deposition of 13 Ma). These cherts correspond to siliceous pelagic sediments that have recrystallized to porcellanite and chert as a result of subsidence during diagenesis. Predominance of siliceous microfossils in Unit III is probably indicative of high surface bioproductivity when these sediments deposited near the Equator. The transition from Unit III (cherts) to Unit II (pelagic clays) suggests a significant change in sedimentation rates but this also suggests that sediments were deposited in oligotrophic waters provoking an abrupt decrease in biogenous silica in the sedimentary pile (Plank et al. 2000). Dating of the base of the sediment pile (sediment/chert contact) yielded an age of 134 Ma (Plank et al. 2000; Ludden et al. 2006). Basement was encountered at 408 mbsf (meters below seafloor) (Figure III.14).

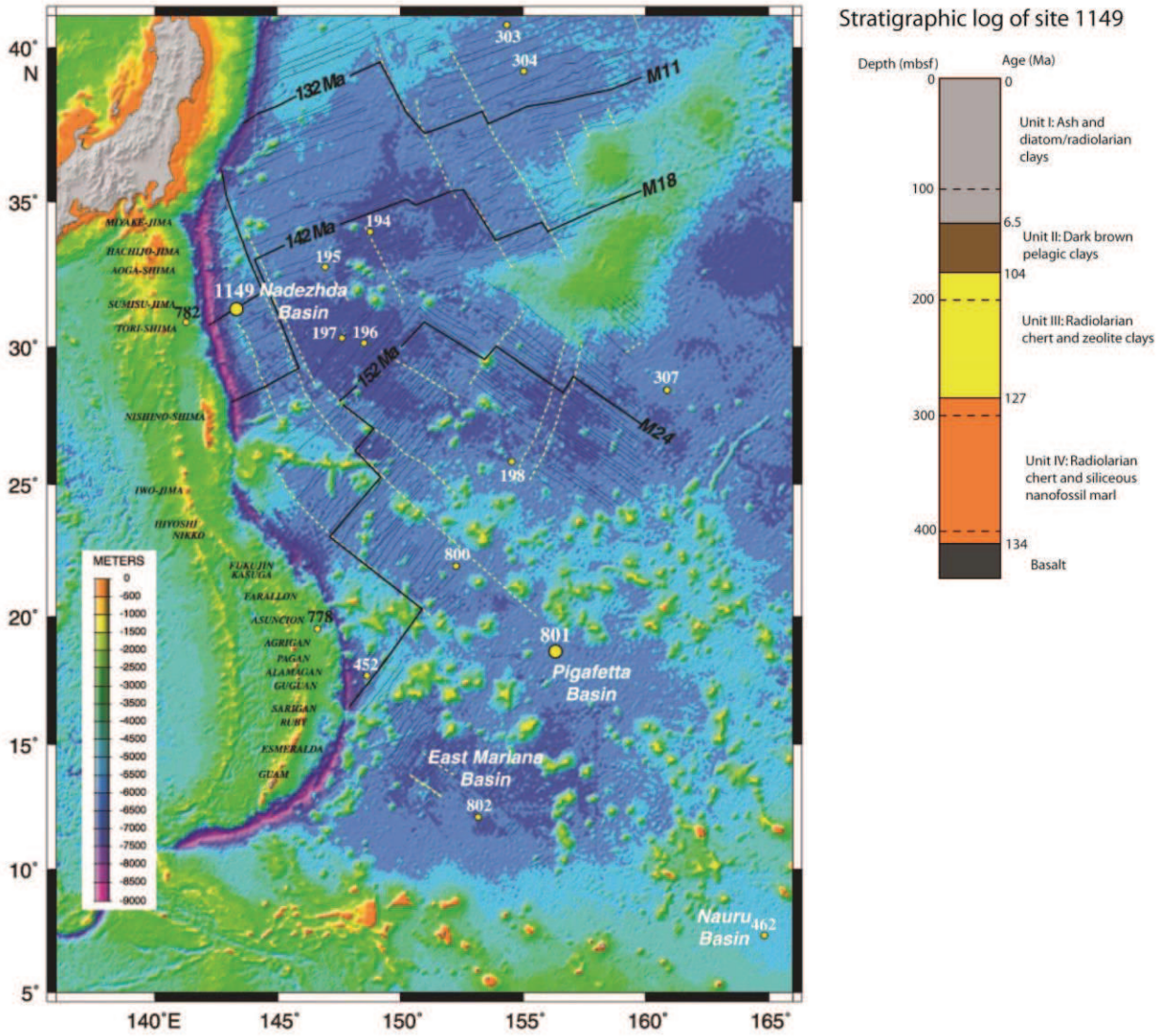

Figure III.14*: Map of drilling core position and stratigraphic log of site 1149 (map from Ludden et al., 2006 and stratigraphic log modified from Plank et al. (2000)).*

3. Results

3.1. Geochemical profiles

The major and trace elements geochemistry is already published in previous papers (Rouxel et al. 2003; Ludden et al. 2006) and representative analysis are reported in Table III.5. Radiogenic isotope geochemistry (Pb-Sr-Nd) was also reported for this sedimentary sequence in order to evaluate the composition of the lithogenic component entering the mantle in the “subduction factory” (Hauff et al. 2003). Elemental geochemistry of the samples shows that along the stratigraphic sequence, Mn, Ni, Cu, Co and Zn concentrations increase with depth. Mn/Al varies from 0.006 at 1.4 mbsf to a maximum of 0.078 at 160 mbsf, which means a 10-fold increase of Mn/Al ratio (Figure III.15 and Table III.5). Ni concentrations are comprised between ~30 ppm at top of the sediment column to more than 400 ppm at the base of the core, hence there is also a ten-fold increase in Ni/Al ratios from 0.00021 to 0.0027.

Table III.5: Elemental geochemistry (µg/g) and Ni isotope composition (‰) of pelagic clays from ODP site 1149.

Sample name	1149A-01H1,140	1149A-04H2,140	1149A-05H5,140	1149A-07H4,140	1149A-09H3,140	1149A-10H3,140	1149A-12H3,140	1149A-16H3,140	1149A-18H3,140	1149A-20X1,140
Depth (mbsf)	1,4	26,1	40,1	57,6	75,1	84,6	103,6	141,6	160,4	171,2
$\delta^{60/58}$Ni (‰)	0,044	0,020	0,154	0,094	0,191	0,149	0,280	0,450	1,032	0,772
2se	0,037	0,034	0,027	0,030	0,033	0,032	0,032	0,043	0,031	0,026
1/[Ni]	0,030	0,018	0,019	0,031	0,025	0,022	0,018	0,014	0,004	0,002
Mn/Al	0,006	0,006	0,005	0,013	0,015	0,028	0,025	0,037	0,078	0,077
Ni/Al	0,000	0,000	0,000	0,000	0,000	0,000	0,000	0,000	0,002	0,003
Mn/Ni	28,2	17,3	14,8	60,9	59,7	103,3	73,3	83,3	49,7	28,4
Ni/Mn	0,035	0,058	0,068	0,016	0,017	0,010	0,014	0,012	0,020	0,035
Al	157534,71	151194,62	156357,49	141811,41	157908,06	159062,24	159352,52	156620,19	184250,10	149037,33
Fe	38295,54	49494,16	40657,50	28457,73	50943,93	45175,98	38808,47	41715,13	54559,88	54786,64
Mn	922,03	936,30	772,31	1893,71	2290,46	4524,97	4023,02	5741,32	14308,86	11497,10
Cu	62,46	84,02	81,87	46,97	201,55	131,36	148,43	205,67	221,87	213,76
Zn	89,74	95,93	97,05	96,24	93,63	88,54	97,12	105,67	141,12	152,26
Co	16,42	15,80	19,39	14,99	21,38	32,81	24,39	59,60	158,55	114,05
Cr	40,58	61,57	59,81	32,75	49,34	35,70	60,41	29,99	67,77	60,69
Ni	32,69	53,97	52,15	31,10	38,36	43,80	54,90	68,93	287,72	405,31
V	157,60	123,05	130,25	92,51	136,90	131,81	117,45	60,20	125,57	127,26
Rb	77,45	98,81	109,90	62,02	91,35	71,89	117,11	78,32	141,37	120,49
Sr	143,29	130,14	138,56	149,18	151,20	143,04	116,57	88,51	167,72	202,75
Nb	6,24	8,82	9,99	5,43	7,79	6,31	10,25	10,06	13,34	13,76
Ga	16,77	17,81	18,03	16,07	18,76	16,38	19,23	17,48	22,02	18,00
Hf	2,51	2,58	2,76	2,77	2,55	2,72	2,82	3,98	4,16	4,78
Y	24,87	23,10	27,51	30,64	29,03	27,06	29,60	38,02	65,76	246,01
Zr	84,72	90,41	97,06	92,08	89,82	94,56	99,40	133,74	142,61	146,79
La	17,05	22,02	24,61	14,78	21,62	16,92	26,77	25,72	48,51	154,32
Ce	39,27	51,49	58,25	34,86	50,85	39,75	66,17	73,08	144,69	186,15
Pr	4,36	5,53	6,48	4,12	5,85	4,45	7,02	7,55	14,04	52,16
Nd	17,33	21,55	24,49	17,42	22,42	18,15	26,24	29,58	55,49	226,30
Sm	3,89	4,57	5,22	4,27	4,97	4,19	5,49	6,73	12,42	53,14
Eu	1,00	1,13	1,31	1,17	1,34	1,11	1,35	1,50	2,93	12,26
Gd	3,99	4,29	5,09	4,66	5,09	4,43	5,49	6,87	12,70	55,09
Tb	0,66	0,69	0,83	0,78	0,84	0,72	0,89	1,16	2,06	8,50
Dy	3,92	3,94	4,83	4,80	4,99	4,34	5,21	6,80	11,63	48,53
Ho	0,82	0,80	0,99	1,05	1,04	0,92	1,06	1,38	2,32	9,75
Er	2,38	2,26	2,79	2,98	2,91	2,62	3,00	3,92	6,39	25,71
Yb	2,42	2,26	2,79	3,08	2,82	2,63	2,99	3,84	5,84	21,51
Lu	0,38	0,36	0,44	0,48	0,45	0,41	0,47	0,59	0,91	3,25
Sc	19,73	17,90	16,39	18,53	20,83	20,14	17,86	17,33	23,10	37,00
Ta	0,47	0,64	0,76	0,41	0,59	0,46	0,77	0,77	0,99	1,17
Th	6,75	9,26	9,59	5,54	7,51	6,27	10,14	11,07	17,38	25,13
Li	38,03	55,63	47,53	33,52	37,00	33,13	49,56	80,40	66,01	45,70
Ba	604,82	684,52	672,18	516,26	570,48	524,11	487,08	370,05	399,68	439,32
Cs	5,85	7,43	8,71	4,91	7,68	5,84	9,88	6,37	11,92	10,03
Pb	17,32	25,02	26,34	14,89	19,41	20,87	28,84	35,79	56,74	52,01
U	1,35	1,51	1,71	1,17	1,47	1,34	1,94	1,44	2,34	2,79

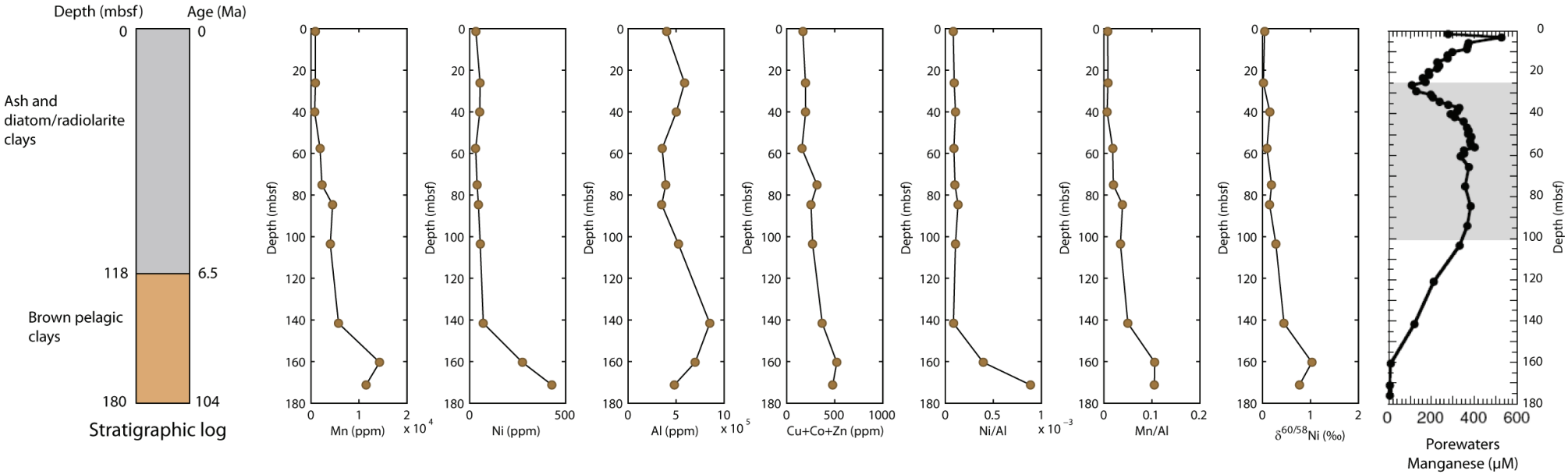

***Figure III.15**: Stratigraphic log of the sediment sequence including samples investigated in this study, and geochemical composition of sediments (Mn, Ni, Al, Cu+Co+Zn, Ni/Al and Mn/Al) and Ni isotope composition with depth below seafloor (mbsf). The right panel shows a depth profile of dissolved Mn (µM) in sediment porewaters (plot taken from Ludden et al. 2006).*

PAAS-normalized (Post Archean Australian Shale (Taylor and McLennan 1995)) REE patterns show a slight positive Ce anomaly excepted for the deepest deep-sea clay sample displaying a negative Ce anomaly (Figure III.16). The two deepest samples are also enriched in REE compared to the remaining top sequence.

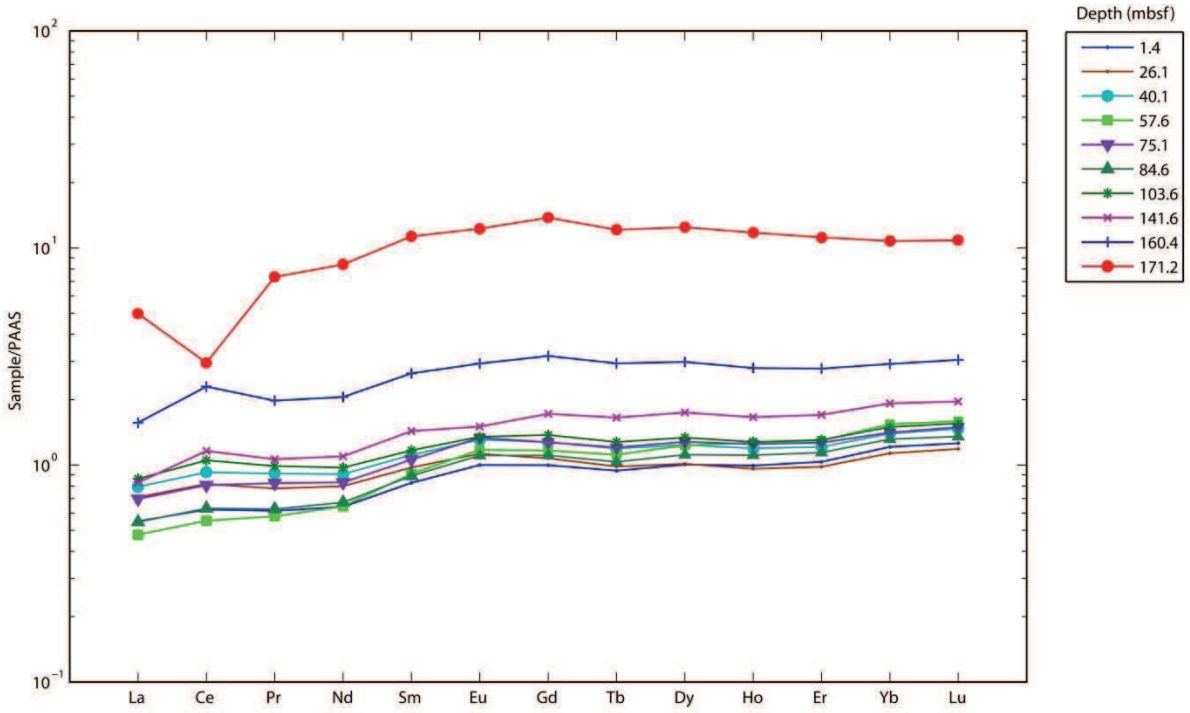

Figure III.16: *Rare Earth Elements patterns normalized to PAAS (Post Archean Australian Shale (Taylor and McLennan 1995)) of pelagic clays. Symbols stands for depth (mbsf) of samples in the stratigraphic sequence.*

3.2. Ni isotope composition of deep-sea-clays with depth in the stratigraphic sequence

In Figure III.17 we see that $\delta^{60/58}$Ni values vary from +0.04 to +1.03 ‰ which is significant in comparison to values already published in the literature (Gall et al. 2012; Gall et al. 2013; Gueguen et al. 2013). A correlation between $\delta^{60/58}$Ni values and 1/Ni (panel A) and Al/Ni (panel B) suggests that Ni derives from two sources, one enriched in heavy Ni isotopes and enriched in Ni, the other one close to 0 ‰ and more depleted in Ni. Note that the first top clay samples of the sequence as well as fresh and altered basalts forming the hard substrate were analyzed previously for their Ni isotope composition and yielded near-zero values (Gueguen et al. 2013).

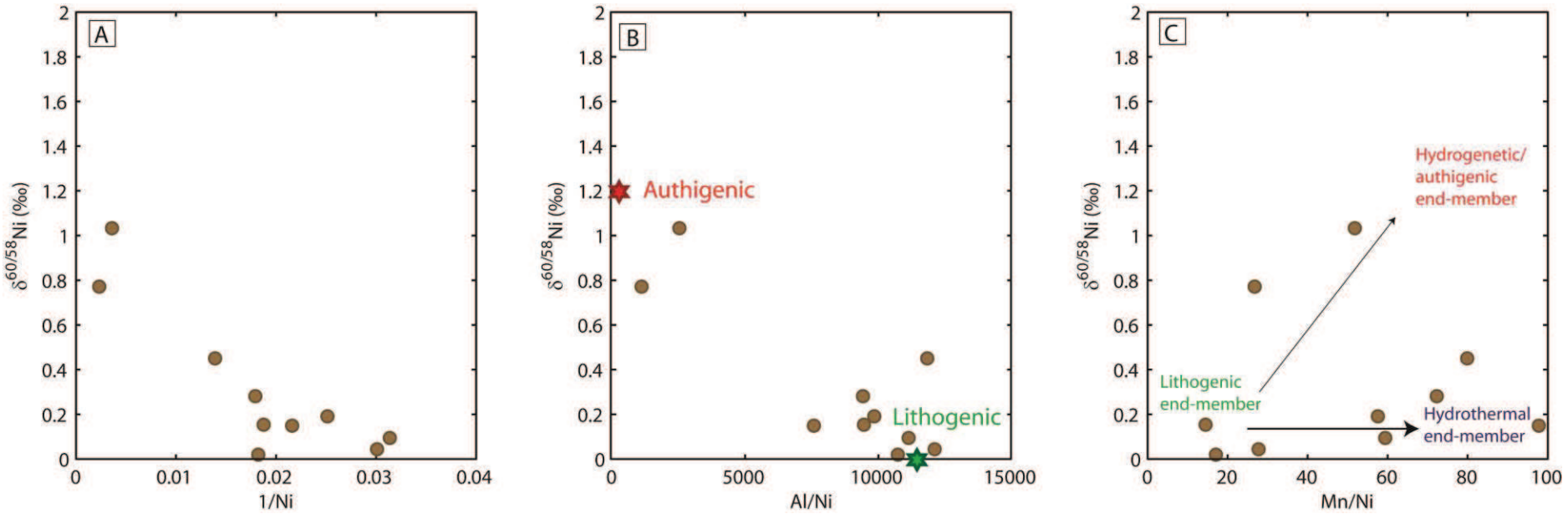

***Figure III.17**: Plots showing Ni isotope composition of pelagic clays versus inverse Ni concentration (panel A), versus Al/Ni ratio (panel B) and versus Mn/Ni ratio (panel C). The assumed authigenic and lithogenic end-members are plotted on panel B, intersection of the linear trend between these two end-members with the y-axis is the assumed Ni isotope composition of authigenic Ni in pelagic sediments. In panel C, three hydrogenetic, lithogenic and hydrothermal end-members are shown on the figure.*

4. Discussion

4.1. Deciphering hydrothermal, authigenic and diagenetic Mn enrichment in pelagic clays

The stratigraphic sequence from which samples were collected consists of pelagic clays deposited in the western Pacific oceanic crust. Our observations indicate that $\delta^{60/58}$Ni value of these deep-sea clays is positively correlated with increasing transition metal concentrations like Ni, Mn, Cu, Co and Zn (Figure III.15). The increasing Mn/Al and decreasing Ni/Al probably is consistent with authigenic precipitation of Mn-oxides within deep-sea clays. In addition, these parameters are correlated with increasing depth of the sediment and $\delta^{60/58}$Ni values. Previously established models for the sedimentation history of the sequence indicate that organic supply to the sediment was low and that sedimentation rates varied between 7 and 13 m/Ma for Unit I and were below 2 m/Ma for Unit II (Ludden et al. 2006). Hence, it is unlikely that organic matter decay contributed significantly to the increase in transition metals. It is however important to note that pelagic clays are underlayered by a 179 meters-thick chert sequence. Diagenetic processes affecting these cherts produced fluids that may have possibly affected the base of the pelagic clay sequence.

The general trend showing a negative correlation between Ni isotope values and inverse Ni concentration (or Al/Ni) is likely indicative of mixing between a near-zero $\delta^{60/58}$Ni value end-member and a positive end-member between +0.8 and +1.2‰ (Figure III.17). High Al/Ni and near-zero $\delta^{60/58}$Ni is consistent with the high detrital component of deep sea clay that are expected to have similar composition than average continental Crust (Gueguen et al. 2013). The isotopically heavy and metal-rich end-member probably corresponds to authigenic Mn-oxides. Ni isotope composition of Fe-Mn deposits such as Fe-Mn crusts and Mn-nodules have been already investigated in previous studies (Gueguen et al. 2011; Gall et al. 2013) (and Part 1 of this chapter III). Results show that Mn-nodules range from +0.36 to +1.03 ‰ (Gall et al. 2012; Gall et al. 2013; Gueguen et al. 2013) while hydrogenous Fe-Mn crusts (Pacific and Atlantic) range from +0.9 and +2.5 ‰ (Gall et al. 2013). Hence, although average $\delta^{60/58}$Ni value of about +1.6‰ have been reported in Fe-Mn crust with no clear differences between oceanic basins, our estimated $\delta^{60/58}$Ni value of authigenic Ni sink in deep sea clay is lower by 0.4 to 0.8 ‰. This value is also lower than seawater value determined at about ~+1.5 ‰ (Cameron and Vance). Although it is possible that seawater $\delta^{60/58}$Ni value has varied in the past, we discuss below the different processes explaining such differences, (1) diagenetic processes, (2) hydrothermal contribution, (3) metal enrichment as a result of slow sedimentation rates.

(1) Several lines of evidence suggest significant diagenetic Mn recycling through the sedimentary section at ODP Site 1149. The examination of the dissolved concentration profile of Mn in porewaters indicates an increase in Mn contents between 25 and 100 mbsf that is likely the result of bacterial reduction of Mn (Plank et al. 2000; Ludden et al. 2006) (Figure III.15). Below 100 mbsf Mn continuously decreases until the base of the pelagic sediment sequence where Mn concentration in the sediment increases. This suggests that Mn oxidation occurs upward (closer to the sediment-seawater interface) while deeper sediments undergo partial Mn reduction. This diagenetic sequence has been well identified in pelagic sediment where low sediment rates and oxic conditions favor the enrichment of Mn in surface sediment. Yet, the amount of Mn oxide deposits and associated metals that remains preserved in the sedimentary column remains poorly known.

(2) At 1149, shallower samples display moderate or no positive Ce anomalies and no REE enrichment relatively to PAAS, whereas deeper clays are enriched in REE, and with the exception of the deepest sample other samples display moderate positive Ce anomalies (Figure III.16). Positive Ce anomaly is typical of hydrogenous Mn-Fe deposits forming deep ocean (De Carlo and McMurtry 1992) due to the oxidation of Ce^{3+} to Ce^{4+} promoting the formation of insoluble CeO_2 (Elderfield et al. 1981; Elderfield et al. 1981; De Baar et al. 1985; German and Elderfield 1990; German et al. 1990). However, the deepest sample of the sequence (the closest to the chert sequence) deviates from this observation since it has a negative Ce anomaly typical to that observed in seawater and the pattern shows the highest enrichment in REE. A plausible hypothesis explaining this negative Ce anomaly involves the contribution of hydrothermal Fe-Mn input. For example, at the time when the sediment deposited, the location of the core could have been affected by inputs from hydrothermal activity emanating from off-axis volcanism (active seamounts). Delivery of important amount of Mn and Fe by hydrothermal fluids would have promoted precipitation of Mn- and Fe-rich particles in the water column along with incorporation of trace metals like Ni, Cu, Co and Zn and REE. The later would explain the seawater-like REE pattern with a negative Ce anomaly inherent to seawater (German and Elderfield 1990; German et al. 1990). Hence, we assume that only the deepest sample showing positive Ce anomaly could be used as the best proxy for authigenic Ni sink in associated with Mn oxides. This allows to refining the estimate of the Ni isotope composition of the authigenic sink preserved in pelagic sediments to between +1.0 to +1.2 ‰.

(3) Finally, it is important to note that this sample is located within a sequence with very low sedimentation rates < 2 m/Ma (50 meters represent ~90 Ma), explaining the enrichment in Mn and other metals at this depth.

4.2. Implications for global Ni budget

Based on our estimate of Ni/Mn ratios and $\delta^{60/58}$Ni values of Fe-Mn oxides dispersed and buried in the sediment, it is possible to estimate the isotope composition in the authigenic Ni sink associated with Fe-Mn oxides. As explained above, $\delta^{60/58}$Ni values of the end-member authigenic pool in Site 1149 is estimated between 1.0 to 1.2 ‰ with Ni/Mn molar ratio about 0.02. The USGS (Hein et al. 2013) have compiled data on the chemical composition of crusts and nodules from selected areas of the global ocean. Estimated Ni/Mn ratios of Fe-Mn crusts from the Atlantic and Indian oceans are 0.017 and 0.014 respectively, which is very similar to the range of Ni/Mn values for North and South Pacific (0.017 to 0.020). In contrast, nodules yield systematically higher Ni/Mn ratios, ranging from 0.043 for the large nodule fields in the Clarion-Clipperton Zone of the Pacific and 0.042 for the Indian ocean. Hence, authigenic sink recorded at Site 1149 is more similar to the authigenic sink associated with Fe-Mn crusts than with Mn-nodules.

Elderfield and Schultz (1996) estimated a global hydrothermal flux of Mn between 1.1 to 3.4×10^{10} mol/yr, which is higher than riverine Mn flux of 0.5×10^{10} mol/yr and thus the principal source of Mn to the oceans (Elderfield and Schultz 1996). With this estimate and assuming steady-state conditions in the oceans thus implying that the source flux is equal to the sink flux, and considering that Ni sink is controlled by the Mn sink we can estimate an output Ni flux. Thus, using our estimated Ni/Mn ratio of the authigenic Mn sink in pelagic sediment and considering that such sink represent the vast majority of Mn sink, we determine an oxic Ni sink of 2.2 to 6.8×10^8 mol/yr. This is equivalent, within uncertainty, to

the dissolved riverine input of Ni that has been estimated at 4.9-5.2x10^8 mol/yr (Gall et al. 2013).

Another important consideration is whether it is possible to establish a reliable mass balance of Ni isotopes in seawater. Such approach would be possible when new data of Ni isotope composition of the riverine source would be available.

Finally, the results suggest that the Ni input flux to the mantle may be also affected by authigenic Ni enrichment. It has been already demonstrated that ferromanganese sediments entering in the mantle may explain Tl isotope variations recorded in Hawaiian basalts (Nielsen et al. 2006). Although Ni inputs to the mantle through subduction zones are small in comparison to Ni concentration in peridotites from the mantle, Ni isotope composition of this Mn-rich sink is highly fractionated relatively to peridotites and the Bulk Silicate Earth estimated at ~0.05 ‰ (Gueguen et al. 2013). We did not test this hypothesis, but it should be evaluated in the future.

5. Summary

Isotopically heavy Ni and enrichment in transition metals within the pelagic clays sequence reflect different processes, (1) accumulation of Fe- and Mn-rich particles delivered by hydrothermal plumes from the off-axis volcanic and hydrothermal activity especially in Unit II of the sequence as promoted by very slow rates of sediment deposition < 2 m/Ma, (2) authigenic precipitation of Ni (and other trace metals) in Mn-oxides by scavenging from porewaters dissolved trace metals, probably produces Ni with an isotopic composition alike that of seawater. The whole of these metal enrichment processes are further enhanced by slow sedimentation rates of these marine sediments.

Finally, this study has important implications for the global oceanic Ni budget since we were able to estimate the Ni isotope composition of the major Ni sink (pelagic sediments) at ~+1.0 to +1.2 ‰ and an output Ni flux of 2.2 to 6.8x10^8 mol/yr in pelagic clays which is similar to the riverine input flux.

6. References

Boström, K. and Peterson, M. N. A. (1966). "Precipitates from hydrothermal exhalations on the East Pacific rise." Economic Geology 61(7): 1258-1265.

Boström, K., Peterson, M. N. A., Joensuu, O. and Fisher, D. E. (1969). "Aluminum-poor ferromanganoan sediments on active oceanic ridges." Journal of Geophysical Research 74(12): 3261-3270.

De Baar, H. J. W., Bacon, M. P., Brewer, P. G. and Bruland, K. W. (1985). "Rare Earth elements in the Pacific and Atlantic Oceans." Geochimica Et Cosmochimica Acta 49(9): 1943-1959.

De Carlo, E. H. and McMurtry, G. M. (1992). "Rare-earth element geochemistry of ferromanganese crusts from the Hawaiian Archipelago, central Pacific." Chemical Geology 95(3–4): 235-250.

Elderfield, H., Hawkesworth, C. J., Greaves, M. J. and Calvert, S. E. (1981). "Rare-earth element geochemistry of oceanic ferromanganese nodules and associated sediments." Geochimica Et Cosmochimica Acta 45(4): 513-528.

Elderfield, H., Hawkesworth, C. J., Greaves, M. J. and Calvert, S. E. (1981). "Rare-earth element zonation in Pacific ferromanganese nodules." Geochimica Et Cosmochimica Acta 45(7): 1231-1234.

Elderfield, H. and Schultz, A. (1996). "Mid-ocean ridge hydrothermal fluxes and the chemical composition of the ocean." Annual Review of Earth and Planetary Sciences 24: 191-224.

Gall, L., Williams, H., Siebert, C. and Halliday, A. (2012). "Determination of mass-dependent variations in nickel isotope compositions using double spiking and MC-ICPMS." Journal of Analytical Atomic Spectrometry 27(1): 137-145.

Gall, L., Williams, H. M., Siebert, C., Halliday, A. N., Herrington, R. J. and Hein, J. R. (2013). "Nickel isotopic compositions of ferromanganese crusts and the constancy of deep ocean inputs and continental weathering effects over the Cenozoic." Earth and Planetary Science Letters 375(0): 148-155.

German, C. R. and Elderfield, H. (1990). "Application of the Ce Anomaly as a Paleoredox Indicator: The Ground Rules." Paleoceanography 5(5): 823-833.

German, C. R., Klinkhammer, G. P., Edmond, J. M., Mitra, A. and Elderfield, H. (1990). "Hydrothermal scavenging of rare earth elements in the ocean." Nature 345(6275): 516-518.

Glasby, G. P. (1991). "Mineralogy, geochemistry, and origin of Pacific red clays: a review." New Zealand Journal of Geology and Geophysics 34(2): 167-176.

Gueguen, B., Rouxel, O., Ponzevera, E., Bekker, A. and Fouquet, Y. (2013). "Nickel Isotope Variations in Terrestrial Silicate Rocks and Geological Reference Materials Measured by MC-ICP-MS." Geostandards and Geoanalytical Research 37(3): 297-317.

Gueguen, B., Rouxel, O., Ponzevera, E., Sorensen, J. V., Toner, B. M., Bekker, A. and Fouquet, Y. (2011). Ni biogeochemical cycle through geological time: insights from Ni isotope variations in modern and ancient marine metallifereous deposits. AGU Fall Meeting 2011. San Francisco, USA.

Hauff, F., Hoernle, K. and Schmidt, A. (2003). "Sr-Nd-Pb composition of Mesozoic Pacific oceanic crust (Site 1149 and 801, ODP Leg 185): Implications for alteration of ocean crust and the input into the Izu-Bonin-Mariana subduction system." Geochemistry, Geophysics, Geosystems 4(8): 8913.

Heggie, D., Kahn, D. and Fischer, K. (1986). "Trace metals in metalliferous sediments, MANOP Site M: interfacial pore water profiles." Earth and Planetary Science Letters 80(1–2): 106-116.

Hein, J. R., Mizell, K., Koschinsky, A. and Conrad, T. A. (2013). "Deep-ocean mineral deposits as a source of critical metals for high- and green-technology applications: Comparison with land-based resources." Ore Geology Reviews 51(0): 1-14.

Kato, Y., Fujinaga, K., Nakamura, K., Takaya, Y., Kitamura, K., Ohta, J., Toda, R., Nakashima, T. and Iwamori, H. (2011). "Deep-sea mud in the Pacific Ocean as a potential resource for rare-earth elements." Nature Geoscience 4(8): 535-539.

Klinkhammer, G. P. (1980). "Early diagenesis in sediments from the eastern equatorial Pacific, II. Pore water metal results." Earth and Planetary Science Letters 49(1): 81-101.

Krishnaswami, S. (1976). "Authigenic transition elements in Pacific pelagic clays." Geochimica Et Cosmochimica Acta 40(4): 425-434.

Ludden, J. N., Plank, T., Larson, R. and Escutia, C. (2006). "Leg 185 Synthesis: Sampling the Oldest Crust in the Ocean Basins to Understand Earth's Geodynamic and Geochemical Fluxes " Proceedings of the Integrated Ocean Drilling Program, Scientific Results 185.

Lupton, J. (1998). "Hydrothermal helium plumes in the Pacific Ocean." Journal of Geophysical Research: Oceans 103(C8): 15853-15868.

Lupton, J. E. (1995). Hydrothermal Plumes: Near and Far Field. Seafloor Hydrothermal Systems: Physical, Chemical, Biological, and Geological Interactions, American Geophysical Union, Geophysical Monograph Series. 91**:** 317-346.

Nielsen, S. G., Rehkämper, M., Norman, M. D., Halliday, A. N. and Harrison, D. (2006). "Thallium isotopic evidence for ferromanganese sediments in the mantle source of Hawaiian basalts." Nature 439(7074): 314-317.

Plank, T., Ludden, J. N., Escutia C. and Party, S. S. (2000). "Site 1149." Proceedings of the Ocean Drilling Program, Initial Reports 185.

Rouxel, O., Dobbek, N., Ludden, J. and Fouquet, Y. (2003). "Iron isotope fractionation during oceanic crust alteration." Chemical Geology 202(1-2): 155-182.

Sawlan, J. J. and Murray, J. W. (1983). "Trace-metal remobilization in the interstitial waters of red clay and hemipelagic marine-sediments." Earth and Planetary Science Letters 64(2): 213-230.

Taylor, S. R. and McLennan, S. M. (1995). "The geochemical evolution of the continental crust." Reviews of Geophysics 33(2): 241-265.

Thomson, J., Carpenter, M. S. N., Colley, S., Wilson, T. R. S., Elderfield, H. and Kennedy, H. (1984). "Metal accumulation rates in northwest Atlantic pelagic sediments." Geochimica Et Cosmochimica Acta 48(10): 1935-1948.

Partie III.3 - Temps de résidence du Ni dans les océans modernes et bilan de masse

Dans l'introduction générale de ce manuscrit de thèse, nous avons mentionné le fait qu'il restait des incertitudes sur l'estimation du temps de résidence du Ni dans les océans modernes en raison d'une mauvaise évaluation des sources et des puits. Quel est le flux global réel de Ni apporté par les sources hydrothermales ? La concentration en Ni naturel des rivières est-elle bien estimée et dans quelle proportion les activités anthropiques peuvent influencer le flux de Ni des rivières vers les océans ? En effet, il est probable que l'apport anthropique en Ni crée une surestimation du flux de Ni en provenance des rivières, et l'on peut faire un raisonnement similaire pour les particules atmosphériques d'origine anthropique. Enfin, le flux de Ni provenant de l'altération du plancher océanique lors de la serpentinisation est encore inconnu.

Au cours de ces travaux de thèse, une équipe de chercheurs de l'Université d'Oxford en Angleterre (Gall et al. 2013), a publié les premières données en isotopes du Ni dans les encroûtements de fer-manganèse. Dans leur étude ils ont également établi de nouvelles estimations du temps de résidence du Ni dans les océans modernes en publiant une synthèse des flux de Ni entrants et sortants.

Nos estimations des flux des sources et des puits de Ni aux océans nous ont permis de calculer un temps de résidence océanique du Ni d'environ 15800 ans, ce qui est légèrement supérieur aux valeurs de 3600 et 14500 ans reportées par Gall et al. (2013). Par ailleurs, en supposant que le bilan de masse du Ni dans les océans est à l'état stationnaire, alors le flux entrant doit être égal au flux sortant (E.1). Or ce n'est pas le cas dans les calculs présentés par Gall et al. (2013) indiquant que le flux total sortant est plus élevé que le flux entrant impliquant qu'il y a donc des incertitudes importantes dans l'estimation des flux.

$$F_{IN} = F_{OUT} \qquad (E.1)$$

Où F_{IN} et F_{OUT} sont les flux entrant et sortant.

La synthèse des données de flux nous ayant permis de calculer notre valeur du temps de résidence du Ni est présentée dans le tableau III.6 avec les compositions isotopiques en Ni de chaque flux. L'apport continental (particules atmosphériques et rivières) constitue la source en Ni la plus importante, c'est donc ce flux qui va essentiellement contrôler l'apport de Ni aux océans. Néanmoins, ce flux peut être surestimé en raison de l'apport anthropique (Nriagu 1989; Nriagu 1990; Duce et al. 1991). Par exemple, sans prendre en compte le flux de Ni anthropique, notre estimation du flux continental naturel de Ni correspond à ~60% du flux de Ni total lorsque les apports anthropiques sont pris en compte dans le calcul. L'apport anthropique peut donc introduire une considérable incertitude dans la détermination des flux continentaux.

Table III.6 : Table summarizing input and output fluxes of Ni to the oceans with best estimates of Ni isotope composition of each flux.

	Ni flux (g/yr)	Ni flux (g/yr) corrected*	Reference	$\delta^{60/58}$Ni (‰) best estimate/measured**
Inputs				
Continental erosion (dissolved load in rivers)	$3{,}00.10^{10}$	$3{,}00.10^{10}$	(Gaillardet et al. 2003)***	0,8***
Continental erosion (particulate load in rivers), but not contributing to budget (Chester, 2002; Jickells, 1995)	$1.40.10^{12}$	-	(Duce et al. 1991; Chester 2003)	0,05
Meteorites (cosmic dust)	$8{,}19.10^{7}$	$3{,}11.10^{7}$	(Levasseur et al. 1999; Bland and Artemieva 2006; Gueguen et al. 2013)	0,25
Atmosphere (natural)*	$3{,}00.10^{10}$	$1{,}14.10^{10}$	(Duce et al. 1991; Rehkämper and Nielsen 2004)	0,05
Atmosphere (anthropogenic)*	$5{,}60.10^{10}$	$2{,}13.10^{10}$	(Nriagu 1989)	0,14
Ni from basalt alteration: serpentine/altered basalt	~0 ?	~0 ?	-	0,00
Hydrothermal	$2{,}91.10^{8}$	$2{,}91.10^{8}$	(Elderfield and Schultz 1996; Wheat et al. 2002; German and Von Damm 2003)	0,00
Total input flux (g/yr) *without anthropogenic inputs*		$4{,}17.10^{10}$		0.59
Residence time of Ni in oceans (yrs)		15684		
Outputs				
Fe-Mn crusts	$6{,}67.10^{5}$		(Hein et al. 2003) (This study)	1,50
Mn-nodules	$5{,}72.10^{6}$		(Hein et al. 2003) (This study)	0,71
Pelagic sediments (oxic sediments)	$4{,}00.10^{10}$		(Elderfield and Schultz 1996), this study	1,20
Ni accumulated in anoxic sediments (organic matter-rich sediments)	$1{,}53.10^{9}$		(Brumsack 2006; Piper and Calvert 2009; Porter 2012)	1,50
Total output flux (g/yr)	**$4{,}15.10^{10}$**			1,21
Residence time of Ni in oceans (yrs)	**15755**			
[Ni] in deep oceans (µg/L)	0,6		(Sohrin and Bruland 2011)	
[Ni] in surface oceans (µg/L)	0,1		(Sohrin and Bruland 2011)	1,4***
Mass of oceans (g)	$1{,}348.10^{24}$		Rehkämper et al. (2004)	
Average [Ni] (µg/L) in deep oceans	0,5		(Sohrin and Bruland 2011)	
Average Ni in oceans (g)	$6{,}54369.10^{14}$		-	
Area of deep-sea floor covered by pelagic sediments (km²)	$3{,}00.10^{8}$		(Rehkämper and Nielsen 2004)	
Average accumulation rate of pelagic sediments (g/cm^3/kyr)	0,22		(Chester 2003)	
Average Ni accumulation rate in anoxic basin (µg/m²/yr)	$2{,}00.10^{3}$			
Area of deep-sea floor depleted in oxygen (0,2% of total seafloor) (km²)	$7{,}64.10^{5}$		(Brumsack 2006)	

* Ni atmospheric flux (g/yr) entering oceans is calculated based on the assumption that only 38% of atmospheric particles are effectively dissolved in seawater (Duce et al., 1991).

** Data from this study.

*** Ni isotope values are from Cameron and Vance (2013) and Vance and Cameron (2013) (both at Goldschmidt, 2013).

Dans la partie 2 de ce chapitre III, nous avons calculé une estimation du puits de Ni dans les sédiments profonds grâce au rapport Ni/Mn mesuré dans les sédiments pélagiques du site ODP 1149. L'affinité très forte du Ni pour les phases d'oxydes de Mn suggère que la précipitation d'oxydes de Mn authigènes dans les sédiments profonds est le puits majeur de Ni, en comparaison au Ni piégé dans les dépôts métallifères océaniques tels que les encroûtements et les nodules de Mn qui est finalement un puits relativement mineur (Tableau III.6). Contrairement à Gall et al. (2013), nous avons également inclus dans nos calculs un puits de Ni dans les sédiments riches en matière organique qui, selon nos estimations, équivaudrait au deuxième puits le plus important après les minéralisations authigènes de manganèse dans les sédiments pélagiques.

Références bibliographiques :

Bland, P. A. and Artemieva, N. A. (2006). "The rate of small impacts on Earth." Meteoritics & Planetary Science 41(4): 607-631.

Brumsack, H.-J. (2006). "The trace metal content of recent organic carbon-rich sediments: Implications for Cretaceous black shale formation." Palaeogeography, Palaeoclimatology, Palaeoecology 232(2-4): 344-361.

Chester, R. (2003). Marine Geochemistry, Blackwell.

Duce, R. A., Liss, P. S., Merrill, J. T., Atlas, E. L., Buat-Menard, P., Hicks, B. B., Miller, J. M., Prospero, J. M., Arimoto, R., Church, T. M., Ellis, W., Galloway, J. N., Hansen, L., Jickells, T. D., Knap, A. H., Reinhardt, K. H., Schneider, B., Soudine, A., Tokos, J. J., Tsunogai, S., Wollast, R. and Zhou, M. (1991). "The atmospheric input of trace species to the world ocean." Global Biogeochem. Cycles 5(3): 193-259.

Elderfield, H. and Schultz, A. (1996). "Mid-ocean ridge hydrothermal fluxes and the chemical composition of the ocean." Annual Review of Earth and Planetary Sciences 24: 191-224.

Gaillardet, J., Viers, J. and Dupré, B. (2003). Trace Elements in River Waters. Treatise on Geochemistry. D. H. Editors-in-Chief: Heinrich and K. T. Karl. Oxford, Pergamon**:** 225-272.

Gall, L., Williams, H. M., Siebert, C., Halliday, A. N., Herrington, R. J. and Hein, J. R. (2013). "Nickel isotopic compositions of ferromanganese crusts and the constancy of deep ocean inputs and continental weathering effects over the Cenozoic." Earth and Planetary Science Letters 375(0): 148-155.

German, C. R. and Von Damm, K. L. (2003). Hydrothermal Processes. Treatise on Geochemistry. D. H. Editors-in-Chief: Heinrich and K. T. Karl. Oxford, Pergamon**:** 181-222.

Gueguen, B., Rouxel, O., Ponzevera, E., Bekker, A. and Fouquet, Y. (2013). "Nickel Isotope Variations in Terrestrial Silicate Rocks and Geological Reference Materials Measured by MC-ICP-MS." Geostandards and Geoanalytical Research 37(3): 297-317.

Hein, J. R., Koschinsky, A. and Halliday, A. N. (2003). "Global occurrence of tellurium-rich ferromanganese crusts and a model for the enrichment of tellurium." Geochimica et Cosmochimica Acta 67(6): 1117-1127.

Levasseur, S., Birck, J. L. and Allègre, C. J. (1999). "The osmium riverine flux and the oceanic mass balance of osmium." Earth and Planetary Science Letters 174(1–2): 7-23.

Nriagu, J. O. (1989). "A global assessment of natural sources of atmospheric trace metals." Nature 338(6210): 47-49.

Nriagu, J. O. (1990). "Global metal pollution." Environment 32(7): 6-&.

Piper, D. Z. and Calvert, S. E. (2009). "A marine biogeochemical perspective on black shale deposition." Earth-Science Reviews 95(1-2): 63-96.

Porter, S. J. (2012). Nickel and osmium isotope and trace element geochemistry of organic-rich sedimentary rocks: the first investigation of Ni isotope systematics in marine sediments. Doctor of Philosophy, Durham University.

Rehkämper, M. and Nielsen, S. G. (2004). "The mass balance of dissolved thallium in the oceans." Marine Chemistry 85(3-4): 125-139.

Sohrin, Y. and Bruland, K. W. (2011). "Global status of trace elements in the ocean." Trends in Analytical Chemistry 30(8): 1291-1307.

Wheat, C. G., Mottl, M. J. and Rudnicki, M. (2002). "Trace element and REE composition of a low-temperature ridge-flank hydrothermal spring." Geochimica Et Cosmochimica Acta 66(21): 3693-3705.

Conclusion du Chapitre III :

Les travaux présentés dans ce chapitre III ont constitué un volet important de la réflexion qui a été menée au cours de ces trois années de thèse sur le développement d'un nouveau traceur biogéochimique que sont les isotopes du Ni. Dans la première partie nous avons présenté un modèle qui montre que les variations isotopiques du Ni observées dans les dépôts métallifères océaniques riches en Fe et Mn peuvent s'expliquer par des processus d'enrichissement, en invoquant notamment le temps de formation des dépôts et de précipitation des oxydes de Fe et de Mn, plutôt que par des variations isotopiques inhérentes aux sources de Ni (Figure C.3a). La Figure C.3b est une vue synthétique et schématique des compositions isotopiques en Ni dans les différents réservoirs océaniques et également terrestres et prenant en compte les données de la littérature et celles de cette étude.

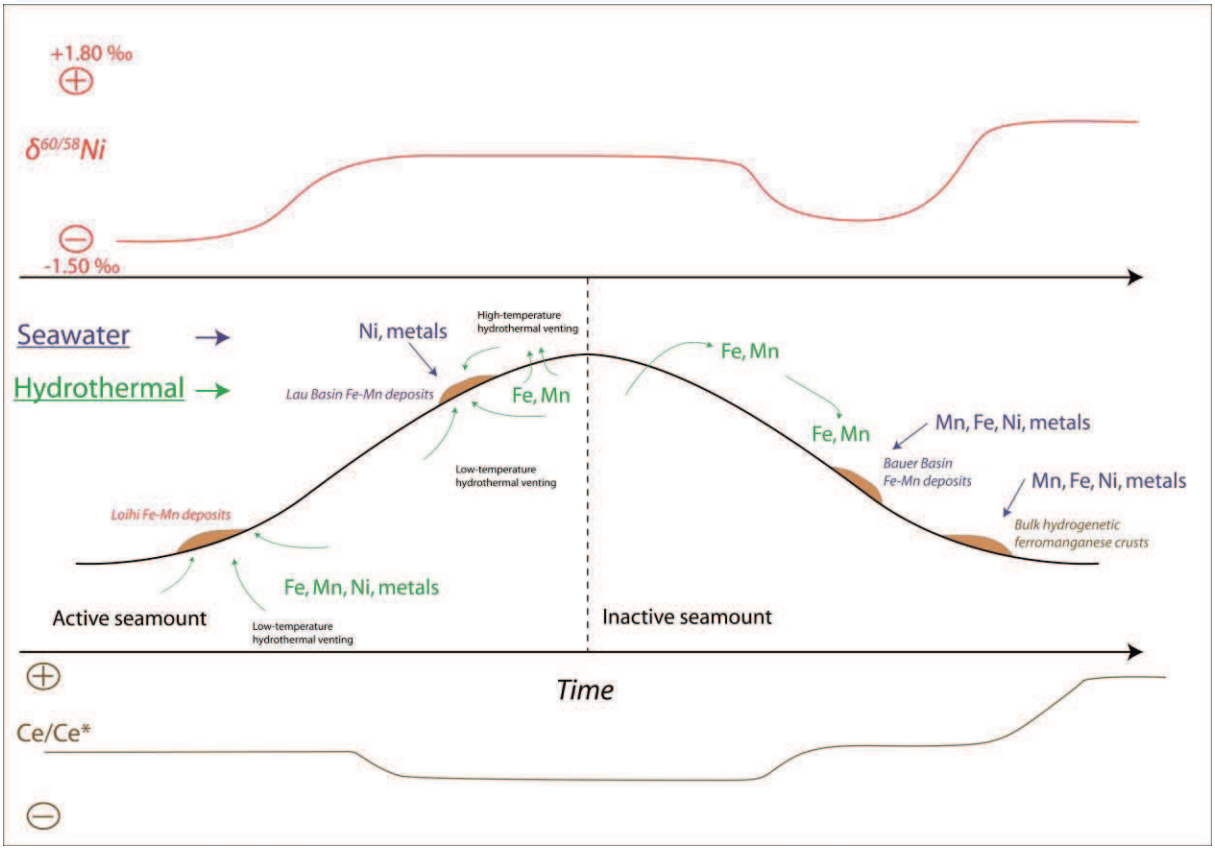

***Figure C.3a** : Modèle expliquant la variabilité isotopique du Ni dans les dépôts métallifères océaniques des océans modernes (figure de la partie 1 du chapitre III).*

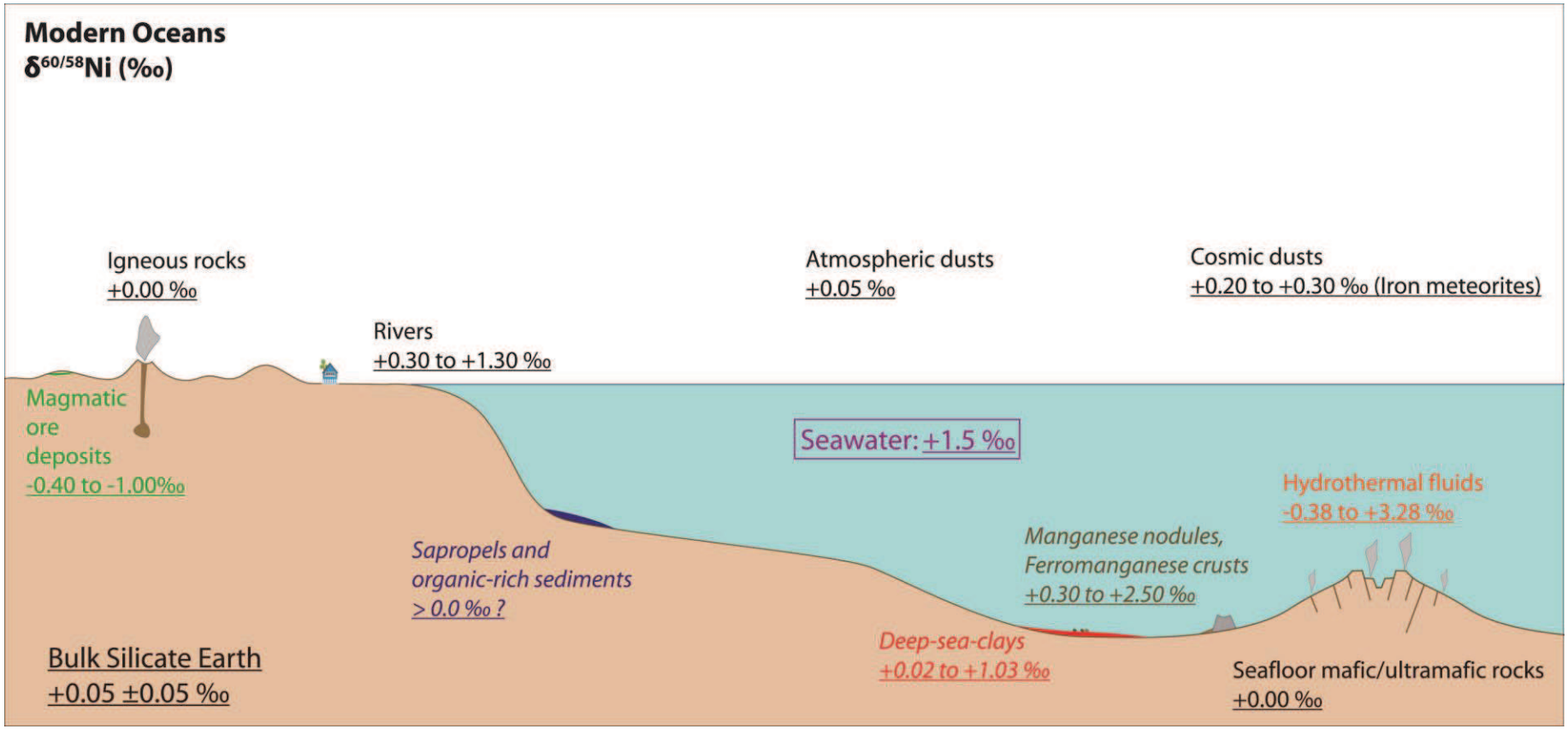

Figure C.3b : *Coupe schématique à travers un bassin océanique indiquant les compositions isotopiques en Ni des différences réservoirs sources et puits de Ni dans les océans. Les puits sont distingués des sources par un figuré en italique. Les données reportées proviennent de Gall et a. (2012), Gall et al. (2013), Gueguen et al. (2013). Les valeurs reportées pour les sulfures hydrothermaux (chalcopyrites) sont des données encore non publiées.*

Chapitre IV - Stratigraphie haute résolution dans des encroûtements de fer-manganèse de l'Océan Pacifique : minéralogie, géochimie et composition isotopique du Ni

Chapter IV – Mineralogy, elemental geochemistry and Ni isotope composition of ferromanganese crusts from the North and South Pacific Oceans

Avant-propos :

Les dépôts de fer-manganèse ont des vitesses de croissance très lentes (de l'ordre de 1 à 6 mm/Ma) et certains enregistrent donc jusqu'à 60 Ma constituant ainsi une archive géologique de l'évolution de la composition isotopique des métaux dissous dans l'eau de mer au cours du Cénozoïque. Au cours de ce projet de thèse, Gall et al. (2013) ont publié une série temporelle d'isotopie du Ni réalisée dans un encroûtement du Pacifique qui montre une excursion en isotopes légers du Ni et qu'ils expliquent comme étant le résultat d'un apport hydrothermal dont la composition isotopique en Ni serait enrichie en isotopes légers par rapport au Ni l'eau de mer. Cependant, nos résultats des compositions isotopiques en Ni dans différents dépôts métallifères marins hydrogénés et hydrothermaux dans le chapitre III, nous ont permis de montrer que la variabilité des compositions isotopiques en Ni s'expliquait par les processus de formation et d'enrichissement des métaux dans les phases d'oxyhydroxydes de Mn et de Fe, au cours lesquels la cinétique de formation des dépôts joue un rôle prédominant, et non pas par des variations des sources en Ni.

Avant la publication des résultats de Gall et a. (2013) nous avions mis en place une étude sur des séries temporelles d'encroûtements de fer-manganèse afin d'évaluer la variabilité isotopique du Ni au cours du temps et de les comparer aux résultats obtenus sur les échantillons roche totale (chapitre III), mais aussi aux résultats de Gall et al. (2013) publiés entre temps. Ainsi, ce chapitre IV a pour objectif d'étudier quatre séries temporelles d'isotopie en Ni effectuées sur des échantillons d'encroûtements de fer-manganèse de l'Océan Pacifique. Deux échantillons proviennent de l'Océan Pacifique Nord (mont sous-marin Apuupuu dans l'archipel d'Hawaii), tandis que les deux autres encroûtements ont été échantillonnés dans l'Océan Pacifique Sud (archipel de Tahiti). Pour établir des profils temporels des variations de la géochimie élémentaire et isotopique dans chacune des croûtes, un échantillonnage haute-résolution a été réalisé tous les 1 à 2 millimètres.

Abstract:

Four new ferromanganese (Fe-Mn) crusts from the North and South Pacific Oceans near Hawaii and Tahiti areas were characterized for their mineralogy, elemental geochemistry and Ni isotope composition. This study aims at unlocking whether Ni isotope composition of Fe-Mn crusts could (1) trace the evolution of Ni biogeochemical cycling in the ocean and (2) provide new tracers for understanding formation mechanisms and metal enrichment processes in these deposits. Analyses were performed on subsamples collected at a high resolution millimeter scale in order to assess the time-resolved record of Ni isotopes over the last ~17 Ma.

Samples were dated and growth rates were determined using a combination of cosmogenic ^{10}Be isotope and Co concentration analyses. Average $\delta^{60/58}$Ni values of +1.72 ±0.18 ‰ (2sd) and +1.87 ±0.10 ‰ were found in two Fe-Mn crusts in the South Pacific, while North Pacific Fe-Mn crusts yield averages of +1.64 ±0.18 ‰ and +1.79 ±0.13 ‰. These results indicate that Fe-Mn crusts recorded Pacific deep waters with fairly homogenous Ni isotopes over the last ~10 Ma. At the base of one sample (older part of the crust) from the South Pacific and directly in contact with its altered substrate, anomalously low $\delta^{60/58}$Ni values were observed, from +1.01 to +0.25 ‰. Those layers are also characterized by high ^{10}Be/^{9}Be ratios correlating with elevated Ni/Mn ratios. Such patterns are best explained by the local inputs of late stage halmyrolitic fluids that formed through seawater circulation within fractures in the underlying substrate. Those results do not confirm any effect of dust deposition and hydrothermal venting in affecting Ni isotope composition of Fe-Mn crusts, but prompt for additional studies of Ni isotope fractionation processes during Ni uptake and enrichment in Fe-Mn deposits.

1. Introduction

Ferromanganese (Fe-Mn) crusts are metal-rich marine mineral deposits forming through slow accumulation of Fe- and Mn-oxides colloids from seawater (Craig et al. 1982; Halbach et al. 1983; Hein et al. 1988; Hein et al. 1992; Koschinsky and Halbach 1995). Fe-Mn crusts are particularly abundant in the Northwest Pacific (e.g. the Pacific Prime Zone (Hein et al. 2013)) and South Central Pacific (e.g. French Polynesia) in connection with the formation and aging of Jurassic to Cretaceous volcanic seamounts (Halbach et al. 1983; Halbach and Puteanus 1984; Halbach et al. 1984; Aplin and Cronan 1985; De Carlo et al. 1987; Hein et al. 1988; Hein et al. 1992).

Enrichment of Fe-Mn crusts in transition and high-technology metals draw the attention of mining industries as potential resources in Ni, Co, Te, REE and Pt for instance (Hein et al. 2013). In particular, many studies have identified that South Pacific Fe-Mn crusts, especially in the French Polynesia area, are among the richest in Co, Te and Pt, although the inventory of crusts deposits is far from complete (Halbach et al. 1984; Pichocki and Hoffert 1987; Hein et al. 1988; Halbach et al. 1989; Lesuave et al. 1989; ISA 2002; Hein et al. 2003).

Because of their very slow growth rates, many studies have been dedicated to understanding the controlling factors of the formation of Fe-Mn crusts and enrichment processes of trace metals in relation to important paleoceanographic processes (Koschinsky and Halbach 1995; Bau et al. 1996; Koschinsky et al. 1997; Hein et al. 2003; Koschinsky and Hein 2003; Koschinsky et al. 2003). Sources of metals in Fe-Mn crusts include essentially dissolved trace metals in seawater that are scavenged onto Fe- and Mn-colloids forming in the water column. Traditionally, the distinction between hydrothermal and hydrogenous

enrichment of metals in Fe-Mn crusts has been made using trace element geochemical signatures (Bonatti and Joensuu 1966; Bonatti et al. 1972c; De Carlo et al. 1987; Nicholson et al. 1997; Hein et al. 2012). The importance of oceanographic parameters such as depth of the oxygen-minimum-zone (OMZ), the calcite-compensation-depth (CCD) and phosphatization events that occurred during the Cenozoic at 39-34 Ma and 27-21 Ma has also been well-recognized (Hein et al. 1993).

In rare case, metallic cosmic spherules were reported in some South Pacific crusts (Kosakevitch 1987; Halbach et al. 1989; Lesuave et al. 1989; Kosakevitch and Disnar 1997) but it remains unclear whether such extra-terrestrial input could affect bulk Fe-Mn crusts composition. While clear evidences of cosmic contributions are inferred from He isotopes (Stuart and Lee 2012), the contribution of cosmic spherules to the Pt and Ni budget in Fe-Mn crusts remains uncertain (Halbach et al. 1984; Hein et al. 1988; Halbach et al. 1989).

The radiogenic isotopes geochemistry (Pb, Sr, Nd, Os, Hf) of Fe-Mn crusts has been thoroughly investigated in the past (Frank 2002). This approach allowed to successfully resolve many fundamental paleoceanographic processes such as the evolution of oceanic circulation resulting from opening or closure of oceanic passages (e.g. closure of the Panama gateway, opening of the Drake passage), modifications in continental erosion fluxes after major climatic changes (O'Nions et al. 1998; Reynolds et al. 1999; Frank 2002; Frank et al. 2002; van de Flierdt et al. 2003), and for instance the impact of hydrothermal inputs (van de Flierdt et al. 2004).

More recently, transition metal stable isotope geochemistry (Fe, Zn, Cu, Cd, Tl, Mo, Ni) of Fe-Mn crusts and nodules has been used as promising proxies for paleoceanography (Zhu et al. 2000; Barling et al. 2001; Rehkämper et al. 2002; Siebert et al. 2003; Levasseur et al. 2004; Rehkämper et al. 2004; Anbar and Rouxel 2007; Schmitt et al. 2009; Horner et al. 2010; Nielsen et al. 2011). Because many of transition metals are actively recycled in the water column through biological activity (Fe, Zn, Cd, Cu) while others show conservative behavior (Tl, Mo), metal isotopes are promising proxies to unravel changes in marine biogeochemical cycles through time. However, unlocking the potential of using those new tracers is not straightforward since both changes of metal sources/sinks and internal biogeochemical cycling as well as fractionation processes during precipitation may all contribute to metal isotope variability in Fe-Mn crusts.

In this context, Ni isotopes can be considered as one of the latest metal isotope proxy for paleoceanography (Anbar and Rouxel 2007; Gall et al. 2013). Previous studies by Gall et al. (2013) have shown that in spite of large variations from +0.9 to +2.5 ‰ in $\delta^{60/58}$Ni of Fe-Mn crusts, the absence of Ni isotope variability related to different locations over the oceans implies that the composition of different water masses do not affect Ni isotopes. Further, no relationships were found between Ni isotopes, surface water productivity and bottom water oxygenation. However, Fe-Mn crusts collected closest to continental margins tend to display heavier Ni isotopes values, that were ascribed by the authors to continental Ni input and heavy isotopes fractionation during continental weathering (Gall et al. 2013). In contrast, lower $\delta^{60/58}$Ni values together with Mn enrichment in the Fe-Mn crusts were interpreted as reflecting the extent of hydrothermal input. A follow-up study (chapter III part 1 of this manuscript) investigated a range of Fe-Mn deposits, including hydrothermally-affected deposits and hydrogenous crusts from various locations. Results revealed that Ni isotope variations in these Fe-Mn deposits can be explained by mechanisms of precipitation and enrichment processes produced by different precipitation rates rather than source effects. Seawater Ni incorporated in slow precipitated hydrogenous Fe-Mn crusts is not significantly isotopically fractionated from its seawater source. On the other hand, rapidly precipitated

hydrothermal deposits such as young pure hydrothermal deposits from Loihi seamount (Hawaii, North Pacific) and other mixed hydrothermal/hydrogenous Fe-Mn deposits from the Lau basin (Southwestern Pacific) are fractionated from their source producing a large range of $\delta^{60/58}$Ni values. Interpretations are in agreement with experimental results of isotope fractionation occurring during adsorption of Ni on Fe- and Mn-oxyhydroxides which show enrichment of the mineral phase in light Ni isotopes up to 1 ‰ for Mn-oxide birnessite (Gueguen et al. 2011; Sorensen et al. 2011).

In this study we report a full description of four new Fe-Mn crusts samples collected on seamounts from the North (Hawaii archipelago) and South (Tahiti archipelago) Pacific Oceans. Although crusts from the north central Pacific Ocean have been intensively investigated (Goldstein and Onions 1981; Abouchami et al. 1997; Burton et al. 1997; Ling et al. 1997; O'Nions et al. 1998; Ling et al. 2005), including for their Ni isotope composition (Gall et al. 2013), paleoceanographic studies in the south equatorial Pacific, in particular from the French Polynesia area were generally restricted to a small number of samples (Frank 2002). We first used a combination of XRD analyses on bulk samples of the crusts with elemental mapping of polished section of the four crusts using Electron Microprobe that allows us to establish relationships between transition metal distribution in the crusts and mineralogy of hosting phases. Then, we carried out a subsampling at the millimeter scale to obtain a high-resolution profile of the precipitated Fe- Mn-oxides layers of each crust. After dating the crusts using both Co and cosmogenic isotope ^{10}Be contents, subsamples were analyzed for their elemental geochemistry including major, trace and Rare Earth elements as well as Ni isotope composition. With this detailed characterization of the crusts, we aim to test the following hypothesis, (1) Ni isotope compositions of the upper crust surface between the North and the South Pacific Ocean are similar, which is expected considering the residence time of Ni in seawater, (2) potential secular variations of Ni isotope in seawater should be reflected by co-variations in all the crusts of this study, (3) local Ni isotope variations provide useful proxy for resolving sources and enrichment processes of Ni and other elements such as Pt in relation to OMZ dynamics and potentially cosmic or hydrothermal contribution.

2. Materials and methods

2.1. Sample description: microsampling of Pacific Fe-Mn crusts

The first set of samples comprises two Fe-Mn crusts (samples J2-480 and J2-480-R14) collected on Apuupuu seamount ~50 km south of Hawaii during FeMO 2009 cruise on the R/V Kilo Moana (University of Hawaii) in October 2009 (Figure IV.1). The other set of samples are two Fe-Mn crusts collected in the South Pacific in the Tahiti archipelago during ZEPOLYF2 cruise on the R/V L'Atalante (Ifremer-Genavir) in July-August 1999 (samples ZEP2-DR-05-04 and ZEP2-DR-06-03). While crusts from Tahiti area were recovered by dredging, crusts from Apuupuu seamount were sampled by ROV Jason2 allowing a precise determination of their location and depth. Unfortunately, sample J2-480 could not be located since it originates from several set of samples that got mixed together in ROV sampling basket. Apuupuu Fe-Mn crusts grew on a basaltic substrate but the sample J2-480 was not collected attached with its substrate (Figure IV.1). The total thickness of Apuupuu crusts recovered was ~60 mm thick each. ZEP2-DR05-04 (Tahiti Fe-Mn crusts) substrate consists of altered brecciated basalt mixed with phosphorites and carbonates and was collected attach to the crust. The substrate of crust ZEP2-DR06-03 is assumed to be basaltic but it

was not recovered in the dredges. The total thickness of the crusts is 25 mm and 90 mm for ZEP2-DR05-04 and ZEP2-DR06-03 respectively. The smooth top surface indicating the part in contact with seawater allows unambiguous determination of their growth direction and top to bottom. Accordingly, each crust is defined by its “Outer” and “Inner” regions which correspond to the top/youngest and the bottom/oldest crust respectively (Figure IV.2).

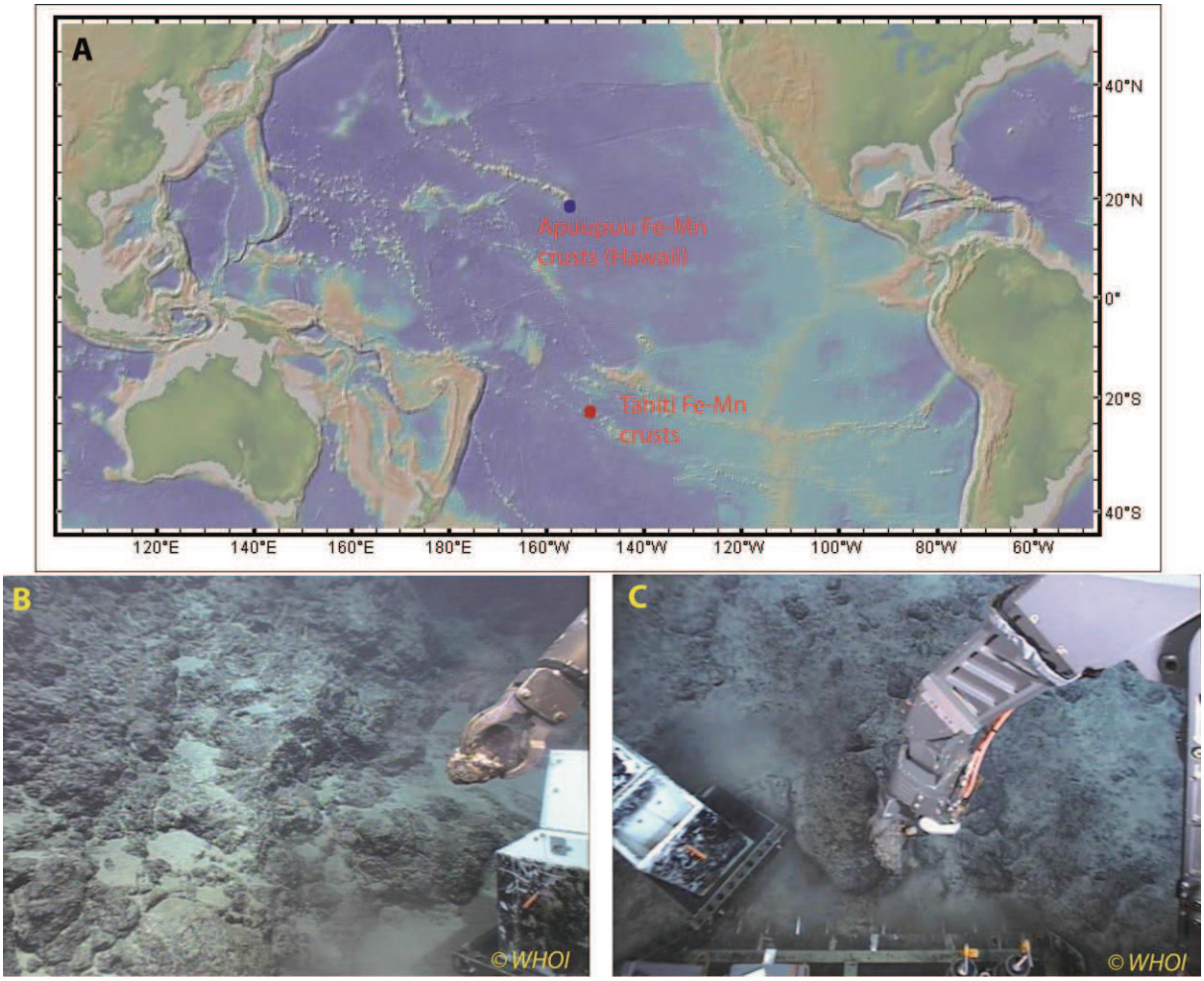

Figure IV.1*: Locations of Apuupuu and Tahiti Fe-Mn crusts (panel A) and photographs of Apuupuu Fe-Mn crusts sampling (panels B and C) using ROV Jason2 during FeMO cruise 2009 on the R/V Kilo Moana (University of Hawaii). Photographs are courtesy of Woods Hole Oceanographic Institution.*

Each crust was split and a section perpendicular to growth layers (including the top surface) and a total thickness between 20 and 25 mm was embedded in epoxy resin. The surface was polished for petrographic examination and spatially resolved geochemical analysis (see below). Fe-Mn crusts were then subsampled with a microdrilling device (New Wave Micromill®). Lines perpendicular to the direction of growth were drilled by the machine to carry out a high resolution microsampling (from 0 mm to 20-25 mm with 1-2 mm thick layers) of the crust growth layers (Figure IV.2). Powders were subsequently recovered in small plastic centrifuge tubes. The total amount of powder collected in each row was generally between ~30 and 50 mg.

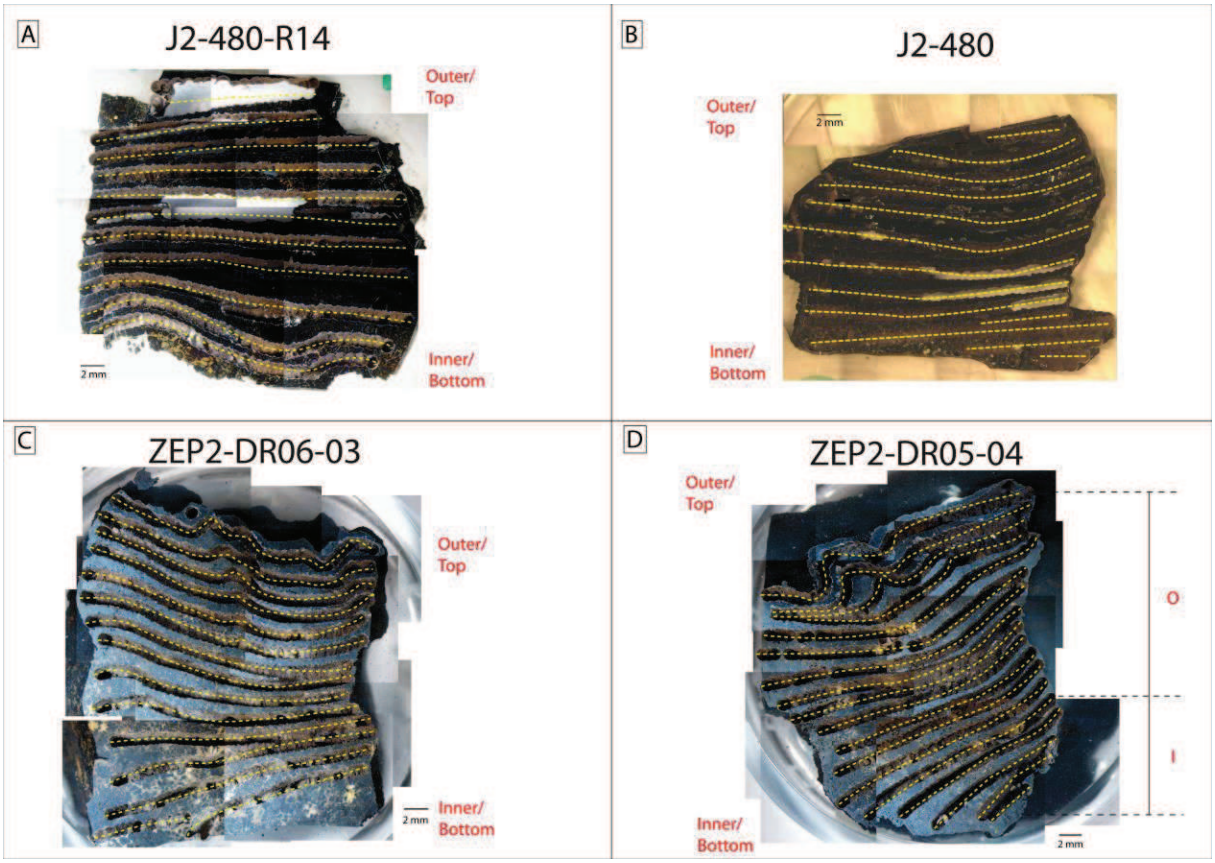

***Figure IV.2**: Photographs of the four Fe-Mn crusts samples after microdrill sampling using Micromill apparatus system. Yellow lines correspond to the positions drilled for making one sample per line drilled.*

2.2. Electron Microprobe analyses

Elemental maps (Mn, Fe, Ni, Cu, Co, Zn) and contents of elements were acquired on carbon coated polished sections using an Electron Microprobe Analyzer (CAMECA SX-100) (Ifremer-CNRS Brest, France) using the following parameters: V=15 kV, I=20 nA, electron beam diameter of 1 µm. Standards used were standards of albite, wollastanite, $MnTiO_2$, Fe, Co, ZnS, apatite, Ni, Cu, Al_2O_3 and Forsterite. Elemental maps were done for selected regions (1.5 mm²) in the crusts (top, middle and bottom regions of each crust) while elements concentration were measured along a complete profile through each crust with a step of ~200 µm.

2.3. Major, trace and Rare Earth elements concentrations

Between 10 and 20 mg of powder were weighed in Teflon vials. Reagents used for digestion and chemical procedures were prepared from sub-boiled distilled concentrated chlorhydric and nitric acid using a Cleanacids® device (Analab, France).

Fe-Mn crusts Subsamples were digested in a mixture of 5 mL concentrated HNO_3 and 5 mL 6 mol/L HCl. Evaporation at 80°C on hot Teflon plates left a residue that was dissolved in 5 mL 6 mol/L HCl and then evaporated to dryness at 80°C. This operation was reiterated once to ensure efficient dissolution of the samples. Residues were dissolved in 10 mL 6 mol/L HCl to be kept as archive solutions.

Major and trace elements, including Rare Earth elements were measured either by ICP-MS-Quadrupole (X-Series, Thermo Scientific) or by HR-ICP-MS (Element 2, Thermo Scientific) at the Pôle-Spectrométrie-Océan (IUEM-Ifremer, Brest, France). Geostandards of manganese nodules Nod-A-1 and Nod-P-1 (US Geological Survey) were systematically analyzed along with samples together with multi-elemental solutions.

2.4. Nickel isotope compositions

Ni isotopes were measured at the Pôle-Spectrométrie-Océan (IUEM-Ifremer, Brest, France) by MC-ICP-MS (Neptune, Thermo Scientific). Ni was corrected from instrumental mass bias using the double-spike method as described in (Gueguen et al. 2013).
Nickel was separated from the geological matrix by ion-exchange chromatography columns involving two steps. First, samples were processed through AG1-X8 in 6 mol/L HCl to separate Ni from Fe, Zn and most of Co and Cu that are retained on the column. Elution of Ni was made in 6 mol/L HCl. Afterwards, Ni was repurified with Ni-spec resin (Eichrom) by complexation of Ni with a DMG molecule allowing elution of the remaining matrix elements. Eluted Ni fractions were evaporated and dissolved in 2% HNO_3 for MC-ICP-MS analyses. The experimental and analytical method is described in details in Gueguen et al. (2013).
Nickel isotopic compositions are reported in delta notation $\delta^{60/58}$Ni (per mil) (1):

$$\delta^{60/58}Ni = (^{60}Ni/^{58}Ni_{sample}/^{60}Ni/^{58}Ni_{NIST986} - 1) \times 1000 \quad (1)$$

Precision on Ni isotope delta values are determined as a two-standard error of the mean (2se) calculated with the 50 run cycles used for double-spike calculations (Gueguen et al. 2013).

2.5. Beryllium isotope compositions

Selected Fe-Mn crusts sub-samples were analyzed for $^{10}Be/^{9}Be$ ratio on a Accelerator Mass Spectrometer (AMS ASTER) at CEREGE (Aix-En-Provence, France) using previously established methods (Bourles et al. 1989; Arnold et al. 2010). Chemical extraction of Be was made using a lixiviation method which consists in a smooth chemical extraction of Be from its matrix.

3. Results

3.1. Age and growth rates of Fe-Mn crusts

The rate of Co precipitation have been widely used to determine age of Fe-Mn crusts because the seawater Co flux is assumed to be constant over time due to its short residence time in seawater and its efficient scavenging by Mn-colloids (Halbach and Puteanus 1984). Therefore, Co concentration in Fe-Mn crusts layers is indicative of their growth rates, with higher concentrations of Co being expected at slower growth rate. We used the following equation (1) described by Frank et al. (1999) for Pacific Fe-Mn crusts to determine the growth rates in mm/Ma:

$$\frac{0.68}{(\mathrm{Co}\% - 0.0012)^{1.67}} \quad (1)$$

Co% is the Co concentration in wt% where 0.0012 wt% corresponds to the detrital contribution of Co removed from the bulk Co concentration.

However, Frank et al. (1999) suggested that different equations should be used according to whether Fe-Mn crusts are rich in Co (>0.24 wt%) or poor in Co (<0.24 wt%), equations (1) and (2) respectively. In fact, Co enrichment in Fe-Mn crusts is sensitive to the water depth of crust formation, with crust forming closest to the OMZ being the most enriched in Co (and other Mn-associated trace elements).

$$\frac{0.25}{\mathrm{Co}\%^{2.69}} \quad (2)$$

Where Co% is the Co concentration in wt%.

Since our samples have Co concentrations higher than 0.24 wt% we used equation (1) for calculating the growth rates of each layer Table IV.1.

An absolute method for dating Fe-Mn crusts is the use of cosmogenic isotope ^{10}Be. Radioactive ^{10}Be is only produced in the atmosphere by spallation of N and O while ^{9}Be occur naturally in the continental crust. It is then rapidly adsorbed onto particles and mixed in the atmosphere to eventually reach the oceans through rainfalls. Therefore, this method is based on the assumption that ^{10}Be is supplied at a constant rate to the oceans implying and so is the ^{10}Be/^{9}Be ratio at the ocean-basin scale (Ku et al. 1990; von Blanckenburg et al. 1996). Therefore, ^{10}Be/^{9}Be ratio should be uniform in the surface layer of Fe-Mn crusts. The advantage of this method is to obtain an absolute age of Fe-Mn crust and to avoid possible hiatuses. However, because ^{10}Be half-life of 1.36 Ma is short, only the youngest 10 Ma can be dated with Be isotopes (Tanaka and Inoue 1979; Segl et al. 1984; Bourles et al. 1989; Morris 1991; Ling et al. 1997; Frank et al. 1999; Frank et al. 2002; Ling et al. 2005; Amend et al. 2011). Preliminary dating of our Fe-Mn crusts subsamples using the Co-dating method indicates that they are not older than 12 Ma, thus validating the use of the Be-dating method for the interval of time considered here. ^{10}Be/^{9}Be ratios are presented in Table IV.2 and plots of logarithms of ^{10}Be/^{9}Be ratios versus depth (mm) are shown in Figure IV.3 for each Fe-Mn crust (panels C, D, E and F).

Table IV.1: Elemental geochemistry (ppm), growth rates and ages of Fe-Mn crusts time-series from Apuupuu (North Pacific) and Tahiti (South Pacific).

Sample Name	ZEP2-DR05-04-L1	ZEP2-DR05-04-L2	ZEP2-DR05-04-L3	ZEP2-DR05-04-L4	ZEP2-DR05-04-L5	ZEP2-DR05-04-L6
	ZEP2-DR05-04 Fe-Mn crust					
Depth in the crust (mm)	0,5	1	2,5	3,5	4,5	6,5
Be*	2,56	2,03	2,63	2,49	1,94	2,90
Na	11516,06	10010,54	10451,61	7568,56	5377,87	6388,71
Mg	9625,64	8389,28	9407,52	7314,16	4918,64	5867,75
Al	3603,52	2809,03	3998,24	3351,20	2867,86	3697,48
Ca	17876,49	14011,96	15973,22	12022,51	8592,64	10926,89
Ti	11864,45	9051,20	10936,70	8808,37	6519,79	7181,12
V	738,08	624,02	618,45	514,44	461,73	495,37
Cr	5,30	5,78	4,95	19,19	21,88	12,83
Mn	170703,76	135257,55	157114,88	110150,45	73693,60	83326,16
Fe	89549,03	81238,56	87718,99	72260,96	65908,65	79551,06
Co	12405,56	8921,98	8495,36	5536,44	3046,53	3749,59
Ni**	2789,98	2482,96	2918,72	2063,49	1287,47	1258,84
Cu	383,49	409,81	563,67	435,20	327,79	421,80
Zn	394,52	334,55	417,31	327,16	229,26	260,62
Rb	1,64	1,29	1,44	1,07	1,00	1,08
Sr	1114,07	878,77	1054,36	776,86	520,60	679,28
Y	120,03	80,44	90,59	63,84	47,25	66,83
Nb	84,64	61,51	67,93	42,17	44,35	56,51
Mo	334,90	284,04	310,67	204,20	127,42	160,86
Cd	3,90	3,11	3,41	2,52	1,51	1,75
Te	98,48	71,26	74,50	66,88	45,71	54,26
Ba	818,49	744,90	972,99	764,51	538,53	750,59
La	120,18	83,52	98,11	74,32	53,21	73,73
Ce	575,17	456,24	614,96	564,05	420,18	558,12
Pr	23,68	15,04	17,64	13,47	9,74	13,38
Nd	102,39	64,09	73,89	54,53	39,99	54,31
Sm	20,26	12,13	14,07	10,54	7,39	10,37
Eu	4,84	2,93	3,49	2,60	1,86	2,52
Gd	25,86	16,60	18,96	13,35	9,89	13,27
Tb	3,76	2,40	2,70	1,97	1,38	1,88
Dy	25,06	15,92	17,83	12,57	8,84	11,95
Ho	5,55	3,67	4,10	2,84	2,01	2,65
Er	17,19	11,67	13,15	9,13	6,41	8,63
Tm	2,56	1,78	2,05	1,40	0,95	1,31
Yb	15,93	11,31	13,06	9,04	6,24	8,52
Lu	2,57	1,85	2,12	1,49	1,05	1,41
Pt	0,55	0,41	0,51	0,46	0,37	0,57
Tl	142,61	138,04	174,19	128,38	80,16	91,91
Pb	1530,85	1155,28	1299,81	869,81	539,22	667,87
Bi	42,03	35,29	36,04	21,64	14,06	18,00
Th	5,09	1,96	3,29	3,73	3,05	4,47
U	12,21	9,26	11,16	7,61	4,99	6,14
Fe/Mn	0,52	0,60	0,56	0,66	0,89	0,95
Ni/Mn	0,02	0,02	0,02	0,02	0,02	0,02
Cu/Mn	0,0022	0,0030	0,0036	0,0040	0,0044	0,0051
Zn/Mn	0,0023	0,0025	0,0027	0,0030	0,0031	0,0031
Co/Mn	0,073	0,066	0,054	0,050	0,041	0,045
Ca/Mn	0,10	0,10	0,10	0,11	0,12	0,13
Age (Ma)***	1,1	1,7	3,3	3,9	4,1	4,6

* Concentrations (µg/g) were measured by ICP-MS-Quad or by HR-ICP-MS (Element 2).

** Ni concentration (µg/g) were first measured by ICP-MS-Quad and then recalculated by isotopic dilution after analysis through MC-ICP-MS. The latter value is reported.

*** Ages (Ma) determined with Be isotopes with the exception of crust ZEP2-DR05-04 dated with the Co-method (see text for explanations).

Table IV.1 continued

Sample Name	ZEP2-DR05-04-L7	ZEP2-DR05-04-L8	ZEP2-DR05-04-L9	ZEP2-DR05-04-L10	ZEP2-DR05-04-L11	ZEP2-DR05-04-L12	ZEP2-DR05-04-L13	ZEP2-DR05-04-L14
Depth in the crust (mm)	8,5	10	11,5	12,5	13,5	15,5	16,5	17,5
Be*	4,06	3,43	3,21	2,95	2,55	2,46	2,20	3,96
Na	9184,71	7656,97	7103,58	6977,27	5579,72	5595,91	5034,85	8821,29
Mg	8244,46	6967,75	6419,17	6375,54	5395,65	5813,52	5079,13	10117,08
Al	4883,48	3916,75	3478,48	3208,23	2884,72	3558,25	3139,85	6808,87
Ca	19371,53	13742,83	17581,82	11674,68	10238,24	11680,58	11421,18	21638,22
Ti	9760,48	7784,68	7014,43	6555,22	5668,58	5760,30	5435,50	9820,65
V	684,19	612,77	587,40	571,60	509,98	484,74	492,89	714,69
Cr	8,77	7,14	8,79	7,72	9,11	7,97	7,39	11,34
Mn	127572,98	98375,24	93190,33	99121,13	81876,08	76037,62	73325,96	129795,86
Fe	118962,72	95009,75	86217,81	96233,05	83035,84	74391,36	76851,33	113657,46
Co	5882,24	4781,64	4683,76	5482,58	4225,68	3952,30	3674,81	6345,99
Ni**	1919,10	1464,48	1365,23	1459,44	1239,75	1335,55	1187,98	2753,46
Cu	674,08	576,34	544,88	532,59	475,78	514,88	465,35	947,13
Zn	414,23	340,59	315,96	314,48	260,28	275,62	247,94	528,57
Rb	1,71	1,47	1,30	1,29	1,07	1,43	1,36	2,65
Sr	1075,82	821,62	754,57	728,09	599,07	609,88	539,76	941,82
Y	160,87	91,94	111,13	70,85	64,59	79,09	90,88	209,51
Nb	88,05	71,09	65,61	64,82	53,75	52,34	49,37	96,07
Mo	263,48	214,44	196,32	210,31	173,63	168,25	153,48	269,95
Cd	2,61	1,95	1,94	1,79	1,73	1,56	1,47	3,22
Te	82,31	68,13	65,09	66,86	50,01	47,58	44,50	78,53
Ba	1195,98	942,78	847,22	832,04	661,44	694,95	622,91	1155,53
La	138,26	94,30	97,54	79,19	67,30	72,02	72,14	148,22
Ce	838,37	650,52	611,89	622,32	464,76	475,86	466,56	880,60
Pr	26,52	17,46	18,80	14,11	12,03	13,15	13,64	28,85
Nd	110,66	73,30	78,11	57,63	50,42	55,52	57,78	124,68
Sm	21,40	13,80	15,28	10,95	9,47	10,70	11,04	24,50
Eu	5,29	3,28	3,68	2,62	2,30	2,63	2,72	6,04
Gd	27,46	17,62	19,45	13,94	11,97	13,88	14,83	32,96
Tb	3,87	2,49	2,74	1,95	1,73	1,96	2,06	4,58
Dy	25,22	15,84	17,41	12,60	11,10	12,47	13,32	29,55
Ho	5,53	3,47	3,80	2,76	2,42	2,79	3,00	6,41
Er	17,70	10,83	11,94	8,81	7,80	8,75	9,20	19,76
Tm	2,57	1,69	1,73	1,37	1,14	1,27	1,29	2,77
Yb	16,27	10,55	11,18	8,61	7,48	8,19	8,23	16,99
Lu	2,62	1,74	1,78	1,44	1,23	1,35	1,34	2,76
Pt	1,24	1,09	1,04	1,34	1,30	1,46	1,39	2,34
Tl	139,48	110,85	101,67	102,18	80,88	81,54	72,50	137,51
Pb	1023,32	746,41	696,94	668,56	499,46	532,97	485,82	929,07
Bi	25,72	18,85	17,46	16,84	11,98	11,77	10,91	19,14
Th	7,37	6,48	6,13	7,04	5,32	5,28	5,27	8,58
U	9,06	7,06	6,52	6,30	5,07	5,01	4,62	8,18
Fe/Mn	0,93	0,97	0,93	0,97	1,01	0,98	1,05	0,88
Ni/Mn	0,02	0,01	0,01	0,01	0,02	0,02	0,02	0,02
Cu/Mn	0,0053	0,0059	0,0058	0,0054	0,0058	0,0068	0,0063	0,0073
Zn/Mn	0,0032	0,0035	0,0034	0,0032	0,0032	0,0036	0,0034	0,0041
Co/Mn	0,046	0,049	0,050	0,055	0,052	0,052	0,050	0,049
Ca/Mn	0,15	0,14	0,19	0,12	0,13	0,15	0,16	0,17
Age (Ma)****	5,9	6,5	7,1	7,7	8,0	8,6	8,9	9,6

Table IV.1 continued

Sample Name	ZEP2-DR05-04-L15	ZEP2-DR05-04-L16	ZEP2-DR05-04-L17	ZEP2-DR06-03-L1	ZEP2-DR06-03-L2	ZEP2-DR06-03-L3	ZEP2-DR06-03-L4	ZEP2-DR06-03-L5
				ZEP2-DR06-03 Fe-Mn crust				
Depth in the crust (mm)	19	20	22	0,5	2,5	4	5,5	7,5
Be*	2,15	2,72	1,35	2,00	3,05	2,99	2,61	3,13
Na	5038,25	6958,69	3883,99	8243,44	8944,52	8430,53	6660,28	6033,72
Mg	6131,58	9580,57	8797,92	6443,06	7423,61	6978,35	5627,07	5560,10
Al	3965,54	6069,84	5693,60	2079,23	3483,52	3660,27	2763,99	3620,83
Ca	14892,16	17987,52	16288,85	12804,35	14623,42	14249,51	10725,95	11741,08
Ti	5251,17	8279,93	5089,42	8037,39	10527,08	11516,69	8890,40	10998,71
V	429,38	538,53	434,85	530,02	557,56	528,67	462,29	527,61
Cr	6,63	8,41	4,87	3,80	7,05	6,07	4,49	13,10
Mn	74750,80	101268,09	66381,50	114078,03	123840,28	124559,80	95254,73	77204,56
Fe	69515,62	79857,65	50740,46	78675,93	97722,03	99579,48	83277,75	100889,73
Co	3150,31	5205,01	3321,01	8693,85	7774,21	7225,22	5385,04	3948,10
Ni**	1871,11	3237,84	3395,27	1682,30	1745,22	1776,62	1320,11	1010,56
Cu	554,99	810,49	669,61	293,07	450,57	483,45	393,28	420,46
Zn	337,00	472,68	402,62	254,74	303,50	317,40	254,18	327,81
Rb	1,61	1,57	1,17	0,91	1,36	1,25	0,87	0,96
Sr	503,97	672,46	334,51	812,08	973,87	993,86	764,27	731,22
Y	143,84	138,21	134,35	82,38	88,81	80,79	53,37	48,28
Nb	51,18	92,48	65,99	61,35	85,18	72,75	54,61	56,63
Mo	138,56	190,18	90,10	227,08	223,01	212,91	162,25	146,63
Cd	1,90	3,31	2,66	2,43	2,69	2,55	2,03	1,81
Te	42,56	66,94	35,29	75,31	77,12	71,38	57,18	48,82
Ba	631,64	937,30	487,05	636,58	928,64	1004,81	796,54	801,52
La	91,74	103,81	81,86	97,91	107,41	104,35	76,59	71,11
Ce	474,93	681,32	303,74	469,90	619,38	653,31	516,86	406,69
Pr	18,92	20,38	17,76	18,65	18,98	18,48	13,89	13,70
Nd	84,07	89,12	79,78	80,80	81,57	77,71	57,59	56,27
Sm	16,60	17,64	16,57	15,43	15,21	14,64	10,95	10,85
Eu	4,09	4,25	3,92	3,86	3,72	3,60	2,63	2,70
Gd	22,81	23,40	21,29	20,34	20,61	19,29	13,91	13,15
Tb	3,10	3,17	2,87	2,86	3,01	2,83	1,99	1,96
Dy	19,39	20,35	18,52	18,89	19,91	18,80	13,20	12,28
Ho	4,29	4,53	3,83	4,19	4,44	4,13	2,79	2,53
Er	12,96	13,76	11,49	12,99	14,06	13,03	8,79	8,05
Tm	1,76	1,91	1,53	1,94	2,08	1,94	1,37	1,21
Yb	10,68	11,62	9,15	12,08	13,29	12,57	8,67	7,67
Lu	1,70	1,88	1,45	1,90	2,18	1,99	1,35	1,21
Pt	1,19	1,72	0,91	0,43	0,52	0,59	0,41	0,54
Tl	77,66	110,76	68,74	98,80	115,37	117,77	92,73	84,43
Pb	510,41	900,97	561,32	1250,95	1411,38	1302,20	884,26	855,95
Bi	10,15	16,17	8,90	30,87	32,72	29,11	20,22	14,74
Th	4,38	5,05	2,70	3,85	3,61	4,48	3,60	4,10
U	4,26	6,14	3,15	9,28	11,17	11,59	8,79	7,94
Fe/Mn	0,93	0,79	0,76	0,69	0,79	0,80	0,87	1,31
Ni/Mn	0,03	0,03	0,05	0,01	0,01	0,01	0,01	0,01
Cu/Mn	0,0074	0,0080	0,0101	0,0026	0,0036	0,0039	0,0041	0,0054
Zn/Mn	0,0045	0,0047	0,0061	0,0022	0,0025	0,0025	0,0027	0,0042
Co/Mn	0,042	0,051	0,050	0,076	0,063	0,058	0,057	0,051
Ca/Mn	0,20	0,18	0,25	0,11	0,12	0,11	0,11	0,15
Age (Ma)****	9,9	10,4	10,9	0,91	1,62	1,98	2,29	5,06

Table IV.1 continued

Sample Name	ZEP2-DR06-03-L6	ZEP2-DR06-03-L7	ZEP2-DR06-03-L8	ZEP2-DR06-03-L9	ZEP2-DR06-03-L10	ZEP2-DR06-03-L11	ZEP2-DR06-03-L12	ZEP2-DR06-03-L13	ZEP2-DR06-03-L14
Depth in the crust (mm)	9,5	11	12,5	14	16	17,5	19	21	23,5
Be*	2,33	2,31	2,62	2,42	2,20	2,36	2,11	2,17	2,16
Na	7153,69	6488,98	6559,50	6537,71	5639,14	6306,59	5626,88	6086,24	6189,49
Mg	6181,02	5907,78	6155,12	6858,60	6279,49	6526,04	5808,15	6393,31	5572,60
Al	3793,69	4379,75	4312,25	4276,94	3742,60	3948,31	3288,66	3723,14	3334,94
Ca	21138,72	21185,20	27977,17	48599,65	74906,04	73244,32	71143,99	95379,13	118433,95
Ti	7393,06	7062,45	7047,16	6782,60	5681,73	6102,23	5545,70	5553,54	5061,98
V	444,06	424,68	436,70	469,93	420,20	474,86	451,85	497,54	428,35
Cr	5,43	5,03	5,75	8,66	6,43	6,87	7,23	10,06	6,78
Mn	96945,74	85584,81	83835,88	83554,24	69333,30	74942,06	69638,80	68178,24	62670,27
Fe	82957,17	77826,83	81988,49	85206,60	74146,11	81387,73	70320,04	74625,36	64043,91
Co	4907,48	3552,29	3951,84	4298,64	3551,08	3954,40	3569,71	3728,54	3255,24
Ni**	1687,40	1278,91	1134,34	1145,89	971,82	1015,30	916,40	911,73	881,43
Cu	476,53	479,83	504,18	556,87	492,36	562,28	499,82	516,04	489,84
Zn	258,72	238,61	245,26	257,57	229,85	246,72	221,64	225,52	210,57
Rb	2,10	2,43	2,14	2,02	1,63	1,82	1,42	2,24	1,81
Sr	743,07	713,59	735,85	762,57	736,42	793,58	736,20	808,33	903,28
Y	59,42	76,87	89,11	88,05	114,65	109,86	105,18	138,19	136,71
Nb	53,34	64,35	70,31	74,32	63,12	71,48	62,24	62,04	51,08
Mo	162,51	129,24	133,79	145,54	122,22	137,02	124,96	126,35	117,27
Cd	2,16	1,90	1,89	2,26	2,15	2,14	1,80	1,97	1,52
Te	69,18	72,13	64,89	61,46	54,88	61,78	53,03	56,46	50,75
Ba	693,71	711,94	725,86	707,17	588,46	643,67	563,69	560,74	514,98
La	66,91	74,19	80,05	73,68	78,40	76,11	68,73	83,63	79,76
Ce	586,71	649,85	643,38	570,94	462,32	503,84	434,57	455,48	407,92
Pr	13,19	14,65	15,90	14,32	15,56	14,09	12,68	15,53	13,84
Nd	54,03	61,72	67,38	60,08	68,14	61,23	53,91	68,10	60,09
Sm	10,98	12,37	13,43	11,94	13,22	11,83	10,33	12,97	11,45
Eu	2,74	2,95	3,31	2,93	3,26	2,95	2,64	3,27	2,90
Gd	14,46	16,13	17,61	16,18	18,19	16,18	14,88	18,54	16,24
Tb	1,99	2,21	2,42	2,20	2,53	2,22	2,02	2,56	2,30
Dy	12,29	14,06	15,20	13,95	16,16	14,88	13,63	17,05	15,39
Ho	2,56	2,95	3,32	3,06	3,64	3,40	3,12	3,90	3,67
Er	8,02	9,17	10,03	9,61	11,31	10,57	10,00	12,58	11,98
Tm	1,18	1,29	1,42	1,37	1,57	1,54	1,43	1,83	1,74
Yb	7,53	8,19	8,91	8,52	9,85	9,81	9,06	11,19	11,28
Lu	1,20	1,29	1,40	1,38	1,60	1,60	1,51	1,90	1,89
Pt	0,49	0,55	0,61	0,73	0,68	0,66	0,65	0,69	0,51
Tl	105,98	90,48	85,40	84,53	69,09	74,73	63,81	64,80	59,12
Pb	617,61	566,20	571,05	549,81	461,04	487,17	423,44	427,70	386,77
Bi	17,78	14,40	13,25	13,81	11,42	12,26	10,69	10,36	9,10
Th	3,98	5,34	6,37	6,42	5,16	5,80	5,18	5,27	4,60
U	6,89	6,21	6,20	6,12	5,12	5,49	5,16	5,54	5,90
Fe/Mn	0,86	0,91	0,98	1,02	1,07	1,09	1,01	1,09	1,02
Ni/Mn	0,02	0,01	0,01	0,01	0,01	0,01	0,01	0,01	0,01
Cu/Mn	0,0049	0,0056	0,0060	0,0067	0,0071	0,0075	0,0072	0,0076	0,0078
Zn/Mn	0,0027	0,0028	0,0029	0,0031	0,0033	0,0033	0,0032	0,0033	0,0034
Co/Mn	0,051	0,042	0,047	0,051	0,051	0,053	0,051	0,055	0,052
Ca/Mn	0,22	0,25	0,33	0,58	1,08	0,98	1,02	1,40	1,89
Age (Ma)****	5,37	5,68	5,71	5,74	5,78	5,99	6,15	6,37	6,76

Table IV.1 continued

Sample Name	J2-480-R1	J2-480-R2	J2-480-R3	J2-480-R4	J2-480-R5	J2-480-R6	J2-480-R7	J2-480-R8	J2-480-R9
	J2-480 Fe-Mn crust								
Depth in the crust (mm)	0,2	2,5	5	7	9	11	12,5	14	15
Be*	6,09	4,58	4,27	5,31	4,85	5,74	6,06	5,33	6,20
Na	8718,04	8181,36	6916,59	10336,68	13047,76	11742,59	11899,46	11327,52	12527,14
Mg	4852,43	4650,21	3993,54	6017,72	8026,03	6876,58	6614,87	6500,65	7052,56
Al	2794,04	1664,62	1470,93	2132,39	2175,99	2485,02	2828,90	2844,96	4223,65
Ca	67980,28	47308,13	31367,26	45545,18	35155,55	69904,45	84689,85	61954,43	66488,18
Ti	10065,66	8038,99	6220,37	8925,16	8790,39	9251,54	9899,89	7906,16	7231,35
V	nd	nd	nd	nd	nd	nd	nd	nd	nd
Cr	15,29	12,68	10,27	16,93	12,27	11,89	10,21	10,06	15,77
Mn	109540,61	112338,57	99086,12	148710,30	228105,20	198347,20	183225,97	172050,73	152987,96
Fe	92950,82	77974,65	70956,50	95937,64	102712,32	115535,88	108130,18	98357,78	119625,85
Co	1506,98	1725,55	1390,99	2307,61	3798,00	3136,58	3189,14	3216,50	2991,27
Ni**	730,08	1628,63	1354,88	2118,37	3596,79	2813,92	2862,65	3001,06	2816,88
Cu	663,10	842,83	795,08	1204,33	1836,53	1410,92	1330,67	1299,88	1309,75
Zn	582,33	465,23	457,72	613,75	760,86	692,23	708,52	658,82	644,37
Rb	1,34	1,11	0,93	1,34	1,86	1,53	1,79	1,67	1,72
Sr	1259,52	1102,20	929,33	1314,29	1474,91	1496,91	1501,35	1326,58	1454,23
Y	131,54	69,33	49,70	71,14	49,60	84,12	156,57	287,50	255,94
Nb	30,80	22,55	18,52	28,20	26,88	34,80	38,81	27,64	29,71
Mo	298,32	355,42	326,11	465,04	700,77	487,01	416,23	407,16	404,34
Cd	2,82	2,55	2,41	3,83	5,32	3,68	3,79	3,46	3,42
Te	53,83	38,33	35,85	64,65	61,22	74,41	80,11	40,77	41,93
Ba	2253,79	1794,69	1565,31	1857,57	2143,87	1939,78	2071,20	1764,10	1815,66
La	265,26	174,79	131,71	195,76	143,59	223,57	214,34	250,62	235,68
Ce	1129,01	849,07	716,92	1135,14	1047,22	1198,70	1220,79	988,68	1030,68
Pr	37,02	27,20	21,15	31,73	25,91	36,48	30,76	32,69	29,63
Nd	150,04	111,44	86,02	128,28	104,49	148,27	125,40	136,78	125,86
Sm	28,29	21,94	16,91	25,28	21,72	29,89	25,08	26,45	24,03
Eu	7,29	5,68	4,47	6,56	5,75	7,59	6,60	7,01	6,58
Gd	36,29	28,28	22,62	32,37	29,32	36,60	32,07	32,83	31,23
Tb	4,35	3,25	2,50	3,71	3,13	4,23	3,66	4,21	3,92
Dy	28,89	21,04	15,96	23,62	19,46	26,12	23,41	28,95	27,17
Ho	6,23	4,31	3,23	4,74	3,76	5,15	4,95	6,74	6,38
Er	18,92	12,62	9,39	13,67	10,80	14,74	15,02	21,15	20,17
Tm	2,94	1,93	1,44	2,11	1,69	2,25	2,30	3,14	3,04
Yb	22,25	15,08	11,65	16,76	13,79	17,41	17,78	23,30	23,52
Lu	4,07	2,62	1,97	2,86	2,31	3,05	3,36	4,59	4,68
Pt	0,18	0,18	0,19	0,26	0,39	0,37	0,44	0,43	0,52
Tl	44,65	44,48	42,79	74,87	110,38	76,88	81,77	70,76	67,06
Pb	1181,30	853,40	754,72	922,60	863,33	828,73	820,33	636,08	659,36
Bi	60,19	49,19	46,78	76,82	97,93	84,85	62,21	47,48	40,06
Th	16,30	12,37	6,80	5,01	6,05	6,08	6,10	4,28	4,99
U	7,82	7,27	5,91	8,40	9,80	8,88	8,62	6,81	7,23
Fe/Mn	0,85	0,69	0,72	0,65	0,45	0,58	0,59	0,57	0,78
Ni/Mn	0,01	0,01	0,01	0,01	0,02	0,01	0,02	0,02	0,02
Cu/Mn	0,0061	0,0075	0,0080	0,0081	0,0081	0,0071	0,0073	0,0076	0,0086
Zn/Mn	0,0053	0,0041	0,0046	0,0041	0,0033	0,0035	0,0039	0,0038	0,0042
Co/Mn	0,014	0,015	0,014	0,016	0,017	0,016	0,017	0,019	0,020
Ca/Mn	0,62	0,42	0,32	0,31	0,15	0,35	0,46	0,36	0,43
Age (Ma)****	6,98	7,12	7,24	7,53	7,97	8,28	8,45	8,56	8,73

Table IV.1 continued

Sample Name	J2-480-R10	J2-480-R12	J2-480-R14-L11	J2-480-R14-L10	J2-480-R14-L9	J2-480-R14-L8	J2-480-R14-L7	J2-480-R14-L6
			J2-480-R14 Fe-Mn crust					
Depth in the crust (mm)	16,5	19	0,2	3	5	7	9	10
Be*	6,14	4,74	3,62	3,74	4,01	3,88	3,50	3,64
Na	8836,13	9805,70	12450,24	10764,79	11909,29	12091,53	12042,39	12375,34
Mg	5582,13	5268,54	7670,55	6725,16	7493,76	7656,60	7258,00	7813,43
Al	9244,67	13203,80	4951,52	5972,49	5935,92	6500,35	3440,72	2179,53
Ca	59716,14	30825,60	13237,31	11778,13	13635,20	13693,15	13502,70	14657,70
Ti	4765,19	4498,54	9778,53	9718,56	10458,31	9819,39	9087,31	8542,22
V	nd	nd	nd	nd	nd	nd	nd	nd
Cr	15,28	98,21	17,79	15,06	24,09	12,82	14,67	16,85
Mn	80126,10	61627,34	155571,37	129458,14	146604,20	173068,86	160345,70	173808,81
Fe	115375,81	90270,15	118162,54	107305,67	108699,34	103644,49	93703,31	97090,46
Co	1288,86	1201,63	3047,64	2553,91	3035,96	3325,29	3443,26	3819,37
Ni**	1224,80	1189,54	2884,85	2426,55	2969,15	3147,40	3275,24	3735,55
Cu	888,09	779,32	711,90	707,38	841,03	910,89	948,37	1037,06
Zn	432,22	293,05	850,07	944,82	923,62	630,20	575,97	734,70
Rb	3,65	6,96	3,35	3,57	3,58	3,95	2,24	1,88
Sr	1038,81	719,05	1038,48	912,96	1014,19	1019,48	1028,24	1100,27
Y	166,87	252,98	96,47	81,86	89,23	106,17	68,20	60,79
Nb	30,43	27,74	55,76	51,09	55,03	58,99	62,10	58,12
Mo	160,85	109,86	360,08	274,07	333,24	360,35	423,15	515,99
Cd	1,85	1,62	3,70	3,45	4,25	4,08	4,99	4,79
Te	29,63	18,35	35,34	37,98	45,47	43,04	45,87	43,36
Ba	1327,07	1041,73	1262,56	1240,48	1297,39	1478,82	1245,17	1289,93
La	153,92	181,93	174,94	154,50	170,15	166,39	152,67	150,22
Ce	694,64	487,45	694,55	720,11	796,92	757,59	792,67	710,98
Pr	16,72	24,93	29,91	26,72	29,72	29,25	26,38	24,64
Nd	71,31	112,10	127,53	113,22	126,21	125,09	109,95	101,47
Sm	13,51	21,10	26,89	23,99	26,75	26,96	22,81	21,11
Eu	3,90	5,92	6,92	6,25	6,87	6,99	5,90	5,42
Gd	19,04	26,27	31,75	28,71	31,70	32,18	27,83	26,00
Tb	2,28	3,68	4,27	3,78	4,20	4,19	3,51	3,20
Dy	15,93	26,58	28,56	25,18	27,57	27,48	22,92	20,69
Ho	3,86	6,38	5,92	5,21	5,67	5,64	4,67	4,19
Er	12,68	19,99	17,50	15,19	16,58	16,39	13,68	12,33
Tm	1,98	2,90	2,65	2,30	2,50	2,45	2,08	1,89
Yb	16,57	22,44	20,00	17,24	18,66	17,76	16,56	15,33
Lu	3,32	4,20	3,56	3,10	3,35	3,23	2,83	2,60
Pt	0,38	0,34	0,25	0,27	0,32	0,39	0,41	0,36
Tl	34,39	19,59	89,43	80,95	100,08	100,03	115,03	120,30
Pb	502,51	345,03	962,76	822,27	852,62	779,04	763,94	724,58
Bi	17,76	12,81	29,01	34,23	42,06	33,50	29,30	24,29
Th	5,29	2,62	9,34	9,58	10,35	10,60	8,35	6,83
U	5,54	2,61	8,64	7,95	8,42	7,86	7,78	7,89
Fe/Mn	1,44	1,46	0,76	0,83	0,74	0,60	0,58	0,56
Ni/Mn	0,02	0,02	0,02	0,02	0,02	0,02	0,02	0,02
Cu/Mn	0,0111	0,0126	0,0046	0,0055	0,0057	0,0053	0,0059	0,0060
Zn/Mn	0,0054	0,0048	0,0055	0,0073	0,0063	0,0036	0,0036	0,0042
Co/Mn	0,016	0,019	0,020	0,020	0,021	0,019	0,021	0,022
Ca/Mn	0,75	0,34	0,09	0,09	0,09	0,08	0,08	0,08
Age (Ma)****	8,78	11,78	3,61	4,40	6,60	7,65	8,68	9,35

Table IV.1 continued

Sample Name	J2-480-R14-L5	J2-480-R14-L4	J2-480-R14-L3	J2-480-R14-L2	J2-480-R14-L1	NOD-A-1	NOD-P-1
						USGS geostandards	
Depth in the crust (mm)	12	14	16	18	20	-	-
Be*	5,04	4,03	4,49	3,94	3,89	4,95	2,10
Na	11598,97	11539,29	12254,52	10316,05	9364,10	7475,53	15422,48
Mg	7556,15	7507,88	7995,82	7180,37	6791,08	27334,68	18871,97
Al	2917,36	2457,84	3467,67	4445,29	5480,46	20288,88	22404,23
Ca	13802,25	14323,08	14248,87	12142,49	11554,43	102495,77	20563,69
Ti	8317,13	6754,94	5845,07	5019,57	4522,32	3505,68	2897,88
V	nd	nd	nd	nd	nd	686,49	504,78
Cr	12,95	18,98	12,24	16,06	19,99	24,25	14,20
Mn	137373,43	163956,78	185050,41	131796,99	112307,53	176519,44	282228,26
Fe	105311,22	100040,04	117607,51	104419,30	89638,05	101253,11	52519,07
Co	3156,01	3447,33	3680,14	3047,59	2737,12	3302,00	2279,90
Ni**	3217,37	3252,38	3429,85	2881,37	2631,97	4577,88	10806,03
Cu	1007,97	1060,67	1192,98	1074,65	950,16	1117,42	11490,89
Zn	592,89	758,27	649,69	551,59	471,40	625,76	1557,05
Rb	3,25	1,88	2,46	3,50	5,28	9,35	21,82
Sr	1093,95	1086,93	1097,40	901,99	786,52	1468,30	620,54
Y	66,40	48,36	44,95	52,98	80,43	106,43	80,30
Nb	73,39	57,25	58,64	49,81	48,03	304,35	265,52
Mo	457,98	542,40	511,05	376,31	307,68	46,89	19,84
Cd	4,29	4,00	4,15	3,51	3,43	334,70	575,70
Te	40,81	35,04	37,87	31,19	26,48	33,46	5,02
Ba	1328,99	1291,86	1370,70	1467,23	1476,94	1412,51	2420,03
La	147,27	123,92	103,27	82,17	78,60	91,23	90,53
Ce	700,25	567,14	580,46	486,55	417,89	669,47	290,27
Pr	28,85	21,66	17,91	14,79	17,01	21,84	30,06
Nd	119,62	88,94	74,04	63,08	75,37	90,99	126,79
Sm	25,31	18,66	15,67	13,53	16,23	20,05	31,27
Eu	6,48	4,87	4,19	3,80	4,62	4,79	7,40
Gd	30,82	23,98	20,72	19,14	22,83	23,70	30,31
Tb	3,71	2,72	2,32	2,04	2,49	3,48	4,51
Dy	23,63	17,29	14,84	13,18	16,19	20,73	25,60
Ho	4,74	3,45	2,99	2,70	3,37	4,21	4,64
Er	13,72	10,05	8,76	7,84	9,66	12,85	12,94
Tm	2,09	1,55	1,35	1,18	1,38	1,86	1,89
Yb	15,99	13,49	10,71	10,24	12,05	11,75	12,19
Lu	2,82	2,18	1,86	1,68	1,93	1,89	1,83
Pt	0,39	0,36	0,48	0,43	0,43	0,64	0,18
Tl	99,39	111,84	102,75	84,28	69,28	93,88	191,63
Pb	672,69	557,25	487,51	366,05	292,63	676,13	370,34
Bi	20,34	17,51	15,00	12,64	11,99	8,32	4,73
Th	7,88	5,87	5,46	5,55	4,84	18,06	14,00
U	8,35	7,02	5,81	5,15	4,48	5,51	3,59
Fe/Mn	0,77	0,61	0,64	0,79	0,80	0,57	0,19
Ni/Mn	0,02	0,02	0,02	0,02	0,02	0,03	0,04
Cu/Mn	0,0073	0,0065	0,0064	0,0082	0,0085	0,0063	0,0407
Zn/Mn	0,0043	0,0046	0,0035	0,0042	0,0042	0,0035	0,0055
Co/Mn	0,023	0,021	0,020	0,023	0,024	0,019	0,008
Ca/Mn	0,10	0,09	0,08	0,09	0,10	0,58	0,07
Age (Ma)****	10,35	11,27	12,00	12,95	16,61	-	-

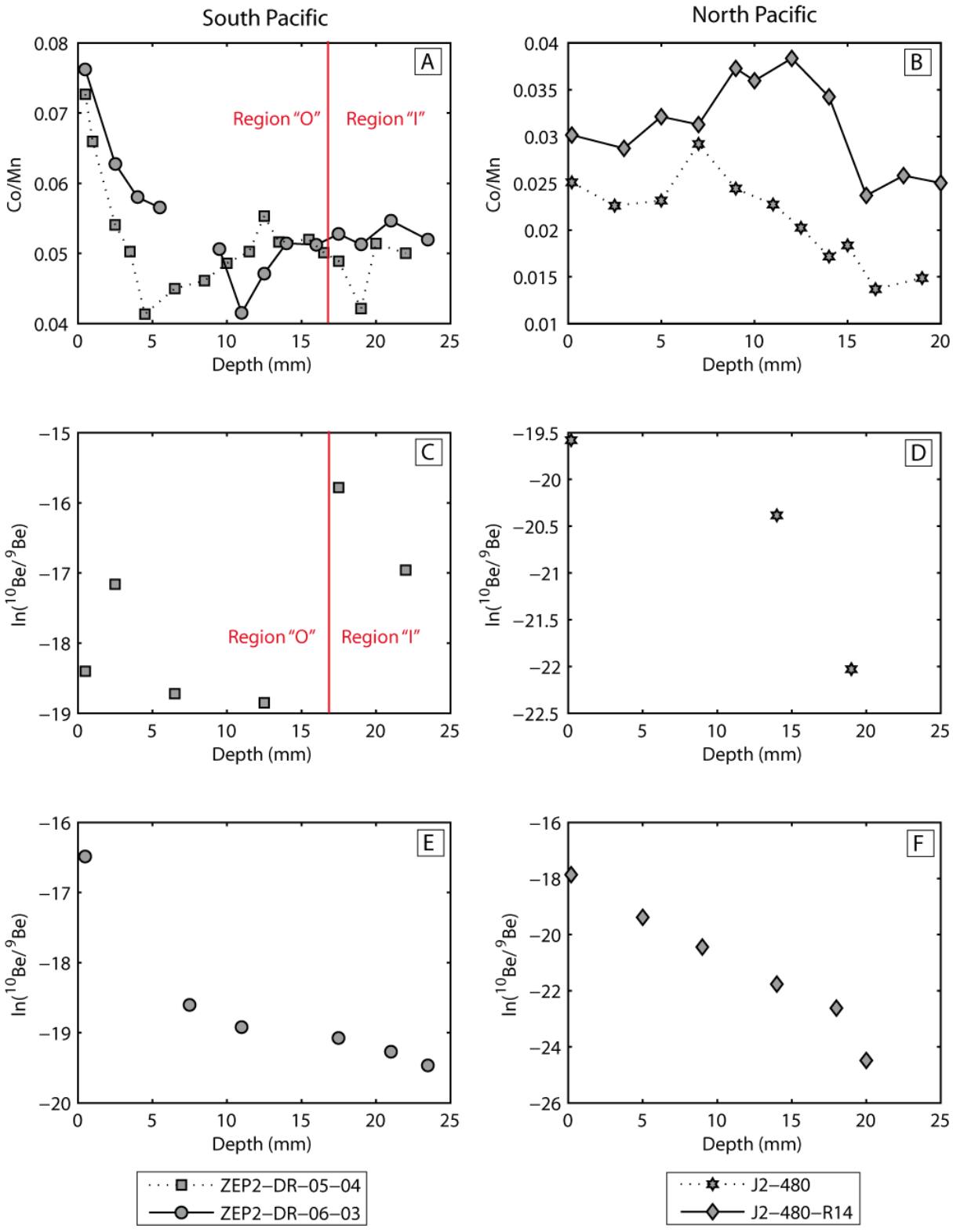

***Figure IV.3**: Plots of Co/Mn ratios versus depth in the crusts (mm) in Tahiti Fe-Mn crusts (South Pacific) (panel A) and Apuupuu Fe-Mn crusts (North Pacific) (panel B) showing variations in the growth rates. The lower panels show the logarithm of $^{10}Be/^{9}Be$ ratios vs depth inTahiti crusts (panels C and E) and in Apuupuu Fe-Mn crusts (panels D and F). The red line delimits region "I" and region "O" of ZEP2-DR05-04 crust identified in Figure IV.2.*

$^{10}Be/^{9}Be$ ratios were not measured on all subsamples, but only on a selection comprising at least the top and bottom of the crust (Figure IV.3). These data provide absolutes ages at different depth in the crust, while Co dating method allows to determining the different growth rates and ages between those depths. We used an initial $^{10}Be/^{9}Be$ ratio of $1.1x10^{-7}$ (von Blanckenburg et al. 1996) for calculating absolute ages. Then, combining growth rates calculated with Co concentrations and absolute ages determined with Be isotopes of some subsamples of the crusts we calculated ages of the remaining subsamples.

However, one sample, ZEP2-DR05-04 (Tahiti, South Pacific), displays anomalously high $^{10}Be/^{9}Be$ ratios in the deeper, i.e. older, part of the crust (Figure IV.3, panel C). Potential reasons for the aberrant youth of the crust are explained below. Therefore, we cautiously avoid using these data for dating the crust and we preferred reporting Co-dated ages. In addition, even if the crusts are dated by two different methods the geochemical time-series of the two South Pacific Fe-Mn crusts is very similar which validates this strategy of using Co concentrations for dating ZEP2-DR05-04.

Subsamples of J2-480 span a range from 7.0 to 11.8 Ma (Be-dating) and J2-480-R14 from 4.5 to 8.6 Ma (be-dating). Growth rates are 4.4 mm/Ma for J2-480, 0.5 mm/Ma and 1.4 mm/Ma for J2-480-R14. ^{10}Be dating on ZEP2-DR06-03 indicates a range from 0.9 to 6.8 Ma with growth rates between of 1.9 and 10.5 mm/Ma. These growth rates are in the range reported in the literature for hydrogenetic Fe-Mn deposits (Frank et al. 1999; Frank 2002). As a means of comparison, high growth rates comprised between ~5 and ~9 mm/Ma were calculated for hydrothermally-affected hydrogenous Fe-Mn crusts from the Bauer Basin (van de Flierdt et al. 2004).

Table IV.2: Ni isotope composition (‰) in Fe-Mn crusts time-series from Apuupuu (North Pacific) and Tahiti (South Pacific).

Sample name	Depth (mm) in the crust	$\delta^{60/58}$Ni	2se*	Growth rates (mm/Ma)***	Age (Ma) Co-dating	^{10}Be/^{9}Be	Age (Ma) (Be-dating)
ZEP2-DR05-04 Fe-Mn crust							
ZEP2-DR05-04-L1	0,5	1,89	0,04	0,5	1,1	1,02E-08	-
ZEP2-DR05-04-L2	1	1,82	0,05	0,8	1,7	na	-
ZEP2-DR05-04-L3	2,5	1,69	0,03	0,9	3,3	na	-
ZEP2-DR05-04-L4	3,5	1,71	0,03	1,8	3,9	na	-
ZEP2-DR05-04-L5	4,5	1,65	0,02	5,0	4,1	na	-
ZEP2-DR05-04-L6	6,5	1,75	0,04	3,5	4,6	7,41E-09	-
ZEP2-DR05-04-L7	8,5	1,74	0,03	1,7	5,9	na	-
ZEP2-DR05-04-L8	10	1,81	0,03	2,3	6,5	na	-
ZEP2-DR05-04-L9	11,5	1,72	0,03	2,4	7,1	na	-
ZEP2-DR05-04-L10	12,5	1,67	0,04	1,9	7,7	6,50E-09	-
ZEP2-DR05-04-L11	13,5	1,63	0,03	2,9	8,0	na	-
ZEP2-DR05-04-L12	15,5	1,54	0,03	3,2	8,6	na	-
ZEP2-DR05-04-L13	16,5	1,69	0,02	3,6	8,9	na	-
ZEP2-DR05-04-L14	17,5	1,08	0,03	1,5	9,6	1,40E-07	-
ZEP2-DR05-04-L15	19	1,01	0,04	4,7	9,9	na	-
ZEP2-DR05-04-L16	20	0,63	0,04	2,0	10,4	na	-
ZEP2-DR05-04-L17	22	0,25	0,05	4,3	10,9	4,31E-08	-
ZEP2-DR06-03 Fe-Mn crust							
ZEP2-DR06-03-L1	0,5	1,88	0,04	0,9	0,9	6,906E-08	0,9
ZEP2-DR06-03-L2	2,5	1,94	0,02	1,0	2,8	na	1,6
ZEP2-DR06-03-L3	4	1,86	0,04	1,2	4,1	na	2,0
ZEP2-DR06-03-L4	5,5	1,89	0,04	1,9	4,9	na	2,3
ZEP2-DR06-03-L5	7,5	1,84	0,03	3,2	5,5	8,349E-09	5,1
ZEP2-DR06-03-L6	9,5	1,95	0,03	2,2	6,4	na	5,4
ZEP2-DR06-03-L7	11	1,89	0,03	3,9	6,8	6,073E-09	5,7
ZEP2-DR06-03-L8	12,5	1,89	0,03	3,2	7,3	na	5,7
ZEP2-DR06-03-L9	14	1,87	0,03	2,8	7,8	na	5,7
ZEP2-DR06-03-L10	16	1,80	0,03	3,9	8,3	na	5,8
ZEP2-DR06-03-L11	17,5	1,84	0,04	3,2	8,8	5,197E-09	6,0
ZEP2-DR06-03-L12	19	1,87	0,04	3,8	9,2	na	6,2
ZEP2-DR06-03-L13	21	1,86	0,03	3,6	9,7	4,280E-09	6,4
ZEP2-DR06-03-L14	23,5	1,75	0,03	4,5	10,3	3,506E-09	6,8

* 2se corresponds to a two-standard error of the mean calculated on the 50 measurement cycles through MC-ICP-MS and corrected using double-spike.

** Duplicate of attack and chemistry procedure.

na: not analyzed

*** Same as Table IV.1.

Table IV.2 continued

Sample name	Depth (mm) in the crust	$\delta^{60/58}$Ni	2se*	Growth rates (mm/Ma)***	Age (Ma) Co-dating	^{10}Be/^{9}Be	Age (Ma) (Be-dating)
J2-480 Fe-Mn crust							
J2-480-R1	0,2	1,72	0,07	5,9	7,0	3,14E-09	7,0
J2-480-R2	2,5	1,74	0,03	6,8	7,3	na	7,1
J2-480-R3	5	1,65	0,07	8,0	7,6	na	7,2
J2-480-R4	7	1,66	0,03	2,8	8,4	na	7,5
J2-480-R5	9	1,67	0,04	1,8	9,5	na	8,0
J2-480-R6	11	1,65	0,07	2,6	10,2	na	8,3
J2-480-R7	12,5	1,72	0,05	3,6	10,7	na	8,5
J2-480-R8	14	1,65	0,03	5,2	10,9	1,40E-09	8,6
J2-480-R9	15	-	-	5,7	11,1	na	8,7
J2-480-R10	16,5	1,64	0,04	27,8	11,2	na	8,8
J2-480-R12	19	1,41	0,03	37,6	11,2	2,71E-10	11,8
J2-480-R14 Fe-Mn crust							
J2-480-R14-L11	0,2	1,94	0,03	5,7	8,4	1,7464E-08	3,6
J2-480-R14-L10	3	1,81	0,03	4,1	8,0	na	4,4
J2-480-R14-L9	5	1,75	0,03	2,7	7,5	3,8068E-09	6,6
J2-480-R14-L8	7	1,78	0,04	1,8	6,8	na	7,7
J2-480-R14-L7	9	1,86	0,03	2,0	5,7	1,32E-09	8,7
J2-480-R14-L6	10	1,80	0,05	1,5	4,7	na	9,3
J2-480-R14-L5	12	1,74	0,05	1,6	4,0	na	10,3
J2-480-R14-L4	14	1,78	0,03	1,9	2,8	3,5312E-10	11,3
J2-480-R14-L3	16	1,81	0,04	2,4	1,7	na	12,0
J2-480-R14-L2	18	1,74	0,03	3,6	0,9	1,50E-10	12,9
J2-480-R14-L1	20	1,70	0,03	2,4	0,1	2,3132E-11	16,6
NOD-P-1	-	0,34	0,03	-	-	-	-
NOD-P-1**	-	0,34	0,03	-	-	-	-
NOD-P-1**	-	0,33	0,03	-	-	-	-
NOD-A-1	-	1,06	0,02	-	-	-	-
NOD-A-1**	-	1,07	0,02	-	-	-	-
NOD-A-1**	-	1,06	0,03	-	-	-	-

3.2. Mineralogy and Electron Mircroprobe analyses

3.2.1. North Pacific Fe-Mn crusts

Mineralogy by X-Ray diffraction does not permit the detection of amorphous phases (Fe-oxyhydroxides and δ-MnO_2 vernadite) which are the predominant mineralogy in Fe-Mn crusts (Koschinsky and Halbach 1995; Koschinsky and Hein 2003). However, it allows to determining the presence of secondary phases like phosphates and carbonates or remnant of detrital phases. Our results indicate a predominance of the Mn-oxide (birnessite and todorokite) and the presence of fluorapatite and traces of detrital phases like plagioclase. Elemental maps produced by Electron Microprobe analyses (EMPA) show that Zn, Cu, Co and notably Ni are associated with Mn - the higher Mn the higher Ni concentration (supplementary Figures S1, S3, appendix 6). In crust J2-480 there is an evolution in the mineral texture. In the top map of the crust Mn-oxides phases and to a lesser extent Fe-oxides form columnar textures while the base is composed of dense successive laminated

Mn-oxides and Fe-oxides layers (supplementary Figure S1, appendix 6). Fe is also located in the matrix surrounding the columnar textures (predominantly composed of Mn) in the form of Fe-oxides “patches”. Extremities of the columnar textures are highly enriched in Mn. Note that regardless of mineral textures, Zn, Cu Co and Ni are always co-located with Mn consistent with the literature (Aplin and Cronan 1985; Hein et al. 1988; Koschinsky and Halbach 1995; Koschinsky and Hein 2003).

The three regions that were mapped in crusts J2-480-R14 (top, middle and bottom) also show an evolution in the mineralogical texture (supplementary Figure S3, appendix 6). The “top” map indicates relatively spaced rounded to columnar textures which are notably composed of Mn-oxides. Fe-rich areas are located as disseminated patches in between the Mn-oxides structures. On the other hand the “bottom” map of the crust shows that it is composed of dense columnar textures with little matrix in between and there are no Fe-rich patches as observed in the top region. Mineral textures in the middle region are essentially constituted by successive layers of Mn-oxides and Fe-oxides.

Elemental profiles made with the Electron Microprobe through the whole crusts implemented with a 200 µm step show similar results in both crusts (supplementary Figure S9 and Tables S1 and S2, appendix 6). In the middle section of J2-480 crust (~2 mm in total), there is an increase in Mn concentrations from ~25 wt% to ~35 wt% and a decrease in Fe concentrations from ~15 wt% to ~8 wt%. Co concentrations do not specifically vary on average, but highest concentrations of ~0.9 wt% in comparison to ~0.5 wt% are found in this region. Ni and Cu are also twice more concentrated in this region reaching values of ~0.8 wt% and ~0.3 wt% respectively. Therefore, enrichment in Mn is followed by increasing concentration in Ni, Cu and Co which is consistent with the strong affinity of these elements for the Mn-phase. These variations are not related to any compositional variations in Si, Al, Ti, Mg, P and Ca (supplementary Table S1, appendix 6). In crust J2-480-R14, the increase in transition metals spreads a larger area than in crust J2-480 where the increase in transition metals is more localized (supplementary Table S2, appendix 6). Similar to J2-480 crust, mineral phases that are enriched in Mn are also enriched in Ni, Cu but depleted in Fe.

3.2.2. South pacific Fe-Mn crusts

Similarly to Apuupuu crusts Tahiti crusts are poorly crystallized, and are probably essentially composed of δ-MnO_2. The only detectable phase by XRD is todorokite. An assemblage of δ-MnO_2 and todorokite have been already reported in Fe-Mn crusts from Pacific seamounts (Craig et al. 1982).

ZEP2-DR-06-03 contains some fluorapatite and some calcite. As expected, elemental mapping by Electron Microprobe indicates that Ni, Cu, Zn and Co are systematically associated with Mn whatever the mineral texture (supplementary Figures S5, S7, appendix 6) and Ti and P with Fe (supplementary Figures S6, S8, appendix 6). In crust ZEP2-DR06-03 Mn-oxides (and Fe-oxides) mineralizations forming columnar textures (a composite of Mn- and Fe-oxides) are denser at the top of the crust than in the base. In the top and middle profiles, Fe-oxides also systematically occur in located regions either in between the large Mn-oxides textures or at the extremities of the columnar textures. However, in the middle profile, Fe occurs in very little abundance within the columnar texture in comparison to Mn (supplementary Figure S7, appendix 6). Al and Si are generally present in the matrix outside the Mn-rich textures probably in silicate phases. At the base of the crust the columnar textures are made of successive layers rich in Mn-oxides and rich in Fe-oxides. Some Ca

and P are also present within these columnar structures but the highest abundances are found outside the structures. It is consistent with the presence of fluorapatite and calcite.

The “Inner“ region of crust ZEP2-DR05-04, is made of Mn-oxides columnar structures while the “Outer” region of the crust is composed of dense structures of both Mn-oxides and Fe-oxides mineralizations. In the “Outer” profile, regions with high Ca concentrations are present but outside the columnar structures (supplementary Figure S6, appendix 6). Regardless of mineral textures, partitioning of the elements with either the Mn-phase or the Fe-phase (e.g. Ni and Cu with the Mn-phase) does not vary along the crust.

Electron Microprobe elemental profile through ZEP2-DR06-03 reveals that with the exception of the “Inner“ region of the crust which comprises many phosphate- and carbonate-rich phases as shown by high Ca and P contents of the phases, no specific variations in transition metal contents occur (supplementary Table S4, appendix 6). These data also show that in the ‘Inner” region of the crust some Fe-Mn oxides precipitations are interlayered with phosphates/carbonates.

ZEP2-DR05-04 profile shows interesting results in the “Inner” region of the crust, therefore we defined two different areas named “I” (over a thickness of ~4 mm) and “O” (Figure IV.2). The area “I” shows significantly enriched Mn, Ni, Cu, Zn and Al concentrations in comparison to the area “O”. Mn concentrations vary from an average of ~25 wt% whereas at the base of the crust they reach values of 39 wt%. In this layer, Ni and Cu concentrations reach up to 4 wt% and 0.6 wt% respectively, whereas concentrations in remaining crust generally cluster around 0.5 wt % and 0.1 wt% respectively. Zn is four times more enriched in this region than the other regions of the crust. There is almost a ten-fold increase in Al with concentrations as high as 3 wt% and Mg is five times more enriched. On the other hand, Fe and Ti decrease drastically. Fe concentrations are systematically below 5 wt% in comparison to usual concentrations encountered in the crust of ~12-15 wt% and the decrease in Ti is of the same order as Fe. We observe that the more Mn enriched the more depleted in Fe and enriched in Ni, Cu and Zn consistent with affinity of the elements for the Mn-phase. Finally, Si concentrations are lower and P, Na and Ca do not show any particular variations. Microscope observations (supplementary Figure S11, appendix 6) probably indicate that the restricted region “I” of the crust is formed by newly crystallized Mn-oxides minerals.

In summary, the four Fe-Mn crusts investigated here are dominated by a mineralogical assemblage of Fe- and Mn-oxyhydroxides, while silicates, phosphates and carbonates are present as accessory phases. Unlike Fe that also occur as scattered patches in the “matrix” (the material surrounding the columnar structures), Mn is always present within organized mineral textures (columnar, dense, laminated,…).

3.3. Elemental and isotope geochemistry

3.3.1. North Pacific Fe-Mn crusts

On average, Fe/Mn ratios of different growth layers range from 0.45 to 1.46 (Table IV.1) which is typical of values already reported for hydrogenetic Fe- and Mn-rich deposits (Halbach et al. 1983; De Carlo et al. 1987; Hein et al. 1988; Puteanus and Halbach 1988; Koschinsky and Halbach 1995; Koschinsky et al. 1997). At smaller spatial scale, however, larger variations of Fe/Mn ratios reflect the modal abundances of Fe- and Mn-rich minerals that are heterogeneously distributed among different textures. Typically enriched elements in Fe-Mn crusts like Co and Te yield similar enrichment than other Pacific crusts (Hein et al.

2013), i.e. between ~1200 and ~4000 ppm for Co and between 18 and 80 ppm for Te (Table IV.1). Platinum concentrations range from 0.18 and 0.52 ppm with a gradual decrease from inner towards the top of the crusts especially in J2-480 (Figure IV.4). Finally, Pb concentration patterns are similar in both crusts showing a continuous increase from the base of the crusts (~450 ppm) to the top of the crusts (~1200 ppm). REE patterns are very similar between and within both crusts displaying a typical HREE enrichment and a strong positive Ce anomaly (supplementary Figure S9, appendix 6).

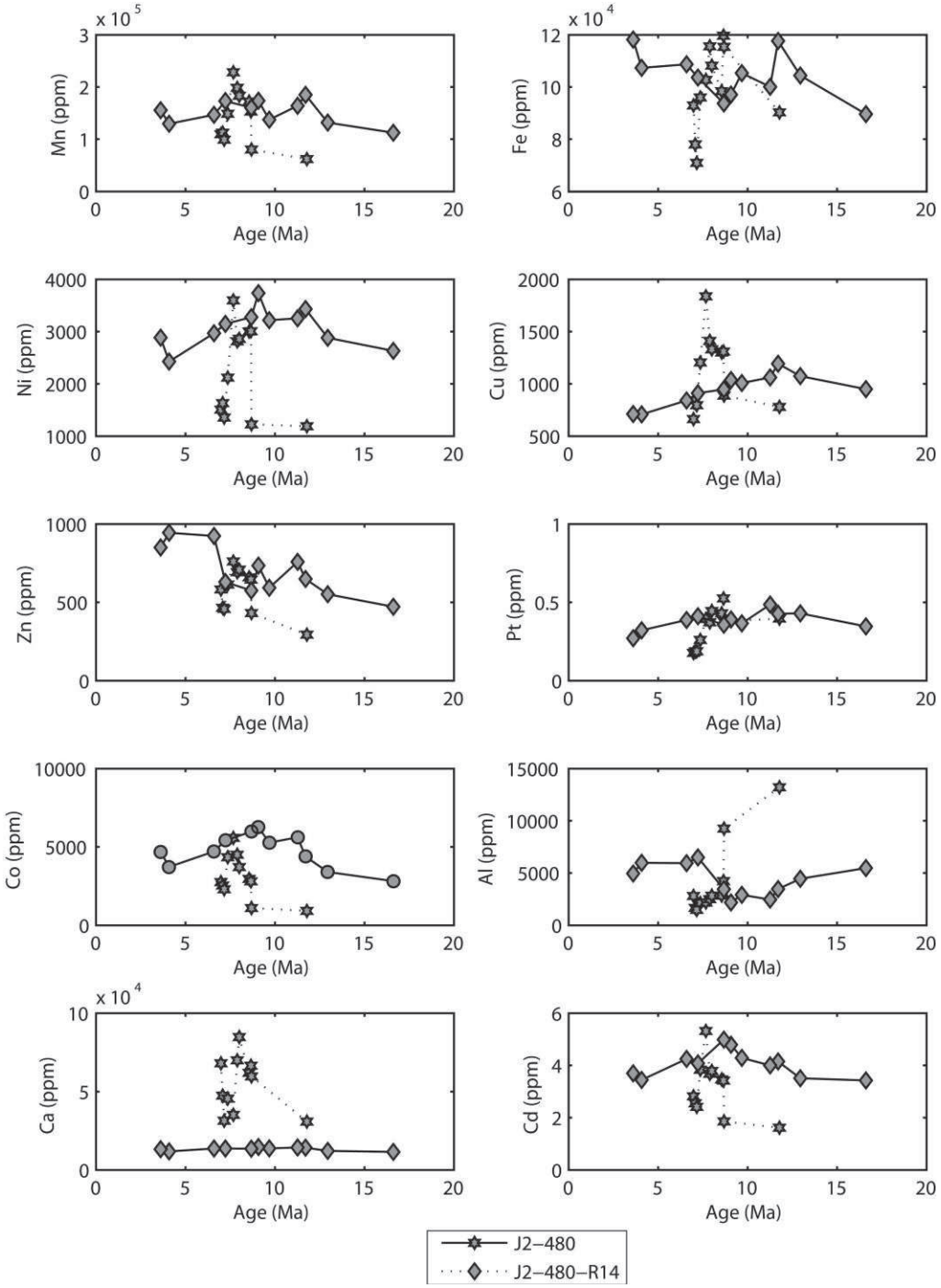

Figure IV.4*: Elemental concentrations (ppm) time-series of Apuupuu Fe-Mn crusts (North Pacific) J2-480 (grey stars) and J2-480-R14 (diamonds).*

Metals such as Mn, Cu, Ni, Co, Cd, Mo, Bi and Tl (moderately for Zn) show an increase of concentration from ca. 9.9 to 8.6 Ma in J2-480 and from ~13 to 8.1 Ma in J2-480-R14, thus slightly shifted temporally (Figure IV. and Table IV.1). The overall increase in transition metals is less pronounced in J2-480-R14 than in J2-480 (Figure IV.4). On the other hand, Fe concentration decreases in J2-480 from ~9.9 to 8.6 Ma but it remains stable in J2-480-R14.

Overall concentration patterns of Ni, Co, Cu, Zn, Tl and Cd covary with Mn concentrations and indicate that these elements are hosted by the Mn-phase which controls their abundance in the crust. Similar observations can be established for Pt content evolution. This is consistent with what we know from the literature (Koschinsky and Halbach 1995; Koschinsky and Hein 2003). Other elements show association with Fe such as Pb that has been shown to be mostly associated with the Fe-phase rather than with Mn-oxides and also Ti (Koschinsky and Hein 2003; Takahashi et al. 2007). Elemental association can also be visualized with correlation coefficients matrices (supplementary Tables S5a and S5b, appendix 6).

Ni isotope composition is rather uniform in the range of +1.64 to +1.72 ‰ for crust J2-480 with the exception the most basal point with $\delta^{60/58}$Ni = +1.40 ‰. On the other hand, J2-480-R14 displays variations in the +1.70 to +1.86 ‰ with the exception of the top of J2-480-R14 with a higher $\delta^{60/58}$Ni of +1.94 ‰ (Table IV.2 and Figure IV.7). For comparison these results show smaller range of $\delta^{60/58}$Ni values than those reported in other Fe-Mn crusts reported in chapter III of this manuscript ($\delta^{60/58}$Ni from +0.76 to +1.80 ‰) and Gall et al. (2013) ($\delta^{60/58}$Ni from +0.9 and +2.5 ‰).

3.3.2. South Pacific Fe-Mn crusts

The range of Fe/Mn ratios, i.e. from 0.53 and 1.31, is globally more homogeneous than for Apuupuu Fe-Mn crusts. The correlation coefficient matrix for selected elements (supplementary Tables S5c and S5d, appendix 6) shows similar group of elements associated with either Mn or Fe phases. On the other hand, differences are observed in terms of enrichment factors, such as Co contents which are globally higher than for North Pacific Fe-Mn crusts with values comprised between ~3000 and ~12000 ppm (Table IV.1). Tellurium generally varies within the range of 50-100 ppm (Figure IV.5). The REE patterns of the South Pacific samples show a strong positive Ce anomaly and an overall enrichment in HREE. The spread of the pattern is more important for ZEP2-DR05-04 than for ZEP2-DR06-03, hence the latter have a larger range of REE enrichment. As observed for Apuupuu Fe-Mn crusts, there is a positive Gd anomaly, but the REE enrichment is less important in South Pacific Fe-Mn crusts in comparison to North Pacific crusts probably because of dilution effects (supplementary Figure S10, appendix 6).

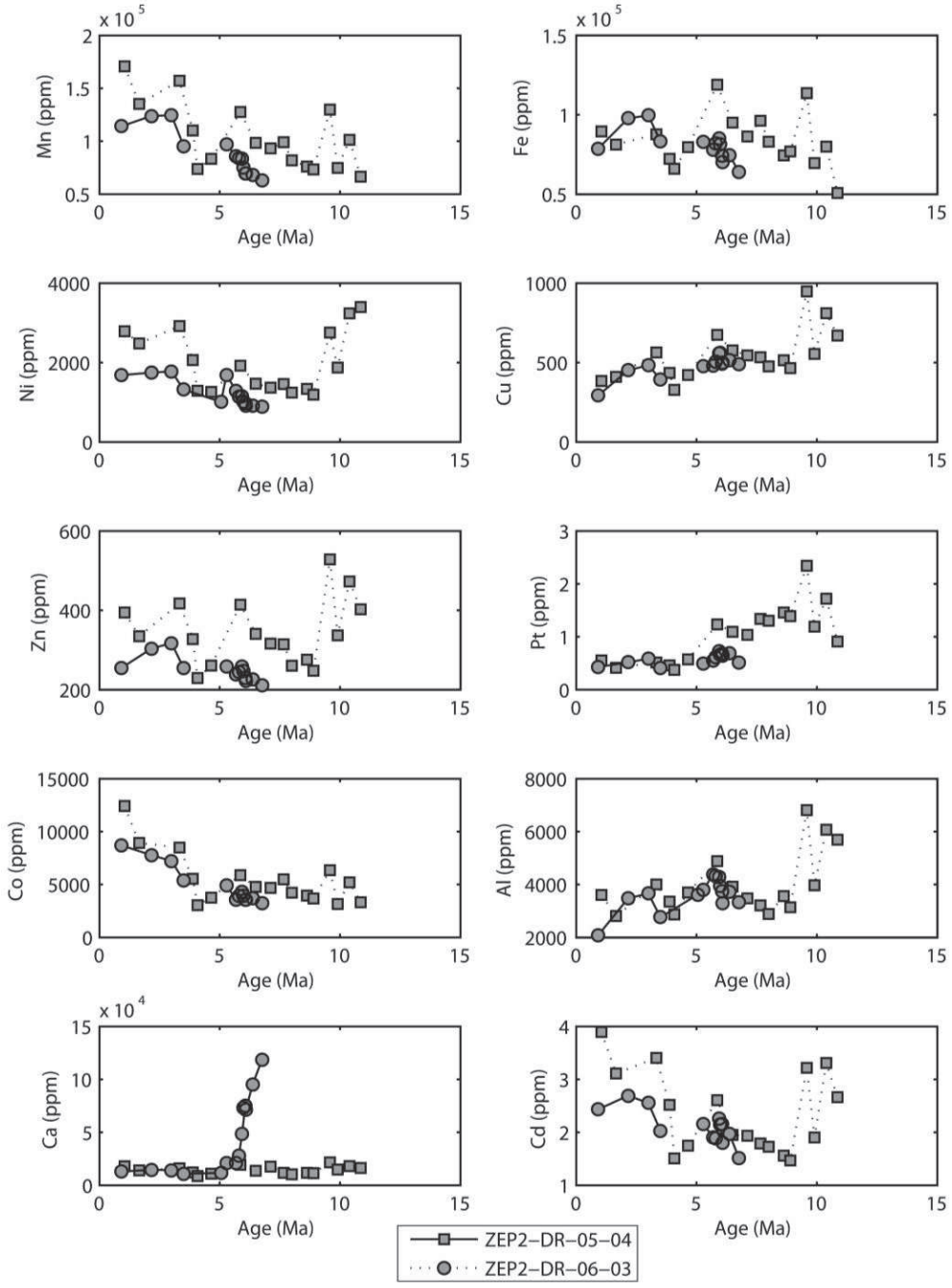

***Figure IV.5**: Elemental concentrations (ppm) time-series of Tahiti Fe-Mn crusts (South Pacific) ZEP2-DR05-04 (grey squares) and ZEP2-DR06-03 (grey circles)*

From ca. 4 Ma until the surface of the crust, there is a trend towards higher Co/Mn whereas Fe/Mn and Cu/Mn decrease (Figure IV.6). Increase in Co/Mn ratios indicates decreasing growth rates. Although both crusts show remarkably identical variations in their geochemical patterns, in particular with respect to Cu/Mn, Zn/Mn, Co/Mn, Fe/Mn and Al/Mn ratios, there is however a specific trend observed for Al, Zn, and Ni in the region “I” of ZEP2-DR05-04 (over a thickness of ~4 mm, (Figure IV.6). Accordingly, it warrants the distinction between two regions in crust ZEP2-DR05-04 as established in previous section: region “I” in the “Inner” crust and region “O” for the outer part of the crust (Figure IV.2). In region “I” Ni, Cu, Zn, Al and Pt are significantly enriched. Pt is four times more enriched (from 0.37 ppm to

more than 2 ppm) than region “O”, while Ni, Cu and Zn concentrations show an average two-fold increase in concentrations in the base of the crust (Figure IV.5). Al concentrations are also particularly elevated in region “I” of ZEP2-DR05-04 crust for which average concentration of 3000 ppm reach values of ~7000 ppm at the base of the crust in comparison to region “O”. There is a decrease in Fe and Ti concentrations, from ~90000 ppm to ~60000 ppm for Fe, and from ~8000 ppm to ~5000 ppm for Ti. In summary the composition of region “I” in crust ZEP2-DR05-04 shows marked differences from the composition of region “O” as highlighted by their elevated Ni, Cu, Zn, Al and Pt, contents but low Fe and Ti concentrations. However, with the exception of region “I”, the overall geochemical patterns of the two South Pacific Fe-Mn crusts are very similar and consistent between each other. In addition, results corroborate observations from microprobe analyses indicating that region ‘I” of ZEP2-DR05-04 has a peculiar geochemistry in comparison to region “O”.

Ni isotope variations are limited to the range of +1.75 to +1.95 ‰ in ZEP2-DR06-03. In ZEP2-DR05-04 two regions must be distinguished as equally highlighted above for the elemental geochemistry: subsamples of the “Inner” region of the crust show an important variability in $\delta^{60/58}$Ni values from +0.25 to 1.08 ‰ on a relatively limited scale, while $\delta^{60/58}$Ni values in the remaining crust are comprised between +1.54 to +1.86 ‰ (Table IV.2 and Figure IV.7) similar to previous values reported in this study or the literature (Gall et al. 2013).

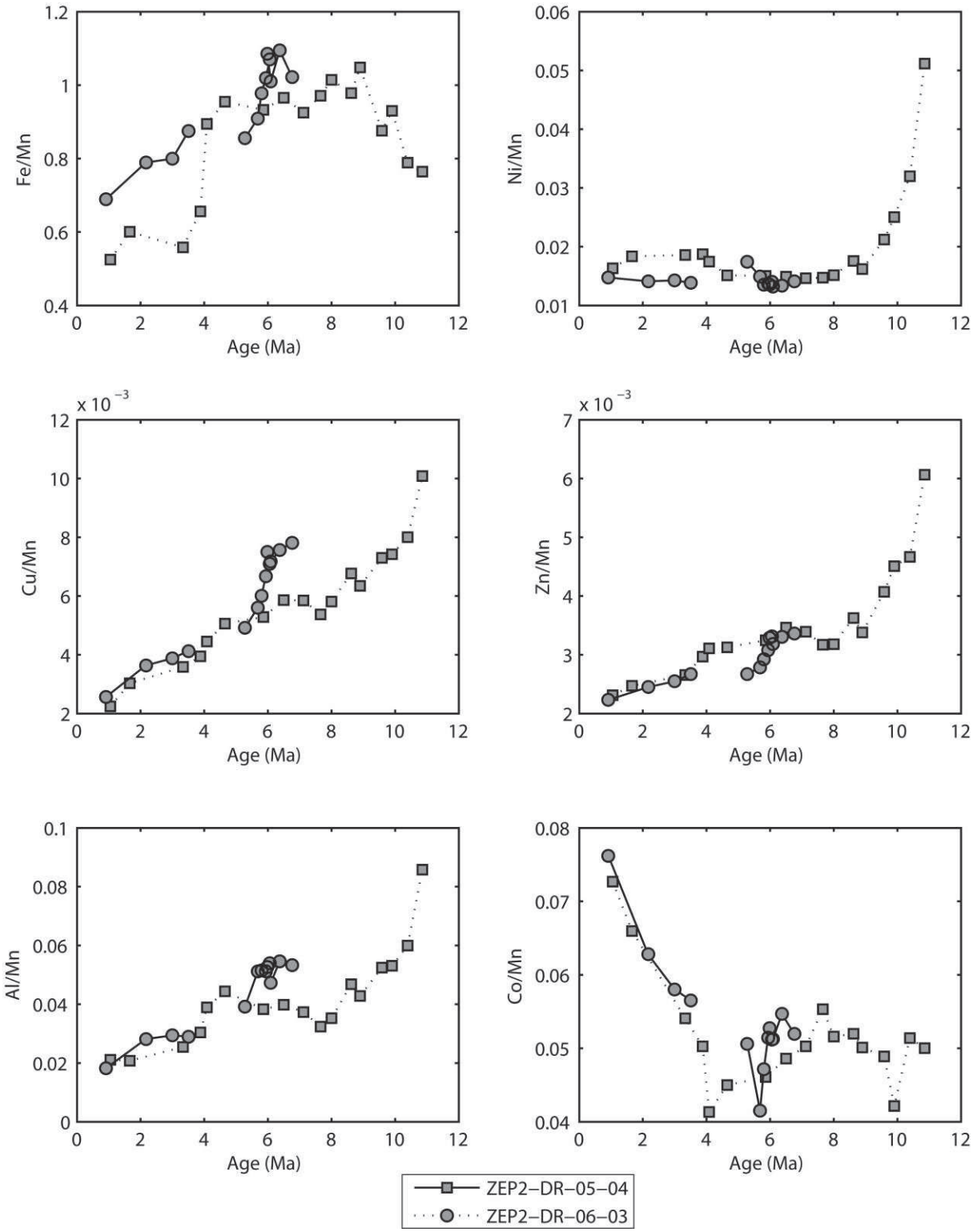

Figure IV.6*: Elemental ratios time-series of Tahiti Fe-Mn crusts (South Pacific) ZEP2-DR05-04 (grey squares) and ZEP2-DR06-03 (grey circles) showing increases in Ni, Cu, Zn and Al in region "I" of ZEp2-DR05-04 Fe6Mn crust.*

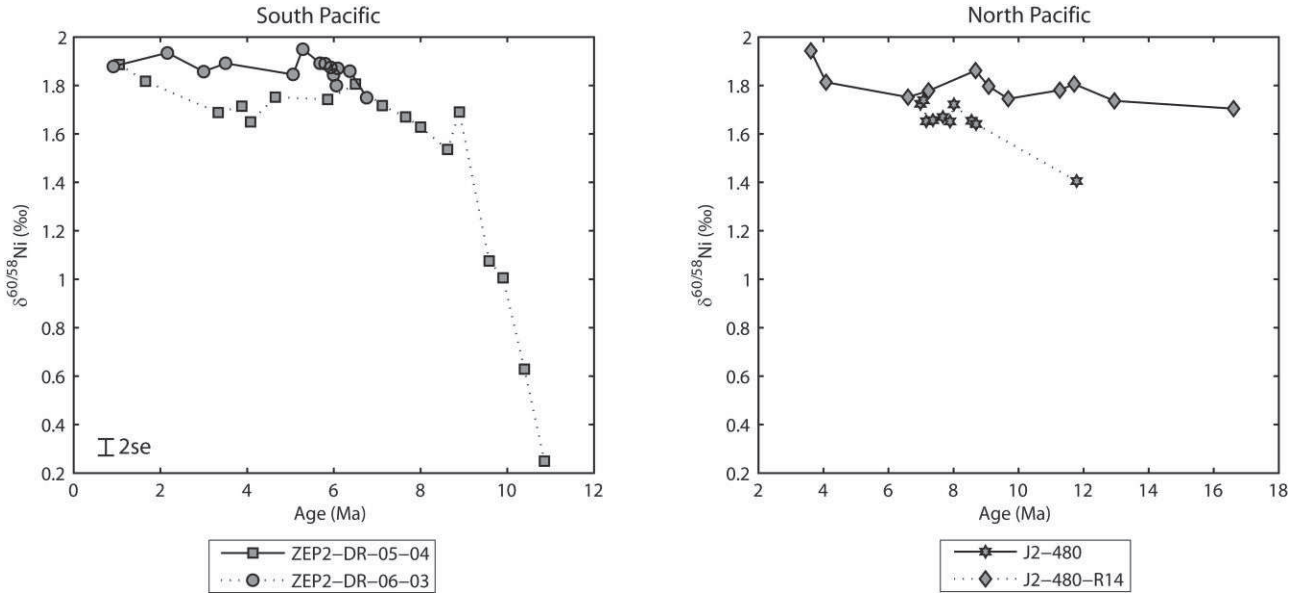

***Figure IV.7**: Ni isotope composition (‰) time-series (South Pacific) (panel A) and Apuupuu Fe-Mn crusts (North Pacific) (panel B). Sample symbols are identical to Figures 4 and 5.*

4. Discussion

4.1. Evidence for the hydrogenetic origin of the crusts and mineralogical control on elements distribution

Mineralogy of the four Fe-Mn crusts indicates an assemblage of poorly-crystallized Fe- and (mostly) Mn-oxides (birnessite, todorokite) that is typically encountered in marine Fe-Mn deposits. Note that due to the poor crystallinity of the mineral phases it was not possible to detect the nature of the Fe-phase neither the presence of δMnO_2-vernadite which is generally considered as the predominant Mn-phase in hydrogenetic Fe-Mn crusts (Koschinsky and Halbach 1995; Koschinsky and Hein 2003), and the abundance of each mineral phase. We also detected in all samples the presence of accessory phases such as fluorapatite and calcite (in South Pacific crusts), and detrital plagioclase (in North Pacific crusts). EMPA elemental profiles show that carbonates and phosphates are present in J2-480 (North Pacific) and in ZEP2-DR-06-03 (South Pacific). These observations are consistent with the geochemistry of subsampled layers of the crusts indicating higher Ca concentrations and more than three times higher Ca/Mn ratios in these two crusts.

Ti, along with Al, is often used as an indicator of the presence of detrital phases or of the presence of any silicate-rich material. However, Koschinsky and Halbach (1995) showed that a large part of Ti in hydrogenetic Fe-Mn crusts is derived from precipitation in seawater of colloidal Ti in the Fe-phase, only 10% of Ti is associated with detrital phases (Koschinsky and Halbach 1995). EMPA elemental maps show that Ti is systematically associated with Fe which supports a hydrogenetic origin of Ti. This association also explains the lack of correlations between Ti and Al in Fe-Mn crusts. Associations of other elements such as Co, Ni, and Zn with Mn oxides are also in agreement previous studies (Koschinsky and Halbach 1995). Likewise, Co, Ni and Zn which are present in seawater as divalent species or chloro-complexes, are preferentially adsorbed on the negatively-charged surface of Mn-colloids,

while Ti forming large uncharged hydroxo-complexes, are adsorbed on the positively-charged Fe-colloids (Koschinsky and Halbach 1995; Koschinsky and Hein 2003). Even if some Ca and P are present in ZEP2-DR06-03, Ca- and P-phases do not retain transition metals.

The slow precipitation rate of Fe- and Mn-rich phases (1-6 mm/Ma) from colloids formed in the water column ultimately controls the enrichment of these elements in Fe-Mn crusts in comparison to the average continental crust (Li and Schoonmaker 2003; Schulz and Zabel 2006). For instance, Pt contents in Fe-Mn crusts mostly ranging between 0.5 and 1.5 ppm, are consistent with Pt concentrations reported in the literature for Central and South Pacific Ocean Fe-Mn crusts (Halbach et al. 1984; Hein et al. 1988; Halbach et al. 1989; Lesuave et al. 1989). These concentrations are more than 1000 times higher than the estimated average in the upper continental crust (Rudnick and Gao 2003). To date such high concentrations are thought to be derived from dissolved seawater Pt that accumulated in Fe-Mn crusts after adsorption on the Mn-phase (Hein et al. 1988; Halbach et al. 1989). By contrast, enrichment of Te in Fe-Mn crusts is possible through the adsorption of Te on Fe-colloids in seawater which then precipitated slowly to form Fe-Mn crusts (Hein et al. 2003). Elevated concentrations of Mo (more than 200 ppm on average) and Tl (more than 50 ppm on average) in the samples are also indicative of enrichment through precipitation of seawater dissolved trace metals from in Fe-Mn crusts (hydrogenetic deposits).

REE patterns normalized to PAAS (Post Archean Australian Shale (Taylor and McLennan 1995)) are typical to that of hydrogenetic Fe-Mn crusts showing a strong positive Ce anomaly and relatively flat patterns or slightly REE enriched (supplementary Figures S9 and S10, appendix 6). REE removal onto Fe-Mn crusts is dominated by surface complexation processes and the positive Ce anomaly is probably indicative of an additional process with precipitation of Ce-hydroxides on the crust surface (Bau et al. 1996) or to oxidation of Ce^{3+} to Ce^{4+} after sorption on Mn-oxides (Takahashi et al. 2007). More elevated Ce anomalies may also be related with depth of occurrence of the crusts (De Carlo and McMurtry 1992). Reduction of Ce from particles entering the OMZ promotes its solubilization and accumulation in the OMZ. Thereafter, it is rapidly oxidized through formation of CeO_2 complexes at the surface of the crust. Hence, this process is expected to be more efficient in shallower crusts close to the OMZ.

In the South Pacific samples the spread of the patterns is more important for ZEP2-DR-05-04 than for ZEP2-DR-06-03 and the latter display slightly less enriched REE patterns than other crusts of this study. This difference could be due depth of the samples (i.e. 1876 and 1530 m depth respectively) and to their distance from the OMZ through time. ZEP2-DR06-03 was globally closer to the OMZ which may explain REE enriched patterns relatively to ZEP2-DR05-04. Alternatively, it could reflect changes in the growth rates of the crusts.

Most Fe/Mn ratios of the four Fe-Mn crusts are comprised in the range of 0.5-1, which is identical to the range reported in the literature for hydrogenetic Fe-Mn crusts (Craig et al. 1982; Halbach et al. 1983; Aplin and Cronan 1985; De Carlo et al. 1987; Hein et al. 1988; Hein et al. 1992; Koschinsky and Halbach 1995; Hein et al. 2010; Hein et al. 2013). However, Fe/Mn ratios in Tahiti Fe-Mn crusts are on average globally slightly higher (averages of 0.85 and 0.91) than Apuupuu Fe-Mn crusts ratios (averages of 0.79 and 0.70) and could be due to lower growth rates in Tahiti Fe-Mn crusts.

4.2. Diagenetic alteration and post-depositional processes in crust ZEP2-DR05-04

Fe-Mn crusts are composed of successive Fe-Mn-rich layers that accumulated in seawater after precipitation on a hard substrate, thus the youngest crust corresponds to the surface and the deepest region of the crust is the oldest. The chronology of the different subsamples in the crusts was determined using Be isotopes and unexpected high $^{10}Be/^{9}Be$ ratios in the region "I" (in the "Inner" region) of the crust ZEP2−DR−05−04 (Table IV.2 and Figure IV.2) yielded aberrant youth ages. Surprisingly, it also corresponds to the region of the crust displaying important geochemical variability with high Ni, Mn, Cu, Co, Al and Pt concentrations and low Fe concentrations.

Three possible explanations may account for these anomalously high $^{10}Be/^{9}Be$ ratios, (1) diffusion of cosmogenic ^{10}Be isotope from outer to inner crust, (2) cosmic inputs with high $^{10}Be/^{9}Be$ ratios, or (3) hydrothermal or halmyrolitic reactions. Hypothesis (1) can be disclaimed because it was demonstrated that on the time-scale considered for dating Fe-Mn crusts diffusion of Be is probably very limited (Henderson and Burton 1999).

There are some arguments against hypothesis (2) and a meteoritic origin. Even if Stuart and Lee (2012) detected the presence of micrometeorites using He isotopic composition, they also dated their Fe-Mn crusts samples using cosmogenic ^{10}Be isotope and seemingly, extraterrestrial inputs have not modified $^{10}Be/^{9}Be$ ratios in their samples. Thus the presence of extraterrestrial material is not the cause to elevated Be isotopes ratios correlating with increase Ni and Pt enrichments.

Several lines of evidence favor hypothesis (3) implying dissolution and recrystallization processes that affected solely the geochemistry of Mn-oxides in region "I" of the crust. This process of recrystallization could have been promoted by continued circulation of seawater through fractures which then reached the empty cavities present between the base of the crust and the attached substrate. This seawater would have brought Be with higher $^{10}Be/^{9}Be$ ratios thus producing the anomalously high Be isotope composition in the region "I" of the crust. Although the element distribution in the minerals is similar to typical hydrogenous crusts; the difference is rather observed in the abundance of Mn-phases over Fe-phases. This is specifically evident with EMPA profiles which indicate that Mn-phases are predominant in the "Inner" crust since very few Fe phases were encountered during analysis of the profile. A substantial recrystallization of Mn-oxides phases in comparison to Fe-oxides would have promoted enrichment in transition metals like Pt, Ni, Cu, Zn and Co in that part of the crust especially because of their strong affinity for this phase. However, as presented in Figure IV.8, elemental ratios relationships between Ni/Mn vs Cu/Mn, Zn/Mn and Al/Mn show positive correlations, suggesting that fluid circulation had an effect on Ni, Cu, Zn and Al enrichment. It is also important to note the decrease of Ti concentrations by a factor of ~3 together with a two-fold increase in Al concentrations.

Petrographical observation of the base of crust ZEP2-DR05-04 revealed that the substrate is extremely altered and that voids (up to 20 mm size) are present between the crust and the substrate. These cavities are likely of secondary origin, resulting from the dissolution of primary precipitates through the circulation of alteration fluids, leaching Al from the rocks and remobilizing Ni from initial Fe-Mn deposits. In addition, the REE pattern of the deepest sample in ZEP2-DR05-04 (region "I" of the sample Figure IV.2) display the smallest positive Ce anomaly (supplementary Figure S10, appendix 6) which might suggest a supply of REE from seawater, the former having a negative Ce anomaly.

As presented in Figure IV.8, Ni isotope compositions are also affected by such fluid circulation. The lower $\delta^{60/58}Ni$ values at the base of Fe-Mn crust ZEP2-DR05-04 +1.06 to +0.25 ‰ are strongly correlated with Ni/Mn ratios (R^2=0.85) suggesting mixing relationships between typical hydrogenous Ni end-member (Ni/Mn = 0.01 for $\delta^{60/58}Ni$ = +1.8 ‰) and low

$\delta^{60/58}$Ni – high Ni/Mn end-member. As discussed above, a plausible candidate for the isotopically light Ni and high Ni/Mn source may be related to the alteration fluid that affected the geochemistry and Be-age of the base of the crust. Ni isotope composition of volcanic rocks has been determined at $\delta^{60/58}$Ni = 0 ‰, which is consistent with the isotope signatures of the alteration fluid that produce the Ni enrichment. The effect of halmyrolitic fluids on Ni isotopes is further discussed in section 4.5 of this chapter.

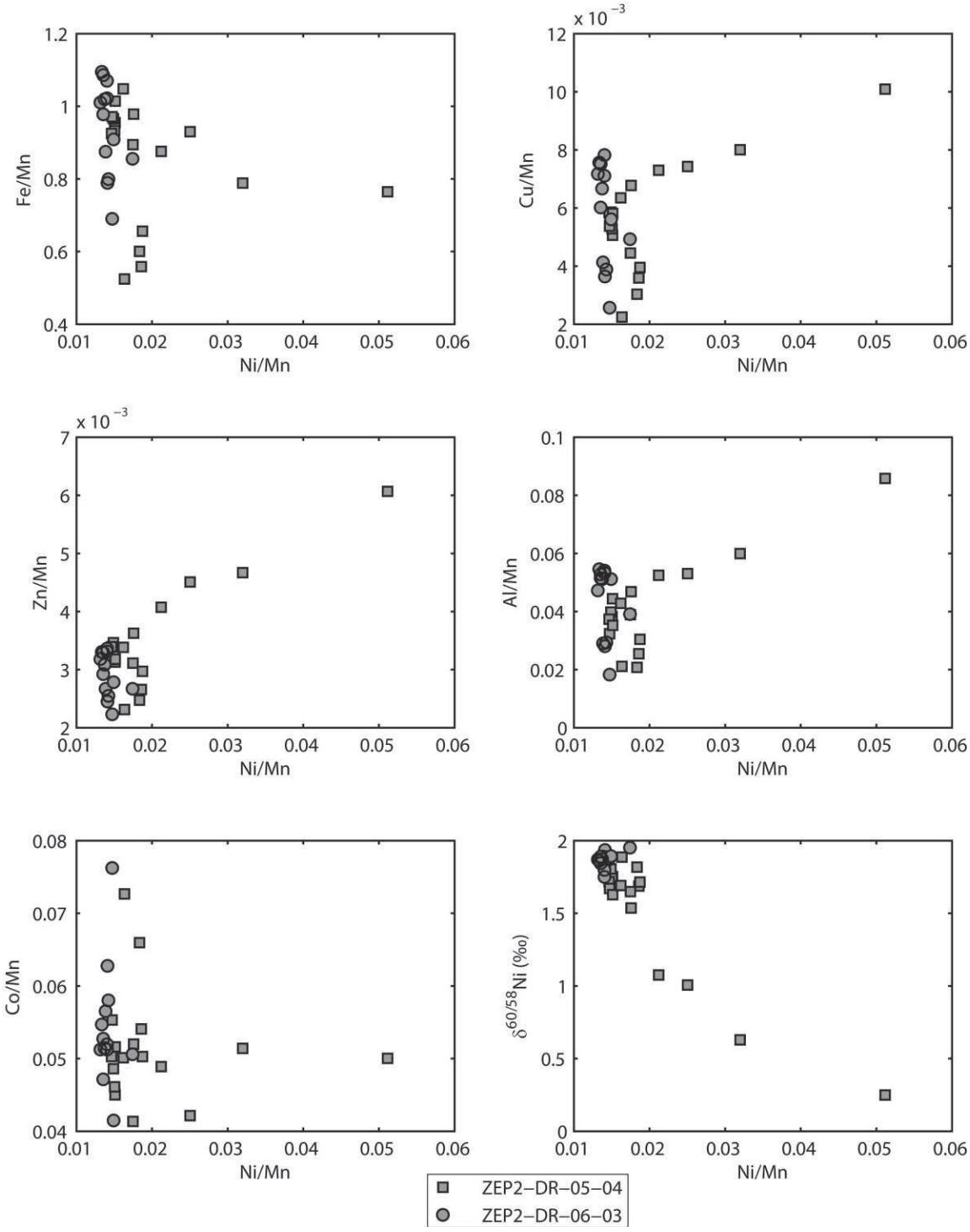

Figure IV.8*: Ni/Mn ratios versus Fe/Mn, Cu/Mn Zn/Mn, Al/Mn Co/Mn and Ni isotopes values (‰) in Tahiti Fe-Mn crusts.*

Due to the high residence time of oceanic Ni, it is very likely that if modifications of erosional inputs from the continents have an impact on Ni isotopes this effect would have been visible on both South Pacific crusts and probably also in North Pacific crusts (Apuupuu crusts). Further, it is unlikely the Ni isotope composition of continental fluxes would have significantly vary through the Cenozoic, since unlike radiogenic isotopes, Ni isotopes in the continental crust are relatively homogenous (Gueguen et al. 2013). Therefore, the atypical geochemical variations observed in ZEP2-DR5-04 are probably the result of local rather than global processes occurring in ambient seawater.

4.3. Revisiting the extraterrestrial sources of metals to Fe-Mn crusts

Although South Pacific crusts from are clearly more enriched in Pt (up to 2.34 ppm) than Apuupuu crusts (up to 0.52 ppm), the range of values are within the range reported elsewhere (Halbach et al. 1984; Hein et al. 1988; Halbach et al. 1989; Lesuave et al. 1989; Hein et al. 2013). We note, however, that Pt concentrations are overall more elevated in the inner "I" region of ZEP2-DR05-04 than in crust ZEP2-DR06-03. Micrometeorites (i.e. cosmic spherules) have already been observed in Fe-Mn crusts from the South Pacific (Halbach et al. 1984; Kosakevitch 1987; Halbach et al. 1989; Lesuave et al. 1989; Kosakevitch and Disnar 1997). Accumulation of micrometeorites in Fe-Mn crusts is favored by the slow precipitation rate of Fe-Mn crusts (1-6 mm/ma) combined to sluggish water masses (e.g. no major continental inputs, low surface bioproductivity, downwelling currents). Considering the enrichment in Pt in cosmic materials (and notably iron meteorites), it is important to test whether such Pt enrichment could be related to the presence of extraterrestrial materials.

Alternatively, Halbach et al. (1989) argued that the general Pt enrichment in Fe-Mn crusts is related to the adsorption of tetra-chloro complexes of Pt present in seawater (Hodge et al. 1985). Hein et al. (1988) also suggested the participation of organic species for complexing Pt in seawater.

The flux of extraterrestrial material in deep-sea sediments from the Pacific Ocean has been estimated at ~$3.7x10^7$ kg/yr and remained rather constant through the Cenozoic (Peucker-Ehrenbrink 1996). Three types of cosmic spherules are described in the literature, (1) stony spherules with a chondritic elemental composition, (2) iron-rich spherules which generally contain a Fe-Ni-rich core, and (3) iron-sulfur-nickel rich spherules (Brownlee et al. 1997). Stony spherules are by far the predominant type of spherules found in deep-sea sediments but the most enriched source of Pt (and Ni) in Fe-Mn crusts is found in iron-rich type spherules. According to estimates, ~2 to 7 % of the total spherules present in deep-sea sediments are iron-rich spherules (Taylor et al. 2000). There is also evidence that some cosmic spherules that reach the deep seafloor could be in fact much enriched in Pt that average iron meteorites. Pt is not significantly lost by volatilization processes upon the entry of cosmic materials into the atmosphere (Rudraswami et al. 2012). In addition, Pt and other Platinum Group Elements (PGE) may form "PGE nuggets" in stony meteorites, leading to the potential segregation of Pt-rich cosmic spherules (Brownlee et al. 1997; Rudraswami et al. 2012).

Although no cosmic spherules were observed in the inner region of Fe-Mn crust ZEP2-DR05-04, it would be important to further determine whether high Pt contents are of extraterrestrial origin by measuring Os or He isotope compositions. Although changes in extraterrestrial inputs to seawater do not explain the variations of the Os isotope patterns recorded in Fe-Mn crust (Peucker-Ehrenbrink 1996; Peucker-Ehrenbrink and Ravizza 2000), local addition of extraterrestrial Os to ZEP2-DR05-04 Fe-Mn crust would have affected its Os

isotope composition towards less radiogenic values. Such hypothesis should be further evaluated.

Previous studies have reported the Ni isotope composition of meteorites and $\delta^{60/58}$Ni values of +0.20 and +0.30 ‰ were reported for Nantan and Gibeon iron meteorites (Gueguen et al. 2013). Ni/Fe ratios (0.07) of iron meteorites like Nantan Iron and Gibeon Iron, as well as $\delta^{60/58}$Ni values, are similar to those obtained in the inner section of crust ZEP2-DR05-04. Hence, from a mass balance point of view most of Fe and Ni in this sample should be derived from raw meteoritic materials to explain both Ni/Fe and $\delta^{60/58}$Ni values, which is obviously unlikely. Ni/Fe in cosmic spherules is on average comprised between 0.4 and 1.2. Our spatially-resolved Electron Microprobe (EMPA) data show Ni/Fe ratios up to 2.6. However, in contrast to iron-rich cosmic shperules, those values can be directly related to the preferential association of Ni with Mn-oxides (and thus Fe-poor phases) rather to Ni-rich Fe-oxides. Another important aspect to consider is the late-stage dissolution of cosmic materials once they accumulate within the Fe-Mn crust. It is likely that reduced forms of metals within Ni-Fe-alloys of the cosmic spherules would react with the Fe-Mn-oxides matrices of the Fe-Mn crust, resulting in dissolution and element redistribution in the crust.

In addition, Fe-Mn crusts generally occur in areas where important oceanic currents sweep out pelagic particles, including cosmic particles, preventing their deposition in the crusts. Therefore, the presence of cosmic particles in Fe-Mn crusts would more probably be local instead of global contributions to Fe-Mn crusts from the Pacific Ocean. However, although local effects are in agreement with the fact that only ZEP2-DR05-04 was affected by geochemical and Ni isotope variations, it is unlikely that cosmic spherules would impact the overall geochemistry of the crust.

4.4. Assessing sources vs. processes in affecting Ni isotope systematics of Fe-Mn crusts.

The residence time of oceanic Ni is relatively long ~10 kyrs (Sclater et al. 1976; Bruland and Lohan 2003; Gall et al. 2013) in comparison to the mixing time of oceans of 1.5 kyrs. Thus, Ni isotope composition in the oceans should be homogenous, i.e. for similar ages Ni isotopes in different deep oceanic basins would be identical and the influence of local sources on Ni isotopes should be limited. With the exception of crust ZEP2-DR05-04, our results show very limited long-term Ni isotope variations with averages of +1.72 ‰ and +1.87 ±0.10 ‰ in the South Pacific, and +1.64 ‰ and +1.79 ‰ in the North Pacific.

However, despite the fact that halmyrolitic processes during seawater circulation in the localized extremities of the crust can affect Ni isotope composition, assessment of *in-situ* Ni diffusion along the whole section of the crust according to equations from (Henderson and Burton 1999) indicates diffusion rates several orders of magnitude lower than calculated for U. This suggests that Ni isotope composition in Fe-Mn crusts will not be disturbed by diffusion processes and that pristine isotope composition should be preserved at the sampling scale carried out in our Fe-Mn crusts. Therefore, the fairly homogenous Ni isotope composition through time in the four Fe-Mn crusts argued for constant Ni isotopes in deep waters of the South and North Pacific Oceans over the last 17 Ma.

Other Ni isotope composition of surface layers of hydrogenetic Fe-Mn crusts were reported very recently by Gall et al. (2013) and show a compositional range of +0.9 to +2.5 ‰ from various localities. The authors did not observe any relationships between oceanic basins, water depth and Ni isotope composition, suggesting that Ni isotopes variability is probably not controlled by factors such as biological activity or redox conditions. However, they observed that Fe-Mn crusts formed closest to the continents are isotopically heavier

which they attributed to a higher contribution of materials coming from continental weathering (rivers and groundwater) enriched in heavy Ni isotopes. A Ni isotope time-series in a Fe-Mn crust (sample CD29-2) located to the West of Apuupuu Fe-Mn crust from this study reported by Gall et al. (2013) shows a negative excursion ca. 45 Ma ascribed to hydrothermal inputs. By contrast, our Ni isotopes time-series are very homogenous compared to Gall et al. (2013). Such differences may be accounted for by the fact that our Fe-Mn crusts are located in the interior of oceanic basins, therefore we expect limited changes of supply from the continents. Secondly, our time-series sampling was carried out at a higher resolution and on a shorter interval of time in comparison to Gall et al. (~17 Ma in total in our crusts and ~ 70 Ma in Gall et al. crusts samples), and notably their profile does not include the first 10 Ma which is in fact the period investigated in our crusts. Finally, due to plate motion and subsidence, at 45 Ma the crust CD29-2 was located southeast of its present location and in shallower waters. Therefore, we may suppose that seawater was different at that time and at that location.

Gall et al. also argued that no isotope fractionation occurs during Ni adsorption on Fe- and Mn-oxyhydroxides based on the limited difference between average $\delta^{60/58}$Ni values of crust and seawater of ~+1.5 ‰ (Cameron and Vance 2013; Vance et al. 2013). This assumption is however at odd with our recent experimental determination of Ni isotope fractionation during adsorption on Fe- and Mn-phases indicating significant enrichment in light isotopes of the mineral phase (by up to ~-1 ‰) (Gueguen et al. 2011; Sorensen et al. 2011). The apparent lack of Ni isotope fractionation between Fe-Mn crusts and seawater could be explained by the mechanisms of Ni uptake in Fe-Mn crusts which accumulate very slowly from colloids formed in seawater. Therefore, even if the formation of colloids themselves is rapid and probably result in Ni uptake in the water column, most of Ni adsorption should occur directly on the crust surface during precipitation of the colloids. During this process, Ni uptake proceeds through quantitative adsorption of Ni at the layer surface. Hence, Ni isotope fractionation will not be expressed in the final product. Therefore, we would expect that Ni isotope composition of Fe-Mn crusts should be either lower or equal to Ni isotope composition of seawater. The determined average $\delta^{60/58}$Ni values of +1.8 ‰, which is higher than modern seawater values at +1.5 ‰ (Cameron and Vance 2013), suggests either that seawater changed through time, or that other processes affected Ni isotope fractionation during Ni uptake like for example the presence of organic ligands.

4.5. Ni isotope record of halmyrolitic processes versus fluids alteration

The crust ZEP2-DR05-04 was collected with its substrate that clearly shows important traces of alteration. We have previously demonstrated that region “I” of ZEP2-DR5-04 was probably affected by post-depositional alteration processes where inputs of seawater modified ^{10}Be/^{9}Be ratios. Therefore, Ni isotopes might have been affected by these processes either by halmyrolitic reactions or by alteration by circulating fluids.

It has already been demonstrated that alteration of the seafloor (halmyrolysis) could release Fe to the alteration fluids and may have some impact on the Fe isotope budget of the altered basalts (Rouxel et al. 2003). These authors showed that alteration of basalt on the seafloor produces isotopically light Fe fluxes because of preferential leaching of light Fe isotopes. Although Ni is a relatively immobile element, the few data available on Ni isotope fractionation during alteration processes show that fresh and altered basalts have the same $\delta^{60/58}$Ni values (Gueguen et al. 2013). As far as we know, there is no estimation of the real Ni flux that could be produced by alteration of basic and ultrabasic rocks from the seafloor, and as yet it is unknown whether the halmyrolitic Ni flux would have a different Ni isotope

composition than its source. Hein and Morgan (1999) claimed that the nature of the substrate has no influence on the bulk composition of Fe-Mn crusts (Hein and Morgan 1999). However, their sampling method is based on statistical calculations of more than 80 bulk Fe-Mn crusts samples including their substrate which method does not consider internal compositional variations.

Enrichment in Al is unlikely to be brought by seawater which is very poor in Al, instead it could have been supplied by basalt alteration (Staudigel and Hart 1983). Hydrothermal solutions produced by low-temperature diffuse hydrothermal venting from the oceanic crust may have emanated from fractures in the underlying oceanic substrate. Low temperature hydrothermal fluids produced by seawater infiltration into basaltic crusts have already been shown to result in an output flux of Mn, Co, Ni, and Zn (Wheat and Mottl 2000; Wheat et al. 2002).

Seawater input from the substrate could explain why solely the base of the crust was affected by these inputs. This hypothesis is also in agreement with a local origin, since the other nearby Fe-Mn crust presented in the study does not shown any meaningful geochemical variations. Given the large crust/basalt Ni ratio, it is unlikely that basalt alteration at this limited spatial scale provided significant amount of Ni for modifying the isotope composition in the crust. However, such hydrothermal inputs could promote dissolution and recrystallization processes of the primary Mn and Fe mineral phases, therefore this does not specifically require, for instance, inputs of additional Mn, Ni and Pt.

From what we know from the literature and from observations of EMPA elemental maps, Ni is one of the elements having the strongest affinity for the Mn-phase. Therefore, any process of Mn-oxides dissolution/recrystallization will strongly impart the distribution of Ni in the system. Sharp increase in Ni/Co and a decrease in Co/Mn ratio in region “I” of the crust are consistent with rapid precipitation of Mn-oxides. In support of this hypothesis and considering a fractionation factor in the order of ~-1 ‰ during adsorption on Fe- and Mn-oxides (Gueguen et al. 2011; Sorensen et al. 2011), low Ni isotope values are in agreement with Ni isotope fractionation from a source with composition akin to that of Fe-Mn crusts (> +1.5 ‰) after dissolution of initial Mn-phases, or to that of seawater with a composition of +1.5 ‰ (Cameron and Vance 2013) after inputs from seawater Ni. This is also consistent with results reported in chapter III of this manuscript that showed that Ni isotope variations on Fe- and Mn-rich deposits are highly dependent on the rate of precipitation and formation of the mineral phases. Fast precipitated deposits (e.g. hydrothermal deposits) display a larger range of Ni isotope compositions than slowly precipitated deposits (e.g. pure hydrogenetic Fe-Mn crusts).

5. Summary and concluding remarks

In this study we have reported mineralogical, elemental composition, and Ni isotope composition of four hydrogenetic Fe-Mn crusts from the North and South Pacific oceans. Our results indicate that Ni isotopes in the four crusts are similar and remained relatively constant over the last ~17 Ma, suggesting a global oceanic reservoir with. $\delta^{60/58}$Ni values about +1.76 ±0.23 ‰ (2sd).

One of the South Pacific Fe-Mn crust (ZEP2-DR05-04), presents unusual geochemical variations with high, Mn, Ni, Al, and Pt, anomalously high ^{10}Be/^{9}Be ratios, and low Ni isotope values in the range of +1.08 to +0.25 ‰ in contact with the altered substrate. These results suggest that post-depositional processes implying dissolution and recrystallization processes of Mn-rich oxides phases as well as substrate-seawater

interactions have locally affected the composition of Fe-Mn crust. We argue that seawater circulation through fractures best explains anomalously high $^{10}Be/^{9}Be$ ratios in the older layers of the crust, while rapid re-precipitation of Mn-oxides would have produced a large Ni isotope fractionation. Data from this study are consistent with the model suggested for explaining Ni isotope variations in oceanic Fe-Mn deposits in which enrichment processes and rates of precipitation are likely the main factors controlling Ni isotope variations rather than variations of the Ni sources to the oceans. On the other hand, although higher Pt concentrations were observed concomitantly to low Ni isotope values, the hypothesis cosmic spherules input for explaining these values is ruled out because it is not consistent with the overall geochemistry.

Supplementary information is shown in appendix 6 of this manuscript.

6. References

Abouchami, W., Goldstein, S. L., Galer, S. J. G., Eisenhauer, A. and Mangini, A. (1997). "Secular changes of lead and neodymium in central Pacific seawater recorded by a Fe-Mn crust." Geochimica Et Cosmochimica Acta 61(18): 3957-3974.

Amend, J. P., McCollom, T. M., Hentscher, M. and Bach, W. (2011). "Catabolic and anabolic energy for chemolithoautotrophs in deep-sea hydrothermal systems hosted in different rock types." Geochimica Et Cosmochimica Acta 75(19): 5736-5748.

Anbar, A. D. and Rouxel, O. (2007). "Metal stable isotopes in paleoceanography." Annual Review of Earth and Planetary Sciences 35: 717-746.

Aplin, A. C. and Cronan, D. S. (1985). "Ferromanganese oxide deposits from the Central Pacific ocean. 1. Encrustations from the Line islands archipelago." Geochimica Et Cosmochimica Acta 49(2): 427-436.

Arnold, M., Merchel, S., Bourlès, D. L., Braucher, R., Benedetti, L., Finkel, R. C., Aumaître, G., Gottdang, A. and Klein, M. (2010). "The French accelerator mass spectrometry facility ASTER: Improved performance and developments." Nuclear Instruments and Methods in Physics Research Section B: Beam Interactions with Materials and Atoms 268(11–12): 1954-1959.

Barling, J., Arnold, G. L. and Anbar, A. D. (2001). "Natural mass-dependent variations in the isotopic composition of molybdenum." Earth and Planetary Science Letters 193(3-4): 447-457.

Bau, M., Koschinsky, A., Dulski, P. and Hein, J. R. (1996). "Comparison of the partitioning behaviours of yttrium, rare earth elements, and titanium between hydrogenetic marine ferromanganese crusts and seawater." Geochimica Et Cosmochimica Acta 60(10): 1709-1725.

Bonatti, E. and Joensuu, O. (1966). "Deep-sea iron deposit from South Pacific." Science 154(3749): 643-&.

Bonatti, E., Kraemer, T. and Rydell, H. (1972c). Classification and genesis of submarine iron-manganese deposits, Washington DC, Nat. Sci. Found.

Bourles, D., Raisbeck, G. M. and Yiou, F. (1989). "^{10}Be and ^{9}Be in marine sediments and their potential for dating." Geochimica Et Cosmochimica Acta 53(2): 443-452.

Brownlee, D. E., Bates, B. and Schramm, L. (1997). "The Leonard Award address - Presented 1996 July 25, Berlin, Germany - The elemental composition of stony cosmic spherules." Meteoritics & Planetary Science 32(2): 157-175.

Bruland, K. W. and Lohan, M. C. (2003). Controls of Trace Metals in Seawater. Treatise on Geochemistry. D. H. Heinrich and K. T. Karl. Oxford, Pergamon**:** 23-47.

Burton, K. W., Ling, H. F. and Onions, R. K. (1997). "Closure of the Central American Isthmus and its effect on deep-water formation in the North Atlantic." Nature 386(6623): 382-385.

Cameron, V. and Vance, D. (2013). Nickel Isotopic Composition of Modern Seawater and Rivers. Goldschmidt, Florence, Italy, Mineralogical Magazine.

Craig, J. D., Andrews, J. E. and Meylan, M. A. (1982). "Ferromanganese deposits in the hawaiian archipelago." Marine Geology 45(1-2): 127-157.

De Carlo, E. H. and McMurtry, G. M. (1992). "Rare-earth element geochemistry of ferromanganese crusts from the Hawaiian Archipelago, central Pacific." Chemical Geology 95(3–4): 235-250.

De Carlo, E. H., McMurtry, G. M. and Kim, K. H. (1987). "Geochemistry of ferromanganese crusts from the hawaiian archipelago. 1. Northern survey areas." Deep-Sea Research Part a-Oceanographic Research Papers 34(3): 441-467.

Frank, M. (2002). "Radiogenic isotopes: Tracers of past ocean circulation and erosional input." Reviews of Geophysics 40(1).

Frank, M., O'Nions, R. K., Hein, J. R. and Banakar, V. K. (1999). "60 Myr records of major elements and Pb–Nd isotopes from hydrogenous ferromanganese crusts: reconstruction of seawater paleochemistry." Geochimica Et Cosmochimica Acta 63(11–12): 1689-1708.

Frank, M., Whiteley, N., Kasten, S., Hein, J. R. and O'Nions, K. (2002). "North Atlantic deep water export to the Southern Ocean over the past 14 Myr: Evidence from Nd and Pb isotopes in ferromanganese crusts." Paleoceanography 17(2).

Gall, L., Williams, H. M., Siebert, C., Halliday, A. N., Herrington, R. J. and Hein, J. R. (2013). "Nickel isotopic compositions of ferromanganese crusts and the constancy of deep ocean inputs and continental weathering effects over the Cenozoic." Earth and Planetary Science Letters 375(0): 148-155.

Goldstein, S. L. and Onions, R. K. (1981). "Nd and Sr isotopic relationships in pelagic clays and ferromanganese deposits." Nature 292(5821): 324-327.

Gueguen, B., Rouxel, O., Ponzevera, E., Bekker, A. and Fouquet, Y. (2013). "Nickel Isotope Variations in Terrestrial Silicate Rocks and Geological Reference Materials Measured by MC-ICP-MS." Geostandards and Geoanalytical Research 37(3): 297-317.

Gueguen, B., Rouxel, O., Ponzevera, E., Sorensen, J. V., Toner, B. M., Bekker, A. and Fouquet, Y. (2011). Ni biogeochemical cycle through geological time: insights from Ni isotope variations in modern and ancient marine metallifereous deposits. AGU Fall Meeting 2011. San Francisco, USA.

Halbach, P., Kriete, C., Prause, B. and Puteanus, D. (1989). "Mechanisms to explain the platinum concentration in ferromanganese seamount crusts." Chemical Geology 76(1-2): 95-106.

Halbach, P. and Puteanus, D. (1984). "The influence of the carbonate dissolution rate on the growth and composition of Co-rich ferromanganese crusts from Central Pacific seamount areas." Earth and Planetary Science Letters 68(1): 73-87.

Halbach, P., Puteanus, D. and Manheim, F. T. (1984). "Platinum concentrations in ferromanganese seamount crusts from the Central Pacific." Naturwissenschaften 71(11): 577-579.

Halbach, P., Segl, M., Puteanus, D. and Mangini, A. (1983). "Co-fluxes and growth rates in ferromanganese deposits from Central Pacific seamount areas." Nature 304(5928): 716-719.

Hein, J. R., Bohrson, W. A., Schulz, M. S., Noble, M. and Clague, D. A. (1992). "Variations in the fine-scale composition of a Central Pacific ferromanganese crust: paleoceanographic implications." Paleoceanography 7(1): 63-77.

Hein, J. R., Conrad, T. A., Frank, M., Christl, M. and Sager, W. W. (2012). "Copper-nickel-rich, amalgamated ferromanganese crust-nodule deposits from Shatsky Rise, NW Pacific." Geochem. Geophys. Geosyst. 13: Q10022.

Hein, J. R., Conrad, T. A. and Staudigel, H. (2010). "Seamount mineral deposits: a source of rare metals for high-technology industries." Oceanography 23(1): 184-189.

Hein, J. R., Koschinsky, A. and Halliday, A. N. (2003). "Global occurrence of tellurium-rich ferromanganese crusts and a model for the enrichment of tellurium." Geochimica et Cosmochimica Acta 67(6): 1117-1127.

Hein, J. R., Mizell, K., Koschinsky, A. and Conrad, T. A. (2013). "Deep-ocean mineral deposits as a source of critical metals for high- and green-technology applications: Comparison with land-based resources." Ore Geology Reviews 51(0): 1-14.

Hein, J. R. and Morgan, C. L. (1999). "Influence of substrate rocks on Fe–Mn crust composition." Deep Sea Research Part I: Oceanographic Research Papers 46(5): 855-875.

Hein, J. R., Schwab, W. C. and Davis, A. S. (1988). "Cobalt-rich and platinum-rich ferromanagenese crusts and associated substrate rocks from the Marshall islands." Marine Geology 78(3-4): 255-283.

Hein, J. R., Yeh, H. W., Gunn, S. H., Sliter, W. V., Benninger, L. M. and Wang, C. H. (1993). "Two major Cenozoic episodes of phosphogenesis recorded in equatorial Pacific seamount deposits." Paleoceanography 8(2): 293-311.

Henderson, G. M. and Burton, K. W. (1999). "Using ($^{234}U/^{238}U$) to assess diffusion rates of isotope tracers in ferromanganese crusts." Earth and Planetary Science Letters 170(3): 169-179.

Hodge, V. F., Stallard, M., Koide, M. and Goldberg, E. D. (1985). "Platinum and the platinum anomaly in the marine environment." Earth and Planetary Science Letters 72(2–3): 158-162.

Horner, T. J., Schonbachler, M., Rehkämper, M., Nielsen, S. G., Williams, H., Halliday, A. N., Xue, Z. and Hein, J. R. (2010). "Ferromanganese crusts as archives of deep water Cd isotope compositions." Geochemistry Geophysics Geosystems 11: 1525-2027.

ISA, Ed. (2002). Polymetallic Massive Sulphides and Cobalt-Rich Ferromanganese Crusts: Status and Prospects. Kingston, Jamaica, International Seabed Authority (ISA).

Kosakevitch, A. (1987). "Platiniferous Fe-Ni cosmic spherules in a marine metalliferous incrustation from Tuamotu (French Polynesia)." Comptes Rendus De l'Academie Des Sciences 305(2): 105-108.

Kosakevitch, A. and Disnar, J. R. (1997). "Nature and origin of chemical zoning in the metal nucleus and oxide cortex of cosmic spherules from the Tuamotu Archipelago, French Polynesia." Geochimica Et Cosmochimica Acta 61(5): 1073-1082.

Koschinsky, A. and Halbach, P. (1995). "Sequential leaching of marine ferromanganese precipitates: Genetic implications." Geochimica et Cosmochimica Acta 59(24): 5113-5132.

Koschinsky, A. and Hein, J. R. (2003). "Uptake of elements from seawater by ferromanganese crusts: solid-phase associations and seawater speciation." Marine Geology 198(3-4): 331-351.

Koschinsky, A., Stascheit, A., Bau, M. and Halbach, P. (1997). "Effects of phosphatization on the geochemical and mineralogical composition of marine ferromanganese crusts." Geochimica et Cosmochimica Acta 61(19): 4079-4094.

Koschinsky, A., Winkler, A. and Fritsche, U. (2003). "Importance of different types of marine particles for the scavenging of heavy metals in the deep-sea bottom water." Applied Geochemistry 18(5): 693-710.

Ku, T. L., Kusakabe, M., Measures, C. I., Southon, J. R., Cusimano, G., Vogel, J. S., Nelson, D. E. and Nakaya, S. (1990). "Beryllium isotope distribution in the western North Atlantic: a comparison to the Pacific." Deep-Sea Research Part a-Oceanographic Research Papers 37(5): 795-808.

Lesuave, R., Pichocki, C., Pautot, G., Hoffert, M., Morel, Y., Voisset, M., Monti, S., Amosse, J. and Kosakevitch, A. (1989). "Geological and mineralogical study of Co-rich ferromanganese crusts from a submerged atoll in the Tuamotu archipelago (French Polynesia)." Marine Geology 87(2-4): 227-247.

Levasseur, S., Frank, M., Hein, J. R. and Halliday, A. (2004). "The global variation in the iron isotope composition of marine hydrogenetic ferromanganese deposits: implications for seawater chemistry?" Earth and Planetary Science Letters 224(1-2): 91-105.

Li, Y. H. and Schoonmaker, J. E. (2003). Chemical Composition and Mineralogy of Marine Sediments. Treatise on Geochemistry. D. H. Editors-in-Chief: Heinrich and K. T. Karl. Oxford, Pergamon**:** 1-35.

Ling, H.-F., Jiang, S.-Y., Frank, M., Zhou, H.-Y., Zhou, F., Lu, Z.-L., Chen, X.-M., Jiang, Y.-H. and Ge, C.-D. (2005). "Differing controls over the Cenozoic Pb and Nd isotope evolution of deepwater in the central North Pacific Ocean." Earth and Planetary Science Letters 232(3–4): 345-361.

Ling, H. F., Burton, K. W., O'Nions, R. K., Kamber, B. S., von Blanckenburg, F., Gibb, A. J. and Hein, J. R. (1997). "Evolution of Nd and Pb isotopes in Central Pacific seawater from ferromanganese crusts." Earth and Planetary Science Letters 146(1–2): 1-12.

Morris, J. D. (1991). "Applications of cosmogenic ^{10}Be to problems in the Earth sciences." Annual Review of Earth and Planetary Sciences 19: 313-350.

Nicholson, K., Hein, J. R., Buehn, B. and Dasgupta, S., Eds. (1997). Manganese mineralization; geochemistry and mineralogy of terrestrial and marine deposits, Geological Society of London : London, United Kingdom.

Nielsen, S. G., Gannoun, A., Marnham, C., Burton, K. W., Halliday, A. N. and Hein, J. R. (2011). "New age for ferromanganese crust 109D-C and implications for isotopic

records of lead, neodymium, hafnium, and thallium in the Pliocene Indian Ocean." Paleoceanography 26.
O'Nions, R. K., Frank, M., von Blanckenburg, F. and Ling, H. F. (1998). "Secular variation of Nd and Pb isotopes in ferromanganese crusts from the Atlantic, Indian and Pacific Oceans." Earth and Planetary Science Letters 155(1-2): 15-28.
Peucker-Ehrenbrink, B. (1996). "Accretion of extraterrestrial matter during the last 80 million years and its effect on the marine osmium isotope record." Geochimica Et Cosmochimica Acta 60(17): 3187-3196.
Peucker-Ehrenbrink, B. and Ravizza, G. (2000). "The marine osmium isotope record." Terra Nova 12(5): 205-219.
Pichocki, C. and Hoffert, M. (1987). "Characteristics of Co-rich ferromanganese nodules and crusts sampled in French Polynesia." Marine Geology 77(1-2): 109-119.
Puteanus, D. and Halbach, P. (1988). "Correlation of Co concentration and growth rate — A method for age determination of ferromanganese crusts." Chemical Geology 69(1–2): 73-85.
Rehkämper, M., Frank, M., Hein, J. R. and Halliday, A. (2004). "Cenozoic marine geochemistry of thallium deduced from isotopic studies of ferromanganese crusts and pelagic sediments." Earth and Planetary Science Letters 219(1-2): 77-91.
Rehkämper, M., Frank, M., Hein, J. R., Porcelli, D., Halliday, A., Ingri, J. and Liebetrau, V. (2002). "Thallium isotope variations in seawater and hydrogenetic, diagenetic, and hydrothermal ferromanganese deposits." Earth and Planetary Science Letters 197(1-2): 65-81.
Reynolds, B. C., Frank, M. and O'Nions, R. K. (1999). "Nd- and Pb-isotope time series from Atlantic ferromanganese crusts: implications for changes in provenance and paleocirculation over the last 8 Myr." Earth and Planetary Science Letters 173(4): 381-396.
Rouxel, O., Dobbek, N., Ludden, J. and Fouquet, Y. (2003). "Iron isotope fractionation during oceanic crust alteration." Chemical Geology 202(1-2): 155-182.
Rudnick, R. L. and Gao, S. (2003). Composition of the Continental Crust. Treatise on Geochemistry. D. H. Editors-in-Chief: Heinrich and K. T. Karl. Oxford, Pergamon**:** 1-64.
Rudraswami, N. G., Shyam Prasad, M., Babu, E. V. S. S. K., Vijaya Kumar, T., Feng, W. and Plane, J. M. C. (2012). "Fractionation and fragmentation of glass cosmic spherules during atmospheric entry." Geochimica Et Cosmochimica Acta 99(0): 110-127.
Schmitt, A. D., Galer, S. J. G. and Abouchami, W. (2009). "Mass-dependent cadmium isotopic variations in nature with emphasis on the marine environment." Earth and Planetary Science Letters 277(1-2): 262-272.
Schulz, H. D. and Zabel, M. (2006). Marine geochemistry. Federal Republic of Germany, Springer : Berlin, Federal Republic of Germany.
Sclater, F. R., Boyle, E. and Edmond, J. M. (1976). "On the marine geochemistry of nickel." Earth and Planetary Science Letters 31(1): 119-128.
Segl, M., Mangini, A., Bonani, G., Hofmann, H. J., Nessi, M., Suter, M., Wolfli, W., Friedrich, G., Pluger, W. L., Wiechowski, A. and Beer, J. (1984). "^{10}Be-dating of a manganese crust from Central North Pacific and implications for ocean palaeocirculation." Nature 309(5968): 540-543.
Siebert, C., Nagler, T. F., von Blanckenburg, F. and Kramers, J. D. (2003). "Molybdenum isotope records as a potential new proxy for paleoceanography." Earth and Planetary Science Letters 211(1-2): 159-171.
Sorensen, J. V., Toner, B. M., Gueguen, B. and Rouxel, O. (2011). "Ni Speciation and Isotope Fractionation in Marine Ferromangenese Deposits." Goldschmidt Conference 2011 75(3): 1914.
Staudigel, H. and Hart, S. R. (1983). "Alteration of basaltic glass: Mechanisms and significance for the oceanic crust-seawater budget." Geochimica Et Cosmochimica Acta 47(3): 337-350.

Stuart, F. M. and Lee, M. R. (2012). "Micrometeorites and extraterrestrial He in a ferromanganese crust from the Pacific Ocean." Chemical Geology 322–323(0): 209-214.

Takahashi, Y., Manceau, A., Geoffroy, N., Marcus, M. A. and Usui, A. (2007). "Chemical and structural control of the partitioning of Co, Ce, and Pb in marine ferromanganese oxides." Geochimica Et Cosmochimica Acta 71(4): 984-1008.

Tanaka, S. and Inoue, T. (1979). "^{10}Be of North Pacific sediment cores up to 2.5 million years BP." Earth and Planetary Science Letters 45(1): 181-187.

Taylor, S., Lever, J. H. and Harvey, R. P. (2000). "Numbers, types, and compositions of an unbiased collection of cosmic spherules." Meteoritics & Planetary Science 35(4): 651-666.

Taylor, S. R. and McLennan, S. M. (1995). "The geochemical evolution of the continental crust." Reviews of Geophysics 33(2): 241-265.

van de Flierdt, T., Frank, M., Halliday, A. N., Hein, J. R., Hattendorf, B., Günther, D. and Kubik, P. W. (2003). "Lead isotopes in North Pacific deep water - implications for past changes in input sources and circulation patterns." Earth and Planetary Science Letters 209(1-2): 149-164.

van de Flierdt, T., Frank, M., Halliday, A. N., Hein, J. R., Hattendorf, B., Günther, D. and Kubik, P. W. (2004). "Tracing the history of submarine hydrothermal inputs and the significance of hydrothermal hafnium for the seawater budget—a combined Pb–Hf–Nd isotope approach." Earth and Planetary Science Letters 222(1): 259-273.

Vance, D., Cameron, V., Little, S. and Archer, C. (2013). The Oceanic Cycles of the Transition Metals and their Isotopes. Goldschmidt 2013, Florence, Italy, Mineralogical Magazine.

von Blanckenburg, F., O'Nions, R. K., Belshaw, N. S., Gibb, A. and Hein, J. R. (1996). "Global distribution of beryllium isotopes in deep ocean water as derived from Fe-Mn crusts." Earth and Planetary Science Letters 141(1-4): 213-226.

Wheat, C. G. and Mottl, M. J. (2000). "Composition of pore and spring waters from Baby Bare: Global implications of geochemical fluxes from a ridge flank hydrothermal system." Geochimica Et Cosmochimica Acta 64(4): 629-642.

Wheat, C. G., Mottl, M. J. and Rudnicki, M. (2002). "Trace element and REE composition of a low-temperature ridge-flank hydrothermal spring." Geochimica Et Cosmochimica Acta 66(21): 3693-3705.

Zhu, X. K., O'Nions, R. K., Guo, Y. L. and Reynolds, B. C. (2000). "Secular variation of iron isotopes in North Atlantic Deep Water." Science 287(5460): 2000-2002.

Conclusion du chapitre IV :

Les séries temporelles des compositions isotopiques en Ni analysés dans quatre encroûtements différents de l'Océan Pacifique (Nord et Sud) ont révélées que sur les 10 derniers millions d'années la composition isotopique du Ni enregistrée dans les encroûtements n'a pas varié significativement. En revanche, des processus d'altération/recristallisation dans un encroûtement du Pacifique Sud montre que finalement les isotopes du Ni sont très affectés par les processus d'altération et de re-précipitation des phases minérales (Figure C.4).

Ainsi, nos interprétations sont cohérentes avec les résultats obtenus dans le chapitre III qui favorisent l'hypothèse selon laquelle les processus de formation et d'enrichissement du Ni dans les phases minérales peuvent expliquer la variabilité isotopique du Ni dans les dépôts métallifères sans invoquer des variations des sources en Ni (par ex. hydrothermal). Les vitesses de précipitation des dépôts marins hydrothermaux ou hydrogénétiques riches en Fe et en Mn influent d'un part sur les enrichissements en métaux dans les phases minérales, et d'autre part les compositions isotopiques en Ni. Les dépôts formés rapidement, comme c'est le cas des dépôts hydrothermaux, montrent des fractionnements isotopiques du Ni car il est fractionné lors des processus d'adsorption du Ni dans les phases minérales. D'un autre côté, le Ni incorporé dans les dépôts hydrogénétiques formés sur des périodes de temps beaucoup plus longue (de l'ordre du million d'années) n'exprimera pas de facteur de fractionnement isotopique et ces dépôts auront des compositions isotopiques similaires à leur source, l'eau de mer.

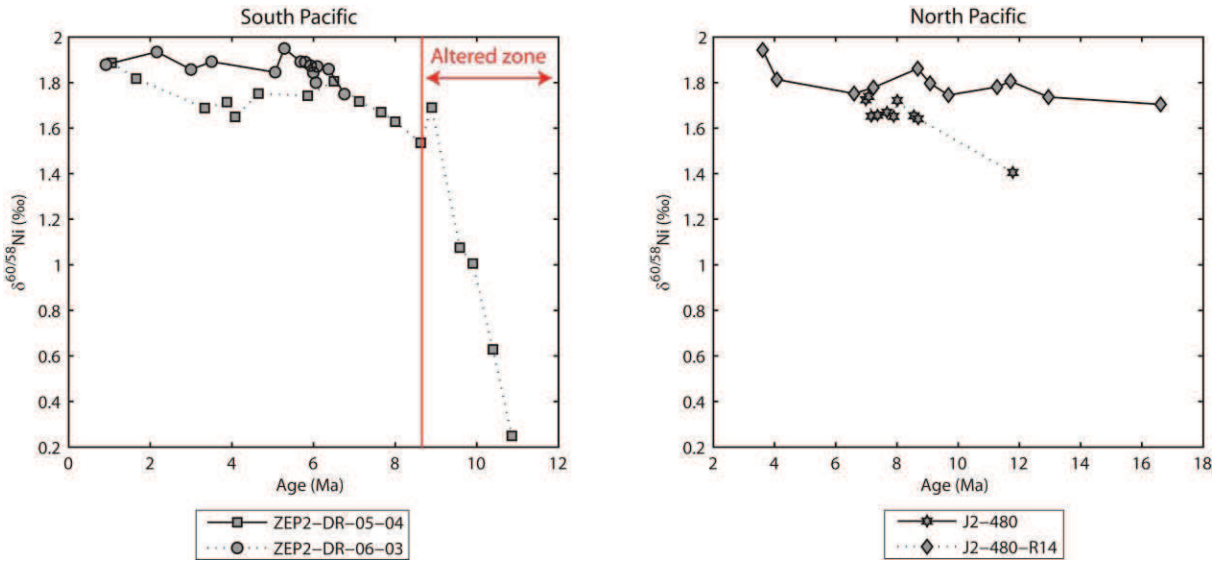

***Figure C.4** : Variations temporelles des compositions isotopiques en Ni dans deux encroûtements de fer-manganèse du Pacifique Sud (Tahiti) (A) et du Pacifique Nord (Apuupuu, Hawaii) (B). La ligne rouge tracée sur le graphe (A) délimite la zone altérée de l'échantillon ZEP2-DR05-04.*

Chapitre V - Stratigraphie haute résolution des variations isotopiques du Fe, Pb, Cu et Zn dans des encroûtements de fer-manganèse de l'Océan Pacifique : une approche multi-proxy

Chapter V – High resolution stratigraphy of Fe, Pb, Cu and Zn isotope variations in ferromanganese crusts from the Pacific Ocean : a multi-proxy approach

Avant-propos :

Dans le chapitre IV nous avons présentés les compositions isotopiques en Ni dans quatre encroûtements de fer-manganèse. Dans les chapitres III et IV nous avons montré que le Ni était un bon traceur des processus d'enrichissement et que les variations isotopiques du Ni s'expliquait donc par les processus de formation et de précipitation *in-situ* des encroûtements, et non par des variations isotopiques dues aux sources de Ni. Par conséquent, l'objectif de ce chapitre V est d'étudié les variations isotopiques en Fe, Cu et Zn de ces mêmes séries temporelles afin de déterminer si ces traceurs isotopiques permettraient de tracer les processus d'enrichissement ou bien les variations des sources de métaux aux océans.

En effet, dans l'introduction du chapitre III nous avons présenté de manière succincte les études réalisées sur d'autres systèmes isotopiques des métaux dans les dépôts métallifères et les sédiments marins et les variations isotopiques significatives que certains de ces systèmes pouvaient présenter. Le comportement biogéochimique étant différent pour chacun de ces métaux, on peut envisager que ces systèmes isotopiques aient eu des réponses différentes aux changements globaux, aux variations des sources et aux processus de formation et de précipitation qui entrent en jeu dans la genèse des encroûtements. Ainsi, l'utilisation conjointe de ces différents systèmes isotopiques pourrait permettre d'avoir une approche multi-proxy. Le fer a typiquement un temps de résidence très court (80 à 200 ans) dans les océans car il est rapidement recyclé par l'activité biologique et piégé dans les particules. Ainsi, la composition isotopique du Fe enregistrée dans les croûtes est très dépendante de la composition isotopique des sources locales en Fe. Au contraire le Cu et le Zn qui ont des temps de résidence plus longs devraient avoir des compositions isotopiques homogènes dans les océans et pourraient permettre de tracer des changements globaux ayant eu lieu dans les océans.

Bien que les isotopes du Fe aient déjà été utilisés comme traceurs paléocéanographiques, avec comme objectif de retracer la variabilité du cycle biogéochimique du Fe et de ses sources dans l'eau de mer au cours du Cénozoïque, une seule étude a pour l'instant porté sur les isotopes du Zn et Cu dans les encroûtements de fer-manganèse (Little et al. 2013).

La première partie s'articule autour des compositions isotopiques en Fe des encroûtements qui ont été collectés dans l'océan Pacifique Nord au Sud de la grande île d'Hawaii sur le mont sous-marin Apuupuu. La deuxième partie propose une discussion autour des variations isotopiques en Cu et Zn dans les quatre encroûtements.

Partie V.1 – Signification des variations isotopiques temporelles dans des encroûtements de fer-manganèse : indice d'apports hydrothermaux dans l'eau de mer profonde ?

Part V.1 - Significance of secular Fe isotope variations in ferromanganese crusts: evidence of hydrothermal inputs in deep seawater ?

Abstract:

Temporal variations of iron (Fe) isotope compositions of two ferromanganese (Fe-Mn) crusts from the North Pacific Ocean (south of Hawaii) were inferred using high resolution profiles. Results of Pb isotope composition reveal a concomitant shift in $^{208}Pb/^{204}Pb$ and $^{207}Pb/^{204}Pb$ ratios from 7 Ma to 12 Ma in the two Fe-Mn crusts. In contrast, $^{206}Pb/^{204}Pb$ ratios and $\delta^{56/54}Fe_{IRMM-14}$ values are different between the crusts. However, comparison of Pb and Fe isotope composition shows remarkable correlations, with one crust (J2-480) showing negative correlation between $\delta^{56/54}Fe_{IRMM-14}$ and $^{206,207,208}Pb/^{204}Pb$ ratios, and the other crust (J2-480-R14) lacking correlation between $\delta^{56/54}Fe_{IRMM-14}$ and $^{206}Pb/^{204}Pb$ but showing positive correlation between $\delta^{56/54}Fe_{IRMM-14}$ and $^{207,208}Pb/^{204}Pb$ ratios. Crust J2-480 also shows a marked increase in $\delta^{56/54}Fe_{IRMM-14}$ from -0.68‰ to -0.03‰ from 8.6 to 11 Ma, while crust J2-480-R14 shows a lower decrease of $\delta^{56/54}Fe_{IRMM-14}$ from +0.06 to -0.30 ‰. Major and trace element composition of both crust are rather similar, although variations in transition metal concentrations are more prominent in crust J2-480, in particular for Co, Ni, and Mo. Using Co/Mn ratios and $^{10}Be/^{9}Be$ ratios, average growth rate of crust J2-480 is more than twice the growth rate of J2-480-R14 (4.4 vs 1.4 mm/Ma).

These results suggest that both Fe-Mn crusts recorded different Fe reservoir during their growth, and that Fe isotope composition of Fe-Mn crusts is mainly controlled by local water masses mixing. The large negative Fe isotope excursion, increasing growth rate and variations of metal contents in J2-480 are best explained by hydrothermal input of Fe that became prominent by 9 Ma ago. This hydrothermal input could be related to the increase proximity of the seamount with the Hawaiian volcanoes. This hypothesis suggests that hydrothermal venting related to the Hawaii volcanic activity has affected the surrounding areas. Using the present-day vent fluid chemistry at Loihi seamount as modern analogues, where Fe is predominantly precipitated as Fe-oxyhydroxides instead of Fe-sulfides at the seafloor, we consider that hydrothermally release would be characterized by negative Fe isotope compositions. The negative Fe isotope signature is then transported in surrounding water masses having contrasted Pb isotope composition. This localized nature of hydrothermal venting related to mid-plate volcanoes may explain the peculiar correlations observed between Fe and Pb isotopes.

1. Introduction

Transition metals in modern seawater are present as dissolved trace elements (Broecker and Peng, 1982; Bruland, 1983). However, many of them are bioessential elements and involved in major biological reactions as micronutrients (Morel and Price, 2003). Of these metals, Fe is an important but bio-limiting element for primary production in surface waters. For instance, in HNLC zones (High-Nutrient-Low-Chlorophyll), low trace metal concentrations in seawater hamper thriving of microorganisms resulting in low phytoplankton productivity and chlorophyll concentrations and consequently higher concentrations in other nutrients. Recently, much attention was given to iron (Fe), especially because improvements in experimental and analytical developments for measuring Fe concentrations and isotope compositions in seawater allowed to better constraining the biogeochemical cycling of Fe mostly in surface waters (Boyle et al., 2012; John and Adkins, 2010; Lacan et al., 2008; Lacan et al., 2010; Radic et al., 2011; Rouxel and Auro, 2010).

In modern oceans, Fe is extremely particle-reactive resulting in a very short residence time in oceans of 0-200 yrs, (Johnson et al., 1997) compared to the ~1500 yrs required for

homogenizing oceanic water masses, and it generally precipitate close to its source (e.g. estuaries, hydrothermal deposits). Hence, Fe is one of the less concentrated trace metals in the marine environment, generally < 1 nmol/L (Broecker and Peng, 1982; Bruland, 1983; Bruland and Lohan, 2003; Bruland et al., 1994). Iron is delivered to the oceans mainly through rivers, eolian dusts and particles (Duce et al., 1991; Jickells, 1995; Jickells et al., 2005), hydrothermal sources along oceanic ridges (Baker et al., 1995; Bennett et al., 2008; Elderfield and Schultz, 1996; Saito et al., 2013; Tagliabue et al., 2010; Von Damm, 1995) and continental margins sediments (Bergquist and Boyle, 2006; Elrod et al., 2004; Severmann et al., 2006; Severmann et al., 2010). Estimates yield a river flux with the same amplitude as the hydrothermal flux (Anbar and Rouxel, 2007; Dauphas and Rouxel, 2006; Elderfield and Schultz, 1996). Accordingly, Fe isotope composition of global oceans is not spatially uniform and Fe isotope variations are extremely sensitive to local sources - which may be quite Fe rich like for instance hydrothermal fluids - and processes, and to the nature and contribution of each source.

A review of previous work with a reevaluation of the estimation hydrothermal fluxes to the oceans are reported in 1996 by Elderfield and Schultz. The authors pointed out that for many trace metals high-temperature hydrothermal vents were rather sinks than sources because most of trace metals are scavenged by hydrothermal minerals and particles. However, low-temperature and diffuse hydrothermal fluxes are very likely important suppliers of trace metals to oceans (Alt, 1995; Edwards et al., 2011). According to the magnitude of these fluxes, we may assume that the far-field influence of hydrothermal inputs would be greater than expected in the deep oceans. Estimate of the contribution of hydrothermal Fe inputs to the oceans in the total oceanic budget is on the order of 12-22 % (Bennett et al., 2008). Other authors show that the Southern Hemisphere oceans are the most affected by hydrothermal inputs of Fe (Tagliabue et al., 2010). Although, new data on dissolved Fe in the deep Atlantic Ocean emphasize that low temperature diffuse venting from the Mid-Ocean Atlantic ridge delivers important amount of Fe (Saito et al., 2013), yet the real contribution of hydrothermal inputs of Fe to the deep oceans remains poorly constrained. Additionally, iron biogeochemical cycling in the deep oceans and its time-resolved variations in oceans are not completely understood of which the impact of hydrothermal inputs of Fe budget in the oceans.

Fe- and Mn-rich metalliferous crusts are deposits composed of successive Fe-Mn oxides layers of predominantly vernadite (δ-MnO_2) and in a lesser extent Fe-oxides, precipitated at slow rate (1-6 mm/Ma) on the flank of seamount between 1000 and 3000 meters depth. Transition metals are principally hosted in the manganese phase (Koschinsky and Halbach, 1995). The presence of an Oxygen Minimum Zone (OMZ) between 500 and 1000 meters depth would allow Mn to become soluble as a result of its reduction to Mn^{2+}. Thereafter, oxidation of Mn at the base of the OMZ promotes its precipitation in oxides to form Fe-Mn crusts layered deposits. During oxidation and precipitation, Mn- (and Fe-) oxides efficiently scavenge dissolved trace metal present in ambient seawater accounting for enrichment in transition metals of Fe-Mn crusts deposits such as Ni, Cu, Zn and Co, elements which are hosted in the Mn-phase (Frank et al., 1999; Halbach and Puteanus, 1984; Koschinsky and Halbach, 1995; Koschinsky et al., 1997). Interestingly, the slow rate of precipitation provides a temporal record of seawater transition metal isotope composition. The rate of Fe-Mn crusts precipitation (a few mm/Ma) is large in comparison to the short Fe residence time in oceans of ~200 yrs. Therefore, it is very likely that Fe-Mn crusts faithfully record ambient seawater since practically no Fe isotope fractionation between the crusts and

seawater should occur (Chu et al., 2006). The system can be envisioned as if removal of Fe from seawater during precipitation in Fe-Mn crusts was quantitative.

Although large-scale Fe isotope variations in deep oceanic basins deduced from surface layers of precipitated ferromanganese crusts do not reveal meaningful trend that could be ascribed to any particular global variations (Levasseur et al., 2004), yet temporal series of $\delta^{56/54}$Fe values in Fe-Mn crusts could yield important constraints on the variations of Fe sources to the oceans and their impact on the global biogeochemical cycling of Fe through the Cenozoic. In this framework, it is expected that Fe isotope composition of Fe-Mn crusts will be very sensitive to the composition of local sources due the highly particle-reactive behavior of Fe. For instance, it was argued that a negative Fe isotope excursion recorded in a Fe-Mn crust was the result of scattered hydrothermal input in the water column (Chu et al., 2006). However, even though the approach of using Fe isotopes as a valuable tracer of the hydrothermal activity is not straightforward because, for instance, the global Fe isotopes composition of the hydrothermal flux is poorly constrained, there is nevertheless a promising potential and this hypothesis need to be delved. It is hypothesized that Fe isotopes in Fe-Mn crusts may provide valuable information for deciphering spatial spread of hydrothermal inputs that could help us constrain the influence of hydrothermal inputs to the global budget of oceans chemical composition.

On the other hand, a concomitant increase in Fe isotopes and Pb isotopes composition from 2 to 0 Ma in a Atlantic Fe-Mn crusts led the authors to suggest that Fe isotope variations were the result of variable continental sources (Zhu et al., 2000). Due to its short residence time Pb isotopes in Fe-Mn crusts faithfully record water masses, as it is expected from Fe isotopes. The abundant literature available for Pb isotope compositions in Fe-Mn crusts from all the oceans implies that the temporal evolution of deep water Pb isotopes is very well constrained (Abouchami et al., 1997; Burton et al., 1997; Frank, 2002; Frank et al., 1999; Frank et al., 2002; Ling et al., 2005; O'Nions et al., 1998; Reynolds et al., 1999; van de Flierdt et al., 2003; Vlastelic et al., 2001). Therefore, it is expected that combining Pb and Fe isotopes measurements in Fe-Mn crusts will help deciphering whether Fe isotope variations in Fe-Mn crusts are the result of global vs. local effects.

In that perspective, we present in this paper a case study of time series combining elemental geochemistry and Fe isotope and Pb isotope compositions of two ferromanganese crusts collected on the Apuupuu seamount located South West of Hawaii Big Island following approaches of Zhu et al. (2000) and Chu et al. (2006).

2. Materials and methods

The two Fe-Mn crusts collected on Apuupuu seamount (Latitude = 18°34’54’’N; Longitude = 155°28.11’76’’W) ~50 km south of Hawaii were recovered during FeMO 2009 cruise on the R/V Kilo Moana (University of Hawaii) in October 2009. These crusts were collected by ROV (Remotely Operated underwater Vehicle) Jason2 (Woods Hole Oceanographic Institution) at water depths of 2079 for crust J2-480-R14 (Figure V.1). However, the depth of collection of crust J2-480 is not precisely known because it was mixed together with other samples in the ROV basket. Fe-Mn crusts were deposited on a basaltic substrate although it was not collected attached to the crusts. The total thickness of crusts is ~60 mm.

The two crusts were prepared in epoxy resin for subsequent high resolution sampling of Mn-oxides layers using a microdrill (Micromill®) equipped with diamond drill-bits. Pictures of the two crusts after microdrilling are presented in (Figure V.1). The total thickness of each

crust in epoxy resin is between 20 and 25 mm. The “Inner” region of the crust corresponds to the older part of the crust (towards the substrate), and the “Outer” region is the one in contact with seawater.

Dating the crusts was made using the method of the cosmogenic isotope ^{10}Be (Frank et al., 1999; von Blanckenburg et al., 1996) at CEREGE in Aix-en-Provence (France) by Didier Bourlès. Be isotopes were only measured on a selected numbers of samples. Then, combining growth rates calculated with Co concentrations for all samples and absolute ages determined with Be isotopes on some subsamples of the crusts we calculated ages of the remaining subsamples.

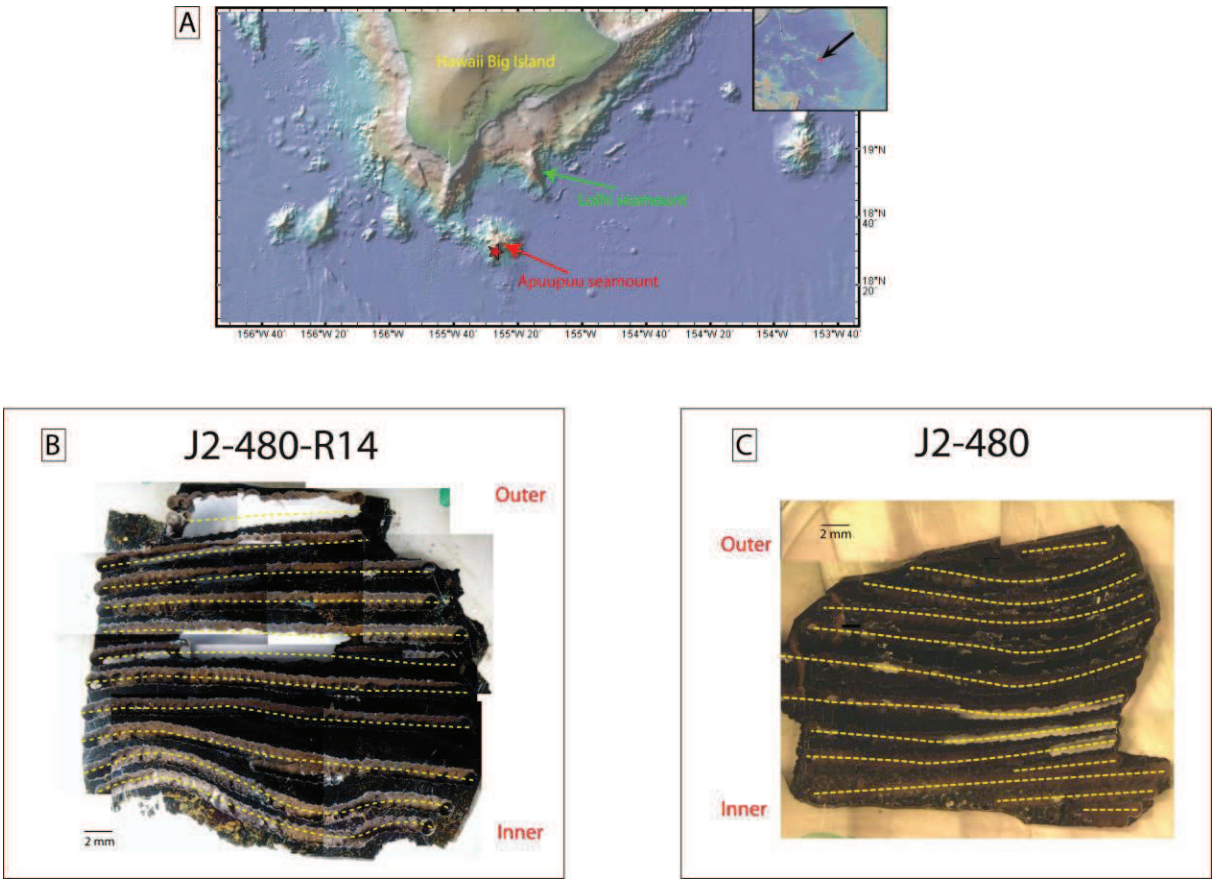

Figure V.1*: Map with sample locations relatively to Hawaii Big Island and Loihi seamount (panel A) and photographs of polished sections of Fe-Mn crusts after microdrilling (yellow stippled lines) (panels B and C).*

Major and trace elements were analyzed by ICP-MS Quadrupole (X Series, Thermo-Finnigan) at Pôle-Spectrométrie-Océan (PSO, IUEM/Ifremer, Brest, France) and Pb and Fe isotope compositions were measured by MC-ICP-MS (Neptune, Thermo-Finnigan) at PSO. A solution of Pb NIST SRM 981 standard was run along with samples and the compilation of analyses was used for calculating the two-standard deviation (2sd) of analytical session. Instrumental mass bias was corrected with Tl added to each sample prior to analysis (Albarède et al., 2004; Collerson et al., 2002; Longerich et al., 1987).

^{56}Fe/^{54}Fe ratios were measured following methods by (Rouxel et al., 2008; Rouxel et al., 2005). ^{56}Fe/^{54}Fe ratios are reported relative to IRMM-14 Reference Material according to the conventional delta notation (1) used for stable isotope systematics.

$$\delta^{56/54}Fe = [(^{56}Fe/^{54}Fe_{sample})/(^{56}Fe/^{54}Fe_{IRMM\text{-}14}) - 1] \times 1000 \quad (1)$$

A nickel-doping method was used to correct our samples for instrumental mass discrimination and a standard-sample-bracketing analysis scheme (Albarede and Beard, 2004; Albarède et al., 2004; Rouxel et al., 2005) allows us to determine a two standard deviation of 0.05 ‰ based on replicate measurements of IRMM-14 isotopic standard.

Eventually, elemental mapping of selected regions in the crusts and elemental profiles were measured with electron microprobe analyses (CAMECA SX-100, Ifremer-CNRS Brest, France). These elemental maps show the distribution of major elements in the mineralogical textures of the crusts and the preferential elemental associations. Elemental profiles were made at a 200 µm interval through the entire crust.

3. Results

Apuupuu Fe-Mn crusts are composed of a mineral assemblage of Mn-oxides and Fe-oxides. Some phosphates and carbonates are present as secondary phases. Elemental maps by electron Microprobe analyses also clearly indicate that Ni, Cu, Zn and Co are always co-located with Mn and that the Mn-phase controls the distribution of these elements in Fe-Mn crusts (see chapter IV). Both samples of hydrogenous crusts were collected on Apuupuu seamount (South of Hawaii) practically in the middle of the Pacific Ocean. If we attempt to reconstruct the geodynamic pathway followed by the crust 10 Ma ago, it was located southeast of its present position and has only moved over ~500 km (Meynadier et al., 2008).

Temporal geochemical variations of the crusts are presented in Figure V.2 and elemental ratios of Mn/Fe, Co/Mn and Pb/Mn in Figure V.3 and in Table V.1, while Fe and Pb isotopes time-series are shown in Figure V.4. There is a general increase in transition metals such as Mn, Ni, Cu, Cd, Mo, Te, Tl and Pb in the middle of the crusts (Figure V.2). In both crusts there is also an increase in Mn/Fe and Co/Mn, ratios indicating a global increase in transition metal contents and growth rates (Figures V.2 and V.3).

Interestingly, in crust J2-480 the increase in $^{207}Pb/^{204}Pb$ and $^{208}Pb/^{204}Pb$ ratios (from 15.61 to 15.66 and from 38.55 to 38.81 respectively) is contemporaneous to the decrease in Fe isotope composition from near-zero value at the base of the crust ($\delta^{56/54}Fe$ = -0.04‰) towards negative values down to -0.68 ‰ (Figure V.4). By contrast, J2-480-R14 crust has a more restricted range of variation from -0.30 to +0.06‰ and the increase in Fe isotope values is concomitant to $^{207}Pb/^{204}Pb$ and $^{208}Pb/^{204}Pb$ ratios increase (from 15.59 to 15.63 and from 38.47 to 38.75 respectively). With the exception of $^{206}Pb/^{204}Pb$ ratio which only increases from 18.63 to 18.78 in crust J2-480, both crusts show similar $^{207}Pb/^{204}Pb$ and $^{208}Pb/^{204}Pb$ ratios with gradual increasing patterns from the “Inner” to the “Outer” of the crust (values range from 15.592 to 15.659 and 38.810 to 38.473 respectively) (Figure V.4 and V.5). Note that J2-480-R14 does not reach high Pb isotopes values as in J2-480, however the amplitude of variation is similar because J2-480-R14 has also lower Pb isotope values in its “Inner” region. The increasing Pb isotopes are correlated with increasing Pb/Mn ratios in both Fe-Mn crusts. Linear correlations between the three Pb isotopes ratios are shown in Figure V.5.

Figure V.6 indicates that $^{206}Pb/^{204}Pb$, $^{207}Pb/^{204}Pb$ and $^{208}Pb/^{204}Pb$ ratios are correlated with Fe isotopes in both Fe-Mn crusts but in two different ways. The correlation is negative in

J2-480 while it is positive in J2-480-R14, with the exception of $^{206}Pb/^{204}Pb$ vs $\delta^{56/54}Fe$ in crust J2-480-R14 (Figure V.6A).

Table V.1: Elemental ratios (µg/µg) of Mn/Fe, Co/Mn and Pb/Mn, Fe isotope composition (‰) and Pb isotopes ratios in Fe-Mn crusts time-series from Apuupuu (North Pacific).

Sample name	Depth (mm) in the crust	Age (Ma)*	Mn/Fe	Co/Mn	Pb/Mn	$\delta^{56/54}$Fe	2sd**	^{206}Pb/^{204}Pb	2sd***	^{207}Pb/^{204}Pb	2sd	^{208}Pb/^{204}Pb	2sd
J2-480 Fe-Mn crust													
J2-480-R1	0,2	7,0	1,18	0,014	0,0108	-0,62	0,05	18,7871	0,0008	15,6586	0,0008	38,8101	0,0023
J2-480-R2	2,5	7,1	1,44	0,015	0,0076	-0,63	0,05	18,7665	0,0008	15,6514	0,0008	38,7802	0,0023
J2-480-R3	5,0	7,2	1,40	0,014	0,0076	-0,57	0,05	18,7642	0,0008	15,6513	0,0008	38,7779	0,0023
J2-480-R4	7,0	7,5	1,55	0,016	0,0062	-0,62	0,05	18,7599	0,0008	15,6529	0,0008	38,7835	0,0023
J2-480-R5	9,0	8,0	2,22	0,017	0,0038	-0,68	0,05	18,7574	0,0008	15,6506	0,0008	38,7751	0,0023
J2-480-R6	11,0	8,3	1,72	0,016	0,0042	-0,46	0,05	18,7406	0,0008	15,6437	0,0008	38,7492	0,0023
J2-480-R7	12,5	8,5	1,69	0,017	0,0045	-0,47	0,05	18,7187	0,0008	15,6355	0,0008	38,7053	0,0023
J2-480-R8	14,0	8,6	1,75	0,019	0,0037	-0,39	0,05	18,6596	0,0008	15,6181	0,0008	38,6219	0,0023
J2-480-R9	15,0	8,7	1,28	0,020	0,0043	-0,22	0,05	18,6409	0,0008	15,6154	0,0008	38,5937	0,0023
J2-480-R10	16,5	8,8	0,69	0,016	0,0063	0,03	0,05	18,6191	0,0008	15,6077	0,0008	38,5488	0,0023
J2-480-R12	19,0	11,8	0,68	0,019	0,0056	-0,04	0,05	18,6323	0,0008	15,6090	0,0008	38,5544	0,0023
J2-480-R14 Fe-Mn crust													
J2-480-R14-L11	0,2	3,6	1,32	0,020	0,0062	0,06	0,05	18,6520	0,0008	15,6326	0,0008	38,7517	0,0023
J2-480-R14-L10	3,0	4,4	1,21	0,020	0,0064	0,00	0,05	18,6455	0,0008	15,6295	0,0008	38,7305	0,0023
J2-480-R14-L9	5,0	6,6	1,35	0,021	0,0058	-0,02	0,05	18,6460	0,0008	15,6285	0,0008	38,7208	0,0023
J2-480-R14-L8	7,0	7,7	1,67	0,019	0,0045	-0,03	0,05	18,6475	0,0008	15,6255	0,0008	38,6973	0,0023
J2-480-R14-L7	9,0	8,7	1,71	0,021	0,0048	-0,10	0,05	18,6497	0,0008	15,6215	0,0008	38,6717	0,0023
J2-480-R14-L6	10,0	9,3	1,79	0,022	0,0042	-0,15	0,05	18,6411	0,0008	15,6128	0,0008	38,6192	0,0023
J2-480-R14-L5	12,0	10,3	1,30	0,023	0,0049	-0,21	0,05	18,6383	0,0008	15,6085	0,0008	38,5788	0,0023
J2-480-R14-L4	14,0	11,3	1,64	0,021	0,0034	-0,30	0,05	18,6498	0,0008	15,6052	0,0008	38,5561	0,0023
J2-480-R14-L3	16,0	12,0	1,57	0,020	0,0026	-0,24	0,05	18,6438	0,0008	15,5975	0,0008	38,5050	0,0023
J2-480-R14-L2	18,0	12,9	1,26	0,023	0,0028	-0,26	0,05	18,6424	0,0008	15,5936	0,0008	38,4838	0,0023
J2-480-R14-L1	20,0	16,6	1,25	0,024	0,0026	-0,26	0,05	18,6373	0,0008	15,5918	0,0008	38,4734	0,0023
NOD-A-1	-	-	1,74	0,019	0,0038	-0,36	0,05	18,6941	0,0008	15,6307	0,0008	38,6833	0,0023
NOD-A-1****	-	-	1,74	0,019	0,0039	-0,34	0,05	-	-	-	-	-	-
NOD-P-1	-	-	5,29	0,008	0,0013	-0,55	0,05	-	-	-	-	-	-

* Age (Ma) were calculated using cosmogenic 10Be isotope (see chapter IV for ample details on the method).
** 2sd stands for two-standard deviation calculated on replicate measurements of IRMM-14 for Fe isotopes.
*** 2sd corresponds to the two-standard deviation calculated on replicate measurements of NIST SRM 981.
**** Duplicate of attack and chemistry procedure.

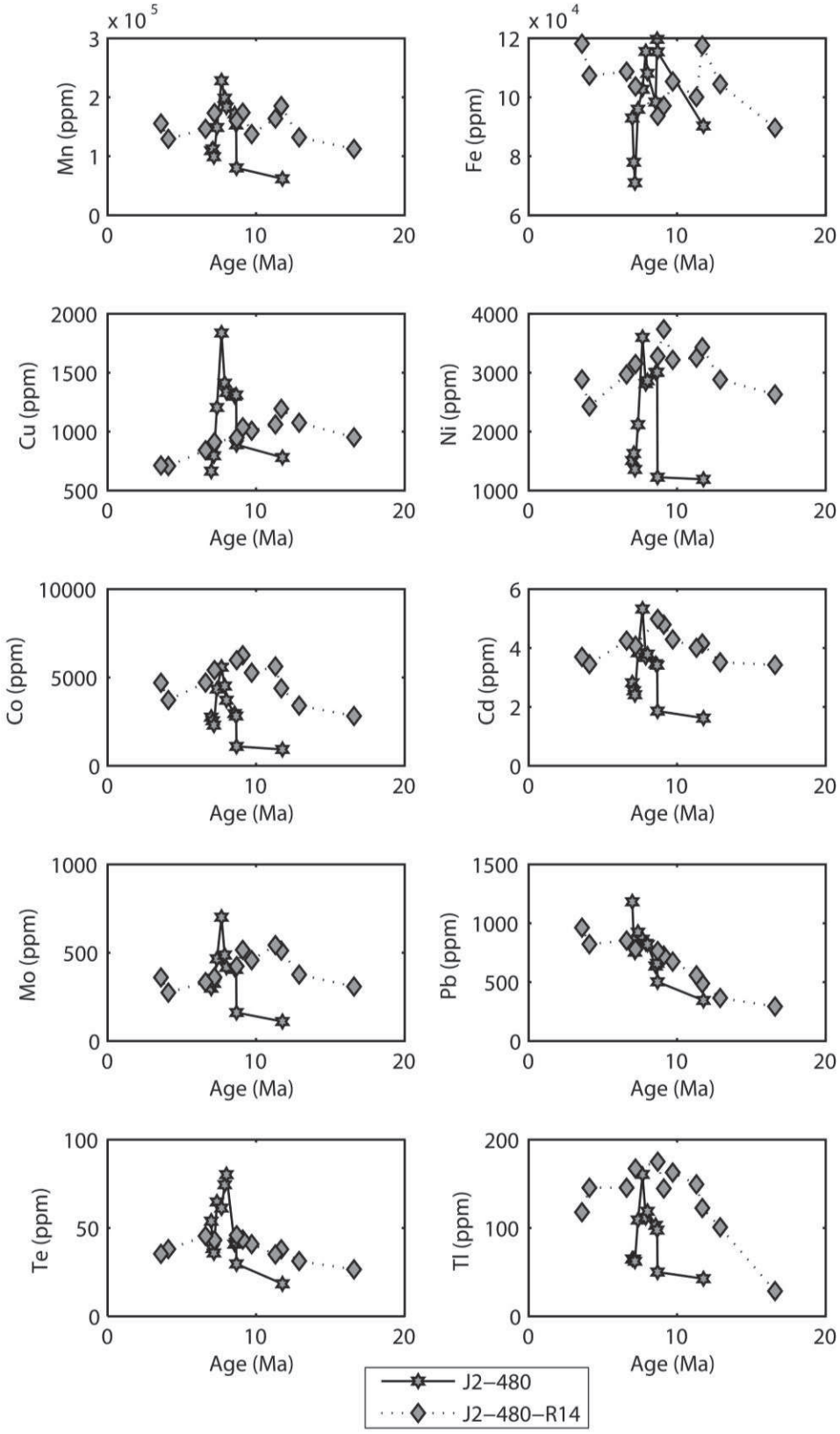

***Figure V.2**: Time-series of elemental concentrations (µg/g) of Mn, Fe, Ni, Cu, Zn, Co, Mo and Pb in Apuupuu Fe-Mn crust.*

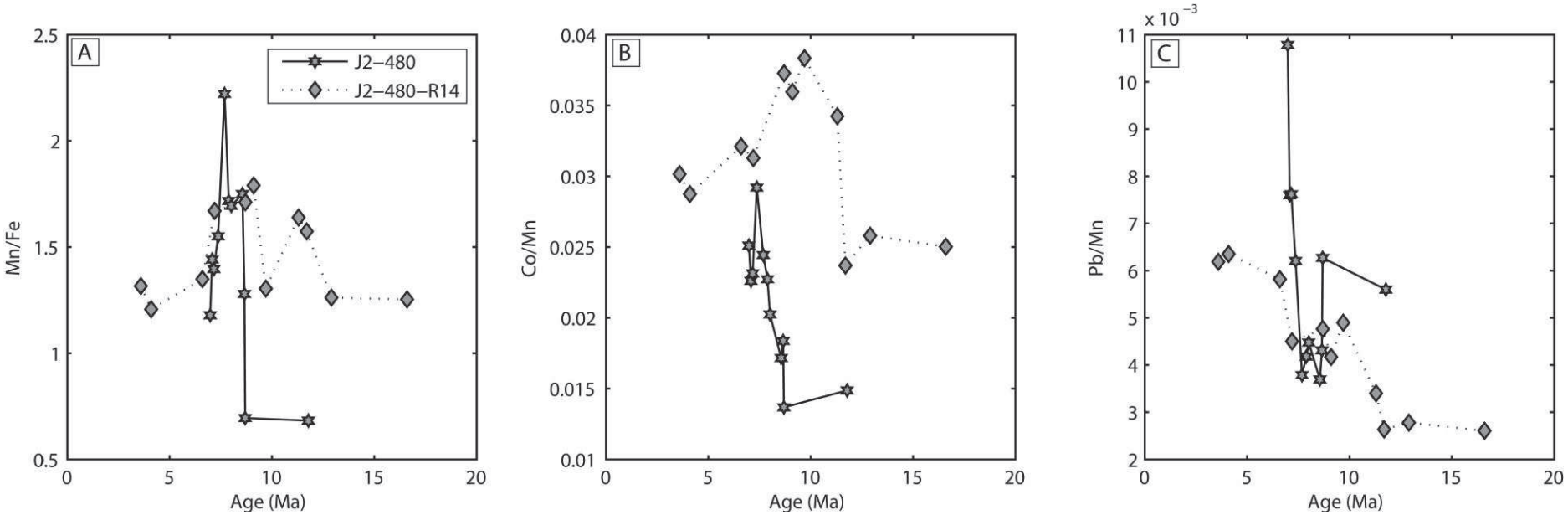

***Figure V.3**: Time-series of elemental ratios of Mn/Fe, Co/Mn and Pb/Mn in Apuupuu Fe-Mn crusts.*

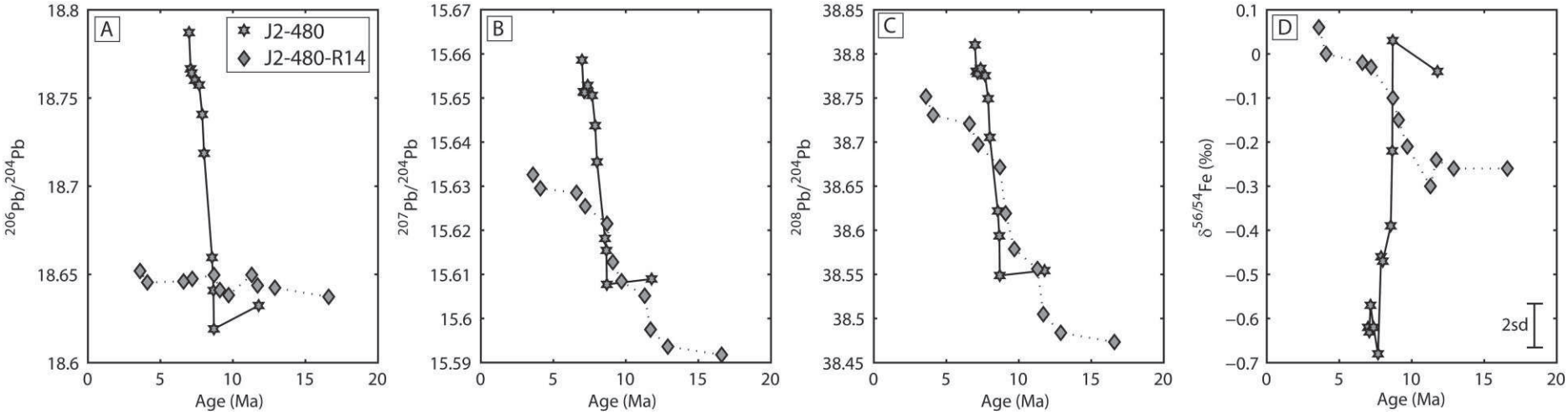

***Figure V.4**: Pb isotopes time-series, $^{206/204}Pb$ (panel A), $^{207/204}Pb$ (panel B) and $^{208/204}Pb$ (panel C) and Fe isotopes time-series (panel D) of Apuupuu Fe-Mn crusts.*

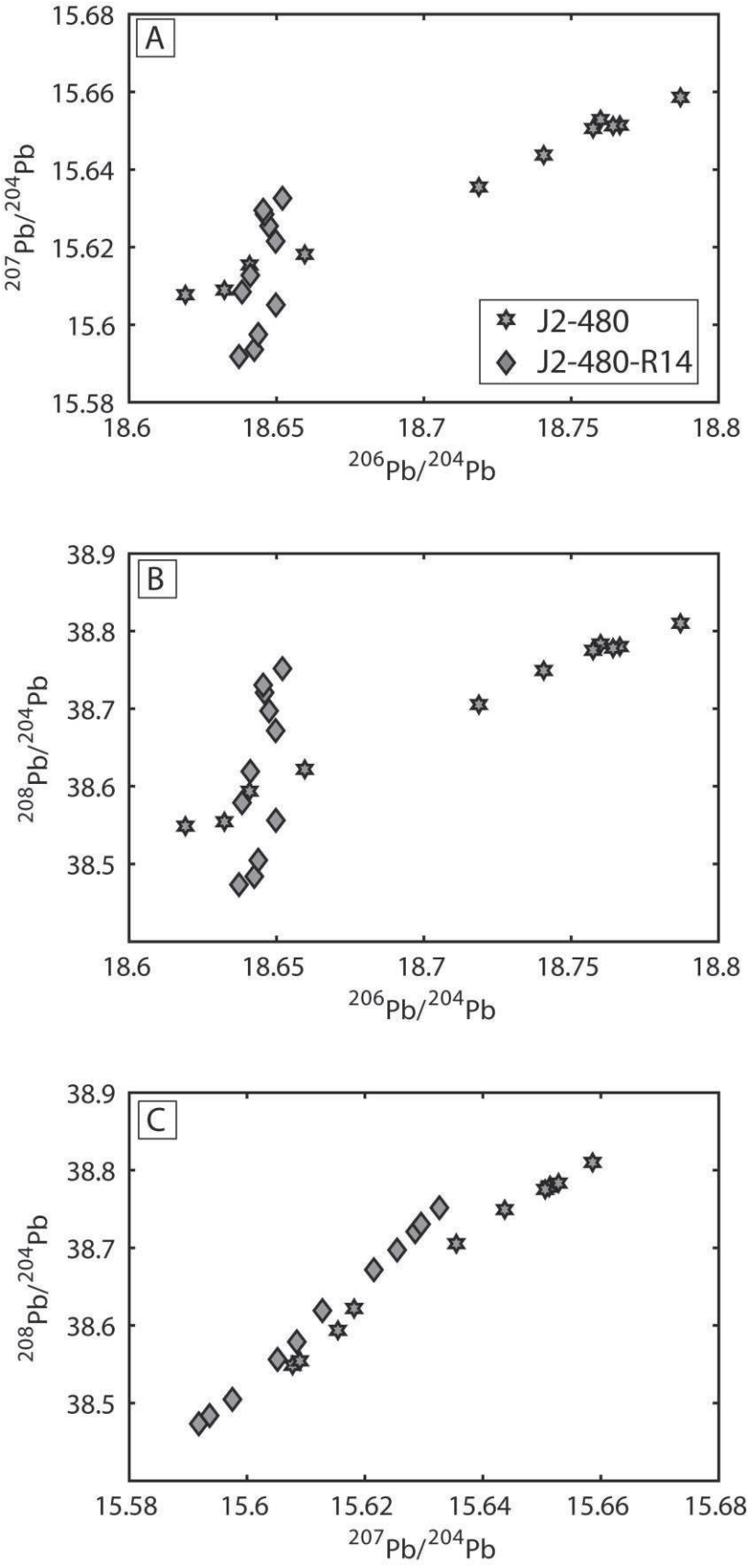

***Figure V.5**: $^{207/204}Pb$ vs $^{206/204}Pb$ (panel A), $^{208/204}Pb$ vs $^{206/204}Pb$ (panel B) and $^{208/204}Pb$ vs $^{207/204}Pb$ (panel C) ratios of Apuupuu Fe-Mn crusts.*

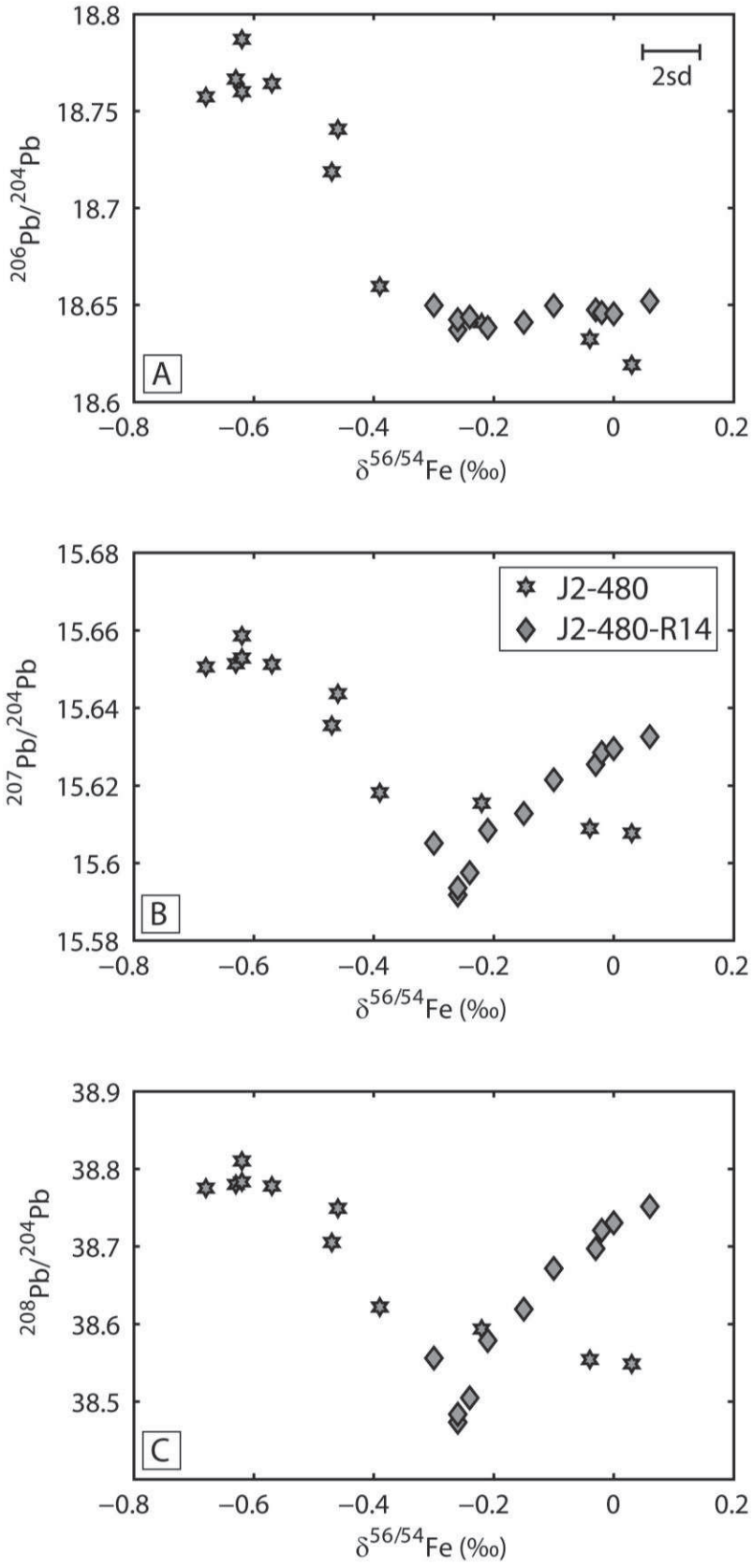

***Figure V.6**: Pb isotopes ratios versus Fe isotopes values (‰) in Apuupuu Fe-Mn crusts.*

4. Discussion

4.1. Deciphering global versus local processes

Iron is a highly particle-reactive element because it is readily trapped in its sinks upon release from its source. Consequently, Fe isotopes in seawater are expected to reflect that of the local sources. $\delta^{56/54}$Fe seawater values reported in the literature are between -0.8 and +0.8‰ (Boyle et al., 2012; Lacan et al., 2008; Lacan et al., 2010; Radic et al., 2011). Similarly to Fe Pb is rapidly retrieved from seawater, however while Pb is mostly supplied by continental sources, especially by continental eolian dusts (Frank, 2002; Frank et al., 1999; Ling et al., 2005), Fe sources include continental erosion and atmospheric particles, hydrothermalism, diagenetic fluxes, and seafloor alteration. Pb and Fe are generally show mineralogical association in Fe-Mn crusts since Pb is generally incorporated in the Fe-phase rather than in the Mn-phase (Koschinsky and Hein, 2003; Takahashi et al., 2007). However, there are still uncertainties regarding the global versus local effects of the different sources on Fe isotope composition of deep waters.

According to correlations between Pb isotopes ratios (Figure V.5) and to correlations between Pb isotopes and Fe isotopes displayed in Figure V.6, isotopic variations are probably the result of mixing between two end-members for each crust. However, the correlations are different between the two crusts, it is negative for J2-480 and positive for J2-480-R14, implying that end-members defining the trends are different for the two crusts. The mixing trends could be explained by mixing between different oceanic water masses.

Geochemical differences between water masses are, in fact, the result of the integration of different sources (e.g. inputs from the continental atmospheric dusts and hydrothermal inputs) in these water masses. Therefore, it is important to highlight that Fe-Mn crusts do not record directly variations of the sources, but instead they record the final product of these integrations in the water masses. For instance, Figure V.7 (panel B) showing Fe isotopes compositions versus Al/Fe as an indicator of lithogenic effect, indicates that Fe isotope variations are not related to any potential variations in Al/Fe ratios, which are other evidence that any isotopic signal recorded in our Fe-Mn crusts only originate from seawater.

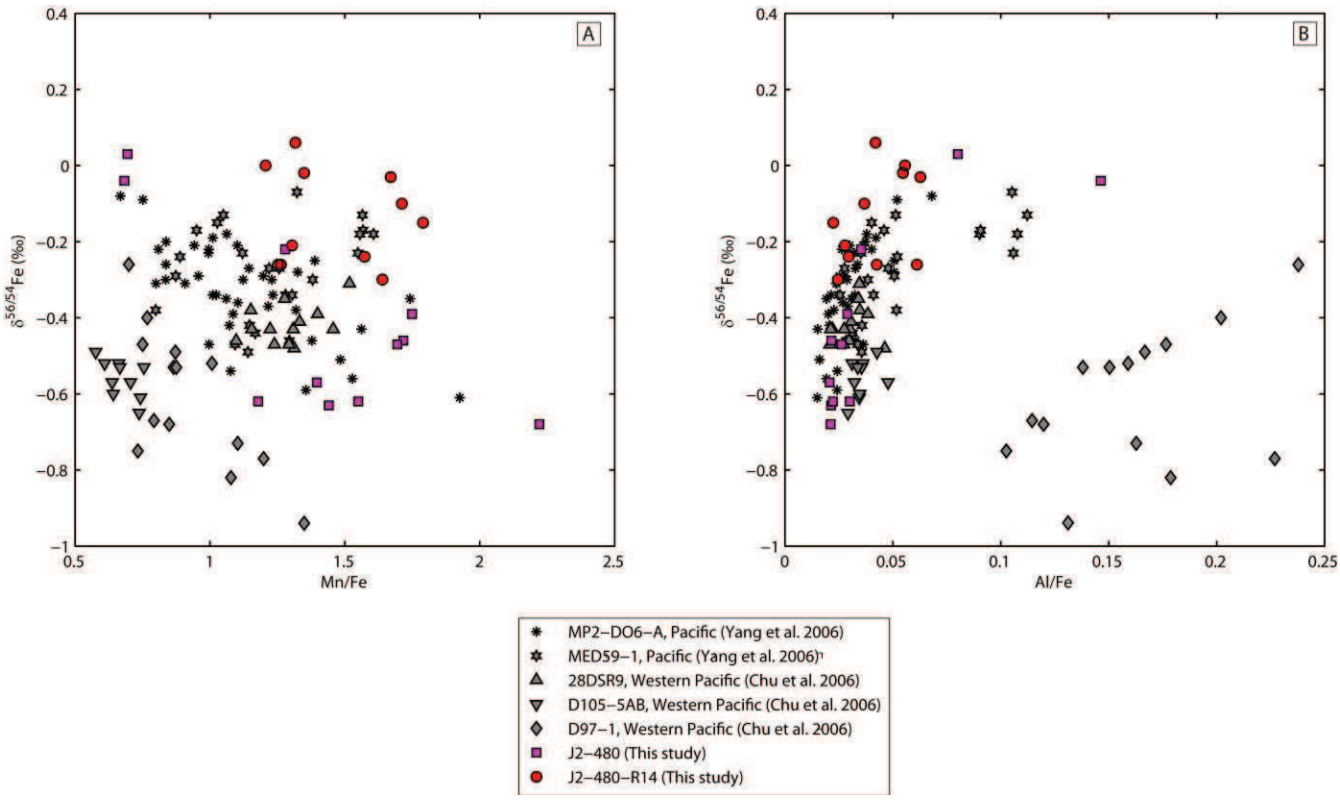

***Figure V.7**: Fe isotopes versus Mn/Fe (panel A) and Al/Fe (panel B) ratios of J2-480 (pink squares) and J2-480-R14 (red circles) Fe-Mn crusts plotted with literature data (grey symbols). Sample names and references are given in legend of the figure.*

Even if it is possible that Pb and Fe isotope systematics are decoupled from each other, i.e. a source will not necessarily affect both Pb isotopes and Fe isotopes in the seawater, the correlation between the two isotope systematics measured in our Fe-Mn crusts is strong evidence that Fe-Mn crusts have recorded mixing between water masses rather than the effect of independent sources. Interestingly, the intersection between the two trends (Figure V.6) corresponds to the time when crust J2-480 underwent higher growth rates (higher Mn/Fe and lower Co/Mn ratios), thus implying that ambient seawater may have undergone a particular event (Figure V.4).However, one should note that J2-480-R14 has recorded a larger period of time than J2-480.

In the next sections, we will explore the potential sources that may have affected Fe isotope and Pb isotope compositions of the different water masses recorded in our two Fe-Mn crusts, (1) variations in the continental sources, (2) seafloor alteration, (3) diagenetic remobilization of Fe from continental margins sediments, (4) hydrothermal inputs. While hypotheses (1) and (2) are related to global processes, hypotheses (3) and (4) will essentially reflect local processes.

4.2. Variations in the continental sources

Pb isotope composition in seawater is essentially controlled by continental sources inputs, mostly through atmospheric dusts and particles, while Fe isotope compositions can be strongly affected by hydrothermal inputs. Therefore, Pb isotope patterns may enable us to reconstruct paleocirculation of oceanic currents and the influence of dust inputs and continental weathering to dissolved trace metals budget in seawater by comparing with other existing Pb isotope patterns recorded in North Pacific Fe-Mn crusts.

Although located further to the North (the central gyre region of the North Pacific), analyses of dusts collected in core GPC3 indicate that eolian particles from Asia are the predominant contributor to overall dust deposition in North Pacific Ocean (Pettke et al., 2002). We may, therefore, reasonably assume that water masses in which our samples are located can also be influenced by Asian dusts. These dusts are characterized by continental lead, i.e. high Pb isotopes values > 18.80 for $^{206}Pb/^{204}Pb$, >15.65 for $^{207}Pb/^{204}Pb$, and > 38.85 for $^{208}Pb/^{204}Pb$ (Pettke et al., 2002). Alternatively, Pb isotope patterns in a hydrothermal crust from Bauer Basin (Eastern Pacific Ocean) showing low radiogenic Pb isotopes are consistent with a hydrothermal composition, i.e. a MORB-like composition and Pb isotopes are correlated with Mn/Fe ratios, the less radiogenic Pb (close to a MORB composition) the lower Mn/Fe ratio (van de Flierdt et al., 2004). However, these deposits are purely hydrothermal whereas Fe-Mn crusts deposits from our study are typical hydrogenetic deposits. Figure V.8 displays Pb isotope compositions of Fe-Mn crusts reported in the literature and shows that Pb isotopes values in our Fe-Mn crusts are globally lower than other Fe-Mn crusts.

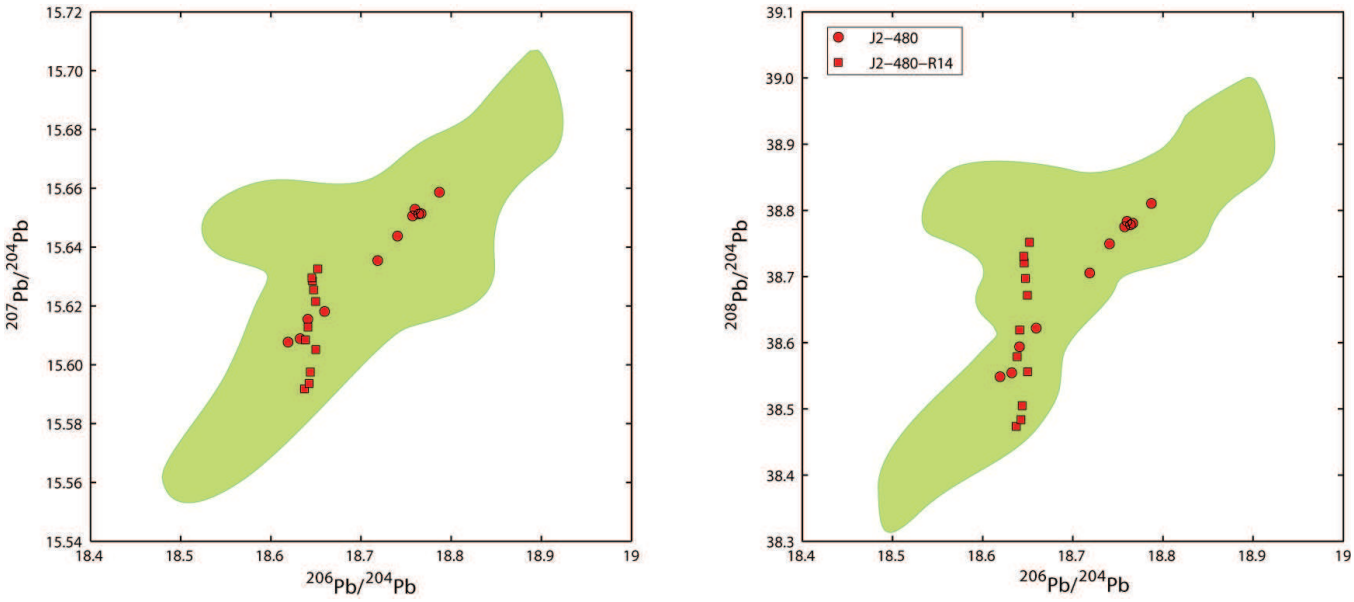

Figure V.8: *$^{207/204}Pb$ vs $^{206/204}Pb$ (panel A) and $^{208/204}Pb$ vs $^{206/204}Pb$ (panel B) ratios with literature data (green field). Samples from this study are represented as red circles (J2-480) and red squares (J2-480-R14).*

In Figure V.5, positive correlations between Pb isotopes ratios indicate mixing between radiogenic Pb from continental atmospheric particles (a continental end-member) and unradiogenic Pb from a hydrothermal/basaltic origin (a mantle end-member). The only

possible means to explain high Pb isotope ratios is to invoke a continental source (atmospheric inputs of continental particles) or to a volcanic arc source (through either weathering or delivery of ashes to the atmosphere). In addition, since the two samples align on two different correlations for $^{207}Pb/^{204}Pb$ and $^{208}Pb/^{204}Pb$ vs. $^{206}Pb/^{204}Pb$ (Figure V.5 panels A and B), this suggests two different end-members for the hydrothermal/basaltic Pb and to account for the two different trends.

Zhu et al. (2000) discussed the possibility of using coupled Fe and Pb isotope compositions. The excellent co-variations between Fe isotope and Pb isotope compositions in a Atlantic Fe-Mn crust with a continuous decrease from 0 to ca.2 Ma was attributed to a variation in the sources of these elements (Zhu et al., 2000). Fe isotope values measured in China loess - assumed to represent the predominant source of Fe to the oceans and to be similar to the composition of the upper continental crust - are comprised between -0.04 and +0.32‰ (Zhu et al., 2000). Therefore, the trend in their data showing that the more elevated Pb isotope ratios the more positive Fe isotope values (from -0.77 to +0.13‰), is consistent with mixing of continental sources. Microbially-mediated isotope fractionation is ruled out because, albeit it could affect Fe isotopes, it is unlikely to impart any Pb isotope signature, and we would not observe a positive correlation between the two isotope systems (Zhu et al., 2000). However, the authors failed to determine exactly the mechanisms responsible for negative Fe isotope fractionation from its sources. Beard et al. (2003) advocate that Fe isotope variability in Fe-Mn crusts is the result of changes in the relative proportion of Fe fluxes to the oceans having distinct Fe isotope compositions (Beard et al., 2003).

As observed by Zhu et al. (2000), there is a positive correlation between Pb isotopes and Fe isotopes in our crust J2-480-R14. Therefore, eolian dusts with positive Fe isotopes and high Pb isotopes values could therefore represent the superior end-member displayed by the correlation in J2-480-R14 (Figure V.6). In contrast, the correlation in crust J2-480 is inversed to that observed by Zhu et al. (2000) in the Atlantic crust and in crust J2-480-R14 showing that the lowest Fe isotope compositions are correlated with the less radiogenic Pb isotopes. Therefore, another end-member must be invoked to explain this end-member.

Noteworthy, while Pb isotope patterns are similar in the two crusts (with the exception of $^{206}Pb/^{204}Pb$ ratio), the extent of Fe isotope variations is different indicating that these two isotope systematics are decoupled in our samples in contrast to results reported by Zhu et al. (2000) and that they are controlled by different geochemical processes.

4.3. Seafloor alteration

In support of hypothesis (2) negative Fe isotope values have also been reported as the result of halmyrolysis processes (Rouxel et al., 2003). These authors demonstrated that alteration of glass on the seafloor may produce fluids enriched in lighter Fe isotopes as a result of preferential leaching of light Fe. Therefore, it is possible that alteration of the seamount onto which the crusts are deposited produced a local flux of Fe as a result of halmyrolitic processes. This source could account for the light Fe isotopes end-member recorded in our two Fe-Mn crusts.

4.4. Diagenetic remobilization of Fe in sediment porewaters in continental margins

Hypothesis (3) was mentioned by Johnson et al. (1999) who argued that Fe from continental margins may be an important source of Fe for phytoplankton growth in seawater (Johnson et al., 1999). Then Elrod at al. (2004) suggested that an important flux of iron to the

oceans originate from continental shelf sediments (Elrod et al., 2004). Staubwasser et al. (2006) demonstrated with analyses of Fe isotopes in porewaters and sediments from two cores that diagenetic remobilization of Fe within sediment porewaters produces light Fe isotope compositions down to ~-0.8 ‰ (Staubwasser et al., 2006). Diffusion of Fe from these porewaters towards the overlying water column could be a non-negligible source of light Fe to the oceanic Fe isotope budget. Fe isotopes in porewaters from the Amazon shelf also reveal that the produced Fe flux could be severely enriched in light isotopes by -1.3 ‰ (Bergquist and Boyle, 2006). Further, similar results were found by Severmann et al. (2006 and 2010) in continental shelf sediments for which the authors advocated a that Fe transferred to seawater in continental benthic shelf environments is isotopically light with $\delta^{56/54}$Fe values down to -3.4 ‰ (relatively to average isotope composition of igneous rocks) (Severmann et al., 2006; Severmann et al., 2010). Staubwasser et al. (2006) even suggested that light Fe isotope reported by Levasseur et al. (2004) could be accounted for by this diagenetic Fe source.

Manganese and Fe can be transported from continental margins over long distances in the OMZ acting as a Fe and Mn "shuttle" in the oceans. In the OMZ these elements accumulate under their reduced soluble form after release from particles (Martin and Knauer, 1984). Upon escaping the OMZ, Mn and Fe are either scavenged onto particles or they precipitated as Mn- and Fe-rich colloids which efficiently scavenged other dissolved trace metals in seawater. Samples were collected below 2000 m depth and the OMZ is generally located at water depth between 500 and 1500 m. Therefore, because of plate motion and subsidence of the seamount, the distance of Fe-Mn crusts from the OMZ have varied through time and ~7 to 8 Ma (when lower Fe isotopes values were measured) they were probably located closer to the OMZ implying that they could have been affected by this diagenetic Fe flux from the OMZ. However, the increase in metal/Fe ratios and the shift to negative Fe isotope values in J2-480-R14 are not as significant as in crust J2-480, leaving this hypothesis still uncertain but worth considering.

4.5. Hydrothermal venting and potential effects on Fe isotopes in the deep oceans

Negative Fe isotopes excursions down to -0.95 ‰ have already been reported in Fe-Mn crusts from Western Pacific (close to Izu-Bonin arc) (Chu et al., 2006). Similarly this negative excursion is coupled to an increase in Mn, Mg, Ni, Cu, Zn, Mo and V contents of the crust layers. However, another crust collected ~100 km north of the Izu-Bonin arc in a very close region to this crust does not record this hydrothermal pulse. The difference was accounted for by either different depths between the two sites or a localized hydrothermal pulse. The authors proposed several explanations that may account for this discrepancy, (1) crusts were not collected at locations close enough so that the diffuse and localized hydrothermal plume haven't imprinted the two crusts, (2) precision on the determination of growth rate using Co-dating method is low and could explain the apparent gap for the transition metal contents increase (Chu et al., 2006).

Apuupuu Fe-Mn crusts from this study were collected in an active volcanic setting (Hawaii hotspot) where continuous hydrothermal venting occurred since its initiation. Loihi seamount is the presently active region of the Hawaiian hotspot with highly active hydrothermal sources exhibiting uncommon fluid geochemistry. Therefore, even if Loihi has not always been the active source, their geochemical composition offers an excellent opportunity to obtain an estimate of the overall geochemical signature of the incoming hydrothermal flux in ambient seawater produced by the magmatic activity of the Hawaiian

hotspot. Our assumption is that hydrothermal fluids produced on Hawaii active volcanoes in the past had similar fluids geochemistry than present-day Loihi fluids.

Loihi hydrothermal activity was first discovered by nontronite deposits on dredged lavas, and methane concentrations, temperature and ^{3}He anomalies in seawater (Garcia et al., 2006). In 1987, the first dive on Loihi active hydrothermal vents took place with ALVIN submersible and provided direct observation of Loihi hydrothermal activity. Loihi hydrothermal influence over several hundreds of kilometers has already been advocated with helium enrichment measured in the water column and high $^{3}He/^{4}He$ ratios together with anomalous methane concentration for instance. Excess in ^{3}He in the water column was even observed at 400 km North Loihi seamount, albeit the largest trace of the plume is toward the East, hence providing strong evidence of intensive hydrothermal activity (Lupton, 1998; Lupton, 1995). This far-field helium signal was ascribed to Loihi due to the particularly high $^{3}He/^{4}He$ ratios measured in Loihi basalts (Garcia et al., 2006; Lupton, 1998). $^{3}He/^{4}He$ ratios (>30 Ra) of Loihi basalts is among the highest ever observed in oceanic basalts. Similar anomalies were detected in the Lau-Fiji basin in the South Pacific (Lupton et al., 2004). The present observations indicate that He isotope anomalies may be used to trace the far-field influence of hydrothermal activity on the global oceans. Altogether, these results show that hydrothermal inputs to the oceans are probably underestimated.

The discovery of such hydrothermal solutions was first reported for hydrothermal vents from Pele's summit and surprisingly they observed that Ni was enriched and correlates with Si concentrations (Sedwick et al., 1992). Interestingly, Loihi fluids are enriched in CO_2, CH_4, NH_4, PO_4 and Fe and Mn but they are depleted in H_2S and have a low pH (Glazer and Rouxel, 2009; Sedwick et al., 1992). Association of this particular fluid geochemistry to the presence of the oxygen-minimum-zone (OMZ) implies the presence of depleted O_2 waters at ~1000 m water depth. Conjunction of these factors also hampers abiotic oxidation of Fe in the water column upon delivery at vent chimneys. Therefore, while Fe precipitation at vent chimneys is generally controlled by rapid sulfide precipitation producing positive Fe isotope values in remaining Fe in the water column, Fe delivered at Loihi hydrothermal vents is not quantitatively removed by sulfide precipitation (Edwards et al., 2011; Glazer and Rouxel, 2009) and oxidation of Fe^{2+} will be slower. In addition, although most hydrothermal activity takes place close to Loihi hydrothermal active vents important ultra-diffuse venting releasing significant quantities of Fe also occurs. The delivery of Fe through this diffuse venting promotes the deposition of massive Si- and Fe-rich deposits formed by microbial activity through biological oxidation of incoming Fe^{2+}, altogether coated by thin ferromanganese crusts, thus revealing an important bacterial ecosystem (Edwards et al., 2011). The ancient counterpart have already been documented for late Cretaceous Pacific seamounts (Hein et al., 1994). Further, these authors advocated that Loihi hydrothermal fluids rich in Fe, CO_2 (and Ni) may be the precursor to these Fe-rich and that silica was of hydrothermal origin – and not detrital. These observations support the essential role of Fe in Loihi hydrothermal system. An important outcome of this process is that Fe oxidation from the hydrothermal flux generates negative isotope composition in remaining Fe in the water column. Further, the oxidation rate of Mn is slower than Fe, hence the transport of Mn away from the vent over long distance could have been possible.

Finally, carbon-rich particles released by hydrothermal vents can stabilize the Fe delivered by hydrothermal sources through the formation of organic ligand complexes with Fe, thus hampering its oxidation and precipitation near the vents and favoring its transport through the water column (Bennett et al., 2008; Toner et al., 2009). Other studies also show that stabilization of Fe in the oceans could be strongly enhanced by organic complexation

allowing its transport away from the vents and preventing its oxidation and precipitation in the hydrothermal plume (Hawkes et al., 2013; Sander and Koschinsky, 2011; Toner et al., 2009). Clearly, our Fe-Mn crusts samples are pure hydrogenetic metalliferous deposits and did not precipitated in proximity to the vent and to the buoyant plume and they are not hydrothermal Fe-Mn deposits. However, scattered hydrothermal inputs in the overlying seawater emanating from Hawaii hotspot hydrothermal activity (consistent with present-day geochemistry of hydrothermal fluids of Loihi vents) may have affected the geochemistry of surrounding water masses.

A combination of higher growth rates in J2-480 (e.g. lower Co/Mn) in comparison to J2-480-R14, lowest $\delta^{56/54}$Fe values and transition metals enrichment could be evidence that seawater in which the crust formed was affected by these hydrothermal inputs. This scattered hydrothermal flux in the water column may have locally produced enhanced Mn-oxides precipitation in the crust (and Fe-oxides) with efficient scavenging of Ni, Cd, Zn, Mo, Te and Tl, the latter three elements having a typically pure hydrogenetic origin. However, since low Fe isotopes values are correlated with high Pb isotope ratios, it indicates that the geochemical composition of these water masses is also controlled by continental dusts inputs. However, we must recognized that it is still unclear whether higher growth rates in J2-480 in comparison to J2-480-R14 are the result of the particular geochemistry of the hydrothermally-affected water mass it-self as suggested above, or that higher growth rates allow J2-480 to record hydrothermal isotopic signal affecting water masses while lower growth rates in J2-480-R14 do no permit the crust to archive this signal.

Alternatively, the reason why crust J2-480-R14 does not display such negative $\delta^{56/54}$Fe values could be related to the position of both crusts relatively to the direction of hydrothermal fluxes. The position of Apuupuu seamount has varied over the last 10 Ma and it was located farther and to the southeast of the Hawaiian hotspot and its hydrothermal activity than today. Since both crusts were not exactly located in the same area on the seamount, the overall hydrothermal input flux from Hawaii may have imprinted a crust more importantly than the other. For instance, crust J2-480 could have been located strictly in the pathway of the scattered hydrothermal flux, whereas J2-480-R14 was located aside of this flux.

5. Concluding remarks

This study has presented Pb and Fe isotope compositions of two Fe-Mn crusts collected in the North Pacific on the Apuupuu seamount to the southwest of Hawaii Island. Our results show that Pb isotopes and Fe isotopes are correlated in each crust according to two different trends. J2-480 displays a negative correlation, while J2-480-R14 exhibits a positive correlation between the two isotope systematics. These correlations are clear evidence that Fe-Mn crusts recorded mixing between different water masses according to two different trends. Low Pb isotopes ratios in seawater are attributed to a hydrothermal/basaltic end-member, while radiogenic Pb isotope compositions are the result of inputs from continental atmospheric dusts. Low Fe isotope values down to -0.68 ‰ in one crust (J2-480) may have been produced by hydrothermal inputs which affected the geochemistry of water masses. Therefore, J2-480 may have recorded mixing between hydrothermally-affected water masses and non-affected water masses.

Altogether, these results show combining different isotopic systematics may provide interesting constraints for understanding metal isotope variations in deep seawater.

Abouchami, W., Goldstein, S. L., Galer, S. J. G., Eisenhauer, A., and Mangini, A., 1997, Secular changes of lead and neodymium in central Pacific seawater recorded by a Fe-Mn crust: Geochimica Et Cosmochimica Acta, v. 61, no. 18, p. 3957-3974.

Albarede, F., and Beard, B., 2004, Analytical Methods for Non-Traditional Isotopes: Reviews in Mineralogy and Geochemistry, v. 55, no. 1, p. 113-152.

Albarède, F., Telouk, P., Blichert-Toft, J., Boyet, M., Agranier, A., and Nelson, B., 2004, Precise and accurate isotopic measurements using multiple-collector ICPMS: Geochimica Et Cosmochimica Acta, v. 68, no. 12, p. 2725-2744.

Alt, J. C., 1995, Subseafloor Processes in Mid-Ocean Ridge Hydrothermal Systems, Seafloor Hydrothermal Systems: Physical, Chemical, Biological, and Geological Interactions, Volume 91, American Geophysical Union, Geophysical Monograph Series, p. 85-114.

Anbar, A. D., and Rouxel, O., 2007, Metal stable isotopes in paleoceanography: Annual Review of Earth and Planetary Sciences, v. 35, p. 717-746.

Baker, E. T., German, C. R., and Elderfield, H., 1995, Hydrothermal Plumes Over Spreading-Center Axes: Global Distributions and Geological Inferences, Seafloor Hydrothermal Systems: Physical, Chemical, Biological, and Geological Interactions, Volume 91, American Geophysical Union, Geophysical Monograph Series, p. 47-71.

Beard, B. L., Johnson, C. M., Von Damm, K. L., and Poulson, R. L., 2003, Iron isotope constraints on Fe cycling and mass balance in oxygenated Earth oceans: Geology, v. 31, no. 7, p. 629-632.

Bennett, S. A., Achterberg, E. P., Connelly, D. P., Statham, P. J., Fones, G. R., and German, C. R., 2008, The distribution and stabilisation of dissolved Fe in deep-sea hydrothermal plumes: Earth and Planetary Science Letters, v. 270, no. 3-4, p. 157-167.

Bergquist, B. A., and Boyle, E. A., 2006, Iron isotopes in the Amazon River system: Weathering and transport signatures: Earth and Planetary Science Letters, v. 248, no. 1–2, p. 54-68.

Boyle, E. A., John, S., Abouchami, W., Adkins, J. F., Echegoyen-Sanz, Y., Ellwood, M., Flegal, A. R., Fornace, K., Gallon, C., Galer, S., Gault-Ringold, M., Lacan, F., Radic, A., Rehkamper, M., Rouxel, O., Sohrin, Y., Stirling, C., Thompson, C., Vance, D., Xue, Z. C., and Zhao, Y., 2012, GEOTRACES IC1 (BATS) contamination-prone trace element isotopes Cd, Fe, Pb, Zn, Cu, and Mo intercalibration: Limnology and Oceanography-Methods, v. 10, p. 653-665.

Broecker, W., and Peng, T., 1982, Tracers in the Sea, Eldigio, Palisades, NY.

Bruland, K. W., 1983, Trace elements in sea water, London, Academic Press, Chemical Oceanography.

Bruland, K. W., and Lohan, M. C., 2003, Controls of Trace Metals in Seawater, *in* Heinrich, D. H., and Karl, K. T., eds., Treatise on Geochemistry: Oxford, Pergamon, p. 23-47.

Bruland, K. W., Orians, K. J., and Cowen, J. P., 1994, Reactive trace metals in the stratified central North Pacific: Geochimica Et Cosmochimica Acta, v. 58, no. 15, p. 3171-3182.

Burton, K. W., Ling, H. F., and Onions, R. K., 1997, Closure of the Central American Isthmus and its effect on deep-water formation in the North Atlantic: Nature, v. 386, no. 6623, p. 382-385.

Chu, N. C., Johnson, C. M., Beard, B. L., German, C. R., Nesbitt, R. W., Frank, M., Bohn, M., Kubik, P. W., Usui, A., and Graham, I., 2006, Evidence for hydrothermal venting in Fe isotope compositions of the deep Pacific Ocean through time: Earth and Planetary Science Letters, v. 245, no. 1-2, p. 202-217.

Collerson, K. D., Kamber, B. S., and Schoenberg, R., 2002, Applications of accurate, high-precision Pb isotope ratio measurement by multi-collector ICP-MS: Chemical Geology, v. 188, no. 1–2, p. 65-83.

Dauphas, N., and Rouxel, O., 2006, Mass spectrometry and natural variations of iron isotopes: Mass Spectrometry Reviews, v. 25, no. 5, p. 831-832.

Duce, R. A., Liss, P. S., Merrill, J. T., Atlas, E. L., Buat-Menard, P., Hicks, B. B., Miller, J. M., Prospero, J. M., Arimoto, R., Church, T. M., Ellis, W., Galloway, J. N., Hansen, L., Jickells, T. D., Knap, A. H., Reinhardt, K. H., Schneider, B., Soudine, A., Tokos, J. J.,

Tsunogai, S., Wollast, R., and Zhou, M., 1991, The atmospheric input of trace species to the world ocean: Global Biogeochem. Cycles, v. 5, no. 3, p. 193-259.
Edwards, K. J., Glazer, B. T., Rouxel, O. J., Bach, W., Emerson, D., Davis, R. E., Toner, B. M., Chan, C. S., Tebo, B. M., Staudigel, H., and Moyer, C. L., 2011, Ultra-diffuse hydrothermal venting supports Fe-oxidizing bacteria and massive umber deposition at 5000m off Hawaii: The ISME journal, p. 1-11.
Elderfield, H., and Schultz, A., 1996, Mid-ocean ridge hydrothermal fluxes and the chemical composition of the ocean: Annual Review of Earth and Planetary Sciences, v. 24, p. 191-224.
Elrod, V. A., Berelson, W. M., Coale, K. H., and Johnson, K. S., 2004, The flux of iron from continental shelf sediments: A missing source for global budgets: Geophysical Research Letters, v. 31, no. 12, p. L12307.
Frank, M., 2002, Radiogenic isotopes: Tracers of past ocean circulation and erosional input: Reviews of Geophysics, v. 40, no. 1.
Frank, M., O'Nions, R. K., Hein, J. R., and Banakar, V. K., 1999, 60 Myr records of major elements and Pb–Nd isotopes from hydrogenous ferromanganese crusts: reconstruction of seawater paleochemistry: Geochimica Et Cosmochimica Acta, v. 63, no. 11–12, p. 1689-1708.
Frank, M., Whiteley, N., Kasten, S., Hein, J. R., and O'Nions, K., 2002, North Atlantic deep water export to the Southern Ocean over the past 14 Myr: Evidence from Nd and Pb isotopes in ferromanganese crusts: Paleoceanography, v. 17, no. 2.
Garcia, M. O., Caplan-Auerbach, J., De Carlo, E. H., Kurz, M. D., and Becker, N., 2006, Geology, geochemistry and earthquake history of Lo'ihi Seamount, Hawai'i's youngest volcano: Chemie Der Erde-Geochemistry, v. 66, no. 2, p. 81-108.
Glazer, B. T., and Rouxel, O. J., 2009, Redox Speciation and Distribution within Diverse Iron-dominated Microbial Habitats at Loihi Seamount: Geomicrobiology Journal, v. 26, no. 8, p. 606 - 622.
Halbach, P., and Puteanus, D., 1984, The influence of the carbonate dissolution rate on the growth and composition of Co-rich ferromanganese crusts from Central Pacific seamount areas: Earth and Planetary Science Letters, v. 68, no. 1, p. 73-87.
Hawkes, J. A., Connelly, D. P., Gledhill, M., and Achterberg, E. P., 2013, The stabilisation and transportation of dissolved iron from high temperature hydrothermal vent systems: Earth and Planetary Science Letters, v. 375, no. 0, p. 280-290.
Hein, J. R., Yeh, H. W., Gunn, S. H., Gibbs, A. E., and Wang, C. H., 1994, Composition and origin of hydrothermal ironstones from Central Pacific seamounts: Geochimica Et Cosmochimica Acta, v. 58, no. 1, p. 179-189.
Jickells, T., 1995, Atmospheric inputs of metals and nutrients to the oceans - Their magnitude and effects: Marine Chemistry, v. 48, no. 3-4, p. 199-214.
Jickells, T. D., An, Z. S., Andersen, K. K., Baker, A. R., Bergametti, G., Brooks, N., Cao, J. J., Boyd, P. W., Duce, R. A., Hunter, K. A., Kawahata, H., Kubilay, N., laRoche, J., Liss, P. S., Mahowald, N., Prospero, J. M., Ridgwell, A. J., Tegen, I., and Torres, R., 2005, Global iron connections between desert dust, ocean biogeochemistry, and climate: Science, v. 308, no. 5718, p. 67-71.
John, S. G., and Adkins, J. F., 2010, Analysis of dissolved iron isotopes in seawater: Marine Chemistry, v. 119, no. 1–4, p. 65-76.
Johnson, K. S., Chavez, F. P., and Friederich, G. E., 1999, Continental-shelf sediment as a primary source of iron for coastal phytoplankton: Nature, v. 398, no. 6729, p. 697-700.
Johnson, K. S., Gordon, R. M., and Coale, K. H., 1997, What controls dissolved iron concentrations in the world ocean?: Marine Chemistry, v. 57, no. 3-4, p. 137-161.
Koschinsky, A., and Halbach, P., 1995, Sequential leaching of marine ferromanganese precipitates: Genetic implications: Geochimica et Cosmochimica Acta, v. 59, no. 24, p. 5113-5132.

Koschinsky, A., and Hein, J. R., 2003, Uptake of elements from seawater by ferromanganese crusts: solid-phase associations and seawater speciation: Marine Geology, v. 198, no. 3-4, p. 331-351.

Koschinsky, A., Stascheit, A., Bau, M., and Halbach, P., 1997, Effects of phosphatization on the geochemical and mineralogical composition of marine ferromanganese crusts: Geochimica et Cosmochimica Acta, v. 61, no. 19, p. 4079-4094.

Lacan, F., Radic, A., Jeandel, C., Poitrasson, F., Sarthou, G., Pradoux, C., and Freydier, R., 2008, Measurement of the isotopic composition of dissolved iron in the open ocean: Geophysical Research Letters, v. 35, no. 24.

Lacan, F., Radic, A., Labatut, M., Jeandel, C., Poitrasson, F., Sarthou, G., Pradoux, C., Chmeleff, J., and Freydier, R., 2010, High-Precision Determination of the Isotopic Composition of Dissolved Iron in Iron Depleted Seawater by Double Spike Multicollector-ICPMS: Analytical Chemistry, v. 82, no. 17, p. 7103-7111.

Levasseur, S., Frank, M., Hein, J. R., and Halliday, A., 2004, The global variation in the iron isotope composition of marine hydrogenetic ferromanganese deposits: implications for seawater chemistry?: Earth and Planetary Science Letters, v. 224, no. 1-2, p. 91-105.

Ling, H.-F., Jiang, S.-Y., Frank, M., Zhou, H.-Y., Zhou, F., Lu, Z.-L., Chen, X.-M., Jiang, Y.-H., and Ge, C.-D., 2005, Differing controls over the Cenozoic Pb and Nd isotope evolution of deepwater in the central North Pacific Ocean: Earth and Planetary Science Letters, v. 232, no. 3–4, p. 345-361.

Longerich, H. P., Fryer, B. J., and Strong, D. F., 1987, Determination of lead isotope ratios by inductively coupled plasma-mass spectrometry (ICP-MS): Spectrochimica Acta Part B: Atomic Spectroscopy, v. 42, no. 1–2, p. 39-48.

Lupton, J., 1998, Hydrothermal helium plumes in the Pacific Ocean: Journal of Geophysical Research: Oceans, v. 103, no. C8, p. 15853-15868.

Lupton, J. E., 1995, Hydrothermal Plumes: Near and Far Field, Seafloor Hydrothermal Systems: Physical, Chemical, Biological, and Geological Interactions, Volume 91, American Geophysical Union, Geophysical Monograph Series, p. 317-346.

Lupton, J. E., Pyle, D. G., Jenkins, W. J., Greene, R., and Evans, L., 2004, Evidence for an extensive hydrothermal plume in the Tonga-Fiji region of the South Pacific: Geochemistry, Geophysics, Geosystems, v. 5, no. 1, p. Q01003.

Martin, J. H., and Knauer, G. A., 1984, VERTEX: manganese transport through oxygen minima: Earth and Planetary Science Letters, v. 67, no. 1, p. 35-47.

Meynadier, L., Allegre, C., and O'Nions, R. K., 2008, Plate tectonics, radiogenic isotopic tracers and paleoceanography - The case of the manganese crusts in the Pacific: Earth and Planetary Science Letters, v. 272, no. 3-4, p. 513-522.

Morel, F. M. M., and Price, N. M., 2003, The Biogeochemical Cycles of Trace Metals in the Oceans: Science, v. 300, no. 5621, p. 944.

O'Nions, R. K., Frank, M., von Blanckenburg, F., and Ling, H. F., 1998, Secular variation of Nd and Pb isotopes in ferromanganese crusts from the Atlantic, Indian and Pacific Oceans: Earth and Planetary Science Letters, v. 155, no. 1-2, p. 15-28.

Pettke, T., Halliday, A. N., and Rea, D. K., 2002, Cenozoic evolution of Asian climate and sources of Pacific seawater Pb and Nd derived from eolian dust of sediment core LL44-GPC3: Paleoceanography, v. 17, no. 3.

Radic, A., Lacan, F., and Murray, J. W., 2011, Iron isotopes in the seawater of the equatorial Pacific Ocean: New constraints for the oceanic iron cycle: Earth and Planetary Science Letters, v. 306, no. 1-2, p. 1-10.

Reynolds, B. C., Frank, M., and O'Nions, R. K., 1999, Nd- and Pb-isotope time series from Atlantic ferromanganese crusts: implications for changes in provenance and paleocirculation over the last 8 Myr: Earth and Planetary Science Letters, v. 173, no. 4, p. 381-396.

Rouxel, O., Dobbek, N., Ludden, J., and Fouquet, Y., 2003, Iron isotope fractionation during oceanic crust alteration: Chemical Geology, v. 202, no. 1-2, p. 155-182.

Rouxel, O., Shanks, W. C., Bach, W., and Edwards, K. J., 2008, Integrated Fe- and S-isotope study of seafloor hydrothermal vents at East Pacific rise 9-10 degrees N: Chemical Geology, v. 252, no. 3-4, p. 214-227.

Rouxel, O. J., and Auro, M., 2010, Iron Isotope Variations in Coastal Seawater Determined by Multicollector ICP-MS: Geostandards and Geoanalytical Research, v. 34, no. 2, p. 135-144.

Rouxel, O. J., Bekker, A., and Edwards, K. J., 2005, Iron Isotope Constraints on the Archean and Paleoproterozoic Ocean Redox State: Science, v. 307, no. 5712, p. 1088-1091.

Saito, M. A., Noble, A. E., Tagliabue, A., Goepfert, T. J., Lamborg, C. H., and Jenkins, W. J., 2013, Slow-spreading submarine ridges in the South Atlantic as a significant oceanic iron source: Nature Geosci, v. advance online publication.

Sander, S. G., and Koschinsky, A., 2011, Metal flux from hydrothermal vents increased by organic complexation: Nature Geoscience, v. 4, no. 3, p. 145-150.

Sedwick, P. N., McMurtry, G. M., and Macdougall, J. D., 1992, Chemistry of hydrothermal solutions from Pele vents, Loihi seamount, Hawaii: Geochimica Et Cosmochimica Acta, v. 56, no. 10, p. 3643-3667.

Severmann, S., Johnson, C. M., Beard, B. L., and McManus, J., 2006, The effect of early diagenesis on the Fe isotope compositions of porewaters and authigenic minerals in continental margin sediments: Geochimica Et Cosmochimica Acta, v. 70, no. 8, p. 2006-2022.

Severmann, S., McManus, J., Berelson, W. M., and Hammond, D. E., 2010, The continental shelf benthic iron flux and its isotope composition: Geochimica Et Cosmochimica Acta, v. 74, no. 14, p. 3984-4004.

Staubwasser, M., von Blanckenburg, F., and Schoenberg, R., 2006, Iron isotopes in the early marine diagenetic iron cycle: Geology, v. 34, no. 8, p. 629-632.

Tagliabue, A., Bopp, L., Dutay, J. C., Bowie, A. R., Chever, F., Jean-Baptiste, P., Bucciarelli, E., Lannuzel, D., Remenyi, T., Sarthou, G., Aumont, O., Gehlen, M., and Jeandel, C., 2010, Hydrothermal contribution to the oceanic dissolved iron inventory: Nature Geoscience, v. 3, no. 4, p. 252-256.

Takahashi, Y., Manceau, A., Geoffroy, N., Marcus, M. A., and Usui, A., 2007, Chemical and structural control of the partitioning of Co, Ce, and Pb in marine ferromanganese oxides: Geochimica Et Cosmochimica Acta, v. 71, no. 4, p. 984-1008.

Toner, B. M., Fakra, S. C., Manganini, S. J., Santelli, C. M., Marcus, M. A., Moffett, J., Rouxel, O., German, C. R., and Edwards, K. J., 2009, Preservation of iron(II) by carbon-rich matrices in a hydrothermal plume: Nature Geoscience, v. 2, no. 3, p. 197-201.

van de Flierdt, T., Frank, M., Halliday, A. N., Hein, J. R., Hattendorf, B., Günther, D., and Kubik, P. W., 2003, Lead isotopes in North Pacific deep water - implications for past changes in input sources and circulation patterns: Earth and Planetary Science Letters, v. 209, no. 1-2, p. 149-164.

-, 2004, Tracing the history of submarine hydrothermal inputs and the significance of hydrothermal hafnium for the seawater budget—a combined Pb–Hf–Nd isotope approach: Earth and Planetary Science Letters, v. 222, no. 1, p. 259-273.

Vlastelic, I., Abouchami, W., Galer, S. J. G., and Hofmann, A. W., 2001, Geographic control on Pb isotope distribution and sources in Indian Ocean Fe-Mn deposits: Geochimica Et Cosmochimica Acta, v. 65, no. 23, p. 4303-4319.

Von Damm, K. L., 1995, Controls on the Chemistry and Temporal Variability of Seafloor Hydrothermal Fluids, Seafloor Hydrothermal Systems: Physical, Chemical, Biological, and Geological Interactions, Volume 91, American Geophysical Union, Geophysical Monograph Series, p. 222-247.

Zhu, X. K., O'Nions, R. K., Guo, Y. L., and Reynolds, B. C., 2000, Secular variation of iron isotopes in North Atlantic Deep Water: Science, v. 287, no. 5460, p. 2000-2002.

Partie V.2 – Co-variation des compositions isotopiques du Cu et du Zn dans les encroûtements de fer-manganèse de l'Océan Pacifique au cours du Cénozoïque tardif

Part V.2 - Co-variation of Zn and Cu isotope compositions in North and South Pacific ferromanganese crusts in the late Cenozoic

Abstract:

This study presents a high resolution record of Cu and Zn isotopes in four Fe-Mn crusts from the North and South Pacific oceans. Northern Pacific crusts were collected on the Apuupuu seamount south of Hawaii archipelago and South Pacific crusts were recovered near Rurutu Island in the Tahiti archipelago. Major and trace element composition suggests that Fe-Mn crusts have a hydrogenous origin with Cu and Zn precipitated from seawater and therefore reflect deep seawater metal isotope composition. We show that Cu and Zn display different isotopic patterns between North and South Pacific but show similar temporal evolution within each geographical area.

Cu and Zn isotope composition of both Hawaiian crusts varies between +0.57 to +0.73 ‰ for $\delta^{65/63}Cu_{NIST976}$ and +1.91 to +2.19 ‰ for $\delta^{66/64}Zn_{NIST3168a}$. In contrast, both South Pacific crusts show resolvable temporal variations, with Cu and Zn isotopic ratios increasing sharply over the last ~6 Ma from +1.61 to +2.01 ‰ and +0.16 to +0.51‰ respectively. The results contrast with recent studies of Cu and Zn compositions of Fe-Mn crusts from Pacific, Atlantic and Indian Oceans yielding fairly homogeneous values over the last 20 Ma. Noteworthy, we observed a remarkable positive correlation between $\delta^{65/63}Cu_{NIST976}$ and $\delta^{66/64}Zn_{NIST3168a}$ values in Fe-Mn crusts from the South Pacific suggesting mixing between two components, one being defined by crustal or hydrothermal values and the other being similar to hydrogenous values encountered in the North Pacific seawater. Two possible hypotheses may account for these observations, (1) the South Pacific received higher hydrothermal inputs of Cu and Zn from the East Pacific Rise and, or (2) the South Pacific recorded deep water masses with distinct Cu-Zn isotope composition as a response to major oceanic circulation changes.

1. Introduction

Our understanding of metal biogeochemical cycles in the oceans has increased significantly since the development of new methods for measuring low trace metal concentrations in seawater (Bruland et al. 1994; Sohrin et al. 1998; Sohrin et al. 2008; Sohrin and Bruland 2011; Biller and Bruland 2012). Surface bioproductivity has long been recognized as an important parameter influencing distribution of transition metals in seawater because many of those trace elements are essential, and in some cases bio-limiting for primary productivity (e.g. Fe, Zn, Cd, Ni) (Morel and Price 2003). However, our knowledge of the deep ocean biogeochemical cycles of metals is relatively incomplete, in particular with respect to benthic sources and oceanic water masses dynamics. For instance, the importance of hydrothermal inputs in the oceanic Mn, Fe and Cu budget was demonstrated to be important in the South Pacific, notably because of hydrothermal vents along the South East Pacific Rise (SEPR) contributing to large hydrothermal fluxes in seawater (Boström et al. 1969; Lupton and Craig 1981; Baker and Massoth 1986; Baker et al. 1995; Urabe et al. 1995; Lupton 1998; Hannington 2013) and variations of these fluxes through time could potentially have impinged global metals biogeochemical cycles.

Among trace metals, particular attention is now given to Cu and Zn. These elements are mostly supplied to the oceans via the riverine input from the continents, whereas the most important sink is associated with the precipitation of Fe-Mn-oxides at the seafloor (Little et al. 2013). Zn exhibits a nutrient-type profile in seawater as a result of biological uptake in surface waters and recycling of settling organic matter in deep waters (Bruland 1980; Bruland 1983; Morel and Price 2003). By contrast, Cu behaves more closely to a particle-

reactive element and shows relatively stable concentrations in the water column, albeit it is also depleted in surface waters by biological uptake but at a much lower level than for Zn (Boyle et al. 1977; Bruland 1980). Subsequently to the development of efficient methods for measuring metal concentration in seawater, some studies took an interest at measuring seawater Cu and Zn isotope compositions as new biogeochemical tools (Bermin et al. 2006; Vance et al. 2008; Boyle et al. 2012; Conway et al. 2013; Takano et al. 2013). Besides their important implications in biological reactions, Cu and Zn are elements sensitive to many geochemical processes including precipitation, adsorption and speciation in solution that could modify isotope compositions (Zhu et al. 2002; Albarede 2004; Johnson et al. 2004; Anbar and Rouxel 2007).

$\delta^{65/63}Cu_{NIST976}$ values in seawater range from +0.56 to +0.72 ‰ in the Atlantic Ocean (Boyle et al. 2012), and from +0.47 to +0.63 ‰ in the Northwestern Pacific Ocean (Takano et al. 2013). Larger range of $\delta^{65/63}Cu$ values was also reported in South Central Indian Ocean and Northeast Pacific Ocean from +0.90 to +1.44 ‰ (Vance et al. 2008). Seawater $\delta^{66/64}Zn_{NIST3168a}$ varies from +1.01 to 1.49 ‰ in the Atlantic Ocean and from +1.12 to +1.46 ‰ in the Pacific Ocean (Conway et al. 2013). There are still important uncertainties on the residence time of Cu and Zn in seawater with ~3100 years estimated for Cu (Algeo and Maynard 2008) and 3000-6000 years for Zn (Maréchal et al. 2000) while other estimates of 5400 and 11000 years for Cu and Zn respectively were recently determined (Little et al. 2013). Despite those uncertainties, residence times are well above the oceanic mixing time of ~1500 years, suggesting that deep waters should be fairly homogenous in regards of their isotope compositions. On the other hand, biological activity fractionates Zn and Cu isotopes, thus it may impart specific isotopic signatures particularly in surface waters (Zhu et al. 2002; Ehrlich et al. 2004; John et al. 2007). Investigation of marine carbonates indicates that Zn isotope variations may reflect seasonal variations and nutrient availability in relation to the intensities of the trade winds. Weak trade winds will prevent mixing of deep waters with surface waters, thus promoting depletion of surface waters in light isotopes by biology, whereas replenishment of surface waters during strong trade winds does not promote important isotope fractionation (Pichat et al. 2003).

A promising target for investigating deep waters metal isotope compositions over longer time scale is the hydrogenetic ferromanganese (Fe-Mn) crusts record. These metalliferous deposits are composed of an assemblage of Mn- and Fe-oxides which are highly enriched in Ni, Co, Cu, Zn, Mo, Te, Pt, Tl relatively the average continental crust (Li and Schoonmaker 2003; Hein et al. 2010; Hein et al. 2013). The preferred model for explaining metal enrichment is that they are exclusively derived from seawater (i.e. hydrogenous precipitation). Fe-Mn crusts formation process is promoted by the presence of an Oxygen Minimum Zone (OMZ) in the water column which allows accumulation of soluble reduced Mn^{2+} due to low oxygen concentration. Dissolved Mn can be reoxidized and then it precipitates as Mn-oxides at the surface of rocks outcropping beneath the base of the OMZ. They are generally deposited on the flank of seamounts which serves as a substrate (but some are formed on a sedimentary substrate) at depths between 1000 and 3000 meters at very slow growth rates between 1 and 6 mm/Ma. The depositional environment of Fe-Mn crusts has to be preserved from high sedimentation rates areas in order to prevent transition metals dilution by sedimentary particles (Halbach et al. 1983; Hein et al. 1988; Hein et al. 1992; Koschinsky and Halbach 1995; Koschinsky et al. 1997).

So far, Fe-Mn crusts deposits were essentially investigated for their radiogenic isotopes composition (Pb, Nd, Hf) as a means of tracing the evolution of oceanic circulation and its relation to climate variations and continental fluxes of material to the oceans (see for

example the review by (Frank 2002)). Zn isotope composition of surface scraping of manganese nodules surface layers collected in the Atlantic, Pacific, Indian oceans and in the Circum-Antarctic Current vary from +1.49 to +2.12 ‰ for $\delta^{66/64}Zn_{NIST3168a}$ (Maréchal et al. 2000). In this early study it was unknown whether those values were representative of the present-day seawater Zn isotope composition. Using the same sample set (Albarede 2004) obtained an average for $\delta^{65/63}Cu_{NIST976}$ of +0.31‰ with a range of +0.09 to +0.60 ‰. However, no relationship could be established with geographical locations or any other specific biogeochemical processes. More recently, Little et al. (2013) reported a large range of $\delta^{66/64}Zn_{NIST3168a}$ values in three Fe-Mn crusts from the Atlantic, Indian and Pacific oceans from +1.56 to +2.38 ‰ for (Little et al. 2013). $\delta^{65/63}Cu_{NIST976}$ values on these same crusts also yield a wide range from -0.16 to +1.19 ‰. However, no specific explanations were given to interpret the temporal Cu and Zn variations in these crusts. These data clearly show that Cu and Zn isotopes in oceanic metalliferous deposits vary in significant range, but that the causes to isotopic variations remain largely unresolved.

Here, we aim at unraveling spatial and temporal variations of Cu and Zn isotope compositions recorded in four Fe-Mn crusts from the Pacific Ocean. After discussing the reliability of using Fe-Mn crusts as a proxy of deep seawater Cu and Zn isotope composition, several hypotheses pertaining to Cu and Zn variations in seawater are addressed including, (1) influence of the OMZ and CCD depths, (2) influence of surface productivity, (3) impact of hydrothermal inputs on oceanic Cu and Zn, and (4) variations of continental inputs to the oceans and oceanic circulation.

2. Materials and methods

2.1. Sample description: microsampling of Pacific Fe-Mn crusts

Four Fe-Mn crusts were selected for implementing high resolution depth profiles. The sample set comprises two Fe-Mn crusts collected on Apuupuu seamount ~50 km south of Hawaii during FeMO 2009 cruise on the R/V Kilo Moana (University of Hawaii) in October 2009, and two crusts collected in the South Pacific in the Tahiti archipelago by dredges during ZEPOLYF 2 cruise on the R/V L'Atalante (Ifremer-Genavir) in July-August 1999 (Table V.1). Hawaii Fe-Mn (J2-480 and J2-480-R14) crusts were collected at 2079 m depth while Tahiti crusts were collected at shallower depths at 1826 and 1530 m (ZEP2-DR-05-04 and ZEP2-DR-06-03 respectively).

Each crust was split and a representative cross section was taken off (including whenever possible the top surface) and embedded into epoxy resin. Each section was polished for petrographic observation and electron microprobe analysis. Growth layers of Fe-Mn crusts were subsampled at mm-scale using a microdrilling device (Micromill®). Lines perpendicular to the direction of growth were drilled to obtain sufficient crust powder for subsequent geochemical analysis. The total amount of powder collected in each line was generally between ~30 and 50 mg. A complete description of the samples is provided in chapter IV of this manuscript.

For each sample of Fe-Mn crust we defined the "Inner" region as the bottom/older crust, whereas the "Outer" region defined the top/younger crust (see Figure 2 of chapter IV).

Dating of the crusts was made by the mean of cosmogenic ^{10}Be isotope measurement (Segl et al. 1984; Bourles et al. 1989), with the exception of crust ZEP2-DR05-04 (this issue is discussed in chapter IV of this manuscript) which was dated using Co concentrations (Halbach et al. 1983; Puteanus and Halbach 1988; Frank et al. 1999).

2.2. Cu and Zn isotope compositions

Cu and Zn isotope compositions were measured at Pôle-Spectrométrie-Océan (IUEM-Ifremer, Brest, France) by MC-ICP-MS (Neptune, Thermo-Finnigan). Cu and Zn isotope ratios were corrected with internal isotopic standards of Zn NIST SRM 3168a and Cu NIST SRM 976 respectively coupled to a standard-sample-bracketing scheme (Marechal et al. 1999; Albarede 2004). Basically, the fractionation factor calculated for the doped element for which the isotope composition is known is applied to the isotopic ratios of the measured element assuming that isotopes of both the doped element and the element to be measured follow a similar exponential mass fractionation law (Marechal et al. 1999; Albarede 2004).
Prior to isotope analyses, Cu and Zn were separated with ion-exchange chromatography columns using AG-MP1 resin. 2 mL of resin were loaded in polypropylene columns. Prior to loading on the resin, a split from the samples archive solutions was taken off and evaporated to dryness on hot Teflon plates and redissolved in 1.2 mol/L HCl. Both Cu and Zn were purified twice through the columns.

Isotopic compositions are expressed as $\delta^{65/63}Cu_{NIST976}$ and $\delta^{66/64}Zn_{NIST3168a}$ (‰) calculated with the following the equations (1) and (2) respectively :

$$\delta^{65/63}Cu_{NIST976} = 1000 \times [(^{65}Cu/^{63}Cu_{sample})/(^{65}Cu/^{63}Cu_{NIST976}) - 1] \quad (1)$$

$$\delta^{66/64}Zn_{NIST3168a} = 1000 \times [(^{66}Zn/^{64}Zn_{sample})/(^{66}Zn/^{64}Zn_{NIST3168a}) - 1] \quad (2)$$

Precisions on the Cu and Zn isotope delta values are reported as a two-standard deviation (2sd) calculated on replicate measurements of the isotopic standards Cu NIST SRM 976 and Zn NIST SRM 3168a respectively. Zn isotope values are often reported relatively to the JMC Lyon Zn standard in the literature. For comparison, JMC Lyon Zn isotopic standard is fractionated from Zn NIST SRM 3168a by a factor of -0.96 ‰ (Rouxel, unpublished data).

Analysis of GRMs Nod-A-1 and Nod-P-1 yields average values of +0.26 ±0.01 ‰ (2sd, n=2) and +0.32 ±0.03 ‰ (2sd, n=3) for $\delta^{65/63}Cu_{NIST976}$ and +1.91 ±0.10 ‰ (2sd, n=2) and +1.79 ±0.09 ‰ (2sd n=3) for $\delta^{66/64}Zn_{NIST3168a}$ (Table V.2) consistent with previous studies (Chapman et al. 2006; Bigalke et al. 2010).

Table V.2: Mn/Fe, Cu/Mn and Zn/Mn ratios (µg/µg), and Cu and Zn isotopes (in ‰) in ferromanganese crusts time-series from Tahiti, South Pacific, and Apuupuu, North Pacific.

Sample name	Depth (mm) in the crust	Age (Ma)*	Mn/Fe	Cu/Mn	Zn/Mn	$\delta^{65/63}$Cu	2sd**	$\delta^{66/64}$Zn	2sd**
ZEP2-DR05-04 Fe-Mn crust									
ZEP2-DR05-04-L1	0,5	1,1	1,91	0,0022	0,0023	0,52	0,03	2,03	0,03
ZEP2-DR05-04-L2	1	1,7	1,66	0,0030	0,0025	0,51	0,03	2,04	0,03
ZEP2-DR05-04-L3	2,5	3,3	1,79	0,0036	0,0027	0,49	0,03	2,01	0,03
ZEP2-DR05-04-L4	3,5	3,9	1,52	0,0040	0,0030	0,51	0,03	2,00	0,03
ZEP2-DR05-04-L5	4,5	4,1	1,12	0,0044	0,0031	0,43	0,03	1,88	0,03
ZEP2-DR05-04-L6	6,5	4,6	1,05	0,0051	0,0031	0,34	0,03	1,83	0,03
ZEP2-DR05-04-L7	8,5	5,9	1,07	0,0053	0,0032	0,32	0,03	-	-
ZEP2-DR05-04-L8	10	6,5	1,04	0,0059	0,0035	0,27	0,03	1,74	0,03
ZEP2-DR05-04-L9	11,5	7,1	1,08	0,0058	0,0034	0,27	0,03	1,75	0,03
ZEP2-DR05-04-L10	12,5	7,7	1,03	0,0054	0,0032	0,32	0,03	1,76	0,03
ZEP2-DR05-04-L11	13,5	8,0	0,99	0,0058	0,0032	0,23	0,03	1,73	0,03
ZEP2-DR05-04-L12	15,5	8,6	1,02	0,0068	0,0036	0,24	0,03	1,74	0,03
ZEP2-DR05-04-L13	16,5	8,9	0,95	0,0063	0,0034	0,21	0,03	1,68	0,03
ZEP2-DR05-04-L14	17,5	9,6	1,14	0,0073	0,0041	0,21	0,03	1,76	0,03
ZEP2-DR05-04-L15	19	9,9	1,08	0,0074	0,0045	0,21	0,03	1,76	0,03
ZEP2-DR05-04-L16	20	10,4	1,27	0,0080	0,0047	0,19	0,03	1,76	0,03
ZEP2-DR05-04-L17	22	10,9	1,31	0,0101	0,0061	0,16	0,03	1,76	0,03
ZEP2-DR06-03 Fe-Mn crust									
ZEP2-DR06-03-L1	0,5	0,6	1,45	0,0026	0,0022	0,51	0,03	2,00	0,03
ZEP2-DR06-03-L2	2,5	2,5	1,27	0,0036	0,0025	0,44	0,03	1,99	0,03
ZEP2-DR06-03-L3	4	3,8	1,25	0,0039	0,0025	0,50	0,03	2,02	0,03
ZEP2-DR06-03-L4	5,5	4,6	1,14	0,0041	0,0027	0,46	0,03	2,02	0,03
ZEP2-DR06-03-L5	7,5	5,2	0,77	0,0054	0,0042	0,47	0,03	-	-
ZEP2-DR06-03-L6	9,5	6,1	1,17	0,0049	0,0027	0,48	0,03	1,90	0,03
ZEP2-DR06-03-L7	11	6,5	1,10	0,0056	0,0028	0,40	0,03	1,81	0,03
ZEP2-DR06-03-L8	12,5	6,9	1,02	0,0060	0,0029	0,34	0,03	1,73	0,03
ZEP2-DR06-03-L9	14	7,5	0,98	0,0067	0,0031	0,25	0,03	1,71	0,03
ZEP2-DR06-03-L10	16	8,0	0,94	0,0071	0,0033	0,27	0,03	1,63	0,03
ZEP2-DR06-03-L11	17,5	8,5	0,92	0,0075	0,0033	-	-	1,62	0,03
ZEP2-DR06-03-L12	19	8,8	0,99	0,0072	0,0032	0,21	0,03	1,63	0,03
ZEP2-DR06-03-L13	21	9,4	0,91	0,0076	0,0033	0,22	0,03	1,61	0,03
ZEP2-DR06-03-L14	23,5	10,0	0,98	0,0078	0,0034	0,18	0,03	1,61	0,03
J2-480 Fe-Mn crust									
J2-480-R1	0,2	7,0	1,18	0,0061	0,0053	0,73	0,06	2,10	0,04
J2-480-R2	2,5	7,1	1,44	0,0075	0,0041	0,54	0,06	2,19	0,04
J2-480-R3	5	7,2	1,40	0,0080	0,0046	0,59	0,06	2,10	0,04
J2-480-R4	7	7,5	1,55	0,0081	0,0041	0,66	0,06	2,13	0,04
J2-480-R5	9	8,0	2,22	0,0081	0,0033	0,65	0,06	2,19	0,04
J2-480-R6	11	8,3	1,72	0,0071	0,0035	0,67	0,06	2,18	0,04
J2-480-R7	12,5	8,5	1,69	0,0073	0,0039	0,64	0,06	2,14	0,04
J2-480-R8	14	8,6	1,75	0,0076	0,0038	0,66	0,06	2,13	0,04
J2-480-R9	15	8,7	1,28	0,0086	0,0042	0,63	0,06	2,15	0,04
J2-480-R10	16,5	8,8	0,69	0,0111	0,0054	0,56	0,06	1,97	0,04
J2-480-R12	19	11,8	0,68	0,0126	0,0048	0,57	0,06	1,91	0,04

Table V.2 continued

Sample name	Depth (mm) in the crust	Age (Ma)*	Mn/Fe	Cu/Mn	Zn/Mn	$\delta^{65/63}Cu$	2sd**	$\delta^{66/64}Zn$	2sd**
J2-480-R14 Fe-Mn crust									
J2-480-R14-L11	0,2	3,6	1,32	0,0046	0,0055	0,65	0,06	2,19	0,04
J2-480-R14-L10	3	4,4	1,21	0,0055	0,0073	0,63	0,06	2,16	0,04
J2-480-R14-L9	5	6,6	1,35	0,0057	0,0063	0,66	0,06	2,06	0,04
J2-480-R14-L8	7	7,7	1,67	0,0053	0,0036	0,65	0,06	2,14	0,04
J2-480-R14-L7	9	8,7	1,71	0,0059	0,0036	0,72	0,06	2,18	0,04
J2-480-R14-L6	10	9,3	1,79	0,0060	0,0042	0,67	0,06	2,18	0,04
J2-480-R14-L5	12	10,3	1,30	0,0073	0,0043	0,67	0,06	2,12	0,04
J2-480-R14-L4	14	11,3	1,64	0,0065	0,0046	0,69	0,06	2,20	0,04
J2-480-R14-L3	16	12,0	1,57	0,0064	0,0035	0,63	0,06	2,09	0,04
J2-480-R14-L2	18	12,9	1,26	0,0082	0,0042	0,60	0,06	2,05	0,04
J2-480-R14-L1	20	16,6	1,25	0,0085	0,0042	0,56	0,06	2,03	0,04
NOD-P-1	-	-	1,74	0,0415	0,0055	0,32	0,03	1,75	0,03
NOD-P-1***	-	-	1,74	0,0407	0,0055	0,32	0,03	1,82	0,03
NOD-A-1	-	-	5,29	0,0063	0,0035	0,24	0,03	1,94	0,03
NOD-A-1***	-	-	5,37	0,0063	0,0037	0,26	0,03	1,88	0,03
NOD-A-1***	-	-	-	-	-	0,28	0,03	-	-
Average NOD-A-1 (2sd)	-	-	-	-	-	**0,26**	**0,01**	**1,91**	**0,10**
Average NOD-P-1 (2sd)	**-**	**-**	**-**	**-**	**-**	**0,32**	**0,03**	**1,79**	**0,09**

* Age (Ma) were calculated using cosmogenic 10Be isotope, except sample ZEP2-DR05-04 dated with the Co-method (see chapter IV for ample details on the method).
** 2sd stands for two-standard deviation calculated on replicate measurements of NIST976 for Cu isotopes and NIST3168a for Zn isotopes.
*** Duplicate of attack and chemistry procedure.

3. Results

Full descriptions of the mineralogy, major, trace and REE elements concentrations of Apuupuu Fe-Mn crusts (Hawaii, North Pacific) are reported in chapter IV of this manuscript. Evolution of Cu/Mn and Zn/Mn ratios are shown in Figure V.9. Zn/Mn and Cu/Mn ratios are similar in both Fe-Mn crusts from Tahiti, and display a continuous decrease from the “Inner” region (i.e. older) to the “Outer” region (i.e. younger). In contrast, Fe-Mn crusts from Apuupuu seamount display opposite trends in Zn/Mn ratios although both crusts show similar features with a sharp decrease at about 7-8 Ma Figure V.9. Fe-Mn crusts from Apuupuu and Tahiti show similar increase in Cu/Mn ratios, with higher values observed for crust J2-480.

Mn/Fe ratios in Apuupuu Fe-Mn crusts show an important increase through time ~10 Ma until ~9 Ma from 0.68 to 2.22 in J2-480 and from 1.25 to 1.79 in J2-480-R14. Fe-Mn crusts from Tahiti also exhibit an increase in Mn/Fe ratios from ~6 Ma to the top of the crust from 0.98 to 1.45 in ZEP2-DR06-03 and from 0.99 to 1.91 in ZEP2-DR05-04 (Figure V.9).
Temporal patterns of geochemical composition Cu and Zn isotope compositions in both crusts from Apuupuu seamount (North Pacific, Hawaii) show a relatively restricted range of variations with values of +0.57 to +0.67 ‰ for $\delta^{65/63}Cu_{NIST976}$ and +1.91 + to 2.18 ‰ for $\delta^{66/64}Zn_{NIST3168a}$ in J2-480, and from +0.56 to +0.72 ‰ $\delta^{65/63}Cu_{NIST976}$ and +2.09 + to 2.18 ‰ for $\delta^{66/64}Zn_{NIST3168a}$ in J2-480-R14 (Table V.2 and Figure V.10). On the other hand, South Pacific Fe-Mn crusts show a concomitant increase in $\delta^{65/63}Cu_{NIST976}$ and $\delta^{66/64}Zn_{NIST3168a}$ at about 6 Ma to 4 Ma, from +0.16 to +0.51‰ for $\delta^{65/63}Cu_{NIST976}$ and from +1.61 to +2.03 ‰ for $\delta^{66/64}Zn_{NIST3168a}$ values(Table V.2 and Figure V.10).

This translates into a remarkable positive correlation between $\delta^{65/63}Cu_{NIST976}$ and $\delta^{66/64}Zn_{NIST3168a}$ values (Figure V.11), with correlation coefficient of about 1 and coefficient of determination R^2=0.90.

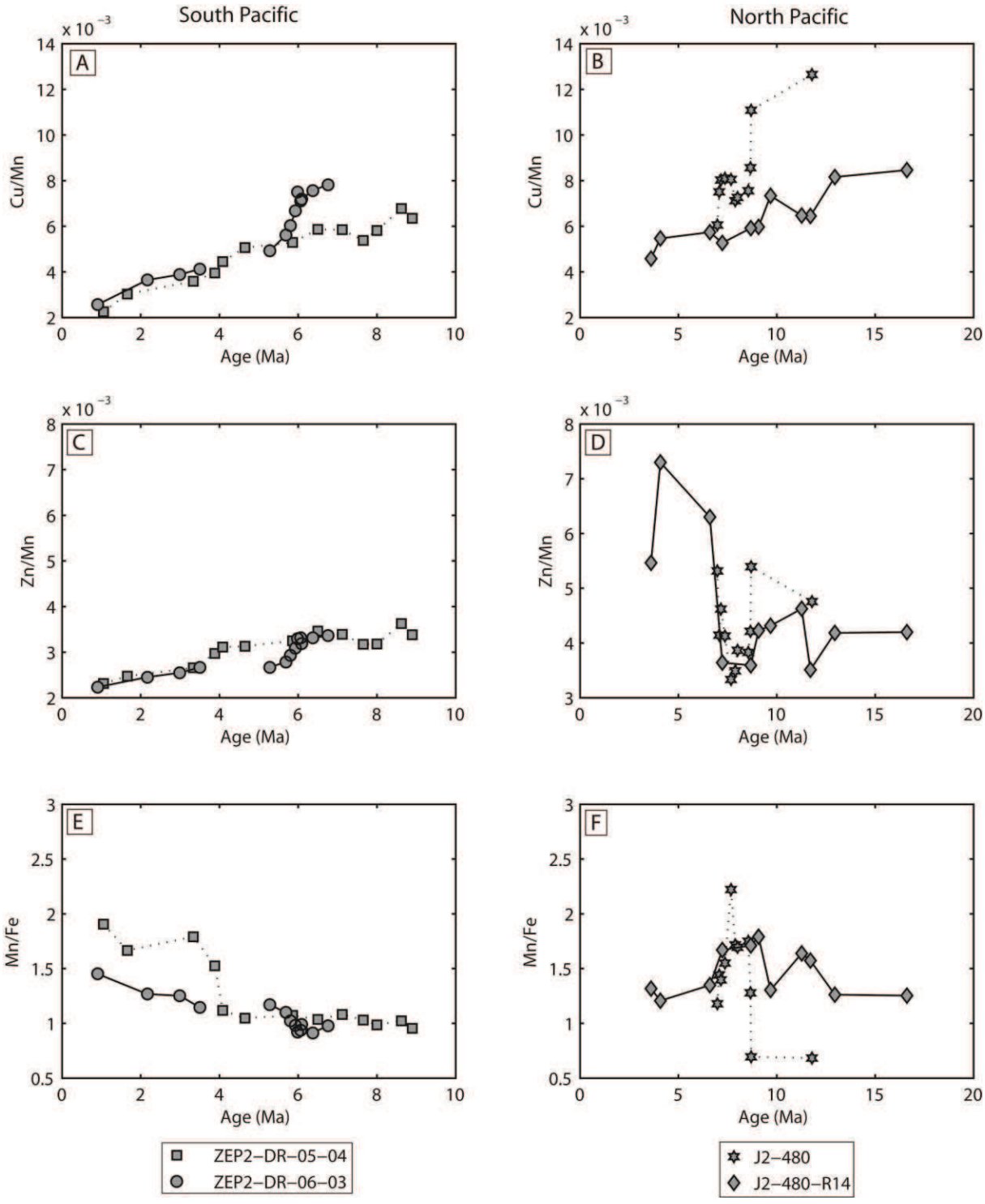

Figure V.9: Cu/Mn (panels A and B), Zn/Mn (panels C and D) and Mn/Fe (panels E and F) ratios time-series in Tahiti Fe-Mn crusts (South Pacific) and Apuupuu Fe-Mn crusts (North Pacific) respectively.

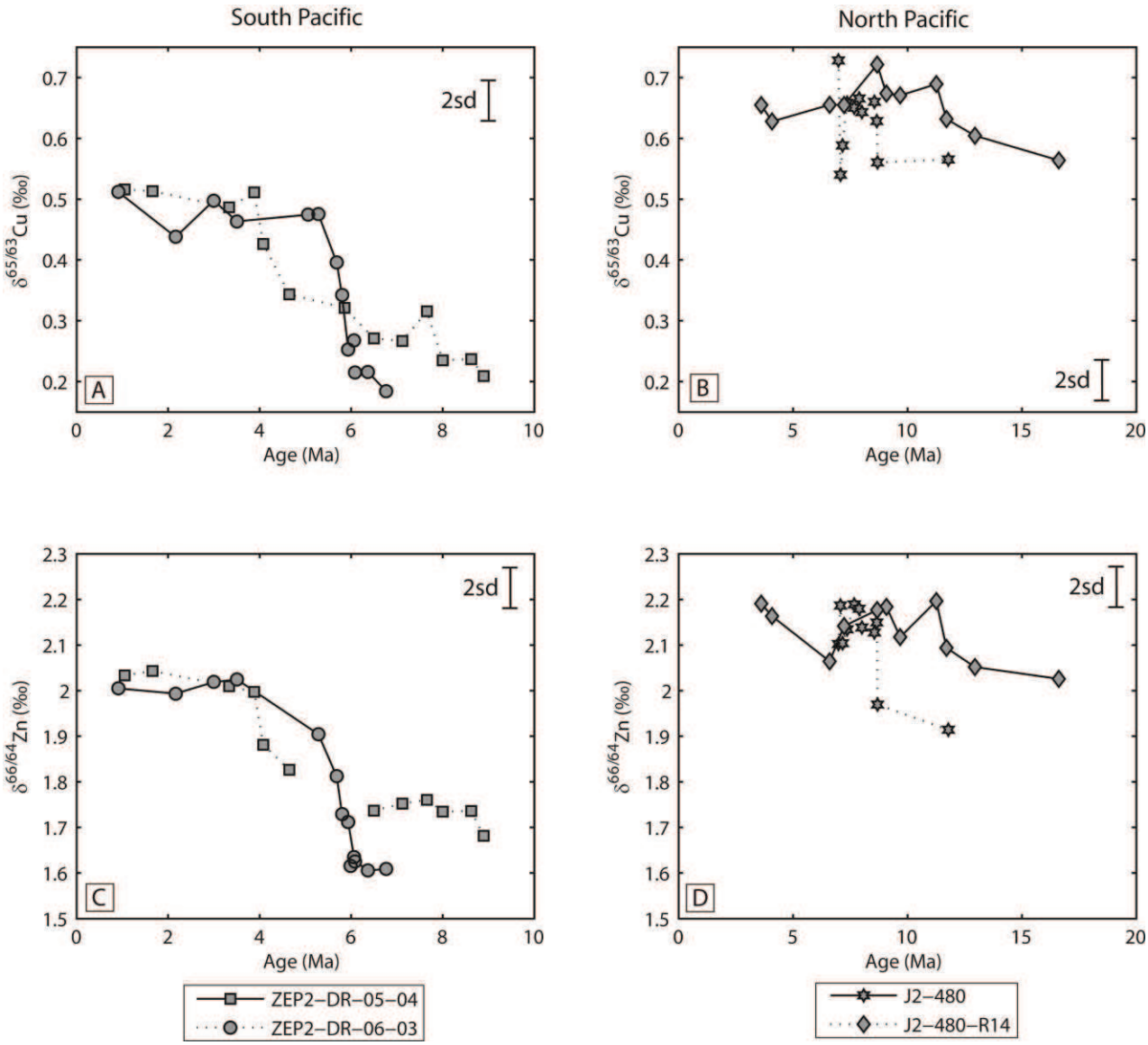

Figure V.10: *Cu and Zn isotopes (‰) time-series in Tahiti (South Pacific) Fe-Mn crusts (panel A and C) and Apuupuu (North Pacific) Fe-Mn crusts (panel B and D).*

4. Discussion

4.1. Zn and Cu isotope composition of hydrogenetic Fe-Mn-rich deposits: a proxy of deep seawater chemistry?

It has been widely accepted that hydrogenetic Fe-Mn crusts record dissolved trace metals from seawater, and that they can archive the isotopic composition of deep seawater water masses through time (Hein et al. 1988; Koschinsky and Halbach 1995; Hein et al. 2003; Koschinsky and Hein 2003; Hein et al. 2010). However, in the case of stable isotope systematics, isotopic composition recorded in the crusts may differ from that of seawater due to mass-dependent fractionation during precipitation and/or adsorption onto Fe-Mn oxides minerals. Such processes have been well demonstrated for Tl and Mo isotopes both through laboratory experiments and by comparing modern seawater values and surface scraping of Fe-Mn crusts (Rehkämper et al. 2002; Barling and Anbar 2004; Rehkämper et al. 2004;

Wasylenki et al. 2008; Wasylenki et al. 2011; Nielsen et al. 2013). On the other hand, Cd isotopes in Fe-Mn crusts are considered to provide a reliable archive of deep seawater isotope composition with minimal isotope fractionation during uptake (Horner et al. 2010; Wasylenki and Swihart 2013). Similar feature for other metal isotope systems such as Cu and Zn isotopes remain debated.

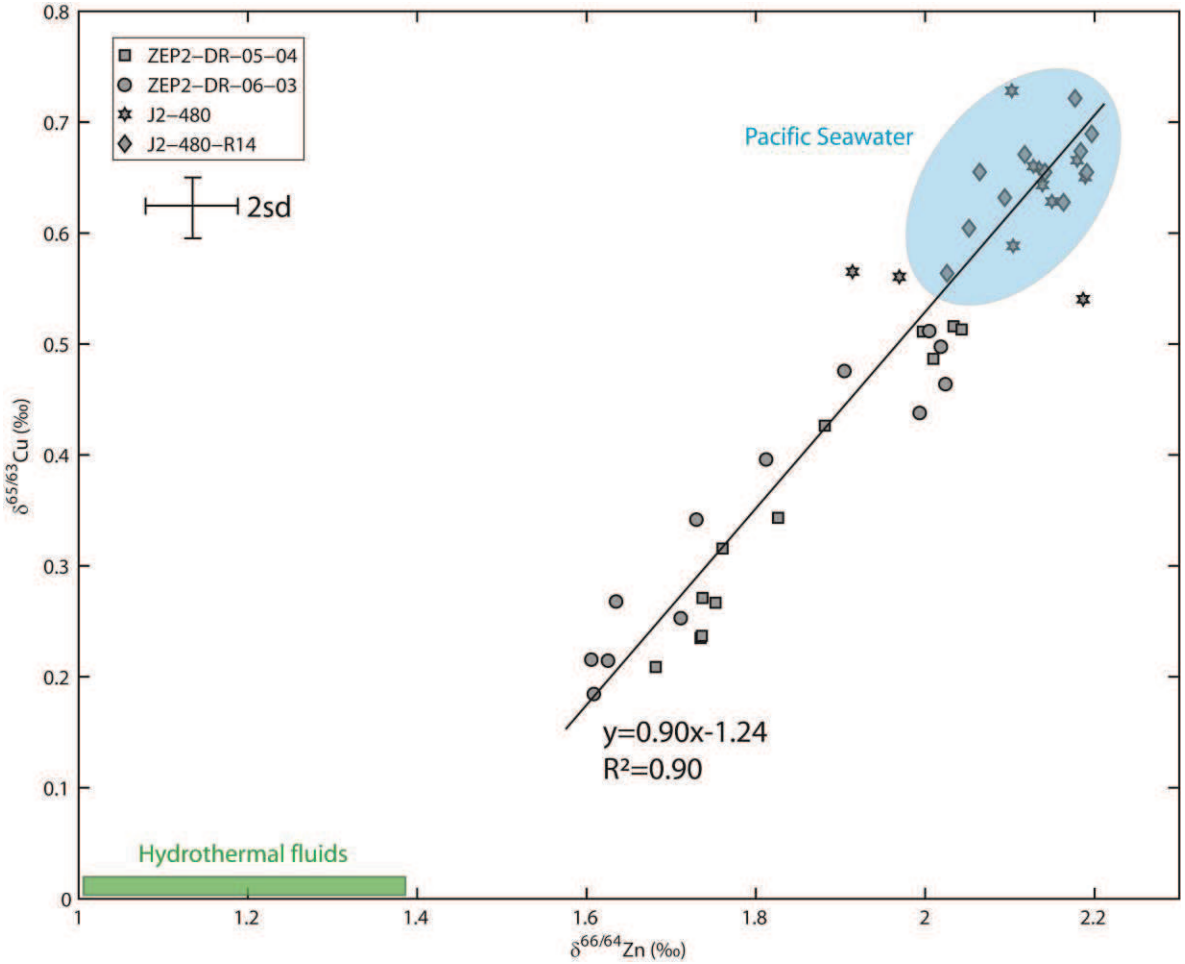

Figure V.11 *: Plot showing the positive correlation between $\delta^{65/63}Cu$ and $\delta^{66/64}Zn$ values (‰) in Tahiti Fe-Mn crusts. Apuupuu Fe-Mn crusts isotopic values are also plotted and they are clustered in the blue area which represents the Pacific seawater end-member. The green area represents the hydrothermal end-member. The linear correlation is plotted and the equation and coefficient of determination are equally shown on the figure.*

Experiments show little Zn isotope fractionation during adsorption on Mn-oxide birnessite $\Delta^{66/64}Zn_{solid/sol}$ = -0.17 ‰ indicating modest but significant enrichment of the solid phase in light isotopes (Pokrovsky et al. 2005). Experimental determination of Cu isotope fractionation during adsorption processes has been documented only for Fe-oxides ($\Delta^{65/63}Cu_{solid/sol}$ = +0.58 and +0.98 ‰) (Pokrovsky et al. 2008). These experimental data show that (1) Cu and Zn isotopes should fractionate in opposite directions during adsorption on Fe- and Mn-oxides, and (2) Cu isotopes should be more fractionated than Zn isotopes relative to seawater values. However, the direction of Zn isotope fractionation factor is at odds with the range of values measured for seawater by Boyle et al. (2012) and Conway et al. (2013) (+1.01 and +1.49 ‰) and values measured in Fe-Mn deposits, suggesting enrichment in heavy Zn isotopes during Zn adsorption. Data from Little et al. (2013) support this observation, the Cu output flux is isotopically lighter of ~0.5 ‰ than deep waters, whereas it

is ~0.5 ‰ heavier for Zn isotopes. Authors advocated that since Fe-Mn crusts and Mn-nodules encompass a similar range of values, Fe-Mn oxides are a good representative of the Cu and Zn isotope composition of the output flux.

The effect of diffusion was estimated using equation from (Henderson and Burton 1999) and calculations show that Cu and Zn diffusion rates are several orders of magnitude lower than diffusion of U, thus Cu and Zn can be considered as immobile elements in Fe-Mn crusts at least at the scale of our sampling. We can reasonably assume that Fe-Mn crusts are reliable archives of Cu and Zn isotope compositions.

The positive relationship observed between $\delta^{65/63}Cu_{NIST976}$ and $\delta^{66/64}Zn_{NIST3168a}$ with a correlation coefficient close to unity is thus at odd with a mineralogical control of Cu and Zn isotope fractionation during adsorption processes. In addition, mineralogical effects can be ruled out since Cu and Zn isotope shifts occurring at 6-4 Ma in Tahiti Fe-Mn crusts do not correspond to any significant variations of Cu/Mn and Zn/Mn ratios (Table V.2). In opposite, large fluctuations of Cu/Mn and Zn/Mn ratios observed in Apuupuu Fe-Mn crusts do not result in significant excursion of Zn and Cu isotopes.

Co concentrations in Fe-Mn crusts are commonly used for dating the crusts because the flux of Co to the oceans is assumed to be constant through time (Halbach et al. 1983; Puteanus and Halbach 1988). Therefore, the absence of co-variations between Co/Mn ratios and isotope values likely indicates that growth rates are not the factor that controlled Cu and Zn isotope fractionation (Figure V.12).

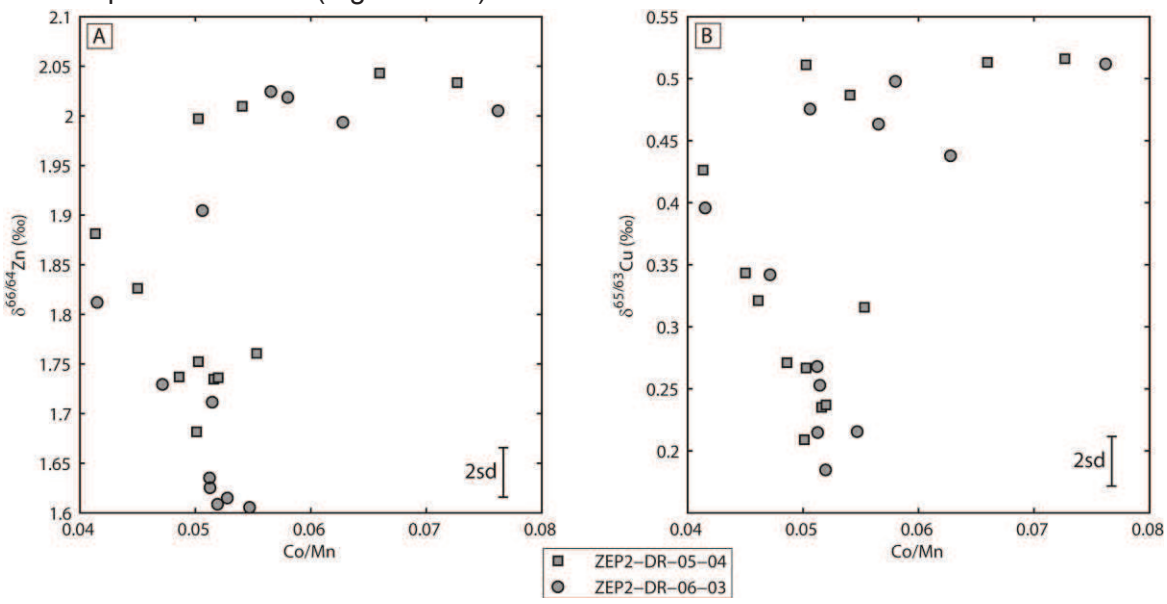

***Figure V.12**: Zn and Cu isotope compositions (‰) versus Co/Mn ratios in Tahiti Fe-Mn crusts (South Pacific) showing that isotope variations are not related to crusts growth rates.*

The examination of Cu and Zn isotope compositions of the surface layers of Fe-Mn crusts (i.e. < 4 Ma) shows relatively similar values for both North and South Pacific Ocean, with $\delta^{65/63}Cu_{NIST976}$ between +0.52 to +0.65‰ and $\delta^{66/64}Zn_{NIST3168a}$ +2.0 to +2.2 ‰. Compared to modern seawater values, Fe-Mn crusts show that (1) $\delta^{65/63}Cu_{NIST976}$ values are similar or slightly lighter, suggesting minor enrichment in light Cu isotopes during Cu precipitation, which differs from experimental studies of Cu isotope fractionation during sorption onto Fe-oxyhydroxide; (2) $\delta^{66/64}Zn_{NIST3168a}$ values are heavier with an average maximum shift of ~0.8 ‰. This fractionation factor contrasts with results of Zn adsorption on birnessite indicating that Fe-Mn crusts should be enriched by a factor of -0.17 ‰ relatively to seawater (Pokrovsky et al. 2005).

Hence, taken at face values, the process responsible for the fractionation between seawater and crusts is still unclear. Although it is possible that modern seawater values have changed significantly over relatively short period that cannot be recorded by Fe-Mn crusts, it is likely that mechanisms of Cu and Zn isotope fractionation during formation of Fe-Mn crusts deviate significantly from laboratory experiments. In particular, it is crucial to consider the importance of metal speciation in seawater and the effect of preferential incorporation of one species over another. This mechanism could be expressed, for example, in the case of a significant isotope fractionation between organic and inorganic dissolved species. These processes were already suggested to be important for Mo isotopes and Ni isotopes (Rehkämper et al. 2002; Barling and Anbar 2004; Tossell 2005; Fujii et al. 2011). Although such effects on Cu and Zn isotopes has not been documented yet, Cu and Zn speciation in seawater with organic ligands is important (Coale and Bruland 1988; Bruland 1989; Robbins et al. 2013; Scott et al. 2013) and need to be considered to explain the differences. It would be also important to further document the range of Cu and Zn isotopes in deep water masses through the oceans.

Phosphatization events are important oceanographic events that may impact Fe-Mn crusts geochemistry (Hein et al. 1993; Koschinsky et al. 1997). An increase in the strength of oceanic circulation promoted redistribution of accumulated phosphorus in the OMZ which produced carbonate-fluorapatite precipitation on seamounts where Fe-Mn crusts were growing. Although the lower section of the crust ZEP2-DR06-03 was significant affected by phosphatization, as revealed by increased Ca concentrations, crust ZEP2-DR05-04 was not affected by this process. Hence, it is unlikely that secondary processes related to phosphatization had any impact on Cu and Zn isotope concentrations and isotopic ratios.

4.2. Factors controlling the co-variations in Cu and Zn isotope variations in seawater

As discussed above, the positive correlation observed between $\delta^{65/63}Cu_{NIST976}$ and $\delta^{66/64}Zn_{NIST3168a}$ is rather the reflection of different water masses mixing than local in-situ processes affecting Cu and Zn isotope fractionation during precipitation in Fe-Mn crusts. This implies that both Fe-Mn crusts from the South Pacific recorded a major oceanographic change between 6 to 4 Ma, while North Pacific remain relatively stable from the perspectives of Cu and Zn isotope compositions. It is also important to note that the record provided by the South Pacific crusts starts before 6 Ma with relatively low $\delta^{65/63}Cu$ and $\delta^{66/64}Zn$ values, before increasing to values similar to North Pacific after 4 Ma. Therefore, the mixing relationship defined by the diagram $\delta^{65/63}Cu$ vs. $\delta^{66/64}Zn$ (Figure V.11) could be explained by mixing of two end-members (1) average Pacific oceanic values with higher Cu and Zn isotope composition similar to North Pacific values; (2) near-crustal values with $\delta^{65/63}Cu$ and $\delta^{66/64}Zn$ values at 0 and 1.4 ‰ which is similar to average basalt values e.g. (Moeller et al. 2012). In addition, both end-members should have similar Cu/Zn ratios to produce such linear relationships.

Below, we discuss the different hypothesis that could potentially explain shifts in Cu and Zn isotope signatures of oceanic water masses.

4.2.1. Influence of OMZ depth

The oxygen-depleted layer is generally present between 500 and 1500 m water depth. However, the thickness and water depth of this layer can vary as a result increasing surface bioproductivity. In addition, the subsidence and derive of seamounts during plate

motion imply that Fe-Mn crusts deepen through time and thus keeps them away from the OMZ. Since Mn-oxides colloids formation with scavenging of trace metals is probably more efficient at the base of the OMZ due to enhanced oxidation of Mn from the OMZ where dissolved reduced Mn accumulates (Koschinsky and Halbach 1995), Fe-Mn crusts formed closely to the OMZ would be preferentially enriched in transition metals. The effect of depth of OMZ base has already been suggested by previous authors to explain the highest enrichment in Co, Ni and Mn in the shallowest crusts (Halbach et al. 1984; Aplin and Cronan 1985; De Carlo et al. 1987).

Although Zn isotopes in the water column strongly vary between 0 and ~500 m depth (with the most important variations in the first 200 m below the seawater surface) and exhibit heavier values with increasing depth (Boyle et al. 2012), there are no significant variations related to the presence of the OMZ, and in deep waters below ~1000 m depth $\delta^{66/64}$Zn values remain constant (Boyle et al. 2012). Similarly, Cu isotopes are not affected by the OMZ and most Cu isotope variations occur in surface waters (Takano et al. 2013).

The four crusts are located below the ~1500 m maximum depth of the OMZ (1826 and 1530 m for ZEP2-DR05-04 and ZEP2-DR06-03 respectively, and ~2000 and 2079 m for J2-480 and J2-480-R14 respectively). If the location of Fe-Mn crusts relatively to the base of the OMZ has varied through time as a consequence of seafloor subsidence and plate motion, so that the older parts sampled in the crusts were located in shallower waters than their present-day location and more proximate to the base of the OMZ, thus we would expect to have higher Mn/Fe ratios in older part of the crusts (the “Inner” region). In fact, this is the inverse trend that is observed in Tahiti crusts where increasing Mn/Fe ratios are found in the youngest parts of the crusts (Figure V.9). As a consequence, we suggest that water depth and OMZ position cannot account for the shift in $\delta^{65/63}$Cu and $\delta^{66/64}$Zn recorded in Fe-Mn crust from the South Pacific.

4.2.2. Effect of surface bioproductivity on Zn and Cu isotope composition of deep water

It has been experimentally shown that biological activity fractionates Zn isotopes by the preferential incorporation of light isotopes (John et al. 2007). The extent of fractionation depends on the concentration of free Zn^{2}+ in such a way that in presence of high Zn concentrations (low-affinity Zn transport) diatoms will be more fractionated towards lighter Zn isotope compositions than at low Zn concentrations (high-affinity Zn transport). This difference is related to the process by which Zn is incorporated in the cell, i.e. high- versus low-affinity transport of Zn (John et al. 2007). Zinc is involved in many biological reactions making Zn a bio-essential element for biological productivity (Morel and Price 2003). In High-Nutrient-Low-Chlorophyll (HNLC) areas, despite high concentrations in major nutrients, limited productivity has been related to the very low trace metal concentrations (e.g. Zn and Fe). Three regions are primarily concerned: the Eastern Equatorial Pacific, Subarctic Pacific and Southern Oceans (e.g. Antarctic).

Pichat et al. (2003) demonstrated that the carbonate fractions of deep-sea sediments from eastern equatorial Pacific were enriched in heavy Zn isotopes and that Zn isotope variations are explained by variable intensities of the trade winds controlled by precession cycles. At the end of the summer, the presence of a thermocline due to implementation of weak trade winds prevents mixing of surface waters with deep waters. Biological activity will deplete surface waters (the euphotic zone) in light Zn isotopes during uptake leaving an isotopically heavy Zn residual pool. Accordingly, carbonate shells of organisms growing in these waters will incorporate Zn enriched in heavy isotopes – if assumption is made that no

isotopic fractionation occurs during shell growth with respect to seawater. By contrast, when intense trade winds form, the thermocline does not develop and does not promote upwelling of deep waters that would homogenized Zn isotope composition of surface seawater (Pichat et al. 2003).

The magnitude of Zn isotope variations in Fe-Mn crusts from Tahiti is of the same order as the one reported by Maréchal et al. (2000) in marine particles but lower than the range reported by Pichat et al. (2003) in carbonate sediments. However, by contrast with Zn isotopes in carbonates which are a proxy of surface seawater composition, Fe-Mn crusts are instead a proxy of deep seawater. Therefore, any Cu and Zn isotope variations produced by biological-induced processes would have to be preserved during transport in the water column from surface to deep waters.

Locations of the depositional environment of our Fe-Mn crusts correspond to different hemispheres but to approximately similar latitudes (22° and 18° for South and North Pacific samples respectively). Nowadays, these open-ocean regions are known as having oligotrophic waters and present one of the lowest bioproductivity rates. They are far from continental runoff (and to a lesser extent from large fluxes of atmospheric particles) and nutrients sources and they are located in downwelling regions, hence availability of nutrients and micronutrients is limited and the deep Pacific Ocean is characterized by old water masses (thermohaline circulation).

Cu and Zn have relatively high residence times (in the order of 5400 and 11000 for Cu and Zn respectively (Little et al. 2013). Therefore we would expect to record similar patterns in North and South Pacific crusts due to homogenization of deep waters masses over the time scale of crust formation. If a modification in marine productivity resulted in specific Cu and Zn isotope signatures, then North Pacific crusts should also have recorded this event. In addition, while Zn has clearly a nutrient-type profile in the water column (it is a micronutrient), Cu does not display the same mid-depth maximum than Zn. In fact, Cu concentrations increase continuously with depth as a result of dissolution of sinking particles. Hence, it seems unlikely that surface productivity would be able to affect both Cu and Zn isotopes in a similar manner, which in turns cannot explain the relationships observed in South Pacific crusts.

4.2.3. Inputs from continental erosion (rivers) and atmospheric particles and oceanic circulation

Continental erosion and atmospheric particles are the main sources of Cu and Zn in the seawater pool (Little et al. 2013). The average isotope composition of rivers are +0.68 ‰ for $\delta^{65/63}Cu_{NIST976}$ (range of +0.02 to +1.45 ‰) (Vance et al. 2008; Little et al. 2013) and +1.29 ‰ for $\delta^{66/64}Zn_{NIST3168a}$ (range of +1.15 to +1.52 ‰) (Little et al. 2013). The extent of isotopic values in rivers is thus in the range of Cu and Zn isotope variations in our Fe-Mn crusts. However, since the timescale spans by Fe-Mn crusts from this study is not larger than ~17 Ma, it is hardly conceivable that the isotopic composition of the continental sources (mostly rivers) has dramatically changed over this period to the point of modifying the isotope composition of the deep seawater. On the other hand, oceanic circulation may have varied through time due to plate motion and continental drift. These changes could have brought different water masses with different isotopic compositions. Given the position of our samples and the current oceanic circulation we may expect that these currents come from the Southern Ocean or the Indian Ocean.

So far, no systematic differences of Cu and Zn isotope compositions have been observed between oceanic basins. Hence, although the input of different water masses would easily account for the co-variations of Cu and Zn isotope compositions (Figure V.11), it is incompatible with current knowledge of oceanic values. With additional surveys of Cu and Zn isotope composition of water masses through basin-scale transect, such issues could be tested in the future.

4.2.4. Hydrothermal fluxes in the South Pacific Ocean

The influence of hydrothermal activity on transition metals enrichment in Eastern Pacific sediments was first mentioned by (Boström et al. 1969). Although most transition metals delivered by hydrothermal fluids are precipitated in the vicinity of vent sites, a significant proportion of Cu and Fe may enter the deep ocean through complexation with organic ligands (Coale and Bruland 1988; Toner et al. 2009; Sander and Koschinsky 2011). Recent model of Cu transport from hydrothermal vents by complexation with organic ligands may account for 14% of the Cu dissolved in seawater, especially in ultramafic-hosted hydrothermal sites where abiotic production of organic compounds is enhanced (Sander and Koschinsky 2011). Organic complexation of Zn from hydrothermal fluids is not specifically documented in the literature, but it was demonstrated elsewhere that Zn also forms strong organic ligands in seawater (Bruland 1989; Robbins et al. 2013). Accordingly, we can possibly assume that transport of Cu and Zn far away from hydrothermal sites would be enhanced by speciation in organic ligands which stabilize the Cu and Zn in seawater. Hannington (2013) recently highlighted that accumulation of Cu in South Pacific deep-sea sediments through time may exceed the total amount of Cu deposited at ridge axis. The far-field sedimentation of hydrothermal materials in the South Pacific has been also confirmed by the studies of Rare Earth Elements in deep-sea sediments deposited in the Pacific. It was shown that area affected by hydrothermal input are also associated with enhanced scavenging of seawater-derived REE (Kato et al. 2011).

Considering the location of our South Pacific Fe-Mn crusts, the Tahiti archipelago is clearly within the area of the Pacific Ocean (between 10-20°S) that are characterized by a large scale ^{3}He enrichment at 2500m depth (Lupton and Craig 1981; Lupton 1995; Urabe et al. 1995), it can be suggested that the area has been receiving large hydrothermal input from the superfast EPR segments for some time. Hence, we posit that the difference in Cu and Zn isotope records between the South and North Equatorial Pacific crusts are related to the global hydrothermal contribution of trace metals that are different at the scale of the oceanic basin and that would affected water masses of the South Pacific Ocean.

Zn isotopes in hydrothermal fluids from EPR hydrothermal vent sites are enriched in heavy isotopes in comparison to the source rock for Zn in the fluids as a result of precipitation of isotopically light Zn in sulfides (John et al. 2008). These authors argued that hydrothermal fluids may possibly affect Zn isotopes budget of seawater. However, $\delta^{66/64}Zn_{NIST3168a}$ values from these vent fluids vary from +0.96 to +2.00 ‰, albeit most values cluster between +1.16 to +1.26 ‰, which is generally below the range reported for Apuupuu and Tahiti Fe-Mn crusts (+1.61 to +2.19 ‰). Cu isotope composition of hydrothermal fluids has not been reported in the literature yet but preliminary studies suggest near-basaltic values for high-temperature hydrothermal fluid end-members (Dekov and Rouxel 2012). Hence, it is reasonable to assume that hydrothermal input of Cu and Zn would be characterized by near to above crustal values, which is identical to the lowest values recorded in the older section of Fe-Mn crusts from Tahiti (i.e. older than 6 Ma).

If correct, this finding suggest either that hydrothermal input in the South Pacific area recorded by the Fe-Mn crust was stronger before 6 Ma or that oceanic circulation changed substantially, which deviated the major pathways of hydrothermal export to its present location. Further knowledge of isotope fractionation during Cu and Zn transport and precipitation, in particular with respect to the importance of organic ligands is now required to further address this issue. It would be also important to investigate other Fe-Mn crusts from other locations in the South Pacific to confirm such large-scale event.

5. Summary and conclusions

Cu and Zn isotope patterns during the last ~17 Ma are distinct whether Fe-Mn crusts formed in the North Pacific or in the South Pacific Ocean. North Pacific (Apuupuu) Fe-Mn crusts show limited Cu and Zn isotope variations through time with values between +0.57 and +0.73 ‰ for $\delta^{65/63}Cu_{NIST976}$ and between +1.91 to +2.19 ‰ for $\delta^{66/64}Zn_{NIST3168a}$. The extent of isotopic variations is higher in South Pacific crusts than in North Pacific crusts with Zn isotopes varying from +1.61 to +2.03 ‰ and Cu isotopes are comprised in the +0.16 to +0.51 ‰ range.

Strikingly, South Pacific Fe-Mn crusts display a strong positive correlation between $\delta^{65/63}Cu$ values and $\delta^{66/64}Zn_{NIST3168a}$ values. These variations are probably not related to precipitation processes and mineralogical effects, but they are rather the results of variations in the sources of Cu and Zn to the oceans. Two possible explanations are envisaged, (1) hydrothermal inputs from the East Pacific Rise where transport of Cu and Zn with organic ligands may have favor their dispersion in deep seawaters, (2) modification of oceanic circulation and inputs of water masses with different Cu and Zn isotope compositions. While the first hypothesis is consistent with the geodynamic setting of samples and current knowledge of isotope composition of hydrothermal sources, testing further the second hypothesis would require more in-depth knowledge of present-day distribution of Cu and Zn isotopes in seawater including the effect of hydrothermal inputs on Cu and Zn. Overall, this study demonstrated for the first time that a major oceanographic event occurred about 6 Ma ago affecting both Cu and Zn isotope compositions of the South Equatorial Pacific.

6. References

Albarede, F. (2004). "The Stable Isotope Geochemistry of Copper and Zinc." Reviews in Mineralogy and Geochemistry 55(1): 409-427.

Algeo, T. J. and Maynard, J. B. (2008). "Trace-metal covariation as a guide to water-mass conditions in ancient anoxic marine environments." Geosphere 4(5): 872-887.

Anbar, A. D. and Rouxel, O. (2007). "Metal stable isotopes in paleoceanography." Annual Review of Earth and Planetary Sciences 35: 717-746.

Aplin, A. C. and Cronan, D. S. (1985). "Ferromanganese oxide deposits from the Central Pacific ocean. 1. Encrustations from the Line islands archipelago." Geochimica Et Cosmochimica Acta 49(2): 427-436.

Baker, E. T., German, C. R. and Elderfield, H. (1995). Hydrothermal Plumes Over Spreading-Center Axes: Global Distributions and Geological Inferences. Seafloor Hydrothermal Systems: Physical, Chemical, Biological, and Geological Interactions, American Geophysical Union, Geophysical Monograph Series. 91**:** 47-71.

Baker, E. T. and Massoth, G. J. (1986). "Hydrothermal Plume Measurements: A Regional Perspective." Science 234(4779): 980-982.

Barling, J. and Anbar, A. D. (2004). "Molybdenum isotope fractionation during adsorption by manganese oxides." Earth and Planetary Science Letters 217(3-4): 315-329.

Bermin, J., Vance, D., Archer, C. and Statham, P. J. (2006). "The determination of the isotopic composition of Cu and Zn in seawater." Chemical Geology 226(3-4): 280-297.

Bigalke, M., Weyer, S., Kobza, J. and Wilcke, W. (2010). "Stable Cu and Zn isotope ratios as tracers of sources and transport of Cu and Zn in contaminated soil." Geochimica Et Cosmochimica Acta 74(23): 6801-6813.

Biller, D. V. and Bruland, K. W. (2012). "Analysis of Mn, Fe, Co, Ni, Cu, Zn, Cd, and Pb in seawater using the Nobias-chelate PA1 resin and magnetic sector inductively coupled plasma mass spectrometry (ICP-MS)." Marine Chemistry 130–131(0): 12-20.

Boström, K., Peterson, M. N. A., Joensuu, O. and Fisher, D. E. (1969). "Aluminum-poor ferromanganoan sediments on active oceanic ridges." Journal of Geophysical Research 74(12): 3261-3270.

Bourles, D., Raisbeck, G. M. and Yiou, F. (1989). "^{10}Be and ^{9}Be in marine sediments and their potential for dating." Geochimica Et Cosmochimica Acta 53(2): 443-452.

Boyle, E. A., John, S., Abouchami, W., Adkins, J. F., Echegoyen-Sanz, Y., Ellwood, M., Flegal, A. R., Fornace, K., Gallon, C., Galer, S., Gault-Ringold, M., Lacan, F., Radic, A., Rehkamper, M., Rouxel, O., Sohrin, Y., Stirling, C., Thompson, C., Vance, D., Xue, Z. C. and Zhao, Y. (2012). "GEOTRACES IC1 (BATS) contamination-prone trace element isotopes Cd, Fe, Pb, Zn, Cu, and Mo intercalibration." Limnology and Oceanography-Methods 10: 653-665.

Boyle, E. A., Sclater, F. R. and Edmond, J. M. (1977). "The distribution of dissolved copper in the Pacific." Earth and Planetary Science Letters 37(1): 38-54.

Bruland, K. W. (1980). "Oceanographic distributions of Cadmium, Zinc, Nickel, and Copper in the North Pacific." Earth and Planetary Science Letters 47(2): 176-198.

Bruland, K. W. (1983). Trace elements in sea water. London, Academic Press.

Bruland, K. W. (1989). "Complexation of zinc by natural organic-ligands in the Central North Pacific." Limnology and Oceanography 34(2): 269-285.

Bruland, K. W., Orians, K. J. and Cowen, J. P. (1994). "Reactive trace metals in the stratified central North Pacific." Geochimica Et Cosmochimica Acta 58(15): 3171-3182.

Chapman, J. B., Mason, T. F. D., Weiss, D. J., Coles, B. J. and Wilkinson, J. J. (2006). "Chemical separation and isotopic variations of Cu and Zn from five geological reference materials." Geostandards and Geoanalytical Research 30(1): 5-16.

Coale, K. H. and Bruland, K. W. (1988). "Copper complexation in the Northeast Pacific." Limnology and Oceanography 33(5): 1084-1101.

Conway, T. M., Rosenberg, A. D., Adkins, J. F. and John, S. G. (2013). "A new method for precise determination of iron, zinc and cadmium stable isotope ratios in seawater by double-spike mass spectrometry." Analytica Chimica Acta 793(0): 44-52.

De Carlo, E. H., McMurtry, G. M. and Kim, K. H. (1987). "Geochemistry of ferromanganese crusts from the hawaiian archipelago. 1. Northern survey areas." Deep-Sea Research Part a-Oceanographic Research Papers 34(3): 441-467.

Dekov, V. and Rouxel, O. (2012). Cu- and Zn-isotope systematics of seafloor hydrothermal vent fluids from a back-arc setting (Manus Basin). EGU. Vienna, Austria, Geophysical Research Abstracts. 14**:** 13020.

Ehrlich, S., Butler, I., Halicz, L., Rickard, D., Oldroyd, A. and Matthews, A. (2004). "Experimental study of the copper isotope fractionation between aqueous Cu(II) and covellite, CuS." Chemical Geology 209(3-4): 259-269.

Frank, M. (2002). "Radiogenic isotopes: Tracers of past ocean circulation and erosional input." Reviews of Geophysics 40(1).

Frank, M., O'Nions, R. K., Hein, J. R. and Banakar, V. K. (1999). "60 Myr records of major elements and Pb–Nd isotopes from hydrogenous ferromanganese crusts: reconstruction of seawater paleochemistry." Geochimica Et Cosmochimica Acta 63(11–12): 1689-1708.

Fujii, T., Moynier, F., Dauphas, N. and Abe, M. (2011). "Theoretical and experimental investigation of nickel isotopic fractionation in species relevant to modern and ancient oceans." Geochimica et Cosmochimica Acta 75(2): 469-482.

Halbach, P., Puteanus, D. and Manheim, F. T. (1984). "Platinum concentrations in ferromanganese seamount crusts from the Central Pacific." Naturwissenschaften 71(11): 577-579.

Halbach, P., Segl, M., Puteanus, D. and Mangini, A. (1983). "Co-fluxes and growth rates in ferromanganese deposits from Central Pacific seamount areas." Nature 304(5928): 716-719.

Hannington, M. D. (2013). "The role of black smokers in the Cu mass balance of the oceanic crust." Earth and Planetary Science Letters(0).

Hein, J. R., Bohrson, W. A., Schulz, M. S., Noble, M. and Clague, D. A. (1992). "Variations in the fine-scale composition of a Central Pacific ferromanganese crust: paleoceanographic implications." Paleoceanography 7(1): 63-77.

Hein, J. R., Conrad, T. A. and Staudigel, H. (2010). "Seamount mineral deposits: a source of rare metals for high-technology industries." Oceanography 23(1): 184-189.

Hein, J. R., Koschinsky, A. and Halliday, A. N. (2003). "Global occurrence of tellurium-rich ferromanganese crusts and a model for the enrichment of tellurium." Geochimica et Cosmochimica Acta 67(6): 1117-1127.

Hein, J. R., Mizell, K., Koschinsky, A. and Conrad, T. A. (2013). "Deep-ocean mineral deposits as a source of critical metals for high- and green-technology applications: Comparison with land-based resources." Ore Geology Reviews 51(0): 1-14.

Hein, J. R., Schwab, W. C. and Davis, A. S. (1988). "Cobalt-rich and platinum-rich ferromanagenese crusts and associated substrate rocks from the Marshall islands." Marine Geology 78(3-4): 255-283.

Hein, J. R., Yeh, H. W., Gunn, S. H., Sliter, W. V., Benninger, L. M. and Wang, C. H. (1993). "Two major Cenozoic episodes of phosphogenesis recorded in equatorial Pacific seamount deposits." Paleoceanography 8(2): 293-311.

Henderson, G. M. and Burton, K. W. (1999). "Using ($^{234}U/^{238}U$) to assess diffusion rates of isotope tracers in ferromanganese crusts." Earth and Planetary Science Letters 170(3): 169-179.

Horner, T. J., Schonbachler, M., Rehkämper, M., Nielsen, S. G., Williams, H., Halliday, A. N., Xue, Z. and Hein, J. R. (2010). "Ferromanganese crusts as archives of deep water Cd isotope compositions." Geochemistry Geophysics Geosystems 11: 1525-2027.

John, S. G., Geis, R. W., Saito, M. A. and Boyle, E. A. (2007). "Zinc isotope fractionation during high-affinity and low-affinity zinc transport by the marine diatom Thalassiosira oceanica." Limnology and Oceanography 52(6): 2710-2714.

John, S. G., Rouxel, O. J., Craddock, P. R., Engwall, A. M. and Boyle, E. A. (2008). "Zinc stable isotopes in seafloor hydrothermal vent fluids and chinmeys." Earth and Planetary Science Letters 269(1-2): 17-28.

Johnson, C. M., Beard, B. L. and Albarède, F. (2004). "Overview and General Concepts." Reviews in Mineralogy and Geochemistry 55(1): 1-24.

Kato, Y., Fujinaga, K., Nakamura, K., Takaya, Y., Kitamura, K., Ohta, J., Toda, R., Nakashima, T. and Iwamori, H. (2011). "Deep-sea mud in the Pacific Ocean as a potential resource for rare-earth elements." Nature Geoscience 4(8): 535-539.

Koschinsky, A. and Halbach, P. (1995). "Sequential leaching of marine ferromanganese precipitates: Genetic implications." Geochimica et Cosmochimica Acta 59(24): 5113-5132.

Koschinsky, A. and Hein, J. R. (2003). "Uptake of elements from seawater by ferromanganese crusts: solid-phase associations and seawater speciation." Marine Geology 198(3-4): 331-351.

Koschinsky, A., Stascheit, A., Bau, M. and Halbach, P. (1997). "Effects of phosphatization on the geochemical and mineralogical composition of marine ferromanganese crusts." Geochimica et Cosmochimica Acta 61(19): 4079-4094.

Li, Y. H. and Schoonmaker, J. E. (2003). Chemical Composition and Mineralogy of Marine Sediments. Treatise on Geochemistry. D. H. Editors-in-Chief: Heinrich and K. T. Karl. Oxford, Pergamon**:** 1-35.

Little, S. H., Vance, D., Walker-Brown, C. and Landing, W. M. (2013). "The oceanic mass balance of copper and zinc isotopes, investigated by analysis of their inputs, and outputs to ferromanganese oxide sediments." Geochimica Et Cosmochimica Acta(0).

Lupton, J. (1998). "Hydrothermal helium plumes in the Pacific Ocean." Journal of Geophysical Research: Oceans 103(C8): 15853-15868.

Lupton, J. E. (1995). Hydrothermal Plumes: Near and Far Field. Seafloor Hydrothermal Systems: Physical, Chemical, Biological, and Geological Interactions, American Geophysical Union, Geophysical Monograph Series. 91**:** 317-346.

Lupton, J. E. and Craig, H. (1981). "A Major Helium-3 Source at 15°S on the East Pacific Rise." Science 214(4516): 13-18.

Maréchal, C. N., Nicolas, E., Douchet, C. and Albarède, F. (2000). "Abundance of zinc isotopes as a marine biogeochemical tracer." Geochem. Geophys. Geosyst. 1(5): 1-15.

Marechal, C. N., Telouk, P. and Albarede, F. (1999). "Precise analysis of copper and zinc isotopic compositions by plasma-source mass spectrometry." Chemical Geology 156(1-4): 251-273.

Moeller, K., Schoenberg, R., Pedersen, R.-B., Weiss, D. and Dong, S. (2012). "Calibration of the New Certified Reference Materials ERM-AE633 and ERM-AE647 for Copper and IRMM-3702 for Zinc Isotope Amount Ratio Determinations." Geostandards and Geoanalytical Research 36(2): 177-199.

Morel, F. M. M. and Price, N. M. (2003). "The Biogeochemical Cycles of Trace Metals in the Oceans." Science 300(5621): 944.

Nielsen, S. G., Wasylenki, L. E., Rehkämper, M., Peacock, C. L., Xue, Z. and Moon, E. M. (2013). "Towards an understanding of thallium isotope fractionation during adsorption to manganese oxides." Geochimica Et Cosmochimica Acta 117(0): 252-265.

Pichat, S., Douchet, C. and Albarede, F. (2003). "Zinc isotope variations in deep-sea carbonates from the eastern equatorial Pacific over the last 175 ka." Earth and Planetary Science Letters 210(1-2): 167-178.

Pokrovsky, O. S., Viers, J., Emnova, E. E., Kompantseva, E. I. and Freydier, R. (2008). "Copper isotope fractionation during its interaction with soil and aquatic microorganisms and metal oxy(hydr)oxides: Possible structural control." Geochimica et Cosmochimica Acta 72(7): 1742-1757.

Pokrovsky, O. S., Viers, J. and Freydier, R. (2005). "Zinc stable isotope fractionation during its adsorption on oxides and hydroxides." Journal of Colloid and Interface Science 291(1): 192-200.

Puteanus, D. and Halbach, P. (1988). "Correlation of Co concentration and growth rate — A method for age determination of ferromanganese crusts." Chemical Geology 69(1–2): 73-85.

Rehkämper, M., Frank, M., Hein, J. R. and Halliday, A. (2004). "Cenozoic marine geochemistry of thallium deduced from isotopic studies of ferromanganese crusts and pelagic sediments." Earth and Planetary Science Letters 219(1-2): 77-91.

Rehkämper, M., Frank, M., Hein, J. R., Porcelli, D., Halliday, A., Ingri, J. and Liebetrau, V. (2002). "Thallium isotope variations in seawater and hydrogenetic, diagenetic, and hydrothermal ferromanganese deposits." Earth and Planetary Science Letters 197(1-2): 65-81.

Robbins, L. J., Lalonde, S. V., Saito, M. A., Planavsky, N. J., Mloszewska, A. M., Pecoits, E., Scott, C., Dupont, C. L., Kappler, A. and Konhauser, K. O. (2013). "Authigenic iron oxide proxies for marine zinc over geological time and implications for eukaryotic metallome evolution." Geobiology: n/a-n/a.

Sander, S. G. and Koschinsky, A. (2011). "Metal flux from hydrothermal vents increased by organic complexation." Nature Geoscience 4(3): 145-150.

Scott, C., Planavsky, N. J., Dupont, C. L., Kendall, B., Gill, B. C., Robbins, L. J., Husband, K. F., Arnold, G. L., Wing, B. A., Poulton, S. W., Bekker, A., Anbar, A. D., Konhauser, K. O. and Lyons, T. W. (2013). "Bioavailability of zinc in marine systems through time." Nature Geosci 6(2): 125-128.

Segl, M., Mangini, A., Bonani, G., Hofmann, H. J., Nessi, M., Suter, M., Wolfli, W., Friedrich, G., Pluger, W. L., Wiechowski, A. and Beer, J. (1984). "^{10}Be-dating of a manganese crust from Central North Pacific and implications for ocean palaeocirculation." Nature 309(5968): 540-543.

Sohrin, Y. and Bruland, K. W. (2011). "Global status of trace elements in the ocean." Trends in Analytical Chemistry 30(8): 1291-1307.

Sohrin, Y., Iwamoto, S., Akiyama, S., Fujita, T., Kugii, T., Obata, H., Nakayama, E., Goda, S., Fujishima, Y., Hasegawa, H., Ueda, K. and Matsui, M. (1998). "Determination of trace elements in seawater by fluorinated metal alkoxide glass-immobilized 8-hydroxyquinoline concentration and high-resolution inductively coupled plasma mass spectrometry detection." Analytica Chimica Acta 363(1): 11-19.

Sohrin, Y., Urushihara, S., Nakatsuka, S., Kono, T., Higo, E., Minami, T., Norisuye, K. and Umetani, S. (2008). "Multielemental determination of GEOTRACES key trace metals in seawater by ICPMS after preconcentration using an ethylenediaminetriacetic acid chelating resin." Analytical Chemistry 80(16): 6267-6273.

Takano, S., Tanimizu, M., Hirata, T. and Sohrin, Y. (2013). "Determination of isotopic composition of dissolved copper in seawater by multi-collector inductively coupled plasma mass spectrometry after pre-concentration using an ethylenediaminetriacetic acid chelating resin." Analytica Chimica Acta 784(0): 33-41.

Toner, B. M., Fakra, S. C., Manganini, S. J., Santelli, C. M., Marcus, M. A., Moffett, J., Rouxel, O., German, C. R. and Edwards, K. J. (2009). "Preservation of iron(II) by carbon-rich matrices in a hydrothermal plume." Nature Geoscience 2(3): 197-201.

Tossell, J. A. (2005). "Calculating the partitioning of the isotopes of Mo between oxidic and sulfidic species in aqueous solution." Geochimica Et Cosmochimica Acta 69(12): 2981-2993.

Urabe, T., Baker, E. T., Ishibashi, J., Feely, R. A., Marumo, K., Massoth, G. J., Maruyama, A., Shitashima, K., Okamura, K., Lupton, J. E., Sonoda, A., Yamazaki, T., Aoki, M., Gendron, J., Greene, R., Kaiho, Y., Kisimoto, K., Lebon, G., Matsumoto, T., Nakamura, K., Nishizawa, A., Okano, O., Paradis, G., Roe, K., Shibata, T., Tennant, D., Vance, T., Walker, S. L., Yabuki, T. and Ytow, N. (1995). "The Effect of Magmatic Activity on Hydrothermal Venting Along the Superfast-Spreading East Pacific Rise." Science 269(5227): 1092-1095.

Vance, D., Archer, C., Bermin, J., Perkins, J., Statham, P. J., Lohan, M. C., Ellwood, M. J. and Mills, R. A. (2008). "The copper isotope geochemistry of rivers and the oceans." Earth and Planetary Science Letters 274(1-2): 204-213.

Wasylenki, L. E., Rolfe, B. A., Weeks, C. L., Spiro, T. G. and Anbar, A. D. (2008). "Experimental investigation of the effects of temperature and ionic strength on Mo isotope fractionation during adsorption to manganese oxides." Geochimica Et Cosmochimica Acta 72(24): 5997-6005.

Wasylenki, L. E. and Swihart, J. (2013). Cd Isotope Fractionation during Sorption to Mn Oxide at Low and High Ionic Strength. Goldschmidt, Florence, Italy.

Wasylenki, L. E., Weeks, C. L., Bargar, J. R., Spiro, T. G., Hein, J. R. and Anbar, A. D. (2011). "The molecular mechanism of Mo isotope fractionation during adsorption to birnessite." Geochimica Et Cosmochimica Acta 75(17): 5019-5031.

Zhu, X. K., Guo, Y., Williams, R. J. P., O'Nions, R. K., Matthews, A., Belshaw, N. S., Canters, G. W., de Waal, E. C., Weser, U., Burgess, B. K. and Salvato, B. (2002). "Mass fractionation processes of transition metal isotopes." Earth and Planetary Science Letters 200(1-2): 47-62.

Conclusion du chapitre V:

Afin de renforcer nos interprétations sur les variations isotopiques des métaux en général dans les dépôts métallifères océaniques, l'idée de ce travail est également de développer une approche multi-proxys utilisant plusieurs systèmes isotopiques des métaux tels que Fe, Cu, Zn et le Ni (Figure C.5). Nous avons notamment examiné l'évolution des compositions isotopiques de ces éléments enregistrées dans les encroûtements de fer-manganèse et les relations que l'on pouvait établir en fonction des caractéristiques géochimiques de chacun des systèmes isotopiques considéré.

Les corrélations entre les compositions isotopiques en Fe et en Pb dans les encroûtements d'Apuupuu près d'Hawaii dans le Pacifique Nord sont probablement le résultat de mélanges entre différentes masses d'eau océanique. Les valeurs négatives en isotopes du Fe observées dans un des encroûtements pourraient être liées à un apport hydrothermal en provenance l'activité magmatique ayant lieu au niveau du point chaud d'Hawaii et qui aurait affecté la masse d'eau océanique dans laquelle ont précipité les dépôts. Les encroûtements du Pacifique Sud (Tahiti) ne montrent aucune variation dans les profils isotopiques en Fe.

En revanche, ces encroûtements du Pacifique Sud montrent une co-variation des compositions isotopiques en Cu et Zn entre ~4 et 6 Ma. Ces variations se traduisent par une parfaite corrélation positive et les échantillons d'Apuupuu du Pacifique Nord s'alignent sur cette tendance et forment le « pôle » supérieur de cette corrélation. Cette corrélation montre probablement un mélange entre des masses d'eau océanique entre ce « pôle » et un « pôle » inférieur ayant des compositions isotopiques en Cu et Zn enrichies en isotopes légers probablement apportées par des apports hydrothermaux en provenance de la dorsale Est Pacifique.

Ainsi, cette étude montre que les dépôts hydrogénétiques, formés a priori lors de processus simples tels que la précipitation de colloïdes d'oxydes de Fe et de Mn, présentent parfois de variations significatives des compositions isotopiques des métaux. Le cycle biogéochimique des métaux dans l'eau de mer a donc un impact significatif sur les compositions isotopiques des masses d'eau et donc également sur les compositions isotopiques des encroûtements permettant ainsi de tracer des processus inédits.

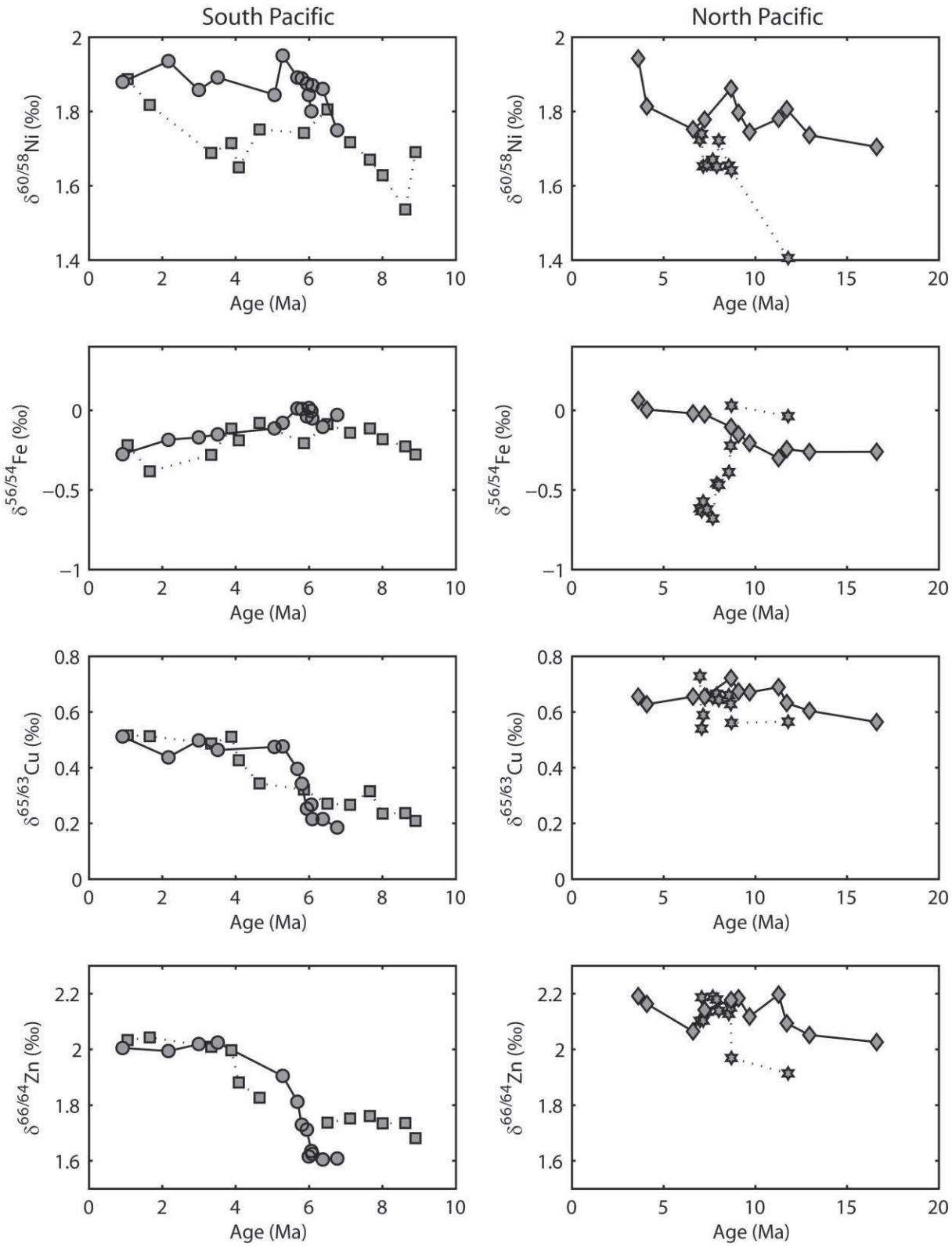

Figure C.5 *: Séries temporelles des compositions isotopiques en Ni, Fe, Cu et Zn dans les encroûtements de Tahiti (Sud Pacifique) et de Apuupuu (Nord Pacifique).*

Conclusions et perspectives

Foreword:

This study has been undertaken following two main objectives. First, we evaluated the utility of Ni isotopes as new biogeochemical tracers of metal sources and formation of Fe-Mn-rich marine deposits. This objective was led by applying both classical and required tools of elemental geochemistry, mineralogy and new isotope geochemistry tools of metal stable isotope systematics such as Ni, Fe, Cu and Zn. We essentially focused on Ni isotope systematics due to its potential as a new biogeochemical tracer of past and present oceans. This approach allows to emphasizing major results. Hydrothermal Fe-Mn deposits have variable Ni isotope compositions which are related to processes of formation and to relatively rapid reactions kinetics during precipitation producing important Ni isotope fractionation. On the other hand, hydrogenous deposits show a more restricted range of isotopic values indicating that Ni is not fractionated from its seawater source. This study also benefited from experimental results showing that Ni isotope fractionation is significant during its adsorption on Fe- and Mn-phases, consistent with previous interpretation of Ni isotopes in hydrothermal deposits. A compilation of isotopic data is presented in Figure F.1 and shows the large variability of Ni isotopes in terrestrial rocks.

Then, we explored Ni, Fe, Pb, Cu and Zn isotope compositions in Fe-Mn crusts time-series. Using this approach we have demonstrated that, (1) correlation of Pb and Fe isotope compositions indicating mixing between water masses, and Fe isotopes are sensitive to local inputs in seawater such as hydrothermal inputs, (2) Ni isotopes do not show any temporal variations but they can be affected by post-depositional and alteration processes and recrystallization, (3) correlation between Cu and Zn isotopes also indicate mixing between water masses.

This work has provided important advances for our understanding of factors controlling metals biogeochemical cycling over the last few million years. In the following synthesis, after giving the major findings of this work, we will propose perspectives and we will present preliminary work reported in the appendices of this manuscript as projects or published collaborative work.

Avant-propos :

Cette étude a été menée suivant deux principaux objectifs. Il a fallu dans un premier temps, évaluer l'utilité des isotopes du Ni comme nouveaux traceurs de sources de métaux et des processus de formation des dépôts marins riches en Fe et Mn. Cet objectif a été mené en appliquant à la fois les outils classiques et indispensables de géochimie élémentaire, minéralogie et les outils de la géochimie des isotopes stables des métaux tels que le Ni, Fe, Cu et Zn. Notre attention s'est porté essentiellement sur la systématique isotopique du Ni du fait de son potentiel en tant que nouveau traceur biogéochimique dans les océans actuels et anciens. Cette approche a permis de mettre en évidence des résultats majeurs. Les dépôts hydrothermaux ont des compositions isotopiques variables qui sont liées aux processus de formation et à une cinétique relativement rapide de formation des phases minérales produisant des fractionnements isotopiques importants, alors que les dépôts hydrogénés montrent une gamme de valeurs isotopiques beaucoup plus restreinte indiquant que le Ni n'est pas fractionné par rapport à sa source, l'eau de mer. Cette étude a également bénéficié des résultats d'expérimentation en laboratoire qui montrent des fractionnements isotopiques du Ni significatifs lors de l'adsorption dans les oxydes de Fe et de Mn qui sont cohérents avec nos interprétations des variations isotopiques du Ni dans les

dépôts hydrothermaux. Une compilation des données isotopiques est présentée dans la Figure F.1 et montre la grande variabilité des compositions isotopiques en Ni dans les roches terrestres.

Dans un second temps, nous avons exploré les variations isotopiques conjointes du Pb, Ni, Fe, Cu et Zn dans les enregistrements temporels préservés dans les encroûtements de fer-manganèse. Cette approche a permis de mettre en évidence des résultats majeurs (1) les isotopes du Fe sont sensibles aux apports locaux de type hydrothermal, (2) les isotopes du Ni ne montrent pas de variations temporelles significatives mais par contre ils peuvent être affectés par des processus tardifs d'altération et de recristallisation, (3) les isotopes du Cu et du Zn peuvent être affectés par des variations des sources aux masses d'eau océanique (tels qu'un apport hydrothermal) et pourraient ainsi permettre de tracer le mélange de ces différentes masses d'eau océaniques. Ultimement, ce travail a permis d'apporter des premiers éléments de réponse afin d'améliorer notre compréhension des facteurs ayant influencé les cycles biogéochimiques des métaux dans les océans modernes au cours des derniers millions d'années.

Dans cette synthèse, après avoir passé en revue les résultats majeurs, nous aborderons les perspectives en insistant particulièrement sur les résultats préliminaires déjà obtenue dans cette étude, dont certains ont été détaillé en annexe sous la forme de projet de recherche ou de publications en collaboration.

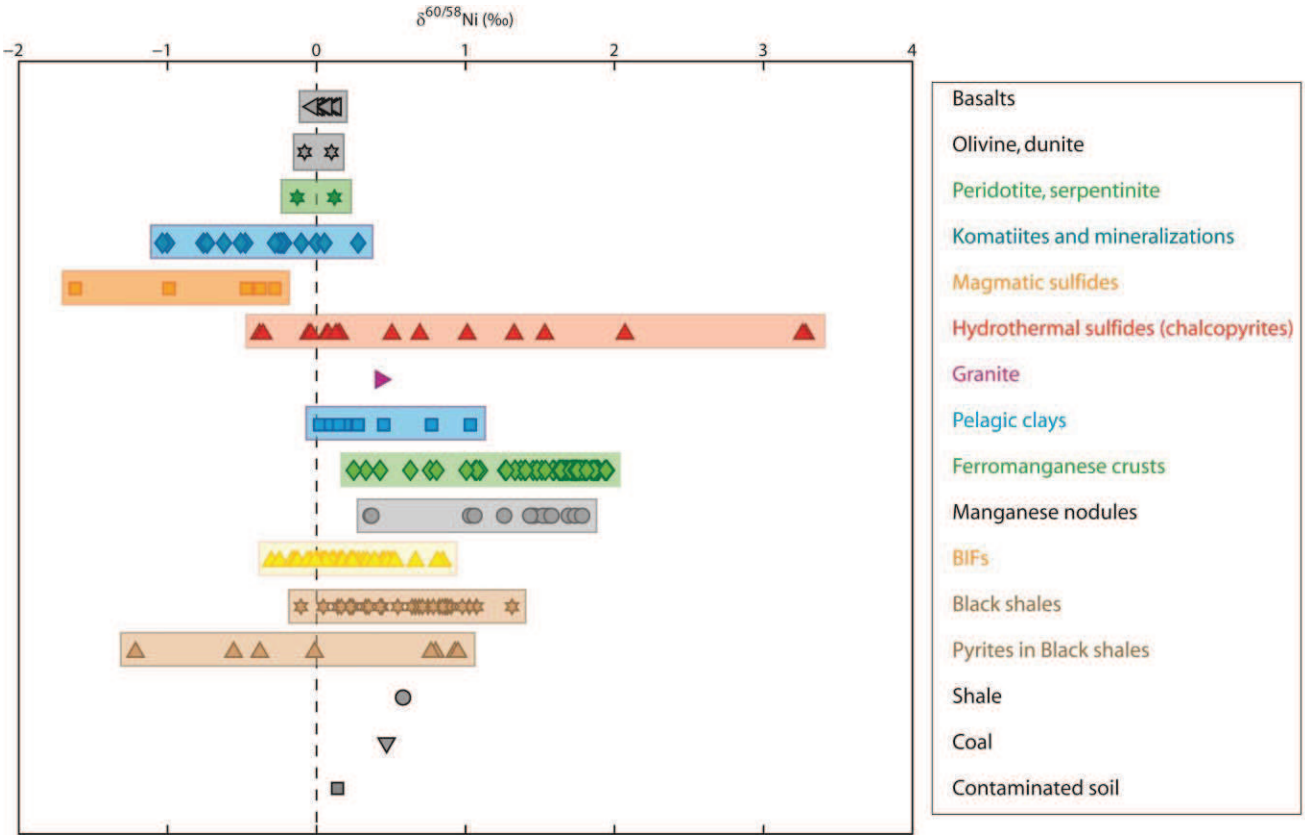

Figure F.1 *: Compilation of Ni isotope data (‰) measured in the course of this study showing the large variability of Ni isotope compositions in terrestrial rocks.*

1. Synthèse générale des principaux résultats obtenus et conclusion

1.1. Variations isotopiques du Ni dans les dépôts métallifères océaniques et les roches terrestres

1.1.1. Variabilité naturelle des compositions du Ni dans différents matériaux terrestres

Une partie de ce travail a consisté à développer la systématique isotopique du Ni. Les développements analytiques ont permis d'établir un protocole de séparation des isotopes du Ni adaptés à une large gamme de matrices géologiques différentes ainsi que des matrices d'eau de mer, et la méthode du double-spike pour l'analyse des compositions isotopiques en Ni est adaptée à un large ensemble de matrices géologiques.

Une fois les techniques analytiques mises au point, nous avons exploré la variabilité des compositions isotopiques du Ni dans différents matériaux terrestre et nous avons pu montrer qu'elle est significative et que les variations ont un lien avec le type de roche. Par exemple les sulfures magmatiques riches en Ni (donc formés lors de processus de haute température) sont systématiquement enrichis en isotopes légers jusqu'à moins de -1 ‰, tandis que les dépôts sédimentaires (donc formés à basse température) présentent majoritairement des enrichissements en isotopes lourds pouvant atteindre des valeurs jusqu'à +2 ‰.

En revanche, les compostions isotopiques de basaltes typiques de rides médio-océaniques (MORBs frais ou altérés) ainsi que les roches ultrabasiques telles que les dunites, péridotites ou serpentinites présentent une gamme restreinte des valeurs de $\delta^{60/58}$Ni autour de 0‰ suggérant que le réservoir terrestre silicaté global (ou Terre silicatée) a une composition isotopique proche de +0.05 ±0.05 ‰. Ces résultats sont en accord avec les études précédentes (Cameron et al., 2009; Gall et al., 2012) qui ont reportés les premières données isotopiques en Ni dans les roches terrestres. Par ailleurs, lors de la réalisation de ce travail d'autres résultats ont été générés sur des dépôts sédimentaires riches en matière organique (Porter, 2012) et sur des encroûtements hydrogénés (Gall et al., 2013).

1.1.2. Variabilité naturelle des compositions du Ni dans les dépôts métallifères océaniques des océans modernes et temps de résidence du Ni

Ensuite, nous nous sommes intéressés aux dépôts métallifères océaniques sensu-stricto et nous avons étudié les compositions isotopiques du Ni des encroûtements de Fe-Mn ainsi que des dépôts hydrothermaux riches en Mn afin de tester la variabilité isotopique du Ni dans l'eau de mer profonde et des sources potentielles en fonction des contextes géologiques, des localisations des bassins océaniques dans lesquels se sont formés ces dépôts. L'approche est en ce sens similaire à celles qui ont été mises en place lors des premières études sur les isotopes du Tl (Rehkämper et al., 2002) mais peu appliquées pour les isotopes du Fe, Cu et Zn dans les dépôts métallifères.

Les compositions isotopiques du Ni sur les encroûtements de notre étude ne montrent pas de variation systématique avec les positions géographiques des échantillons en lien avec les différentes masses d'eau des océans du globe, ce qui est cohérent avec les conclusions de Gall et al. (2013). Les variations observées dans ces encroûtements seraient plutôt associées à des paramètres tels que la distance des encroûtements par rapport à la base de la zone d'oxygène minimum. En revanche, Gall et al. (2013) ont montré à partir

d'une série temporelle dans un encroûtement de fer-manganèse que l'enregistrement des compositions isotopiques en Ni permettait de tracer l'apport hydrothermal aux océans et qu'on pourrait ainsi tracer les variabilités de cette source dans les océans profonds.

Outre les encroûtements de fer-manganèse nous avons élargi notre étude à l'analyse d'une sélection de dépôts d'oxydes de Fe-Mn hydrothermaux de manière à avoir une série d'échantillons formant un continuum d'un pôle hydrothermal à un pôle hydrogénétique. Ainsi, nous avons montré que la variabilité isotopique du Ni dans les dépôts métallifères océaniques est en fait liée aux mécanismes de formation, notamment leur taux de précipitation. Par exemple, les processus et/ou les apports hydrothermaux ont pour effet de d'augmenter la cinétique de formation des dépôts de Fe-Mn. Les dépôts hydrothermaux encore actifs échantillonnés à Loihi montrent que le Ni incorporé dans les phases minérales riches en Fe (et Mn) (et probablement les autres métaux traces) provient du fluide hydrothermal et que les variations isotopiques du Ni (de -1.49 à -0.69 ‰) sont le résultat de fractionnements isotopiques lors de l'adsorption sur les phases d'oxydes de Fe principalement. En revanche, les compositions isotopiques du Ni dans les dépôts hydrogénétiques de fer-manganèse, formés par précipitation des métaux dissous dans l'eau de mer, ne montrent pas de fractionnement isotopique par rapport à leur source océanique car ils se sont formés très lentement dans l'eau de mer. Ainsi le piégeage du Ni de l'eau de mer au niveau de la couche de surface des encroûtements en cours de formation s'est fait de manière quantitative et il n'y a pas de fractionnement isotopique exprimé.

Ces interprétations sont cohérentes avec les résultats des travaux expérimentaux sur les fractionnements isotopiques du Ni lors de son adsorption sur des oxyhydroxydes de Fe et de Mn menés en collaboration avec Brandy Toner et Jeffry Sorensen de l'Université du Minnesota aux Etats-Unis. L'adsorption du Ni sur les oxydes de Fe et de Mn produit systématiquement un enrichissement en isotopes légers de la phase minérale, la goethite étant plus fractionnée ($\Delta^{60/58}Ni_{min/sol}$ = ~-0.9 ‰) que la ferrihydrite ($\Delta^{60/58}Ni_{min/sol}$ = ~-0.4 ‰), alors que l'oxyde de Mn birnessite est la phase minérale montrant le plus fort facteur de fractionnement ($\Delta^{60/58}Ni_{min/sol}$ = ~-1.0 ‰).

Ainsi, non sans rejeter définitivement les conclusions établies par Gall et al. sur les effets d'un apport hydrothermal sur la variabilité isotopique du Ni dans les encroûtements hydrogénétiques, nos résultats indiquent que les effets minéralogiques et la cinétique de formation des dépôts peuvent à eux seuls expliquer les compositions isotopiques du Ni plutôt que des variations dans les sources. Il convient néanmoins de souligner que la contribution hydrothermale des dorsales médio-océaniques dans le cycle océanique du Ni est probablement négligeable, puisque seuls quelques environnements hydrothermaux spécifiques montrent des enrichissements en Ni dans les fluides. Il s'agit en particulier des sites hydrothermaux en contexte ultrabasiques des dorsales lentes, ainsi que certains volcans intra-plaques tel que Loihi (archipel d'Hawaii).

1.2. Stratigraphie haute résolution des encroûtements de fer-manganèse : étude spatio-temporelle des variations isotopiques du Ni dans l'Océan Pacifique

Les séries temporelles de la composition isotopique du Ni dans les encroûtements hydrogénétiques collectés sur le mont sous-marin Apuupuu (Hawaii) et dans l'archipel de Tahiti montre que la composition isotopique du Ni dissout dans l'eau de mer n'a quasiment pas varié sur la période des ~17 derniers millions d'années et était relativement homogène dans tout l'océan Pacifique. Les moyennes des compositions isotopiques des quatre encroûtements étudiés sont très proches, de +1.72 ±0.18 ‰ (2sd) et +1.87 ±0.10 ‰ pour les encroûtements du Pacifique Sud, tandis que les échantillons collectés dans le Pacifique Nord ont des compositions similaires de +1.64 ±0.18 ‰ et +1.79 ±0.13 ‰

Toutefois, il faut noter que l'un des deux encroûtements récoltés dans l'archipel de Tahiti montre des valeurs isotopiques en Ni particulièrement basses de +0.25 à +1.08 ‰ à la base de la croûte. Cette excursion isotopique n'a pas été enregistrée dans aucune autre série temporelle du Pacifique. Les analyses multi-élémentaires sur les différentes couches échantillonnées dans les encroûtements montrent une augmentation importante du rapport Ni/Mn et les analyses par microsonde électronique montrent que les phases minérales sont enrichies en Mn (et Ni, Cu, Zn et Co) mais appauvries en Fe (et Ti) dans cette partie de la croûte. Ces résultats suggèrent une précipitation importante d'oxydes de Mn incorporant Ni, Cu, Zn et Co au détriment de la précipitation d'oxydes de Fe auxquels est associé le Ti. Cet évènement très local aurait pu être provoqué par un apport, à la base de la croûte, d'eau de mer « hydrothermalisée » issue de l'infiltration dans les fractures du substrat basaltique sous-jacent. Cette hypothèse est cohérente avec les rapports en $^{10}Be/^{9}Be$ anormalement hauts qui auraient pu être apportés par l'eau de mer. Ainsi, la précipitation rapide de nouvelles phases de Mn expliqueraient les fractionnements isotopiques du Ni. Ces interprétations sont en accord avec les conclusions établies précédemment préconisant des fractionnements isotopiques du Ni importants lorsque la formation des phases minérales a une cinétique rapide.

1.3. Variations isotopiques du Fe, Cu, et Zn dans l'Océan Pacifique profond : une approche multi-proxys à travers l'analyse d'encroûtements de fer-manganèse

Alors que les isotopes du Ni seraient plutôt des traceurs des processus de formations et d'enrichissement des métaux dans les dépôts métallifères océaniques, les isotopes du Fe, Cu et Zn permettraient en revanche de tracer les sources de métaux aux océans.

Les facteurs contrôlant les variations isotopiques du Fe dans les océans modernes sont encore très débattus en particulier concernant l'influence de l'hydrothermalisme ou des variations des sources continentales atmosphériques. Ainsi, les analyses des compositions isotopiques en Fe et en Pb (dont les variations sont uniquement dues à des variations des sources des différentes masses d'eau) des séries temporelles des encroûtements de fer-manganèse du Pacifique Nord (Apuupuu, Hawaii) montrent d'excellentes corrélations entre ces deux systèmes isotopiques avec des variations en isotopes du Fe significatives de 0 à -0.7 ‰. Ces résultats suggèrent que les variations isotopiques en Fe soient dues à des mélanges de masse d'eau océanique ayant été affectées par des sources différentes. Même si cela reste encore incertain, il est possible que les valeurs isotopiques les plus négatives en Fe soient dues à un apport hydrothermal ou à des processus de dissolution des particules atmosphériques ayant affecté certaines masses d'eau profondes.

D'un autre côté, les compositions isotopiques en Cu et Zn dans les encroûtements du Pacifique Sud (Tahiti) montrent une augmentation significative des valeurs isotopiques au cours du temps, or ce résultat n'est pas observé dans les encroûtements d'Apuupuu (Pacifique Nord). Mais ce qui est très marquant dans les encroûtements de Tahiti est l'excellente corrélation positive entre les compositions isotopiques en Cu et Zn qui indiquerait un mélange entre différentes masses d'eau océaniques. Il est également intéressant de noter que les valeurs isotopiques des encroûtements de Apuupuu s'alignent sur cette tendance et forme le pôle supérieur; alors que le pôle inférieur est identique aux valeurs "crustales" ou hydrothermales des isotopes du Cu et Zn. Ces résultats, après confirmation par l'étude d'autres encroûtements, pourraient suggérer qu'un apport hydrothermal important ait affecté le Pacifique Sud Equatorial, en particulier avant 6 Ma. Ces résultats permettraient d'expliquer l'enrichissement unique en métaux des sédiments marins du Pacifique Sud sur plusieurs milliers de kilomètres, ce qui avait déjà été identifié dès la fin des années 60 (Boström et al., 1969).

1.4. Conclusion : processus biogéochimiques et formation des encroûtements hydrogénétiques

Plusieurs processus biogéochimiques participent à la formation des encroûtements de fer-manganèse hydrogénétiques qui vont directement influencer la géochimie de ces dépôts. Ainsi, nous avons montré que les compositions isotopiques des métaux permettaient de tracer certains de ces processus biogéochimiques. Ils sont résumés dans la Figure F.2 et présentés ci-dessous :

(1) Les isotopes du Ni sont un bon traceur de la formation des colloïdes dans la colonne d'eau aux processus de précipitation in-situ des encroûtements.

(2) La dynamique de l'OMZ influe directement sur l'efficacité de la formation des colloïdes de Mn et Fe. Alors que les isotopes du Ni semblent donc être le proxy le plus sensible au taux de croissance des encroûtements, les traceurs isotopiques sensibles aux conditions redox tels que le Fe et Cu semblent peu affectés.

(3) Les isotopes du Pb et Fe sont couplés notamment parce que ces deux éléments présentent des similitudes, ils sont associés dans les mêmes phases minérales et leur temps de résidence océanique sont courts. Cette approche permet non seulement de tracer la circulation océanique des différentes masses d'eau océanique profondes mais également de leurs modifications par des processus locaux.

(4) Alors que les isotopes du Cd dans les encroûtements pourraient permettre de tracer la productivité biologique de surface, les isotopes du Zn ne semblent pas affectés par les même processus.

(5) Les isotopes du Fe, Cu, Ni et du Zn seraient des traceurs des apports hydrothermaux dans la colonne d'eau, mais avec des caractéristiques différentes: les isotopes du Fe constituent un traceur local, alors que les isotopes du Zn et Cu semblent mieux tracer les processus hydrothermaux globaux. Quant au Ni, seules les sources *in-situ* riches en Ni peuvent produire des variations isotopiques du Ni.

(6) Les signatures isotopiques des apports continentaux par les rivières et les particules atmosphériques sont préservées pour les isotopes du Pb mais sont systématiquement fractionnées pour les isotopes du Cu, Ni, Zn et Fe dans une moindre mesure.

(7) Il convient maintenant d'utiliser une approche "muti-proxy" pour l'étude de la géochimie des encroûtements de fer-manganèse afin de distinguer les processus océaniques à différents échelles, ainsi que les processus d'halmyrolyse "in-situ". Cette approche est indispensable afin de définir ou valider les modèles de métallogénie d'enrichissement en éléments traces et "stratégique" tels que les terres rares, Co, Pt, Te qui font maintenant l'objet d'intérêts particuliers en vue d'exploitation minière.

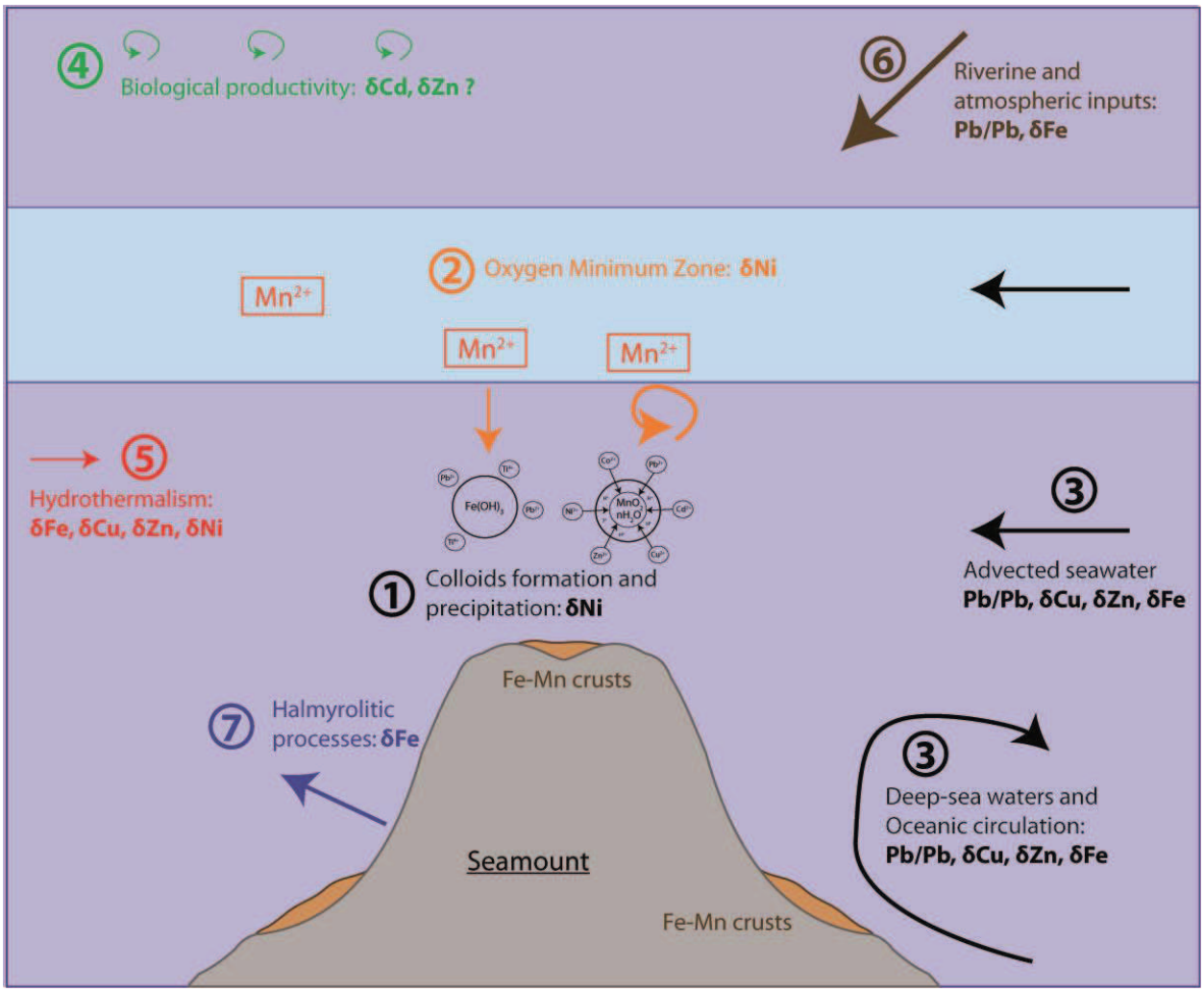

Figure F.2 : *Biogeochemical processes influencing the geochemical composition and metal enrichment of ferromanganese crusts. For each process potential useful isotopic tracers are mentioned.*

2. Des travaux préliminaires aux perspectives à court-terme

A travers cette étude nous avons souligné un fait important ; les séries temporelles des compositions isotopiques des métaux enregistrées dans les encroûtements de fer-manganèse - qui ne présentent a priori que peu de complexité dans les facteurs qui contrôlent leur mode de formation (enrichissement en métaux à partir de la précipitation des colloïdes de Fe et de Mn dissous dans l'eau de mer) - montrent des variations importantes dont les causes sont variées et complexes. Il est donc fondamental de bien comprendre

l'origine des variations isotopiques des métaux dans les dépôts modernes, là où les environnements de dépôts sont généralement mieux connus.

Dès lors, les perspectives qui émergent de ces travaux sont de s'intéresser à des dépôts plus complexes tels que les nodules polymétalliques, ou bien des dépôts anciens formés dans les océans précambriens où dans ce cas la fiabilité des proxys est plus incertaine car les facteurs qui influent sur ces proxys sont eux aussi moins bien établis.

2.1. Campagne océanographique BIONOD 2012 sur les zones à nodules polymétalliques de l'Océan Pacifique Central

La campagne océanographique BIONOD 2012 s'est déroulée en Avril-Mai 2012 dans l'Océan Pacifique équatorial sur les zones de permis minier français et allemand à bord du navire océanographique L'Atalante de l'Ifremer-Genavir. Ce projet a consisté à mener un projet collaboratif dédié à l'étude fine et détaillée des nodules polymétalliques. Le détail de ce projet, les problématiques et les objectifs sont présentés dans l'annexe 3 de ce manuscrit.

Depuis les années 1970 de nombreuses campagnes ont été réalisées sur cette zone notamment pour évaluer la ressource en métaux que pourrait constituer dans le futur les nodules polymétalliques. Néanmoins, il faut reconnaître qu'il y a finalement encore de fortes inconnues relatives à la formation de ces nodules, de la ou des source(s) de métaux, et des processus d'enrichissement. La France et l'Allemagne (parmi d'autres pays) disposent chacun d'un permis minier pour les nodules dans la zone Clarion/Clipperton de l'Océan Pacifique équatorial et cette campagne a été réalisée en collaboration avec une équipe française et une équipe allemande. Dans la zone française se trouve une petite zone nommée « NIXO 45 » dans laquelle de nombreuses campagnes océanographiques ont déjà eu lieu à la fois pour des échantillonnages de nodules et de sédiment mais également pour étudier la faune qui peuple ces plaines abyssales.

La zone NIXO 45 a donc déjà été bien caractérisée en termes de faciès de nodules, sédiments et de topographie des fonds lors des campagnes précédentes. Néanmoins aucune des campagnes n'a réalisé un échantillonnage intégrant nodules, sédiment et eaux interstitielles uniquement dédié à l'étude détaillée et approfondie des métaux de transition, leur enrichissement dans les nodules, et leur comportement géochimique dans les sédiments superficiels et les eaux interstitielles.

L'objectif de ce projet est donc d'effectuer une étude fine et approfondie des nodules polymétalliques et de leur environnement de dépôt en s'intéressant aux processus biogéochimiques qui ont lieu à l'échelle du nodule et des premiers centimètres de sédiment. Nous avons échantillonné à la fois les nodules, le sédiment sous-jacent (avec un échantillonnage haute résolution tous les centimètres le long de la carotte) et les eaux interstitielles associées aux sédiments prélevés. Nous avons également collecté par tamisage les micronodules présents dans les dix premiers centimètres de sédiment. De plus, grâce à la méthode expérimentale de pré-concentration des métaux traces dans l'eau de mer tels que Ni, Cu, Zn, Mo et les Terres Rares décrite dans ce manuscrit il est donc potentiellement possible de réaliser des analyses multi-isotopiques des métaux sur les eaux interstitielles. A terme, une étude incluant l'utilisation de plusieurs systèmes isotopiques des métaux permettrait de tester les hypothèses suivantes:

(1) mécanismes d'enrichissement des métaux dans les nodules

(2) influence des processus de diagenèse précoce dans le sédiment sur l'apport des métaux lors de la croissance des nodules.

(3) impact de la productivité biologique sur l'apport en métaux au sédiment.

(4) influence des sources de métaux aux océans au cours du temps sur la géochimie des nodules et leur croissance.

2.2. Variations isotopiques du Ni dans les dépôts marins Précambriens

Au cours de la dernière décennie de nombreux travaux sur les dépôts marins précambriens montrent que les isotopes des métaux sont très prometteurs pour étudier les environnements primitifs et l'évolution biogéochimique des océans anciens (Anbar and Rouxel, 2007). Ces problématiques concernent notamment l'étude des premières traces de vie et l'évolution de la biosphère primitive.

Ainsi, une des perspectives intéressantes qui a été initié au cours de ces travaux de thèse (en collaboration notamment avec Andrey Bekker de l'Université du Minnesota au Canada) est l'application des compositions isotopiques en Ni aux dépôts anciens tels que les formations ferrifères (BIFs) et les sédiments riches en matière organique que sont les schistes noirs ou « Black Shales ». L'hypothèse est d'utiliser cet outil isotopique comme traceur de l'utilisation du Ni par la biosphère précoce et la disponibilité du Ni dans les océans anciens et les liens que l'on pourrait établir avec l'évolution de la biosphère précambrienne et de la géochimie des océans de cette époque.

Des résultats prometteurs en déjà été obtenus sur les formations sédimentaires d'âges différents avec une large gamme de variations de -0.30 à +0.85 ‰ dans les échantillons paléoprotérozoïques, alors qu'une série d'échantillons néoprotérozoïques provenant d'une même séquence sédimentaire montrent une gamme de variations aussi large que +0.05 à +1.31 ‰. D'un autre côté, les schistes noirs montrent des valeurs positives de +0.05 à +1.31 ‰ alors que les fractions séparées de pyrite dans ces schistes montrent systématiquement des valeurs négatives jusqu'à -1 ‰ dans l'unité plus vieille que 2.5 Ga, et des valeurs positives jusqu'à +1 ‰ plus jeune que 2.5 Ga. Une partie de ces résultats sont présentés dans l'annexe 4 avec le poster qui a été présenté lors de l'AGU en décembre 2011 à San Francisco.

3. Références

Anbar, A. D., and Rouxel, O., 2007, Metal stable isotopes in paleoceanography: Annual Review of Earth and Planetary Sciences, v. 35, p. 717-746.

Boström, K., Peterson, M. N. A., Joensuu, O., and Fisher, D. E., 1969, Aluminum-poor ferromanganoan sediments on active oceanic ridges: Journal of Geophysical Research, v. 74, no. 12, p. 3261-3270.

Cameron, V., Vance, D., Archer, C., and House, C. H., 2009, A biomarker based on the stable isotopes of nickel: Proceedings of the National Academy of Sciences of the United States of America, v. 106, no. 27, p. 10944-10948.

Gall, L., Williams, H., Siebert, C., and Halliday, A., 2012, Determination of mass-dependent variations in nickel isotope compositions using double spiking and MC-ICPMS: Journal of Analytical Atomic Spectrometry, v. 27, no. 1, p. 137-145.

Gall, L., Williams, H. M., Siebert, C., Halliday, A. N., Herrington, R. J., and Hein, J. R., 2013, Nickel isotopic compositions of ferromanganese crusts and the constancy of deep ocean inputs and continental weathering effects over the Cenozoic: Earth and Planetary Science Letters, v. 375, no. 0, p. 148-155.

Porter, S. J., 2012, Nickel and osmium isotope and trace element geochemistry of organic-rich sedimentary rocks: the first investigation of Ni isotope systematics in marine sediments [Doctor of Philosophy: Durham University.

Rehkämper, M., Frank, M., Hein, J. R., Porcelli, D., Halliday, A., Ingri, J., and Liebetrau, V., 2002, Thallium isotope variations in seawater and hydrogenetic, diagenetic, and hydrothermal ferromanganese deposits: Earth and Planetary Science Letters, v. 197, no. 1-2, p. 65-81.

Annexe 1 : Article publié dans *Mineralium Deposita* : “Comparing orthomagmatic and hydrothermal mineralization models for komatiite-hosted nickel deposits in Zimbabwe using multiple-sulfur, iron, and nickel isotope data”

Appendix 1 : Article published in Mineralium Deposita : “Comparing orthomagmatic and hydrothermal mineralization models for komatiite-hosted nickel deposits in Zimbabwe using multiple-sulfur, iron, and nickel isotope data”

Comparing orthomagmatic and hydrothermal mineralization models for komatiite-hosted nickel deposits in Zimbabwe using multiple-sulfur, iron, and nickel isotope data

Axel Hofmann, Andrey Bekker, Paul Dirks, Bleuenn Gueguen, Doug Rumble & Olivier J. Rouxel

Mineralium Deposita
International Journal for Geology, Mineralogy and Geochemistry of Mineral Deposits

ISSN 0026-4598

Miner Deposita
DOI 10.1007/s00126-013-0476-1

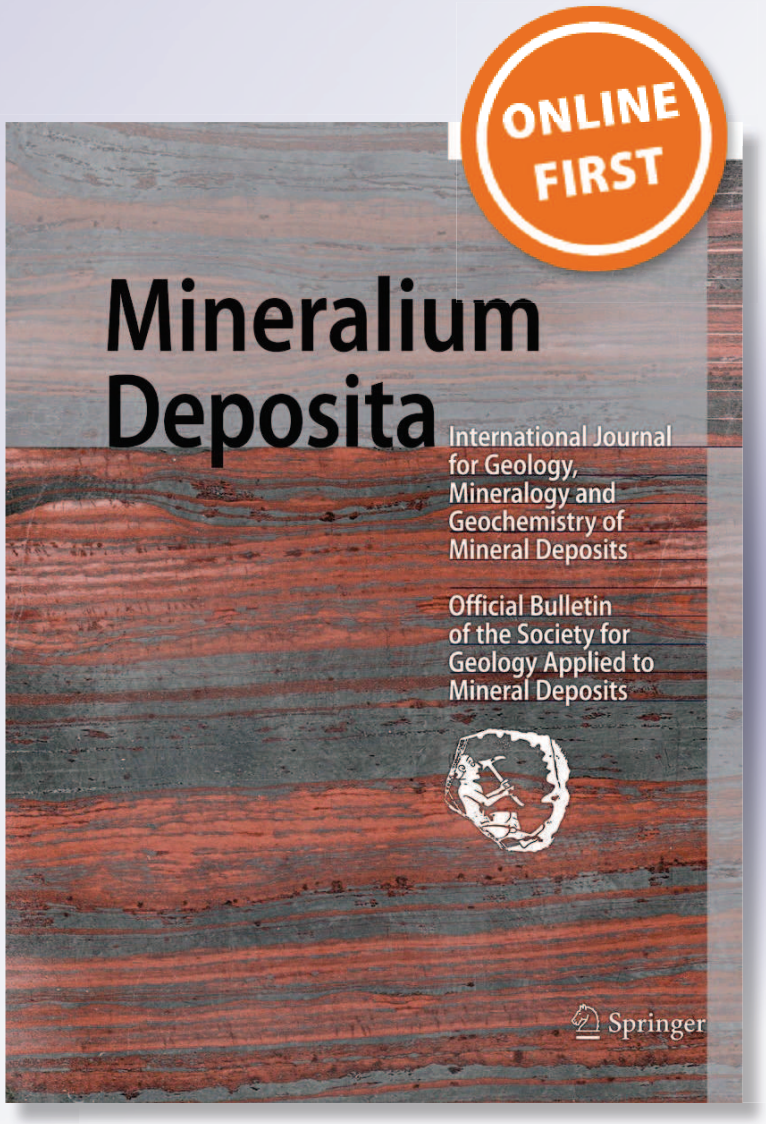

Springer

Miner Deposita
DOI 10.1007/s00126-013-0476-1

ARTICLE

Comparing orthomagmatic and hydrothermal mineralization models for komatiite-hosted nickel deposits in Zimbabwe using multiple-sulfur, iron, and nickel isotope data

Axel Hofmann · Andrey Bekker · Paul Dirks · Bleuenn Gueguen · Doug Rumble · Olivier J. Rouxel

Received: 13 August 2012 / Accepted: 12 June 2013

Abstract Trojan and Shangani mines are low-grade (<0.8 % Ni), komatiite-hosted nickel sulfide deposits associated with ca. 2.7 Ga volcano-sedimentary sequences of the Zimbabwe craton. At both mines, nickel sulfide mineralization is present in strongly deformed serpentinite bodies that are enveloped by a complex network of highly sheared, silicified, and sulfide-bearing metasedimentary rocks. Strong, polyphase structural–metamorphic–metasomatic overprints in both the Trojan and Shangani deposits make it difficult to ascertain if sulfide mineralization was derived from orthomagmatic or hydrothermal processes, or by a combination of both. Multiple S, Fe, and Ni isotope analyses were applied to test these competing models. Massive ores at Shangani Mine show mass-dependent fractionation of sulfur isotopes consistent with a mantle sulfur source, whereas S-isotope systematics of net-textured ore and disseminated ore in talcose serpentinite indicates mixing of magmatic and sedimentary sulfur sources, potentially via post-magmatic hydrothermal processes. A restricted range of strongly mass-independent $\Delta^{33}S$ values in ore samples from Trojan Mine likely reflects high-temperature assimilation of sulfur from supracrustal rocks and later superimposed low-temperature hydrothermal remobilization. Iron isotope values for most Ni-bearing sulfides show a narrow range suggesting that, in contrast to sulfur, nearly all of iron was derived from an igneous source. Negative Ni isotope values also agree with derivation of Ni from ultramafic melt and a significant high-temperature fractionation of Ni isotopes. Fe isotope values of some samples from Shangani Mine are more fractionated than expected to occur in high-temperature magmatic systems, further suggesting that hydrothermal processes were involved in either low-grade ore formation (liberation of Ni from olivine by sulfur-bearing hydrothermal fluids) or remobilization of existing sulfides potentially inducing secondary Ni-sulfide mineralization.

Keywords Komatiite-hosted nickel deposit · Zimbabwe craton · Archean · Sulfur isotopes · Iron isotopes · Nickel isotopes

Editorial handling: B. Lehmann

A. Hofmann (✉)
Department of Geology, University of Johannesburg, Auckland Park 2006, South Africa
e-mail: ahofmann@uj.ac.za

A. Bekker
Department of Geological Sciences, University of Manitoba, Winnipeg, MB R3T 2N2, Canada

A. Bekker · D. Rumble
Geophysical Laboratory, Carnegie Institution, Washington, DC 20015, USA

P. Dirks
School of Earth and Environmental Sciences, James Cook University, Townsville, QLD 4812, Australia

B. Gueguen
Technopôle Brest-Iroise, European Institute for Marine Studies, University of Brest, UEB, Place Nicolas Copernic, 29280 Plouzané, France

B. Gueguen · O. J. Rouxel
IFREMER, Centre de Brest, 29280 Plouzané, France

Published online: 28 June 2013

Introduction

Komatiite-hosted nickel sulfide deposits are common in Neoarchean greenstone belts of the Yilgarn craton of Western Australia, the Superior Province of North America, and the Zimbabwe craton in southern Africa as well as in Proterozoic greenstone belts of Canada (Naldrett 2004). The Kambalda area of Western Australia is regarded as the type locality for komatiite-hosted nickel sulfide deposits (Lesher

1989; Hronsky and Schodde 2006). Two main types of deposits have been recognized (Lesher 1989; Lesher and Keays 2002; Barnes 2006). Type 1 deposits occur near or along the base of ultramafic volcanic sequences and hypabyssal sills and are considered to result from the separation of an immiscible sulfide liquid from an ultramafic magma (Lesher and Keays 2002; Naldrett 2004; Arndt et al. 2005). Massive sulfides typically occur at the base of ultramafic bodies or within their footwall embayments. Massive ore is commonly overlain by net-textured (= matrix) ore with sulfides surrounding cumulate olivine and pyroxene. Matrix ore is in turn overlain by peridotite or dunite with disseminated sulfide (disseminated ore), which grades into unmineralized, locally spinifex-textured ultramafic rocks toward the stratigraphic top. Mineralization is regarded to have formed at the base of inflated lava flows representing feeder channels for large komatiite flow fields. Sulfides are concentrated at the base of the channels, characterized by cumulate-textured dunites that pass laterally into thin komatiite flow lobes with spinifex texture (Hill et al. 1995). Type 2 deposits are low-grade disseminations in the central part of cumulate-textured, lenticular dunite bodies. While sulfides may have been precipitated simultaneously with olivine to form interstitial ores (Barnes 2006), some of the Ni in finely disseminated sulfides may have been derived from subsolidus hydration processes under the influence of sulfur-bearing fluids (Eckstrand 1975; Grguric et al. 2006).

Most komatiite-hosted nickel deposits are interpreted to have been derived from sulfide-undersaturated magmas (Keays 1995; Naldrett 2004; Arndt et al. 2005). Sulfide saturation of the magma and the formation of an immiscible sulfide liquid trapping nickel, copper, and platinum-group elements are attributed to the addition of crust-derived sulfur. Sulfide-bearing carbonaceous sedimentary rocks, including shale and chert, sulfidized iron formation, and base-metal barren massive sulfides are commonly intercalated with komatiite flows in mineralized ultramafic sequences (Bavinton 1981; Hopwood 1981). The exact relation between nickel sulfide mineralization and the sedimentary horizons has not yet been conclusively resolved, but many authors have suggested that the sulfidic sediments provided the sulfur for the ultramafic magmas to reach sulfide saturation (Lesher 1989; Naldrett 1989; Lesher and Burnham 2001; Bekker et al. 2009). The most commonly inferred model for sulfur contamination of type 1 deposits is by thermal erosion and assimilation or devolatilization of the sulfidic sediments beneath ultramafic lava channels (Huppert et al. 1984; Groves et al. 1986; Naldrett 2004; Barnes 2006; Williams et al. 2011). In contrast, some authors argued that thermal erosion of the substrate by ultramafic lava flows is unlikely to occur (Rice and Moore 2001; Cas and Beresford 2001). In addition, sulfide-hosting troughs and embayments have been regarded as structural rather than primary footwall features (Cowden 1988; Cowden and Roberts 1990; Stone and Archibald 2004).

A further problem in unraveling the origin of komatiite-hosted nickel deposits is their presence in greenstone belts that experienced multiple episodes of deformation and metamorphism, generally interpreted to have affected already existing mineralization. However, many deposits consist of tabular or elongate ore bodies that are parallel to regional, penetrative linear fabrics, including fold axes, and mineral lineations, which formed during the peak of a dynamic regional metamorphic event at upper greenschist to upper amphibolite facies (e.g., Viljoen et al. 1976; Barrett et al. 1977; Gresham and Loftus-Hills 1981; Lesher 1989; Stone and Archibald 2004). It is unlikely that in all these cases, deformation was focused along pre-existing primary magmatic linear trends. The co-linearity of ore bodies with regional structural trends (cf. Gresham and Loftus-Hills 1981; Naldrett 1981) strongly suggests considerable ore redistribution and, possibly, ore generation in response to dynamic metamorphic and metasomatic processes.

In Zimbabwe (Fig. 1), general aspects of the stratigraphy, ore composition, and geochemistry of nickel sulfide deposits are known (e.g., Shangani Mine, Viljoen et al. 1976; Trojan Mine, Chimimba and Ncube 1986; Epoch Mine, Baglow 1986; Hunters Road Deposit, Moubray et al. 1979, Prendergast 2001; Damba Deposit, Williams 1979, Killick 1986), but a detailed description and interpretation of structures and metamorphic textures formed by regional deformation events is mostly lacking. As a result, all deposits have been interpreted as orthomagmatic (Prendergast 2003), i.e., the Ni-bearing sulfides crystallized from a melt and did not form during sub-solidus processes. However, every nickel deposit in Zimbabwean greenstone belts is centered on structural discontinuities, such as faults or fold hinges, and an evaluation of the structural and metamorphic imprints on these deposits must be made to fully appreciate what role deformation and metamorphism may have played in affecting these low-grade deposits. Furthermore, it has been shown that many of the sulfidic sedimentary horizons that are associated with mineralized ultramafic volcanics have been intensely sheared (Hofmann et al. 2003), possibly resulting in the redistribution of primary sedimentary to diagenetic sulfides and potentially inducing secondary sulfide mineralization. The spatial association of sulfide-bearing high-strain zones with nickel sulfide mineralization in komatiites may thus point to a secondary, hydrothermal origin or redistribution/enrichment of at least some of the Ni mineralization. Cases of this type of mineralization are known to exist elsewhere (type 4, Barnes 2006).

In this paper, we present field and petrographic observations from the Trojan and Shangani Ni mines in Zimbabwe in combination with trace element geochemistry and multiple sulfur, nickel, and iron isotope data. We critically evaluate mineralization style and test if multiple S, Ni, and Fe isotope data can provide constraints on the relative importance of

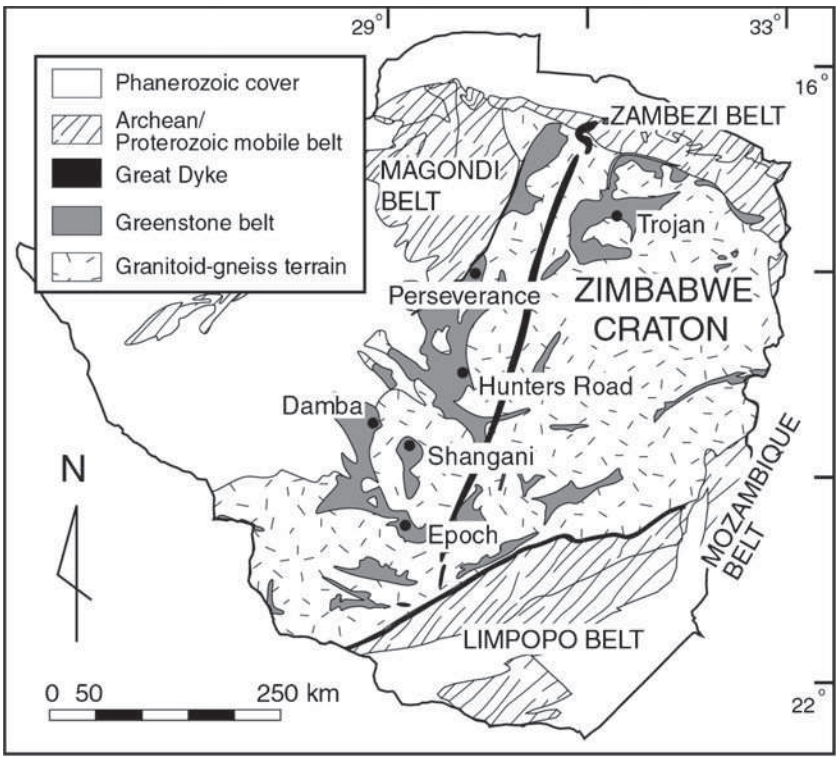

Fig. 1 Geological map of the Zimbabwe craton showing major nickel deposits

orthomagmatic vs. hydrothermal processes in the generation of komatiite-hosted Ni sulfide mineralization. The study is focused on Trojan Mine, but multiple S, Ni, and Fe isotope data are also presented for the Shangani Mine nickel deposit.

Geology of the Shangani Mine and Ni sulfide mineralization

Shangani Mine (Fig. 1) is situated in the Shangani Mineralized Complex of the Shangani greenstone belt (Harrison 1969) and is associated with the Shangani Layered Ultramafic Complex that intruded into greenstone units assigned to the Lower Bulawayan Group (Fig. 2; Wilson et al. 1995). It is a low-grade type 2 deposit with some occurrences of type 1 massive sulfides. Production at the mine in 2002 was 0.93 Mt/year of ore at an average grade of 0.48 % nickel (C. Makuni, personal communication, 2003). The Shangani Mineralized Complex is intrusive into the Esmyangene Formation, a succession of felsic tuffaceous sedimentary rocks and agglomerates that is capped by sulfidic carbonaceous shale (Viljoen et al. 1976; Viljoen and Bernasconi 1979). It consists of two lobes on both sides of a central stem (Fig. 2b) resulting in a mushroom-shaped body in cross section that was interpreted by Viljoen et al. (1976) as a lopolith. Dirks and Sithole (1996) reported a more complex geometry resulting from deformation (Fig. 2c). Their mapping has shown that the ultramafic lobes occur as folded lensoidal bodies within a complex network of highly sheared sedimentary rocks that include carbonaceous and sulfidic cherts, and carbonaceous shale with mylonitic texture. Prendergast (2003) argued for an extrusive origin for the Shangani Mineralized Complex, possibly related to the observation of apparent spinifex texture in a pyroxenite-gabbro layer, features not considered by Viljoen et al. (1976) to represent a true quench texture.

The east and west lobes of the Shangani Mineralized Complex correspond to the Main and Far West ore bodies, respectively. The massive sulfide bodies, which are much better developed in the eastern lobe, generally occur at the assumed stratigraphic base of both lobes, consistent with a magmatic control of mineralization (Viljoen et al. 1976). In contrast, Dirks and Sithole (1996)) noted a structural control over the ore bodies since they are highly linear and are parallel to a mineral lineation developed in sheared sedimentary rocks as well as fold axes of several generations of colinear folds.

Sedimentary rocks of the Esmyangene Formation constitute the footwall to the Main and Far West ore bodies and consist of siliceous felsic tuff locally interleaved with carbonaceous shale with abundant pyrite and pyrrhotite. Lenses of layered siliceous tuff and carbonaceous shale occur both along the footwall and hanging wall contacts and within the ultramafic rocks along shear zones (Fig. 2c). Sulfide mineralization is developed within the tuff, especially where it underlies Ni sulfide mineralization in ultramafic rocks. Sulfide grains in tuff display an orientation parallel to the compositional layering.

The mineralized complex consists of massive green and talcose serpentinites and carbonated talc schist. These rocks

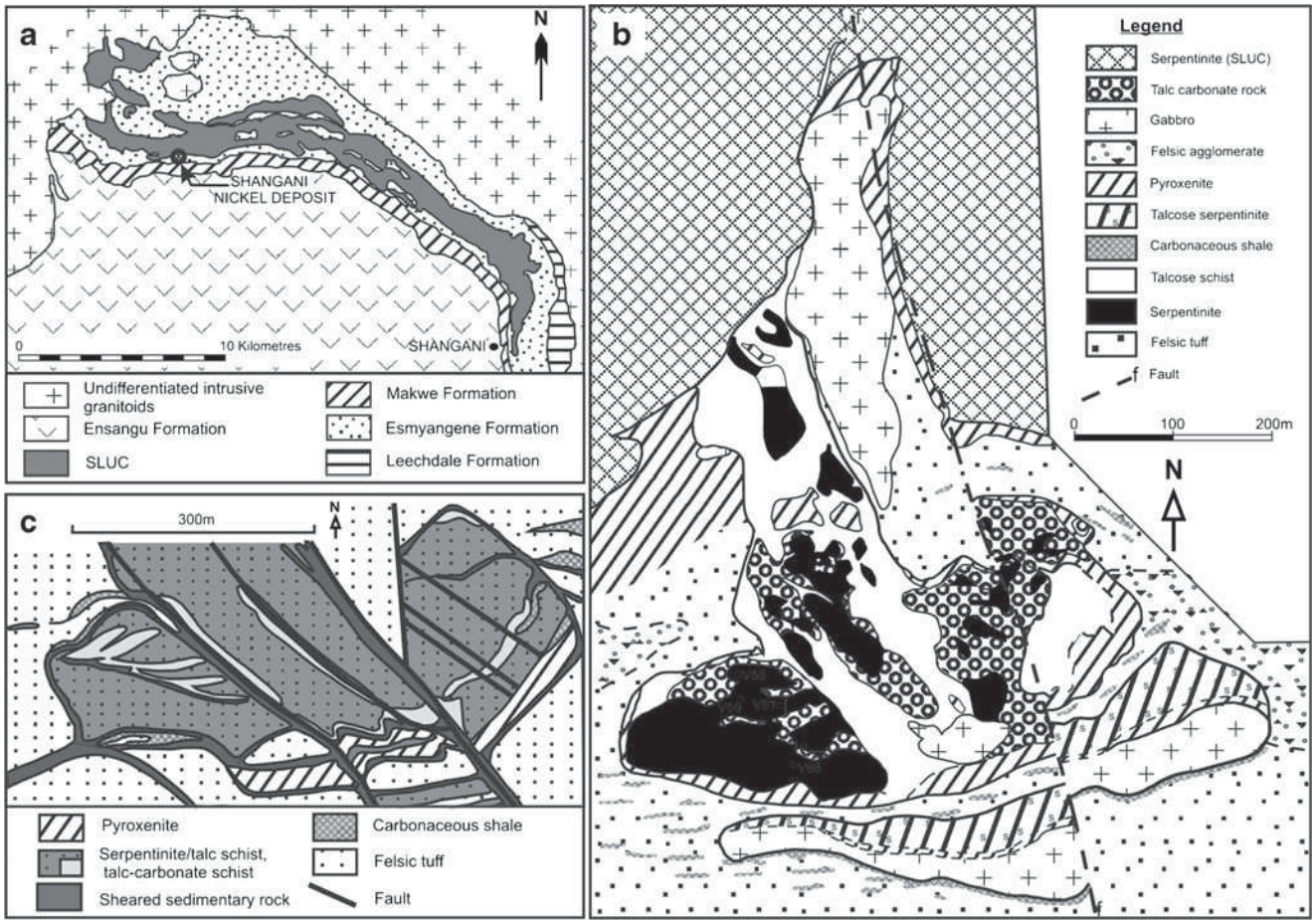

Fig. 2 **a** Regional geological setting of the Shangani nickel deposit (after Viljoen and Bernasconi 1979). **b** Detailed geology of the Shangani Mineralized Complex (after Viljoen and Bernasconi 1979). **c** Detailed geological map of the southern portion of the Shangani Mineralized Complex (after Dirks and Sithole 1996), showing a much more complex geometry for the lobes and stem. *SLUC* Shangani Layered Ultramafic Complex

are enveloped and interleaved with black shale, chloritic siliceous tuff, and chlorite–actinolite schist. Massive green serpentinite occurs throughout the mineralized complex and commonly contains disseminated pyrrhotite and pentlandite, which occur as blebs and trails along the margins of serpentinite patches resembling cumulate textures. The sulfides are intergrown with serpentine and subhedral grains of magnetite. Much of the sulfide is, however, within carbonate-filled fractures, which also contain abundant magnetite. Talcose serpentinite is more abundant in the eastern lobe of the complex and occurs along shear zones dissecting the massive green serpentinite. Mineralization occurs as either disseminated sulfide or several centimeter-wide massive sulfide veins. Coarse-grained, carbonated talc schists are associated with the talcose serpentinite and form the most common rock type within the eastern lobe and the stem of the Shangani Mineralized Complex. Disseminated sulfide is rare in carbonated talc schist; instead, sulfides occur either as schlieren parallel to foliation or within veins. Sulfide-bearing carbonate veins are common within the rock. The association of sulfides with secondary carbonates indicates sulfide mineralization during carbonatization of the ultramafic rocks, a feature common to low-grade type 2 deposits (Grguric et al. 2006).

Geological setting of Trojan Mine

Trojan Mine is the largest nickel producer in Zimbabwe. Mining of this type 1 deposit started in 1968, and production in 2002 was 1.03 Mt/year of ore at an average grade of 0.62 % nickel (C. Makuni, personal communication, 2003). The Trojan nickel deposit is hosted by the Upper Bulawayan Group metavolcanic rocks within the southern flank of the Bindura–Shamva greenstone belt (Fig. 3a). The basal unit of the greenstone succession overlies the Chinamora granitoid gneiss dome along a tectonic contact and is represented by the 2715±15-Ma Iron Mask Formation (Jelsma et al. 1996), a sequence of calc-alkaline rhyodacitic volcanic and volcaniclastic rocks that are intercalated with lenses of banded iron formation, chert, conglomerate, and basalt. The overlying Arcturus Formation hosts

the Trojan nickel deposit and is a sequence of pillowed and massive tholeiitic basalt, komatiitic basalt, ultramafic schist, and serpentinite. The volcanic rocks are intercalated with thin horizons of banded iron formation, chert, slate, sandstone, and marble. The Arcturus Formation is overlain by siliciclastic metasedimentary rocks of the Shamvaian Supergroup (Hofmann et al. 2002).

Ultramafic rocks that host the nickel mineralization at Trojan Mine (Fig. 3b) have been interpreted as extrusive komatiitic flows in a consistently N-younging volcano-sedimentary sequence (Chimimba 1984; Chimimba and Ncube 1986; Baglow 1992). Gravity settling within the flows has been described as the dominant means of nickel sulfide concentration with minor remobilization along later shear zones, resulting in localized veins of massive sulfides (Chimimba 1984; Chimimba and Ncube 1986; Maiden et al. 1986).

Geology and Ni sulfide mineralization at Trojan Mine

Lithological units and structural–metamorphic history

The lithological units around Trojan Mine form discontinuous blocks with sheared, discordant contacts and sigmoidal outcrop pattern (Fig. 3; Dirks and Jelsma 1998; Jelsma and Dirks 2000). Table 1 summarizes lithological, mineralogical, and structural features of the rock units. The mineralization is generally associated with cumulate-textured peridotitic to dunitic rocks, altered to serpentinite, that occur as a horizon of partly overlapping lensoidal bodies within a metabasalt sequence (Table 1; Fig. 3b). Near the mine site at Cardiff Hill, several stacked serpentinite lenses are tectonically intercalated with metasedimentary units (Fig. 4a). Serpentinite is variably carbonated and silicified. The ultramafic rocks are strongly schistose near lithological contacts and within the mineralized zones, but massive, coarse-grained, and cumulate-textured in the center of ultramafic lenses. They have been considered as extrusive flows (Chimimba and Ncube 1986), and their volcanic origin is supported by the intimate association with metabasalts. However, an intrusive origin as shallow-level sills cannot be discounted.

Layers and lenses composed of a variety of silicified and sulfide-bearing, highly deformed metasedimentary rocks (Table 1) are intercalated with the volcanic rocks. Silicified carbonaceous schist and black chert are confined to the immediate vicinity of ultramafic units (Fig. 4b). The rocks become less silicic both vertically and laterally away from the ultramafic rocks. A vein network of sulfides (mostly pyrrhotite) is common in silicified metasedimentary rocks.

A detailed description of the structural and metamorphic history of the Trojan Mine area was presented in Dirks and Jelsma (1998) and Jelsma and Dirks (2000). These authors differentiated three major events that affected the greenstone succession. D_1 resulted in a pervasive schistosity (S_1) that trends between 040° and 100° and is steeply dipping toward the NW (Fig. 5a). The intensity of S_1 is the greatest along an anastomosing network of 1–30-m-wide shear zones hosted by silicified metasedimentary rocks (Fig. 3b). D_1 shear zones preserve mylonitic features and are associated with a shallowly SW-plunging mineral lineation (L_1, Fig. 5b). D_1 was associated with a metamorphic event (M_1) at lower amphibolite facies metamorphic grade, with a temperature of ~500 °C and a pressure of 3–4 kbar (Dirks and Jelsma 1998).

D_2 gave rise to a second foliation (S_2) related to the solid-state emplacement of the Chinamora granite gneiss dome south of the mine area (Fig. 2a). S_2 is a shallow to moderate N-dipping, penetrative schistosity and contains a NE-plunging mineral lineation (L_2, Fig. 5b). Metamorphism (M_2) reached a grade of 565 °C and 3.5 kbar at Trojan Mine (Dirks and Jelsma 1998). Brittle strike-slip faulting during D_3 reactivated D_1 shear zones. Faulting was accompanied by the brecciation of competent units and the infiltration of sulfide and quartz carbonate veins.

Structural setting of the ore bodies and mineralization patterns

All nickel ores at Trojan Mine consist of pyrrhotite and pentlandite with lesser amounts of chalcopyrite, pyrite, and, locally, millerite. Disseminated ore (cutoff <0.4 % Ni, average 0.6 % Ni) is pervasive and makes up ~95 % of the reserves. The remaining 5 % of the reserves are composed of matrix or net-textured ore (30–40 % sulfides, 4 % Ni) and massive ore (60–90 % sulfides, 10 % Ni). The average Ni/Cu ratio is ~15 (Chimimba 1984), similar to that in other komatiite-hosted nickel sulfide deposits (Naldrett 2004).

Ore is concentrated in a number of ultramafic bodies separated by sheared sedimentary units. Ore bodies currently mined include the Main and Hanging Wall ore bodies (Figs. 3b, 6, and 7). The ore bodies as well as the lenses of ultramafic host rock are elongated. Constructed from mine plans, the average orientations of the long axes of Main, Hanging Wall, and Cardiff South ore bodies parallel one another in a general direction of 320/70 (Fig. 5c), which is nearly identical to the intersection lineation between the anastomosing S_1 orientations and the primary layering S_0 in the area (Fig. 5d). In plain view, the Main ore body (MOB) extends about 100–150 m along strike with a maximum width of 60–100 m. It is situated along two anastomosing shear zone branches that outline a broad synformal feature (Fig. 7), which has previously been interpreted as a footwall embayment (Chimimba 1987). This shear zone is not a simple planar feature, but consists of a 20–50-m-wide zone of anastomosing branches that envelop lenses of metabasalt, chert, metasediment, and feldspathic schist.

The Hanging Wall ore body is more irregular and has a strike length of about 200 m (Figs. 6 and 7). It is underlain and separated from the Main ore body by a 20–60-m-wide shear zone (Fig. 7) in which lenses of spinifex-textured komatiitic metabasalt, feldspathic schist, and metagabbro are present. In places, the shear zones are entirely situated within the ultramafic rocks and consist of talc-carbonate schist with high proportions of magnetite and thin quartz veinlets. Small lenses (<2 m long) of footwall schist are locally present within the shear zones.

Massive ore occurs near the base of the Main, Hanging Wall, and Cardiff South ore bodies. Matrix ore is present as shoots in the Main and Hanging Wall ore bodies. The contacts between massive, matrix, and disseminated ores are sharp and parallel to the foliation. With the exception of the Footwall 2 ore body, massive and matrix ores are generally restricted to the stratigraphically lower parts of the ultramafic host rock and occur in direct contact with a strongly silicified metasedimentary unit resembling chert. In the Hanging Wall ore body, massive ore is only present in the extreme west where it overlies silicified sedimentary rock. Massive ore is absent in places where the sedimentary horizon pinches out (Figs. 6 and 7).

Chimimba and Ncube (1986) reported that the nickel content of disseminated ores gradually decreases from the stratigraphic base to the top of the ultramafic host rocks. However, this is an idealized view as, in general, the Ni-content drops off sharply away from the basal massive and matrix ores. In detail, Ni and MgO concentrations vary greatly across ultramafic lenses and change sharply across shear zones.

Ore environment

Massive ore is represented by banded to massive sulfide intervals conformable with the principal tectonic fabric and in places transgressing primary igneous layering (Fig. 7a). Lenses of massive ore contain significant proportions (up to 40 %) of footwall metasedimentary lithologies, carbonate, and vein quartz fragments, but no ultramafic host rock fragments. Many footwall rock fragments, including vein quartz, are well-rounded and enveloped by foliated sulfide similar to "durchbewegung" structures (Marshall and Gilligan 1989) indicative of non-coaxial flow. In places, deformed footwall rock fragments with D_1 and D_2 fabric elements become so abundant that massive ore is more aptly described as breccia ore. The margins of both massive and breccia ore shoots typically contain sulfide veins that extend into the adjacent footwall lithologies. These veins are commonly developed along D_3 shear zones.

Massive sulfide ore consists of pyrrhotite with minor chalcopyrite, pyrite, and chromite. Pentlandite occurs as grains and exsolution lamellae in pyrrhotite or as small grains along the boundaries of larger pyrrhotite crystals. Pentlandite grain aggregates are common and are elongated parallel to S_1 and the contact with the wall rock. The proportion of chalcopyrite is the highest in the contact zone with the footwall rock and along the margins of wall rock fragments. The chalcopyrite content also increases in injection veins.

Matrix ore consists of densely disseminated sulfide in an ultramafic host. Pyrrhotite and pentlandite, which are the main sulfide phases, form aggregates that are commonly banded parallel to S_1. Chalcopyrite occurs in the matrix as small aggregates elongated parallel to S_1. Pyrite occurs as subhedral grains. Magnetite, chromite, and carbonate are accessory minerals.

Both the massive and matrix ores are foliated. The foliation is defined by preferred orientation of silicate fragments in the sulfide matrix and silicate inclusions within pyrrhotite grains, orientation of pentlandite bands, shape of matrix pyrrhotite grains, and cleavage orientation in matrix pyrrhotite and pentlandite grains. Matrix pyrrhotite is generally granoblastic due to post-kinematic recrystallization.

Disseminated sulfides are intergrown with metamorphic alteration products and are present in talc-carbonate schist, talc-antigorite schist, and massive serpentinite. They frequently occur as elongated matrix grains or grain aggregates oriented parallel to S_1.

Ore texture

Silicate–sulfide textures and mineralogy in the ore bodies at Trojan Mine generally reflect post-magmatic alteration, mobilization, and recrystallization processes. Most sulfides in the metasedimentary schist do not show features consistent with a primary origin. They commonly form veins parallel to and cutting across foliation planes and occur in pressure shadows of metamorphic minerals or in association with ribbon quartz and quartz veins (Fig. 8). Primary sulfides in the form of nodules in metasedimentary rocks are rare and form a minor part of total sulfide budget at best. The secondary, cross-cutting nature of the sulfides in the metasedimentary rocks is a common feature on the mine scale, as indicated by orientation of massive sulfide veins with respect to foliation and stratification of the footwall rocks (Fig. 7).

Sulfide grains in the ultramafic rocks show a variety of textures, but unequivocal evidence for unrecrystallized, primary, magmatic sulfide has not been observed. Intergrowth of sulfides with serpentine, talc, tremolite, and chlorite in serpentinized ultramafic rocks is common (Fig. 9a). Some

Fig. 3 **a** Geological map of the southern part of the Bindura–Shamva greenstone belt, showing the main lithologies and the orientation of L_1 and L_2 lineations. Map is modified from Baglow (1992). **b** Map of the area around Trojan Mine (modified from Dirks and Jelsma 1998) and cross section through Cardiff Hill. *MOB* Main ore body, *HWOB* Hanging Wall ore body, *CSOB* Cardiff South ore body, *CEOB* Cardiff East ore body, *FW2OB* Footwall no. 2 ore body, *CWOB* Cardiff West ore body, *CFWOB* Cardiff Far West ore body

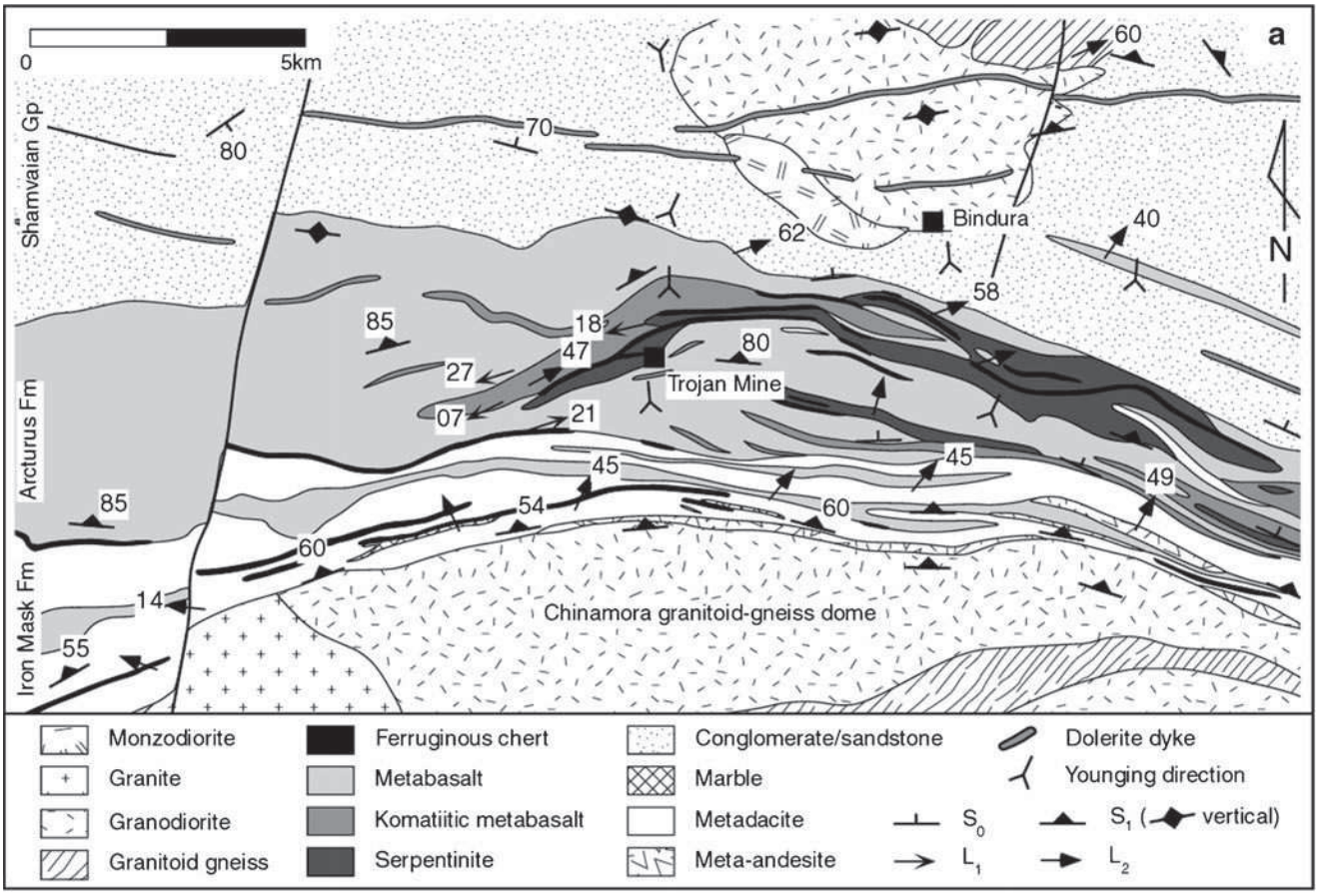

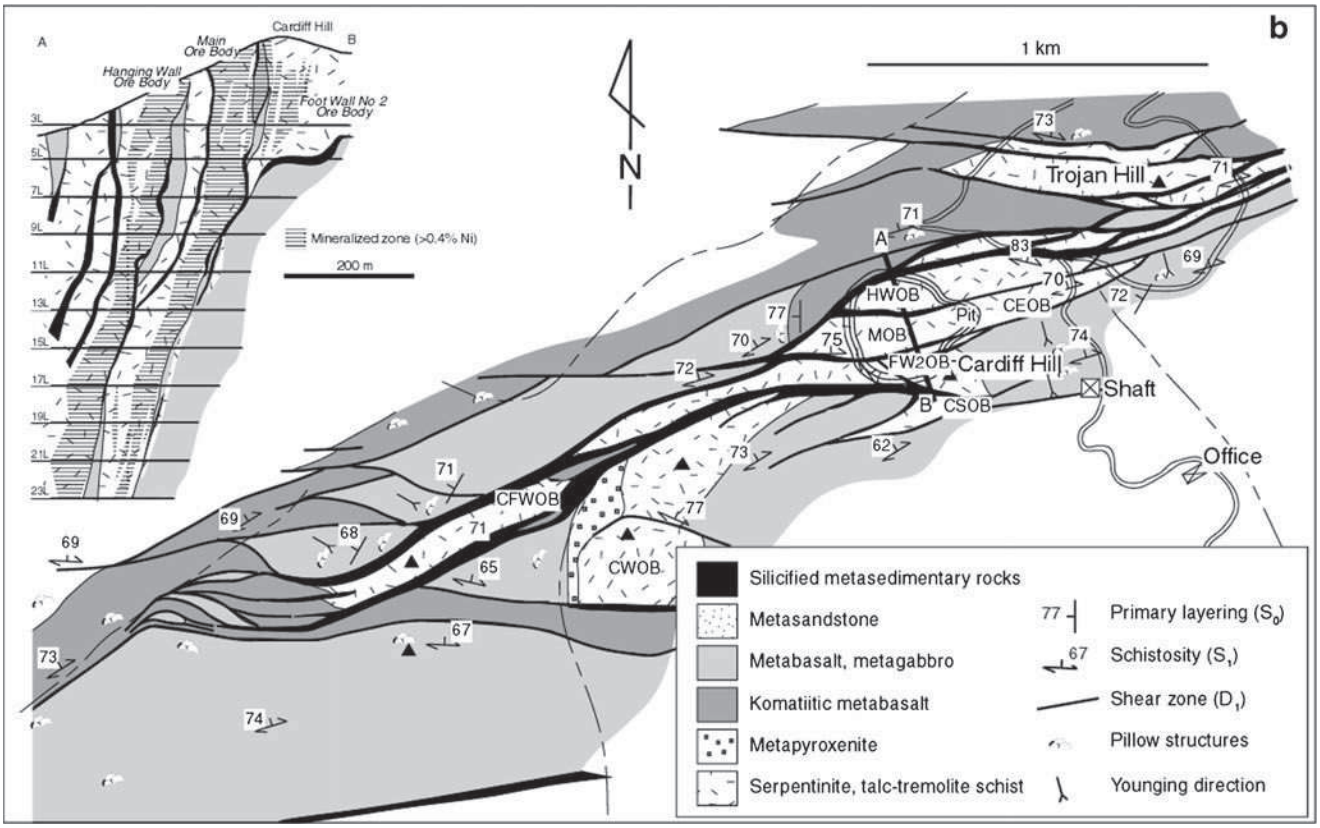

Table 1 Lithological description, mineralogy, and structural features of the geological units around Trojan Mine

Lithology	Description	Mineralogy	Structure
Tholeiitic metabasalt	Pillowed to massive basalt. Pillows (mostly c. 0.5 m in diameter) contain carbonate–quartz–filled vesicles	Poorly oriented amphibole needles in an aphanitic groundmass of plagioclase, chlorite, and biotite with minor opaques and secondary quartz and carbonate; interpillow domains contain coarse-grained plagioclase, quartz, and carbonate with minor chlorite and amphibole	Massive to foliated. Pillows are elongated (typical width-to-length ratio = 1:3) within the foliation plane; elongation is the highest along lithological contacts
Metagabbro	Massive, homogeneous, coarse-grained rock	Pyroxene is replaced by green hornblende embedded in a dark-gray aphanitic matrix of plagioclase with minor chlorite, actinolite and quartz	Interstratified with metabasalt; undeformed
Komatiitic metabasalt	Pillowed (<0.5 m in diameter) to massive rock with local spinifex textures. The rock is locally deformed to talc-chlorite schist	Massive rock consists of poorly oriented tremolite–actinolite needles, talc, chlorite, variable amounts of magnetite, and secondary carbonate and quartz. Schistose varieties have high talc content. Spinifex texture is defined by 2–10-cm-long needles of pyroxene replaced by tremolite	Undeformed to strongly schistose. Stretched pillows have a maximum width-to-length ratio of 1:3. Schistose zones are common along lithological contacts, but also occur at an angle to stratification
Ultramafic rock	Serpentinite with locally preserved cumulate texture; pyroxenite occurs at the top of some ultramafic bodies; the primary grain size is mostly less than 3 mm	Massive serpentinite is composed of antigorite and talc with minor metamorphic olivine, tremolite, chromite and carbonate. Schist consists of talc, magnesite, and antigorite, with minor chlorite, tremolite, magnetite, and chromite. Quartz is locally common along fine fractures in magnetite-rich zones. Cumulate-textured rock consists of closely packed antigorite rimmed by magnetite in a talcose matrix. Pyroxene in metapyroxenite is replaced by amphibole with minor chlorite and talc	Massive to strongly schistose
Silicified meta-sedimentary rocks	Various metasedimentary schists	Graphitic schist (chlorite, sericite, graphite, quartz, biotite), chlorite–sericite–quartz–feldspar schist, biotite–tremolite/actinolite–quartz–feldspar schist, rare lenses of biotite–muscovite–cordierite–quartz schist	Strongly schistose anastomosing horizons exhibiting foliation truncations, S–C fabrics and intense disharmonic folding
	Metasandstone intercalated with metasedimentary schist	Quartz augen (rare sericitized feldspar augen) set in a matrix of quartz, plagioclase, and biotite. Biotite foliation is overgrown by unoriented, radiating aggregates of hornblende and up to 1 cm large, anhedral garnet	
	Black metachert and carbonaceous schist associated with ultramafic rock. Chert is well-layered to massive	Metachert consists of quartz with variable amounts of graphite, chlorite, sericite, and carbonate. Carbonaceous schist is composed of quartz with variable amounts of aligned hornblende and biotite	
	Metaconglomerate lenses (rare)	Equal proportions of elongate, hornblende-bearing basaltic and quartz–feldspathic fragments embedded in a schistose, chlorite–carbonate-rich matrix	
Feldspathic schist	Lensoidal bodies of schist associated with metasedimentary rocks	Medium-grained (<3 mm) hornblende intergrown with plagioclase with minor matrix quartz, biotite, and secondary carbonate. Two generations of hornblende occur; an early one parallel to the regional foliation and a later unoriented one	Schistose horizons parallel to the regional foliation

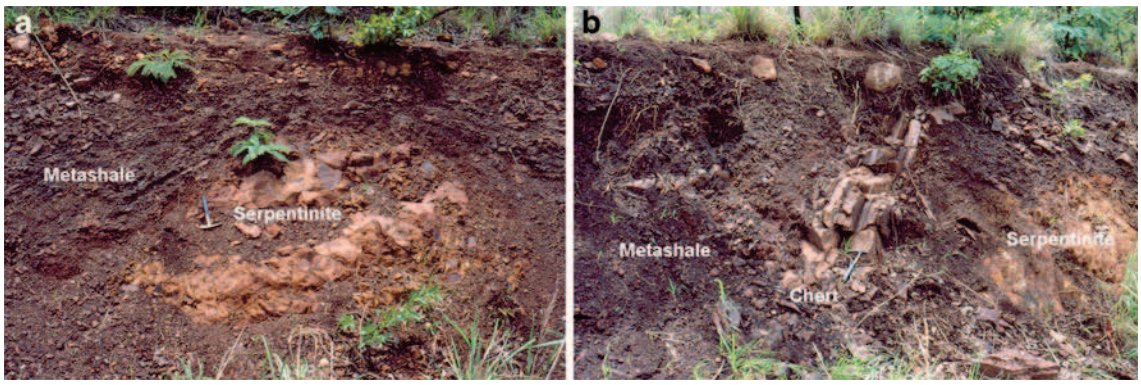

Fig. 4 **a** Boudin of serpentinized ultramafic rock within sheared and sulfide-impregnated carbonaceous metashale. **b** Contact between sheared carbonaceous metashale (*left*) and serpentinite (*right*). A thin unit of carbonaceous metachert is present along the contact (*center*)

sulfide aggregates in serpentinized dunite occur as cross-cutting veins that were apparently formed both before and after the serpentinization process (Fig. 9b, c). Sulfides that formed prior to the alteration could represent remobilized primary magmatic sulfides. Metadunites with relict cumulate texture are common toward the core of the disseminated ore bodies (Fig. 7). Magnetite frequently rims olivine, now replaced by serpentine and talc or talc and carbonate, and is commonly intergrown with pyrrhotite and pentlandite. Sulfide-bearing reaction rims along margins of olivine crystals suggest sulfide formation during metamorphic processes (Fig. 9d, e). Sulfide globules are commonly aligned along

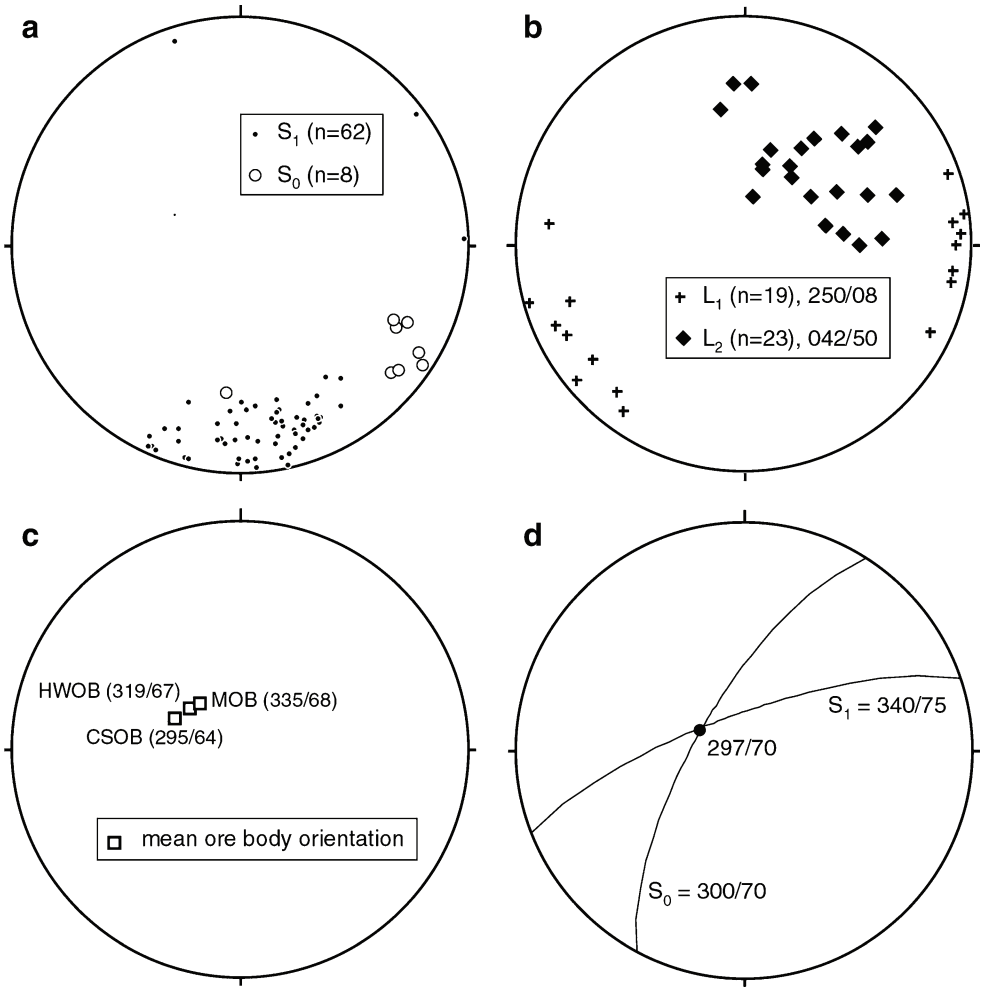

Fig. 5 Lower hemisphere stereographic projections of structural data from the Trojan Mine area. **a** S_0 and S_1; **b** L_1 and L_2; **c** mean orientations of the long axes of ore bodies constructed from mine plans (*MOB* Main ore body, *HWOB* Hanging Wall ore body, *CSOB* Cardiff South ore body); **d** intersection between average S_0 and S_1 orientations. Note that the ore bodies are parallel to the S_0–S_1 intersection lineation

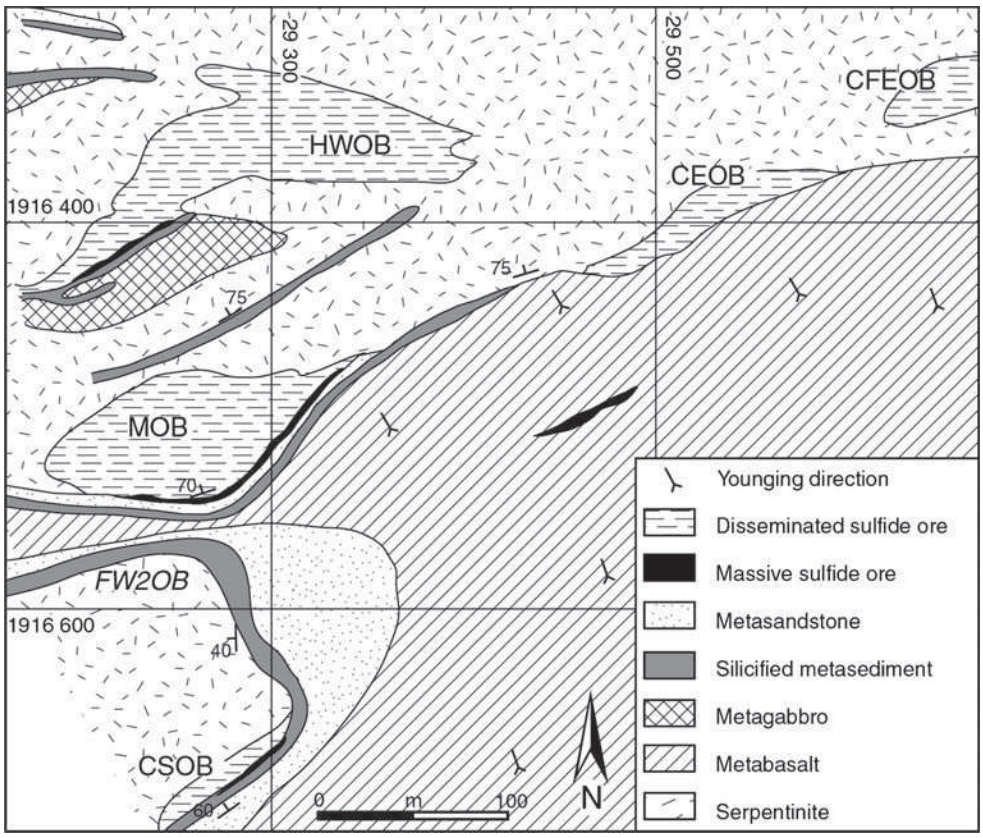

Fig. 6 Geological plan of the seventh level showing the distribution of the principal ore bodies (modified from Chimimba 1984). *MOB* Main ore body, *HWOB* Hanging Wall ore body, *CSOB* Cardiff South ore body, *FW2OB* Footwall no. 2 ore body, *CEOB* Cardiff East ore body, *CFEOB* Cardiff Far East ore body. Note that the distribution of the CSOB and the FW2OB along an inferred fold structure (Chimimba 1984) is inconsistent with younging directions to the east as well as subsequent mapping (Fig. 3b)

fine cracks both within and interstitial to variably replaced olivine grains likely indicating secondary origin for these globules (Fig. 9f).

Timing of sulfide mobilization relative to deformation

Textural evidence indicates sulfide mobility during each deformation stage. Sulfur mobility during the initial serpentinization process is indicated by the intergrowth of sulfides and unoriented laths of metamorphic talc, tremolite, and antigorite in serpentinite (Fig. 9a). Metamorphism and serpentinization coincided with the development of the penetrative regional foliation and network of shear zones during D_1, and many nickel sulfide crystals in disseminated and massive ores are aligned parallel to S_1. In metasedimentary schist, it is common to find sulfide patches parallel to S_1, such as in asymmetric pressure shadows around porphyroclasts and porphyroblasts (Fig. 8b). During progressive folding of the schist, massive sulfide veins formed parallel to axial planes.

Garnet-bearing schist contains unoriented hornblende patches that are intergrown with sulfides, reflecting sulfide mobility during D_2/M_2. Similar relationships exist between sulfides and unoriented antigorite replacing metamorphic olivine (Chimimba 1987). Most deformation textures in massive and matrix ores appear to post-date D_2, considering that blocks of strongly foliated and folded footwall rock fragments and fragments of garnet-bearing schist containing unoriented M_2 minerals are common within the massive ores. In addition, invasion of sulfide into metasandstone is controlled by D_3 brittle–ductile faults.

Analytical procedures

We analyzed major and trace element contents of selected samples. Fresh-rock samples were reduced with jaw crusher into small chips. Vein-free chips were handpicked, ultrasonically cleaned, and pulverized using an agate mill. Major element concentrations were measured by X-ray fluorescence spectrometry (Philips X'Unique XRFS) on glass tablets at the School of Geological Sciences, University of KwaZulu-Natal (UKZN). Accuracy for major elements was checked against international standard NIM-G and was found to be better than 3 %.

Trace elements were measured using a Perkin-Elmer Elan 6100 inductively coupled plasma mass spectrometry (ICP-MS), also at the School of Geological Sciences (UKZN), calibrated against primary standard solutions, and validated with certified standard rock materials. Fifty milligrams of sample was dissolved in HF-HNO_3 in an Anton-Paar Multiwave high-pressure and temperature microwave digester with 40-min digestion time and evaporated to dryness in Teflon beakers before being taken up in 5 % HNO_3 for analysis. The final solution was topped up to 50 ml for

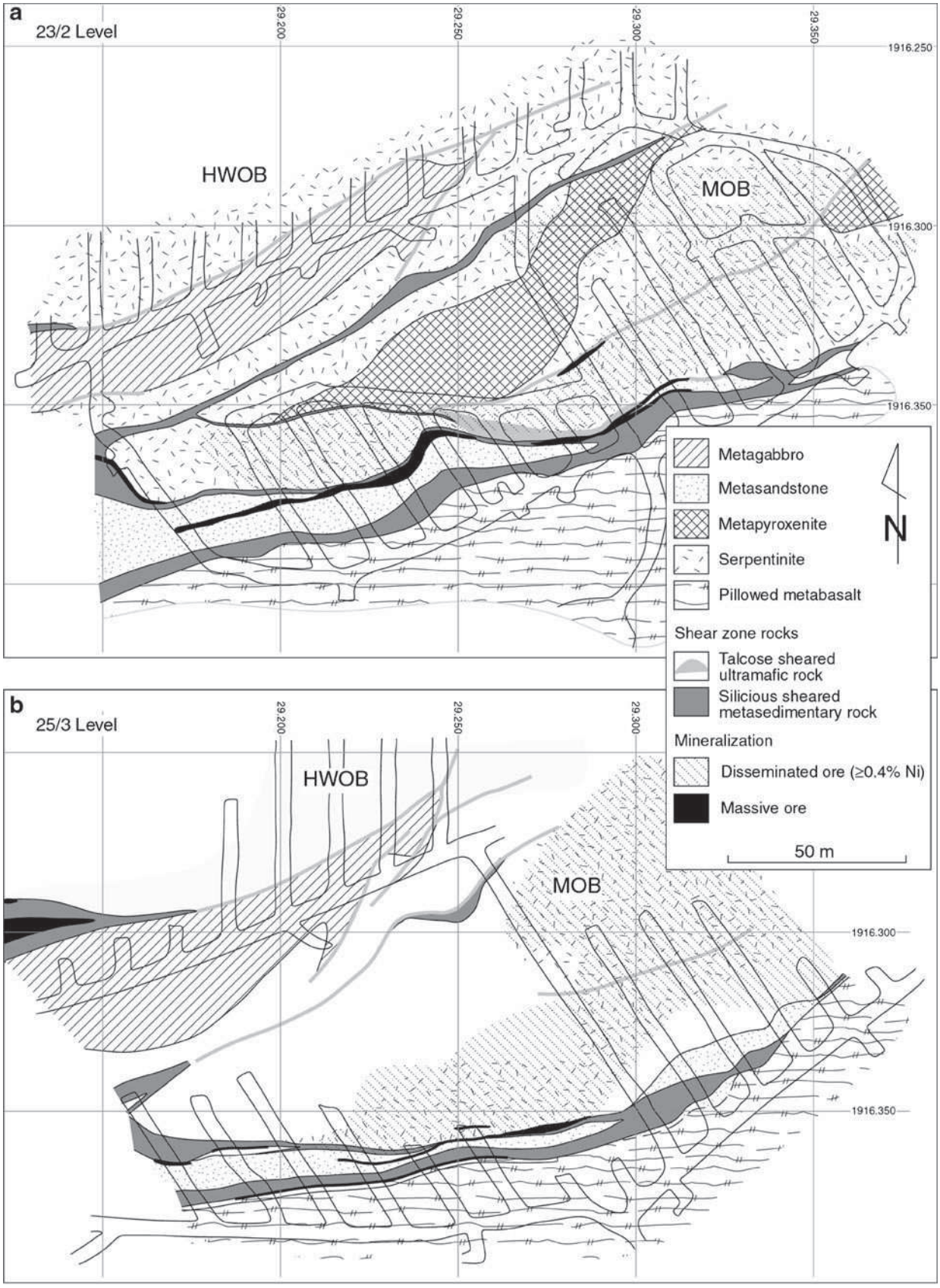

Fig. 7 Geological plan of the 23/2 (**a**) and 25/3 (**b**) levels. *MOB* Main ore body, *HWOB* Hanging Wall ore body

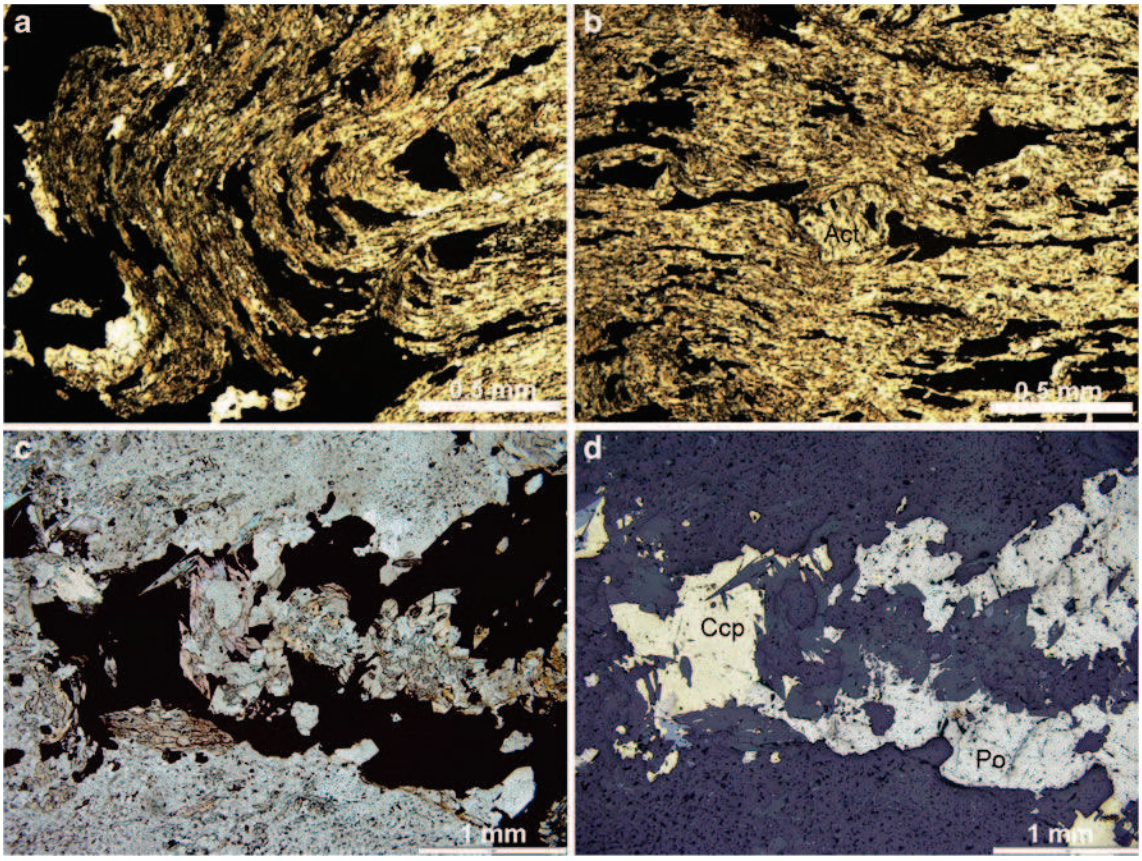

Fig. 8 Photomicrographs of sulfide-bearing metasedimentary rocks. **a** Crenulated chlorite–actinolite schist; sulfides (pyrrhotite and minor chalcopyrite) occur within the foliation plane (preferentially along fold hinges) and as veins cutting across the crenulations (plane-polarized light). **b** Chlorite–actinolite schist; sulfides (mainly pyrrhotite) are irregularly dispersed or occur in pressure shadows of actinolite (*Act*) porphyroblasts (plane-polarized light). **c** Chert cut by vein filled with quartz, actinolite, and sulfides (pyrrhotite (*Po*) and chalcopyrite (*Ccp*); plane-polarized light). **d** Same as in **c** (reflected light)

analysis. Internal standards (10 ppb Rh, In, Re, and Bi) and calibration solutions were prepared from certified single and multi-element standard solutions. Quality of data was monitored using the international standards BCR-1, BHVO-1, and BIR-1. For this analysis, precision was better than 5 % except for Sc, V, and Sr (better than 7 %), on the basis of four repeat analysis of BCR-1. Accuracy was better than 15 % for most elements except for V, Ni, and Cu (better than 25 %) and Cr and Zn (better than 35 %). Lower limit of detection was typically well below 0.1 ppm for rare earth elements and below 1 ppm for all other elements except for Cu (below 2.5 ppm) and Zn (below 3.7 ppm). One sample (ZTR-1) was analyzed using a Fisons PQ2+ ICP-MS at the University of Queensland, Australia (see Bolhar et al. 2005 for analytical methods and details on accuracy and precision).

Sulfur isotope ratios were determined at the Geophysical Laboratory, using technique described by Hu et al. (2003) and under the same analytical conditions as described in Hofmann et al. (2009). The sulfur isotope compositions are reported with respect to VCDT. The intralaboratory precision for $\delta^{34}S$, $\delta^{33}S$, and $\Delta^{33}S$ values based on multiple S isotope analysis of CDT material and internal laboratory standards (Maine Light and Alpha Aesar pyrite) is better than 0.34, 0.19, and 0.03 ‰, respectively. Iron isotope and chemical analyses of sulfides were performed on the same aliquots of mineral separates that were used for S-isotope work. Sulfides were digested in Teflon beakers using concentrated HCl and HNO_3 acid mixture and dry residue obtained after evaporation was then dissolved in 6 N HCl. A fraction of the solution was diluted for S, Fe, Cu, Ni, and Zn chemical analyses using high-resolution ICP-MS or ICP-atomic emission spectroscopy at the Pole Spectrometrie Ocean (PSO, Brest, France). For each element, instrument sensitivity was calibrated using matrix-matched standard solutions corresponding to synthetic sulfide matrices. The detection limit was better than 0.01 wt.%, and analytical precision was estimated at ~2 %. Iron isotope ratios were measured on the Neptune multi-collector inductively coupled plasma mass-spectrometer (MC-ICP-MS, Thermo Fisher Scientific; Waltham, MA, USA) operated at the PSO (Brest, France) following previously published methods (Rouxel et al. 2005, 2008). The MC-ICP-MS was operated in a medium-resolution mode, and we used Ni as an internal

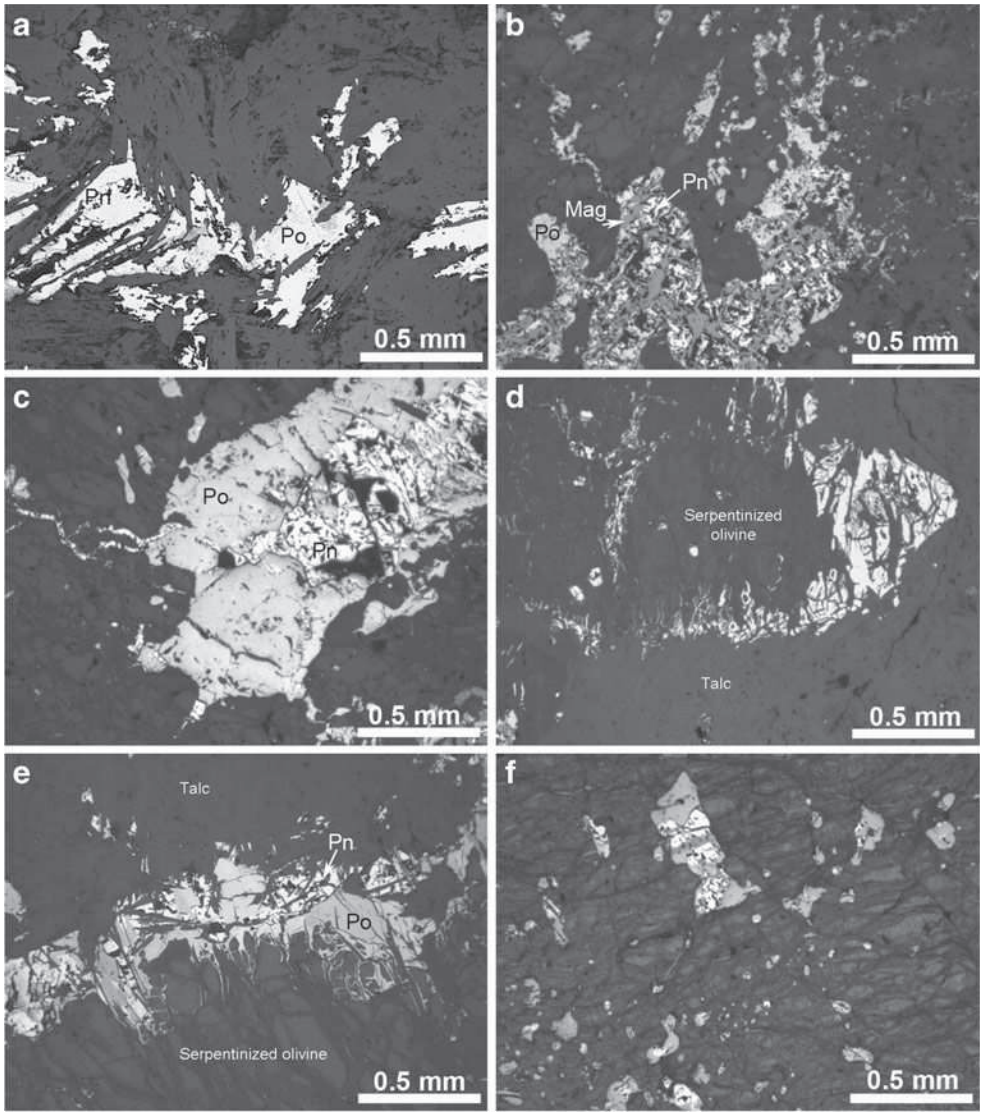

Fig. 9 Photomicrographs (reflected light) of sulfide-bearing ultramafic rocks. **a** Coarse-grained serpentine and tremolite are intergrown with sulfides (pyrrhotite (*Po*), pentlandite (*Pn*), and minor chalcopyrite). The sulfides form stringers parallel to S_1. **b** Mesh texture of serpentinized dunite is cut by a sulfide vein. Sulfide in turn is also cut by magnetite (*Mag*) veins that are parallel to the mesh texture of the surrounding metadunite, suggesting that serpentinization and magnetite formation took place after sulfide veining. **c** Mesh texture of serpentinized dunite is cut by a sulfide vein with a weak fabric parallel to mesh texture indicating that veining took place prior to serpentinization. **d**, **e** Sulfide-bearing reaction rim between serpentinized dunite and massive talc-serpentine rock. **f** Globular sulfide blebs both interstitial and within serpentinized olivine. The globules are generally aligned along fractures

standard for mass bias correction. Fe isotope values are reported relative to the international isotopic standard IRMM-14 using the conventional delta notations. Several georeference materials, including banded iron formation (IF-G) and Hawaiian Basalt (BHVO-1) standards, were also measured and results were similar to previously reported values (Dauphas and Rouxel 2006). Based on duplicate chemical purifications and isotope analyses, the long-term external reproducibility is 0.08 ‰ for δ^{56}Fe and 0.11 ‰ for δ^{57}Fe values (2 standard deviations).

Ni isotopes were measured by MC-ICP-MS (PSO, Brest, France) using a double-spike method for correction of the instrumental mass bias. The experimental and analytical methods are described in Gueguen et al. (2013). Samples were digested in double-distilled, concentrated HCl and HNO_3. Ni was purified with a two-step column separation procedure using AG1-X8 anionic resin for removal of most Fe, Cu, and Zn and a specific resin for Ni (manufactured by Eichrom) for elution of remaining matrix elements. Prior to loading samples on Ni-spec resin, a known amount of double-spike solution containing ^{61}Ni and ^{62}Ni isotopes was added to the samples. ^{60}Ni/^{58}Ni ratios are reported in conventional delta notation using the NIST SRM 986 international standard. Pure NIST SRM 986 standard solution was also analyzed during each MC-ICP-MS session in a standard-sample-bracketing manner in order to monitor the external error. The error associated with Ni isotope analyses is 0.02 ‰ (2 standard error). It was calculated from the data for 50 measurement cycles performed on each sample during MC-ICP-MS analysis. The double-spike correction method is based on iterative calculations using three isotopic ratios (^{60}Ni/^{58}Ni, ^{61}Ni/^{58}Ni, and ^{62}Ni/^{58}Ni) as previously described by Siebert et al. (2001) for Mo isotopes. We estimate that this number of measurement cycles is necessary in order to calculate a satisfactory error on samples.

Geochemistry of metasedimentary horizons at Trojan Mine

Variably silicified and carbonaceous metasedimentary units were analyzed for their major and trace element contents. These include nine samples of fine-grained siliciclastic rock, representing metamorphosed shale and siltstone, and two samples of metachert. Some samples are from surface exposures, while others were collected from the drillcore 35-1-20 that intersected the MOB and the footwall on the 35th level. For this aspect of our study, samples of metasedimentary rocks with sulfide mineralization were avoided as the focus was on the composition of the siliciclastic material of the rocks. Results of major and selected trace element analyses are presented in Table 2.

Excluding two chert samples, selected element concentrations for the average composition of the samples of siliciclastic metasedimentary rocks normalized to PAAS (post-Archean average Australian shale, Taylor and McLennan 1985) are plotted in Fig. 10. Most elements have concentrations lower than PAAS, possibly due to silicification resulting in apparent element depletion due to silica dilution, as SiO_2 content has a large range with values as high as 82 %. Compared to PAAS (Fig. 10), Al_2O_3 and TiO_2 values are relatively low (average Al_2O_3=13.3 %). Samples with the highest Al_2O_3 contents do not necessarily have the lowest SiO_2 contents, as would be expected for siliciclastic sedimentary rocks, again suggesting that the primary mineralogy has been modified by silicification. Na_2O contents are strongly enriched relative to PAAS, with values as high as 6.9 %, indicating albitization. Transition metals correlate positively with each other and with Fe_2O_3 content and are generally slightly depleted relative to PAAS, with the exception of Ni, which is slightly enriched, with values as high as 419 ppm. Base metals are strongly enriched in the sample set, yielding average values of 212 ppm for Cu, 2,841 ppm for Zn, and 70 ppm for Pb.

High-field-strength element ratios show a moderate range of variation (Nb/Ta=9–14.4; Zr/Hf=38–42; Th/U=1.1–6.3), which possibly suggests contributions from compositionally different sources, but they are generally close to the chondritic values, suggesting no significant fractionation as a result of metasomatic or hydrothermal processes during silicification (Bau 1996). ΣREE contents range widely from 46 to 430 ppm and are on average higher than that for PAAS (Fig. 10). There is a moderate positive correlation with P_2O_5 content (R^2=0.58), suggesting a possible control by detrital minerals such as monazite. All samples show LREE enrichment (average La_N/Sm_N=3.81; Fig. 11), while the HREE are relatively unfractionated (average Gd_N/Yb_N=1.36). Both negative and positive Eu anomalies (Eu/Eu*=0.64–1.99) are present in the sample set.

Useful and widely employed proxies for the bulk composition of the provenance are the Cr/Th and Th/Sc ratios (Condie and Wronkiewicz 1990; McLennan and Taylor 1991). The average Cr/Th ratio of 14.6 and Th/Sc ratio of 0.6 for the siliciclastic metasediments in our study suggest a source of intermediate to felsic composition. A comparison with geochemical data (Tomschi 1987; Jelsma 1993) for rhyodacite of the Iron Mask Formation and basalt of the Arcturus Formation, both in terms of REE systematics and Cr/Th ratios (Figs. 11 and 12), suggests that a major proportion of the clastic material was derived from a source that may have had a composition intermediate between the two end members. However, this source is unlikely to represent a simple mix of the two lithologies as a result of erosion. An intermediate to felsic volcanic source is also indicated by a large proportion of felsic volcanic detritus in metasandstone intercalated with the metashale. However, difference in composition between the metasedimentary rocks and rhyodacite of the Iron Mask Formation (e.g., the latter have strongly fractionated HREE, see Fig. 11) makes it unlikely that felsic material was simply derived from erosion of stratigraphically underlying rocks. Instead, synsedimentary volcanism providing pyroclastic material of intermediate to felsic volcanic composition seems more likely. Contemporary mafic and felsic volcanism has been reported from several greenstone belts that host Ni sulfide deposits (Barrie 1999; Trofimovs et al. 2004).

The chert samples consist predominantly of SiO_2 and Fe_2O_3 and likely represent either exhalites precipitated at the seafloor or replacement products of siliciclastic sediments. Replacement may have taken place near the sediment–water interface shortly after deposition during hydrothermal activity and silicification, or during later episodes of hydrothermal alteration. Trace element ratios and REE patterns of the cherts are very similar to those of the clastic rocks, suggesting that they do contain minor amounts of compositionally similar detrital material.

Multiple S, Fe, and Ni isotope systematics

A recent study of several komatiite-hosted Ni deposits from Western Australia (Yilgarn craton) and Canada (Abitibi greenstone belt, superior craton) using multiple isotopes of sulfur ($\Delta^{33}S$, $\delta^{34}S$) and iron isotopes ($\delta^{56}Fe$) has confirmed previous inferences that S is predominantly derived from crustal sources (Bekker et al. 2009; Hiebert et al. 2012). A sedimentary source was also indicated for some Archean Ni–Cu–(PGE) sulfide deposits in mafic–ultramafic intrusions of Botswana (Fiorentini et al. 2012) and Finland (Konnunaho et al. 2013). Mass-independent fractionation (MIF) of S isotopes is defined by non-zero $\Delta^{33}S$ values, where $\Delta^{33}S \approx \delta^{33}S - 0.515 \times \delta^{34}S$ (Hulston and Thode 1965), and accompanies SO_2 photolysis under ultraviolet radiation (Farquhar et al. 2001). MIF of S

Table 2 Major element (in weight percent oxide) and trace element (in parts per million) concentrations of metasedimentary rocks from Trojan Mine

	TM6.9 Shale	TM7.5 Shale	TM9.5 Shale	TM12.7 Shale	ZTR-2 Shale	ZTR-3 Chert	ZTR-4 Shale	ZTR-6 Shale	ZTR-7 Shale	ZTR-8 Shale	ZTR1 Chert
SiO_2	65.65	60.74	61.62	63.37	48.20	88.19	70.05	81.97	73.92	56.02	98.26
TiO_2	0.52	0.48	0.44	0.52	0.42	0.02	0.56	0.26	0.46	0.35	0.01
Al_2O_3	12.42	12.37	15.13	15.62	13.63	0.04	16.89	8.56	11.34	14.08	bd
Fe_2O_3	8.17	11.84	6.58	1.42	11.60	7.61	0.67	0.58	0.65	1.42	0.37
MnO	0.12	0.15	0.11	0.03	0.05	0.02	0.04	0.02	0.01	0.03	0.01
MgO	1.65	2.13	2.16	2.52	2.23	0.11	0.87	0.48	1.02	9.53	bd
CaO	0.83	1.84	0.96	2.05	2.16	0.10	0.02	0.01	1.77	0.88	0.07
Na_2O	5.34	4.13	4.94	1.50	6.94	0.05	0.16	0.18	3.87	4.61	bd
K_2O	1.40	1.86	4.14	12.15	0.02	bd	5.49	2.83	0.12	0.03	0.12
P_2O_5	0.07	0.08	0.08	0.17	0.08	0.03	0.02	0.02	0.04	0.02	bd
LOI	1.56	0.92	2.07	0.69	11.92	0.98	5.49	4.67	6.54	12.55	0.46
Total	97.73	96.55	98.24	100.03	97.25	97.15	100.26	99.58	99.74	99.52	99.3
Sc	12.5	13.1	10.5	8.0	28.2	0.1	6.4	5.5	8.2	6.7	0.1
V	48.6	74.5	86.5	49.5	85.5	0.7	89.4	38.4	44.5	41.5	0.5
Cr	80.4	120.4	78.5	23.9	114.4	0.8	59.4	44.2	54.9	56.1	0.9
Co	26.9	40.5	29.0	3.3	65.5	15.2	0.8	0.2	4.1	8.2	0.9
Ni	93.5	83.9	50.4	7.9	224.5	41.3	20.4	12.3	38.9	419.0	5.5
Cu	196	354	268	145	357	751	22	18	189	361	21
Zn	3639	1695	5191	117	11881	226	60	26	113	2848	17
Rb	59.8	94.2	75.3	160.7	0.4	0.1	98.6	61.4	1.3	0.3	0.1
Sr	109.4	128.6	61.3	233.6	83.2	0.7	11.1	10.8	134.3	64.3	1.2
Y	24.2	20.7	11.8	25.2	20.5	1.3	3.3	4.8	9.1	14.1	1.1
Zr	222.2	168.7	162.4	223.4	110.9	0.4	200.9	100.3	167.3	135.4	2.6
Nb	9.62	5.74	4.96	8.25	4.86	0.03	8.74	5.36	7.23	4.04	0.05
Ba	67	79	286	1486	17	1	318	350	69	28	4
La	20.0	17.2	8.4	34.4	14.3	0.4	2.9	17.3	10.3	13.7	0.4
Ce	41.2	35.3	20.5	66.2	33.6	0.7	4.5	30.2	21.3	24.6	0.9
Pr	5.07	4.34	1.82	6.41	4.35	0.10	0.51	3.19	2.09	3.73	0.12
Nd	20.93	17.80	7.20	23.21	18.26	0.48	1.90	11.94	7.80	15.73	0.50
Sm	4.47	3.86	1.42	4.33	4.26	0.13	0.28	2.11	1.61	3.67	0.11
Eu	1.31	0.98	0.74	1.11	1.74	0.04	0.12	0.40	1.08	1.31	0.06
Gd	4.41	3.78	1.60	4.61	3.97	0.17	0.37	1.74	1.74	3.62	0.14
Tb	0.67	0.56	0.27	0.76	0.62	0.03	0.08	0.21	0.33	0.49	0.02
Dy	4.23	3.48	1.79	4.88	3.76	0.18	0.61	1.12	1.67	2.67	0.15
Ho	0.87	0.71	0.39	0.98	0.74	0.04	0.14	0.20	0.34	0.51	0.04
Er	2.58	2.11	1.23	2.78	2.12	0.12	0.52	0.57	1.03	1.46	0.10
Tm	0.39	0.32	0.20	0.39	0.32	0.02	0.10	0.09	0.16	0.22	0.02
Yb	2.64	2.20	1.40	2.30	2.17	0.11	0.79	0.63	1.45	1.51	0.11
Lu	0.42	0.35	0.24	0.31	0.36	0.02	0.14	0.10	0.22	0.25	0.02
Hf	5.36	4.19	4.19	5.32	2.81	bd	4.91	2.64	4.14	3.43	0.02
Ta	0.69	0.40	0.55	0.57	0.39	bd	0.63	0.40	0.61	0.34	0.00
W	0.21	0.23	1.29	1.08	0.57	0.06	3.27	1.37	1.03	0.50	0.02
Pb	198.5	118.9	123.7	61.2	51.6	332.2	6.7	29.4	16.4	27.4	0.9
Th	5.83	4.61	6.08	7.22	5.22	0.03	2.33	3.92	4.78	8.19	0.01
U	1.85	1.36	2.49	3.20	1.71	0.08	2.22	1.18	1.95	1.31	0.04

Total iron is reported as Fe_2O_3

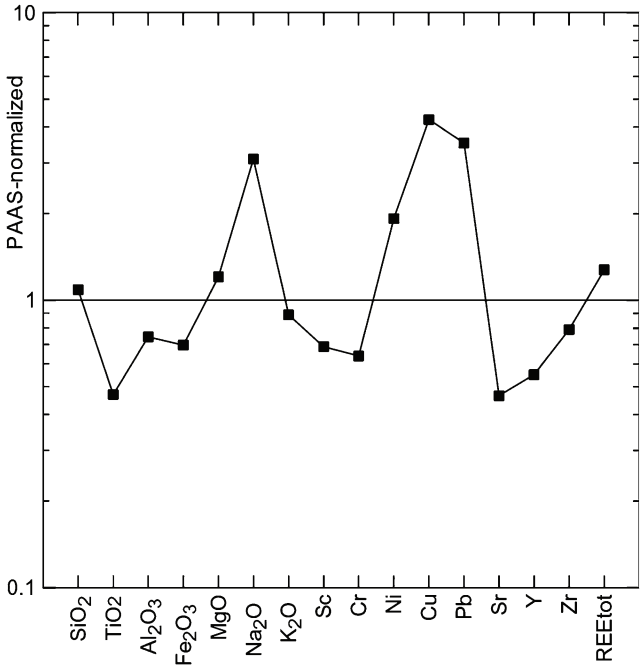

Fig. 10 PAAS-normalized distribution of selected major and trace elements of the average clastic metasedimentary rock from Trojan Mine

isotopes in Archean sulfides and sulfates has been attributed to the absence of an ozone shield in the anoxic Archean atmosphere (Farquhar et al. 2000; Pavlov and Kasting 2002; Bekker et al. 2004). Multiple S isotope analysis thus allows differentiation between S with $\Delta^{33}S \neq 0$ ‰ that passed through the Archean atmosphere and magmatic S with $\Delta^{33}S = 0$ ‰. Bekker et al. (2009) observed both negative and positive $\Delta^{33}S$ values of Ni-bearing sulfide ore. For several deposits, these values were similar to those of base-metal barren massive sulfides and sulfidic shales present in the footwall of the ore bodies. The sulfur in the Ni ores was interpreted by the authors to have likely been derived from the footwall sedimentary sulfides.

Fe isotope fractionation occurs during redox changes, fluid–mineral interactions, and biological processes (e.g., Anbar and Rouxel 2007; Johnson et al. 2008). While igneous and siliciclastic sedimentary rocks have near-zero δ^{56}Fe values that cluster at 0.1 ‰ relative to the IRMM-14 standard, iron sulfides in Archean black shales, and volcanogenic massive sulfides of various ages systematically show negative iron isotope values as low as −3.2 ‰ (Rouxel et al. 2005, unpublished data). In contrast, banded iron formations generally yield more positive δ^{56}Fe values up to 1.8 ‰, although distinct Fe isotope compositions are observed depending on Fe-bearing minerals, such as Fe-carbonate, magnetite, or hematite (Johnson et al. 2008; Planavsky et al. 2012). Bekker et al. (2009) reported iron isotope composition of Archean komatiite-hosted Ni sulfides of the Yilgarn and Superior cratons to be close to 0 ‰, suggesting a predominantly magmatic source of iron in the sulfides.

To date, Ni stable isotope studies were mainly applied to cosmochemical processes (Moynier et al. 2007; Cook et al. 2008), with only few studies (Cameron et al. 2009; Tanimizu and Hirata 2006) dealing with Ni isotope systematics of terrestrial rocks. Recently, Gueguen et al. (2013) estimated the bulk silicate Earth $\delta^{60/58}$Ni value to be around +0.05±0.05 ‰ relative to SRM 986 standard. Recently reported $\delta^{60/58}$Ni values of komatiite-hosted Ni-rich sulfides from the Agnew–Wiluna greenstone belt in Western Australia and the Abitibi greenstone belt in Canada vary from −0.10 to −1.03±0.03 ‰, which indicates significant abiotic fractionations at high temperature in magmatic systems (Gueguen et al. 2013).

Sulfide mineral separates of selected samples were subjected to multiple S, Fe, and Ni isotope analyses.

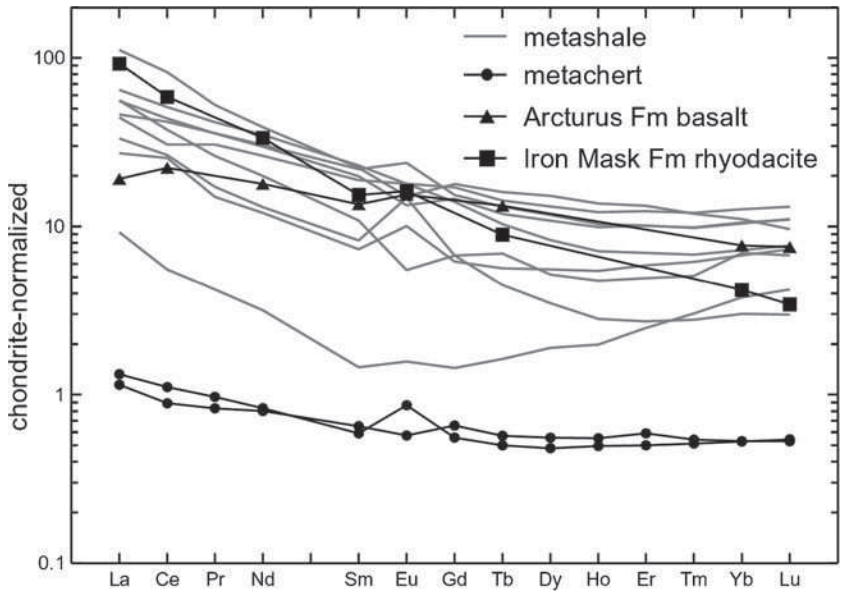

Fig. 11 Chondrite-normalized REE plots of clastic metasediment and metachert samples from the Trojan Mine area as well as the average compositions of rhyodacite of the Iron Mask Formation and basalt of the Arcturus Formation

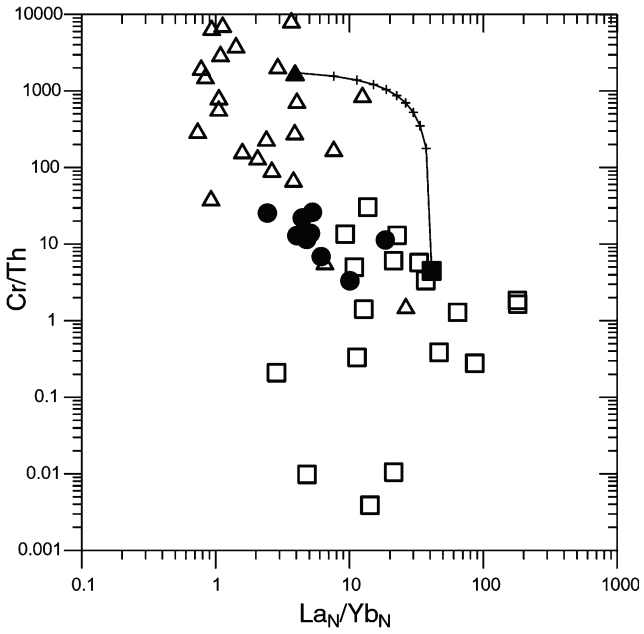

Fig. 12 Cr/Th vs. La_N/Yb_N diagram showing siliciclastic metasediments (*filled circles*), rhyodacite of the Iron Mask Formation (*open squares*), and basalt of the Arcturus Formation (*open triangles*). Also shown is the average composition of the Iron Mask Formation rhyodacite (*filled square*) and Arcturus Formation basalt (*filled triangle*) as well as a mixing trajectory between the two end-member compositions in steps of 10 %. Note that the Trojan Mine samples do not plot near the proposed mixing trajectory, thus not supporting a simple mixing relationship between the two potential end-member compositions

Trojan Mine

We separated sulfides from 11 samples from drillcore 35-1-20. Samples include sediment-hosted sulfide and sulfide from massive, net-textured, and disseminated ore (Table 3). Sulfides show $\delta^{34}S$ values from −0.1 to 4.1 ‰ (Fig. 13a). All samples have a MIF signal with $\Delta^{33}S$ values ranging from 0.58 to 1.12 ‰. The metasedimentary sulfides have the highest $\delta^{34}S$ and the lowest $\Delta^{33}S$ values. The ore sulfides have relatively constant $\Delta^{33}S$ values irrespective of mineralization type. $\delta^{34}S$ and $\Delta^{33}S$ values of the metasedimentary sulfides and some ore sulfide samples show an apparent negative linear correlation. Iron isotope values of ore sulfides (Fig. 14) show a narrow range of $\delta^{56}Fe$ values from −0.28 to 0.07 ‰ with the average of −0.11 ‰, which is slightly lower than that for Eoarchean peridotites (Dauphas et al. 2009) and fertile upper-mantle derived from measurements of modern peridotites (Weyer and Ionov 2007) and defined at ~0.02 ‰. The metasedimentary sulfides have the lowest $\delta^{56}Fe$ values ranging between −1.36 and −1.52 ‰, which are within the range of $\delta^{56}Fe$ values of Neoarchean sedimentary sulfides in metashales that have highly negative Fe isotope values (e.g., Rouxel et al. 2005).

Nickel isotope values of massive and net-textured ore samples from Trojan Mine display a restricted range of negative $\delta^{60/58}Ni$ values from −0.23 to −0.43 ‰ (Table 3) with the average value of −0.38 ‰ within the range of, albeit less variable than, values for komatiite-hosted Ni sulfides reported by Gueguen et al. (2013).

Shangani Mine

We separated sulfides from nine samples of hand specimens and the drillcore 855/50W/2. Samples include sulfides from massive and net-textured ore from the Main ore body, disseminated sulfides, mainly present in carbonate veins in talcose serpentinite from the Main ore body, and pyrite nodules from carbonaceous shale associated with the Far West ore body (Table 3). The sedimentary pyrites in carbonaceous shale have the highest $\delta^{34}S$ (3.8 to 5.1 ‰) and $\Delta^{33}S$ (1.8 ‰) values (Fig. 13a), while $\delta^{56}Fe$ values show systematic enrichment in light isotope and are as low as −1.4 ‰ (Fig. 14). Disseminated sulfides in carbonate veins in talcose serpentinite as well as samples of net-textured ore have $\delta^{34}S$ values ranging from 0.8 to 2.8 ‰, with the average $\Delta^{33}S$ value of 0.7 ‰ and $\delta^{56}Fe$ values of −0.75 to 0.58 ‰. $\Delta^{33}S$ values of massive ore are within the range of mass-dependent fractionation of sulfur isotopes (0.0±0.2 ‰, Farquhar and Wing 2003) and have $\delta^{34}S$ and $\delta^{56}Fe$ values of 0.9 to 1.3 and 0.25 to 0.26 ‰, respectively. Only one Ni isotope analysis of the net-textured ore from Shangani Mine has been performed, and it yielded a $\delta^{60/58}Ni$ value of −0.47 ‰, which is similar to that for ore samples from Trojan Mine.

Discussion

When considering the genesis of the Trojan and Shangani nickel deposits, it is important to differentiate between primary magmatic and secondary metamorphic–hydrothermal processes. Previously, the preferred model for the Trojan and Shangani deposits has been one in which gravity settling of sulfides in ultramafic flows resulted in nickel concentration toward the footwall of the flows, with massive sulfides forming in depressions. It was thought that the effect of structural–metamorphic processes during subsequent events was limited to minor remobilization (Chimimba and Ncube 1986). Considering the complex deformation and alteration experienced by the rocks in the Trojan and Shangani mine areas, it is necessary to explore to what extent other processes may have affected the distribution and grade of Ni sulfide mineralization. Although both deposits share a similar geological history, we focus our discussion on Trojan Mine for which more data are currently available.

Gravity settling of sulfide melt vs. secondary hydrothermal processes

According to Chimimba (1984), the main observations supporting a magmatic origin of the sulfides include the presence of intercumulus sulfides in matrix ore, the basal position of

Table 3 Description of samples used for sulfur, iron, and nickel isotope and element concentration analyses and analytical results

Drillcore	Depth (m)	Sample #	Rock type	$\delta^{34}S^*$	$\delta^{33}S^*$	$\Delta^{33}S_{ln}$	$\delta^{56/54}Fe$	$\delta^{57/54}Fe$	$\delta^{60/58}Ni$	S (wt.%)	Fe (wt.%)	Ni (wt.%)	Cu (wt.%)	Sulfide type
Trojan Mine														
35-1-20	7.5	TM7.5	Silicious meta-greywacke	3.5	2.7	0.84	−1.41	−2.12		37.29	59.44	0.04	0.02	2 mm layer of Po
35-1-20	9.5	TM9.5	Silicious meta-shale	4.1	2.7	0.58	−1.52	−2.24		33.81	54.14	0.05	0.40	Po nodule
35-1-20	10.4	TM10.4	Silicious meta-greywacke	4.0	2.6	0.60	−1.36	−2.12		14.38	25.04	0.02	0.15	Po veinlets
35-1-20	20.4	TM20.4	Massive ore	2.6	2.4	1.05	0.07	0.14	−0.40	35.52	41.36	16.88	0.51	Po–Pn
35-1-20	20.8	TM20.8	Massive ore	1.1	1.5	0.96	0.03	−0.01	−0.39	35.90	42.80	16.44	0.41	Po–Pn
35-1-20	22.55	TM22.55	Massive ore	2.7	2.3	0.96	−0.18	−0.26	−0.43	36.78	47.52	8.94	0.62	Po–Pn
35-1-20	25.6	TM25.6	Massive ore	−0.1	0.9	0.95	−0.22	−0.32	−0.38	36.73	48.02	8.72	0.36	Po–Pn
35-1-20	27.9	TM27.9	Massive ore	−0.1	0.9	0.95	−0.08	−0.15		37.14	47.98	10.10	0.35	Po–Pn
35-1-20	30.55	TM30.55	Massive ore	2.7	2.3	0.97	−0.07	−0.16		36.23	45.03	12.77	0.63	Po–Pn
35-1-20	34.2	TM34.2	Net-textured ore, serpentinite	2.4	2.4	1.12	−0.28	−0.44	−0.28	31.89	39.59	15.10	0.03	Po–Pn
35-1-20	37.9	TM37.9	Disseminated ore, serpentinite	2.9	2.5	1.01	−0.18	−0.27		14.18	24.55	1.91	0.26	Po
Shangani Mine														
Hand specimen		FWOB-1	Carbonaceous shale	5.1	4.4	1.84	−0.25	−0.37		30.07	25.81	0.01	0.00	Cubic Py forming nodules
Hand specimen		FWOB-2	Carbonaceous shale	3.8	3.8	1.83	−1.41	−2.09		33.85	51.02	0.11	0.11	Cubic Py–Po forming nodules
Hand specimen		MOB-1	Massive ore	0.9	0.5	0.03	0.26	0.42		33.80	29.18	0.25	29.09	Ccp
Hand specimen		MOB-3	Massive ore	1.3	0.7	0.03	0.25	0.34		34.81	30.70	0.22	31.06	Ccp
Hand specimen		MOB-2	Net-textured ore, serpentinite	0.8	1.1	0.69	0.58	0.87	−0.47	32.45	33.47	23.83	0.13	Po–Pn
Hand specimen		MOB-2B	Net-textured ore, serpentinite	1.0	1.2	0.68	−0.10	−0.22		34.03	42.41	13.53	0.04	Po–Pn
855/SOW	8.9	855-MOB-8.9	Talcose serpentinite	2.2	1.8	0.69	0.04	0.08		7.61	7.18	0.07	0.01	Po in carbonate vein
855/SOW	56.7	MOB-56.7	Talcose serpentinite	2.8	2.2	0.73	−0.75	−1.11		31.69	32.98	14.35	0.22	Blebs/veinlets of Po–Pn
855/SOW	103	855-MOB-103	Talcose serpentinite	2.0	1.7	0.72	−0.02	0.00		33.07	31.03	4.96	1.36	Blebs/veinlets of Po–Pn

$\delta^{33}S^*$ and $\delta^{34}S^*$ are defined as $\delta^{x}S^* = 1{,}000\ln([\delta^{x}S/1{,}000]+1)$, where x is 33 and 34, respectively (cf. Miller 2002). $\delta^{33}S$ and $\delta^{34}S$ are conventional δ notations with respect to VCDT defined as $\delta^{x}S = 1{,}000[({}^{x}S/{}^{32}S)_{sample}/({}^{x}S/{}^{32}S)_{VCDT}-1]$, where x is 33 and 34, respectively. $\Delta^{33}S_{ln} \approx \delta^{33}S^* - 0.515 \times \delta^{34}S^*$

Py pyrite, *Ccp* chalcopyrite, *Po* pyrrhotite, *Pn* pentlandite

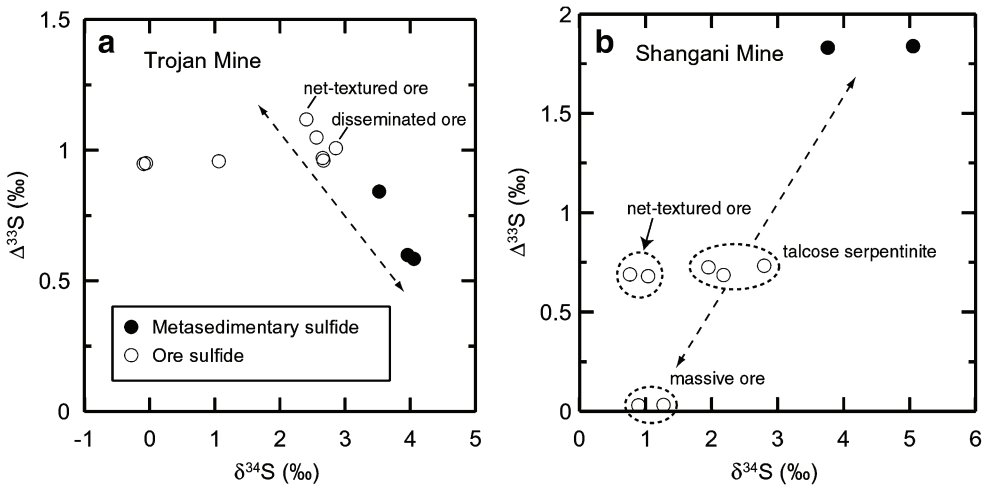

Fig. 13 Plots of $\Delta^{33}S$ vs. $\delta^{34}S$ values for metasedimentary and ore sulfides from **a** Trojan Mine and **b** Shangani Mine. *Dashed arrows* indicate possible mixing trends

massive and matrix ore, and the ordered sequence of massive, matrix, and disseminated ore upward from the footwall of the mineralized serpentinite bodies. However, the following observations argue against a simple gravity-settling model:

1. Although whole-rock Ni-content profiles in disseminated ore are gradual (Chimimba and Ncube 1986), sudden changes in Ni sulfide content can be present between the different ore zones and may testify to tectonic disturbance, as shear zones have been observed at the contact between the disseminated ore and the underlying more massive ore. In fact, when disseminated ore overlies a massive sulfide layer, a barren, 2–3-m-wide zone is usually developed (Chimimba and Ncube 1986).
2. The Ni content in most of the ore bodies increases from the stratigraphic top to the bottom. The conspicuous exception to this rule is the Footwall no. 2 ore body (FW2OB) immediately north of the summit of Cardiff Hill (Fig. 3b). This ore body, which was mined to the third level before it became erratic, occurs in the hanging wall of an ultramafic lens. Its position has been explained by a synclinal fold that overturned the stratigraphy around the ore body (see Fig. 6), but the existence of this fold structure conflicts with an apparent lack of younging reversals to the east of the fold (Fig. 6). Consequently, the nickel sulfide enrichment of the FW2OB cannot be attributed to simple orthomagmatic processes.
3. The distribution of disseminated ore of the MOB is irregular and cuts through lithological contacts (Fig. 7a).
4. The deformation textures observed in schist horizons indicate high strain. Consequently, the current arrangement of lithologies bears little resemblance to the original stratigraphy, and existing geometries cannot be unequivocally used to infer "depressions" responsible for the distribution of massive ore.
5. Fleet and Pan (1994) pointed out that Ni and Cu contents and their ratios in massive and disseminated ores at Trojan and Shangani mines are inconsistent with segregation of an immiscible sulfide liquid and may instead be related to subsolidus sulfide–silicate alteration reactions.
6. Although sulfides are recorded in interstitial position in matrix ore, a relation generally interpreted as primary magmatic, these sulfides are intergrown with metamorphic silicates (Fig. 9a). This means that such textures are not genuinely primary, but at least underwent modification during metamorphism.
7. Metasedimentary schists represent volcaniclastic deposits of intermediate to felsic composition that have been affected by synsedimentary hydrothermal processes resulting in base-metal enrichment as well as by metasomatic processes including silicification and albitization. They are more siliceous and carbonaceous adjacent to mineralized ultramafic units in comparison with those associated with metabasalt. Silica is mobile during serpentinization of ultramafic rocks (e.g., Frost and Beard 2007) and may have migrated from the ultramafic rocks into the adjacent sedimentary horizons

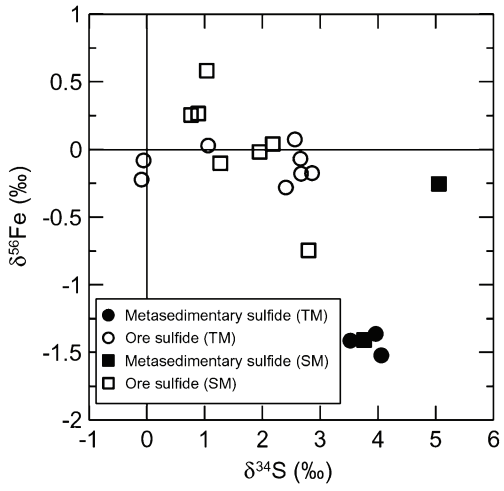

Fig. 14 Plot of $\delta^{34}S$ vs. $\delta^{56}Fe$ values for metasedimentary and ore sulfides from Trojan Mine (*TM*) and Shangani Mine (*SM*)

upon shearing. Massive and near-massive nickel sulfide ore bodies only occur in direct contact with chert and silicified, carbonaceous metasedimentary schist enriched in sulfide. The content of sulfide and carbonaceous matter are commonly correlated in organic matter-rich shales (e.g., Morse and Berner 1995), which might explain why economic mineralization in ultramafic bodies is present only in the vicinity of highly sulfidic and carbonaceous shales. This could indicate that ore bodies developed only in the vicinity of black sulfidic shales due to crustal assimilation. Alternatively, it is conceivable that sulfur, derived from the breakdown reaction of pyrite into pyrrhotite in carbonaceous shale at lower-amphibolite facies conditions (Craig and Vokes 1993; Tomkins 2010), may have entered the ultramafic rocks with hydrothermal fluids channeled along shear zones bounding the ultramafic bodies. This process would also require Ni liberation from the ultramafic rocks during serpentinization and their subsequent migration into ore horizons.

Structural vs. stratigraphic controls on ore body geometry

The complicated intercalation of basalt, ultramafic rocks, and metasedimentary units is not an original volcano-sedimentary stratigraphy. Many lithological contacts in the area are strongly sheared. In addition, the siliceous schists are not primary chemical sedimentary deposits but strongly silicified and sheared metasedimentary rocks.

An important indication that structural–metamorphic processes played a role in the mobilization of the nickel ore deposit at Trojan Mine is the linear nature of the ore bodies and lensoidal geometry of ultramafic host rocks parallel to the S_0/S_1 intersection lineation (Fig. 5d). A similar relationship exists at Shangani Mine (Dirks and Sithole 1996) and has also been described from other deposits in Western Australia (e.g., Barrett et al. 1977; Gresham and Loftus-Hills 1981). To explain this alignment, it has been suggested that the linear nature of ore bodies reflects the shape of volcanic flow channels and that massive sulfide deposits are responsible for strength heterogeneity in the crust localizing strain (e.g., Gresham and Loftus-Hills 1981). Although such linear flow channels may have existed, it appears highly unlikely that they are, almost as a rule, parallel to the orientation of peak-metamorphic linear deformation features of regional significance. Regarding Trojan Mine, this means that the intersection lineation, which is identical in a large area around the mine, cannot possibly be dictated by relatively small linear bodies that occur within the sequence, and it is much more likely that the linear nature of the ore bodies and the host ultramafic rocks resulted from regional tectonics. An alternative suggestion that ore bodies may have rotated to be parallel with the regional strain (e.g., Lacroix and Darling 1991) is also unlikely. First, to attain the near perfect alignment, very high penetrative strain is required, yet not recorded. Second, high strain would align the ore bodies with the direction of maximum elongation (L_1), which in the Trojan Mine area is plunging shallowly to the SW (Fig. 5b), yet the ore bodies dip steeply NW parallel to the S_0–S_1 intersection lineation (Fig. 5c). For these reasons, it is compelling that the linear nature of the ore bodies and their host rocks has a structural–metamorphic origin.

Hydrothermal control on sulfide mineralization at Trojan Mine

The area around Trojan Mine has been strongly deformed during several phases of deformation. Extensive metamorphic reworking of the ultramafic rocks has likely taken place. It is possible that reworking was associated with remobilization of Ni and S, resulting in a hydrothermal control over ore formation. Faults represent zones of high permeability and act as conduits for hydrothermal fluids. There is abundant evidence for hydrothermal activity within the metasedimentary units that were preferentially affected by shearing. Deformation increased permeability of massive ultramafic bodies and may have allowed a pervasive hydrothermal fluid circulation, intense water–rock interaction, and enhanced serpentinization. In contrast to Cr, Ni in ultramafic rocks can be mobile during hydrothermal alteration, such as silicification (Hofmann and Harris 2008), and is liberated from olivine during serpentinization (e.g., Eckstrand 1975; Donaldson 1981). Sulfur could have been sourced from pyrite breakdown in sulfidic shales, entered altered volcanic rocks along shear zones, and preferentially scavenged siderophile elements, such as Ni and Fe. Ore shoots developed along structural features controlled by thrusting of the greenstone sequences, coaxial to the σ_3 direction characterized by a pervasive regional mineral lineation. During subsequent deformation and metamorphic events related to gneiss doming and strike-slip shearing, ore bodies were rotated and reoriented. Locally, massive sulfide ore bodies were extensively reworked, resulting in injection veins into footwall rocks and brecciated ores.

The problem with a hydrothermal–metamorphic origin for nickel sulfide mineralization is the role of primary sulfides in ultramafic rocks. Were primary disseminated sulfides present in the ultramafic rocks and were subsequently upgraded and remobilized by hydrothermal and metamorphic processes? Did disseminated sulfides form by secondary, hydrothermal, and metamorphic processes? Did a combination of these processes take place? Multiple sulfur and iron isotope data help to differentiate between igneous and sedimentary sulfur sources as well as low- and high-temperature processes (Bekker et al. 2009). We therefore further explore below the question whether these proxies, in combination with Ni isotopes, can help to differentiate between a hydrothermal–metamorphic and orthomagmatic control on Ni sulfide mineralization.

Constraints from multiple S, Fe, and Ni isotope analyses

We consider that the distinct MIF signal of samples from Trojan Mine (Fig. 13) suggests derivation of sulfur from crustal, sedimentary sources. Positive $\Delta^{33}S$ values suggest that sulfur was most likely derived from disseminated pyrite in shale, which commonly have highly positive $\Delta^{33}S$ values in Neoarchean sedimentary successions (e.g., Farquhar and Wing 2005; Ono et al. 2009). The sulfides in shales at Trojan Mine are predominantly secondary in origin and were formed by sulfur remobilization. Interestingly, they have lower $\Delta^{33}S$ values compared to the ore sulfides, which may indicate that secondary sulfide in the shale was derived from a mixture of sources, possibly also including sulfur with negative and even zero $\Delta^{33}S$ values.

MDF of S isotopes of massive ore from Shangani Mine most likely suggests a magmatic source of the sulfur as sedimentary to early diagenetic sulfides in associated metashales show distinctly positive $\Delta^{33}S$ values. Alternatively, it might suggest crustal assimilation and subsequent sulfur isotope homogenization in a large crustally derived sulfur reservoir, removing mass-independent fractionation of sulfur isotopes unique to a particular lithology (Fiorentini et al. 2012). In contrast, the S isotope values of sulfides in veins in talcose serpentinite and in net-textured ore appear to lie on a mixing line between magmatic and sedimentary end-members, suggesting a contribution of both.

The small range of iron isotope values in ore sulfides from Trojan Mine suggests that, in contrast to sulfur, most of iron could have been derived from magmatic sources (cf. Hiebert et al. 2013). As recently discussed by Craddock and Dauphas (2011), ultramafic and mafic rocks have an iron isotopic composition similar to that in chondrites (−0.01±0.01 ‰) and different from that in more evolved and differentiated rocks. Hence, our results suggest Fe isotope fractionation of less than 0.2 ‰ between Ni sulfides and silicates by high-temperature magmatic processes, which is consistent with previous studies (Schuessler et al. 2007). Fe isotope data for secondary sulfides in the metashales and metagraywackes cluster at −1.45 ‰ (Fig. 14) suggesting that they were derived from either sedimentary or hydrothermal sulfides remobilized on the scale of their hosting units during deformation and metamorphism. Although negative $\delta^{56}Fe$ values in sedimentary pyrite have been previously interpreted as reflecting microbial Fe reduction (e.g., Archer and Vance 2006; Severmann et al. 2008), it is now widely accepted that abiotic Fe sulfide precipitation in aqueous systems, both in sedimentary and hydrothermal settings, produces Fe isotope fractionations of up to ~1.5 ‰, with light Fe isotopes being enriched in Fe sulfide relative to Fe^{2+}_{aq} (Butler et al. 2005; Polyakov et al. 2007; Rouxel et al. 2008; Bennett et al. 2009; Guilbaud et al. 2011).

In contrast, the negative Fe isotope values as low as −1.4 ‰ for pyrite nodules from shales in the Shangani Mine area are likely to reflect low-temperature fractionation processes during sulfide formation during early diagenesis. Although hydrothermal fluid circulation may also produce isotopically light pyrite (Rouxel et al. 2008), the distinctly positive $\Delta^{33}S$ values in these pyrites suggest rather a sedimentary origin.

In contrast to slightly negative $\delta^{56}Fe$ values of massive ore from Trojan Mine, massive ore at Shangani Mine has positive $\delta^{56}Fe$ values of around 0.25 ‰. Although we currently lack experimental constraints, such difference can be explained by the different mineralogy of the ore deposits. The Shangani Mine ore samples investigated in this study are essentially composed of chalcopyrite, while only pyrrhotite–pentlandite assemblages were analyzed from Trojan Mine. As discussed by Rouxel et al. (2008), it is likely that the equilibrium Fe isotope fractionation between chalcopyrite and Fe^{2+} in either aqueous or melt phase is slightly positive, yielding more positive $\delta^{56}Fe$ values for chalcopyrite. Iron isotope values of disseminated sulfides in serpentinite show a narrow range of $\delta^{56}Fe$ values between −0.10 and 0.04 ‰ with the exception of two outliers with −0.75 and 0.58 ‰ values. The narrow range can be explained by iron isotope fractionation between sulfides and silicates in a magmatic system, while the two outliers might reflect composition of sulfide xenomelt formed by assimilation of crustal lithologies that was not completely homogenized with the magma. However, there is no correlation between the values of MIF of S isotopes and Fe isotope values as would be expected if both Fe and S were derived from crustal (sedimentary) source. In modern seafloor-basalt weathering environments, hydrothermal alteration may release iron with negative iron isotope values, leaving altered rocks enriched in heavy isotopes (Rouxel et al. 2003). Hence, Fe mobility during hydrothermal alteration might be responsible for these two outliers having both negative and positive $\delta^{56}Fe$ values. In addition, there is also negative iron isotope fractionation during precipitation of sulfides from cooling hydrothermal fluids (e.g., Rouxel et al. 2005). These two processes can explain the highly negative iron isotope value in the talcose serpentinite. The positive iron isotope value in the net-textured serpentinite might reflect final stages in Rayleigh distillation by either sulfide precipitation from hydrothermal fluids or iron leaching from ultramafic rocks. Resolution between these two alternatives requires further detailed study, which is beyond the scope of this paper.

Whole-rock Ni concentrations in sedimentary rocks are typically much lower than in mantle-derived ultramafic rocks, which are the likely source for Ni in magmatic sulfides. Ni isotope composition of pyrrhotite–pentlandite ore revealed systematic enrichment in light isotopes to values as low as −0.47 ‰ relative to their ultramafic magma source for which we assumed Ni isotopic composition to be close to the Bulk Silicate Earth value of 0.05±0.05 ‰ (Gueguen et al. 2013). $\delta^{60/58}Ni$ values for both the Trojan and Shangani mines Ni ores form a narrow range from −0.47 to −0.28 ‰, which clearly

indicates a unique mechanism responsible for this light isotope enrichment. For instance, for the Trojan Mine deposit, the average $\delta^{60/58}$Ni value is −0.38 ‰ (n=5), which is consistent with the negative fractionation of −0.3 ‰ between metal and silicate phases obtained by Huh et al. (2009). These authors suggested that Ni isotope fractionation between these two phases was due to nucleation, growth, and annealing mechanisms in the experimental setup, leading to significant fractionation of Ni isotopes at high temperature. These negative values contrast with the strictly positive Ni isotope composition measured in modern marine metalliferous sediments, such as ferromanganese crusts and manganese nodules, which varies from + 0.36 to +1.80 ‰ (Gueguen et al. 2013), arguing further against a sedimentary source of Ni in komatiites, in contrast to S. Although at this stage it is difficult to establish the exact cause of Ni isotope fractionation in magmatic sulfides due to limited experimental and theoretical studies of this new isotopic system, the data provide interesting information on Ni isotope behavior under high-temperature conditions. Specifically, they suggest that there is significant fractionation of Ni isotopes, even higher than that for Fe isotopes, and that Ni sulfide (or sulfide melt) formation produces systematic enrichment in light Ni isotopes with respect to the composition of silicate melt.

Can multiple S and Fe isotope data constrain the origin of Ni sulfide mineralization at Trojan and Shangani mines?

The presence of mass-independent fractionation of multiple sulfur isotopes in Archean komatiite-hosted Ni sulfide deposits implies that the sulfur was previously processed through the atmosphere and then accumulated on the ocean floor prior to incorporation into the ultramafic magmas. Several Archean komatiite-hosted Ni-sulfide deposits show mass-independent sulfur isotope fractionation, suggesting incorporation of sulfur from seafloor hydrothermal sulfide accumulations or sulfidic shales (Bekker et al. 2009; Fiorentini et al. 2012; Hiebert et al. 2013; Konnunaho et al. 2013). Nickel sulfides of the Kambalda deposit show only mass-dependent fractionation of sulfur isotopes, which has been explained by either a magmatic sulfur source or assimilation of multiple crustal sulfur sources, mixing with mantle-derived sulfur and sulfur homogenization removing a mass-independent signal (Bekker et al. 2009). On the scale of a single ore body, assimilation of sedimentary or seafloor, hydrothermal sulfides by thermal erosion in a lava channel and mixing with magmatic sulfur in the turbulent flow, followed by gravitational settling of sulfides upon lava ponding should lead to a relatively homogeneous isotopic composition of sulfides. In contrast, sulfidization with sulfur derived from sedimentary sources via hydrothermal fluid circulation should result in a more heterogeneous sulfur isotope composition of Ni sulfides with sulfides in and close to shear zones (fluid conduits) and sedimentary units having values reflecting a post-magmatic source of S derived from the hosting sedimentary succession. Similarly, iron and nickel isotope values can be used to test between the orthomagmatic and hydrothermal models. If Ni sulfides formed in an isotopic equilibrium with silicate melt in a high-temperature magmatic system, iron and nickel isotope values of unaltered olivine and sulfide should reflect limited fractionation under high-temperature conditions and the mantle source of metals. Alternatively, if hydrothermal processes led to formation of Ni sulfides, they will not be in high-temperature equilibrium with adjacent silicates and will likely show a larger range of iron and nickel isotope values depending on pathways and kinetics of sulfide precipitation (Rouxel et al. 2008) as well as redox transformations and low-temperature fractionations among minerals and with fluids.

Sulfides in metasedimentary rocks at Trojan and Shangani mines show distinctly positive Δ^{33}S values. Early diagenetic pyrite nodules in ca. 2.7 Ga organic matter-rich shales from different greenstone belts in Zimbabwe (Bekker et al. 2008) carry predominantly negative Δ^{33}S values, likely reflecting seawater sulfate reduction in sediments during diagenesis or in the water column. They occur in a matrix of shale with disseminated pyrite having highly positive Δ^{33}S values, likely inherited from photochemically produced, reduced S species such as elemental S (Farquhar and Wing 2005; Ono et al. 2009). Sulfides in metasedimentary rocks at Trojan Mine occur in secondary veinlets, while those at Shangani Mine are strongly recrystallized. However, their positive Δ^{33}S values strongly suggest that the precursor sulfides in the sediment were predominantly derived from photochemically processed elemental sulfur. At both mines, all ore samples that show mass-independent fractionation have positive Δ^{33}S values, again suggesting that the bulk of the sulfur was derived from disseminated pyrite that did not form by reduction of seawater sulfate. This is unlike some other Neoarchean komatiite-hosted Ni-sulfide deposits that have negative Δ^{33}S values indicating that they may have assimilated sulfur from distal, barren volcanogenic massive sulfides (e.g., Bekker et al. 2009). The latter sulfides formed by seawater circulation through hydrothermal systems and seawater sulfate reduction and commonly carry near to zero or small negative Δ^{33}S values (Farquhar and Wing 2005; Ueno et al. 2008; Bekker et al. 2009; Jamieson et al. 2013).

At Shangani Mine, massive ore shows mass-dependent fractionation of sulfur isotopes, which is most easily attributed to a predominantly magmatic sulfur source. Alternatively, assimilation and subsequent sulfur isotope homogenization in a large crustally derived sulfur reservoir, erasing mass-independent fractionation of sulfur isotopes, might be responsible for this signal. Adding support to the former interpretation, disseminated sulfides in talcose serpentinite record evidence for mass-independent fractionation and plot along a mixing line between sedimentary and massive sulfides (Fig. 13b). It is plausible that the sulfur in the disseminated ore may represent a mixture of hydrothermally remobilized magmatic and sedimentary sulfur. Net-textured ore differs from disseminated ore only in slightly

lower $\delta^{34}S$ values, possibly due to mass-dependent equilibrium fractionation among sulfide minerals in the ore. Iron isotope values of Ni sulfides show a narrow range consistent with their predominantly magmatic iron source with the exception of two samples from talcose serpentinite that were likely strongly affected by Fe remobilization during hydrothermal activity.

At Trojan Mine, ore sulfides show a restricted range of positive $\Delta^{33}S$ values, inconsistent with a hydrothermal control over sulfide mineralization. Sulfides in metasediments, albeit secondary in origin, have slightly lower but still positive $\Delta^{33}S$ values, which could indicate that most, if not all, of the sulfur in the ore body was derived from a sedimentary rather than a magmatic source. Net-textured and disseminated ores and metasedimentary rocks lie on a distinct trend on the $\Delta^{33}S$ vs. $\delta^{34}S$ diagram (see Fig. 13a), indicating that during komatiite emplacement and assimilation of crustal sulfur to reach sulfur saturation sulfur isotope systematics of crustal source was inherited with little modification (cf. Hiebert et al. 2013). However, subsequent hydrothermal processes may have led to exchange between adjacent metasediments and Ni sulfide in komatiite. As a result of this exchange, S, Ni, and possibly other chalcophile elements (e.g., Cu) were added to the metasediments, and in other cases, sedimentary sulfur was introduced to komatiite. Iron isotope values of Ni sulfides from Trojan Mine have a narrow range suggesting that the iron inventory in komatiite is predominantly of mantle derivation.

Conclusions

A combination of petrological, geochemical, and structural data for the komatiite-hosted Trojan and Shangani Ni deposits in Zimbabwe indicates a complex geological history of ore-forming processes. Both deposits are associated with mineralized serpentinite bodies that occur in direct contact with sulfidic metasedimentary units. Multiple episodes of deformation and metamorphism have obliterated primary contact relationships and have modified ore mineralogy. Lithological contacts have been sheared, sulfide minerals have been remobilized, and ore bodies have been reoriented, inconsistent with the previously proposed model of simple, orthomagmatic nickel sulfide mineralization. We have, however, shown that the combination of multiple S, Fe, and Ni isotope data provides a "see-through" proxy to test whether magmatic or metamorphic–hydrothermal processes played a major role in ore genesis. For the Zimbabwean Ni sulfide deposits described herein, which are generally of low grade (0.5–0.6 % Ni), a magmatic origin with subsequent hydrothermal reworking is indicated. While massive nickel sulfides at the Shangani Mine deposit could have formed via high-temperature magmatic processes without the addition of sedimentary sulfur, assimilation of crustal sulfur was critical for the origin of net-textured and disseminated ore mineralization at Trojan Mine. The net-textured and disseminated ore mineralization at Shangani Mine could have been formed by post-magmatic hydrothermal processes with sulfur derived from a mixture of magmatic and sedimentary sources. This study indicates that the post-magmatic geological history of komatiite-hosted nickel sulfide deposits should not be discounted in genetic models for mineralization and that metamorphic and hydrothermal processes could be a controlling factor in the formation and upgrading of low-grade nickel sulfide deposits in terrains strongly affected by tectono-metamorphic overprints.

Acknowledgments AH acknowledges support by NAI International Collaboration Grant and NRF grant FA2005040400027. AB participation was supported by NSF grant EAR 05-45484, NAI award no. NNA04CC09A, and NSERC Discovery grant. Research by PD was supported by Stichting Schürmannfonds grants 1996-2003/13 and by extensive support by AngloAmerican PLC in allowing access to Zimbabwean Ni deposits. Support for OR and BG was provided by Europole Mer, ISOMAR, and NSF-EAR grant. We thank Charles Makuni for access to drill core; the Department of Geology, University of Zimbabwe for logistical support; and Emmanuel Ponzevera, Yoan Germain, and Celine Liorzou (PSO, Brest, France) for analytical support. Constructive comments by journal editor Bernd Lehmann, Boswell Wing, and two additional reviewers are gratefully acknowledged.

References

Anbar AD, Rouxel O (2007) Metal stable isotopes in paleoceanography. Annu Rev Earth Planet Sci 35:717–746

Archer C, Vance D (2006) Coupled Fe and S isotope evidence for Archean microbial Fe (III) and sulfate reduction. Geology 34:153–156

Arndt NT, Lesher CM, Czamanske GK (2005) Mantle-derived magmas and magmatic Ni–Cu–(PGE) deposits. Econ Geol, 100th Anniv 5:23

Baglow N (1986) The Epoch nickel deposit, Zimbabwe. In: Anhaeusser CR, Maske S (eds) Mineral deposits of Southern Africa. Geological Society of South Africa, Johannesburg, pp 255–262

Baglow N (1992) Bindura, geological survey of Zimbabwe, 1: 100,000 geological map sheet

Barnes SJ (2006) Komatiite-hosted nickel sulfide deposits: geology, geochemistry, and genesis. In: Barnes SJ (ed) Nickel deposits of the Yilgarn Craton. Soc Econ Geol Spec Publ 13. Society of Economic Geologists, Littleton, pp 51–97

Barrett FM, Binns RA, Groves DI, Marston RJ, McQueen KG (1977) Structural history and metamorphic modification of Archean volcanic-type nickel deposits, Yilgarn Block, Western Australia. Econ Geol 72:1195–1223

Barrie CT (1999) Komatiite flows of the Kidd Creek footwall, Abitibi Subprovince, Canada. Econ Geol Monographs 10:143–161

Bau M (1996) Controls on the fractionation of isovalent trace elements in magmatic and aqueous systems: evidence from Y/Ho, Zr/Hf, and lanthanide tetrad effect. Contrib Mineral Petrol 123:323–333

Bavinton OA (1981) The nature of sulfidic sediments at Kambalda and their broad relationships with associated ultramafic rocks and nickel ores. Econ Geol 76:1606–1628

Bekker A, Barley ME, Fiorentini ML, Rouxel OJ, Rumble D, Beresford SW (2009) Atmospheric sulfur in Archean komatiite-hosted nickel deposits. Science 326:1086–1089

Bekker A, Hofmann A, Rumble D, Rouxel O (2008) Sulfidic organic-rich shales in the Archean low-sulfate ocean: evidence for transient oxygenated conditions, enhanced volcanism, or low sedimentation rates? Geochim Cosmochim Acta 72(Supplement 1):A69

Bekker A, Holland HD, Wang PL, Rumble D III, Stein HJ, Hannah JL, Coetzee LL, Beukes NJ (2004) Dating the rise of atmospheric oxygen. Nature 427:117–120

Bennett SA, Rouxel OJ, Schmidt K, Garbe-Schönberg D, Statham PJ, German CR (2009) Iron isotope fractionation in a buoyant hydrothermal plume from the Mid-Atlantic Ridge at 5°S. Geochim Cosmochim Acta 73:5619–5634

Bolhar R, Van Kranendonk MJ, Kamber BS (2005) A trace element study of siderite–jasper banded iron formation in the 3.45 Ga Warrawoona Group, Pilbara Craton—formation from hydrothermal fluids and shallow seawater. Precambrian Res 137:93–114

Butler IB, Archer C, Vance D, Oldroyd A, Rickar D (2005) Fe isotope fractionation on FeS formation in ambient aqueous solution. Earth Planet Sci Lett 236:430–442

Cameron V, Vance D, Archer C, House CH (2009) A biomarker based on the stable isotopes of nickel. Proc Natl Acad Sci USA 106:10944–10948

Cas RAF, Beresford SW (2001) Field characteristics and erosional processes associated with komatiitic lavas: implications for flow behavior. Can Mineral 39:505–524

Chimimba LR (1984) Geology and mineralization at Trojan nickel mine, Zimbabwe. In: Buchanan DL, Jones MJ (eds) Sulfide deposits in mafic and ultramafic rocks. Institution of Mining and Metallurgy, London, pp 147–155

Chimimba LR, Ncube SMN (1986) Nickel sulfide mineralisation at Trojan mine, Zimbabwe. In: Anhaeusser CR, Maske S (eds) Mineral deposits of Southern Africa. Geological Society of South Africa, Johannesburg, pp 249–253

Chimimba LR (1987) The geology and mineralisation of Trojan nickel mine, Bindura area, Zimbabwe. Ph.D. thesis, University of Zimbabwe, Harare

Condie KC, Wronkiewicz DJ (1990) The Cr/Th ratio in Precambrian pelites from the Kaapvaal Craton as an index of craton evolution. Earth Planet Sci Lett 97:256–267

Cook DL, Clayton RN, Wadhwa M, Janney PE, Davis AM (2008) Nickel isotopic anomalies in troilite from iron meteorites. Geophys Res Lett 35, L01203

Cowden A (1988) Emplacement of komatiite lava flows and associated nickel sulfides at Kambalda, Western Australia. Econ Geol 83:436–442

Cowden A, Roberts DE (1990) Komatiite hosted nickel sulfide deposits, Kambalda. In: Hughes FE (ed) Geology of the mineral deposits of Australia and Papua New Guinea. Australasian Institution of Mining and Metallurgy, Melbourne, pp 567–581

Craddock PR, Dauphas N (2011) Iron and carbon isotope evidence for microbial iron respiration throughout the Archean. Earth Planet Sci Lett 303:121–132

Craig JR, Vokes FM (1993) The metamorphism of pyrite and pyritic ores: an overview. Mineral Mag 57:3–18

Dauphas N, Rouxel O (2006) Mass spectrometry and natural variations of iron isotopes. Mass Spectrom Rev 25:515–550

Dauphas N, Craddock PR, Asimow PD, Bennett VC, Nutman AP, Ohnenstetter D (2009) Iron isotopes may reveal the redox conditions of mantle melting from Archean to Present. Earth Planet Sci Lett 288:255–267

Dirks PHGM, Sithole TA (1996) Report on structural controls on nickel mineralisation at Shangani Mine. Consultant report. Anglo American Corporation, Zimbabwe

Dirks PHGM, Jelsma HA (1998) Silicic layer-parallel shear zones in a Zimbabwean greenstone sequence; horizontal accretion preceding doming. Gondwana Res 1:177–194

Donaldson MJ (1981) Redistribution of ore elements during serpentinization and talc–carbonate alteration of some Archean dunites, Western Australia. Econ Geol 76:1698–1713

Eckstrand OR (1975) The Dumont serpentinite: a model for control of opaque nickeliferous mineral assemblages by alteration reactions in ultramafic rocks. Econ Geol 70:183–201

Farquhar J, Wing BA (2003) Multiple sulfur isotopes and the evolution of the atmosphere. Earth Planet Sci Lett 213:1–13

Farquhar J, Wing BA (2005) The terrestrial record of stable sulfur isotopes: a review of the implications for evolution of Earth's sulfur cycle. In: McDonald I, Boyce AJ, Butler IB, Herrington RJ, Polya DA (eds) Mineral deposits and earth evolution. Geol Soc London Spec Publ 248. Geological Society of London, London, pp 167–177

Farquhar J, Bao H, Thiemens M (2000) Atmospheric influence of Earth's earliest sulfur cycle. Science 289:756–758

Farquhar J, Savarino J, Airieau S, Thiemens MH (2001) Observation of wavelength-sensitive mass-independent sulfur isotope effects during SO_2 photolysis: implications for the early atmosphere. J Geophys Res 106:1–11

Fiorentini ML, Bekker A, Rouxel O, Wing BA, Maier W, Rumble D (2012) Multiple sulfur and iron isotope composition of magmatic Ni–Cu–(PGE) sulfide mineralization from Eastern Botswana. Econ Geol 107:105–116

Fleet ME, Pan Y (1994) Fractional crystallization of anhydrous sulfide liquid in the system Fe–Ni–Cu–S, with application to magmatic sulfide deposits. Geochim Cosmochim Acta 58:3369–3377

Frost BR, Beard JS (2007) On silica activity and serpentinization. J Petrol 48:1351–1368

Gueguen B, Rouxel O, Ponzevera E, Bekker A, Fouquet Y (2013) Nickel isotope variations in terrestrial silicate rocks and geological reference materials measured by MC-ICP-MS. Geostand Geoanal Res. doi:10.1111/j.1751-908X.2013.00209.x

Gresham JJ, Loftus-Hills GD (1981) The geology of the Kambalda nickel field, Western Australia. Econ Geol 76:1373–1416

Groves DI, Korkiakoski EA, McNaughton NJ, Lesher CM, Cowden A (1986) Thermal erosion by komatiites at Kambalda, Western Australia, and the genesis of nickel ores. Nature 319:136–139

Grguric BA, Rosengren NM, Fletcher CM, Hronsky JM (2006) Type 2 deposits: geology, mineralogy and processing of the Mt. Keith and Yakabindie orebodies, Western Australia. In: Barnes SJ (ed) Nickel deposits of the Yilgarn Craton. Soc Econ Geol Spec Publ 13. Society of Economic Geologists, Littleton, pp 119–138

Guilbaud R, Butler IB, Ellam RM (2011) Abiotic pyrite formation produces a large Fe isotope fractionation. Science 332:1548–1551

Harrison NM (1969) The geology of the country around Ford Rixon and Shangani. Rhod Geol Surv Bull 61

Hiebert RS, Bekker A, Houle MG, Lesher CM, Wing BA (2012) Multiple sulphur isotopes as a method to evaluate sulphur sources and a potential exploration tool in the komatiite associated nickel-copper-(Platinum Group Elements) Hart Deposit, Shaw Dome, Abitibi Greenstone Belt, Ontario. Ontario Geological Survey, Open File Report 6280:45-1–45-9

Hiebert R, Bekker A, Wing BA, Rouxel OJ (2013) The role of paragneiss assimilation in the origin of the Voisey's Bay Ni–Cu sulfide deposit, Labrador: multiple S and Fe isotope evidence. Econ Geol (in press)

Hill RET, Barnes SJ, Gole MJ, Dowling SE (1995) The volcanology of komatiites as deduced from field relationships in the Norseman–Wiluna greenstone belt, Western Australia. Lithos 34:158–188

Hofmann A, Harris C (2008) Stratiform alteration zones in the Barberton greenstone belt: a window into subseafloor processes 3.5–3.3 Ga ago. Chem Geol 257:224–242

Hofmann A, Dirks PHGM, Jelsma HA (2002) Late Archaean clastic sediments (Shamvaian Group) of the Zimbabwe craton: first

observations from the Bindura–Shamva greenstone belt. Can J Earth Sci 39:1689–1708

Hofmann A, Dirks PHGM, Jelsma HA, Matura N (2003) A tectonic origin for ironstone horizons in the Zimbabwe craton and their significance for greenstone belt geology. J Geol Soc London 160:83–97

Hofmann A, Bekker A, Rouxel O, Rumble D, Master S (2009) Multiple sulphur and iron isotope composition of detrital pyrite in Archaean sedimentary rocks: a new tool for provenance analysis. Earth Planet Sci Lett 286:436–445

Hopwood T (1981) The significance of pyritic black shales in the genesis of Archean nickel sulfide deposits. In: Wolf KH (ed) Handbook of strata-bound and stratiform ore deposits, 9. Elsevier, Amsterdam, pp 411–468

Hronsky JMA, Schodde RC (2006) Nickel exploration history of the Yilgarn craton: from the nickel boom to today. In: Barnes SJ (ed) Nickel deposits of the Yilgarn Craton. Soc Econ Geol Spec Publ 13. Society of Economic Geologists, Littleton, pp 1–11

Hu GX, Rumble D, Wang PL (2003) An ultraviolet laser microprobe for the in situ analysis of multisulfur isotopes and its use in measuring Archean sulfur isotope mass-independent anomalies. Geochim Cosmochim Acta 67:3101–3118

Hulston JR, Thode HG (1965) Variations in the S33, S34, and S36 contents of meteorites and their relation to chemical and nuclear effects. J Geophys Res 70:3475–3484

Huh MC, Lazar C, Young ED, Manning CE (2009) High temperature fractionation of Ni stable isotopes between metal and silicates: constraints from experimental study at 800°C and 10kbar. 2009AGUFM.V11C1974H

Huppert HE, Sparks RSJ, Turner JS, Arndt NT (1984) Emplacement and cooling of komatiite lavas. Nature 309:19–22

Jamieson JW, Wing BA, Farquhar J, Hannington MD (2013) Neoarchaean seawater sulphate concentrations from sulphur isotopes in massive sulphide ore. Nature Geosci 6:61–64

Jelsma HA (1993) Granites and greenstones in northern Zimbabwe, tectono-thermal evolution and source regions. Ph.D. thesis, Free University of Amsterdam

Jelsma HA, Dirks PHGM (2000) Tectonic evolution of a greenstone sequence in northern Zimbabwe: sequential early stacking and pluton diapirism. Tectonics 19:135–152

Jelsma HA, Vinyu ML, Valbracht PJ, Davies GR, Wijbrans JR, Verdurmen EAT (1996) Constraints on Archaean crustal evolution of the Zimbabwe craton: a U–Pb zircon, Sm–Nd and Pb–Pb whole-rock isotope study. Contrib Mineral Petrol 124:55–70

Johnson CM, Beard BL, Roden EE (2008) The iron isotope fingerprints of redox and biogeochemical cycling in modern and ancient Earth. Annu Rev Earth Planet Sci 36:457–493

Konnunaho JP, Hanski EJ, Bekker A, Halkoaho TAA, Hiebert RS, Wing BA, Karinen TT (2013) The Archean komatiite-hosted, PGE-bearing Ni–Cu sulfide deposit at Vaara, eastern Finland. Miner Deposita. doi:10.1007/s00126-013-0469-0

Keays RR (1995) The role of komatiitic and picritic magmatism and S-saturation in the formation of ore deposits. Lithos 34:1–18

Killick AM (1986) The Damba sulfide nickel deposits, Zimbabwe. In: Anhaeusser CR, Maske S (eds) Mineral deposits of Southern Africa. Geological Society of South Africa, Johannesburg, pp 263–273

Lacroix S, Darling R (1991) Tectonized Cu–Ni deposits of the Aulneau–Redcliff area, Central Labrador Trough, Quebec. Econ Geol 56:718–739

Lesher CM (1989) Komatiite-associated nickel sulfide deposits. Rev Econ Geol 4:45–101

Lesher CM, Burnham OM (2001) Multicomponent elemental and isotopic mixing in Ni–Cu–(PGE) ores at Kambalda, Western Australia. Can Mineral 39:421–446

Lesher CM, Keays RR (2002) Komatiite-associated Ni–Cu–(PGE) deposits: mineralogy, geochemistry, and genesis. Canadian Institute of Mining, Metallurgy and Petroleum Special Volume 54:579–617

Maiden KJ, Chimimba LR, Smalley TJ (1986) Cuspate ore-wall rock interfaces, piercement structures, and the localization of some sulfide ores in deformed sulfide deposits. Econ Geol 81:1464–1472

Marshall B, Gilligan LB (1989) Durchbewegung structure, piercement cusps, and piercement veins in massive sulfide deposits: formation and interpretation. Econ Geol 84:2311–2319

McLennan SM, Taylor SR (1991) Sedimentary rocks and crustal evolution: tectonic setting and secular trends. J Geol 99:1–21

Miller MF (2002) Isotopic fractionation and the quantification of 17O anomalies in the oxygen three-isotope system: an appraisal and geochemical significance. Geochim Cosmochim Acta 66:1881–1889

Morse JW, Berner RA (1995) What determines sedimentary C/S ratios? Geochim Cosmochim Acta 59:1073–1077

Moubray RJ, Brand EL, Hofmeyr PK, Potter M (1979) The Hunters Road nickel prospect. In: Anhaeusser CR, Foster RP, Stratten T (eds) A symposium on mineral deposits and the transportation and deposition of metals: Geol Soc S Afr Spec Publ 5. Geological Society of South Africa, Johannesburg, pp 109–116

Moynier F, Blichert-Toft J, Telouk P, Luck JM, Albarede F (2007) Comparative stable isotope geochemistry of Ni, Cu, Zn, and Fe in chondrites and iron meteorites. Geochim Cosmochim Acta 71:4365–4379

Naldrett AJ (1981) Nickel sulfide deposits: classification, composition, and genesis. Econ Geol 75:628–685

Naldrett AJ (1989) Magmatic sulfide deposits. Oxford University Press, Oxford

Naldrett AJ (2004) Magmatic sulfide deposits: geology, geochemistry, and exploration. Springer, Berlin

Ono S, Beukes NJ, Rumble D (2009) Origin of two distinct multiple-sulfur isotope compositions of pyrite in the 2.5 Ga Klein Naute Formation, Griqualand West Basin, South Africa. Precambrian Res 169:48–57

Pavlov AA, Kasting JF (2002) Mass-independent fractionation of sulfur isotopes in Archean sediments: strong evidence for an anoxic Archean atmosphere. Astrobiology 2:27–41

Planavsky NJ, Rouxel O, Bekker A, Hofmann A, Little C, Lyons TW (2012) Iron isotope composition of some Archean and Paleoproterozoic iron formations. Geochim Cosmochim Acta 80:158–169

Polyakov VB, Clayton RN, Horita J, Mineev SD (2007) Equilibrium iron isotope fractionation factors of minerals: reevaluation from the data of nuclear inelastic resonant X-ray scattering and Mössbauer spectroscopy. Geochim Cosmochim Acta 71:3833–3846

Prendergast MD (2001) Komatiite-hosted Hunters Road nickel deposit, central Zimbabwe: Physical volcanology and sulfide genesis. Aus J Earth Sci 48:681–694

Prendergast MD (2003) The nickeliferous late Archean Reliance komatiitic event in the Zimbabwe craton—magmatic architecture, physical volcanology, and ore genesis. Econ Geol 98:865–891

Rice A, Moore JM (2001) Physical modeling of the formation of komatiite-hosted nickel deposits and a review of the thermal erosion paradigm. Can Mineral 39:491–503

Rouxel O, Dobbek N, Ludden J, Fouquet Y (2003) Iron Isotope Fractionation During Oceanic Crust Alteration. Chem Geol 202:155–182

Rouxel O, Bekker A, Edwards K (2005) Iron isotope constraints on the Archean and Paleoproterozoic ocean redox state. Science 307:1088–1091

Rouxel O, Shanks WC, Bach W, Edwards KJ (2008) Integrated Fe and S-isotope study of seafloor hydrothermal vents at East Pacific rise 9–10 degrees N. Chem Geol 252:214–227

Schuessler JA, Schoenberg R, Behrens H, von Blanckenburg F (2007) The experimental calibration of the iron isotope fractionation factor

between pyrrhotite and peralkaline rhyolitic melt. Geochim Cosmochim Acta 71:417–433

Severmann S, Lyons TW, Anbar A, McManus J, Gordon G (2008) Modern iron isotope perspective on the benthic iron shuttle and the redox evolution of ancient oceans. Geology 36:487–490

Siebert C, Nägler TF, Kramers JD (2001) Determination of molybdenum isotope fractionation by double-spike multicollector inductively coupled plasma mass spectrometry. Geochem Geophys Geosyst 2, 2000GC000124

Stone WE, Archibald NJ (2004) Structural controls on nickel sulphide ore shoots in Archaean komatiite, Kambalda, WA: the volcanic trough controversy revisited. J Struct Geol 26:1173–1194

Tanimizu M, Hirata T (2006) Determination of natural isotopic variation in nickel using inductively coupled plasma mass spectrometry. J Anal At Spectrom 21:1423–1426

Taylor SR, McLennan SM (1985) The continental crust: its composition and evolution. Blackwell, Oxford

Tomkins AG (2010) Windows of metamorphic sulfur liberation in the crust: implications for gold deposit genesis. Geochim Cosmochim Acta 74:3246–3259

Tomschi HP (1987) Goldvorkommen im Archaischen Harare–Bindura–greenstone belt, Zimbabwe: Zusammenhänge zwischen Lagerstättenbildung und greenstone belt Entwicklung. Ph.D. thesis, University of Köln

Trofimovs J, Davis BK, Cas RAF (2004) Contemporaneous ultramafic and felsic intrusive and extrusive magmatism in the Archaean Boorara Domain, Eastern Goldfields Superterrane, Western Australia, and its implications. Precambrian Res 131:283–304

Ueno Y, Ono S, Rumble D, Maruyama S (2008) Quadruple sulfur isotope analysis of ca. 3.5 Ga Dresser Formation: New evidence for microbial sulfate reduction in the early Archean. Geochim Cosmochim Acta 72:5675–5691

Viljoen MJ, Bernasconi A (1979) The geochemistry, regional setting and genesis of the Shangani–Damba nickel deposits, Rhodesia. In: Anhaeusser CR, Foster RP, Stratten T (eds) A symposium on mineral deposits and the transportation and deposition of metals. Geol Soc S Afr Spec Publ 5. Geological Society of South Africa, Johannesburg, pp 67–98

Viljoen MJ, Bernasconi A, van Coller N, Kinloch E, Viljoen RP (1976) The geology of the Shangani nickel deposit, Rhodesia. Econ Geol 71:76–95

Weyer S, Ionov DA (2007) Partial melting and melt percolation in the mantle: the message from Fe isotopes. Earth Planet Sci Lett 259:119–133

Williams DAC (1979) The association of some nickel sulfide deposits with komatiite volcanism in Rhodesia. Can Mineral 17:337–350

Williams DA, Kerr RC, Lesher CM (2011) Mathematical modeling of thermomechanical erosion beneath Proterozoic komatiitic basaltic sinuous rilles in the Cape Smith Belt, New Québec, Canada. Miner Deposita 46:943–958

Wilson JF, Nesbitt RW, Fanning CM (1995) Zircon geochronology of Archaean felsic sequences in the Zimbabwe craton: a revision of greenstone stratigraphy and a model for crustal growth. In: Coward MP, Ries AC (eds) Early Precambrian processes. Geol Soc Spec Publ 95, pp 109–126

Annexe 2 - Article soumis à Geochimica et Cosmochimica Acta, spéciation du Fe dans un nodule de manganèse récolté dans l'Océan Pacifique Sud : « Iron mineral diversity and stability trends in a South Pacific Gyre ferromanganese nodule"

Appendix 2 – Manuscript submitted to Geochimcia et Cosmochimica Acta : "Iron mineral diversity and stability trends in a South Pacific Gyre ferromanganese nodule"

Iron mineral diversity and stability trends in a South Pacific Gyre ferromanganese nodule

Matthew A. Marcus[1], Katrina J. Edwards[2], Sirine C. Fakra[1], Bleuenn Gueguen[3,4], Gregory Horn[2], Olivier Rouxel[3], Jeffry Sorensen[5], Brandy M. Toner[5]

[1]Advanced Light Source, Lawrence Berkeley National Laboratory, Berkeley CA USA 94720

[2]Departments of Biological Sciences and

Earth Sciences, University of Southern California, Los Angeles, CA, USA

[3]IFREMER, Centre de Brest, Unité Géosciences Marines, 29280 Plouzané, France

[4]Institut Universitaire Européen de la Mer, UMR 6538, Université de Brest, BP 80 F- 29280 Plouzané, France

[5]Department of Soil, Water, and Climate, University of Minnesota, St. Paul, MN, USA 55108

Submitted to Geochimica et Cosmochimica Acta

Abstract – Deep-sea ferromanganese nodules accumulate trace elements from seawater and underlying sediment porewaters during the growth of concentric mineral layers over long periods of time. Here we use micro X-ray fluorescence (μXRF) and electron microprobes to examine the fine-scale Fe mineralogy of a hydrogenetic South Pacific Gyre nodule. XRF mapping of the nodule reveals Mn, Ni, Cu-rich botryoidal microstructures along with an Fe-rich "matrix" in between. The “matrix” is found associated with V and Ti, whereas Ni, Cu, and Zn are co-located with Mn-rich botryoidal features. Bulk chemical and electron microprobe analyses of successive growth layers of the nodule further suggest that Ni, Co and to a lesser extent Zn are closely associated with Mn, with enrichment factors dependent on growth rate and metal availability during nodule formation. Two distinct regions of the nodule exhibiting differing morphologies and Mn-Fe-Co ratios were analyzed. The first region called "Outer", is closest to the surface and thus presumably more-recently deposited, while the second, named "Inner", lies deeper within the nodule and presumably consists of older deposits. X-ray absorption spectroscopy (μXAS), and X-ray diffraction (μXRD) measurements in both regions reveal the omnipresence of Fe oxyhydroxides in a wide variety of forms: goethite (α-FeOOH), goethite polymorphs feroxyhite (δ'-FeOOH), lepidocrocite (γ-FeOOH), and biogenic-like ferrihydrite. Fe speciation within the Fe-rich matrix shows a positive correlation between the abundance of stable Fe oxyhydroxides (goethite) and age (presumed) of deposition. Goethite is found to be more abundant in the Inner (older) than in the Outer (younger) deposits, 53 mol % and 18 mol %, respectively. The Outer matrix consists of biogenic-like ferrihydrite > lepidocrocite > goethite. However, the strong basal reflection expected for lepidocrocite was not detected, suggesting a very small coherent domain size in the basal direction. The Inner matrix consists of goethite > feroxyhite. The botryoids consist of variable mixtures of goethite and feroxyhite plus an end-member that does not fit to any combination of oxy(hydr)oxides attempted. These findings demonstrate the fine-scale complexity of natural marine Fe oxyhydroxide phases. We propose that Fe species evolve over time with currently unknown implications for biological processes and trace metal retention.

1. INTRODUCTION

Marine ferromanganese nodules (MFN) have attracted interest for many decades due to their economic potential and their possible use as recorders of the marine geochemical environment over millions of years (Calvert and Cronan, 1978; Koschinsky and Hein, 2003). These nodules are among the slowest-growing natural materials known, with growth rates measured in mm/My, and characterized by alternating layers of Mn-rich and Fe-rich phases (Banerjee et al., 1999; de Lange et al., 1992). On the other hand, they are made in large part of nanophase materials including ferrihydrite, a phase which in the laboratory ages to goethite in a matter of days or weeks. MFNs occur on the seafloor in water depths > 4000 m, usually below the calcite compensation depth and in well oxygenated environments. They generally form in inactive tectonic settings where very slow rates of sedimentation (<10 cm/1000 yrs) protect metals from dilution with background sediments. The abyssal plains, such as the Clarion/Clipperton zone in the Central Pacific Ocean have the most abundant nodule fields at the seafloor (Hein et al., 2013). Yet the mechanisms of formation, growth of MFN, and processes of metal enrichment remain poorly understood . Unlike ferromanganese crusts, that are deposited in shallower environments mostly on the flanks of seamounts by hydrogenous precipitation from dissolved trace metals in seawater, the sources of metals to MFNs include: (1) a hydrogenetic source, (2) a diagenetic source largely derived from the decay of organic matter , and (3) a hydrothermal source that has been recognized in some cases. The diagenetic source is generally considered predominant, indicating the important role of organic matter decay during early diagenesis processes in oxic sediments that supplies dissolved trace metals to the sediment porewaters (Heggie et al., 1986; Klinkhammer et al., 1982; Morford and Emerson, 1999; Sawlan and Murray, 1983). In addition, microorganisms are believed to play important roles in Mn- and Fe-cycling in sediments leading to the formation of MFN (Wang et al., 2009) .

Studying the Fe mineralogy of MFNs is difficult because MFNs are inhomogeneous and complex mixtures on the micron to millimeter scales, with many of the minerals in poorly-crystalline form. The use of traditional techniques such as powder XRD and ^{57} Fe Mossbauer spectroscopy has been often unsuccessful due to the poor crystallinity, distorted structures, and intergrowth with Mn oxides (Murad and Schwertmann, 1988). Further, most of the literature on MFN mineralogy is largely unreliable; for example, it was once typical to identify a Mn-rich phase as 'todokorite' based on optical microscopy and perhaps a bulk XRD pattern. Synchrotron microprobe (μXRF, μXAS and μXRD) techniques allow us to tackle these issues on unprocessed samples (Manceau et al. 2002). To date, much useful information has been gained on the incorporation of trace elements in nodule nanophase oxides, using nodules and other marine ferromanganese oxides as natural long-term sorption laboratories (Marcus et al., 2004b; Takahashi et al., 2007; Takahashi et al., 2000).

Although the properties of Mn minerals and trace elements in MFNs have been examined many times over the past decades (Aplin and Cronan, 1985; Banakar and Tarkian, 1991; Cronan, 1975; Dymond et al., 1984; Elderfield et al., 1981; Martin-Barajas et al., 1991; Verlaan et al., 2004; Yoshikawa, 1991) , there has been comparatively little research on Fe oxyhydroxide phases. By contrast, iron is often the most or 2nd-most abundant metal in MFNs, and Fe-bearing minerals are known to be reactive serving as host to trace elements. We propose that the fine-scale mineralogy of MFN Fe-bearing phases plays a major role in

trace element uptake by MFNs, and may provide clues on the processes that control mineral precipitation/dissolution, aging, and trace element reactivity over time. For instance, rare earth elements present in MFN are mostly hosted by the Fe-phases (Elderfield et al., 1981). Here, we use μXRF, μXRD and Fe K-edge μXAS to decipher the chemical speciation and trace element uptake of Fe within mineral layers of a MFN from the South Pacific Gyre. In addition to familiar phases such as poorly-crystalline ferric oxyhydroxide (ferrihydrite family) and goethite, we also find evidence for an unusual Fe oxide in which there are disproportionately many edge-sharing FeO_6 octahedra when compared to ferrihydrite or even goethite. In addition, we find that the material deep inside the nodule, which is presumably older than that at the surface, contains more goethite, as one might expect from aging of disordered Fe oxyhydroxides.

In order to relate the Fe speciation to locations within the nodule, we first characterize the nodule in terms of bulk chemistry and patterns of element distribution. We then analyze the two main regions of the nodule, named Outer (recent deposition) and Inner ((older deposition). In each region, a recurring pattern is observed: 1) botryoidal microstructures composed of banded Mn-rich material, and 2) an Fe-rich matrix found between botryoidal features. Subsequently, we describe synchrotron data acquisition and analysis methods, after which we report the Fe mineralogy of the nodule as a function of location (as a proxy for time) and discuss the patterns of co-located trace elements with Fe oxyhydroxides.

2. Nodule description and methods

2.1 Description of the sample

2.1.1 Sample collection

The nodule was collected December 24, 2006 (D'Hondt et al., 2009), at 26°03.09'S, 156°53.65'W, at 5126 m water depth during the Knox02RR cruise of the RV Roger Revelle, using a multicore sampler. The site, SPG-2, is characterized as follows: SPG-2 is located in a region of abyssal hill topography trending roughly NE-SW (065°). Two populations of abyssal hill topography are present. The larger hills have relief ranging from 300-400 m with a spacing of ~ 20 km. The smaller hills are superimposed on the larger abyssal hills and have a relief of about 50-100 m and a spacing of about 5-6 km. Several small seamounts (2 km-wide, 300 m-high) are scattered about the region. The largest seamount is located ~3-4 km south of the coring site.

The coring site is located within magnetic polarity Chron 34n so the crustal age may range from 84 - 124.6 Ma (Gradstein and Ogg, 2002). Based on a tectonic reconstruction of the region (Larson et al., 2002), the crust was accreted along the Pacific-Phoenix spreading center ~95 Mya at ultra-fast spreading rates (~90 km/My, half-rate). The sediment on which the nodule rested (half-buried) was homogeneous dark brown clay with micronodules and no microfossils seen on a smear slide. The nodule described in this study was approximately spherical (diameter was 65 – 68 mm at nine points along three axes) and was observed shipboard to be partially buried in sediment at the top of the sediment core. However, the actual orientation of the nodule at the seafloor is not known. The sample was collected as part of a much larger effort to document the nature of life in slowly-accumulating sediments of low primary productivity and great age.

A polished petrographic thin section of the nodule was prepared by Spectrum Petrographics, Inc. The nodule was embedded in 3M Scotchcast #3, mounted on a fused silica slide with Loctite Impruv 363 adhesive, and sectioned to a 30 μm slice, using a diamond electron-microprobe polish. In addition, 1mm-thick sections were made and cut into 2mm-wide "matchsticks" for X-ray tomography, wet-chemical analysis and μXRD.

2.1.2 Chemical composition

The nodule sample “matchstick” was sectioned length-wise into 10 sub-samples using a microdrill device (Micromill®). Each fraction was dissolved in a mixture of 6 mL concentrated HNO_3 (sub-boiled) and 2 mL concentrated HF (Trace metal or Optima grade) to ensure complete dissolution of silicate phases. Solutions were evaporated on hot plates at 80°C. Dry residues were then dissolved in 5 mL concentrated HNO_3 and 5 mL 6 M HCl and evaporated to dryness at 80°C. This last step was repeated once to ensure completed dissolution of non-siliceous materials including fluorides that could have formed during the first digestion step. Archive solutions were kept in 5 mL 6M HCl. Elemental concentrations were measured on an ICP-AES (HORIBA Jobin YVON, ULTIMA 2) operated by Pôle-Spectrométrie-Océan (PSO, Ifremer/IUEM, Brest, France). Calibration of the concentrations during analysis was done using a multi-elemental solution. A set of georeference nodule materials (USGS Nod P1 and Nod A1) was also analyzed along with the samples.

The fine-scale elemental composition and mineral textures was examined with electron microprobe analysis using a JEOL JXA-8900 Electron Probe Microanalyzer and wavelength-dispersive spectrometer at the Electron Microprobe Laboratory, Department of Earth Sciences, University of Minnesota.

The chemical compositions found for SPG-2 nodule are shown in **Table 1** (ICP-AES) and **Tables EA1 and EA2** (electron microprobe). Due to the process involved in micro-drilling and ICP-AES analysis, the nodule material could not be accurately weighed. Therefore, for consistency and comparison with electron microprobe geochemical data, we did not report ICP-AES data in microgram of element per gram of rock as it is the common usage in geochemistry, but instead data were normalized to Fe and expressed in grams of element per gram of Fe (Table 1).

Geochemical composition measured by Electron Microprobe Analyzer (EMPA) were carried out on two types of transects as shown in **Figure 1** (a whole nodule transect and two micro-transects). EMPA data are expressed in wt%, but note that the sum of the weights is not equal to 100% since nodules are porous materials, rich in H_2O (hydrogen is present in the most common Fe- and Mn-phases) and CO_2. Data of the transect made through the whole nodule section is reported in **Table EA1** and may be considered as bulk data comparable to bulk ICP-AES analyses. Based on **Figure 2** (*v.i.*) we defined in the nodule section the limit between the “Outer” region (Mn-rich structures) and the “Inner” region (e-rich structures). On the other hand, EMPA data acquired in two micro-transects along mineral structures of the Outer and Inner regions of the nodule (**Figure 1**) are reported in **Table EA2** and represent local variations of transition elements concentrations in the two distinct regions of the nodule.

2.1.3 Nodule morphology: Matrix and botryoidal features

Electron microprobe analysis was performed on two areas of the nodule thin section, shown in backscatter scanning electron micrographs in **Figure 1**. In both areas, concretions with layered growth and a “botryoidal” morphology are surrounded by a porous "matrix", as previously reported by (Halbach et al., 1981). .

In order to study the morphology and element distributions in more detail micro X-ray fluorescence (μXRF) maps were acquired at Beamline 10.3.2 of the Advanced Light Source (Marcus et al., 2004a). For a general survey, a long map was acquired over a strip 20 mm long by 1mm wide, with 20 μm pixels. All μXRF maps on the nodule were acquired at 10 keV, using dwell times of 30-50 ms and pixel sizes of 5-10 μm. Fluorescence emission signals for Fe, Mn, Ni, Cu, Zn, Ti, Ca, and additionally in some areas Ce, V, P and Co were recorded with a 7 element Ge solid state fluorescence detector (Canberra).

2.2 XAS and XRD data collection and analysis

X-ray absorption spectra at the Fe K-edge were recorded at beamline 10.3.2 at the Advanced Light Source in fluorescence mode on selected spots on the μXRF maps. . The energy was calibrated with respect to Fe foil, whose inflection-point energy was taken to be 7110.75 eV. Data were calibrated, deadtime-corrected, pre-edge subtracted and post-edge normalized using custom LabVIEW programs available at the beamline website. The data range for micro X-ray absorption near edge structure (μXANES) spectroscopy was 100 eV below up to 300 eV above the edge, while micro extended X-ray absorption fine structure (μEXAFS) spectroscopy data were taken up to 500 eV above the edge. Micro-XANES spectra were fit by least-square linear combination (LCF) to a large Fe database (Marcus et al., 2008). Over-absorption is significant in the more Fe-rich spots, and is taken as a free parameter in a simple model (planar, thick sample). Since the cited paper was published, a number of new spectra were added, including one for feroxyhite, a potentially-important species for nodules. This sample was prepared by the method of Schwertmann and Cornell (Schwertmann and Cornell, 2000) and verified by powder XRD at the Characterization Facility, University of Minnesota, using a Siemens D-500 Diffractometer with cobalt source. The observed [Si]/[Fe] ratios in the nodule are low enough to rule out the presence of a significant (>10%) amount of clays or most other silicates, so these were omitted from the set of fitting references.

Micro-EXAFS spectra were analyzed with $k^3\chi(k)$ weighting, out to k = 11Å^{-1}. For those spectra in which over-absorption was significant, we performed LCF of the XANES spectra to estimate the amount of over-absorption, applied that correction to the post-edge normalized spectra, and extracted the EXAFS signal from these corrected spectra. EXAFS data were then fitted using either linear combinations of reference EXAFS spectra or by shell-by-shell fitting using Artemis (Newville, 2001; Ravel and Newville, 2005). For the latter, the structures of goethite and lepidocrocite were used to create FEFF6l input files from which to extract Fe-O and Fe-Fe paths out to 3.5.Å, which encompasses face, edge, and corner-sharing FeO_6 octahedra. This analysis is similar to the polyhedron-centered analysis which was done for poorly-ordered biogenic Fe oxide (Toner et al., 2009). For some of the spectra, we used a shell-by-shell fitting approach based on experimental amplitudes and phases (feroxyhite and lepidocrocite, for Fe-O and Fe-Fe paths), which gave results consistent with the Artemis fitting.

Micro XRD patterns were recorded with a Bruker SMART6000 CCD at 17keV (λ = 0.7293 Å) and 240 sec. acquisition time. The patterns were radially-integrated and calibrated using alumina powder and fit2D software (Hammersley, 1997). Micro XRD patterns were recorded at the μXAS spot locations on the thin sections, and on a nearby blank spot on the silica substrate so as to background substract the data. In order to improve the sensitivity of the XRD, we also mounted a thick section in such a way that the beam passed through ~1 mm of sample without striking the substrate.

3. Results

3.1 Trace elements associated with Fe

A tricolor map illustrating the distributions of Fe, Mn and Ni is shown in **Figure 2**, along with graphs of the Fe, Mn and Ni signals averaged across the width of the map. A clear transition both in appearance and elemental ratios toward the right-hand-side (Inner) can be observed.. While the Fe signal is roughly constant over the length of the map, the Mn and Co (not shown) signals decreases almost two-fold towards the right (Inner). Also, the rhythmic pattern of growth of the "botryoidal " features, which is obvious in the Outer region and delimited by Ni-rich streaks, is much less clear in the Inner region (**Figures 2,3**). The Fe-rich matrix in between the "botryoidal microstructures" is also more prominent in the Inner region. These distribution patterns hold for other transects taken from outside to inside of the nodule and form the basis for our definition of "Inner" vs. "Outer" regions. Some trace elements, notably Ti, V and, to a lesser extent, Zn, are associated with Fe in the nodule. XRF maps of the Inner and Outer regions are displayed in **Figure 3**. For Ti and V, the correlation with Fe is nearly perfect. The distribution of Zn, on the other hand, shows some features in common with that of Fe, in particular, an enrichment in the "matrix" areas. These patterns of distribution suggest but do not prove that Ti and V are bound to or incorporated in Fe-containing phases, and Zn in the matrix material in particular. Previous studies have shown that Fe oxide phases such as goethite (Manceau et al., 2000) and ferrihydrite (Waychunas et al., 2002) can sorb Zn, which is associated with Fe in our nodule. Thus, we can infer that Fe oxides have important effects on the trace-element geochemistry in MFN.

Figure 4 is a ternary diagram representing Mn, Fe and (Ni+Co) x 10 commonly used for distinguishing between the hydrothermal, hydrogenetic and diagenetic nature (shown by the colored fields) of Fe/Mn-rich deposits. In this diagram we represented EMPA data of the whole nodule transect, bulk ICP-AES measurements made on the nodule section and selected literature data from Halbach et al. (1981) (green and grey fields in **Figure 4**) from North and South Pacific Oceans are shown in the diagram for comparison. Common northern Pacific nodules have generally an important diagenetic contribution as shown by the trend towards higher Mn/Fe and Ni/Fe, whereas our SPG-2 nodule display a trend towards an important hydrogenetic contribution (lower Mn/Fe and Ni contents). Together with (Halbach et al., 1981) data on Southeastern Pacific nodules, bulk analyses of our SPG nodule seems to indicate that South Pacific nodules are more hydrogenetic than North Pacific nodules. This is consistent with the documented low flux of organic matter to the seafloor of the South Pacific Gyre (Jahnke, 1996) possibly reducing diagenetic contributions to the growth of the SPG-2 nodule.

Plots in **Figure 5** show EMPA data acquired along two micro-transects in the Outer and Inner region of the nodule (**Figure 1** and **Table EA2**). Clear correlations are displayed by Ni/Fe and Co/Fe ratios versus Mn/Fe (**Figure 2b**, panels A and B) indicating that Ni and Co are

hosted by Mn-rich minerals. In contrast, the scatter in the Zn/Fe vs Mn/Fe diagram (**Figure 5**, panel C) suggest that Zn may be associated with both Mn and Fe mineral phases. The inverse correlation between Ti/Fe and Mn/Fe ratios (**Figure 5**, panel D) in the Inner nodule region transect indicates that Ti is mostly associated with Fe. Bulk ICP-AES analyses do not show significant variations in metal/Fe or metal/Mn ratios (**Table 1**) across the nodule transect, suggesting homogenization of Fe and Mn-rich phases at the scale of sampling intervals (1 to 3 mm).

3.2 Matrix

The EXAFS data (Fourier transform) and fits are shown in **Figure 6** along with XRF maps indicating the spots at which the data were taken. The spectra did not differ substantially between the various locations within a given region. The bottom Fourier transform plot shows the data for the Inner spots and a comparison with a linear-combination fit using 39% feroxyhite and 53% goethite. As with all such least-squares linear-combination fits, the data do not rule out the presence of a few percent of other species. The phase of higher-shell peaks agrees with those in the fit out to 6 Å, presumably due to the long-range order of crystalline goethite. While μXRD was not done on these specific spots, patterns taken at other matrix spots confirm the presence of goethite.

The Outer matrix is typified by the spectrum and fit shown in the top half of **Figure 6**. This spectrum fits well to 28% lepidocrocite, 39% disordered biogenic oxide and 18% goethite. The XANES also fits to the same three minerals, but in proportions of 46%, 21% and 30%, respectively. However, no diffraction measurements on any spot show the strong basal (020, *d*= 6.26Å) reflection expected for lepidocrocite (for example, **Figure 7**). Other lepidocrocite reflections come close enough to those from other phases such as goethite to make their identification uncertain. The basal reflection, however, is one of the strongest and should therefore appear if well-crystalline lepidocrocite were common in our samples. We refer to this reflection as 'basal' because lepidocrocite has a layered structure consisting of sheets of edge-sharing octahedra, with the conventional *b*-axis as the layering direction.

The feature in the EXAFS spectrum which seems to point to lepidocrocite is the prominent peak at 2.7 Å (as indicated in **Figure 6**), which corresponds to edge-sharing FeO_6 octahedra. The lepidocrocite structure consists of layers of edge-sharing octahedra. The inter-layer spacing gives rise to the basal reflection which is not found by μXRD in our samples at any spot. Thus, what the XAS really indicates is that the material has a large fraction of edge-sharing octahedra relative to ferrihydrite or goethite. Shell-by shell fitting yields an average Fe-O distance in the first shell of 2.01 ± 0.015 Å, an Fe-Fe shell 3.06 ± 0.03 Å with a coordination number between 2 and 6 (highly uncertain due to correlation with $\Delta\sigma^2$), and a weak third Fe-Fe shell at 3.38 ± 0.04 Å. The coordination number of this shell is extremely uncertain due to correlation with $\Delta\sigma^2$, but the fit is significantly better with this shell included. The Fe-Fe distances correspond nicely to edge- and corner-sharing octahedra. By comparison, the edge-sharing distance in lepidocrocite is 3.067 Å and the corner-sharing distances in goethite are 3.30 Å and 3.47 Å. In addition, shells at apparent distances of ~3.6 Å and 4.6 Å match those experimentally found for lepidocrocite, and correspond to Fe-Fe distances within the layers ((0,0,1) and (1,0,1) vectors). Taking the EXAFS evidence and the apparent lack of the lepidocrocite (002) reflection together suggests a picture of lepidocrocite nanoparticles which are thin in the *b*-direction but transversely large enough to show the high shells in EXAFS. Note that the biogenic oxide we used as a reference material also has a

relatively large ratio of edge-sharing to corner-sharing octahedra, but the overall intensity of that shell is smaller than what we find for the lepidocrocite-like material.

3.3 Botryoidal Microstructures

The botryoidal material varies between spots within the nodule. We analyzed spots in both Inner and Outer regions, for which XRF maps are shown in **Figure 8**. Principal components analysis (PCA) suggests that the individual spectra may be represented as weighted sums of signals from two materials, of which one is similar to or the same as that found for the Inner matrix, i.e. mostly a combination of feroxyhite and goethite. The other material, referred to as "botryoidal", has a spectrum which does not fit to a sum of our reference spectra. Spots 5 and 1 in the Inner map are the best examples of the "botryoidal" Fe material, as seen from PCA. The EXAFS signal and Fourier transform for Spot 5 are shown in **Figure 9**. There are strong peaks at distances similar to those found for corner- and edge-sharing octahedra.

The best fit we have found for this spectrum contains four contributions. One is an Fe-O shell represented as the Fe-O first neighbor from feroxyhite. While the Fe-O shell is actually split, the data do not cover a long enough *k*-range to resolve this splitting, and the first shells of our models are well-represented as single shells. Next is an Fe-Fe shell at 3.04 ± 0.038Å with a coordination number (CN) of 2.3-9. The distance found for this shell is consistent with edge-sharing octahedra such as those found in lepidocrocite (3.06 Å), whose edge-sharing peak we used as an experimental reference. This contribution requires an additional mean-square relative displacement (MSRD, second moment of the distance distribution) of 0.014-0.047 $Å^2$, beyond that found in lepidocrocite. This is a significant dispersion, which may reflect an unresolved splitting. The large error bars on this number and the CN reflect parameter correlation between the two.

It was found necessary to add a contribution from goethite, which was used without any adjustment except for amount and included all shells out to 3.5 Å. The result showed that 10-25% of the Fe in the sample had to be assumed to be in the form of goethite, though it is possible that some of the other oxides would provide an acceptable fit in this role. Note that the coordination numbers quoted above and below for non-goethite Fe-Fe shells is the average over all Fe atoms; they should be divided by 1-(goethite fraction) to get the Fe-Fe CNs in the 75-90% of the spot 5 material that is not goethite.

A fit with only these three contributions always showed a discrepancy in the FT at around 3.3 Å (apparent). While the phase would match, the amplitude did not. To solve this problem, an additional Fe-Fe shell at 3.45 ± .0.04Å (CN 0.25-0.9) was added to the fit. This distance is comparable to the longer corner-sharing distance in goethite (3.47 Å), thus we interpret it as coming from corner-sharing octahedra in the non-goethite fraction. The MSRD of this shell was assumed to be the same as that in the reference lepidocrocite edge-sharing shell, in order to reduce the number of free parameters.

The result of fitting is shown in the bottom panel of **Figure 9**, as the FT magnitude and imaginary part of the data compared with the fit, and in the top as the FT magnitudes of the individual components.

4. Discussion

Our results suggest that the Fe speciation in the hydrogenetic South Pacific Gyre nodule is considerably more complex than expected and quite different from the uniform amorphous FeOOH 'background' component typically discussed in the literature. Fe oxyhydroxides in the SPG-2 nodule were present in a wide variety of forms – goethite (α-FeOOH), goethite polymorphs feroxyhite (δ'-FeOOH) and nano-lepidocrocite (γ-FeOOH), and biogenic-like ferrihydrite. Each of these phases is thought to form under different environmental conditions (pH and Eh, as examples). Therefore, although MFNs form in well-oxygenated environments such as abyssal plains, the diversity of phases observed may reflect changes in the deep-sea environment at the sediment-water interface or mineral transformation processes over time (Schwertmann and Cornell, 2000).

The major trend in Fe speciation within the Matrix material is a positive correlation between the abundance of stable Fe oxyhydroxides (goethite) and age (presumed) of deposition. Specifically, Fe EXAFS data reveal that goethite is more abundant in the Inner (older) deposits than in the Outer (younger) deposits, 53 mol % and 18 mol %, respectively. Therefore, the differing compositions and environments present in the SPG-2 nodule make for a series of different 'test conditions' for the crystallization and coarsening of natural Fe oxyhydroxides along a continuum from modern biogenic Fe oxyhydroxides to goethite.

The Outer matrix consists of goethite < lepidocrocite < biogenic-like ferrihydrite. Approximately 1/3 of the Outer matrix is a disordered lepidocrocite-like Fe oxyhydroxide with a large number of edge-sharing octahedra. Lepidocrocite was not detected by XRD, and may occur in thin platelets yielding no basal reflection. Lepidocrocite is typically observed in low oxygen environments with Fe^{2+} present, and is meta-stable with respect to goethite (Schwertmann and Cornell, 2000). The biogenic-like ferrihydrite phase also has an excess of edge-sharing octahedra. In general, the Outer matrix is characterized by poorly-crystalline Fe oxyhydroxide phases consistent with those observed in modern low-temperature, deep-sea deposits where microbial activity is evident (Toner et al., 2012; Toner et al., 2009). Microbial activity is not a necessary condition for the precipitation of poorly-crystalline phases. For example, strongly sorbing ligands such as oxyanions of P, Si, and As produce Fe(III) precipitates with these characteristics, and transition metal impurities are known to slow recrystallization processes (Cornell et al., 1992). However, the structural characteristics and abundance of meta-stable phases suggests that the younger nodule deposits have precipitated in the presence of: 1) Fe^{2+} (lepidocrocite-like phase), and 2) metals, ligands or under the influence of biology (biogenic-like ferrihydrite).

The Inner matrix, can be understood as a mixture of two FeOOH polymorphs, feroxyhite and goethite. In the laboratory, feroxyhite is a meta-stable phase generated by very rapid oxidation of Fe^{2+} in alkaline medium (Chukhrov et al., 1977). In the field, feroxyhite is observed in the pore spaces of sediments hosting Fe^{2+}-rich waters (Carlson and Schwertmann, 1980). In poorly drained soils, where ferrihydrite, lepidocrocite, goethite, and feroxyhite are observed within the profile, feroxyhite is associated with the Mn oxide vernadite (Birnie and Paterson, 1991). While the conditions of feroxyhite formation in laboratory and field studies are consistent one another and with what we know of the SPG-2 nodule – precipitation in pore spaces near Mn-rich phases – there is little consensus in early literature regarding the stability relationship between feroxyhite and goethite. Chukhrov et al. proposed that feroxyhite is meta-stable with respect to goethite (Chukhrov et al., 1977). However, Carlson and Schwertmann concluded that feroxyhite does not recrystallize to form goethite, but that the two phases form under different conditions, namely fast oxidation of Fe^{2+} (feroxyhite) versus slow precipitation of Fe^{3+}(goethite) (Carlson and Schwertmann,

1980). More recently, the stability, and transformation time, for pure oxyhydroxides with respect to hematite in the presence of trace Fe^{2+} was established as: ferrihydrite ≤ feroxyhite < lepidocrocite < akaganeite << goethite (Lu et al., 2011). In agreement with Lu et al., when particle size and mineral surface hydration are considered, goethite was most often the stable phase relative to coarse hematite over a wide range of surface area/particle size conditions; however, at high surface area values ferrihydrite can be the stable phase (Navrotsky et al., 2008). These results may indicate that feroxyhite precipitated from a sediment source (fast oxidation of Fe^{2+}), while goethite precipitated in contact with ambient seawater (slow precipitation of Fe^{3+}). In this conceptual framework, the presence of feroxyhite would reflect the "diagenetic" source of metals (sediment porewaters), while goethite would be indicative of the "hydrogenetic" source of metals (seawater dissolved trace metals).

The botryoidal material is a combination of crystalline minerals similar to those found in the matrix, plus another material whose most distinctive feature is the presence of edge-sharing octahedra with considerable dispersion in Fe-Fe distance. In the botryoidal microstructures, as opposed to the matrix, there is considerable Mn in addition to the Fe. Thus, the possibility should be considered that we have a mixed oxide in which the nearest cation neighbor to Fe is not always Fe but is sometimes Mn, such as an "Fe-vernadite". However, the botryoidal material need not be a single phase, and could include Fe-rich and Mn-rich material too finely intergrown to have been resolved in this study. If the two phases have differing Fe-Fe distances, then the resulting average EXAFS could show a large MSRD. However, because linear-combination fitting did not produce a match, at least one of these phases must be something not found in our spectral database. Consistent with intergrowth between Mn and Fe minerals, the botryoidal material includes several percent of other transition metals such as Cu, Ni, Co and Zn, which are known to be associated primarily with Mn oxide minerals in hydrogenetic ferromanganese crusts (Halbach and Puteanus, 1984; Hein et al., 2003; Koschinsky and Halbach, 1995; Koschinsky and Hein, 2003; Koschinsky et al., 1997).

For the SPG-2 nodule, trace element distributions were observed by μXRF mapping. Trace elements Ti and V are co-located with the Fe-rich matrix materials of the Inner and Outer nodule. In contrast, transition metals Ni, Cu, and Zn are co-located with Mn within the botryoidal materials of the Inner and Outer nodule. These observations are consistent with a vast literature base demonstrating the affinity of oxyanions such as V for Fe oxyhydroxide minerals, and the affinity of divalent cations for Mn oxide minerals, in laboratory experiments and field observations (Brown et al., 1999; Cornell and Schwertmann, 2003; Nicholson and Eley, 1997). More specifically, our μXRF and μXAS observations build on previous investigations of hydrogenetic MFNs that employed operationally defined, wet-chemical approaches. A strong correlation between Co, Ni, Cd, Zn, Cu and Mn in a "δ-MnO_2" phase was observed in hydroxylamine hydrochloride leaching experiments (Koschinsky and Halbach, 1995). Similarly, Ti and V were correlated with an "amorphous FeOOH" phase that dissolved in the presence of oxalic acid (Koschinsky and Halbach, 1995). Our X-ray microprobe observations confirm the interpretation of leaching experiments by showing that Ti and V are co-located with the Fe phases of the matrix throughout the hydrogenetic SPG-2 nodule. However, the existing X-ray microprobe observations fall short of defining the exact nature of the association (e.g. adsorption, co-precipitation) and these aspects of nodule geochemistry will be examined by Ti and V spectroscopy in the next phase of our research.

5. Conclusions

The results presented here provide a framework for addressing the degree to which deep-sea ferromanganese nodules are archives of past ocean conditions. First, we observe a transition from low goethite in the Outer matrix to higher in the Inner matrix that is consistent with transformation of lepidocrocite- and ferrihydrite-like phases to goethite over time. One interpretation of these data is that the incipient Fe matrix is composed of poorly ordered ferrihydrite and lepidocrocite. Therefore, the initial trace element uptake signatures should be determined by the characteristics of the incipient phases and the composition of the seawater at the sediment-water interface. As these phases are buried within the nodule, we observe evidence for mineral transformation. A central question then arises: does the incipient trace element signature persist through mineral transformation processes?

It is known that trace metal associations (Ni, Zn) with Fe minerals (goethite) will change in the presence of Fe^{2+} under laboratory conditions, especially under advective flow conditions (Frierdich and Catalano, 2012; Frierdich et al., 2011). Ferrihydrite in particular has been shown to incorporate additional Cu and Zn during Fe^{2+} catalyzed recrystallization, as reviewed by (Latta et al., 2012). With respect to the goal of using metal speciation and isotope signatures as (biogeo) chemical proxies, processes such as these may result in a blurring or over-writing of signatures. The observation that transition metals such as Ni, Mn, and Co slow the rate of recrystallization of poorly ordered Fe oxyhydroxides is consistent with the slow rate of recrystallization observed in the present study, so perhaps a measurable signature is retained. However, Ni speciation changes have been observed as a result of slow recrystallization processes (Cornell et al., 1992), and must be addressed to develop the trace metal proxies or past ocean conditions. From the Mn perspective, it has also been demonstrated in laboratory studies that Ni uptake by the Mn oxide birnessite is pH dependent, but also reversible, calling into question its use as a paleo-pH indicator (Peacock, 2009).

Laboratory research suggests that Fe and Mn minerals and trace element interactions with those minerals are dynamic in aqueous systems. For MFNs, it is clear that minerals and trace elements will change in response to changing seawater conditions, but are there chemical processes or physical barriers in place to silence or mute the modern seawater signals? Next research steps will include measurements that address the porosity, permeability, and pore water characteristics of nodules to better constrain the potential of MFNs to retain geochemical signatures of past ocean conditions. Finally, the over-arching trends of greater abundance of Mn-rich botryoidal materials in the Outer (younger) regions of the nodule, and greater abundance of Fe-rich matrix materials in the Inner (older) regions has the potential to reveal patterns in changes in oxidation-reduction conditions at the sediment-seawater interface. In future research, we propose to examine these trends through the application of fine-scale age dating of the nodule and redox-sensitive metal isotope proxies such as iron isotopes.

6. Figures and table captions

Figure 1. Backscatter SEM images showing Outer and Inner regions. Red lines and crosses show locations of electron microprobe analyses displayed in Figure 5.

Figure 2. Survey of the sample from Outer (left) to Inner. Top: Visible-light micrograph of the sample. Middle: Tricolor map showing Fe (red), Mn (green) and Ni (blue) in a strip

extending from the surface of the nodule (left). Bottom: Averages Fe, Mn and Ni counts across the map. Ni counts are multiplied by 10 relative to Mn and Fe, for clarity. The micrograph and map are to the same field of view as the plot.

Figure 3. µXRF maps of representative Inner and Outer regions showing several elements. Note that the distributions of V and Ti almost precisely match that of Fe, and that Zn is somewhat enriched in the matrix areas. Brighter pixels correspond to higher concentrations. Scale bars are 500 µm.

Figure 4: Ternary diagram of Fe, Mn and (Ni+Co) x 10 (adapted from Bonatti et al., 1972) of Electron Microprobe data acquired along a transect through the whole nodule and bulk ICP-AES measurements on the nodule section. The distinction between "Inner" and "Outer" regions is explained in Table EA2 and in the text. This diagram allows one to distinguish between three different fields (hydrothermal, hydrogenetic and diagenetic) that indicate the predominant origin of the Fe/Mn-rich deposits formation. Selected literature data from Southeast Pacific nodules (green field) (Halbach et al., 1981) and Northeast Pacific (grey field) (Halbach et al. , 1981) are also included for comparison.

Figure 5: Plots of Ni/Fe (A), Co/Fe (B), Zn/Fe (C) and Ti/Fe (D) ratios versus Mn/Fe ratio of electron microprobe data acquired along two transects in the nodule Outer and Inner regions. Position of the transects in the nodule section are shown in Figure 1. See text for more explanations.

Figure 6. EXAFS data (thick lines, symbols) and fits (thin lines) for matrix spots and corresponding tricolor maps showing location of spots at which EXAFS data were taken. The fit for the Outer is a three-shell fit as discussed in text. The fit for the Inner is a linear combination fit to goethite and feroxyhite. Scale bars are 200µm.

Figure 7. Micro-XRD on Outer matrix spots. Abscissa is $q=2\pi/d$ (nm^{-1}). The numbered peak locations for feroxyhite are from Drits, et. al. Clay Minerals (1993), with the numbers showing the order of intensity. Sharp peaks marked with asterisks match albite.

Figure 8. Tricolor-coded µXRF maps showing botryoidal spots in Outer (a) and Inner (b) regions.

Figure 9. Fit of Inner spot 5 (see bottom panel of Figure 6) to Fe-O, two Fe-Fe shells and goethite. The top panel shows the contributions of each shell (divided by 2). The bottom panel shows the magnitude and imaginary parts of the FT for data and fit.

Table 1. Wet chemical analyses of the nodule section measured by ICP-AES

Table S1 (Electronic Annex). Electron microprobe analyses (in wt %) of 10 transects through the whole nodule section (from outer to inner nodule) and elemental ratios.

Table S2 (Electronic Annex). Electron microprobe analyses (in wt %) of two micro-transects in the Outer and Inner nodule regions and elemental ratios

7. Acknowledgments

We thank the science team, crew, and Chief Scientist Steven D'Hondt of the KNOX02RR cruise for access to the South Pacific Gyre. We thank Lindsey Briscoe for measuring the XRD pattern of feroxyhite (Characterization Facility, University of Minnesota, which receives partial support from NSF through the MRSEC program); Fred Davis for measuring the elemental composition by electron microprobe (Electron Microprobe Laboratory, University of Minnesota); and Shahida Quazi for assistance at ALS BL 10.3.2. The Advanced Light Source is supported by the Director, Office of Science, Office of Basic Energy Sciences, of the U.S. Department of Energy under Contract No. DE-AC02-05CH11231.

Aplin, A. C., and Cronan, D. S., 1985, Ferromanganese oxide deposits from the Central Pacific Ocean, II. Nodules and associated sediments: Geochimica et Cosmochimica Acta, v. 49, p. 437-451.

Banakar, V. K., and Tarkian, M., 1991, Genesis and growth of internal microstructures of manganese nodules: Indian Journal of Marine Sciences, v. 20, p. 20-24.

Banerjee, R., Roy, S., Dasgupta, S., Mukhopadhyay, S., and Miura, H., 1999, Petrogenesis of ferromanganese nodules from east of the Chagos Archipelago, Central Indian Basin, Indian Ocean: Marine Geology, v. 157, p. 145-158.

Birnie, A. C., and Paterson, E., 1991, The mineralogy and morphology of iron and manganese oxides in an imperfectly-drained Scottish soil: Geoderma, v. 50, p. 219-237.

Brown, G. E., Jr, Henrich, V. E., Casey, W. H., Clark, D. L., Eggleston, C., Felmy, A., Goodman, D. W., Gratzel, M., Maciel, G., McCarthy, M. I., Nealson, K. H., Sverjensky, D. A., Toney, M. F., and Zachara, J. M., 1999, Metal oxide surfaces and their interactions with aqueous solutions and microbial organisms: Chemical Reviews, v. 99, no. 1, p. 77-174.

Calvert, S. E., and Cronan, D. S., 1978, Geochemistry of oceanic ferromanganese deposits: Philosophical Transactions of the Royal Society London A, v. 290, p. 43-73.

Carlson, L., and Schwertmann, U., 1980, Natural occurrence of feroxyhite (d'-FeOOH): Clays and Clay Minerals, v. 28, no. 4, p. 272-280.

Chukhrov, F., Zvyagin, B., Gorshkov, A., Yermilova, L., Korovushkin, V., Rudnitskaya, Y. S., and Yakubovskaya, N. Y., 1977, Feroxyhyte, a new modification of FeOOH: International Geology Review, v. 19, no. 8, p. 873-890.

Cornell, R. M., R, G., and Schneider, W., 1992, The effect of nickel on the conversion of amorphous iron(III) hydroxide into more crystalline iron oxides in alkaline media: J. Chem. Tech. Biotechnol., v. 53, p. 73-79.

Cornell, R. M., and Schwertmann, U., 2003, The Iron Oxides: Structure, properties, reactions, occurrences and uses, Darmstadt, Germany, Wiley-VCH.

Cronan, D. S., 1975, Manganese nodules and other ferromangese oxide deposits from Atlantic Ocean: Journal of Geophysical Research-Oceans and Atmospheres, v. 80, p. 3831-3837.

D'Hondt, S., Spivack, A. J., Pockalny, R., Ferdelman, T. G., Fischer, J. P., Kallmeyer, J., Abrams, L. J., Smith, D. C., Graham, D., Hasiuk, F., Schrum, H., and Stancin, A. M., 2009, Subseafloor sedimentary life in the South Pacific Gyre: Proceedings of the National Academy of Sciences, v. 106, no. 28, p. 11651-11656.

de Lange, G. J., van Os, B., and Poorter, R., 1992, Geochemical composition and inferred accretion rates of sediments and manganese nodules from a submarine hill in the Madeira Abyssal Plain, eastern North Atlantic: Marine Geology, v. 109, p. 171-194.

Dymond, J., Lyle, M. W., Finney, B., Piper, D. Z., Murphy, K., Conard, R., and Pisias, N., 1984, Ferromanganese nodules from MANOP Sites H, S, and R - Control of mineralogical and chemical composition by multiple accretionary processes: Geochimica et Cosmochimica Acta, v. 48, p. 931-949.

Elderfield, H., Hawkesworth, C. J., Greaves, M. J., and Calvert, S. E., 1981, Rare-earth element zonation in Pacific ferromanganese nodules: Geochimica et Cosmochimica Acta, v. 45, p. 1231-1234.

Frierdich, A. J., and Catalano, J. G., 2012, Controls on Fe(II)-activated trace element release from goethite and hematite: Environmental Science & Technology, v. 46, p. 1519-1526.

Frierdich, A. J., Luo, Y., and Catalano, J. G., 2011, Trace element cycling through iron oxide minerals during redox-driven dynamic recrystallization: Geology, v. 39, no. 11, p. 1083-1086.

Gradstein, F., and Ogg, J., 2002, Future directions in stratigraphy: Episodes, v. 25, p. 203-208.

Halbach, P., and Puteanus, D., 1984, The influence of the carbonate dissolution rate on the growth and composition of Co-rich ferromanganese crusts from Central Pacific seamount areas: Earth and Planetary Science Letters, v. 68, p. 73-87.

Halbach, P., Scherhag, C., Hebisch, U., and Marchig, V., 1981, Geochemical and mineralogical control of different genetic types of deep-sea nodules from the Pacific Ocean: Mineralium deposita, v. 16, no. 1, p. 59-84.

Hammersley, A., 1997, FIT2D: an introduction and overview: European Synchrotron Radiation Facility Internal Report ESRF97HA02T.

Heggie, D., Kahn, D., and Fischer, K., 1986, Trace metals in metalliferous sediments, MANOP Site M: interfacial pore water profiles: Earth and Planetary Science Letters, v. 80, p. 106-116.

Hein, J. R., Koschinsky, A., and Halliday, A. N., 2003, Global occurrence of tellurium-rich ferromanganese crusts and a model for the enrichment of tellurium: Geochimica et Cosmochimica Acta, v. 67, p. 1117-1127.

Hein, J. R., Mizell, K., Koschinsky, A., and Conrad, T. A., 2013, Deep-ocean mineral deposits as a source of critical metals for high- and green-technology applications: Comparison with land-based resources: Ore Geology Reviews, v. 51, p. 1-14.

Jahnke, R. A., 1996, The global ocean flux of particulate organic carbon: Areal distribution and magnitude: Global biogeochemical cycles, v. 10, no. 1, p. 71-88.

Klinkhammer, G., Heggie, D. T., and Graham, D. W., 1982, Metal diagenesis in oxic marine-sediments: Earth and Planetary Science Letters, v. 61, p. 211-219.

Koschinsky, A., and Halbach, P., 1995, Sequential leaching of marine ferromanganese precipitates: Genetic implications: Geochimica et Cosmochimica Acta, v. 59, no. 24, p. 5113-5132.

Koschinsky, A., and Hein, J. R., 2003, Uptake of elements from seawater by ferromanganese crusts: solid-phase associations and seawater speciation: Marine geology, v. 198, p. 331-351.

Koschinsky, A., Stascheit, A., Bau, M., and Halbach, P., 1997, Effects of phosphatization on the geochemical and mineralogical composition of marine ferromanganese crusts: Geochimica et Cosmochimica Acta, v. 61, p. 4079-4094.

Larson, R. L., Pockalny, R. A., Viso, R. F., Erba, E., Abrams, L. J., Luyendyk, B. P., Stock, J. M., and Clayton, R. W., 2002, Mid-Cretaceous tectonic evolution of the Tongareva triple junction in the southwestern Pacific Basin: Geology, v. 30, no. 1, p. 67-70.

Latta, D. E., Gorski, C. A., and Scherer, M. M., 2012, Influence of Fe^{2+}-catalyzed iron oxide recrystallization on metal cycling: Biochemical Society Transations, v. 40, p. 1191-1197.

Lu, B., Guo, H., Li, P., Liu, H., Wei, Y., and Hou, D., 2011, Comparison study on transformation of iron oxyhydroxides: Based on theoretical and experimental data: Journal of Solid State Chemistry, v. 184, no. 8, p. 2139-2144.

Manceau, A., Schlegel, M. L., Musso, M., Sole, V. A., Gauthier, C., Petit, P. E., and Trolard, F., 2000, Crystal chemistry of trace elements in natural and synthetic goethite: Geochim Cosmochim. Acta, v. 64, p. 3643-3661.

Marcus, M. A., MacDowell, A. A., Celestre, R., Manceau, A., Miller, T., Padmore, H. A., and Sublett, R. E., 2004a, Beamline 10.3.2 at ALS: a hard X-ray microprobe for environmental and materials sciences: Journal of Synchrotron Radiation, v. 11, p. 239-247.

Marcus, M. A., Manceau, A., and Kersten, M., 2004b, Mn, Fe, Zn and As speciation in a fast-growing ferromanganese marine nodule: Geochimica Et Cosmochimica Acta, v. 68, no. 14, p. 3125-3136.

Marcus, M. A., Westphal, A. J., and Fakra, S. C., 2008, Classification of Fe-bearing species from K-edge XANES data using two-parameter correlation plots: Journal of Synchrotron Radiation, v. 15, p. 463-468.

Martin-Barajas, A., Lallier-Verges, E., and Leclaire, L., 1991, Characteristics of manganese nodules from the Central Indian Basin: Relationship with the sedimentary environment: Marine Geology, v. 101, p. 249-265.

Morford, J. L., and Emerson, S., 1999, The geochemistry of redox sensitive trace metals in sediments: Geochimica et Cosmochimica Acta, v. 63, p. 1735-1750.

Murad, E., and Schwertmann, U., 1988, Iron oxide mineralogy of some deep-sea ferromanganese crusts: American Mineralogist, v. 73, p. 1395-1400.

Navrotsky, A., Mazeina, L., and Majzlan, J., 2008, Size-driven structural and thermodynamic complexity in iron oxides: Science, v. 319, no. 5870, p. 1635-1638.

Newville, M., 2001, IFEFFIT: interactive XAFS analysis and FEFF fitting: Journal of Synchrotron Radiation, v. 8, no. 2, p. 322-324.

Nicholson, K., and Eley, M., 1997, Geochemistry of manganese oxides: metal adsorption in freshwater and marine environments, *in* Nicholson, K., Hein, J. R., Bühn, B., and Dasgupta, S., eds., Manganese Mineralization: Geochemistry and Mineralogy of Terrestrial and Marine Deposits. Geological Society Special Publication No. 119: London, The Geological Society, p. 309-326.

Peacock, C. L., 2009, Physiochemical controls on the crystal-chemistry of Ni in birnessite: Genetic implications for ferromanganese precipitates: Geochim Cosmochim Acta, v. 73, p. 3568-3578.

Ravel, B., and Newville, M., 2005, ATHENA, ARTEMIS, HEPHAESTUS: data analysis for X-ray absorption spectroscopy using IFEFFIT: Journal of synchrotron radiation, v. 12, no. 4, p. 537-541.

Sawlan, J. J., and Murray, J. W., 1983, Trace-metal remobilization in the interstitial waters of red clay and hemipelagic marine-sediments: Earth and Planetary Science Letters, v. 64, p. 213-230.

Schwertmann, U., and Cornell, R. M., 2000, The Iron Oxides, Iron oxides in the laboratory. Preparation and characterization, Wiley-VCH, p. 4-18.

Takahashi, Y., Manceau, A., Geoffroy, N., Marcus, M. A., and Usui, A., 2007, Chemical and structural control of the partitioning of Co, Ce, and Pb in marine ferromanganese oxides: Geochimica Et Cosmochimica Acta, v. 71, no. 4, p. 984-1008.

Takahashi, Y., Shimizu, H., Kagi, H., Yoshida, H., Usui, A., and Nomura, M., 2000, A new method for the determination of Ce^{III}/Ce^{IV} ratios in geological materials; application for weathering, sedimentary and diagenetic processes: Earth and Planetary Science Letters, v. 182, no. 3, p. 201-207.

Toner, B. M., Berquo, T. S., Michel, F. M., Sorensen, J. V., Templeton, A. S., and Edwards, K. J., 2012, Mineralogy of iron microbial mats from Loihi Seamount: Frontiers in Microbiological Chemistry, v. 3, p. 1-18.

Toner, B. M., Santelli, C. M., Marcus, M. A., Wirth, R., Chan, C. S., McCollom, T. M., Bach, W., and Edwards, K. J., 2009, Biogenic iron oxyhydroxide formation at Mid-Ocean

Ridge hydrothermal vents: Juan de Fuca Ridge: Geochim. Cosmochim. Acta, v. 73, p. 388-403.

Verlaan, P. A., Cronan, D. S., and Morgan, C. L., 2004, A comparative analysis of compositional variations in and between marine ferromanganese nodules and crusts in the South Pacific and their environmental controls: Progress in Oceanography, v. 63, p. 125-158.

Wang, X., Schloßmacher, U., Wiens, M., Schröder, H. C., and Müller, W. E., 2009, Biogenic origin of polymetallic nodules from the Clarion-Clipperton zone in the Eastern Pacific Ocean: electron microscopic and EDX evidence: Marine Biotechnology, v. 11, no. 1, p. 99-108.

Waychunas, G., Fuller, C., and Davis, J., 2002, Surface complexation and precipitate geometry for aqueous Zn (II) sorption on ferrihydrite I: X-ray absorption extended fine structure spectroscopy analysis: Geochimica et cosmochimica acta, v. 66, no. 7, p. 1119-1137.

Yoshikawa, K., 1991, The relationship between manganese minerals and metallic elements in deep-sea manganese nodules: Marine Geology, v. 101, p. 267-286.

Outer
Inner
1 mm

Outer
50 µm

Inner
100 µm

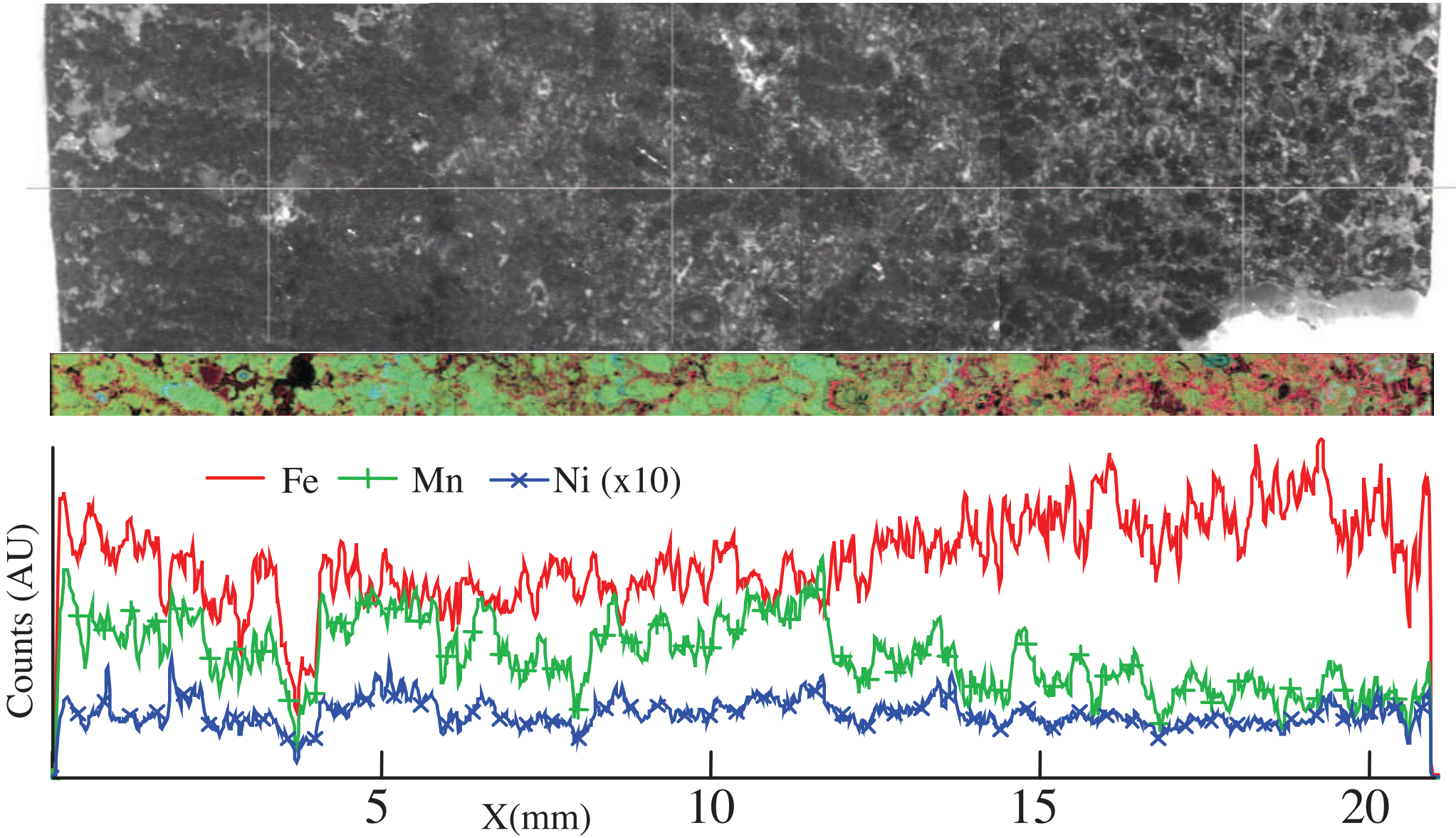
Fe
Mn
Ni (x10)
Counts (AU)
5
10
15
20
X(mm)

Inner

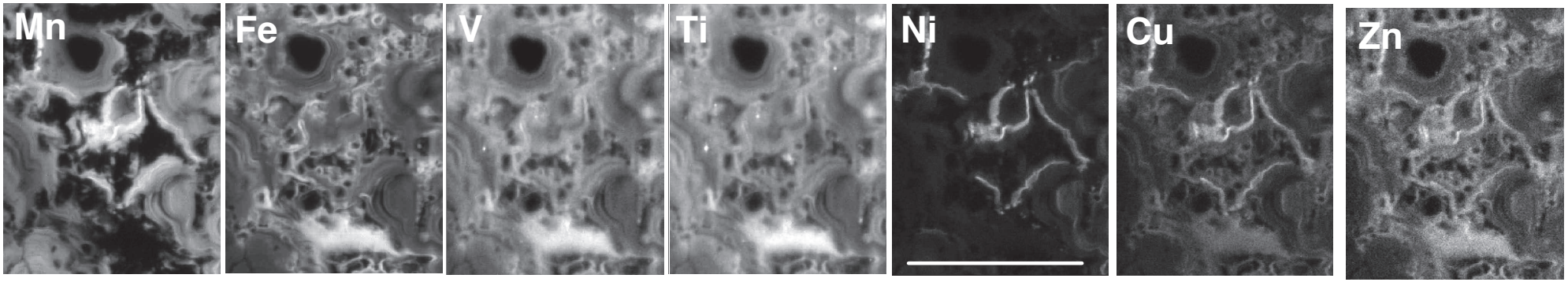

Outer

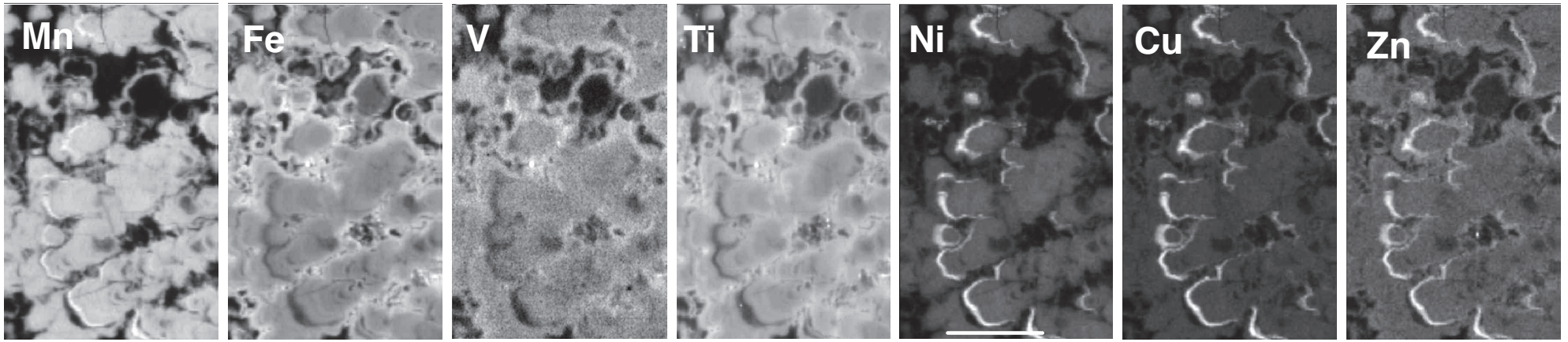

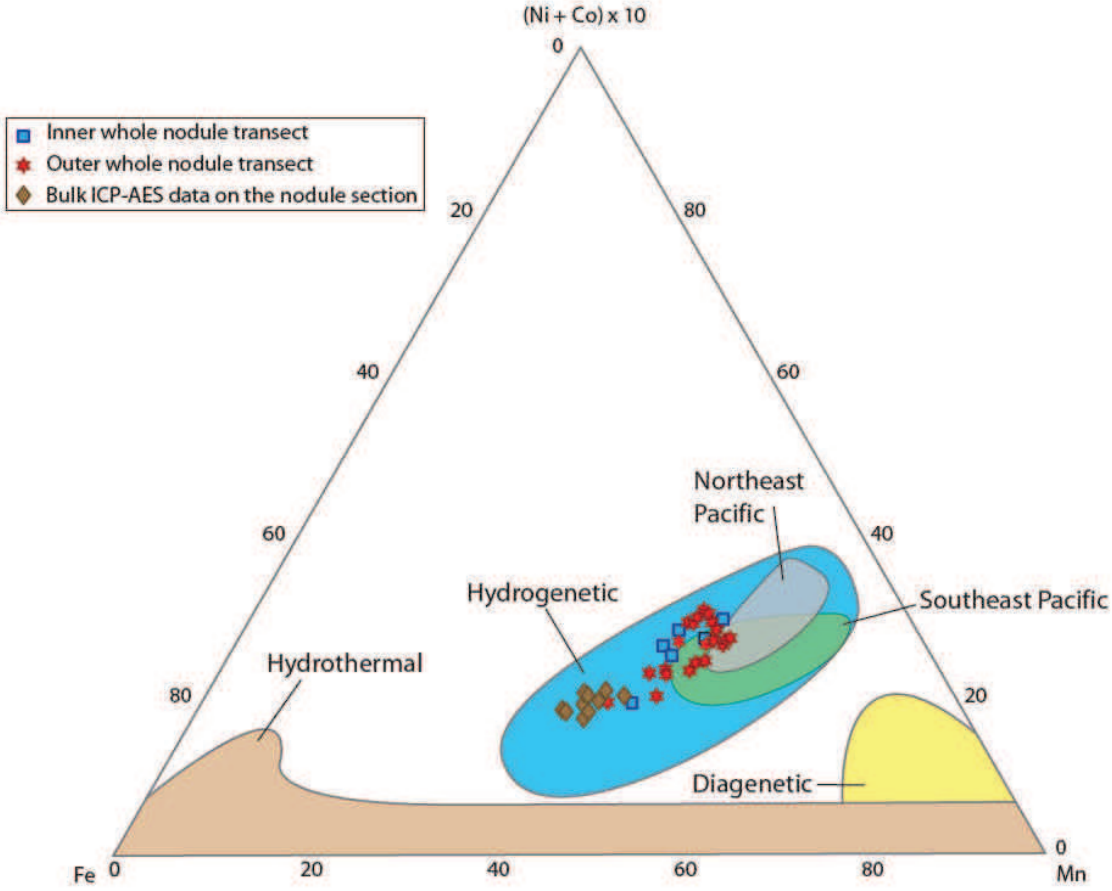
(Ni + Co) x 10
0
20
40
60
80
Inner whole nodule transect
Outer whole nodule transect
Bulk ICP-AES data on the nodule section
Northeast Pacific
Southeast Pacific
Hydrogenetic
Hydrothermal
Diagenetic
Fe
Mn

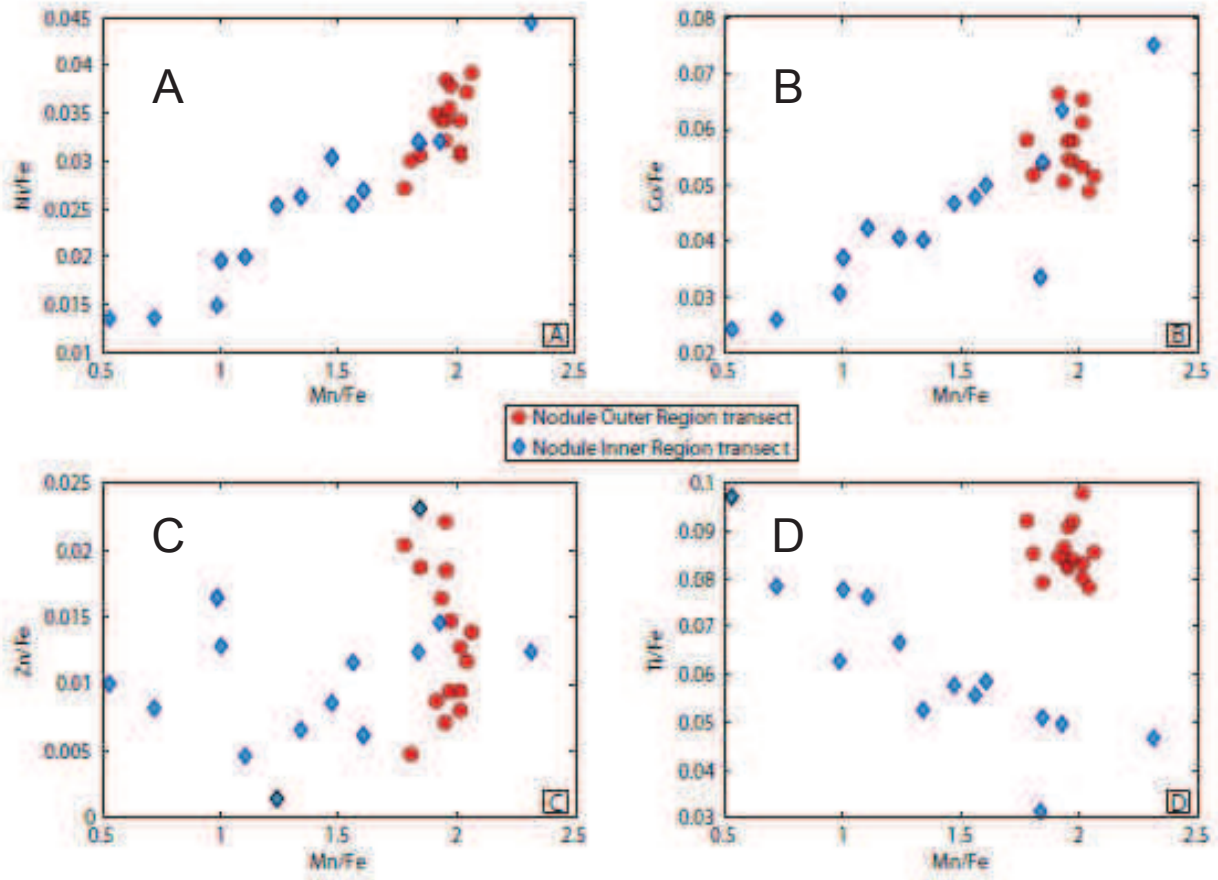
A
B
C
D
Ni/Fe
Co/Fe
Zn/Fe
Ti/Fe
Mn/Fe
Nodule Outer Region transect
Nodule Inner Region transect

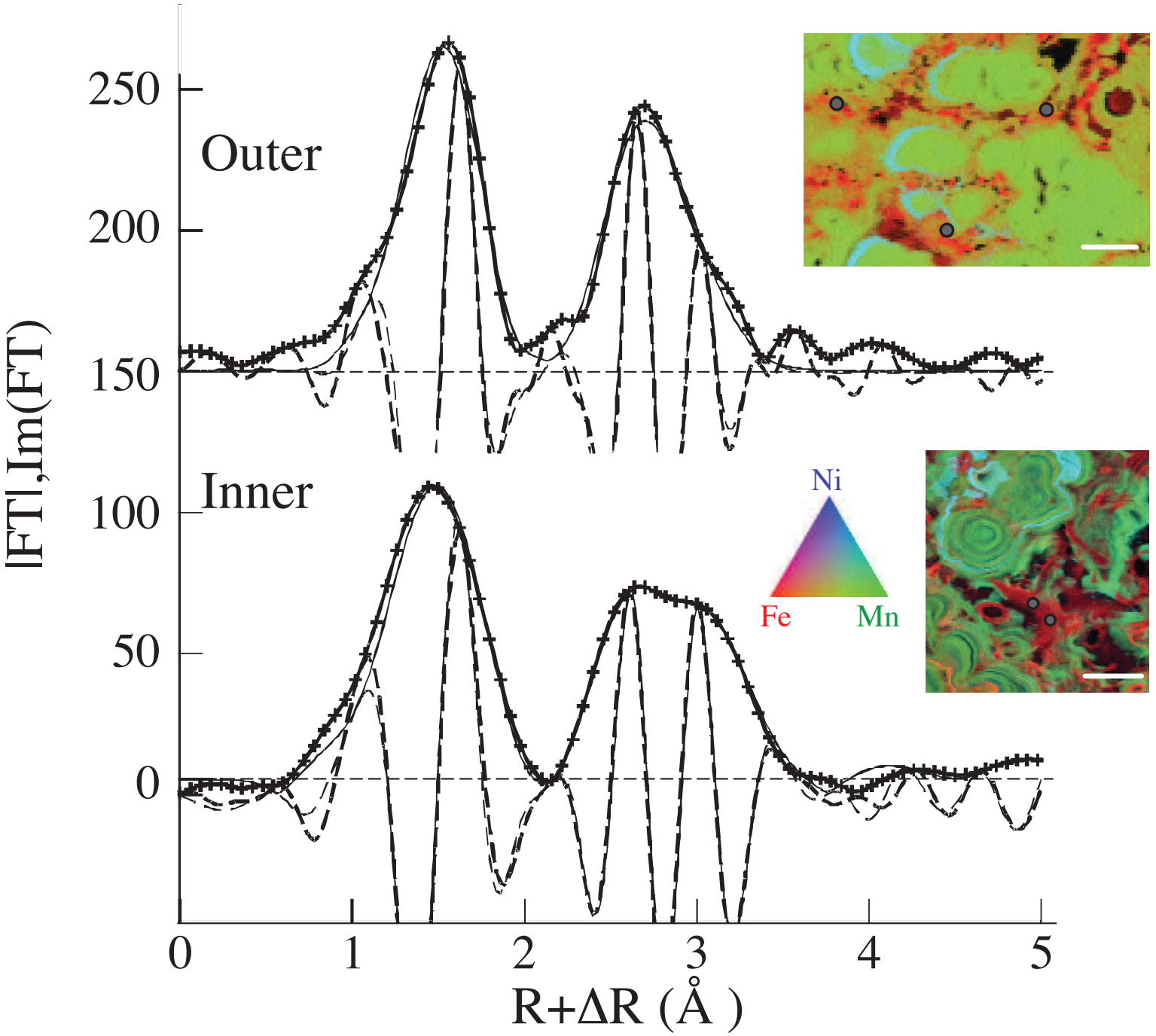
250
200
150
100
50
0
Outer
Inner
|FT|,Im(FT)
Ni
Fe
Mn
0
1
2
3
4
5
R+ΔR (Å)

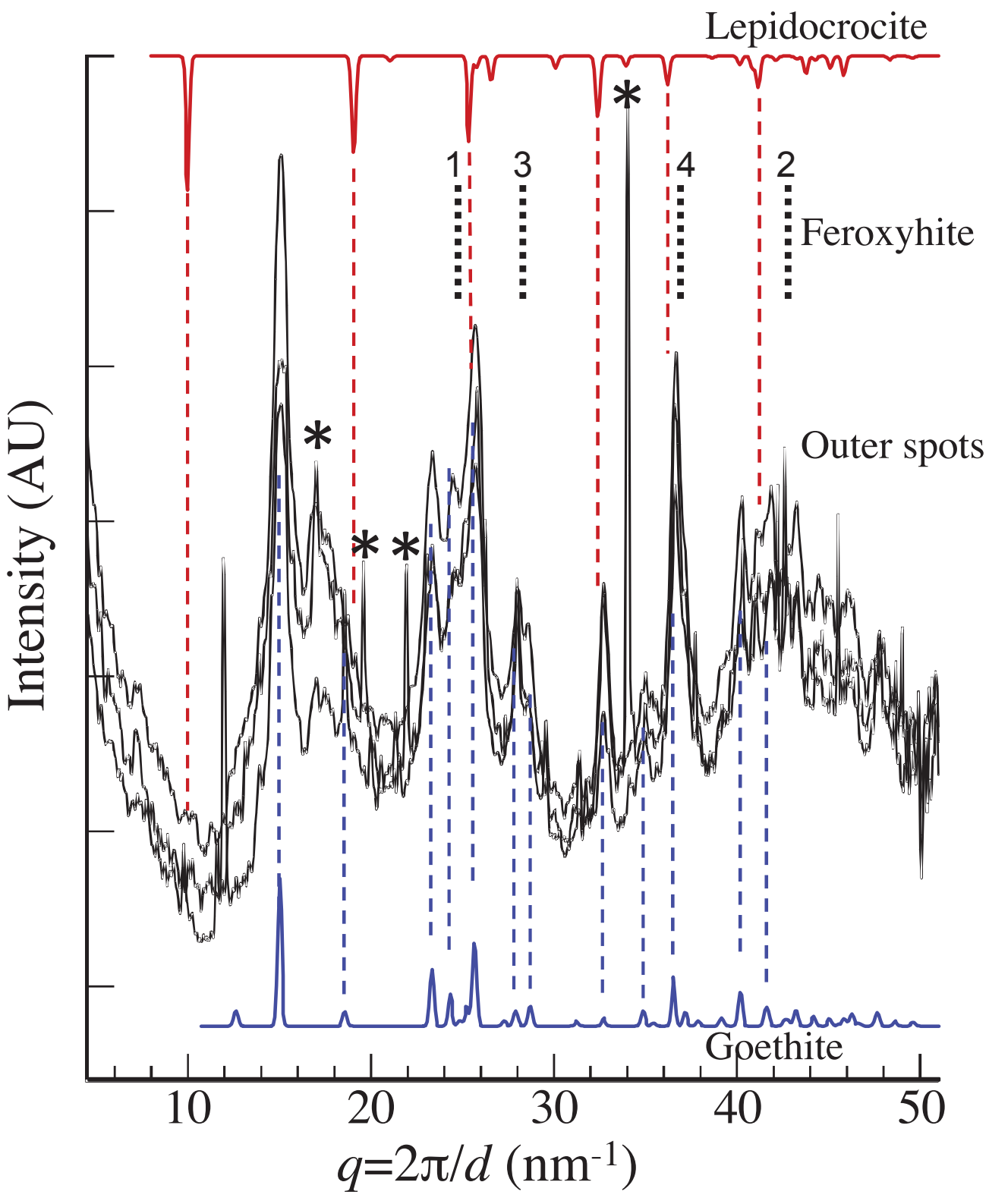
Lepidocrocite
1
3
4
2
Feroxyhite
Outer spots
Goethite
Intensity (AU)
10
20
30
40
50
q=2π/d (nm-1)

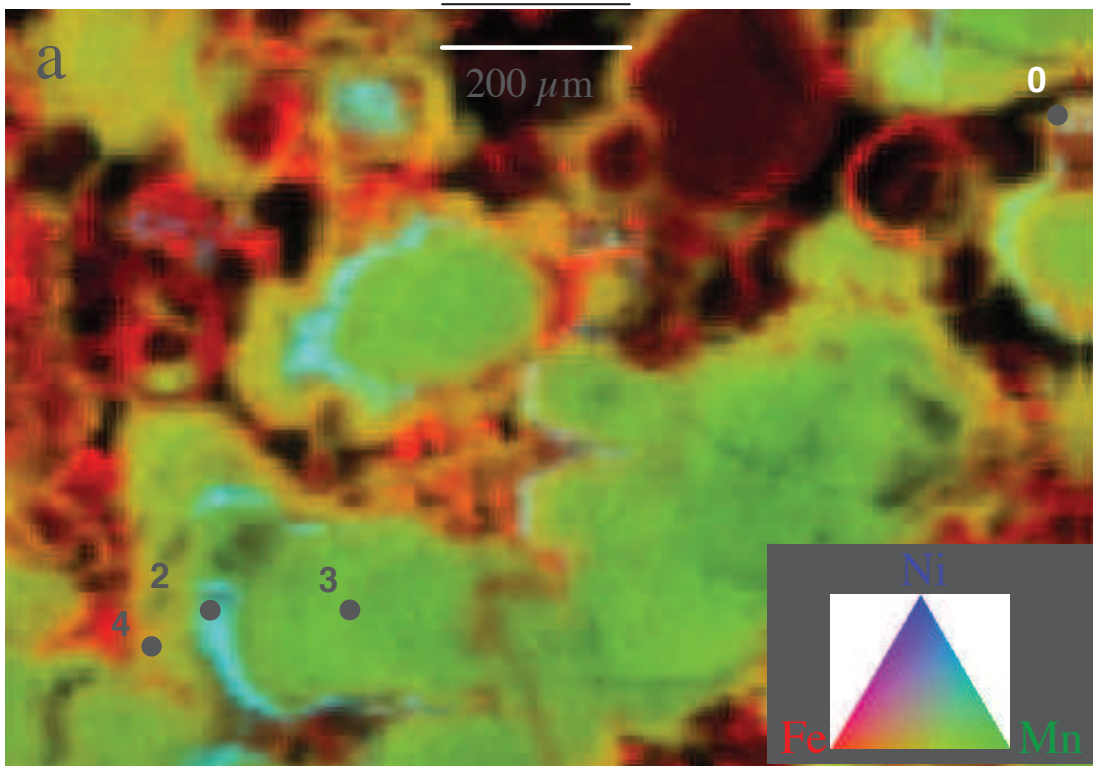
a
200 μm
0
2
3
4
Ni
Fe
Mn

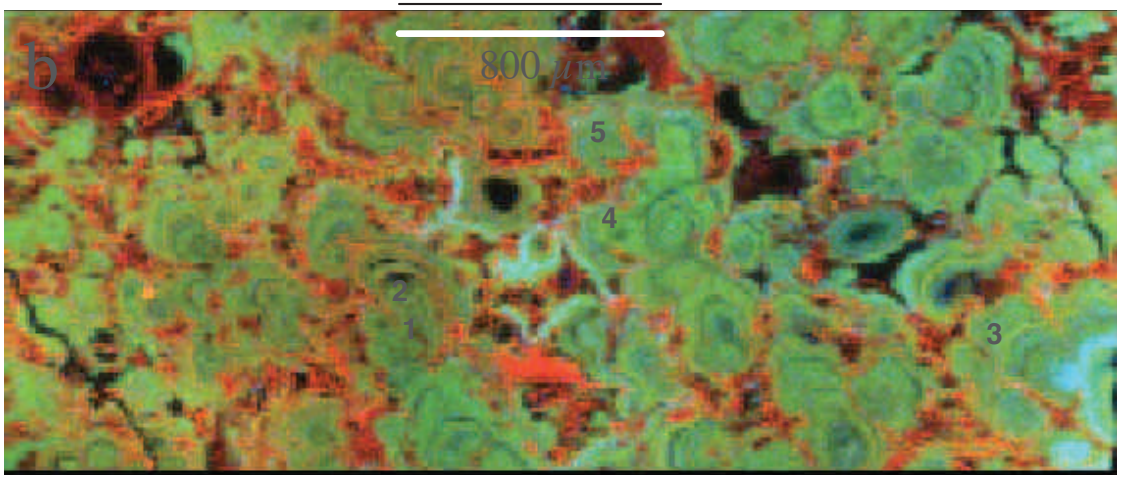
b
800 μm
5
4
2
1
3

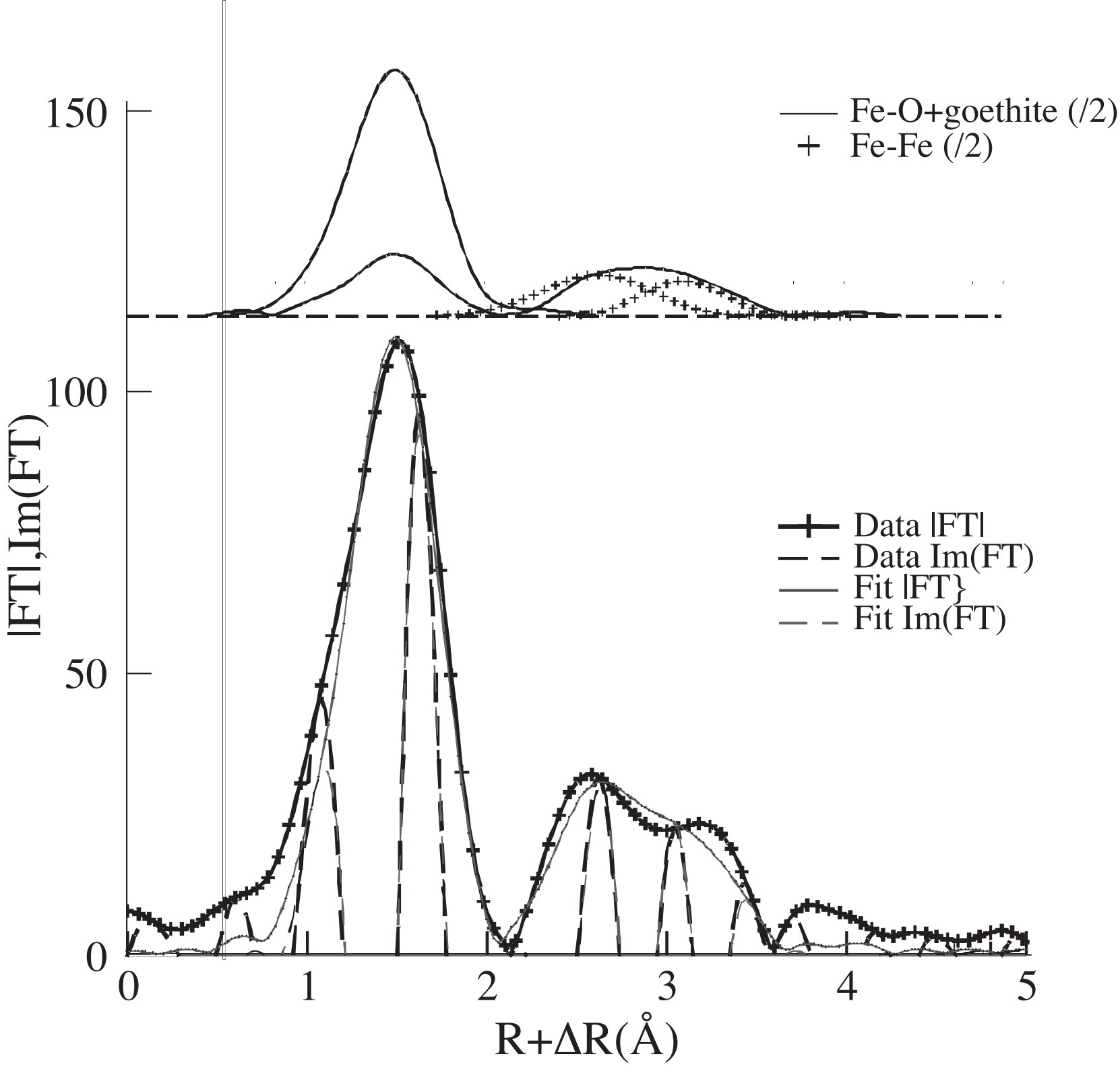
150
100
50
0
|FT|,Im(FT)
0
1
2
3
4
5
R+ΔR(Å)
Fe-O+goethite (/2)
Fe-Fe (/2)
Data |FT|
Data Im(FT)
Fit |FT}
Fit Im(FT)

Table 1: Wet chemical analyses of the nodule section measured by ICP-AES.

Nodule section #	Distance from outer nodule (mm)**	Al/Fe	Ba/Fe	Ca/Fe	Ce/Fe	Co/Fe	Cu/Fe	K/Fe	La/Fe	Mg/Fe	Mn/Fe	Mo/Fe	Na/Fe	Ni/Fe	P/Fe	Sr/Fe	Ti/Fe	Zn/Fe	Cu/Ni
Outer nodule* **																			
N1	3	0,184	0,0085	0,119	0,0114	0,035	0,0096	0,047	0,0015	0,0843	1,14	0,0019	0,123	0,0217	0,017	0,0064	0,106	0,0036	0,45
N2	6	0,165	0,0081	0,109	0,0093	0,030	0,0076	0,040	0,0014	0,0634	0,93	0,0016	0,095	0,0138	0,016	0,0057	0,105	0,0030	0,55
N3	8	0,214	0,0078	0,122	0,0096	0,034	0,0089	0,054	0,0015	0,0763	1,04	0,0018	0,107	0,0184	0,019	0,0060	0,104	0,0035	0,48
N4	10	0,191	0,0080	0,150	0,0095	0,031	0,0095	0,040	0,0015	0,0714	1,10	0,0018	0,106	0,0215	0,022	0,0060	0,095	0,0038	0,44
N5	12,5	0,199	0,0083	0,150	0,0104	0,034	0,0094	0,032	0,0014	0,0747	1,25	0,0022	0,115	0,0241	0,016	0,0066	0,087	0,0039	0,39
N6	13,5	0,215	0,0077	0,141	0,0096	0,028	0,0084	0,032	0,0013	0,0677	1,04	0,0019	0,099	0,0182	0,016	0,0060	0,079	0,0037	0,46
N7	14,5	0,227	0,0072	0,126	0,0089	0,027	0,0084	0,037	0,0011	0,0672	1,02	0,0020	0,103	0,0169	0,015	0,0056	0,071	0,0038	0,50
N8	16	0,193	0,0076	0,112	0,0100	0,031	0,0085	0,038	0,0012	0,0688	1,02	0,0021	0,098	0,0179	0,015	0,0058	0,076	0,0040	0,48
N9	18	0,188	0,0071	0,110	0,0111	0,034	0,0082	0,033	0,0012	0,0724	1,02	0,0022	0,092	0,0183	0,016	0,0056	0,083	0,0040	0,45
N10	19,5	0,160	0,0073	0,099	0,0133	0,026	0,0083	0,022	0,0012	0,0682	0,92	0,0022	0,084	0,0178	0,017	0,0055	0,075	0,0043	0,46
Inner nodule**																			
USGS Nod-P-1	-	0,379	0,0448	0,395	0,0064	0,041	0,2113	0,193	0,0021	0,3360	5,10	0,0106	0,304	0,2504	0,027	0,0114	0,052	0,0306	0,84
USGS Nod-A-1	-	0,197	0,0140	1,129	0,0079	0,031	0,0103	0,048	0,0013	0,2647	1,73	0,0035	0,081	0,0634	0,041	0,0145	0,033	0,0059	0,16

* Concentrations are given in grams of element per gram of Fe (i.e. Element/Fe ratios).

** Distance from outer nodule is reported as the distance from the top surface of the nodule.

*** The "outer nodule" corresponds to the nodule facing seawater or sediment in opposition to the "inner nodule" corresponding to the deeper part of the nodule. See text for ample explanations.

Table S1: Electron microprobe analyses (in wt %) of 10 transects through the whole nodule section (from outer to inner nodule) and elemental ratios.

Position of datapoints in the nodule and transect #	Distance (mm) from outer nodule**	SiO_2†	TiO_2	Al_2O_3	MgO	CaO	MnO	FeO††	CoO	NiO	ZnO	Na_2O	Mn/Fe	Ni/Fe	Zn/Fe	Ti/Fe	Ni/Co
Outer nodule*	-																
Transect 1 - 1	0,5	5,27	2,46	2,77	2,00	3,66	32,60	20,09	1,05	0,44	0,16	1,72	1,62	0,02	0,0081	0,094	0,42
Transect 1 - 2	0,5	4,11	2,08	2,26	1,48	3,10	31,14	17,24	1,32	0,40	0,08	1,92	1,80	0,02	0,0049	0,093	0,30
Transect 1 - 3	0,5	6,50	3,03	3,55	1,72	3,07	27,80	24,01	0,91	0,29	0,16	0,70	1,15	0,01	0,0067	0,097	0,32
Transect 2 - 1	2	4,76	2,06	2,81	2,28	3,87	35,99	17,10	1,58	0,61	0,21	2,40	2,10	0,04	0,0126	0,093	0,39
Transect 2 - 2	2	4,31	2,28	2,77	2,31	3,64	37,43	19,06	1,05	0,68	0,12	2,22	1,96	0,04	0,0066	0,092	0,65
Transect 2 - 3	2	4,73	2,52	2,76	1,65	3,31	32,29	19,89	1,10	0,43	0,14	1,21	1,62	0,02	0,0075	0,098	0,39
Transect 3 - 1	4	4,53	2,62	2,97	2,15	3,63	38,11	17,10	1,74	0,64	0,04	2,40	2,22	0,04	0,0027	0,118	0,37
Transect 3 - 2	4	6,09	2,77	4,00	2,39	3,52	35,76	18,22	1,66	0,50	0,13	2,25	1,96	0,03	0,0075	0,117	0,30
Transect 3 - 3	4	4,88	2,25	2,88	2,32	3,69	36,82	18,11	1,54	0,65	0,11	3,09	2,03	0,04	0,0060	0,096	0,42
Transect 4 - 1	6	4,49	2,20	3,23	2,39	4,19	38,13	18,27	1,08	0,69	0,27	1,80	2,08	0,04	0,0151	0,093	0,64
Transect 4 - 2	6	5,59	1,98	4,03	2,67	3,96	37,18	16,18	1,54	0,71	0,28	1,93	2,29	0,04	0,0176	0,094	0,46
Transect 4 - 3	6	6,35	2,56	4,04	1,98	3,59	31,57	20,86	0,86	0,41	0,21	0,90	1,51	0,02	0,0102	0,095	0,48
Transect 5 - 1	7	4,27	1,86	2,82	2,60	4,13	40,57	15,81	0,92	1,11	0,27	2,95	2,56	0,07	0,0176	0,091	1,20
Transect 5 - 2	7	3,77	2,06	2,65	2,41	4,23	38,55	16,01	1,01	0,90	0,19	2,52	2,40	0,06	0,0121	0,099	0,89
Transect 5 - 3	7	4,07	1,97	2,77	2,27	3,70	39,92	16,11	1,11	0,91	0,13	1,48	2,47	0,06	0,0085	0,094	0,82
Transect 6- 1	10	5,85	1,64	3,81	2,32	4,02	36,30	16,90	1,15	0,71	0,32	1,76	2,14	0,04	0,0196	0,075	0,62
Transect 6- 2	10	4,58	1,82	3,98	2,13	4,00	36,82	19,65	1,04	0,62	0,18	1,58	1,87	0,03	0,0096	0,071	0,59
Transect 6- 3	10	5,71	2,14	4,43	2,15	3,64	32,97	22,33	1,15	0,44	0,12	1,56	1,47	0,02	0,0057	0,074	0,39
Inner nodule *																	
Transect 7 - 1	12	3,51	1,54	2,89	2,16	3,92	37,05	16,27	1,16	0,75	0,29	2,41	2,27	0,05	0,0185	0,073	0,65
Transect 7 - 2	12	3,42	1,83	2,94	2,49	4,00	37,79	16,36	1,37	0,79	0,17	2,41	2,30	0,05	0,0110	0,086	0,57
Transect 7 - 3	12	3,93	1,73	3,45	2,37	4,00	38,05	16,13	1,24	0,82	0,21	2,77	2,35	0,05	0,0137	0,083	0,66
Transect 8 - 1	13,5	4,85	1,78	3,57	2,47	3,94	39,62	15,69	1,39	0,86	0,27	2,62	2,52	0,06	0,0179	0,088	0,62
Transect 8 - 2	13,5	3,41	1,85	2,87	2,48	3,98	38,98	16,17	1,37	0,84	0,23	2,65	2,40	0,05	0,0148	0,088	0,62
Transect 8 - 3	13,5	4,19	1,62	3,75	2,24	3,57	38,02	17,63	1,27	0,75	0,07	2,87	2,15	0,04	0,0041	0,071	0,59
Transect 9 - 1	15	9,32	1,96	5,37	2,94	3,32	26,58	16,31	1,04	0,44	1,05	3,10	1,62	0,03	0,0668	0,093	0,42
Transect 9 - 2	15	4,46	1,88	4,19	2,32	4,03	35,78	19,48	1,46	0,65	0,13	1,75	1,83	0,03	0,0068	0,075	0,45
Transect 9 - 3	15	4,15	1,93	4,11	2,25	3,88	34,91	20,50	1,35	0,44	0,17	2,63	1,70	0,02	0,0087	0,073	0,33
Transect 10 - 3***	17	5,44	1,55	5,06	1,99	3,13	32,18	24,39	0,83	0,48	0,19	1,48	1,31	0,02	0,0080	0,049	0,57

† Concentrations are reported in wt% of the element (not in oxides).
†† Note that Fe in the nodule is in the Fe^{3+} valence state.
* The "Outer nodule" corresponds to the part of the nodule facing seawater or sediment, in opposition to the "Inner nodule" which is the deepest part of the nodule. The limit between "Outer nodule" and "Inner nodule" was defined using Figure 3 (also see text). The nodule was divided into 10 regions fom Outer Region (transect 1) to Inner Region (transect 10) of the nodule. Each transect consists of a serie of three analyses measured orthogonally to the direction of nodule growth (inner to outer), thus the three data points of each transect are roughly at the same distance from outer nodule (mm). See Figure 1 for positions in the sample.
** Depth (mm) in the nodule is calculated from Figure 1.
*** Concentrations of data points 1 and 2 from transect #10 were omited because the sum of the oxides is below 70% (see text for explanations).

Table S2: Electron microprobe analyses (in wt %) of two micro-transects in the Outer and Inner nodule regions and elemental ratios.

Data point # in the nodule transect	SiO_2**	TiO_2	Al_2O_3	MgO	CaO	MnO	FeO***	CoO	NiO	ZnO	Na_2O	Mn/Fe	Ni/Fe	Zn/Fe	Ti/Fe	Ni/Co
Outer Region*																
1	5,33	1,93	2,46	2,11	3,54	33,91	17,65	1,16	0,61	0,15	2,05	1,91	0,03	0,0085	0,084	0,52
2	4,74	2,05	2,67	2,08	3,71	32,65	16,16	1,04	0,50	0,20	2,03	2,01	0,03	0,0126	0,098	0,48
3	4,92	1,89	2,51	2,21	3,75	35,66	17,64	1,07	0,54	0,16	2,19	2,01	0,03	0,0091	0,083	0,50
4	7,96	1,99	2,53	2,01	3,51	32,96	16,64	0,95	0,62	0,24	2,18	1,97	0,04	0,0147	0,092	0,65
5	5,24	1,84	2,53	2,13	3,65	35,70	17,66	0,93	0,60	0,14	2,34	2,01	0,03	0,0083	0,080	0,65
6	5,73	1,85	2,65	2,17	3,67	34,59	16,71	0,86	0,65	0,23	2,11	2,06	0,04	0,0141	0,086	0,75
7	4,65	1,79	2,56	2,32	3,60	36,12	17,63	0,85	0,65	0,20	2,57	2,04	0,04	0,0119	0,078	0,76
8	7,71	1,81	3,20	2,22	3,45	33,09	16,88	0,97	0,57	0,36	1,93	1,95	0,03	0,0219	0,083	0,59
9	5,27	1,94	2,59	2,17	3,63	35,10	17,76	0,96	0,62	0,16	2,26	1,97	0,04	0,0094	0,084	0,65
10	7,66	1,85	3,65	2,01	3,37	32,06	16,51	0,82	0,56	0,26	1,92	1,94	0,03	0,0161	0,087	0,68
11	6,95	1,96	2,78	2,20	3,73	32,78	16,71	0,91	0,64	0,29	1,84	1,95	0,04	0,0182	0,090	0,70
12	8,98	2,04	3,22	1,95	3,37	30,41	17,05	0,98	0,46	0,33	1,78	1,78	0,03	0,0203	0,092	0,47
13	5,12	1,93	2,58	2,20	3,72	35,29	18,02	1,02	0,58	0,12	2,20	1,95	0,03	0,0071	0,083	0,56
14	5,73	1,77	2,28	1,92	3,62	31,88	17,21	0,92	0,53	0,31	1,82	1,85	0,03	0,0189	0,079	0,57
15	4,77	2,08	2,61	2,16	3,72	34,17	18,86	0,96	0,57	0,09	2,00	1,80	0,03	0,0051	0,085	0,59
Inner Region*																
1	4,40	1,13	3,88	1,97	3,28	32,82	16,96	1,11	0,56	0,24	2,00	1,93	0,03	0,0148	0,051	0,51
2	5,57	1,07	4,41	1,81	3,08	28,55	15,43	0,86	0,51	0,36	1,49	1,84	0,03	0,0238	0,053	0,59
3	3,59	1,06	3,54	2,38	3,56	37,89	16,32	1,31	0,78	0,21	1,96	2,31	0,05	0,0133	0,050	0,59
4	5,37	1,20	4,93	1,85	3,07	28,22	18,02	0,79	0,42	0,19	1,22	1,56	0,02	0,0107	0,051	0,53
5	6,93	0,71	5,90	2,13	2,69	25,23	13,69	0,59	0,56	0,21	1,62	1,84	0,04	0,0162	0,040	0,95
6	5,68	1,26	4,67	1,83	3,17	31,62	19,63	0,82	0,44	0,10	1,23	1,60	0,02	0,0053	0,050	0,54
7	4,84	1,21	3,78	1,74	2,77	28,08	20,86	0,70	0,46	0,11	1,07	1,34	0,02	0,0054	0,045	0,65
8	-	-	-	-	-	-	-	-	-	-	-	-	-	-	-	-
9	6,55	1,53	5,03	1,85	2,79	28,94	23,25	0,71	0,45	0,02	1,38	1,24	0,02	0,0010	0,051	0,63
10	5,89	1,23	5,27	2,16	2,61	28,15	19,07	0,76	0,50	0,14	1,47	1,47	0,03	0,0076	0,050	0,65
11	6,89	1,65	5,24	1,89	2,73	28,18	25,41	0,70	0,33	0,07	1,08	1,11	0,01	0,0028	0,050	0,46
12	6,89	1,72	5,17	1,82	2,62	26,59	26,44	0,62	0,33	0,21	1,02	1,00	0,01	0,0083	0,050	0,54
13	7,67	2,27	5,04	1,58	2,03	18,17	34,12	0,44	0,24	0,17	1,02	0,53	0,01	0,0052	0,051	0,54
14	6,85	1,41	5,24	1,62	2,43	22,59	22,82	0,52	0,25	0,28	0,67	0,99	0,01	0,0126	0,048	0,49
15	18,97	1,91	5,32	1,46	2,08	19,14	26,47	0,48	0,25	0,15	0,92	0,72	0,01	0,0058	0,056	0,52

* The "Outer Region" corresponds to the transect measured in the region of the nodule facing seawater or sediment, in opposition to the "Inner Region" which is a transect made in the inside of the nodule (close to the nucleus of the nodule). See Figure 1 for positions of data points in the sample.
** Concentrations are reported in wt%.
*** Note that Fe in the nodule is in the Fe^{3+} valence state.

Annexe 3 - La campagne océanographique BIONOD 2012
Géochimie des nodules polymétalliques et étude du comportement des métaux lors des processus de diagenèse dans les sédiments profonds de la zone Clarion-Clipperton (Pacifique Equatorial)

Appendix 3 - Project description : BIONOD 2012
Geochemistry of Mn-nodules and investigation of early diagenetic behavior of trace metals in deep-sea sediments from the Clarion-Clipperton Fault Zone (Equatorial Pacific)

1. Introduction and rationale of the study

1.1. Background on Mn-nodule formation

Manganese nodules are deep oceanic metalliferous deposits encountered at the surface of dee-sea-clays at very high depth > 4000 meters. These underlying deep-sea clays are characterized by a very low sedimentation rates < 1 mm/1000 yrs which hampers a dilution effect of transition metals accumulating in these deposits and promotes their enrichment.

Metal sources in Mn-nodules are generally thought to have several origins, (1) hydrogenetic source resulting from direct precipitation of metal from seawater leading to similar Fe and Mn enrichment (Mn/Fe ~1) and relatively high contents of Ni, Cu and Co; (2) diagenetic source resulting from metal remobilization from underlying sediment during diagenetic organic matter remineralization leading to higher Mn enrichments relative to Fe (Mn/Fe > 2.5), (3) hydrothermal sources characterized by even higher Mn/Fe ratios (>10) and depleted in Ni (4) additional sources from microbial biofilm may also be an important supply of metals to Mn –nodules, through metal update on organic substrate or direct metal metabolic uptake (Wang et al. 2009) (Figure A3.1). Although local geological and oceanographic settings such as sedimentation rate and sediment composition may account for Mn-nodules geochemical composition variability, the contribution of each source leading to the highest enrichment of strategic metals (e.g. Rare Earth Elements, Platinum Group Elements, Tellurium, etc..) remains unclear. This lack of understanding prevents us from clearly establishing a mode of formation and a model for metal enrichments. A comprehensive understanding Mn-nodules genesis is also critical since they represent a potential mining resource. Co and Te are more than 100-fold enriched relative to crustal abundance, and Ni and Cu are more than 50-fold enriched. Other trace metals such as Mo, Tl, Bi, Pb are also exceptionally enriched by a factor of more than 50 times (Cronan 2000). Mn-nodules having a strong diagenetic component are particularly interesting since they are the most enriched in base metal like Ni or Cu.

Compositional differences exist between nodules from the Atlantic Ocean and those occurring in the Pacific Ocean (Delange et al. 1992). The areas covered by nodules in the Atlantic are less important than in the Pacific Ocean which is characterized by the large nodules fields of the Clarion/Clipperton zone for instance. In the Atlantic Ocean abyssal plains are restricted to small areas in particular because of the presence of Mid-Atlantic ridges implying that about half the seafloor is above the CCD and thus covered by marine carbonate sedimentation. In addition, the configuration of the Atlantic Ocean implies that abyssal plains are more affected by detrital inputs from the neighboring continental margins than abyssal plains from the Pacific (Delange et al. 1992). Therefore, sedimentation rates are generally higher in the Atlantic than in the Pacific Ocean and may be a factor hindering nodule formation.

Many studies have already been conducted to investigate Mn-nodules formation but they generally consist in common geochemistry analyses (major and trace elements) that did not allow to answering all questions concerning how, what, and why these deposits formed. With the advent of transition metal isotopic analyses we have now new tools for reconsidering these processes.

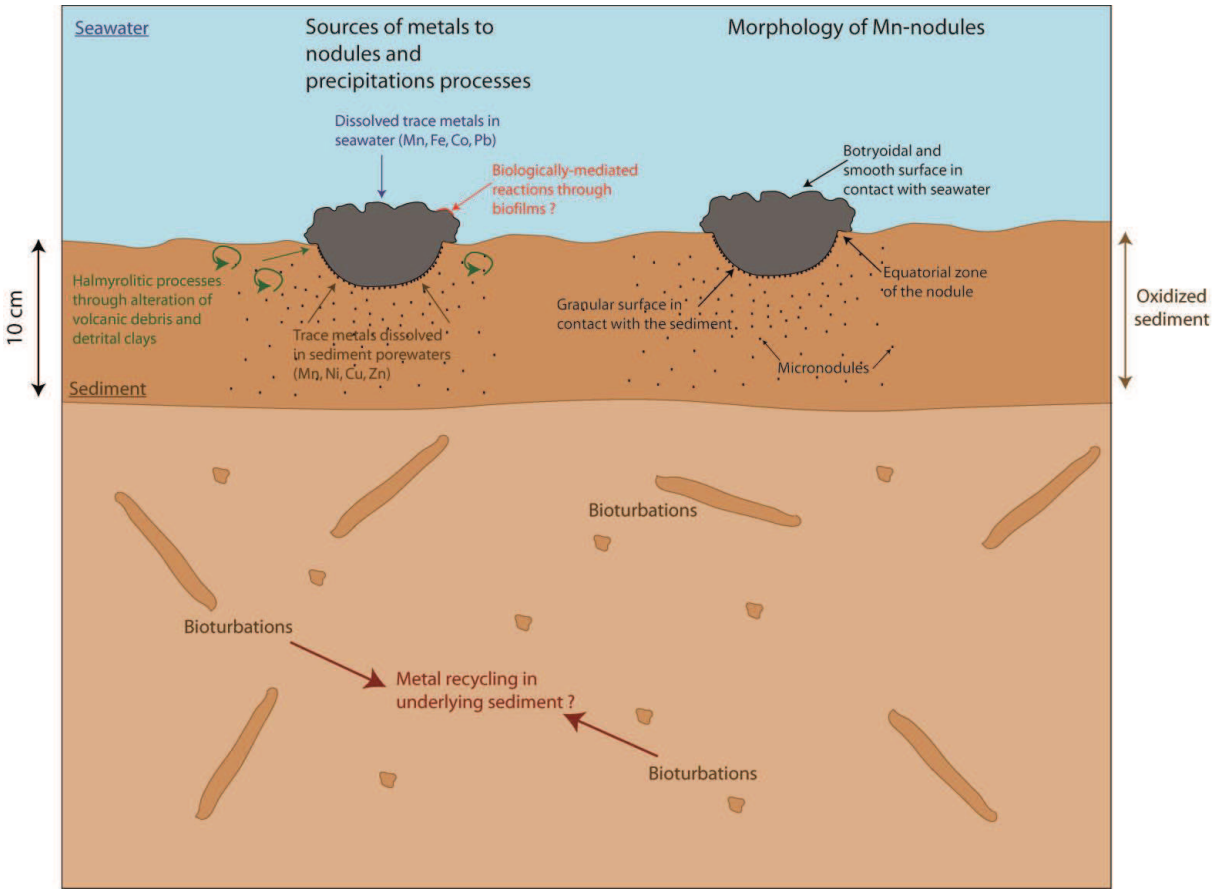

Figure A3.1: *Cartoon showing the deposition environment of manganese nodules and all possible metal sources participating to nodules growth.*

1.2. Metals in seawater and the role of biological activity in surface waters

Cronan (2000) argued that a combination of a high productivity area and a CCD (Carbonate Compensation Depth) near the seafloor where the carbonate sedimentation is lowered due to carbonate dissolution is a prerequisite to provide high contents of metals-bearing organic carbon rich phases to the deep-sea sediments. Organic particles containing metals are then directly supplied to the sediments without being remobilized during their fallout in the water column, and without important dilution by carbonate contents (unlike it occurs above the CCD) (Verlaan et al. 2004). Subsequently, decay of that metals-rich organic matter in the sediments is an important supply of metals to pore waters, especially for Mn, Ni, Cu, and they will potentially contribute to Mn-nodules metals enrichments. Therefore, Mn-nodules precipitated near the CCD and in high productivity surface waters are enriched in Mn, Ni and Cu due to diagenetic input, whereas above the CCD Mn-nodules will be mainly precipitated from hydrogenetic sources. For instance, below the equator, which is an area below the CCD and where siliceous sedimentation is high, concentrations of metals contained in the organic phase are diluted and are not high enough to allow Mn-nodules formation. Thus, in the Peru basin most nodules are found near or below the CCD (Cronan 2000).

1.3. Early diagenesis processes in deep-sea sediments: a reservoir of metals for nodule precipitation and growth

Many transition metals are bioessential elements for biological activity and are present in the biological structure of these organisms. Once the dead organic matter reaches the sediment surface, it is dissolved and oxidized by oxygen contained in porewaters during oxic diagenesis processes (Klinkhammer et al. 1982; Sawlan and Murray 1983; Heggie et al. 1986; Morford and Emerson 1999). Consequently, transition metals such as Mn, Co, Cu and Ni contained in organic matter are released into the sediment porewaters and migrate in the upper part of the sediment to be subsequently incorporated in Mn-oxides of Mn-nodules. Low sedimentation rates are a prerequisite, because it will prevent preservation of organic matter by rapid burial during oxic diagenesis, and transition metals in pore waters are mainly controlled by reactions involving organic matter decay. A high organic matter supply to the sediment coupled to a rapid rate of decaying is critical for Mn-nodules growth (Aplin and Cronan 1985). Early diagenesis processes (sediments close to the sediment-water interface, the few first meters of sediments) are critical for enrichment in Mn-nodules because this is where the highest proportion of organic matter decaying occurs.

This higher metal content in deep-sea-clays is mostly due to remobilization of metal subsequently to organic matter decaying (Heggie et al. 1986). With increasing depth and consumption of oxygen during organic matter decaying, Mn is reduced and become soluble in sediment porewaters. Thereafter, authigenic precipitation of Mn-oxides scavenges trace metals such as Ni, Cu, Co and Zn which have been previously released during organic matter decaying (Klinkhammer 1980; Sawlan and Murray 1983). Ni cycling in oceanic sediment and to a larger extent in oceans is thus strongly controlled by Mn redox cycling.

Aplin and Cronan (1985) (and (Maynard 2003)) suggested that Pacific Mn-nodules having a high diagenetic contribution are found in regions with high biological productivity, which indicates that organic materials play an important role in early diagenetic processes by providing the majority of metals to the sediment surface porewaters, which are then available for being incorporated in Mn-nodules. The diagenetic model invoked in their study involves precipitation of todorokite directly from sediment porewaters.

Occurrence of diagenetic nodules in zones of relatively high biological productivity doesn't only reflect a high metal supply to sediments, but also show a high degree of metals remobilization during sedimentary early diagenesis. Transition metal chemistry is closely related to the oxidation reaction of organic carbon, thereby diagenetic nodules formation is mainly controlled by organic matter supply rates (i.e. biological productivity of surface waters), and organic matter degradation rate (i.e. dissolution and oxidation of organic matter in the sediment surface under low sedimentation rates, which is subsequently followed by release of Mn, Ni and Cu in porewaters). It also implies that variations in the extent of biological productivity in surface waters will impart variations in metals supply to Mn-nodules. Siliceous organisms are also important carriers of transition metal such as Ni and Cu, and their decaying during oxic diagenesis is another possible mechanism of transition metals release to the sediments porewaters (Cronan 2000).

In addition, the role of bacterial activity for nodule growth was mentioned in the literature (Wang and Muller 2009; Wang et al. 2009), and some collaborators observed during previous oceanographic cruises that some nodules were collected completely covered with microbial mats, hence supporting the hypothesis that *in-situ* biological activity could have an influence on metal enrichment of Mn-nodules.

Mn-nodules having an important diagenetic component are the most enriched in metals such as Ni, Cu or Zn. In order to better constrain metals cycling during early diagenesis processes and to distinguish whether metals come from organic matter from

carbonate organisms or from siliceous organisms, seawater or other sources such as hydrothermal vents, we suggest using Ni isotope variations as a biogeochemical tracer and other metal isotope systematics like Fe, Cu and Zn (and Mo). Our first objective is to investigate Ni isotope behavior in the first centimeters of sediments located directly under nodules. The interest lying in Ni isotope systematic is that it's an element strongly associated with biological activity (i.e. nutrient-type profile in ocean, co-factor enzyme, used for assimilation of urea), and given that biological reactions are prone to highly fractionate stable isotopes (Cameron et al. 2009), we expect nodules to record a meaningful isotopic signal.

Mo isotope and Fe isotope fractionation in authigenic precipitated in Mn-oxides during early diagenesis processes have already been documented in previous studies (Severmann et al. 2006; Siebert et al. 2006; Poulson Brucker et al. 2009) which adds further support for using a multi isotope proxy approach, including Ni, to investigate metal sources in Mn-nodules.

1.4. Rationale of the project

The guiding principle of this study is the investigation of early diagenesis processes occurring at the seawater-sediment interface in the first fifty centimeters of the sedimentary column and their effects on metal enrichment in Mn-nodules. Metal stable isotopes studies have blossomed in the past decade as analytical techniques have improved, particularly with the development of high-precision MC-ICP-MS. Although initial attention focused on the potential use of metal isotope systems as biosignatures, they are now emerging as useful geochemical tracers of metal sources and biogeochemical cycling in seawater. Our laboratory and the analytical facilities of the PSO in Ifremer/IUEM is at the forefront of this research field and has the unique capability to investigate a large range of metal and metalloid stable isotope tracers, including Fe, Mo, Cu, Zn, Cd, Ni, Ge, and Se as well as radiogenic isotopes such as Pb and Nd isotopes. This project is therefore at the interface of basic research and applied research since it proposes to apply innovative and promising isotope proxies to investigate the distribution of base metals and other strategic metals in Mn-nodules. This project is expected to strengthen the understanding of formation of the deep oceans mineral resources.

Collaborative work for isotopic and geochemical studies with geologists and geochemists from BGR (Hannover, Germany) and associate partners, Geomar (Kiel, Germany) and AWI (Alfred Wegener Institute, Bermerhaven, Germany) was implemented in the course of this study.

2. Sampling strategy

2.1. Sampling areas locations

2.1.1. The French mining claim area

In 1987 the French government obtained from The United Nations via the International Seabed Authority (ISA) three mining claim areas in the most Mn-nodules concentrated zone, the North-Western part of the Clarion-Clipperton Fault Zone (CCFZ) in the Pacific Ocean, in order to start prospection for mining exploitation perspectives (Figure A3.2). In addition to geological and geochemical exploration and prospection, oceanographic

cruises also include biological studies and inventory of existing faunas to evaluate the potential impact that mining could have on these deep-sea ecosystems. For keeping these claim areas, a contract linking ISA and Ifremer was signed for fifteen years (2001-2016) with obligation to implement explorative oceanographic studies. NODINAUT cruise in 2004 on the R/V L'Atalante and eventually the BIONOD 2012 cruise are the achievement of the contract.

2.1.2. The German mining claim area

The German claim area is located near the Mexican coasts at depth between ~4000 and ~4500 meters, whereas the French claim areas is frankly located in the middle of equatorial Pacific where seafloor depths exceed 5000 meters.

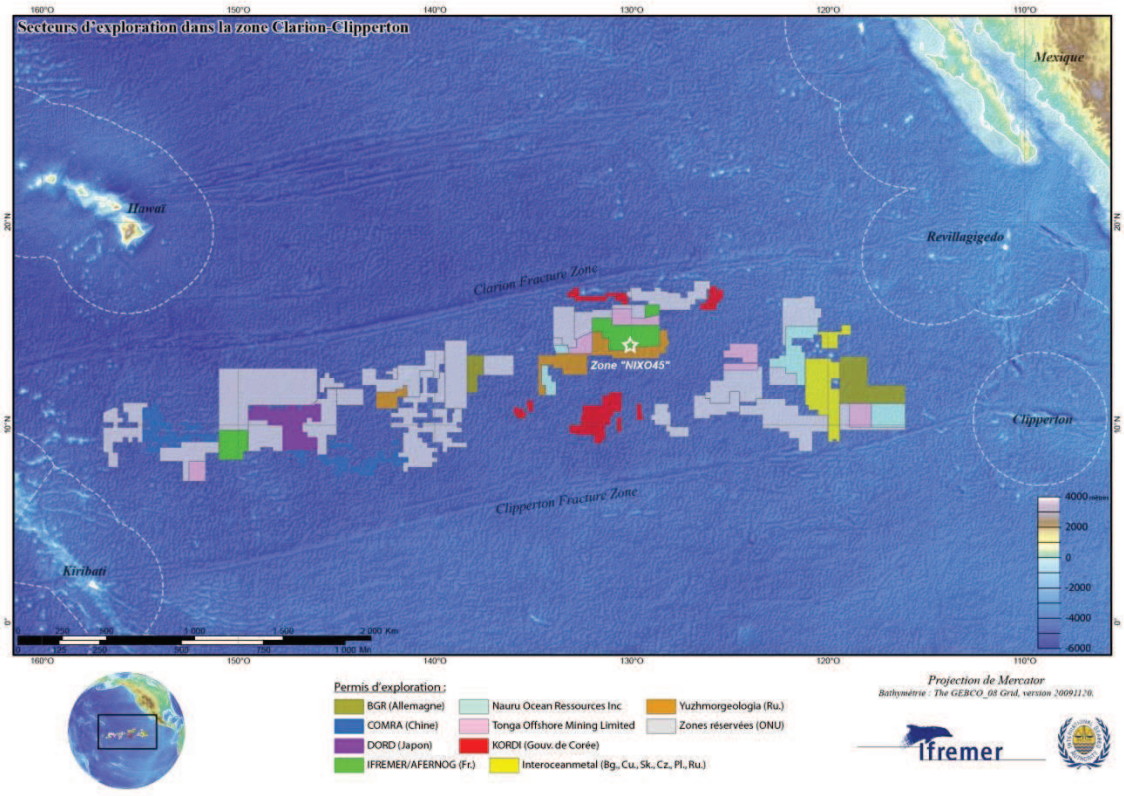

Figure A3.2: *Map of the location of thedifferent mining areas of each country owning a claim area in the Clarion/Clipperton in the Central Pacific Ocean. The French claim area is in green and the German claim area is in brown green. The white star indicates the location of the NIXO 45 zone where sampling was implemented.*

2.2. Samples collected

Surface sediment and Mn-nodule samples will be recovered from Clarion-Clipperton Fracture Zone belt located in the Equatorial Pacific Ocean. Depths range from 4000 to more than 5000 meters. This zone is characterized by a high biological productivity of surface waters and low sedimentation rates (e.g. low continental inputs) implying that high contents of organic matter are likely to be supplied to the sediment surface and undergo intensive

remineralization in the sediment (i.e. organic matter oxidation). Four different nodules facies in this area were defined according to previous studies (e.g. NIXO 45, 1982; NIXONAUT, 1988; NODINAUT, 1994). Facies differ by their nodule sizes, shape, and density: (1) facies “0” with no nodule visible on the zone; (2) facies “A” with small nodules of irregular shape; (3) facies “B” with larger nodules of more regular shape; and (4) facies “C” with large nodules that could reach up to 15 cm in diameter (Figure A3.3).

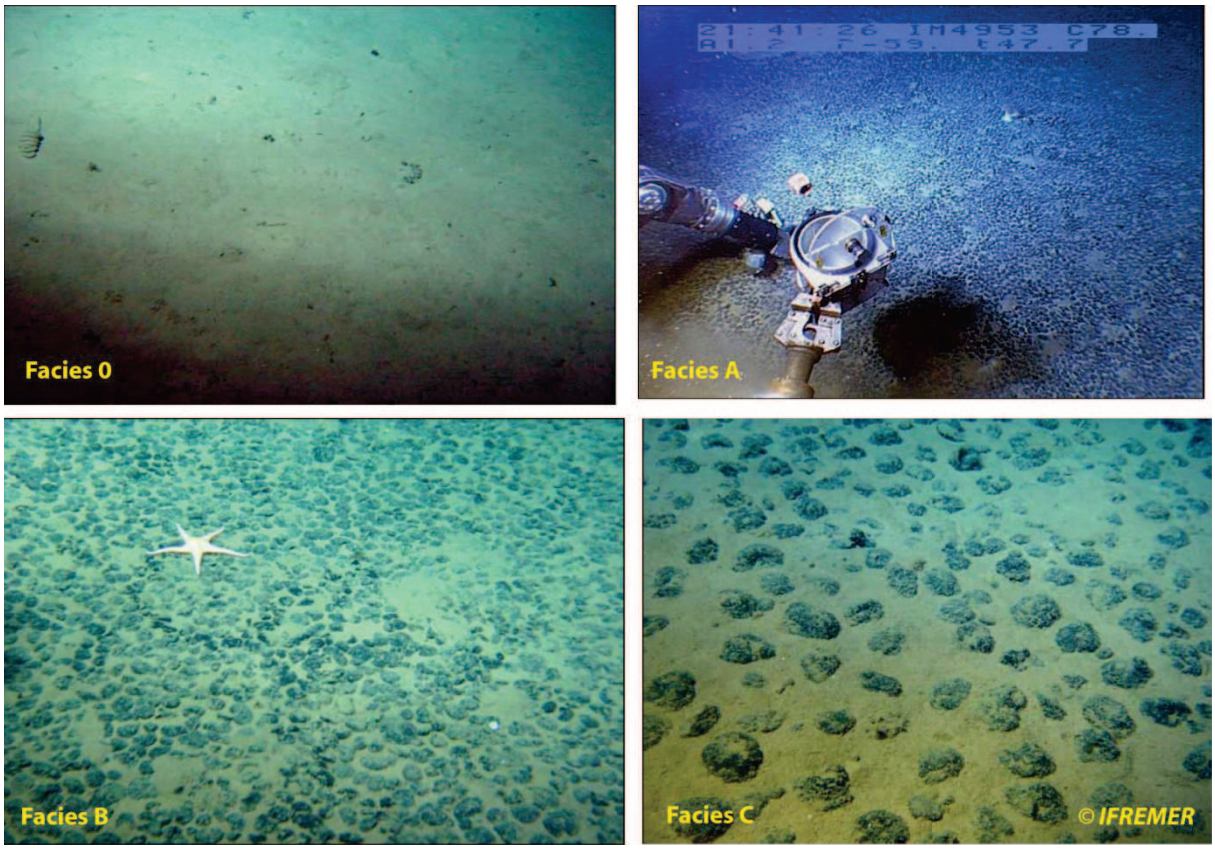

Figure A3.3*: The four different nodule facies A, B, C and 0 encountered in the NIXO 45 zone and more generally in the Clarion/Clipperton area of the Central Pacific Ocean (see text for further descriptions).*

Porewaters were extracted with Rhizons™ samplers following previously used method in Ifremer (Seeberg-Elverfeldt et al. 2005). This technique allows a direct sampling through the core liner where holes will be previously drilled, while preserving the integrity of the sample regarding oxygen contamination. Shore-based work includes (1) major cations and anions by ion chromatography and ICP-AES ; (2) trace elements by ICP-MS; (3) isotopic composition by MC-ICPMS.

Besides conventional major element analysis, we will also investigate metal isotope ratios and the concentrations of a large range of elements (including Rare Earth metals) by ICP-MS following a method modified from (Axelsson et al. 2002).

3. Onboard sampling methods

Onboard sampling consisted in sample archiving and nodules description. No geochemical analyses were carried out during the oceanographic cruise.

3.1. Ferromanganese nodules

In the French claim area we managed to collect samples from facies 0, B and C using box corers and all ferromanganese nodules were collected and weighed (Figure A3.4). It was rather difficult to get any successful sampling in facies A because it occurs in a restricted area with outcrops of pillow-lavas and basalt flows forming small cliffs. Due to this field configuration, we decided that it was too risky to repeat this operation once again. We also archived nodules recovered by epibenthic sledges which generally sampled more than one nodules facies.

In addition, collection of Mn-micronodules were performed by wet sieving (250-300 µm) of the uppermost two sediment layers (0-5 and 5-10 cm) from 33 box corers. We collected 65 samples (wet weight >50 g each) (Table 6) stored in plastic bags for shore-based studies. After sample drying (20-30°C) the micronodules will be separated for further analyses.

3.2. Sediments

Collection of sediment was carried out using plastic push cores with previously drilled holes every centimeter inserted into the sediment retrieved in the box corer. The core was then processed in the cold laboratory for porewaters extraction. Since the extraction of porewaters from the sediment did not disturb the original stratification (only small fractures appeared without any sediment collapsing) we collected sediment samples from this same core. This operation was performed using a piston to push the sediment out of the core and then we sliced it with the exact same resolution as we did for extraction of porewaters with rhizons, i.e. every centimeter for the first 20 centimeters and then every 2 centimeters for the remaining sediment.

One box corer was sampled from each facies 0 and B, whereas on facies C we sampled two box cores. The first push core was placed right under a big nodule and the nodule was collected and archived separately for later analyses. In the second box core the tube was inserted in an area of the box core devoid of any nodule lying on the sediment surface. Sediments were then stored in cold environment (~8°C).

Additionally, sediment from box corers were separately collected for organic matter-related studies using the same procedure as described above. Samples were stored in plastic bags and then frozen to -20°C.

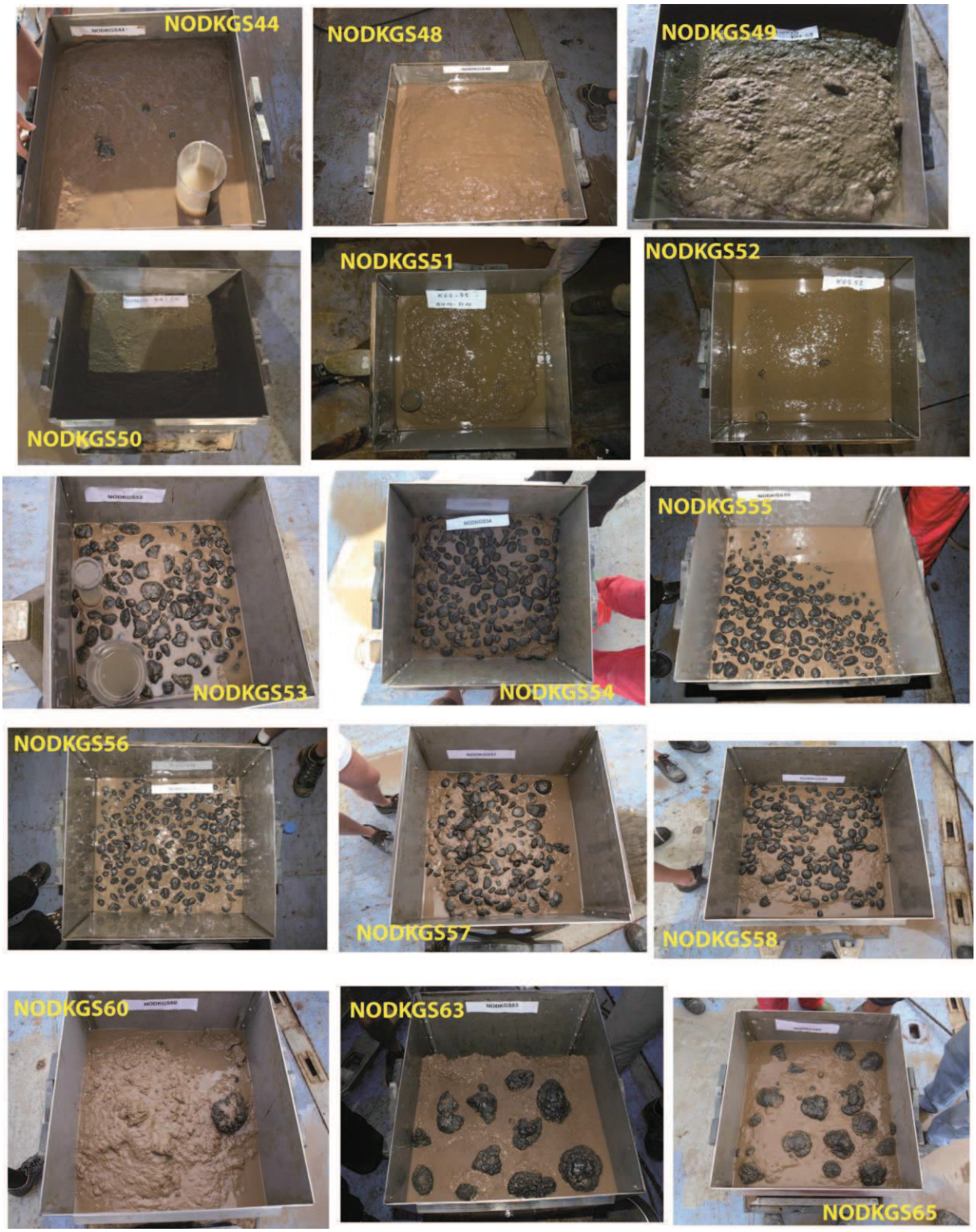

Figure A3.4 *Pictures of box cores collected in the NIXO 45 zone in the French claim area.*

3.3. Porewaters

Porewaters were collected from plastic push cores inserted into the sediment. Core lengths were usually between 30 and 45 cm. The core was processed in a cold laboratory where porewaters were extracted using Rhizons™ (Rhizosphere Research products)

following previously used method in Ifremer (Seeberg-Elverfeldt et al. 2005). Rhizons™ were inserted into the tube holes every centimeter in the first 20 centimeters of the core, and then every 2 centimeters for the remaining core. We waited around one hour and a half until enough porewater was retrieved in the syringe (we usually collected between 5 and 10 ml of porewater per syringe) (Figure A3.5). Porewaters were then transferred in 15 ml Nalgene vials previously washed in cold 10% hydrochloric acid and stored in cold environment (~8°C). Porewaters from box core KGS44 in facies B were sampled both by Rhizons™ and by centrifugation of sediment retrieved in a second core from the same box core.

Figure A3.5 *Picture of porewaters extraction device using Rhizons™ inserted in the sediment core.*

4. Onshore-based sample processing

4.1. Porewater samples processing

Upon receiving porewater samples, they were acidified at pH ~2 with 6 mol/L HCl. Then porewater samples need to be left for a released time of at least three weeks.
Elemental analyses will be made using an HR-ICP-MS (Element 2, Thermo-Finnigan) by applying a dilution of samples of 25 for analyses through the ICP-MS.

4.2. Nodule and sediment samples conditioning

4.2.1 Preparation of rock powders for nodule and sediment samples

Ferromanganese nodules

Prior to transforming nodules in powder, each nodule was dried in an oven at 40°C. Then, nodules powders were made using an agate mortar.

The micronodules fraction was equally collected for analysis of micrometeorites. Possible micrometeorites will be sorted by hand-picking.

Sediments

For each sediment samples of each cores, a split of wet sediment was taken and put in pyrex beakers to be dried in an oven at 40°C. After complete drying, compact sediments were reduced in powder using an agate mortar. Between each sample, the agate mortar was thoroughly washed with pure sand (pure SiO_2). The powder was then placed in HDPE Nalgene vials for archiving. The remaining undried sediment split was frozen and kept as an archive.

4.2.2. Strategy of sample selection

In a first approach, we selected for each mining license area, cores corresponding to each of the three facies B, C and 0 (we did not collect any core from facies A area). We assumed that with this strategy we will have samples from both mining license areas that could be comparable afterwards.

For each selected core correspond the sediment, porewaters extracted from the same sediment core and if available a nodule collected right above the position of the core in the box corer.

4.3. Strategy and planning for sample analyses

With the exception of nodules in the German mining area that were not systematically collected for our study, collection of sediments and porewaters samples from both the French the German mining areas was designed with the ambition of implementing a similar analysis scheme on the two different areas.

4.3.1. Sediment

Our strategy of analysis is three-fold. First, it will consist in determining mineralogy of sediment samples by XRD (X-Ray Diffraction), especially for looking at potential differences between the German area and the French area. Then major and trace elements concentrations will be analyzed by ICP-AES and ICP-MS. Finally, after a good characterization of the samples with these preliminary analyses metal isotope compositions will be measured by MC-ICP-MS.

4.3.2. Nodules

Nodules analyses will be approached in a two-dimensional way. The first approach will be to carry out elemental and isotopic analyses of bulk nodules from the all facies from both the French mining area and the German mining area.

In a second approach a high resolution sampling of discrete Fe-Mn-oxides layers of the nodule will be implemented on selected samples from each of the four facies previously defined using a microdrill device. To avoid dislocation of the nodule when cutting it for obtained a flat section, they will be put into epoxy resin and then cut in half.

Additionally, Electron Microprobe Analyses (EMPA) through the nodule section will be carried out prior to the manual sampling. Using this methodology we can obtain qualitative maps of transition elements (Fe, Mn, Ni, Cu, Co, Zn, Ti) and other major elements like Al, Si, P, Ca, Na, Mg of the nodule section. These maps will show us where elements are located in the crystalline structures and which elements associate together.

Bulk rocks analyses and nodules subsampling analyses of elemental and isotope geochemistry will be done by ICP-AES/ICP-MS and MC-ICP-MS respectively.

4.3.3. Porewaters

After geochemical composition analyses of porewaters by ICP-MS, the second step is to measure metal isotope composition (Ni, Cu, Zn, Mo and Fe) after pre-concentration of metals from the saline matrix following to the experimental method described in chapter 1 of this manuscript.

Designed this way, the whole of the analyses will allow us to make high resolution profiles of trace metal concentrations and isotope compositions in the sediments and associated porewaters.

5. Other relevant analyses to Mn-nodules

Nodules are mainly formed by amorphous and poorly crystalline mineral phases, thus it precludes a clear identification of the mineralogy of the samples by common methods like X-Ray Diffraction. Therefore, besides XRD analyses and Electron Microprobe elemental mapping of nodule cross-sections that will only give a first order picture and evaluation the mineralogy (in particular the presence of detrital phases, carbonates or phosphates), thorough investigation of the mineralogy could be performed using μXRD, XANES and EXAFS. We have previously explained that precipitation Fe- and Mn-oxyhydroxides in polymetallic nodules was the result of several biogeochemical processes which includes three major precursors for these precipitates: seawater, sediment and sediment porewaters, and biological activity. It is expected that mineral phases formed through these different precursors will produce fine-scale variations in the mineralogy. Moreover, these supplementary analyses could be valuable information for understanding metal enrichment in nodules and their effects on elemental and isotopic geochemical variations. In fine, we will obtain a complete and fine picture of the mineralogy and geochemistry of the nodules. An example of such type of study is shown in appendix 2. This article, submitted to *Geochimica et Cosmichimica Acta*, shows the diversity of Fe speciation and fine-scale mineralogy along a nodule transect from the South Pacific gyre.

6. References

Aplin, A. C. and Cronan, D. S. (1985). "Ferromanganese oxide deposits from the Central Pacific Ocean, II. Nodules and associated sediments." Geochimica Et Cosmochimica Acta 49(2): 437-451.

Axelsson, M. D., Rodushkin, I., Ingri, J. and Ohlander, B. (2002). "Multielemental analysis of Mn-Fe nodules by ICP-MS: optimisation of analytical method." Analyst 127(1): 76-82.

Cameron, V., Vance, D., Archer, C. and House, C. H. (2009). "A biomarker based on the stable isotopes of nickel." Proceedings of the National Academy of Sciences of the United States of America 106(27): 10944-10948.

Cronan, D. S., Ed. (2000). Handbook of marine mineral deposits, CRC Press London.

Delange, G. J., Vanos, B. and Poorter, R. (1992). "Geochemical composition and inferred accretion rates of sediments and manganese nodules from a submarine hill in the Madeira abyssal plain, Eastern North Atlantic." Marine Geology 109(1-2): 171-194.

Heggie, D., Kahn, D. and Fischer, K. (1986). "Trace metals in metalliferous sediments, MANOP Site M: interfacial pore water profiles." Earth and Planetary Science Letters 80(1–2): 106-116.

Klinkhammer, G., Heggie, D. T. and Graham, D. W. (1982). "Metal diagenesis in oxic marine-sediments." Earth and Planetary Science Letters 61(2): 211-219.

Klinkhammer, G. P. (1980). "Early diagenesis in sediments from the eastern equatorial Pacific, II. Pore water metal results." Earth and Planetary Science Letters 49(1): 81-101.

Maynard, J. B. (2003). Manganiferous Sediments, Rocks, and Ores. Treatise on Geochemistry. D. H. Editors-in-Chief: Heinrich and K. T. Karl. Oxford, Pergamon**:** 289-308.

Morford, J. L. and Emerson, S. (1999). "The geochemistry of redox sensitive trace metals in sediments." Geochimica Et Cosmochimica Acta 63(11-12): 1735-1750.

Poulson Brucker, R. L., McManus, J., Severmann, S. and Berelson, W. M. (2009). "Molybdenum behavior during early diagenesis: Insights from Mo isotopes." Geochem. Geophys. Geosyst. 10(6): Q06010.

Sawlan, J. J. and Murray, J. W. (1983). "Trace-metal remobilization in the interstitial waters of red clay and hemipelagic marine-sediments." Earth and Planetary Science Letters 64(2): 213-230.

Seeberg-Elverfeldt, J., Schlüter, M., Feseker, T. and Kölling, M. (2005). "Rhizon sampling of porewaters near the sediment-water interface of aquatic systems." Limnology and Oceanography: Methods 3: 361-371.

Severmann, S., Johnson, C. M., Beard, B. L. and McManus, J. (2006). "The effect of early diagenesis on the Fe isotope compositions of porewaters and authigenic minerals in continental margin sediments." Geochimica Et Cosmochimica Acta 70(8): 2006-2022.

Siebert, C., McManus, J., Bice, A., Poulson, R. and Berelson, W. M. (2006). "Molybdenum isotope signatures in continental margin marine sediments." Earth and Planetary Science Letters 241(3–4): 723-733.

Verlaan, P. A., Cronan, D. S. and Morgan, C. L. (2004). "A comparative analysis of compositional variations in and between marine ferromanganese nodules and crusts in the South Pacific and their environmental controls." Progress in Oceanography 63(3): 125-158.

Wang, X. H. and Muller, W. E. G. (2009). "Marine biominerals: perspectives and challenges for polymetallic nodules and crusts." Trends in Biotechnology 27(6): 375-383.

Wang, X. H., Schlossmacher, U., Wiens, M., Schroder, H. C. and Muller, W. E. G. (2009). "Biogenic Origin of Polymetallic Nodules from the Clarion-Clipperton Zone in the Eastern Pacific Ocean: Electron Microscopic and EDX Evidence." Marine Biotechnology 11(1): 99-108.

Annexe 4 – Poster AGU 2011

Appendix 4 – Poster AGU 2011

Ni biogeochemical cycle through geological time: insights from Ni isotope variations in modern and ancient marine metallifereous deposits

Bleuenn Gueguen[1,2]*, Olivier Rouxel[1,2], Emmanuel Ponzevera[2], Jeffry Sorensen[3], Brandy Toner[3], Andrey Bekker[4], and Yves Fouquet[2]
(1)Université de Brest (IUEM), UMR 6538, BP 80 F-29280 Plouzané, France, (2) Ifremer, Département Géosciences Marines, 29280 Plouzané, France, (3) University of Minnesota, Department of Soil Water & Climate, St Paul, MN55108, USA, (4) University of Manitoba, Department of Geological Sciences, Winnipeg, MB R3T 2N2, Canada
*bleuenn.gueguen@univ-brest.fr

1.a. Why using Ni isotope as a biogeochemical tracer?

- **Transition metal isotopes as biogeochemical tracers**

Studies of isotopic composition of transition metals such as Fe, Cu, Zn and Mo (non-traditional stable isotopes) (**Figure 1**) as biogeochemical tracers became popular due to their **important use by the biosphere** (biossential metals) [1]. Ni has one valence state, Ni^{2+} (instead of Fe for instance, which has two valence states, Fe^{2+} and Fe^{3+}), thus shifts of the valence state during redox conditions changes won't dominate mass-dependent fractionations. Ni isotope variations are the results of biotic (e.g. assimilation of Ni by micro-organisms) and/or abiotic fractionations (e.g. chemical precipitation).

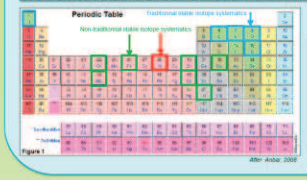

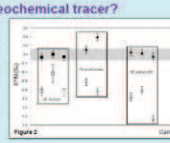

- **Ni is involved in some major biological reactions:**

Ni concentration in oceans is coupled to that of nutrients explaining its **nutrient-type profile** in oceanic waters. Although non-biolimiting, Ni is used by phytoplankton as an **enzyme co-factor** during assimilation of urea. In Archean anoxic oceans, micro-organisms like methanogens which are big consumers of Ni were abundant and probably contributed to methane release in the atmosphere preventing accumulation of oxygen [2]. As **methanogens** fractionate **light Ni isotope** (down to ~1.5‰) (**Figure 2**) [3], Ni isotopic composition of ancient oceans could have been largely controlled by this microbiological activity.

1.b. Ni concentration in oceans has varied through geological time

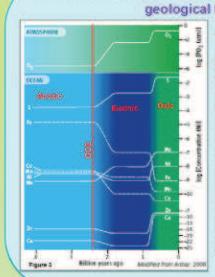

Transition metal concentrations in oceans has varied through geological time especially around 2.5-2.4 Gyr after the so called **Great Oxidation Event (GOE)**, and co-evolved with O_2 concentration in the atmosphere [4]. **Figure 3** is a picture of our best knowledge of metal concentrations in oceans through time. Since the **precambrian mantle was hotter**, volcanic activity at the Earth surface was very high and erupted lavas on continents mostly consisted of **Ni-rich komatiites** that provided high amount of Ni to oceans. Ancient oceans were more than 40-fold enriched in Ni than modern ones [2]. **After ca. 2.4 Gyr**, a marked **decrease in volcanic activity** would have dramatically lowered Ni supply to the oceans leading to a **decrease in methanogen activity** and methane production [2]. This major change could have promoted the **accumulation of oxygen** in the atmosphere leading to the transition towards oxidizing conditions on Earth after GOE.

4.a. Light Ni isotope enrichment during adsorption on Fe-oxyhydroxides

Ni adsorption experiments were conducted on Fe oxy-hydroxides, such as 2-line ferrihydrite and goethite, under varying pH and Ni concentrations in starting solution. The fractionation factor between the solid phase and Ni in solution that was not adsorbed is expressed as $\Delta^{60/58}Ni_{solid} \approx \delta^{60/58}Ni_{bulk} - \delta^{60/58}Ni_{sol}$, i.e. difference in isotopic composition of the mineral and the solution after completion of the experiment. Results indicate that the solid phase is enriched in light isotopes relative to the remaining Ni in solution (**Figure 9**). In addition, we identified a marked difference between **2-line ferrihydrite** which has a maximum fractionation of **~0.4 ‰ and goethite** with a $\Delta^{60/58}Ni_{solid}$ **~0.9 ‰**. Our upcoming EXAFS data (Extended X-ray Absorption Fine Structures) will provide additional information on whether these differences could be due to Ni coordination and speciation changes within mineral or not.

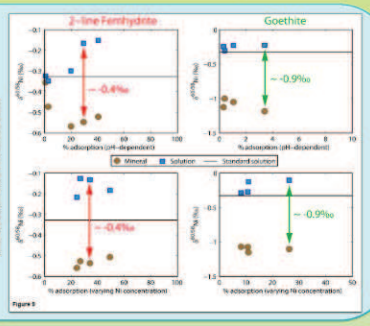

2. Experimental methods

Ni-isotope analyses were performed on a Neptune **MC-ICP-MS** using a double-spike method for instrumental mass bias correction. This method consists in adding a mixture of **^{61}Ni and ^{62}Ni isotopes** for which isotopic composition is perfectly known. To avoid potential isobaric interferences and matrix effects, all geological samples were purified through a **two-step chromatography column separation** procedure (**Figure 5**).

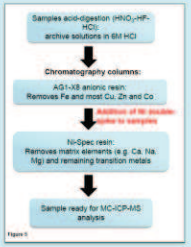

1.c. Modern versus ancient ocean Ni cycling

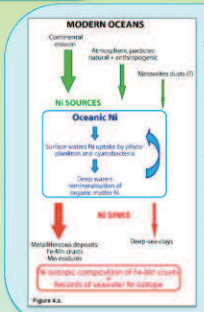

- **Fe-Mn crusts:**

Fe-Mn crusts are composed of **Mn-oxide layers** precipitated from seawater on seamounts. Due to their very low precipitation rate, they can record up to 80 Myr of seawater composition, and are enriched in transition metals such as Ni, Co, Cu and Zn. Isotopic compositions of these metalliferous deposits may directly reflect seawater composition through time (**Figure 4.a**).

- **Iron Formations (IFs):**

IFs consist of very large deposits of interbedded Si-rich layers and Fe-rich layers precipitated in Fe-rich anoxic oceans (**Figure 4.b**). IFs were deposited during the Precambrian and most of them disappeared completely after ~1.8 Gyr with a sharp decrease after ~2.5 Gyr [5].

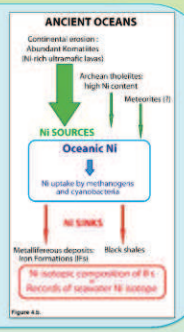

4.b. Heavy Ni isotopic composition of Fe-Mn crusts: implications for Ni isotope in modern seawater

Bulk Fe-Mn crusts were collected in various locations for the Atlantic ocean and in the vicinity of Hawaii archipelago for the Pacific ocean. All Fe-Mn crusts display an **enrichment in heavy Ni isotopes** with $\delta^{60/58}Ni$ ranging from +0.76 ± 0.02 ‰ to +1.80 ± 0.03 ‰ (**Figure 10**). From results of adsorption experiments (Figure 9), we can deduce a minimum Ni isotopic composition of seawater of ~+1.6 ‰ (see dark blue line drawn in **Figure 10**). Ni isotope variations observed among crusts can be explained by fractionation during adsorption on oxy-hydroxides as shown by red and green arrows on **Figure 10**. Nevertheless, since Ni in Fe-Mn crusts occurs mainly within Mn-oxides, we cannot preclude that the fractionation factor for Mn-oxides is different than for goethite and 2-line ferrihydrite.

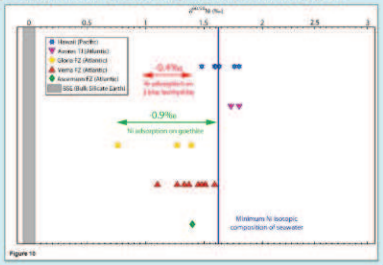

3. Analytical results: high precision with double-spike method

$$\delta^{60/58}Ni\ (‰) = 1000 \times \left(\frac{^{60/58}Ni_{sample}}{^{60/58}Ni_{NIST\ SRM\ 986}} - 1\right)$$

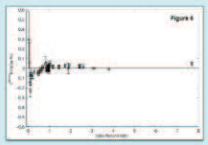

We obtain an overall two-standard error (**2se**) between **0.02 ‰ and 0.04 ‰** for both Ni-depleted samples like BIFs and Ni-enriched samples like Fe-Mn crusts. **Figure 6** presents tests undertaken on the NIST SRM 986 isotopic standard in order to evaluate the **effect of spike/natural ratios on the determination of Ni isotopic composition**. Below a ratio of 0.5, isotopic compositions deviate from the true value of 0.00 ‰ and error bars become larger. Over-spiked NIST SRM 986 up to a ratio of 8 are still well-determined and we used **a ratio of 1 in our procedure**. Different concentrations of spiked NIST SRM 986 analysed through MC-ICP-MS indicate that **20 ppb of Ni in solution is the detection limit** below which isotopic ratios are not determined properly (**Figure 7**). **Figure 8** shows the good reproducibility of the determination of isotopic composition of a mono-elemental solution (Ni Plasma Cal) processed through the entire chromatography procedure with **a two standard deviation of 0.07 ‰**.

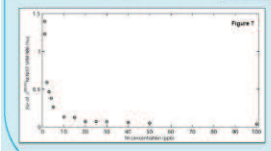

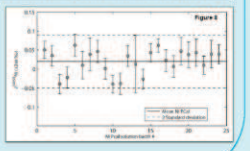

5. Conclusions

- During Ni adsorption on Fe oxy-hydroxides enrichment in light isotopes occurs in the solid phase. Different fractionation factors are obtained according to mineral type: $\Delta^{60/58}Ni_{min/sol}$ ~-0.9‰ for goethite and $\Delta^{60/58}Ni_{min/sol}$ ~-0.4‰ for 2-line ferrihydrite.
- Fe-Mn crusts are enriched in heavy isotopes with a range of variations from +0.76±0.02‰ to +1.80±0.03‰.
- Iron Formations show variations through geological time, especially around 2.4 Gyr during the GOE probably due to globally lower Ni concentrations in oceans. They also indicate that ancient seawater was lighter than modern oceans.

4.c. Ni isotopic composition of IFs through geological time: implications for ancient seawater isotopic composition

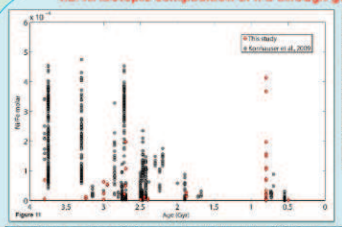

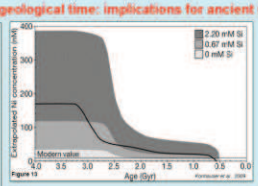

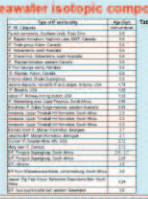

Figure 11 is a compilation of Ni/Fe molar ratios in IFs through time [2]. Ni isotope of IFs versus age are displayed in **Figure 12** (symbols colors are for age and locality) and the blue curve is the best estimate of Ni isotopic composition of IFs through geological time (dashed lines are for period of time which are not enough constrained). The red curve is the extrapolation to archean seawater isotopic composition by considering the 2-line ferrihydrite fractionation factor of -0.4 ‰ (Figure 9). **Table 1** summarizes sample locations. The range of variations of Archean IFs vary between -0.30±0.03‰ and +0.85±0.02‰. Neoproterozoic IFs show a wide range of values from +0.81±0.02‰ to -0.14±0.03‰. **The high variability of Ni isotope around 2.4 Gyr** is correlated to the decrease in Ni concentration in seawater (**Figure 13**), suggests that due to lower Ni concentrations in oceans and to Ni fractionation during adsorption, highest values would imply quantitative scavenging in Fe oxy-hydroxides reflecting seawater composition (or reservoir effects during diagenesis), whereas lowest values would reflect maximum fractionation during Ni precipitation in Fe oxy-hydroxides. In addition, these data suggest that **Ni in ancient oceans was globally lighter than Ni in modern oceans** (see the dark blue line representing modern seawater). High variations in Neoproterozoic IFs could be explained by the presence of an ice-cap during a major glacial event (the « Snowball Earth Events) that provoked a stratification of oceans: an oxic surface layer overlaying deep anoxic waters [6]. This configuration may have modified the scavenging of Ni in Mn-oxides, especially at the oxic/anoxic interface where efficient Mn oxidation occurs and promotes Ni scavenging instead of deeper waters.

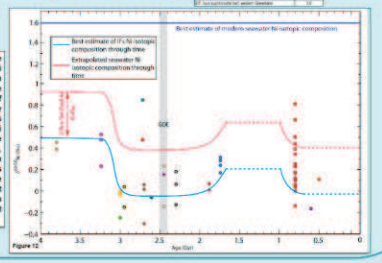

References:
[1] Anbar A.D., Rouxel, O., 2007. Metal stable isotopes in paleoceanography. Annual Review of Earth and Planetary Sciences, 35, 717-746.
[2] Konhauser K.O. et al., 2009. Oceanic nickel depletion and a methanogen famine before the Great Oxidation Event. Nature, 458(7239), 750-753.
[3] Cameron, V., Vance, D., Archer, C., House, C.H., 2009. A biomarker based on the stable isotopes of nickel. Proceedings of the National Academy of Sciences of the United States of America, 106(27), 10944-10948.
[4] Anbar A.D., 2008. Elements and Evolution. Science, 322(5907), 1481-1483.
[5] Bekker, A. et al., 2010. Iron formation: the sedimentary product of a complex interplay among mantle, tectonic, oceanic and biospheric processes. Economic Geology, 105(3), 467-508.
[6] Halverson, G.P. et al., 2011. Fe isotope and trace element geochemistry of the Neoproterozoic syn-glacial Rapitan iron formation. Earth and Planetary Science Letters, 309(1-2), 100-112.

AGU Fall Meeting, 5th-9th December 2011, San Francisco

Annexe 5 - Poster Goldschmidt 2013

Appendix 5 – Poster Goldschmidt 2013

Abstract
3045

Ferromanganese crusts as proxies for deep water Fe and Ni isotope variations

GOLDSCHMIDT MEETING 2013, Florence, 25-30 August 2013

Bleuenn Gueguen[1,2]*, Olivier Rouxel[2] and Yves Fouquet[2]
[1]Institut Universitaire Européen de la Mer, UMR 6538,Université de Bretagne Occidentale, Plouzané, France
[2]IFREMER, Centre de Brest, Unité Géosciences Marines, Plouzané, France
*bleuenn.gueguen@gmail.com

Introductory facts

While ferromanganese (Fe-Mn) crusts have long been characterized by elevated concentrations of Ni, Co, and Cu arising from their very slow growth rates (1-6 mm/Ma), **the sources of metals in hydrogenous seafloor deposits and their record of evolving deep sea metal fluxes remain strikingly unresolved.** Here, we report high resolution Fe and Ni isotope profiles in four dated Fe-Mn crusts in order to evaluate the temporal and spatial isotopic variability of these elements in the Pacific Ocean.

What is the variability of Fe and Ni isotope compositions of seawater in the Pacific Ocean through time ?

1. Fe isotope variations in the Pacific Ocean

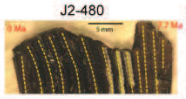

Sample description

- Two Fe-Mn crusts from the North Pacific Ocean (Apuupuu seamount) at ~2000 m depth.
- Two Fe-Mn crusts from the South Pacific Ocean (Tahiti archipelago) between 1500 and 1800 m depth. High resolution patterns were obtained by sampling of Fe- and Mn-oxides microlayers using a microdrilling device system.

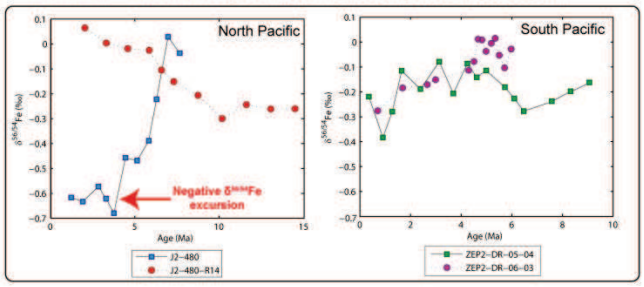

Results

- **Negative Fe isotope excursion** in the **North Pacific**
- Contemporaneous to an **increase in transition metal** scavenging in Mn-oxides (high Mn/Fe, Ni/Fe and Co/Fe)
- **No** Fe isotope variations in the **South Pacific**

Light Fe isotope fractionation ?

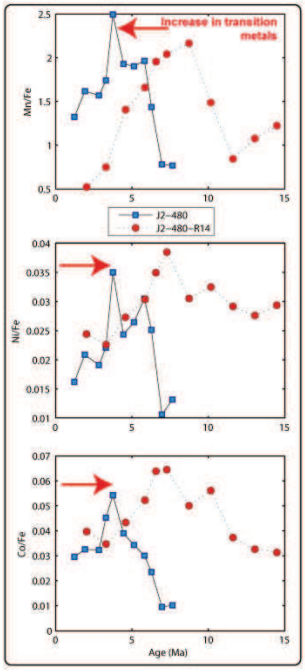

(1) Hydrothermal inputs from Loihi hydrothermal vents

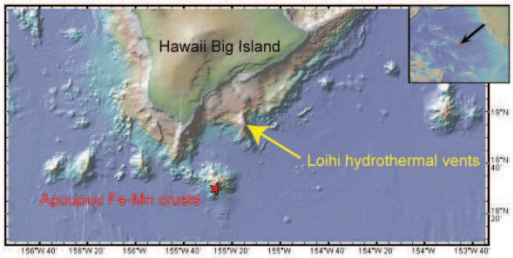

- Geochemistry of Loihi hydrothermal fluids:
  - **high Fe and Mn**
  - low pH
  - **low H_2S**

  → limited sulfides precipitation
- Local effect:
  - limited impact on J2-480-R14 sample
  - constant Fe isotope composition in the South Pacific
- Similar observations by Chu et al. (2006)

(2) Diagenetic remobilization of Fe in sediment porewaters

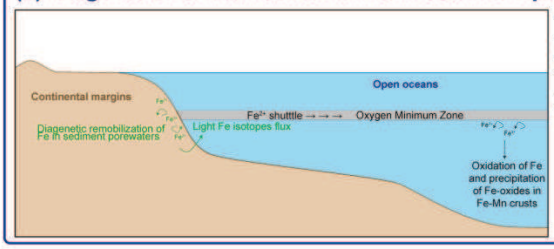

- Diagenetic remobilization of Fe in sediment porewaters produces light Fe isotopes up to ~-0.8 ‰ (Staubwasser et al., 2006): Fe shuttle in the oxygen minimum zone

BUT:
→ Rather a global than a local effect ?
→ Does not explain enrichment in transition metals

→ Hypothesis (1) is preferred
→ Detecting the far-field influence of hydrothermal fluxes with Fe isotopes?

2. Ni isotope variations in the Pacific Ocean

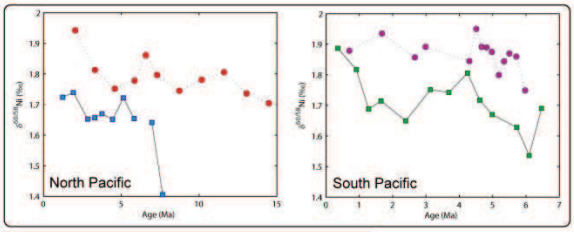

Results

- **Constant Ni** isotopes in **North and South Pacific**: homogenous Ni isotopes in deep waters over the **last ~15 Ma**
- Although suggested by Gall et al. (2013), effect of **hydrothermal inputs** from Loihi vents on Ni isotopes is **not** observed in **North Pacific** crusts (Apuupuu)

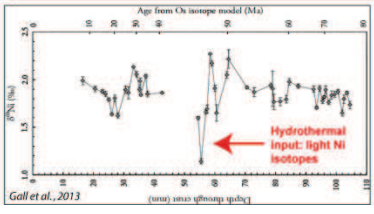

Hypothesis

- **Long residence time** of Ni in oceans ~10 kyrs
- Ni isotope fractionation is rather controlled by mineralogical effects → **Ni adsorption** on Mn-oxides
- Ni **concentration** in hydrothermal **fluids:** amplitude of the flux**?**
- Effect of **organic ligands** on Ni complexation ?

References
Gall, L., Williams, H.M., Siebert, C., Halliday, A.N., Herrington, R.J., Hein, J.R., 2013. Nickel isotopic compositions of ferromanganese crusts and the constancy of deep ocean inputs and continental weathering effects over the Cenozoic. Earth and Planetary Science Letters(0).
Chu, N.C., Johnson, C.M., Beard, B.L., German, C.R., Nesbitt, R.W., Frank, M., Bohn, M., Kubik, P.W., Usui, A., Graham, I., 2006. Evidence for hydrothermal venting in Fe isotope compositions of the deep Pacific Ocean through time. Earth and Planetary Science Letters, 245, 202-217.
Staubwasser, M., von Blanckenburg, F., Schoenberg, R., 2006. Iron isotopes in the early marine diagenetic iron cycle. Geology, 34, 629-632.

Annexe 6 - Informations additionnelles du chapitre IV

Appendix 6 - Chapter IV supplementary information

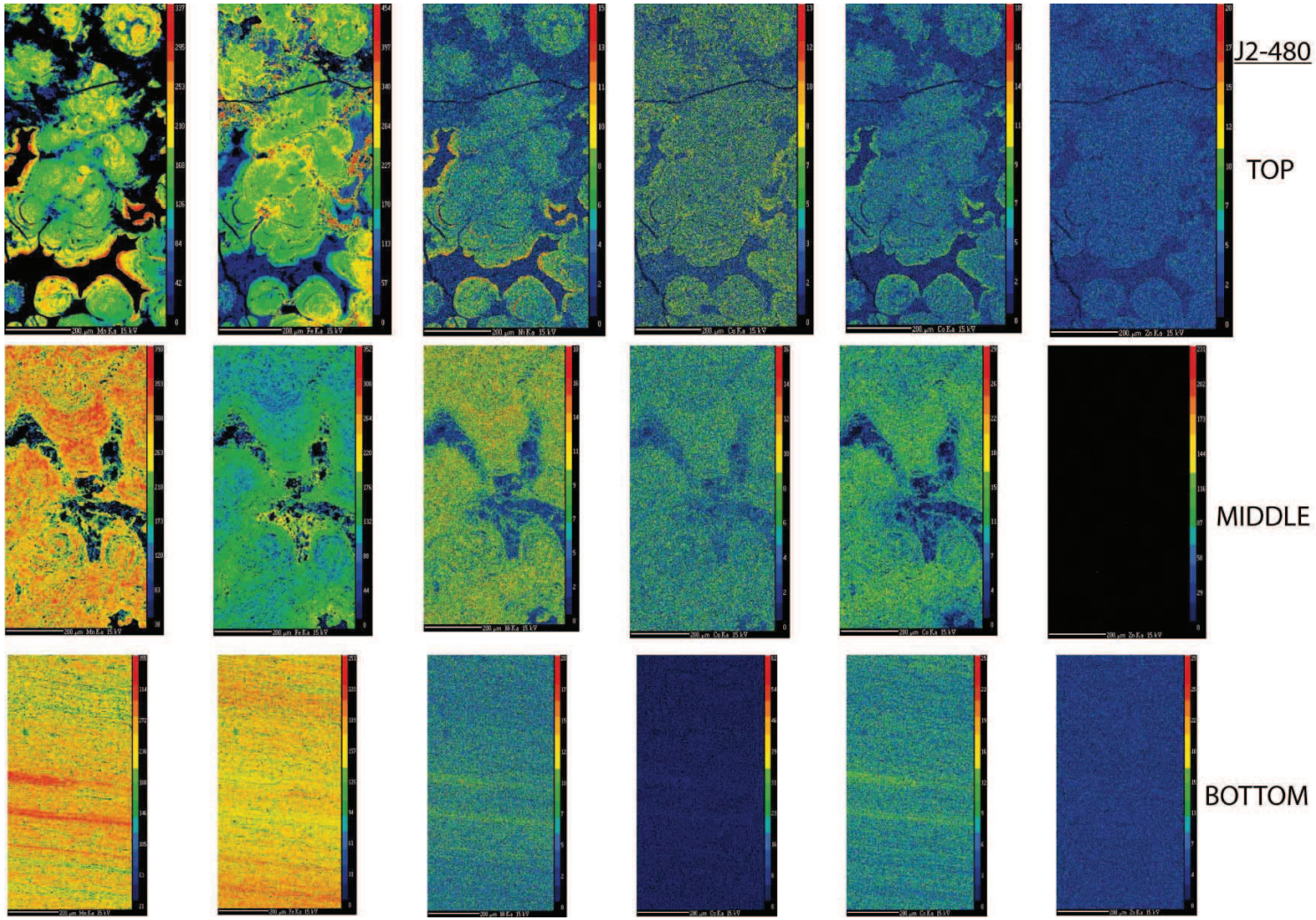

Figure S1 *: Elemental maps of Mn, Fe, Ni, Cu, Co and Zn made with Electron Microprobe analyses (EMPA) for J2-480 Fe-Mn crust (Apuupuu, North Pacific). Colors scale indicates the intensity (low=blue and red=high) of the signal measured by the microprobe, data do not represent concentrations. Three regions, top, middle and bottom, were mapped in the crust.*

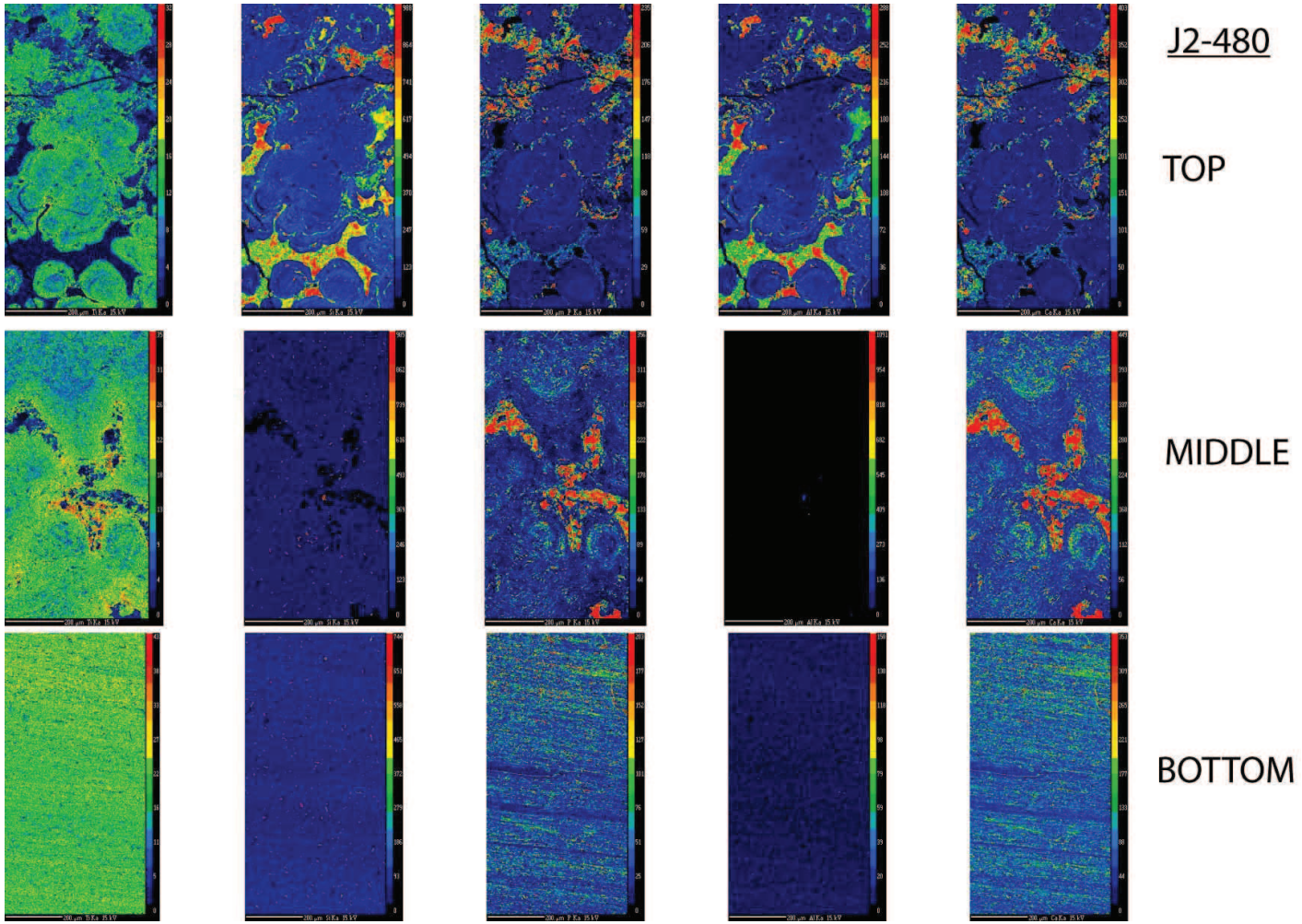

Figure S2 *: Elemental maps of Ti, Si, P, Al and Ca made with Electron Microprobe analyses (EMPA) for J2-480 Fe-Mn crust (Apuupuu, North Pacific). Colors scale indicates the intensity (low=blue and red=high) of the signal measured by the microprobe, data do not represent concentrations. Three regions, top, middle and bottom, were mapped in the crust.*

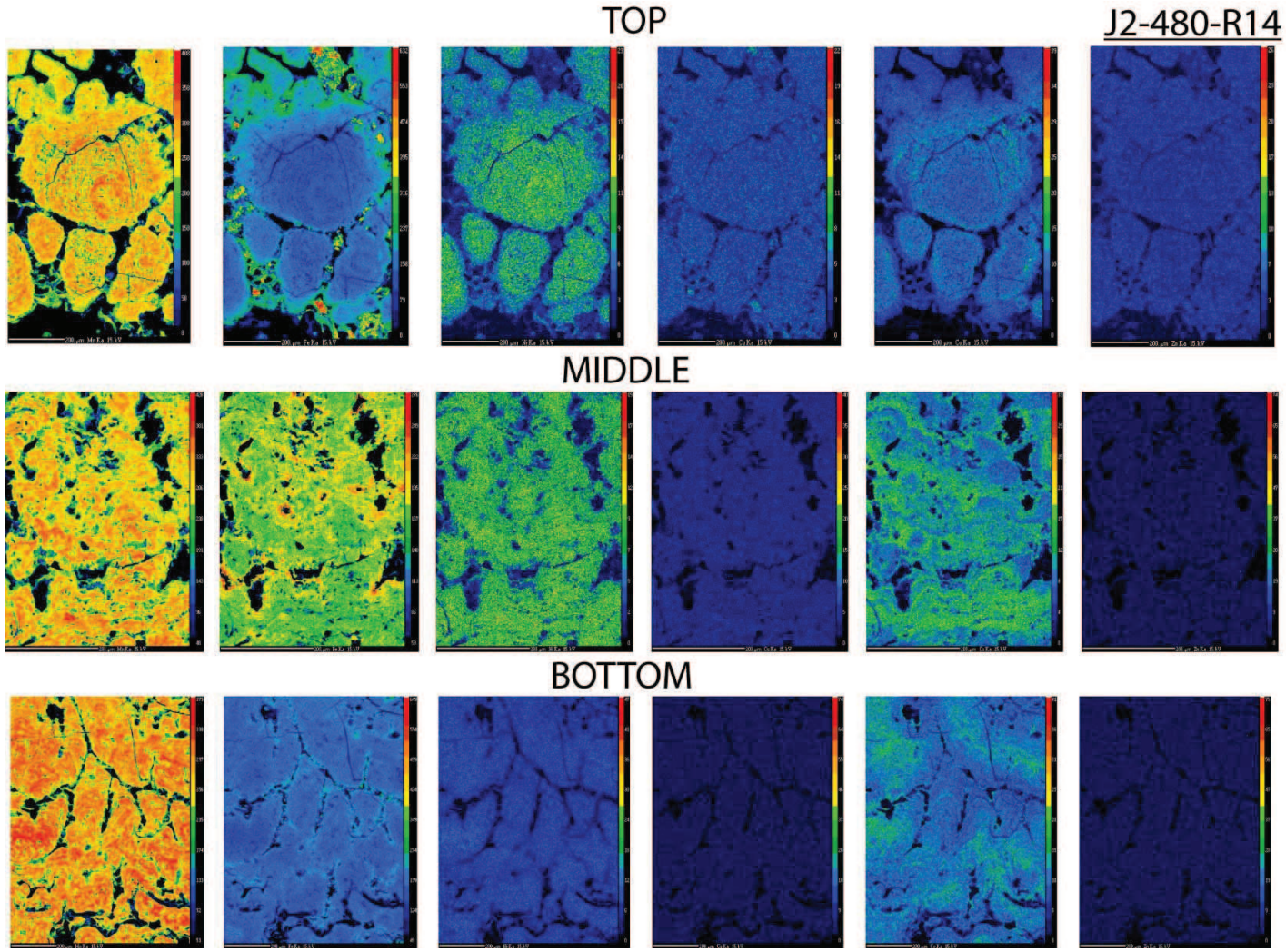

Figure S3 *: Elemental maps of Mn, Fe, Ni, Cu, Co and Zn made with Electron Microprobe analyses (EMPA) for J2-480-R14 Fe-Mn crust (Apuupuu, North Pacific). Colors scale indicates the intensity (low=blue and red=high) of the signal measured by the microprobe, data do not represent concentrations. Three regions, top, middle and bottom, were mapped in the crust.*

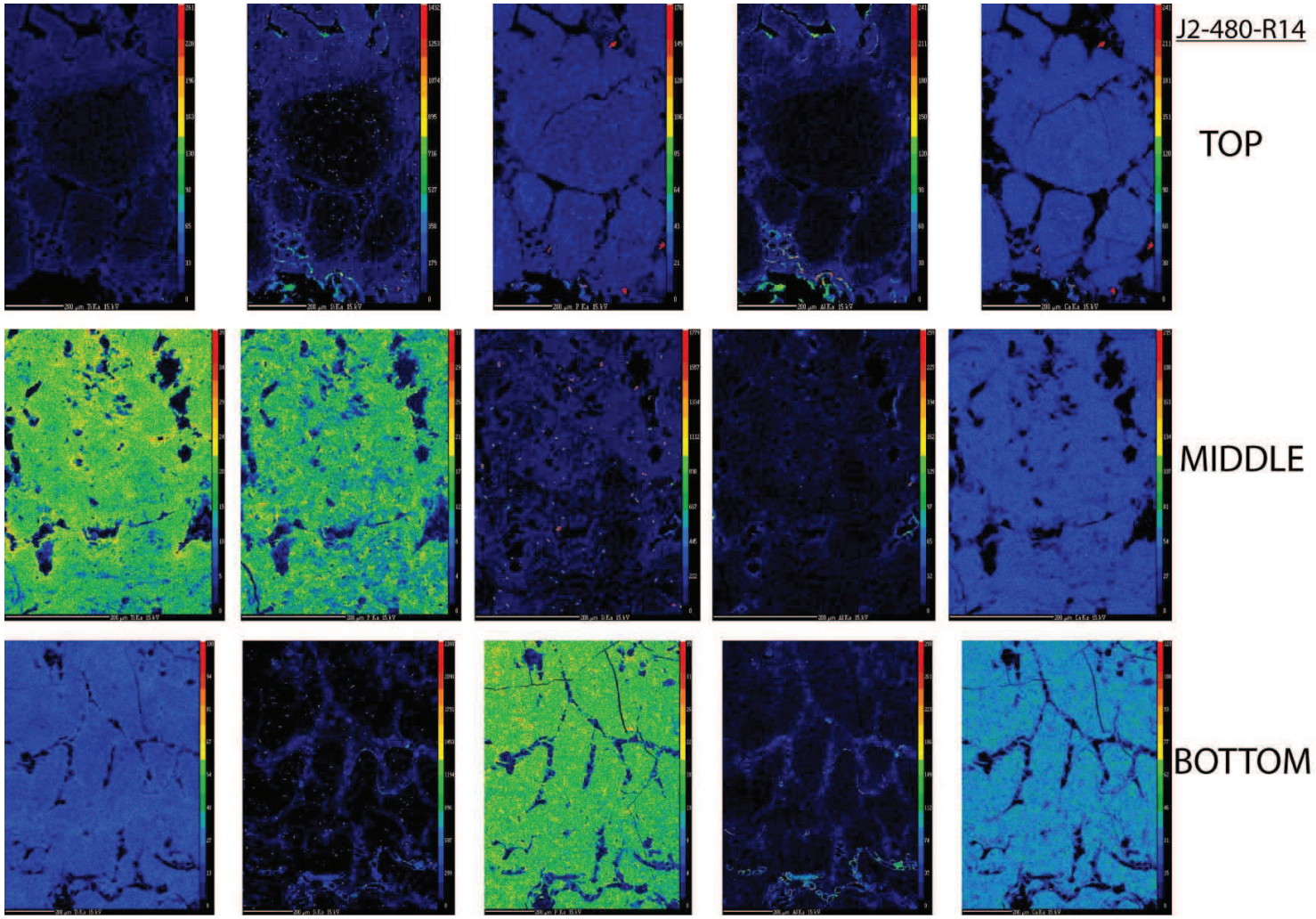

Figure S4 *: Elemental maps of Ti, Si, P, Al and Ca made with Electron Microprobe analyses (EMPA) for J2-480-R14 Fe-Mn crust (Apuupuu, North Pacific). Colors scale indicates the intensity (low=blue and red=high) of the signal measured by the microprobe, data do not represent concentrations. Three regions, top, middle and bottom, were mapped in the crust.*

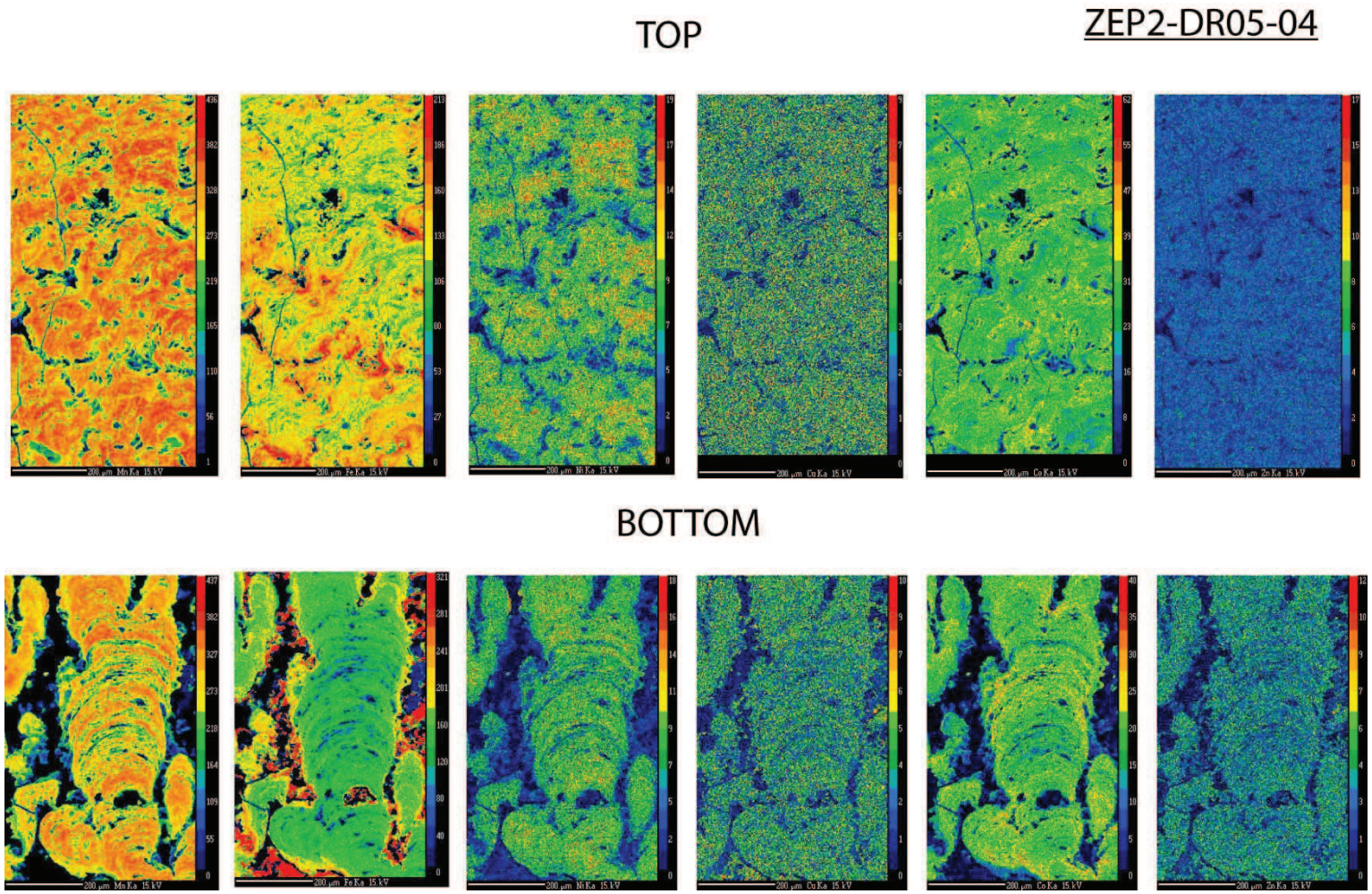

Figure S5 *: Elemental maps of Mn, Fe, Ni, Cu, Co and Zn made with Electron Microprobe analyses (EMPA) for ZEP2-DR05-04 Fe-Mn crust (Tahiti, South Pacific). Colors scale indicates the intensity (low=blue and red=high) of the signal measured by the microprobe, data do not represent concentrations. Two regions, top and bottom, were mapped in the crust.*

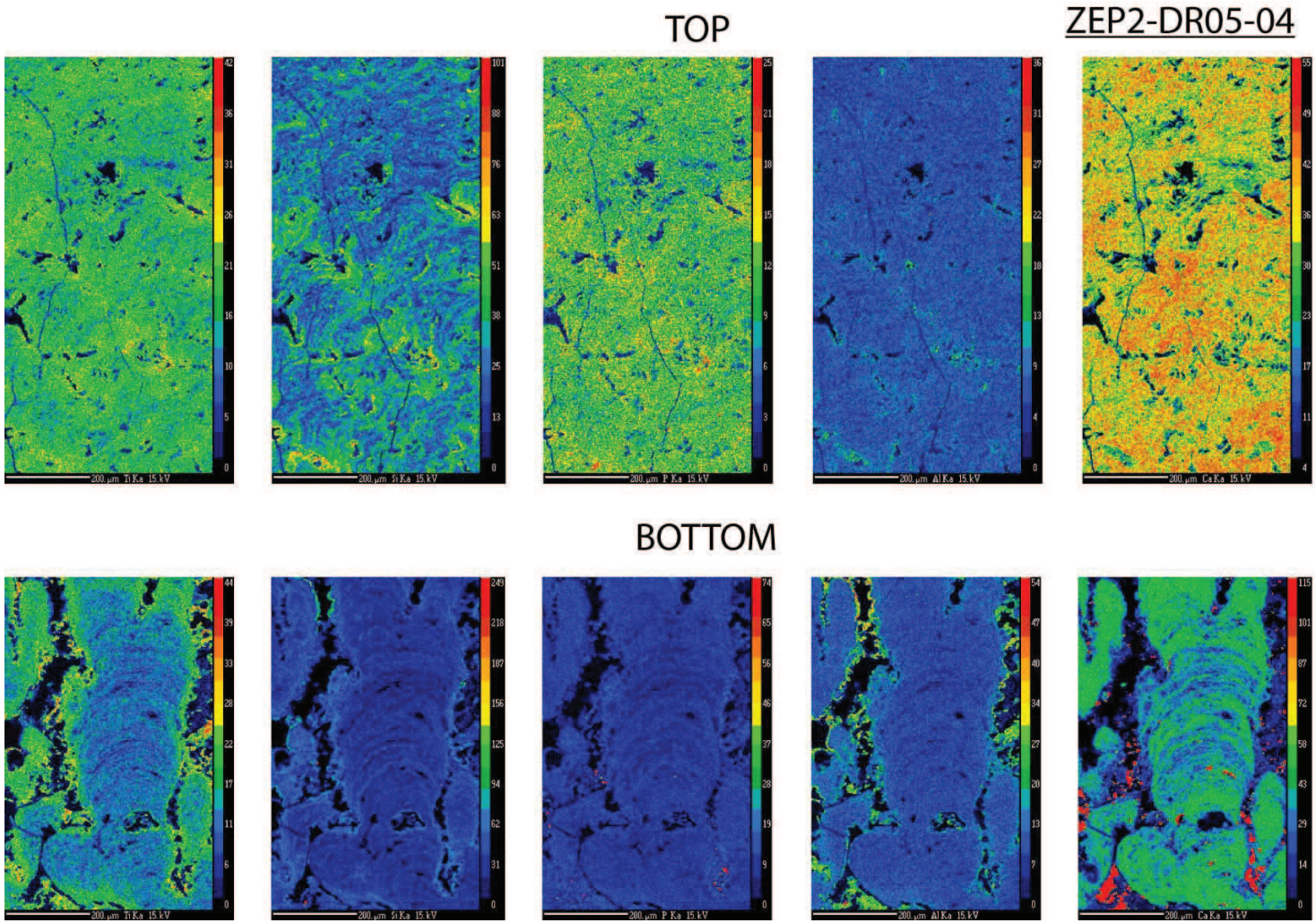

Figure S6 *: Elemental maps of Ti, Si, P, Al and Ca made with Electron Microprobe analyses (EMPA) for ZEP2-DR05-04 Fe-Mn crust (Tahiti, South Pacific). Colors scale indicates the intensity (low=blue and red=high) of the signal measured by the microprobe, data do not represent concentrations. Two regions, top and bottom, were mapped in the crust.*

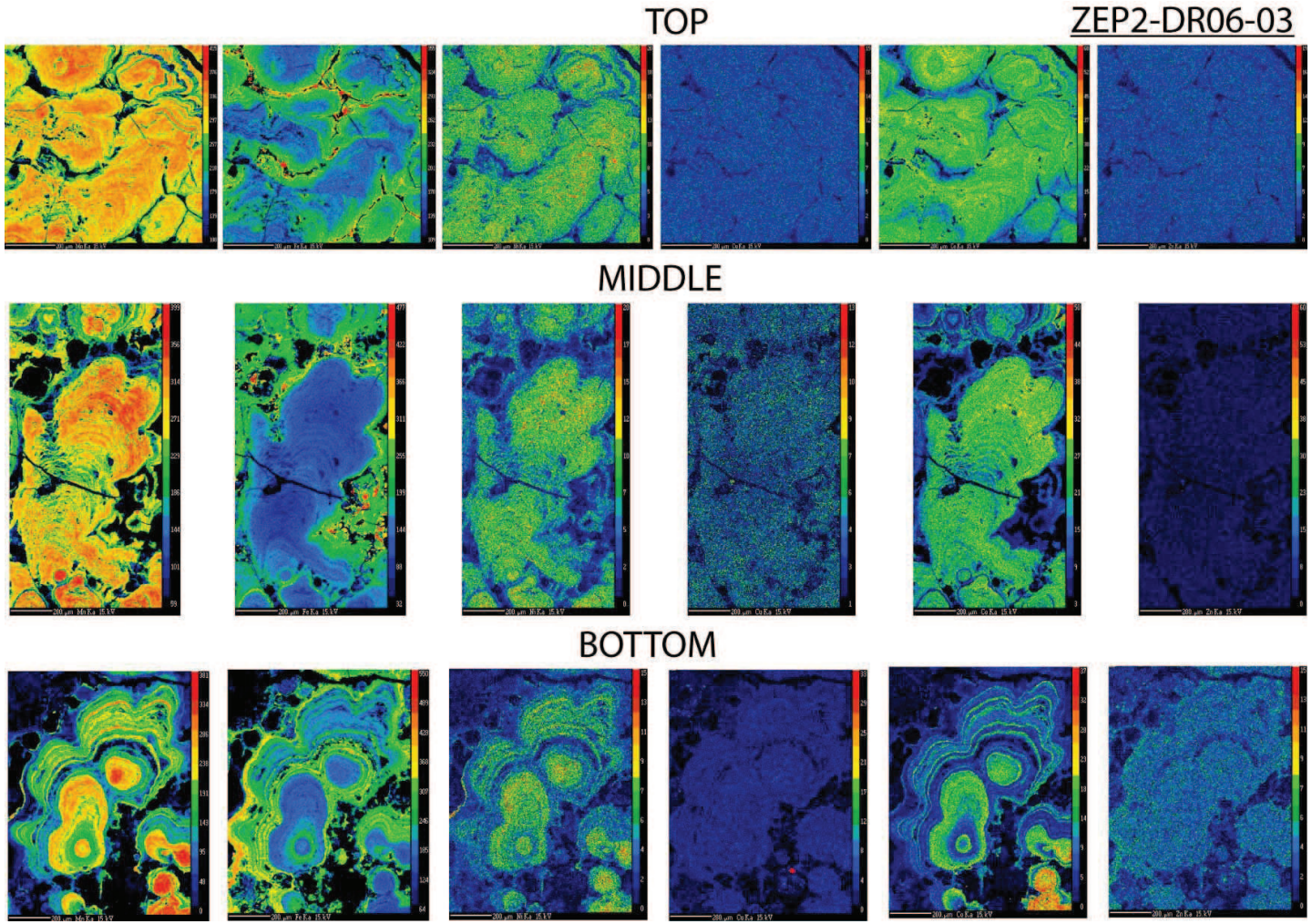

Figure S7 *: Elemental maps of Mn, Fe, Ni, Cu, Co and Zn made with Electron Microprobe analyses (EMPA) for ZEP2-DR06-03 Fe-Mn crust (Tahiti, South Pacific). Colors scale indicates the intensity (low=blue and red=high) of the signal measured by the microprobe, data do not represent concentrations. Three regions, top, middle and bottom, were mapped in the crust.*

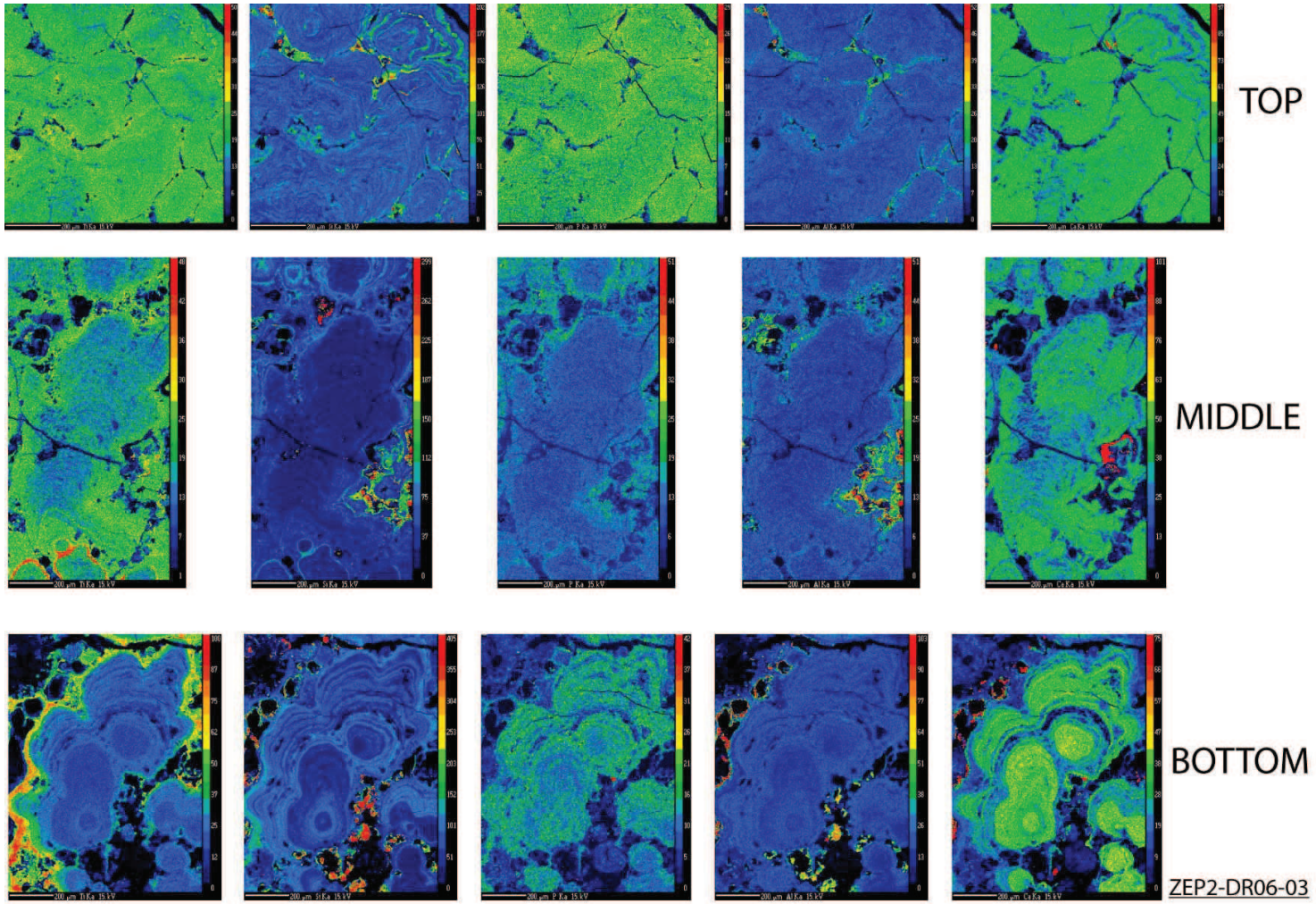

***Figure S8**: Elemental maps of Ti, Si, P, Al and Ca made with Electron Microprobe analyses (EMPA) for ZEP2-DR06-03 Fe-Mn crust (Tahiti, South Pacific). Colors scale indicates the intensity (low=blue and red=high) of the signal measured by the microprobe, data do not represent concentrations. Three regions, top, middle and bottom, were mapped in the crust.*

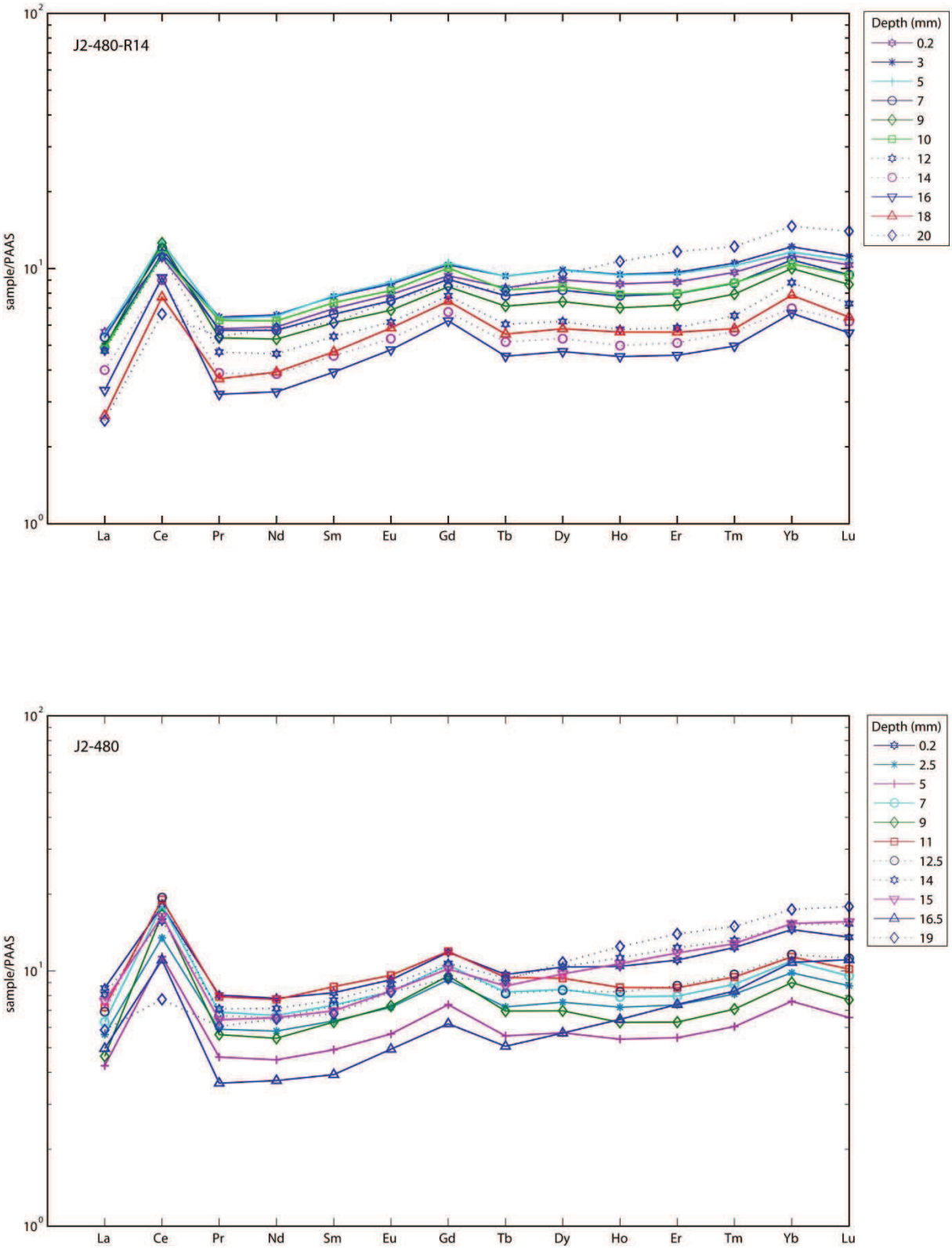

***Figure S9**: Rare Earth Elements patterns normalized to PAAS (Post Archean Australian Shale) for Apuupuu Fe-Mn crusts J2-480 (panel A) and J2-480-R14 (panel B). Each sample is labeled according to its depth in the crust (mm).*

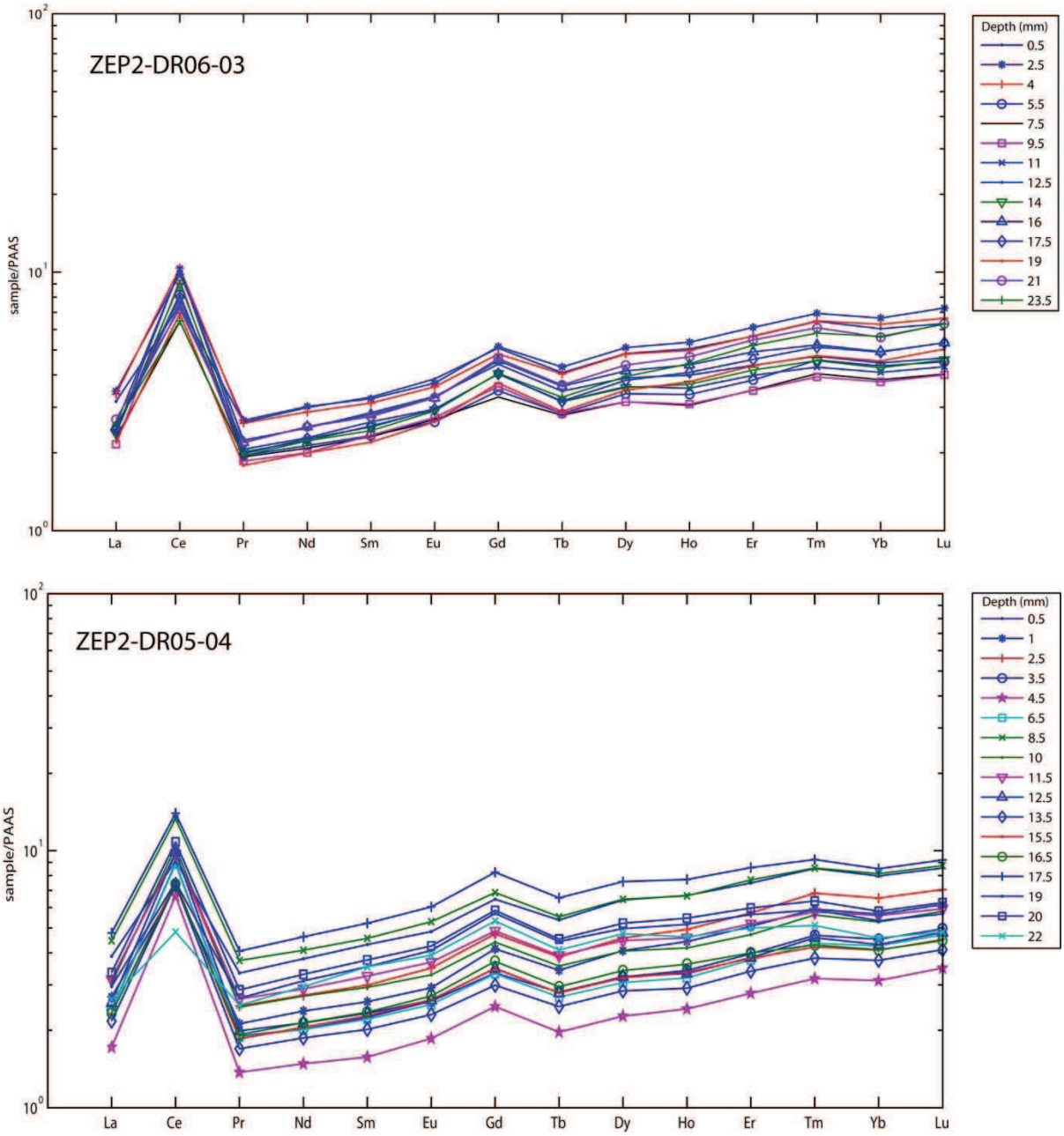

***Figure S10**: Rare Earth Elements patterns normalized to PAAS (Post Archean Australian Shale) for Tahiti Fe-Mn crusts ZEP2-DR05-04 (panel A) and ZEP2-DR06-03 (panel B). Each sample is labeled according to its depth in the crust (mm).*

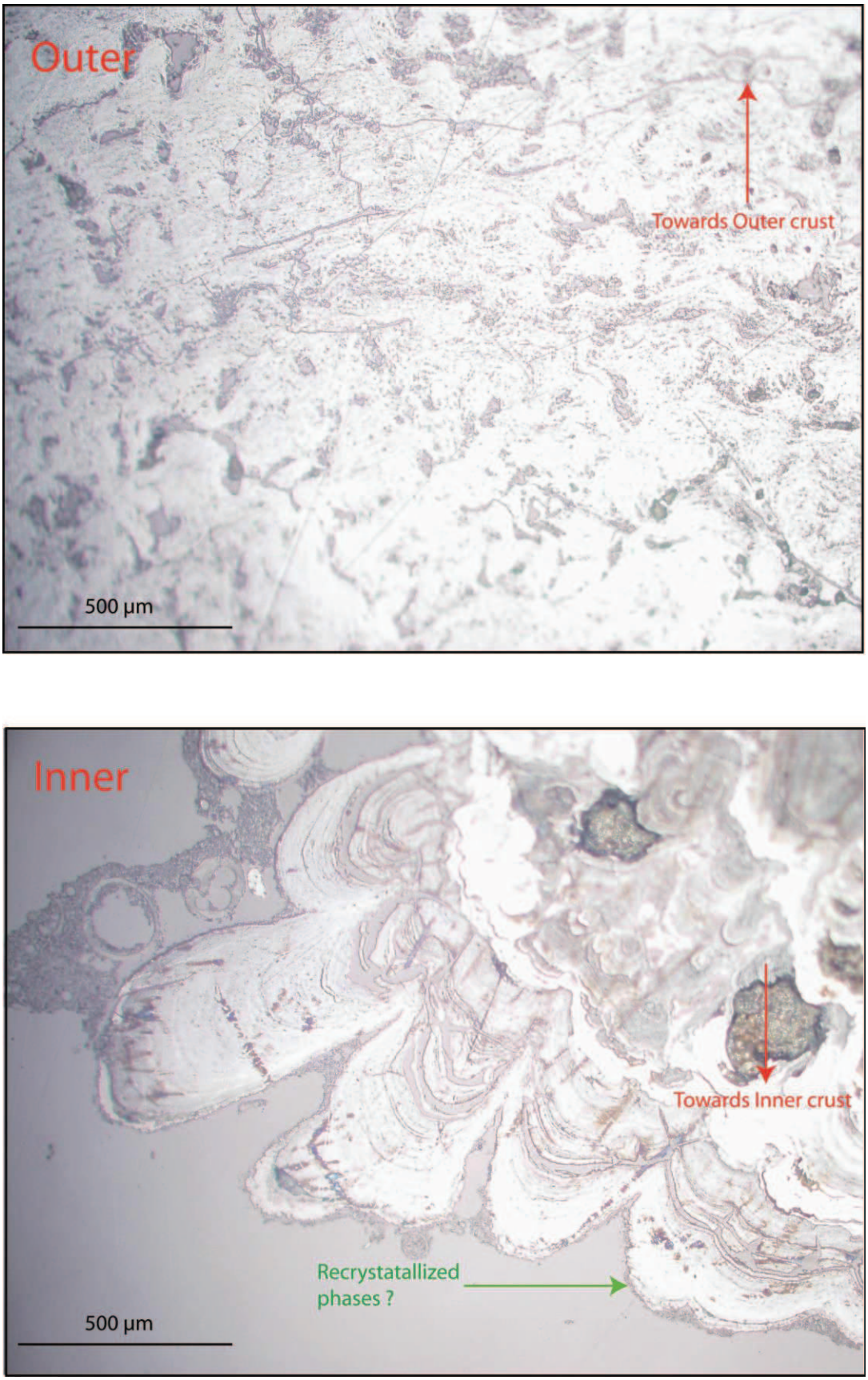

Figure S11: *Photomicrograph of the lowermost part of region "I" of crust ZEP-DR05-04 probably showing recrystallization textures.*

Table S1: Elemental concentrations depth profile in wt% measured by Electron Microprobe Analyser in Apuupuu Fe-Mn crust J2-480, North Pacific.

Depth (mm) in the crust*	Si	Ca	Mn	Fe	Co	Zn	P	Ni	Cu	Al	Ti	Mg	Na	Mn/Fe	Ni/Fe	Co/Fe
0	2,42	2,20	17,89	12,80	0,58	0,05	0,33	0,21	0,07	0,64	0,76	0,62	1,15	1,40	0,016	0,045
0,2	7,77	1,90	16,36	23,87	0,40	0,06	0,61	0,07	0,04	0,99	1,62	0,84	0,62	0,69	0,003	0,017
0,4	6,71	1,16	13,70	14,37	0,08	-	0,27	0,32	0,13	1,59	1,49	0,91	0,74	0,95	0,022	0,006
0,6	2,46	2,93	25,93	17,35	0,51	0,12	0,34	0,28	0,11	0,49	1,53	1,04	1,60	1,49	0,016	0,029
0,8	2,81	4,10	23,35	19,20	0,41	0,02	0,84	0,19	0,06	0,59	1,63	0,90	1,47	1,22	0,010	0,021
1	2,25	6,30	22,94	17,54	0,56	0,04	1,85	0,23	0,12	0,37	1,75	0,76	1,10	1,31	0,013	0,032
1,2	2,04	10,29	20,95	15,12	0,49	0,06	3,50	0,20	0,12	0,35	1,59	0,76	1,30	1,39	0,013	0,033
1,4	2,24	3,36	23,24	17,77	0,64	0,09	0,40	0,22	0,18	0,40	1,74	0,62	0,83	1,31	0,012	0,036
1,8	2,18	7,38	22,41	15,87	0,52	0,06	1,81	0,24	0,17	0,35	1,95	0,52	0,65	1,41	0,015	0,033
2	1,95	7,41	23,49	14,63	0,58	0,08	2,40	0,29	0,10	0,27	1,72	1,05	1,55	1,61	0,020	0,039
2,2	1,86	7,38	23,55	15,10	0,56	0,03	2,42	0,27	0,16	0,25	1,75	1,10	1,64	1,56	0,018	0,037
2,4	2,01	6,71	24,53	15,93	0,55	0,08	1,95	0,25	0,19	0,31	1,71	0,92	1,31	1,54	0,016	0,034
2,6	1,40	4,77	26,34	14,48	0,67	0,11	1,17	0,23	0,20	0,18	1,43	1,13	1,88	1,82	0,016	0,046
2,8	2,03	4,27	30,32	15,86	0,62	0,14	0,70	0,36	0,14	0,28	1,70	1,02	1,62	1,91	0,023	0,039
3	18,73	5,41	18,56	10,19	0,35	0,11	2,05	0,21	0,11	0,19	0,97	0,76	1,06	1,82	0,021	0,034
3,2	1,89	10,56	22,24	13,65	0,44	0,10	3,61	0,30	0,21	0,25	1,32	0,80	1,35	1,63	0,022	0,032
3,4	1,91	11,41	18,09	13,70	0,41	0,07	3,87	0,20	0,20	0,26	1,41	0,65	0,89	1,32	0,015	0,030
3,6	2,56	4,81	25,23	18,09	0,52	0,08	1,04	0,23	0,13	0,39	1,54	0,80	1,04	1,40	0,013	0,029
3,8	1,97	4,91	24,46	16,68	0,42	0,15	1,31	0,25	0,19	0,27	1,27	1,07	1,93	1,47	0,015	0,025
4	1,34	3,41	24,98	17,06	0,44	0,08	0,73	0,28	0,19	0,14	1,17	1,17	1,85	1,46	0,016	0,026
4,2	1,97	4,25	22,11	13,94	0,44	0,13	0,55	0,24	0,17	0,21	1,02	0,28	0,39	1,59	0,017	0,031
4,4	1,80	9,17	13,12	15,57	0,27	0,08	3,42	0,12	0,12	0,44	1,00	0,76	0,79	0,84	0,008	0,017
4,6	1,77	2,85	29,20	14,52	0,55	0,03	0,11	0,28	0,19	0,25	1,12	1,26	1,95	2,01	0,020	0,038
4,8	4,59	4,01	26,25	15,08	0,62	0,10	0,84	0,25	0,15	0,30	1,41	1,12	1,70	1,74	0,016	0,041
5	1,98	3,06	28,22	15,94	0,85	0,06	0,25	0,30	0,16	0,32	1,35	0,98	1,26	1,77	0,019	0,053
5,2	2,25	4,72	26,16	15,77	0,67	0,11	0,97	0,25	0,20	0,31	1,30	0,93	1,23	1,66	0,016	0,042
5,4	2,06	4,08	26,56	16,61	0,68	0,08	0,83	0,27	0,22	0,37	1,41	1,18	1,60	1,60	0,016	0,041
5,6	3,70	2,38	18,19	26,02	0,31	0,13	0,36	0,16	0,16	0,76	1,44	0,80	0,76	0,70	0,006	0,012
5,8	2,08	4,37	26,38	15,43	0,66	0,06	0,82	0,28	0,14	0,33	1,36	0,86	1,29	1,71	0,018	0,043
6	1,94	4,47	28,55	14,11	0,83	0,05	0,98	0,40	0,17	0,29	1,14	0,87	1,24	2,02	0,029	0,058

Depth (mm) in the crust*	Si	Ca	Mn	Fe	Co	Zn	P	Ni	Cu	Al	Ti	Mg	Na	Mn/Fe	Ni/Fe	Co/Fe
6,4	17,80	3,98	22,29	11,32	0,62	0,03	0,91	0,23	0,11	0,19	0,93	0,64	0,88	1,97	0,020	0,055
10,6	1,55	7,28	25,49	13,85	0,49	0,15	2,18	0,37	0,10	0,27	0,98	0,92	1,19	1,84	0,027	0,035
10,8	2,24	5,43	26,79	15,14	0,58	0,04	1,17	0,41	0,08	0,38	1,20	0,93	0,96	1,77	0,027	0,038
11	1,80	8,81	23,56	12,70	0,64	0,03	2,72	0,39	0,17	0,29	1,08	0,75	0,93	1,85	0,031	0,050
11,2	1,67	6,66	28,97	11,38	0,78	0,07	1,72	0,63	0,17	0,30	0,98	0,96	1,21	2,54	0,056	0,069
11,4	1,05	5,87	27,30	12,77	0,78	0,16	1,96	0,39	0,25	0,17	1,07	1,19	1,50	2,14	0,030	0,061
11,6	1,84	6,65	27,27	13,02	0,69	0,07	1,61	0,44	0,23	0,32	1,12	0,85	1,14	2,09	0,034	0,053
11,8	1,82	5,06	27,06	13,73	0,80	0,06	1,03	0,49	0,20	0,31	1,22	1,05	1,22	1,97	0,036	0,058
12	1,90	5,82	27,41	13,56	0,61	0,06	0,91	0,38	0,12	0,32	1,08	0,41	0,55	2,02	0,028	0,045
12,2	1,58	9,60	23,32	11,90	0,42	0,09	3,02	0,38	0,17	0,31	1,02	0,97	1,39	1,96	0,032	0,035
12,4	1,67	8,68	24,17	12,00	0,33	0,15	2,81	0,32	0,14	0,27	1,11	0,96	1,37	2,01	0,027	0,027
12,6	2,28	3,47	25,73	15,24	0,47	0,05	0,54	0,41	0,24	0,42	1,41	1,14	1,37	1,69	0,027	0,031
12,8	1,28	4,41	34,17	9,79	0,74	0,12	0,55	0,93	0,34	0,26	0,85	1,30	1,53	3,49	0,095	0,075
13	1,05	11,03	26,58	8,18	0,67	0,13	3,67	0,70	0,30	0,25	0,78	1,12	1,42	3,25	0,086	0,082
13,2	1,29	4,88	32,75	10,98	0,63	0,10	0,82	0,76	0,31	0,24	0,87	1,22	1,58	2,98	0,069	0,058
13,4	1,05	4,19	31,52	11,96	0,68	0,09	0,75	0,64	0,28	0,17	0,85	1,24	1,48	2,64	0,053	0,057
13,6	1,64	5,93	30,48	9,80	0,67	0,09	1,59	0,82	0,26	0,34	0,84	1,13	1,34	3,11	0,084	0,068
13,8	3,10	2,48	23,53	17,53	0,24	0,08	0,14	0,26	0,14	0,63	1,58	0,59	0,72	1,34	0,015	0,014
14,2	1,75	4,00	29,70	13,18	0,55	0,08	0,71	0,57	0,22	0,36	1,18	1,04	1,56	2,25	0,043	0,042
14,4	2,01	3,07	29,58	13,66	0,50	0,04	0,24	0,56	0,20	0,32	1,04	1,18	1,46	2,17	0,041	0,037
14,6	1,59	4,99	27,88	12,49	0,58	0,11	1,14	0,52	0,15	0,31	0,96	1,20	1,74	2,23	0,041	0,047
15	2,41	5,14	22,75	16,48	0,38	0,13	1,43	0,25	0,06	0,43	1,20	0,88	1,14	1,38	0,015	0,023
15,4	1,91	3,92	27,90	14,85	0,61	0,06	0,66	0,38	0,21	0,35	0,87	1,07	1,30	1,88	0,026	0,041
15,6	2,61	3,75	27,42	16,78	0,46	0,10	0,59	0,51	0,26	0,46	0,82	1,10	1,12	1,63	0,030	0,028
16	1,87	7,05	26,82	14,53	0,44	NaN	1,90	0,44	0,16	0,36	0,78	0,87	0,95	1,85	0,030	0,031
16,2	1,53	6,37	27,18	12,39	0,51	0,10	1,71	0,60	0,10	0,27	0,69	1,01	0,82	2,19	0,048	0,041
16,4	2,61	4,55	26,18	18,50	0,35	0,08	1,05	0,35	0,22	0,61	0,65	0,99	0,95	1,41	0,019	0,019
16,6	2,17	5,36	25,13	15,81	0,44	0,08	1,54	0,33	0,15	0,46	0,66	1,17	1,13	1,59	0,021	0,028
16,8	3,40	3,93	23,01	19,37	0,31	0,07	0,76	0,23	0,13	0,76	0,80	0,79	0,88	1,19	0,012	0,016
17	1,38	7,49	15,51	16,24	0,23	0,05	2,61	0,16	0,17	0,25	0,56	0,80	0,99	0,96	0,010	0,014
17,2	2,47	2,97	26,77	17,82	0,38	0,07	0,54	0,31	0,16	0,49	0,61	1,14	1,42	1,50	0,018	0,021
17,6	3,38	12,29	13,70	18,99	0,15	0,04	4,59	0,09	0,14	0,92	0,75	0,65	0,78	0,72	0,005	0,008

Depth (mm) in the crust*	Si	Ca	Mn	Fe	Co	Zn	P	Ni	Cu	Al	Ti	Mg	Na	Mn/Fe	Ni/Fe	Co/Fe
17,8	2,77	3,11	19,87	23,17	0,19	0,08	0,97	0,20	0,16	0,79	0,68	1,13	0,99	0,86	0,009	0,008
18,2	4,14	2,97	15,62	22,10	0,14	0,16	0,82	0,15	0,19	1,04	0,88	0,67	0,59	0,71	0,007	0,006
18,8	4,47	1,97	18,76	20,88	0,26	0,11	0,42	0,16	0,16	1,01	0,84	1,15	1,46	0,90	0,007	0,013
19	4,83	2,30	17,19	26,55	0,27	0,08	0,89	0,16	0,06	1,57	1,12	1,05	0,80	0,65	0,006	0,010
19,2	4,80	2,66	19,97	25,73	0,33	0,10	1,08	0,18	0,14	1,37	0,90	1,07	0,91	0,78	0,007	0,013
19,6	4,71	2,52	20,83	23,56	0,33	0,07	0,71	0,29	0,21	1,12	0,81	0,92	0,99	0,88	0,012	0,014
20,2	2,99	2,18	18,18	17,34	0,33	0,10	0,58	0,20	0,11	0,64	0,90	1,10	1,32	1,05	0,012	0,019
20,4	2,81	2,85	23,10	17,44	0,39	0,07	1,16	0,36	0,09	0,57	0,76	1,16	1,38	1,32	0,021	0,022
20,6	3,32	4,22	10,44	16,72	0,14	0,08	1,60	0,09	0,12	0,99	1,24	0,34	0,38	0,62	0,005	0,008
20,8	3,00	3,77	21,07	15,74	0,20	0,06	1,05	0,38	0,15	1,04	0,75	0,90	1,17	1,34	0,024	0,013
21,2	5,74	1,68	15,35	20,12	0,17	0,10	0,44	0,26	0,09	1,80	1,31	0,90	0,90	0,76	0,013	0,009
21,4	2,67	2,26	18,90	14,70	0,26	0,13	0,44	0,33	0,11	0,90	0,95	0,66	0,57	1,29	0,023	0,018

* Note that when phosphate and carbonate phases measured along the profile were encountered they were removed from the table.

Table S2: Elemental concentrations depth profile in wt% measured by Electron Microprobe Analyser in Apuupuu Fe-Mn crust J2-480-R14, North Pacific.

Depth (mm) in the crust*	Si	Ca	Mn	Fe	Co	Zn	P	Ni	Cu	Al	Ti	Mg	Na	Mn/Fe	Ni/Fe	Co/Fe
0	2,22	2,46	23,47	16,73	0,59	0,14	0,11	0,26	0,03	0,38	1,30	1,03	0,76	1,40	0,015	0,035
0,6	2,31	2,51	27,37	16,34	0,79	0,07	0,25	0,48	0,07	0,37	1,44	1,35	2,17	1,67	0,030	0,049
0,8	2,61	2,60	27,44	18,03	0,57	0,04	0,20	0,42	0,11	0,48	1,39	1,17	2,06	1,52	0,023	0,032
1	3,34	2,22	20,54	21,23	0,76	0,08	0,48	0,20	0,04	0,59	1,85	0,84	1,11	0,97	0,010	0,036
1,2	2,01	2,51	27,39	15,78	0,75	0,15	0,11	0,46	0,13	0,32	1,28	1,20	1,79	1,74	0,029	0,048
1,4	1,70	2,72	29,59	15,60	0,91	0,01	0,05	0,47	0,06	0,30	1,36	1,25	2,19	1,90	0,030	0,058
1,6	2,68	2,46	25,69	19,02	0,66	-	0,24	0,32	0,08	0,44	1,53	1,24	1,83	1,35	0,017	0,035
1,8	1,93	2,56	28,75	15,56	0,87	0,03	0,15	0,54	0,11	0,35	1,32	1,22	1,90	1,85	0,035	0,056
2	1,89	2,64	29,85	15,44	0,77	0,09	0,12	0,57	0,06	0,34	1,26	1,30	2,12	1,93	0,037	0,050
2,2	2,22	2,69	25,97	16,46	0,64	0,07	0,00	0,41	0,03	0,36	1,46	0,15	0,16	1,58	0,025	0,039
2,4	1,42	2,50	32,09	13,43	1,33	-	0,31	0,68	0,14	0,26	1,43	1,16	1,69	2,39	0,051	0,099
2,6	1,50	2,28	31,46	12,05	1,52	0,06	-	0,89	0,20	0,30	1,60	1,36	2,08	2,61	0,074	0,126
2,8	2,10	2,51	30,90	12,28	1,27	0,05	0,05	0,97	0,18	0,36	1,49	1,51	1,90	2,52	0,079	0,104
3	17,15	1,39	7,04	3,02	0,21	0,02	0,42	0,13	-	0,14	0,42	0,37	0,42	2,33	0,043	0,070
3,2	1,27	1,87	27,75	10,46	1,46	0,04	-	0,82	0,13	0,27	1,08	1,14	1,62	2,65	0,078	0,140
3,4	1,77	2,46	30,20	14,18	0,95	0,01	-	0,64	0,16	0,33	1,30	1,09	1,67	2,13	0,045	0,067
3,6	2,63	2,32	21,75	19,61	0,82	0,04	0,42	0,20	0,09	0,44	1,76	0,98	1,13	1,11	0,010	0,042
3,8	1,60	2,56	29,04	13,62	1,07	0,09	0,37	0,52	0,04	0,24	1,33	1,19	1,59	2,13	0,038	0,079
4	1,85	2,23	28,31	12,81	0,71	0,08	0,11	0,48	0,16	0,24	1,14	1,06	2,45	2,21	0,037	0,055
4,2	2,31	2,97	29,45	15,92	0,59	0,05	0,56	0,50	0,17	0,36	1,41	1,29	1,34	1,85	0,032	0,037
4,4	1,91	2,36	29,18	13,87	0,85	0,05	0,26	0,57	0,13	0,34	1,58	1,23	1,91	2,10	0,041	0,061
4,6	1,71	2,30	29,76	12,64	0,97	0,07	0,19	0,70	0,17	0,30	1,45	0,88	1,21	2,35	0,055	0,077
4,8	2,08	2,60	27,26	14,11	0,54	0,10	0,23	0,46	0,10	0,29	1,47	0,67	0,71	1,93	0,032	0,038
5	2,46	2,45	25,68	15,97	0,66	-	0,20	0,36	0,13	0,38	1,40	0,57	0,59	1,61	0,023	0,041
5,2	1,67	2,51	28,97	14,48	1,09	0,07	0,31	0,46	0,10	0,17	1,35	1,07	1,52	2,00	0,032	0,076
5,4	1,85	2,66	30,26	14,07	1,06	0,07	0,14	0,56	0,15	0,31	1,39	1,27	1,60	2,15	0,040	0,075
5,6	1,51	2,54	28,08	13,46	1,65	0,04	0,28	0,45	0,16	0,19	1,43	0,89	1,21	2,09	0,033	0,123
5,8	1,41	1,95	25,87	11,76	1,44	0,00	0,05	0,57	0,09	0,31	1,25	1,00	1,16	2,20	0,048	0,122
6	2,02	2,42	28,98	12,50	1,15	0,06	0,32	0,69	0,11	0,39	1,42	1,53	1,64	2,32	0,055	0,092
6,2	0,61	1,55	20,46	6,67	0,83	0,04	0,13	0,47	0,09	0,10	0,61	0,63	0,75	3,07	0,070	0,125

Depth (mm) in the crust*	Si	Ca	Mn	Fe	Co	Zn	P	Ni	Cu	Al	Ti	Mg	Na	Mn/Fe	Ni/Fe	Co/Fe
6,4	1,85	2,43	32,83	11,32	1,27	0,15	0,06	0,86	0,21	0,49	1,17	1,50	1,55	2,90	0,076	0,112
6,6	2,26	2,46	27,90	16,89	0,86	0,07	0,23	0,42	0,16	0,40	1,49	1,26	1,74	1,65	0,025	0,051
6,8	1,40	2,33	33,41	11,51	1,40	0,09	0,06	0,92	0,16	0,23	1,21	1,18	1,47	2,90	0,079	0,122
7	0,97	1,66	22,78	8,92	1,20	0,01	-	0,65	0,19	0,21	0,97	0,80	1,19	2,55	0,073	0,135
7,2	2,32	2,57	26,89	16,87	0,55	0,06	0,38	0,32	0,08	0,35	1,24	1,03	1,35	1,59	0,019	0,033
7,4	1,86	2,48	29,56	14,80	1,10	0,01	0,43	0,55	0,12	0,28	1,31	1,02	1,67	2,00	0,037	0,074
7,6	2,49	2,45	26,82	16,71	1,12	0,10	0,40	0,37	0,10	0,54	1,61	1,15	1,51	1,61	0,022	0,067
7,8	1,33	2,44	29,95	13,49	1,17	0,12	0,12	0,55	0,11	0,25	1,13	1,21	1,65	2,22	0,041	0,086
8	1,47	2,15	33,11	11,22	1,24	0,08	0,28	0,97	0,17	0,29	1,14	1,20	1,43	2,95	0,087	0,110
8,2	1,49	2,27	30,84	12,35	1,25	0,10	0,06	0,80	0,17	0,27	1,26	1,07	1,51	2,50	0,065	0,101
8,4	3,24	2,30	25,15	19,82	0,42	0,11	0,19	0,31	0,14	0,55	1,51	0,96	1,21	1,27	0,016	0,021
8,6	2,18	2,25	25,82	14,49	0,92	0,03	0,49	0,43	0,08	0,38	1,19	1,42	2,06	1,78	0,030	0,063
8,8	1,99	2,38	27,87	15,22	0,72	-	0,23	0,50	0,10	0,32	1,42	1,08	1,62	1,83	0,033	0,047
9	2,06	2,52	28,91	15,84	0,76	0,07	0,25	0,50	0,13	0,32	1,43	1,12	1,51	1,83	0,032	0,048
9,2	2,37	2,44	27,21	17,24	0,62	0,07	0,53	0,43	0,06	0,33	1,40	1,18	1,74	1,58	0,025	0,036
9,4	6,96	1,97	20,26	17,83	0,64	0,09	0,17	0,22	0,06	2,11	1,36	1,07	0,98	1,14	0,012	0,036
9,6	1,49	2,37	32,90	12,27	1,16	0,05	0,03	0,81	0,15	0,25	1,25	1,10	1,83	2,68	0,066	0,095
9,8	1,52	2,42	32,74	12,95	1,10	0,07	0,04	0,82	0,15	0,28	1,25	1,15	1,80	2,53	0,064	0,085
10	1,47	2,31	33,88	11,51	1,12	0,05	-	0,92	0,15	0,38	1,09	1,14	1,60	2,94	0,080	0,097
10,2	0,52	1,40	19,95	10,26	1,15	-	-	0,72	0,21	0,10	1,03	0,23	0,19	1,94	0,070	0,112
10,4	1,54	2,39	30,67	13,48	1,10	0,03	0,14	0,55	0,14	0,40	1,19	1,05	1,62	2,28	0,040	0,082
10,6	2,21	2,51	28,88	15,53	0,66	0,14	0,21	0,55	0,09	0,42	1,35	1,05	1,61	1,86	0,035	0,043
10,8	1,54	2,38	30,49	13,25	1,30	0,08	0,06	0,61	0,14	0,21	1,31	0,80	1,05	2,30	0,046	0,098
11,2	1,62	2,52	30,55	13,31	1,64	0,11	0,03	0,62	0,22	0,30	1,34	1,32	2,05	2,29	0,046	0,123
11,4	0,86	2,26	31,86	10,98	0,98	0,08	-	0,53	0,13	0,04	0,99	0,13	0,98	2,90	0,048	0,089
11,8	1,34	2,42	30,14	11,76	1,42	0,05	-	0,66	0,18	0,22	1,18	1,27	1,78	2,56	0,056	0,121
12,2	2,01	3,44	28,39	15,53	1,15	0,06	0,24	0,40	0,16	0,33	1,36	0,77	1,01	1,83	0,026	0,074
12,4	2,52	0,86	8,82	9,82	0,22	0,09	0,17	0,08	0,06	0,52	0,70	0,45	0,43	0,90	0,008	0,023
12,6	1,81	2,61	27,88	13,85	1,17	0,09	0,32	0,52	0,12	0,23	1,10	0,69	0,78	2,01	0,037	0,084
12,8	1,25	2,29	31,28	10,96	1,28	0,07	0,29	0,77	0,15	0,22	0,75	1,02	1,32	2,85	0,070	0,117
13	1,61	2,57	30,22	14,93	1,26	0,09	0,38	0,50	0,10	0,25	1,36	1,14	1,39	2,02	0,033	0,084
13,2	1,56	2,46	27,70	14,47	0,90	0,12	0,46	0,47	0,16	0,22	0,96	1,00	1,21	1,91	0,032	0,062

Depth (mm) in the crust*	Si	Ca	Mn	Fe	Co	Zn	P	Ni	Cu	Al	Ti	Mg	Na	Mn/Fe	Ni/Fe	Co/Fe
13,4	1,82	2,52	28,64	15,76	0,93	0,07	0,19	0,43	0,12	0,27	1,10	1,04	1,29	1,82	0,027	0,059
13,6	2,71	2,04	20,48	16,63	0,67	0,12	0,68	0,20	0,10	0,41	1,19	1,09	1,33	1,23	0,012	0,040
14	1,44	1,85	23,04	13,84	0,90	0,02	0,19	0,43	0,11	0,26	0,87	1,02	1,28	1,66	0,031	0,065
14,4	4,13	1,87	18,62	19,84	0,70	0,06	0,45	0,19	0,13	0,92	1,34	1,15	1,07	0,94	0,010	0,035
14,8	1,33	2,44	29,44	14,52	1,02	0,08	0,20	0,43	0,11	0,19	1,11	1,18	1,55	2,03	0,030	0,070
15	1,83	2,65	27,77	15,55	1,13	0,09	0,26	0,37	0,10	0,29	1,21	1,21	1,61	1,79	0,024	0,073
15,6	1,95	2,51	29,28	14,34	0,97	0,06	0,29	0,58	0,15	0,19	1,01	1,44	2,56	2,04	0,041	0,068
15,8	4,52	1,62	17,17	15,64	0,95	-	0,11	0,15	0,09	0,70	1,23	0,72	1,03	1,10	0,009	0,061
16	2,40	2,78	29,32	14,49	0,74	0,10	0,49	0,45	0,19	0,25	0,96	1,16	1,85	2,02	0,031	0,051
16,2	2,07	2,63	25,49	13,95	0,86	0,12	0,59	0,42	0,13	0,34	1,02	1,13	1,88	1,83	0,030	0,061
16,4	1,82	2,66	30,34	14,89	1,26	0,07	0,10	0,69	0,16	0,34	1,01	1,21	1,95	2,04	0,046	0,085
16,6	2,80	2,49	24,53	20,99	0,52	0,09	0,48	0,31	0,12	0,42	1,40	1,05	1,37	1,17	0,015	0,025
16,8	3,71	2,49	24,43	17,52	0,45	0,05	0,44	0,38	0,12	0,33	1,08	1,18	1,11	1,39	0,022	0,026
17	1,83	2,51	28,34	14,55	0,79	0,00	0,32	0,52	0,26	0,32	0,95	1,06	1,48	1,95	0,036	0,054
17,2	2,06	2,49	26,55	15,55	0,73	0,03	0,41	0,41	0,09	0,31	1,08	0,98	1,17	1,71	0,026	0,047
17,4	1,58	2,21	26,14	14,31	1,04	0,06	0,09	0,61	0,10	0,32	0,87	1,04	1,37	1,83	0,042	0,072
17,6	1,14	2,29	27,35	12,73	1,03	-	0,46	0,57	0,18	0,24	0,64	1,00	1,03	2,15	0,045	0,081
17,8	2,18	1,76	13,27	11,51	0,46	0,03	0,63	0,17	0,11	0,52	0,75	0,65	0,91	1,15	0,014	0,040
18	2,42	2,49	26,88	15,02	0,79	0,04	0,44	0,45	0,13	0,32	0,90	1,00	1,17	1,79	0,030	0,052
18,2	1,89	2,63	28,40	16,24	0,86	0,02	0,64	0,40	0,13	0,31	0,83	1,53	2,01	1,75	0,024	0,053
18,4	1,76	2,42	27,96	15,27	0,57	0,07	0,33	0,46	0,11	0,28	0,81	1,34	1,83	1,83	0,030	0,037
18,6	2,12	2,51	27,23	16,95	0,89	0,04	0,45	0,48	0,11	0,39	0,92	1,34	1,71	1,61	0,028	0,053
18,8	1,00	1,94	22,42	18,07	0,71	0,04	0,35	0,29	0,14	0,15	1,03	0,89	0,96	1,24	0,016	0,040
19	2,56	2,50	26,44	18,14	0,57	0,06	0,67	0,40	0,10	0,48	0,98	1,13	1,21	1,46	0,022	0,031
19,2	2,17	2,18	23,50	20,51	0,41	0,06	0,35	0,29	0,09	0,26	0,95	1,28	1,25	1,15	0,014	0,020
19,4	1,58	2,71	26,90	15,90	0,54	0,06	0,17	0,54	0,18	0,23	0,74	0,50	0,43	1,69	0,034	0,034
19,6	1,57	2,73	28,51	15,33	0,47	-	0,46	0,59	0,16	0,24	0,72	1,48	2,19	1,86	0,038	0,031
20	1,04	2,06	22,56	10,57	0,69	0,07	0,27	0,64	0,13	0,23	0,47	0,90	1,00	2,13	0,061	0,066
20,2	1,31	1,24	14,39	11,88	0,47	0,03	0,24	0,33	0,02	0,31	0,48	0,68	0,78	1,21	0,028	0,040
20,4	1,20	2,49	29,13	13,48	0,85	0,09	0,04	0,66	0,14	0,23	0,50	1,16	1,42	2,16	0,049	0,063
20,8	2,30	2,40	26,07	19,07	0,42	0,17	0,26	0,43	0,13	0,37	0,92	1,05	1,20	1,37	0,023	0,022
21,2	2,13	2,03	21,53	18,49	0,74	0,06	0,13	0,32	0,14	0,50	0,77	0,86	0,73	1,16	0,018	0,040

Depth (mm) in the crust*	Si	Ca	Mn	Fe	Co	Zn	P	Ni	Cu	Al	Ti	Mg	Na	Mn/Fe	Ni/Fe	Co/Fe
22	2,00	2,26	26,32	13,87	0,78	0,08	0,61	0,71	0,14	0,27	0,56	1,38	2,06	1,90	0,051	0,056
22,2	2,38	2,12	23,75	19,59	0,37	0,12	0,39	0,33	0,14	0,59	0,93	1,22	1,54	1,21	0,017	0,019
22,4	2,90	1,40	11,59	38,52	0,20	0,06	0,76	0,07	0,14	0,59	1,59	0,83	0,59	0,30	0,002	0,005
22,6	1,96	2,35	24,94	17,03	0,31	0,08	0,45	0,43	0,16	0,40	0,76	0,98	1,25	1,46	0,025	0,018
23,4	3,26	1,98	19,84	23,54	0,24	0,13	0,30	0,26	0,14	0,75	0,99	0,54	0,66	0,84	0,011	0,010
23,8	4,58	2,08	22,77	16,37	0,48	0,07	0,10	0,56	0,09	1,82	0,52	1,19	1,19	1,39	0,034	0,029

* Note that when phosphate and carbonate phases measured along the profile were encountered they were removed from the table.

Table S3: Elemental concentrations depth profile in wt% measured by Electron Microprobe Analyser in Tahiti (South Pacific) Fe-Mn crust ZEP2-DR05-04.

Depth in the crust (mm)*	Si	Ca	Mn	Fe	Co	Zn	P	Ni	Cu	Al	Ti	Mg	Na	Mn/Fe	Ni/Mn	Al/Mn
0,0	0,54	2,88	34,33	10,70	2,37	0,07	0,19	0,47	0,02	0,23	0,62	1,82	1,62	3,21	0,01	0,01
0,2	0,62	2,95	32,34	11,98	2,82	0,05	0,06	0,52	-	0,21	1,27	1,67	1,46	2,70	0,016	0,006
0,4	0,52	2,66	35,25	10,59	2,31	0,03	0,00	0,81	-	0,20	0,96	1,58	1,78	3,33	0,023	0,006
0,6	0,36	1,41	17,14	7,58	2,13	0,06	-	0,28	-	0,14	0,76	1,03	0,95	2,26	0,017	0,008
0,8	1,15	2,88	30,91	13,87	2,56	0,04	0,16	0,40	0,03	0,27	1,23	1,37	1,18	2,23	0,013	0,009
1,2	0,39	1,07	13,14	5,61	1,50	-	0,05	0,11	0,05	0,23	0,60	0,82	0,70	2,34	0,009	0,017
1,4	0,42	1,66	20,30	8,00	2,59	-	0,03	0,22	0,08	0,18	1,01	1,25	1,03	2,54	0,011	0,009
1,6	0,85	2,35	29,76	11,18	2,39	0,06	0,08	0,42	0,04	0,28	1,24	1,42	1,27	2,66	0,014	0,009
2,0	0,57	2,70	34,95	10,44	2,74	0,08	-	0,67	0,11	0,23	0,95	1,61	1,38	3,35	0,019	0,007
2,2	0,94	2,60	31,27	11,72	2,73	0,05	0,07	0,53	0,02	0,28	1,21	1,60	1,46	2,67	0,017	0,009
2,4	1,36	2,76	29,04	13,24	2,16	0,09	0,19	0,42	0,06	0,34	1,30	1,39	1,44	2,19	0,014	0,012
2,6	1,05	2,79	29,91	14,86	2,08	0,06	0,17	0,41	0,14	0,30	1,37	1,35	1,35	2,01	0,014	0,010
2,8	0,66	2,91	34,30	12,17	2,44	0,06	-	0,61	0,09	0,27	1,14	1,59	1,46	2,82	0,018	0,008
3,0	0,75	2,31	31,89	11,71	2,42	0,07	0,03	0,59	0,17	0,28	1,10	1,65	1,71	2,72	0,018	0,009
3,2	0,53	1,96	27,66	9,79	2,14	0,04	0,09	0,38	0,09	0,25	0,83	1,48	1,11	2,82	0,014	0,009
3,4	0,67	2,50	35,04	10,63	2,67	0,10	-	0,69	-	0,30	1,02	1,59	1,67	3,30	0,020	0,009
3,6	0,76	2,49	36,75	10,34	2,54	0,07	-	0,81	0,15	0,26	0,96	1,63	1,71	3,55	0,022	0,007
3,8	0,67	2,56	37,13	10,91	2,64	0,07	-	0,89	0,11	0,30	0,99	1,75	1,75	3,40	0,024	0,008
4,0	1,03	2,41	36,73	10,14	2,64	0,15	-	0,99	0,06	0,37	1,00	1,69	1,54	3,62	0,027	0,010
4,2	0,51	2,70	34,01	10,60	2,68	0,04	-	0,74	0,07	0,31	1,00	1,72	1,47	3,21	0,022	0,009
4,4	1,15	2,83	31,07	16,33	1,96	0,06	0,14	0,44	0,13	0,42	1,47	1,51	1,48	1,90	0,014	0,013
4,6	0,94	2,82	32,09	13,86	1,55	0,08	0,04	0,66	0,12	0,36	1,10	1,55	1,42	2,32	0,021	0,011
4,8	0,66	2,61	33,49	11,52	2,36	0,04	-	0,72	0,10	0,33	1,05	1,65	1,60	2,91	0,022	0,010
5,0	1,11	2,32	24,18	10,49	2,07	0,14	0,27	0,31	0,08	0,34	1,14	0,98	1,26	2,30	0,013	0,014
5,2	0,87	3,11	31,82	13,60	1,97	0,07	0,07	0,52	-	0,44	1,45	1,68	1,67	2,34	0,016	0,014
5,4	0,96	2,92	31,15	15,50	1,44	0,07	0,06	0,57	0,03	0,52	1,08	1,40	1,61	2,01	0,018	0,017
5,8	1,87	2,55	24,49	21,29	0,96	0,09	0,34	0,39	0,14	0,83	1,34	1,47	1,27	1,15	0,016	0,034
6,0	1,03	2,77	29,73	15,35	1,10	0,09	0,11	0,54	0,15	0,58	1,20	1,49	1,98	1,94	0,018	0,020
6,2	0,91	2,68	30,18	14,54	1,69	0,05	0,06	0,58	0,13	0,58	1,22	1,55	2,20	2,08	0,019	0,019
6,4	0,81	2,66	31,04	13,95	0,99	0,09	0,06	0,65	0,07	0,40	1,14	1,58	2,61	2,22	0,021	0,013
6,6	0,89	2,90	29,56	15,31	0,75	0,07	0,05	0,58	0,08	0,46	1,12	1,53	2,08	1,93	0,020	0,015

Depth in the crust (mm)*	Si	Ca	Mn	Fe	Co	Zn	P	Ni	Cu	Al	Ti	Mg	Na	Mn/Fe	Ni/Mn	Al/Mn
6,8	1,52	2,18	23,45	21,13	0,98	0,03	0,23	0,30	0,05	0,59	1,70	1,22	1,03	1,11	0,013	0,025
7,0	0,93	2,95	31,12	13,51	1,32	0,05	0,03	0,67	0,14	0,35	0,98	1,49	1,70	2,30	0,022	0,011
7,2	1,02	3,06	32,30	14,32	1,17	0,06	-	0,67	0,09	0,38	0,94	1,45	1,64	2,25	0,021	0,012
7,4	0,99	2,83	29,89	14,91	1,69	0,13	0,00	0,49	0,02	0,44	1,09	1,46	1,39	2,00	0,016	0,015
7,6	1,16	3,03	30,29	14,92	1,21	0,03	0,08	0,49	0,18	0,42	1,13	1,37	1,60	2,03	0,016	0,014
7,8	1,19	2,94	29,98	14,30	1,59	0,04	0,05	0,51	0,10	0,43	1,12	1,37	1,60	2,10	0,017	0,014
8,0	1,86	1,98	19,72	25,47	1,01	0,14	0,28	0,14	0,02	0,73	1,95	1,09	0,89	0,77	0,007	0,037
8,2	1,45	2,65	24,83	17,38	0,64	0,09	0,16	0,35	0,08	0,48	1,30	1,38	1,39	1,43	0,014	0,019
8,4	1,18	3,10	30,18	16,04	1,21	0,07	0,14	0,46	0,17	0,45	1,16	1,33	1,60	1,88	0,015	0,015
8,6	1,48	2,56	27,72	16,21	1,27	0,04	0,16	0,42	0,08	0,42	1,07	1,21	1,42	1,71	0,015	0,015
9,0	1,00	2,93	30,37	15,13	1,64	0,08	0,05	0,52	0,05	0,38	0,89	1,22	1,11	2,01	0,017	0,013
9,2	0,90	2,98	34,68	13,06	1,44	0,08	-	0,63	0,14	0,33	0,74	1,48	1,34	2,66	0,018	0,010
9,4	1,99	2,22	20,63	16,82	1,40	0,06	0,23	0,19	0,10	0,58	1,18	0,49	0,44	1,23	0,009	0,028
9,6	0,95	3,23	34,27	13,42	1,45	0,04	0,03	0,61	0,13	0,35	0,81	1,37	1,40	2,55	0,018	0,010
9,8	0,60	2,82	33,08	12,43	1,78	0,09	-	0,66	0,14	0,34	0,68	1,58	1,49	2,66	0,020	0,010
10,0	0,69	3,08	34,39	13,60	1,53	0,04	-	0,67	0,15	0,36	0,70	1,45	1,43	2,53	0,020	0,011
10,2	0,75	1,13	13,83	10,56	0,97	0,05	0,07	0,19	0,06	0,35	0,63	0,78	0,26	1,31	0,014	0,025
10,4	2,09	2,58	23,94	17,03	0,92	0,05	0,23	0,35	0,07	0,53	1,01	1,26	1,30	1,41	0,015	0,022
10,6	1,23	2,91	29,47	15,99	1,53	0,11	0,03	0,48	0,06	0,53	1,01	1,43	1,83	1,84	0,016	0,018
10,8	1,16	2,67	30,50	16,56	2,45	0,01	0,09	0,28	0,05	0,49	1,05	1,32	1,58	1,84	0,009	0,016
11,0	0,67	2,34	23,38	11,96	1,53	0,07	0,03	0,36	0,07	0,37	0,90	1,11	0,71	1,96	0,015	0,016
11,2	1,02	2,87	32,62	12,37	1,60	0,07	-	0,53	0,10	0,43	0,66	1,23	1,18	2,64	0,016	0,013
11,4	1,15	2,75	29,73	12,11	1,70	0,05	0,09	0,62	0,13	0,40	0,75	1,08	1,13	2,46	0,021	0,013
11,6	1,19	2,48	27,59	12,65	1,26	0,05	0,06	0,46	0,08	0,36	0,76	1,04	1,02	2,18	0,017	0,013
11,8	1,22	2,59	25,69	14,15	1,30	0,12	0,05	0,47	0,14	0,42	0,95	1,27	1,21	1,82	0,018	0,017
12,2	1,31	2,67	27,33	15,97	1,62	0,07	0,12	0,38	0,11	0,44	1,04	1,26	1,44	1,71	0,014	0,016
12,4	1,89	2,86	26,09	19,68	0,91	0,06	0,20	0,33	0,13	0,60	1,06	1,06	1,11	1,33	0,013	0,023
12,6	1,82	2,74	24,96	19,24	0,58	0,13	0,19	0,36	0,04	0,53	1,21	1,19	1,31	1,30	0,014	0,021
12,8	1,40	2,94	30,84	15,96	1,38	0,05	0,11	0,57	0,14	0,49	0,97	1,33	1,48	1,93	0,019	0,016
13,0	1,04	2,53	27,10	13,49	1,66	0,08	0,01	0,43	0,09	0,34	0,81	1,06	1,15	2,01	0,016	0,013
13,2	0,76	2,69	24,62	10,97	1,20	0,05	0,20	0,43	0,06	0,42	0,84	1,15	0,37	2,24	0,017	0,017
13,4	1,23	2,01	22,79	16,82	2,11	0,09	0,11	0,26	0,04	0,54	1,15	1,16	0,83	1,35	0,012	0,023

Depth in the crust (mm)*	Si	Ca	Mn	Fe	Co	Zn	P	Ni	Cu	Al	Ti	Mg	Na	Mn/Fe	Ni/Mn	Al/Mn
13,8	1,39	2,51	27,19	16,00	2,36	0,03	0,02	0,33	0,11	0,48	1,06	1,21	1,43	1,70	0,012	0,018
14,0	1,41	2,55	27,01	13,91	1,27	0,09	0,09	0,47	0,07	0,42	0,78	1,18	1,03	1,94	0,017	0,015
14,2	1,24	2,54	27,80	15,85	0,75	0,08	0,02	0,59	0,16	0,69	0,87	1,75	1,81	1,75	0,021	0,025
14,6	1,94	1,88	15,58	32,54	0,39	0,15	0,39	0,19	0,18	0,71	1,58	1,16	0,67	0,48	0,012	0,046
14,8	1,59	2,87	26,87	17,16	1,14	0,09	0,19	0,35	0,13	0,51	0,99	1,26	1,48	1,57	0,013	0,019
15,0	1,51	2,32	22,93	20,53	0,82	0,10	0,20	0,26	0,10	0,60	1,19	0,99	1,09	1,12	0,011	0,026
15,2	1,51	2,77	25,07	21,41	0,59	0,17	0,25	0,28	0,11	0,61	1,32	1,40	1,50	1,17	0,011	0,025
15,4	1,01	2,71	28,33	16,79	2,06	0,12	0,06	0,35	0,06	0,48	1,21	1,28	1,94	1,69	0,012	0,017
15,6	1,03	2,93	30,43	16,19	1,88	0,08	0,05	0,38	0,05	0,47	1,27	1,33	1,67	1,88	0,013	0,015
15,8	0,70	2,74	30,59	13,71	1,89	0,07	-	0,48	0,08	0,33	0,89	1,40	1,87	2,23	0,016	0,011
16,0	1,14	3,00	30,84	15,36	1,80	0,10	0,07	0,40	0,09	0,40	1,00	1,34	1,73	2,01	0,013	0,013
16,2	1,43	2,71	24,27	20,96	1,51	0,14	0,19	0,22	0,06	0,63	1,46	1,35	1,37	1,16	0,009	0,026
16,4	1,93	2,34	20,33	27,52	0,52	-	0,33	0,26	0,15	0,76	1,31	1,23	1,03	0,74	0,013	0,037
16,6	1,97	1,87	16,97	16,52	0,94	0,03	0,06	0,23	0,11	1,22	0,74	0,38	0,18	1,03	0,014	0,072
16,8	2,05	2,19	21,45	17,36	0,41	0,05	0,19	0,25	0,12	0,93	0,67	0,98	0,85	1,24	0,012	0,043
17,0	3,09	2,24	20,08	23,94	0,56	0,11	0,30	0,23	0,17	1,61	0,94	1,39	0,89	0,84	0,011	0,080
17,2	3,92	1,82	18,10	16,16	0,63	0,08	0,18	0,30	0,07	1,65	0,64	0,94	0,70	1,12	0,017	0,091
17,6	1,29	1,49	17,66	28,49	0,83	0,05	0,23	0,20	0,23	0,53	1,42	1,25	0,68	0,62	0,011	0,030
17,8	1,25	1,91	17,93	22,80	0,90	0,13	0,18	0,23	0,08	0,44	1,29	1,03	0,93	0,79	0,013	0,024
18,2	1,05	2,97	29,96	16,58	0,66	0,02	-	0,60	0,10	0,47	0,84	1,46	1,53	1,81	0,020	0,016
18,4	1,43	1,53	15,43	29,66	0,48	0,04	0,32	0,31	0,34	0,54	1,22	1,49	0,82	0,52	0,020	0,035
18,6	0,97	2,90	30,45	15,67	2,09	0,10	0,03	0,41	0,03	0,45	1,03	1,31	2,07	1,94	0,013	0,015
19,0	0,87	2,54	25,98	13,45	2,10	0,09	0,05	0,41	0,15	0,52	0,86	1,55	2,02	1,93	0,016	0,020
19,2	0,75	2,53	27,39	13,66	1,73	0,02	0,03	0,34	0,10	0,37	0,78	1,22	1,66	2,01	0,013	0,013
19,6	0,48	0,26	3,69	2,30	0,14	0,00	0,01	0,07	0,02	0,22	0,08	0,18	0,07	1,61	0,020	0,059
20,2	1,44	2,90	26,50	18,20	1,38	0,08	0,11	0,30	0,09	0,50	1,21	1,30	1,01	1,46	0,011	0,019
20,4	1,10	2,10	20,45	9,91	0,96	0,03	0,12	0,33	-	0,36	0,66	0,93	0,74	2,06	0,016	0,017
20,6	0,93	2,72	28,97	13,88	2,18	0,09	-	0,44	0,09	0,42	0,92	1,20	0,92	2,09	0,015	0,014
20,8	1,00	3,14	33,06	12,85	1,72	0,06	-	0,49	0,11	0,39	0,83	1,19	1,04	2,57	0,015	0,012
21,0	0,82	2,82	29,54	13,31	2,11	-	-	0,42	0,05	0,41	0,98	1,38	1,49	2,22	0,014	0,014
21,2	0,86	3,44	34,38	13,16	2,02	0,12	-	0,52	0,13	0,38	0,98	1,21	1,38	2,61	0,015	0,011
21,4	1,04	2,89	29,95	12,58	1,75	0,09	0,07	0,52	0,14	0,40	0,88	1,28	1,32	2,38	0,017	0,013

Depth in the crust (mm)*	Si	Ca	Mn	Fe	Co	Zn	P	Ni	Cu	Al	Ti	Mg	Na	Mn/Fe	Ni/Mn	Al/Mn
21,6	0,58	1,67	18,31	6,65	0,84	0,04	0,02	0,37	0,04	0,25	0,43	0,78	0,65	2,75	0,020	0,013
21,8	0,57	1,69	18,20	7,19	1,02	0,04	0,02	0,30	0,02	0,20	0,50	0,93	0,82	2,53	0,017	0,011
22,0	1,27	3,07	28,42	18,24	0,97	0,11	0,11	0,42	0,19	0,53	1,21	1,39	1,25	1,56	0,015	0,019
22,2	1,03	2,97	28,95	17,13	0,88	-	0,09	0,51	0,08	0,50	1,12	1,41	1,27	1,69	0,018	0,017
22,4	1,57	2,77	27,46	19,52	1,41	0,10	0,15	0,28	0,12	0,61	1,35	1,28	1,05	1,41	0,010	0,022
22,8	1,55	2,86	27,19	18,56	0,40	0,10	0,18	0,57	0,05	0,56	0,96	1,35	1,27	1,47	0,021	0,021
23,0	1,56	2,82	24,07	19,20	0,67	0,13	0,15	0,35	0,09	0,62	1,14	1,32	1,11	1,25	0,014	0,026
23,2	1,43	2,65	26,79	16,63	2,01	0,07	0,11	0,35	0,08	0,53	1,40	1,15	0,80	1,61	0,013	0,020
23,4	1,83	2,61	23,31	15,94	1,18	0,11	0,17	0,27	0,12	0,50	1,38	1,19	1,11	1,46	0,012	0,021
23,6	0,85	3,07	33,45	13,55	1,59	0,01	-	0,67	0,15	0,39	1,06	1,24	1,14	2,47	0,020	0,012
23,8	1,08	2,81	30,37	13,25	1,84	0,06	-	0,52	0,15	0,40	1,05	1,32	1,31	2,29	0,017	0,013
24,0	1,95	2,39	23,34	22,95	1,04	0,03	0,24	0,34	0,14	0,63	1,73	1,18	0,97	1,02	0,014	0,027
24,2	1,22	1,16	9,95	32,73	0,72	0,09	0,35	0,10	0,18	0,99	2,04	1,34	0,41	0,30	0,010	0,099
24,4	0,62	3,07	34,13	12,71	1,60	0,03	-	0,67	0,17	0,38	0,92	1,47	1,78	2,69	0,020	0,011
24,6	0,78	3,19	30,43	14,19	1,19	0,04	0,08	0,71	0,13	0,79	0,83	1,78	1,34	2,15	0,023	0,026
24,8	0,33	0,98	39,36	1,60	0,09	0,20	-	4,10	0,62	2,77	0,21	5,22	1,00	24,54	0,104	0,071
25,0	0,40	2,26	34,63	2,54	0,19	0,30	0,26	3,31	0,66	2,87	0,26	5,28	1,02	13,61	0,095	0,083
25,2	1,27	1,87	26,59	12,86	0,28	0,17	0,27	2,38	0,55	2,89	0,98	4,42	0,97	2,07	0,090	0,109
25,6	1,13	6,31	10,25	24,66	0,27	0,11	2,84	0,66	0,17	1,09	1,32	1,70	0,71	0,42	0,064	0,106
26,2	0,41	0,95	33,26	4,37	0,90	0,16	-	3,02	0,37	2,97	0,44	5,50	0,88	7,60	0,091	0,089
26,4	0,45	1,00	36,56	4,48	0,81	0,19	-	3,28	0,33	3,07	0,40	5,53	0,92	8,17	0,090	0,084
26,6	0,23	0,97	34,25	4,05	1,08	0,20	-	2,87	0,37	2,27	0,29	5,29	0,89	8,46	0,084	0,066
27,0	0,39	1,22	20,89	6,26	2,79	0,08	-	0,60	0,08	0,64	0,64	2,26	0,86	3,34	0,029	0,030
27,2	0,46	1,91	37,65	6,48	2,78	0,18	-	1,79	0,21	1,26	0,66	3,90	1,83	5,81	0,048	0,033
27,4	0,69	2,94	32,20	10,24	3,88	0,04	0,01	0,65	0,03	0,53	1,41	1,93	2,40	3,15	0,020	0,016

* Note that when phosphate and carbonate phases measured along the profile were encountered they were removed from the table.

Table S4: Elemental concentrations depth profile in wt% measured by Electron Microprobe Analyser in Tahiti (South Pacific) Fe-Mn crust ZEP2-DR06-03.

Depth in the crust (mm)*	Si	Ca	Mn	Fe	Co	Zn	P	Ni	Cu	Al	Ti	Mg	Na	Mn/Fe	Ni/Mn	Al/Mn
0	1,33	2,70	23,67	17,13	1,96	0,09	0,60	0,21	-	0,91	1,26	1,38	1,70	1,38	0,009	0,038
0,2	1,03	2,83	30,19	15,85	1,97	0,06	0,26	0,42	0,09	0,40	1,28	1,42	1,55	1,90	0,014	0,013
0,4	1,20	2,74	28,90	16,66	2,40	0,06	0,27	0,33	0,06	0,31	1,52	1,43	1,67	1,73	0,011	0,011
0,6	1,32	2,86	26,12	18,93	1,90	0,10	0,31	0,22	0,03	0,43	1,73	1,36	1,39	1,38	0,008	0,016
0,8	1,24	2,42	29,09	15,01	2,50	0,06	0,14	0,49	0,02	0,35	1,24	1,40	1,63	1,94	0,017	0,012
1	1,02	2,74	28,92	15,49	1,98	0,06	0,19	0,36	0,08	0,38	1,26	1,36	1,64	1,87	0,012	0,013
1,2	1,27	2,57	25,77	17,39	2,02	0,13	0,24	0,24	0,00	0,42	1,59	1,31	1,35	1,48	0,009	0,016
1,4	1,12	2,57	29,80	15,02	2,49	0,07	0,13	0,36	0,06	0,42	1,49	1,36	1,82	1,98	0,012	0,014
1,6	0,97	2,49	27,43	14,93	1,85	0,10	0,12	0,40	0,08	0,34	1,32	1,31	0,82	1,84	0,015	0,012
2,2	1,22	2,76	28,64	16,64	1,76	0,10	0,13	0,43	0,00	0,43	1,70	1,38	1,66	1,72	0,015	0,015
2,6	1,05	2,89	30,37	16,38	1,78	0,09	0,15	0,31	0,15	0,40	1,35	1,38	1,72	1,85	0,010	0,013
2,8	1,40	2,90	27,56	18,88	1,14	0,09	0,24	0,40	0,10	0,43	1,74	1,39	1,49	1,46	0,015	0,016
3	1,41	3,02	29,09	18,74	1,24	0,12	0,28	0,47	0,10	0,43	1,78	1,33	1,44	1,55	0,016	0,015
3,2	1,03	2,85	30,88	14,40	2,37	0,11	0,04	0,60	0,06	0,33	1,37	1,40	1,34	2,14	0,019	0,011
3,4	1,06	2,41	26,47	14,85	1,94	0,07	0,16	0,27	0,09	0,37	1,18	1,29	1,41	1,78	0,010	0,014
3,6	1,02	2,85	30,42	15,98	2,12	0,06	0,10	0,38	0,10	0,35	1,31	1,37	1,51	1,90	0,013	0,011
3,8	2,47	1,80	17,91	21,86	1,13	0,12	0,32	0,10	0,09	0,53	1,70	0,70	0,89	0,82	0,006	0,029
4	1,70	2,64	24,71	20,66	1,06	0,12	0,29	0,33	0,04	0,48	1,54	1,17	1,19	1,20	0,013	0,019
4,2	1,26	2,94	27,99	18,54	0,94	0,03	0,24	0,34	0,09	0,38	1,37	1,29	0,99	1,51	0,012	0,014
4,4	1,26	2,53	21,40	16,86	0,70	0,08	0,22	0,21	0,14	0,45	1,52	1,02	0,63	1,27	0,010	0,021
4,6	1,35	2,63	22,99	17,58	0,75	0,04	0,26	0,33	0,11	0,47	1,57	1,02	0,62	1,31	0,014	0,020
4,8	1,76	1,53	11,86	9,82	0,34	0,10	0,11	0,09	0,12	0,81	0,86	0,42	0,16	1,21	0,008	0,068
5	0,90	2,70	26,32	13,36	0,56	0,09	0,16	0,42	0,07	0,30	1,31	1,19	2,78	1,97	0,016	0,012
5,2	1,43	2,33	22,63	16,72	1,69	0,06	0,15	0,17	0,06	0,51	1,69	1,04	0,70	1,35	0,008	0,023
5,6	2,23	1,87	17,33	22,17	1,21	0,04	0,40	0,08	0,03	0,58	2,26	0,92	0,62	0,78	0,005	0,033
5,8	0,96	2,52	31,35	10,23	1,55	0,14	-	0,77	0,15	0,30	0,94	1,22	1,06	3,07	0,024	0,010
6	1,10	2,80	29,37	14,59	1,98	0,10	0,07	0,40	0,04	0,39	1,51	1,34	1,45	2,01	0,014	0,013
6,2	1,27	2,74	32,11	12,43	1,87	0,06	-	0,85	0,13	0,43	1,04	1,56	1,50	2,58	0,026	0,013
6,4	2,04	1,96	20,07	20,11	1,34	0,12	0,28	0,15	0,08	0,56	1,78	1,04	1,06	1,00	0,007	0,028
6,6	2,10	2,04	21,67	20,06	1,37	0,08	0,33	0,18	0,06	0,58	1,75	1,03	1,10	1,08	0,008	0,027

Depth in the crust (mm)*	Si	Ca	Mn	Fe	Co	Zn	P	Ni	Cu	Al	Ti	Mg	Na	Mn/Fe	Ni/Mn	Al/Mn
6,8	1,40	2,74	30,77	12,75	2,86	0,09	-	0,64	0,09	0,45	1,47	1,64	1,97	2,41	0,021	0,015
7	1,52	2,37	26,80	9,91	1,63	0,11	0,10	0,64	0,11	0,34	1,02	1,04	1,00	2,70	0,024	0,013
7,2	1,03	2,98	29,05	15,84	0,95	0,10	0,05	0,47	0,15	0,34	1,34	1,36	1,82	1,83	0,016	0,012
7,4	0,95	2,67	32,00	14,43	1,54	0,03	0,01	0,62	0,10	0,39	1,13	1,34	1,75	2,22	0,019	0,012
7,6	1,96	2,34	18,47	21,41	0,93	0,08	0,28	0,16	0,10	0,68	2,07	1,17	0,99	0,86	0,008	0,037
8	4,01	1,80	10,23	32,41	0,18	0,21	0,58	0,12	0,12	0,82	4,44	0,73	0,34	0,32	0,012	0,080
8,2	1,75	4,96	18,40	19,03	0,29	0,10	1,42	0,25	0,06	0,74	1,49	1,09	0,71	0,97	0,014	0,040
8,6	2,34	2,78	24,51	21,31	0,79	0,19	0,43	0,47	0,07	0,89	1,82	1,31	1,37	1,15	0,019	0,036
8,8	1,87	1,00	7,13	22,34	0,18	0,10	0,40	0,09	0,11	0,65	1,21	0,94	0,66	0,32	0,012	0,091
9	1,70	1,05	7,56	22,26	0,21	0,06	0,47	0,12	0,05	0,69	1,19	1,00	0,50	0,34	0,016	0,091
9,2	1,50	2,40	22,18	17,10	1,00	0,10	0,17	0,37	0,19	0,64	1,23	1,17	0,89	1,30	0,017	0,029
9,8	3,02	2,35	17,22	28,81	0,33	0,12	0,58	0,11	0,20	0,93	1,85	1,09	0,75	0,60	0,006	0,054
10,4	0,73	2,53	28,77	12,35	1,91	0,07	-	0,52	0,13	0,47	1,37	1,42	1,09	2,33	0,018	0,016
11,4	5,65	2,67	21,55	15,28	0,38	-	0,17	0,29	0,17	1,35	1,00	0,57	0,12	1,41	0,013	0,063
11,6	3,66	1,71	5,11	34,48	0,06	0,25	0,50	-	0,09	0,70	7,60	0,76	0,23	0,15	-	0,136
13,8	1,68	2,78	23,74	19,07	0,57	0,09	0,23	0,35	0,06	1,03	1,12	1,34	1,06	1,24	0,015	0,043
14,2	1,55	2,91	23,65	20,00	0,48	0,12	0,16	0,34	0,17	0,75	1,27	0,94	0,48	1,18	0,014	0,032
14,4	1,04	3,33	30,75	17,00	0,65	0,08	0,06	0,50	0,13	0,54	0,87	1,29	0,80	1,81	0,016	0,017
14,8	1,03	3,35	30,78	16,36	0,46	0,06	0,03	0,54	0,14	0,54	0,90	1,40	1,49	1,88	0,018	0,017
15	1,42	3,04	28,42	16,33	1,29	0,07	0,10	0,44	0,15	0,48	1,12	1,19	0,97	1,74	0,015	0,017
15,2	1,44	2,29	21,71	12,71	1,34	0,07	0,19	0,30	0,09	0,42	0,91	0,70	0,73	1,71	0,014	0,019
15,8	0,89	2,47	20,70	8,88	0,79	0,16	0,32	0,56	0,08	0,29	0,66	0,81	0,60	2,33	0,027	0,014
16	0,89	2,04	14,79	6,70	0,51	0,09	0,32	0,38	0,13	0,31	0,51	0,58	0,39	2,21	0,025	0,021
16,2	1,42	2,56	24,75	14,41	1,51	0,12	0,10	0,30	0,14	0,45	1,25	1,06	0,78	1,72	0,012	0,018
16,4	0,95	2,34	22,97	13,42	1,17	0,08	0,12	0,26	0,17	0,44	0,86	0,95	0,20	1,71	0,011	0,019
17	1,13	3,17	28,39	14,71	1,13	0,07	0,07	0,50	0,10	0,43	0,87	1,18	0,72	1,93	0,018	0,015
17,4	1,83	1,13	8,62	27,08	0,58	0,10	0,27	0,04	0,15	0,68	1,94	0,95	0,19	0,32	0,004	0,079
17,6	0,58	1,37	12,55	8,36	0,74	0,04	0,04	0,11	0,05	0,35	0,58	0,63	0,10	1,50	0,008	0,028
17,8	1,12	1,71	17,43	11,59	1,49	0,04	0,10	0,21	0,08	0,42	0,74	0,67	0,28	1,50	0,012	0,024
18	1,02	2,67	25,63	12,31	1,13	0,10	0,08	0,39	0,09	0,39	0,75	0,89	0,51	2,08	0,015	0,015
18,4	1,17	3,26	32,48	15,29	0,65	0,03	0,03	0,68	0,11	0,46	0,78	1,31	0,71	2,12	0,021	0,014
19,2	1,46	2,49	20,88	16,98	0,79	0,08	0,29	0,24	0,04	0,65	0,90	1,14	1,21	1,23	0,012	0,031

Depth in the crust (mm)*	Si	Ca	Mn	Fe	Co	Zn	P	Ni	Cu	Al	Ti	Mg	Na	Mn/Fe	Ni/Mn	Al/Mn
19,8	1,20	3,30	24,38	17,69	0,65	0,06	0,19	0,39	0,11	0,65	0,78	1,21	0,87	1,38	0,016	0,026
20	1,40	3,00	27,24	19,43	0,63	0,07	0,16	0,41	0,05	0,72	0,95	1,41	1,62	1,40	0,015	0,026
20,2	2,34	2,68	17,31	28,52	0,56	0,04	0,40	0,21	0,18	1,03	1,30	0,99	0,53	0,61	0,012	0,060
20,4	1,40	3,28	20,94	20,68	0,48	0,01	0,35	0,35	0,09	0,61	0,82	0,64	0,11	1,01	0,017	0,029
21	1,15	3,33	27,33	17,48	0,58	0,07	0,12	0,46	0,07	0,61	0,75	1,30	0,72	1,56	0,017	0,022
21,4	1,34	2,74	24,48	19,64	1,17	0,00	0,14	0,34	0,09	0,62	1,08	0,95	1,09	1,25	0,014	0,025
21,6	1,18	3,08	28,46	14,67	1,35	0,08	0,22	0,34	0,15	0,39	1,12	1,19	1,81	1,94	0,012	0,014
21,8	1,23	3,19	28,87	14,64	1,40	0,01	0,22	0,33	0,11	0,39	1,14	1,23	1,73	1,97	0,012	0,014
22	1,67	11,07	0,11	34,56	0,04	0,08	0,41	-	0,20	0,75	1,35	1,00	0,17	0,00	-	6,669
22,6	1,95	2,45	22,41	19,80	1,76	0,12	0,30	0,21	0,03	0,70	1,67	0,95	1,01	1,13	0,009	0,031
22,8	1,12	3,19	29,43	15,63	1,13	0,00	0,10	0,43	0,12	0,44	0,82	1,19	1,32	1,88	0,015	0,015
23	1,32	1,21	11,18	22,40	1,02	0,06	0,19	0,07	0,11	0,61	1,52	0,96	0,14	0,50	0,006	0,054
23,4	1,91	2,65	23,79	16,66	1,50	0,05	0,13	0,29	0,04	0,58	1,03	1,20	0,76	1,43	0,012	0,025
23,6	0,99	3,31	30,90	16,14	1,84	0,08	0,07	0,39	0,12	0,55	0,96	1,41	1,26	1,91	0,013	0,018
24,8	2,51	1,22	0,07	42,60	0,03	0,11	0,80	0,01	0,35	1,73	1,51	1,35	0,34	0,00	0,079	25,703
25	1,08	3,12	27,41	16,32	1,63	0,00	0,07	0,33	0,17	0,55	1,11	1,39	1,64	1,68	0,012	0,020
25,2	0,68	3,56	33,43	12,66	0,45	0,06	-	0,79	0,18	0,35	0,60	1,46	1,59	2,64	0,024	0,010
25,6	0,90	3,32	30,66	12,63	1,72	0,03	0,39	0,52	0,19	0,41	0,83	1,33	1,90	2,43	0,017	0,013
25,8	1,05	2,80	31,18	12,93	1,86	0,05	-	0,58	0,07	0,39	0,98	1,43	2,15	2,41	0,018	0,013
26,2	0,75	1,66	15,89	9,41	1,21	0,01	0,11	0,12	0,18	0,30	0,67	0,93	0,96	1,69	0,008	0,019
26,4	1,01	3,15	30,22	15,72	2,09	0,10	0,14	0,35	0,21	0,54	1,12	1,37	2,01	1,92	0,012	0,018
26,6	1,36	3,13	28,69	16,00	1,85	0,09	0,08	0,42	0,14	0,51	1,26	1,30	1,79	1,79	0,015	0,018
26,8	1,52	3,20	29,90	17,46	1,72	0,10	0,09	0,30	0,12	0,56	1,31	1,31	1,59	1,71	0,010	0,019
27	0,82	3,61	30,87	14,01	1,72	0,07	0,15	0,46	0,19	0,38	1,03	1,40	1,58	2,20	0,015	0,012
27,4	0,52	2,54	18,50	7,75	1,38	0,05	0,03	0,21	0,05	0,31	0,61	1,28	0,55	2,39	0,012	0,017

* Note that when phosphate and carbonate phases measured along the profile were encountered they were removed from the table.

Table S5a: Correlation coefficients matrix for Fe-Mn crust J2-480 (Apuupuu).

	Na	Mg	Al	Ca	Ti	Mn	Fe	Ni	Co	Cu	Zn	Sr	Mo	Cd	Te	Ba	La	Ce	Pt	Tl	Pb	Bi	Th	U
Na	1,00																							
Mg	0,97	1,00																						
Al	-0,09	-0,12	1,00																					
Ca	0,36	0,30	-0,22	1,00																				
Ti	0,38	0,34	-0,76	0,52	1,00																			
Mn	0,80	0,83	-0,61	0,33	0,69	1,00																		
Fe	0,73	0,75	0,18	0,63	0,12	0,43	1,00																	
Ni	0,89	0,90	-0,48	0,36	0,57	0,97	0,52	1,00																
Co	0,63	0,67	-0,69	0,14	0,77	0,92	0,23	0,81	1,00															
Cu	0,89	0,94	-0,35	0,16	0,41	0,93	0,54	0,95	0,82	1,00														
Zn	0,74	0,76	-0,68	0,51	0,80	0,95	0,48	0,91	0,88	0,82	1,00													
Sr	0,75	0,76	-0,63	0,64	0,79	0,90	0,60	0,87	0,81	0,77	0,97	1,00												
Mo	0,63	0,69	-0,73	0,07	0,68	0,93	0,19	0,85	0,96	0,86	0,87	0,79	1,00											
Cd	0,75	0,79	-0,62	0,17	0,70	0,95	0,33	0,90	0,96	0,90	0,92	0,85	0,97	1,00										
Te	0,52	0,52	-0,63	0,55	0,87	0,78	0,36	0,66	0,83	0,59	0,83	0,83	0,70	0,75	1,00									
Ba	0,39	0,39	-0,80	0,48	0,95	0,72	0,16	0,60	0,78	0,46	0,84	0,82	0,74	0,75	0,80	1,00								
La	0,33	0,20	-0,15	0,70	0,51	0,21	0,36	0,26	0,09	0,01	0,37	0,46	0,01	0,11	0,30	0,42	1,00							
Ce	0,56	0,54	-0,71	0,66	0,93	0,78	0,42	0,70	0,79	0,56	0,90	0,93	0,71	0,76	0,92	0,90	0,56	1,00						
Pt	0,82	0,79	0,23	0,42	-0,07	0,46	0,81	0,65	0,15	0,64	0,42	0,47	0,21	0,34	0,15	-0,03	0,24	0,20	1,00					
Tl	0,78	0,82	-0,61	0,24	0,67	0,97	0,40	0,93	0,94	0,93	0,94	0,87	0,96	0,99	0,77	0,72	0,10	0,76	0,42	1,00				
Pb	-0,03	-0,02	-0,78	0,28	0,86	0,38	-0,16	0,20	0,59	0,08	0,54	0,52	0,51	0,48	0,65	0,88	0,31	0,73	-0,47	0,41	1,00			
Bi	0,46	0,52	-0,75	0,11	0,81	0,84	0,11	0,68	0,97	0,68	0,81	0,74	0,91	0,88	0,84	0,81	0,08	0,78	-0,05	0,85	0,72	1,00		
Th	-0,43	-0,43	-0,42	0,20	0,49	-0,14	-0,35	-0,28	0,02	-0,42	0,02	0,06	-0,01	-0,07	0,13	0,54	0,26	0,26	-0,66	-0,15	0,76	0,19	1,00	
U	0,50	0,56	-0,81	0,41	0,87	0,85	0,30	0,72	0,91	0,67	0,91	0,90	0,88	0,87	0,87	0,91	0,20	0,90	0,09	0,87	0,75	0,91	0,29	1,00

Table S5b: Correlation coefficients matrix for Fe-Mn crust J2-480-R14 (Apuupuu).

	Na	Mg	Al	Ca	Ti	Mn	Fe	Ni	Co	Cu	Zn	Sr	Mo	Cd	Te	Ba	La	Ce	Pt	Tl	Pb	Bi	Th	U
Na	1,00																							
Mg	0,83	1,00																						
Al	-0,30	-0,44	1,00																					
Ca	0,84	0,89	-0,61	1,00																				
Ti	0,63	0,18	0,28	0,28	1,00																			
Mn	0,86	0,86	-0,38	0,86	0,26	1,00																		
Fe	0,48	0,48	0,16	0,19	0,27	0,33	1,00																	
Ni	0,68	0,82	-0,70	0,88	-0,03	0,87	0,01	1,00																
Co	0,80	0,62	-0,54	0,86	0,52	0,72	-0,08	0,74	1,00															
Cu	0,00	0,42	-0,64	0,43	-0,68	0,36	-0,17	0,66	0,15	1,00														
Zn	0,39	0,07	0,23	0,13	0,68	0,14	0,52	-0,19	0,14	-0,61	1,00													
Sr	0,89	0,86	-0,61	0,94	0,39	0,81	0,38	0,77	0,84	0,30	0,25	1,00												
Mo	0,49	0,70	-0,90	0,82	-0,23	0,67	0,00	0,88	0,64	0,75	-0,19	0,77	1,00											
Cd	0,67	0,53	-0,55	0,75	0,36	0,61	-0,22	0,75	0,86	0,30	-0,07	0,68	0,58	1,00										
Te	0,76	0,44	-0,10	0,62	0,78	0,55	0,10	0,45	0,77	-0,10	0,35	0,64	0,21	0,80	1,00									
Ba	-0,50	-0,08	0,33	-0,31	-0,59	-0,20	-0,20	-0,09	-0,48	0,39	-0,67	-0,47	-0,18	-0,40	-0,49	1,00								
La	0,71	0,29	0,18	0,39	0,98	0,34	0,30	0,07	0,61	-0,63	0,65	0,49	-0,11	0,41	0,76	-0,61	1,00							
Ce	0,72	0,29	0,11	0,42	0,95	0,39	0,21	0,18	0,66	-0,46	0,53	0,52	-0,05	0,60	0,93	-0,59	0,93	1,00						
Pt	-0,22	0,16	-0,31	0,11	-0,71	0,16	-0,29	0,41	-0,10	0,87	-0,82	-0,03	0,40	0,19	-0,17	0,60	-0,71	-0,48	1,00					
Tl	0,78	0,68	-0,66	0,91	0,33	0,79	-0,06	0,87	0,94	0,38	0,10	0,85	0,77	0,89	0,73	-0,44	0,41	0,53	0,10	1,00				
Pb	0,69	0,25	0,20	0,30	0,97	0,31	0,39	0,00	0,52	-0,69	0,72	0,45	-0,17	0,33	0,70	-0,67	0,98	0,90	-0,77	0,33	1,00			
Bi	0,46	0,03	0,49	0,12	0,94	0,15	0,22	-0,16	0,33	-0,71	0,70	0,18	-0,41	0,26	0,72	-0,48	0,88	0,88	-0,66	0,20	0,87	1,00		
Th	0,46	0,05	0,55	0,07	0,94	0,12	0,31	-0,23	0,31	-0,74	0,59	0,18	-0,45	0,16	0,66	-0,35	0,90	0,86	-0,65	0,10	0,89	0,94	1,00	
U	0,71	0,32	0,00	0,45	0,94	0,31	0,31	0,10	0,66	-0,55	0,65	0,59	0,02	0,45	0,76	-0,69	0,97	0,91	-0,70	0,47	0,95	0,79	0,82	1,00

Table S5c: Correlation coefficients matrix for Fe-Mn crust ZEP2-DR05-04 (Tahiti).

	Na	Mg	Al	Ca	Ti	V	Mn	Fe	Ni	Co	Cu	Zn	Sr	Mo	Cd	Te	Ba	La	Ce	Pt	Tl	Pb	Bi	Th	U
Na	1,00																								
Mg	0,66	1,00																							
Al	0,05	0,69	1,00																						
Ca	0,50	0,82	0,77	1,00																					
Ti	0,96	0,74	0,22	0,56	1,00																				
V	0,90	0,64	0,24	0,65	0,86	1,00																			
Mn	0,98	0,73	0,12	0,55	0,96	0,87	1,00																		
Fe	0,63	0,34	0,26	0,52	0,58	0,82	0,57	1,00																	
Ni	0,51	0,97	0,68	0,74	0,63	0,46	0,62	0,11	1,00																
Co	0,92	0,66	-0,02	0,43	0,87	0,80	0,94	0,39	0,59	1,00															
Cu	0,04	0,59	0,92	0,75	0,14	0,28	0,09	0,42	0,54	-0,08	1,00														
Zn	0,49	0,93	0,86	0,90	0,60	0,58	0,57	0,44	0,88	0,43	0,82	1,00													
Sr	0,96	0,58	0,09	0,52	0,93	0,92	0,93	0,78	0,40	0,82	0,12	0,48	1,00												
Mo	0,98	0,63	0,05	0,51	0,92	0,91	0,97	0,68	0,48	0,91	0,09	0,49	0,96	1,00											
Cd	0,75	0,95	0,49	0,72	0,82	0,66	0,83	0,27	0,94	0,81	0,36	0,81	0,64	0,72	1,00										
Te	0,94	0,65	0,16	0,58	0,93	0,94	0,92	0,74	0,48	0,85	0,16	0,55	0,95	0,93	0,72	1,00									
Ba	0,67	0,57	0,48	0,69	0,70	0,80	0,64	0,91	0,37	0,41	0,60	0,67	0,80	0,70	0,48	0,77	1,00								
La	0,61	0,75	0,69	0,93	0,66	0,79	0,63	0,75	0,61	0,49	0,69	0,85	0,69	0,63	0,66	0,72	0,83	1,00							
Ce	0,56	0,47	0,50	0,64	0,61	0,73	0,52	0,91	0,27	0,29	0,61	0,62	0,71	0,59	0,36	0,71	0,97	0,81	1,00						
Pt	-0,20	0,14	0,61	0,42	-0,18	0,14	-0,17	0,42	0,08	-0,26	0,79	0,43	-0,08	-0,08	-0,05	-0,02	0,40	0,46	0,50	1,00					
Tl	0,94	0,72	0,18	0,54	0,95	0,81	0,95	0,60	0,60	0,81	0,19	0,60	0,93	0,93	0,77	0,87	0,74	0,62	0,61	-0,16	1,00				
Pb	0,95	0,77	0,14	0,55	0,96	0,81	0,97	0,44	0,69	0,95	0,05	0,57	0,87	0,92	0,88	0,89	0,55	0,59	0,42	-0,27	0,91	1,00			
Bi	0,95	0,59	-0,11	0,35	0,90	0,76	0,95	0,40	0,50	0,94	-0,18	0,34	0,87	0,91	0,74	0,84	0,45	0,43	0,30	-0,44	0,88	0,96	1,00		
Th	0,13	0,07	0,36	0,41	0,12	0,48	0,09	0,79	-0,12	-0,03	0,55	0,31	0,33	0,22	-0,08	0,37	0,67	0,60	0,77	0,75	0,10	-0,04	-0,14	1,00	
U	0,99	0,63	0,00	0,45	0,96	0,86	0,98	0,58	0,50	0,92	-0,03	0,44	0,96	0,97	0,74	0,92	0,63	0,57	0,51	-0,27	0,94	0,96	0,97	0,09	1,00

Table S5d: Correlation coefficients matrix for Fe-Mn crust ZEP2-DR06-03 (Tahiti).

	Na	Mg	Al	Ca	Ti	V	Mn	Fe	Ni	Co	Cu	Zn	Sr	Mo	Cd	Te	Ba	La	Ce	Pt	Tl	Pb	Bi	Th	U
Na	1,00																								
Mg	0,69	1,00																							
Al	-0,32	0,14	1,00																						
Ca	-0,59	-0,20	0,13	1,00																					
Ti	0,67	0,31	-0,17	-0,80	1,00																				
V	0,69	0,55	-0,38	-0,43	0,73	1,00																			
Mn	0,96	0,62	-0,31	-0,76	0,76	0,65	1,00																		
Fe	0,57	0,46	0,10	-0,74	0,93	0,71	0,66	1,00																	
Ni	0,92	0,57	-0,20	-0,79	0,74	0,56	0,97	0,66	1,00																
Co	0,93	0,59	-0,59	-0,60	0,64	0,74	0,92	0,50	0,85	1,00															
Cu	-0,44	0,17	0,82	0,54	-0,44	-0,41	-0,49	-0,16	-0,45	-0,65	1,00														
Zn	0,58	0,38	-0,02	-0,71	0,95	0,75	0,65	0,98	0,66	0,53	-0,27	1,00													
Sr	0,71	0,59	-0,23	0,01	0,43	0,58	0,57	0,33	0,47	0,59	-0,06	0,38	1,00												
Mo	0,95	0,61	-0,51	-0,66	0,73	0,78	0,95	0,61	0,90	0,99	-0,60	0,64	0,61	1,00											
Cd	0,82	0,88	-0,17	-0,52	0,55	0,64	0,84	0,59	0,79	0,82	-0,21	0,54	0,51	0,84	1,00										
Te	0,84	0,66	-0,04	-0,59	0,38	0,36	0,83	0,35	0,85	0,73	-0,27	0,30	0,36	0,74	0,75	1,00									
Ba	0,69	0,48	0,07	-0,77	0,92	0,59	0,79	0,91	0,77	0,58	-0,18	0,87	0,48	0,67	0,63	0,51	1,00								
La	0,84	0,70	-0,34	-0,26	0,52	0,70	0,75	0,41	0,63	0,81	-0,35	0,43	0,84	0,80	0,72	0,61	0,54	1,00							
Ce	0,55	0,53	0,47	-0,56	0,37	0,04	0,61	0,43	0,66	0,31	0,17	0,31	0,21	0,37	0,51	0,76	0,64	0,32	1,00						
Pt	-0,47	0,27	0,65	0,52	-0,43	-0,21	-0,49	-0,15	-0,51	-0,52	0,81	-0,24	-0,17	-0,51	-0,07	-0,30	-0,27	-0,22	-0,03	1,00					
Tl	0,87	0,55	-0,10	-0,85	0,81	0,55	0,95	0,75	0,98	0,79	-0,38	0,73	0,42	0,85	0,77	0,80	0,86	0,57	0,71	-0,47	1,00				
Pb	0,90	0,53	-0,46	-0,72	0,86	0,81	0,93	0,72	0,86	0,93	-0,62	0,76	0,61	0,96	0,77	0,64	0,79	0,81	0,35	-0,54	0,84	1,00			
Bi	0,95	0,59	-0,48	-0,70	0,75	0,74	0,97	0,61	0,91	0,98	-0,61	0,63	0,60	0,99	0,83	0,76	0,71	0,81	0,42	-0,54	0,87	0,97	1,00		
Th	-0,51	0,06	0,70	0,41	-0,56	-0,47	-0,52	-0,31	-0,52	-0,59	0,74	-0,42	-0,37	-0,60	-0,28	-0,19	-0,35	-0,36	0,16	0,82	-0,48	-0,64	-0,62	1,00	
U	0,89	0,48	-0,40	-0,69	0,89	0,77	0,92	0,74	0,85	0,87	-0,54	0,77	0,69	0,91	0,70	0,58	0,85	0,78	0,40	-0,55	0,85	0,97	0,93	-0,66	1,00